New Theories and Technologies in Recycled Infrastructure Materials

Lead Guest Editor: Bowen Guan
Guest Editors: Chunli Wu, Haibin Li, Xinhua Song, Xiaolong Sun, and Di Wang
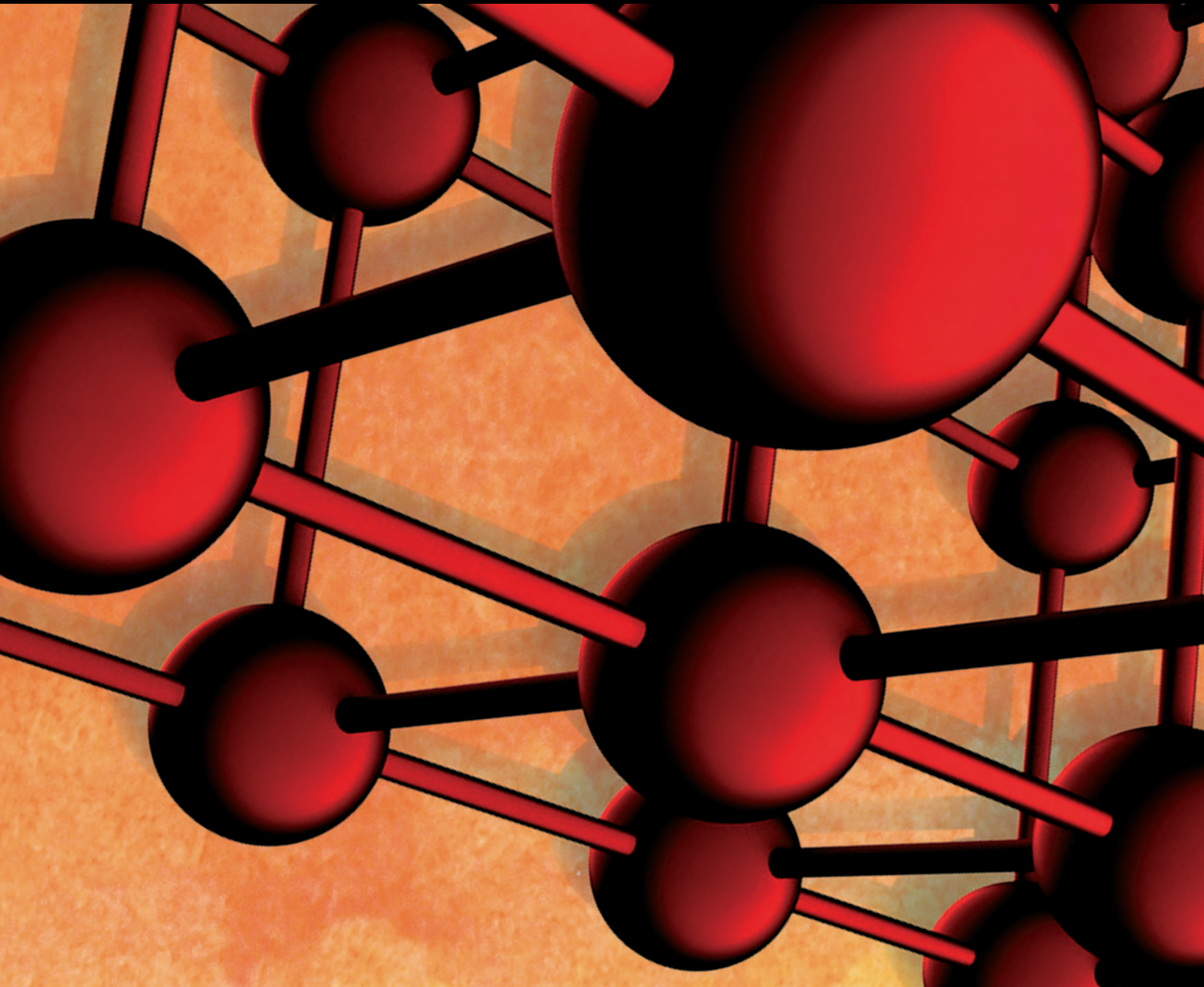
New Theories and Technologies in Recycled Infrastructure Materials

New Theories and Technologies in Recycled Infrastructure Materials

Lead Guest Editor: Bowen Guan
Guest Editors: Chunli Wu, Haibin Li, Xinhua Song, Xiaolong Sun, and Di Wang

Chief Editor

Contents

Research Article

A Practical Swelling Constitutive Model of Anhydrite and Its Application on Tunnel Engineering

Jianxun Wu,[1,2] Fei Lin,[3,4] Xiaohong Zhou,[4] Zhigang Zhang,[4] Jinyang Fan,[2] and Zhenkun Hou [5]

[1]*East China Electric Power Design Institute Co., Ltd. of CPECC, Shanghai 200063, China*
[2]*State Key Laboratory for Coal Mine Disaster Dynamics and Control, Chongqing University, Chongqing 400044, China*
[3]*School of Resources and Safety Engineering, Chongqing University, Chongqing 400030, China*
[4]*China Coal Technology Engineering Group Huaibei Blasting Technology Research Institute Limited Company, Huaibei 235000, China*
[5]*School of Civil and Transportation Engineering, Guangdong University of Technology, Guangzhou 510006, China*

Correspondence should be addressed to Zhenkun Hou; zhenkunhoucqu@163.com

Swelling of anhydrite rock causes serious damage to the tunnel and generates high additional costs in the process of tunnel construction and operation and has gradually become one of the main factors that threaten the safety of the tunnel. It is extremely difficult to predict swelling pressures and deformations accurately based on conventional swelling constitutive models. Thus, a new practical swelling constitutive model of anhydrite for tunnel engineering has been developed. First, swelling tests of natural anhydrite samples focusing on the time effect have been designed and conducted, whose test results show that swelling strain-time can be described by the S-curve model and that swelling stress-strain can be described by the quadratic model. Second, a swelling constitutive model with considering the time effect has been developed to reproduce the swelling behavior of anhydrite observed in swelling tests. This model can track the evolution of swelling activity in tunneling, which has practical significance for process simulation and process control of swelling disaster. Then, this model has been implemented within ANSYS for numerical simulation of the Lirang tunnel. Based on simulation results, useful measures have been proposed. Satisfactory results have been achieved according to the feedback from the site.

1. Introduction

Anhydrite rock is a kind of widely distributed rock; with the high-speed development of the transportation industry, its negative impacts on tunnel engineering are reported increasingly, especially in China [1–3]. Its main composition $CaSO_4$ will transform into $CaSO_4 \cdot 2H_2O$ after meeting water, resulting in an increase of the solid volume by some 61%, and major swelling deformation will occur. During the construction of anhydrite rock tunnel, swelling will cause engineering disasters, such as floor heave, beyond limit or destruction of lining, and collapse of surrounding rock [1, 4].

So the swelling of anhydrite rock is a major threat in tunnel engineering and can cause serious damage to tunnels, which will produce high additional costs.

Research on engineering disaster caused by anhydrite rock in the construction of anhydrite rock tunnel can be triggered in the early 1970's. Luo [5] carried out research on swelling deformation of anhydrite rock samples and accumulated some valuable test data. Rauh et al. [6, 7] conducted some research related to the micromechanism of anhydrite swelling, while Sch¨adlich et al. [8] paid attention to a macroscopic swelling constitutive model. Microscopic swelling models based on mineral transformations in the

anhydrite-gypsum-water system were studied by Anagnostou et al. [9], Ramon Tarragona [10], and Oldecop and Alonso [11]. Alonso et al. [12] and Berdugo [13] also carried out many on-site research works including monitoring and analysis of inverted arch of tunnel. In the abovementioned literature, the swelling process of rock and soil involves the reaction of $CaSO_4$ and water to crystallize and has the characteristics of long swelling duration. Therefore, these long-lasting and chemically reactive expansive rocks can be classified into one category and can be treated differently from other clay-type expansive rocks. Based on the above research results, a great amount of practical experience and experiment research has been gained in the last decades, but tunneling in anhydrite is still a very challenging task. Reliable prediction of swelling pressures and deformations based on conventional swelling constitutive models is extremely difficult for the following reasons:

(a) The anhydrite swelling process can last a very long time. Powder samples instead of natural rock were usually employed to carry out the test for establishing the model [6, 14, 15]. For example, Liu et al. [14] used disk-shaped samples remodeled by anhydrite powder in the swelling test and obtained the relationship between the swelling stress and moisture. Actually, the models based on test results of powder samples cannot accurately reflect swelling behavior, for the structure of the powder sample is different from that of natural rock.

(b) Most constitutive models for swelling rock employ Grob's swelling law [16]. These models were established based on an underlying assumption that the relationship between swelling stress and swelling strain is stable and unchangeable in the whole swelling process. In addition, the swelling stress-strain relationship described by these models usually is under the condition of complete swelling. So, these models are only able to predict a final swelling behavior of surrounding rock but unable to track the evolution of swelling activity in tunneling. Due to the slow evolution of swelling deformations in anhydrite, the dynamic changing of swelling stress-strain before complete swelling cannot be neglected.

(c) Conventional swelling constitution models for swelling rock are usually employed by the logarithmic function to fit test data of swelling stress-strain. In the interval that swelling stress is large, the function fits the data well [17].

As the above reasons, a practical swelling constitutive model of anhydrite, considering the dynamic changing of swelling stress-strain, is the key to solve tunnel engineering problems associated with anhydrite swelling. For reason (a), we employed natural anhydrite rock samples coring from the Lirang tunnel to carry out the experiment study aiming to get closer to on-site swelling performance. For reason (b), we introduced the time effect into the swelling constitutive model; i.e., the relationship between swelling stress and strain changes over time. The time factor was taken into

consideration in the test method with the aim of obtaining swelling stress-strain curves at different points in time. For reason (c), we employed a new function instead of a traditional logarithmic function to fit swelling stress-strain data.

2. Swelling Test

2.1. Sample Preparation. In order to carry out swelling tests, anhydrite rocks belonging to Lower Triassic Jialing River Group were obtained from the Lirang tunnel located in Liangping county, Chongqing, China. As shown in Figure 1(a), the results of X-ray diffraction qualitative analysis show that the compositions of anhydrite samples are $CaSO_4$, $CaSO_4 \cdot 2H_2O$, SiO_2, Fe_2O_3, and $CaCO_3$, respectively. As shown in Table 1, a quantitative analysis was carried out to determine the content of $CaSO_4$, and $CaSO_4 \cdot 2H_2O$ by employing the internal standard method. The $CaSO_4$ content ranges from 88% to 95%, the $CaSO_4 \cdot 2H_2O$ content ranges from 2% to 8%, and the content of other composition (including SiO_2, Fe_2O_3, and $CaCO_3$) ranges from 2% to 5%. As shown in Figure 1(b), these anhydrite rocks were processed into disk-shaped samples with 61 mm in height and 20 mm in diameter according to the recommendations of ISRM [19], whose process was performed air flushed in order to avoid an early activation of the swelling process. What needs illustration is that the expansion time of anhydrite expansive rock is relatively long, and there are relatively few examples for reference in the expansion experiment of this kind of rock. Most of the examples in existing research also refer to the old ISRM suggested methods from 1989. In order to have a better comparative effect with the previous results, the experiment in this paper adopts the ISRM 1989 standard.

2.2. Swelling Test Apparatus. As shown in Figure 2, Single Lever Trigemiry High Pressure Oedometer Apparatus with a maximum capacity of 4000 kPa in the vertical direction was employed to carry out the swelling tests. Besides, TWJ Data Auto Sampling System, which can distinguish a minimum vertical deformation of 0.001 mm, was also employed to assist the swelling test. This system consists of a computer, sensor, servo, and circuit and can be linked with the oedometer apparatuses, which ensures timely recording of data.

2.3. Test Method. Swelling of anhydrite is a complicated process, which is influenced by a lot of factors. In order to establish a practical model, only the time factor is concerned in this paper. A swelling stress-strain relationship is a reflection of swelling potential of rock materials because it changes over contact time with water. It is possible to obtain a complete swelling stress-strain curve at one point in time with the method suggested by ISRM [19]. However, it is not possible to obtain a series of complete swelling stress-strain curves of a separate sample at various points in time during the swelling process, because a separate sample is unable to be reused. Thus, we employed the swelling stress-strain curves of several samples after different contact times with water instead of the swelling stress-strain curves of

(a)

(b)
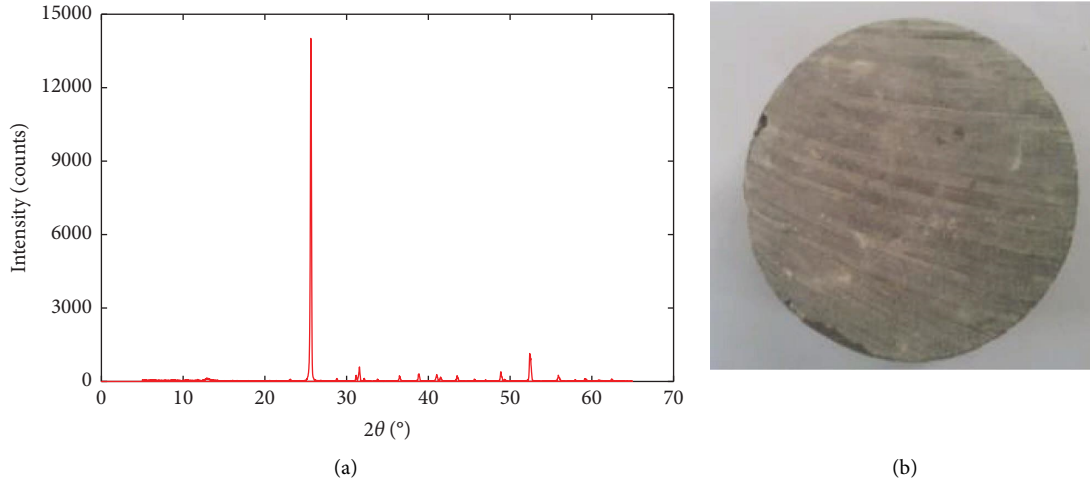
FIGURE 1: (a) One result of X-ray diffraction analysis. All four anhydrite samples for quantitative analysis show similar peaks as above (a). There are differences between X-ray diffraction analysis result of anhydrite in this paper and that reported by [18]. (b) An anhydrite sample after processing which is bluish-grey.

TABLE 1: The mineral composition of the anhydrite rock.

Sample	$CaSO_4$ (%)	$CaSO_4 \cdot 2H_2O$ (%)	Other compositions (%)
1	90	8	2
2	91	4	5
3	88	7	5
4	95	2	3
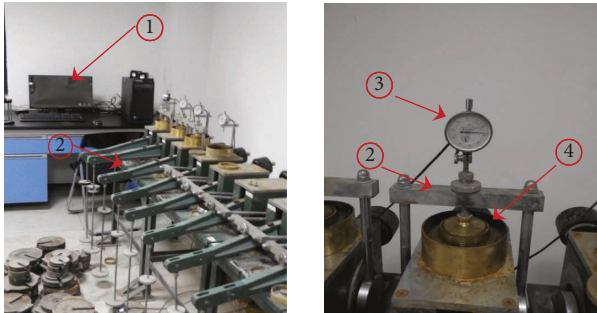
FIGURE 2: The left are the oedometer apparatuses linked with the data auto sampling system. The right is one of the test apparatuses. ① Computer used for indication. ② Loading frame, which can be moved away when measuring the vertical deformation without loading. ③ Dial gauge linking with the computer. ④ Water container, into which a sample is put.

a separate anhydrite sample at various points in time. The specific method is presented as follows:

(a) Free swelling test with lateral confinement (FLC): At this stage, we aimed at establishing the relationship between swelling strain and time. First, a disk-shaped anhydrite sample was embedded into a metal ring, which can be used to confine the lateral of the sample. Then, the sample with the metal was put into the water container of the oedometer apparatus. Both the top and bottom of the sample were placed on a porous plate. Then, water was poured slowly into the water container until the water surface was above the sample by 5 mm. Axial deformation was recorded by the data auto sampling system after reaching design time. Nine disk-shaped anhydrite samples were tested with the above method but different contact times with water. The swelling time of each sample is shown in Table 2.

(b) Axial swelling stress and strain test with lateral confinement (ALC): At this stage, we aimed at obtaining the swelling stress-strain relationship of the above nine samples having experienced different swelling times. After a sample finished design swelling time, the sample is put in a loading frame and loaded stepwise until the measured deformations due to swelling were compensated [19]. The compression deformation under each load was recorded, and its corresponding swelling stress-strain curve was obtained.

2.4. Test Results. Figure 3 shows the relationship between swelling strain and time from FLC. The swelling strain of all samples increases over the time. The swelling strain of No. 9 is still not finished and could continue in a constant rate after a longest swelling time 119 days. The growth rate of swelling strain of anhydrite increases initially in a positive acceleration phase and then declines in a negative acceleration phase until reaching a relatively stable positive value. The swelling process of anhydrite is a complicated physico-chemical reaction. Swelling is able to be controlled by both osmotic effect of water, which is related to the speed of water inflow into the rock, and sulfate hydration, so the growth rate of swelling strain changes [20, 21]. After the rock completely contact water, the dominate reason is the sulfate hydration, whose reaction rate is relatively stable, so the swelling strain can sustain increasing with a relatively stable rate, this is why the latter part of each swelling strain-time curve is approximately an oblique line.

TABLE 2: The swelling time of each sample.

No	1	2	3	4	5	6	7	8	9
Swelling time (days)	7	14	21	35	49	63	77	98	119
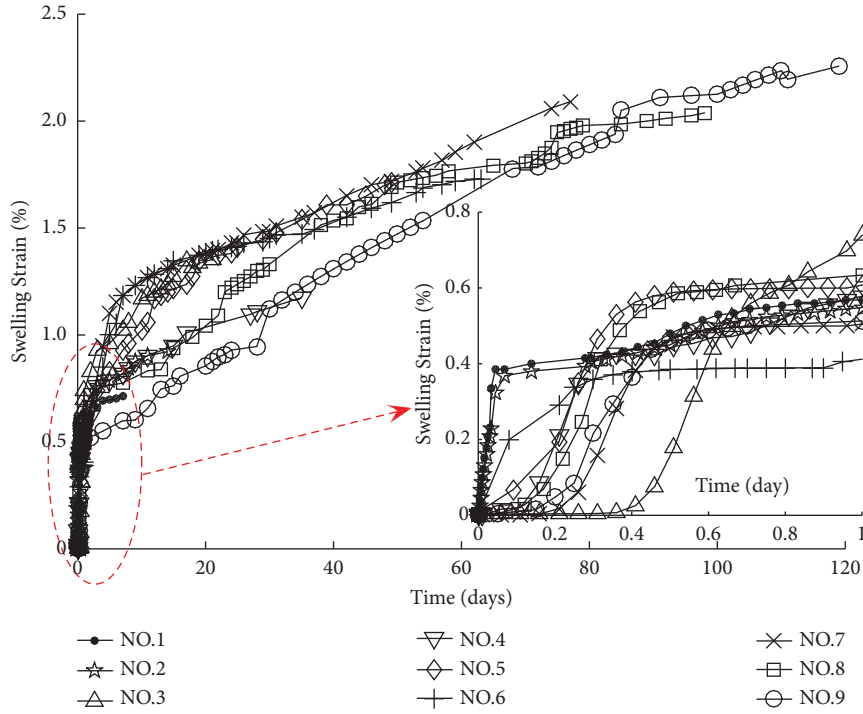
FIGURE 3: The relationship between swelling strain and time from free swelling with lateral confinement. The inner figure is the swelling strain-time on the first day.

Figure 4 shows the relationship between swelling stress and strain from ALC. Swelling stress is defined as the ratio of the force which can inhibit the swelling strain caused by the water seeped into the sample to the sectional area of the sample [22]. As shown in Figure 4, with the increase in swelling stress, the swelling strain decreases and all stress-strain curves behave as concave characteristic. The intersection of each curve with a swelling strain axis, which is the swelling strain of the corresponding sample at the end of FLC, goes up with the increase in sample numbers. It indicates that the longer the swelling time, the larger the swelling strain. By extending the bottom of each curve, the intersection of each curve with a swelling stress axis can be obtained, which also shows an increasing trend with the sample number increase. It indicates that the swelling stress under the condition of completely inhibiting swelling strain goes up with the increasing swelling time.

3. Model Established

3.1. Swelling Strain-Time Model.
As shown in Figure 5, Liu et al. employed the exponential model to describe the swelling strain-time of pure clay rock as follows [23]:

$$\varepsilon_t = \left(\frac{\varepsilon_\infty}{1 + at^{-b}} \right), \tag{1}$$
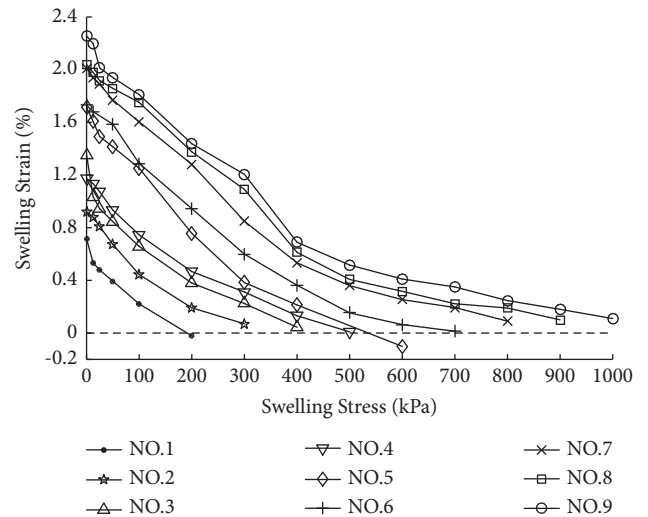
FIGURE 4: The relationship between swelling stress and strain from axial swelling stress and strain with lateral confinement.

where t is the time, ε_t is the swelling strain at time t, ε_∞ is the final swelling strain, and k is the coefficient depending on characteristics of rock.
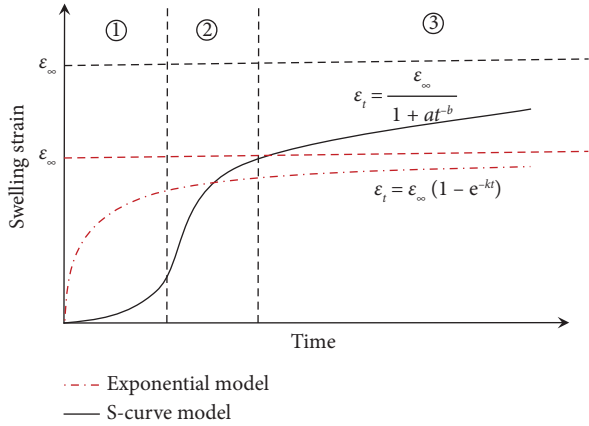
FIGURE 5: Introduction of two kinds of swelling strain-time model. The red line is the exponential model employed in [23]. The black line is the S-curve model employed in this paper. In the representation of the S-curve model, there are three clearly defined phases: ① the growth rate of swelling strain increases over time. This phase can be very short, for example, the data of No. 1 and No. 2 samples in Figure 3. ② Swelling strain increases rapidly, while the growth rate of it decreases over time. ③ The increase of swelling strain is relatively stable and is able to last a long time and will be close to a maximal swelling strain too. ① and ② Unstable phases of the growth rate of swelling strain, which is controlled by the combined effect of both the osmotic effect and hydration effect. ③ A relatively stable increase phase of swelling strain, of which the hydration effect is dominant.

This model is able to describe the swelling stress-time of pure clay rock well but not for anhydrite rock. It cannot describe the changing process of the growth rate of swelling strain, which is controlled by the coupled effect of both the osmotic effect and hydration effect, before the water is in full contact with rock. Although such a changing process lasts a short time in the laboratory test, it can last a long time in the field test [2]; i.e., the changing process will be more obvious with increasing the size of the rock sample. Such a long duration of the changing process has an impact on tunnel construction and design. Second, this model cannot describe well the relatively stable status of the growth rate of swelling strain after water is in full contact with rock, which is very important for predicting the final swelling deformation in tunnel engineering.

Thus, we employed an S-curve model, which has been widely used to show the growth rate of a variable changed over time [24], to describe the swelling strain-time due to the fact that the curve of each sample in Figure 3 is approximately S-shaped. The model is as follows:

$$\varepsilon_t = \left(\frac{\varepsilon_\infty}{1 + at^{-b}} \right), \tag{2}$$

where a and b are coefficients related to characteristics of rock. In this equation, if time tends to infinity, ε_t will tend to a maximal swelling strain ε_∞. It indicates that swelling strain is not able to increase to infinity but has an upper limit. This agrees with the practical situation, and several papers ([6, 25]) point out that the upper limit, i.e., maximal swelling

strain ε_∞, of pure anhydrite is 61%. Actually, 61% is an ideal value and is never obtained in the test. So, in the practical application of this model, ε_∞, just as a coefficient, should be obtained by fitting the test data.

Theoretically, the higher the main component $CaSO_4$ in anhydrite, the more components in the anhydrite can participate in the expansion reaction to produce a greater final expansion strain. In formula (2), the meaning of ε_∞ is the final expansion strain and should have a quantitative relationship with the content of the main component $CaSO_4$. In order to improve the constitutive model, we will conduct further research to clarify this quantitative relationship.

As shown in Figure 6, for a better comparison, we fitted the nine sample data by using the two swelling strain-time models, respectively. It is obvious that the S-curve model is better than the exponential model for anhydrite rock swelling strain-time; especially, it can better describe the continuing increase process of swelling strain. Table 3 is the summary fits of swelling strain-time of nine samples for the two models. In terms of a separate sample, the R-squared of the S-curve model is higher than that of the exponential model, which also indicates the S-curve model is better than the exponential model. It should also be noted that a maximal swelling strain ε_∞ estimated by the S-curve model is more than that by the exponential model.

3.2. Swelling Stress-Strain Model. As shown in Figure 7, based on the laboratory test of clay rocks, Einstein et al. [26–28] formulated a logarithmic model to describe the swelling stress-strain:

$$\varepsilon = K \left[1 - \frac{\lg(\sigma)}{\lg(\sigma_m)} \right], \tag{3}$$

where ε is the swelling strain at a given axial stress σ (i.e., swelling stress based on definition) and K and $\lg(\sigma)$ are coefficients depending on the rock features. As shown in Figure 7, the intersection of the logarithmic curve with the stress axis supplies the coefficient σ_m. For stresses σ larger than σ_m, no more swelling strains occur. For small stresses, the application scope of the swelling law is limited by minimum stress, because unrealistically high swelling strains would result otherwise. Furthermore, very small stresses lead to decomposition processes in the rock, which cannot be described by the swelling law [27].

For this problem, as shown in Figure 4, we employed the left part of a parabola opening upwards, the vertex of which is on the X-axis, to describe the swelling stress-strain due to the curve feature of each sample. As shown in Figure 7, this model is a quadratic function and has intersections with both the X-axis and Y-axis:

$$\varepsilon = p(\sigma - \sigma_m)^2, \tag{4}$$

where ε is the swelling strain, σ is the swelling stress, and p and σ_m are coefficients depending on the feature of rock. In terms of a separate sample, σ_m is the swelling stress under swelling strain inhibited completely, while $p\sigma_m$ is the swelling strain without inhibiting.
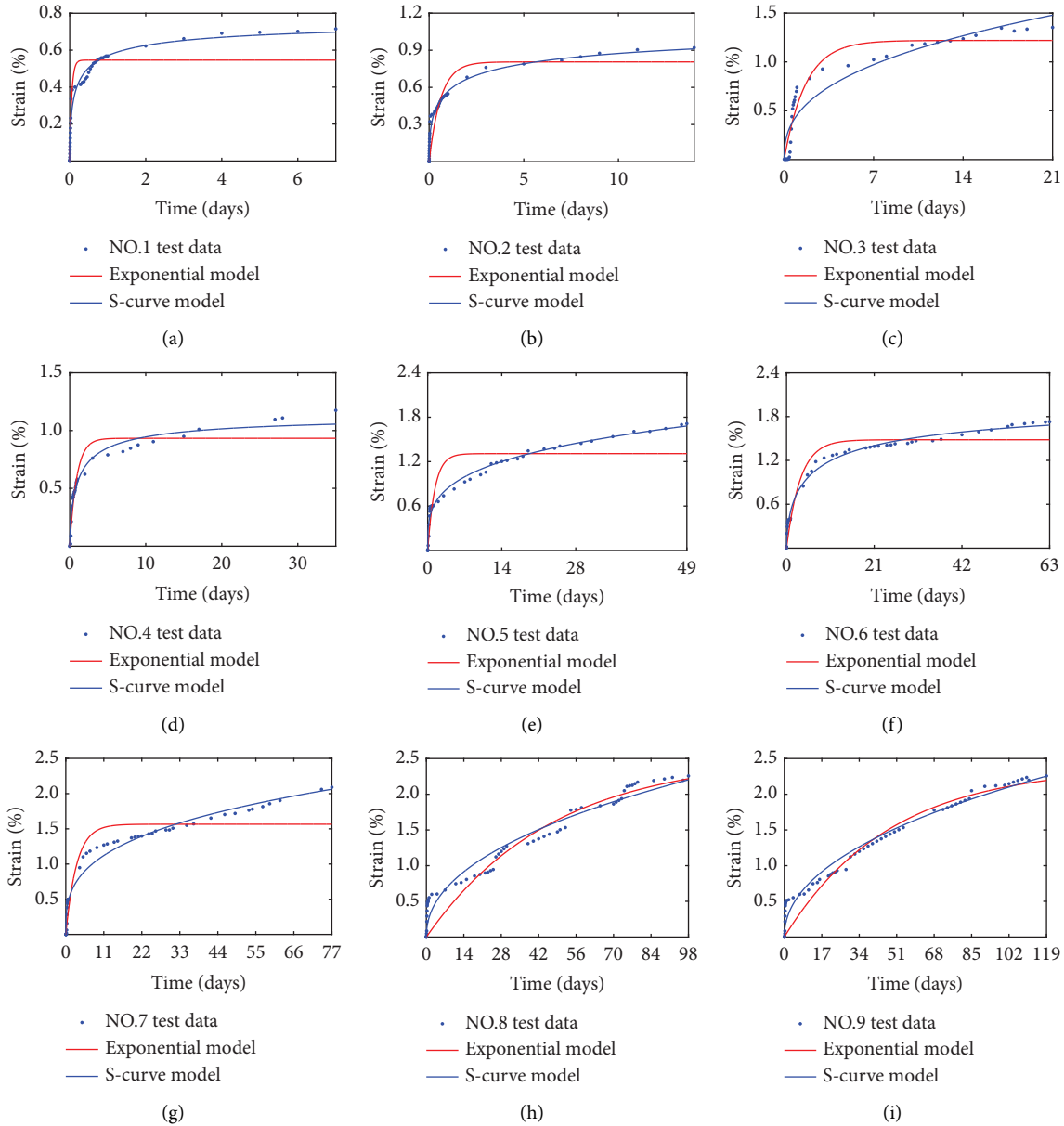
Figure 6: Swelling strain-time fitting results of nine samples of the exponential model and the S-curve model, respectively.

Table 3: Summary fits of swelling strain-time of nine samples for the exponential model and the S-curve model.

No	Exponential model: $\varepsilon_t = \varepsilon_\infty \left(1 - e^{-kt}\right)$			S-curve model: $\varepsilon_t = \varepsilon_\infty / \left(1 + at^{-b}\right)$			
	ε_∞	k	R-square	a	b	ε_∞	R-square
1	0.0055	19.000	0.9082	0.3777	0.5599	0.0079	0.9727
2	0.0081	1.6400	0.8760	1.1290	0.4658	0.0121	0.9839
3	0.0122	0.5943	0.9299	54.370	0.4014	0.2516	0.8806
4	0.0093	1.0900	0.9119	1.0990	0.7054	0.0115	0.9610
5	0.0131	0.7403	0.8310	67.230	0.2789	0.3987	0.9788
6	0.0148	0.3044	0.9412	3.2180	0.5935	0.0215	0.9923
7	0.0157	0.3184	0.9097	138.60	0.3203	0.7320	0.9653
8	0.0253	0.0214	0.9094	196.30	0.4645	0.5360	0.9533
9	0.0239	0.0211	0.9322	194.40	0.4791	0.4666	0.9708

Note. R-square is a number that indicates how well data fit a statistical model and is known as the coefficient of determination. In general, the higher the R-square, the better the model fits data. The above results were obtained using MATLAB Curve Fit Tool.
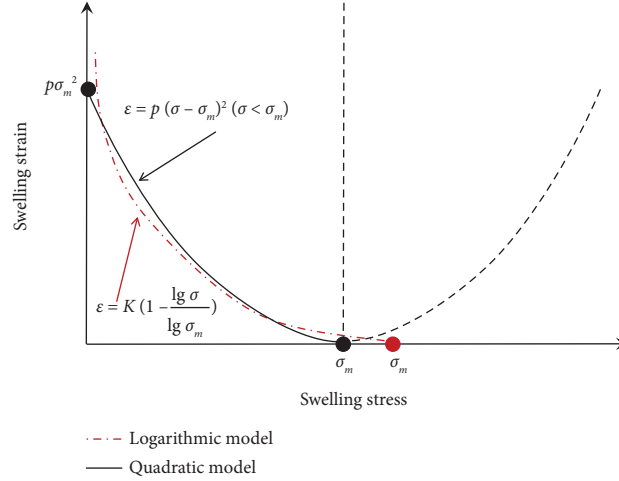
FIGURE 7: Introduction of two kinds of swelling stress-strain model.

As shown in Figure 8, for comparison, we fitted the data of swelling stress-strain by using the two models, respectively. It is obvious that the quadratic model is better than the logarithmic model for anhydrite rock swelling stress-strain, especially in the interval that swelling stress is small. Table 4 is the summary fits of swelling stress-strain of nine samples for the two models. The most R-square of the quadratic model is higher than that of the logarithmic model, which also indicates the quadratic model is better.

3.3. Swelling Constitutive Model with Consideration of Time Effect.

Unlike pure clay swelling rocks, the swelling of anhydrite rock is highly time-dependent [27]. Pure clay rock is able to finish swelling in several days, while anhydrite needs a very long time. In this paper, the swelling of anhydrite rock is still not finished and could continue even though swelling time is up to 119 days. Therefore, the time dependency of anhydrite swelling cannot be neglected. By disregarding the influence of the individual difference of the sample to swelling, the curve of each sample in Figure 4 can be regarded as swelling stress-strain of a separate anhydrite rock at different points in time. So, if making these data corresponds to the time, a swelling constitutive model with consideration of the time effect can be established. This model can describe a dynamic process that the swelling stress-strain curve of an individual anhydrite changes over time.

As illustrated in Section 3.2, data in Figure 4 can be better fitted with a series of parabolas. So, the dependence of swelling stress-strain on time can be established by finding out the movement history of intersections of parabolas with the axis. First, in terms of a separate anhydrite, the intersections of parabolas with the Y-axis, $\rho\sigma_m^2$ (obtained by substituting $\sigma_m = 0$ into equation (4)) represent strain from FLC, so their movement history can be better described by equation (2), that is,

$$
\begin{aligned}
\rho\sigma_m^2 &= \varepsilon_t \\
&= \frac{\varepsilon_\infty}{1 + at^{-b}}.
\end{aligned}
\tag{5}
$$

Second, the intersections of parabolas with the X-axis, σ_m (obtained by substituting $\varepsilon = 0$ into equation (4)) are swelling stresses under the condition of completely inhibiting swelling strain. The relationship between σ_m of parabolas and time is shown in Figure 9. σ_m increases over time, while its increase rate tends to decrease. This is because the longer the expansion time, the smaller the infiltration rate of water in the sample, the denser the sample, and the larger the expansion stress. Previous research [29–31] also indicates that σ_m of swelling rock increases quickly at the early stage and then tends to a constant value. We employed the following equation to describe movement history of σ_m:

$$
\sigma_m = \sigma_{max}\left(1 - e^{-ct}\right),
\tag{6}
$$

where σ_{max} and c are coefficients that depend on the rock feature and σ_{max} is maximal σ_{max} (when time t tends to infinity), i.e., the swelling stress under the condition of inhibiting completely swelling strain when rock completely finishes swelling.

After finding out the movement history of intersections of parabolas with both the X-axis and Y-axis, the swelling constitutive model with consideration of the time effect can be established by substituting equations (5) and (6) into equation (4):

$$
\varepsilon = \frac{\varepsilon_\infty\left[\sigma - \sigma_{max}\left(1 - e^{-et}\right)\right]^2}{\sigma_{max}^2\left(1 + at^{-b}\right)\left(1 - e^{-et}\right)^2}.
\tag{7}
$$

In this model, both time t and swelling stress σ are independent variables, while ε is the dependent variable. This model is a surface in a three-dimensional space and is
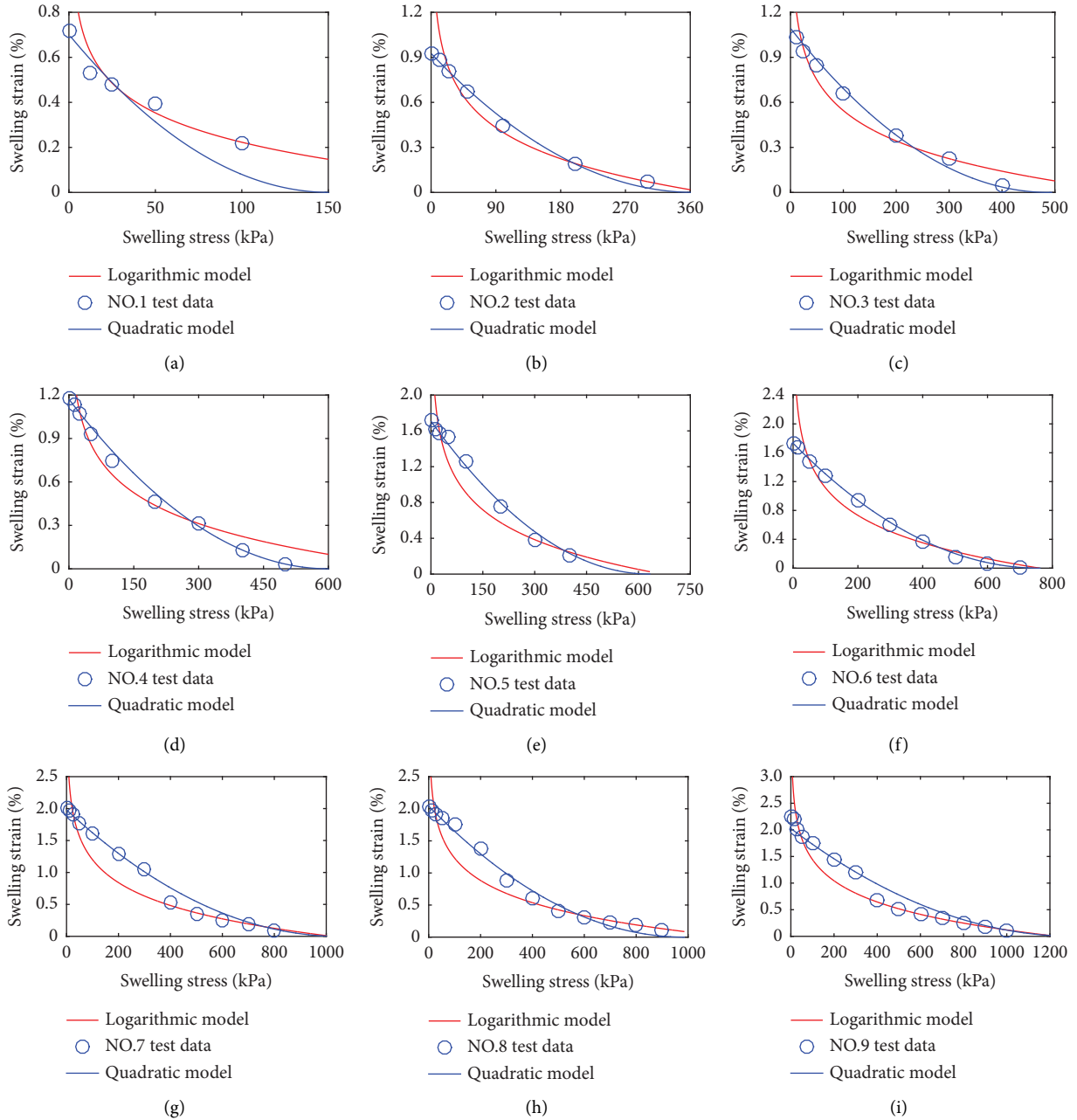
FIGURE 8: Swelling stress-strain fitting results of nine samples of the logarithmic model and the quadratic model, respectively.

established to describe the dynamic process that the swelling stress-strain relationship changes over time with disregarding the influence of the individual difference. As it can be regarded as the swelling stress-strain of an individual anhydrite rock at different points in time, all data in Figure 4 were fitted by this model using MATLAB sftool.

As shown in Figure 10, test data are equably distributed around the fitting surface. It indicates that this model fits the test data well. As shown in Table 5, R-square is close to 1, while both RMSE and SSE are close to 0. All of them also support the view that this model can reflect the dynamic process of swelling stress-strain of anhydrite well. It is very meaningful that the estimated value of ε_∞ of this model,

which is a final swelling strain, is close to its theoretical value of 61% [1, 32] as in pure anhydrite rock. The error between the estimated value and the theoretical value may be caused by the $CaSO_4$ content.

4. Application of the Model

This study is part of a project carried out at the Lirang tunnel in Chongqing, China. The left channel from ZK14 + 582 to ZK14 + 907 and the right channel from K14 + 599 to K14 + 920 in the Lirang tunnel go through about 300 m anhydrite-gypsum stratum. In this section, the swelling constitutive model (7) was implemented within ANSYS to

TABLE 4: Summary fits of swelling stress-strain of nine samples for the logarithmic model and the quadratic model.

No	Logarithmic model: $\varepsilon = K[1 - \lg(\sigma)/\lg(\sigma_m)]$			Quadratic model: $\varepsilon = p(\sigma - \sigma_m)^2$		
	σ_m	K	R-square	p	σ_m	R-square
1	329.60	0.0107	0.8989	$3.077E-7$	151.00	0.8822
2	381.30	0.0177	0.9538	$6.915E-8$	365.00	0.9940
3	650.00	0.0188	0.9327	$4.587E-8$	487.30	0.9841
4	830.00	0.0311	0.9490	$3.243E-8$	600.00	0.9937
5	668.00	0.7403	0.8796	$4.255E-8$	632.90	0.9919
6	759.80	0.0362	0.8692	$3.004E-8$	758.30	0.9988
7	1020.0	0.0357	0.8761	$1.792E-8$	1050.0	0.9840
8	1171.0	0.0352	0.8826	$2.100E-8$	985.30	0.9904
9	1233.0	0.0407	0.9815	$1.169E-8$	1315.0	0.9599
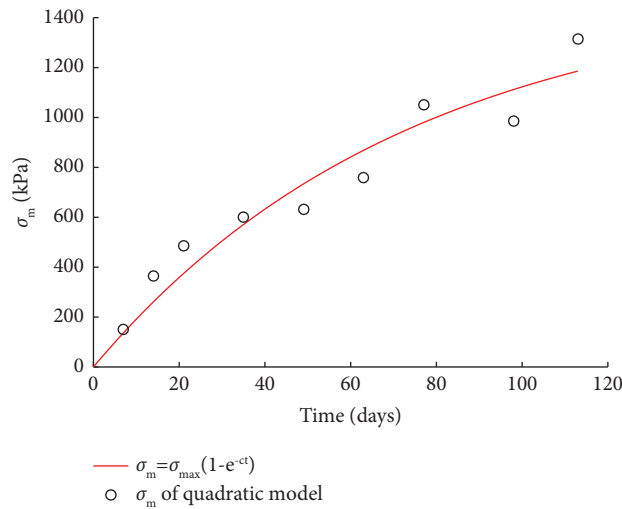
FIGURE 9: The relationship between σ_m of the quadratic model and time.
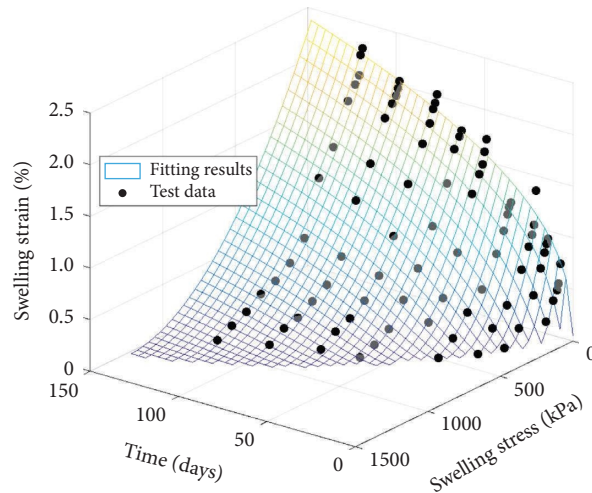
FIGURE 10: Comparisons between test data and prediction of the swelling constitutive model with consideration of the time effect.

simulate the influence of swelling on the tunnel during the construction period, so that some practical measures based on simulation results were proposed to counteract the swelling problem.

A previous simulation for surrounding rock swelling usually used the method of simulating thermal expansion for reference. For example, Miao et al. ever simulated swelling of surrounding rock by corresponding humidity stress field to

TABLE 5: Summary fits of swelling stress-strain changing over time for the swelling constitutive model with consideration of the time effect.

ε_∞ (%)	Parameters				Goodness of fit		
	σ_{max} (kPa)	a	B	c	R-square	RMSE	SSE
52.04	1510	150.30	0.3954	0.0125	0.9750	0.0011	$9.4820E - 5$

Note. Parameter ε_∞ (%) = 52.04% indicates that swelling strain of this type anhydrite is able to reach to 52.04% after complete free swelling. $\sigma_{max} = 1510$ kPa, which indicates that swelling stress under swelling strain inhibited completely of this type anhydrite, is able to reach 1510 kPa. R-square is the coefficient of determination. RMSE (root-mean-square error) is a frequently used measure of the differences between values predicted by a model and the values actually observed. SSE (sum of squares due to error) is used to measure the total deviation of the response values from the fit to the response values. RMSE and SSE values closer to 0 indicate a fit that is more useful for prediction.

temperature field [33]. However, as our model considered the time effect, we used the method of simulating creep for reference to simulate swelling. Our model is essential for describing strain under the effect of stress and time. So with user-defined creep subroutine offered by ANSYS, we can directly simulate swelling.

As shown in Figure 11, based on geologic survey data and design documents of the Lirang tunnel, a 2D finite element model is established using ANSYS. The plane42 element was employed to simulate the surrounding rock, the link1 element was employed to simulate rock bolts, and the beam3 element was employed to simulate first lining. The basic material parameters for both rock stratums and support structure are given in Table 6. As the samples were obtained from the Lirang tunnel, so the parameters listed in Table 5 can be employed for simulating swelling immediately. In this study, we only simulated the process from excavation to the beginning of second lining. Some useful results are presented in Figure 12 and Table 7.

Figures 12(a) and 12(b) show the deformation distribution of surrounding rock on day 36. As shown in Figure 12(a), the arch crowns go down 24.5 cm and the floors are uplifted up to 19.7 cm. It indicates that not only the roof but also the floor of the tunnel are subjected to larger deformation due to the effect of swelling. Figure 12(b) shows that the maximal deformation of surrounding rock is 27.6 cm. Figures 12(c) and 12(d) show the mechanical performance of support structures. As shown in Figure 12(c), the maximal axial force of beam elements on day 36 is 50396 kN coming from arch springing. In the simulation results, the beam elements are mainly subjected to axial force, while both shearing force and bending moment of them are very small. Based on the mechanical performance of beam elements, a maximal compression stress of first lining that is 7.4 MPa is worked out. In Figure 12(d), the maximal axial force of link elements is 197.86 kN, which also comes from the arch springing. Based on the axial force characteristics of link elements, the maximal tensile stress of the rock bolt that is 100.4 MPa was worked out, which is less than the design strength of 130 MPa. Based on the simulation results, we gave some useful and quantitative measures for counteracting the swelling problem:

(a) In consideration that the maximal deformation surrounding the cross section of the tunnel is 27.6 cm, the reserved deformation with 40 cm in thickness was reduced to 30 cm.
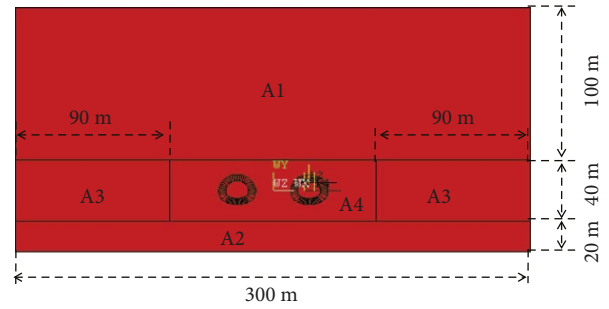
FIGURE 11: 2D finite model. A1 and A2 are limestone stratums, which are unable to swell. A3 and A4 are anhydrite stratums. A4 is subjected to underground water, so it is able to swell, while A3 is far away from the tunnel and free of underground water, so A3 does not need to consider swelling.

(b) The floor of the tunnel got an upheaval of 19.7 cm, and an overbreak of 20 cm in thickness under the inverted arch was set within laying some gravel as a buffer layer.

(c) As maximal tensile stress of the rock bolt is not beyond the strength tensile, the length and ring direction installation intervals of rock bolts still followed initial design. At the same time, considering that arch springing is subjected to a lager force, we suggested increasing the quantity of rock bolts there when necessary.

The above measures have already been applied to the Lirang tunnel, and a satisfactory result was obtained; especially, the revised reserved deformation provides a scientific basis for cost saving. According to the on-site feedback, the updated reserved deformation is reasonable due to no beyond-limit phenomenon, the measures for the inverted arch are also reasonable due to no upheaval phenomenon, and there was no collapse of surrounding rock and damage to the support structure during the construction period, so such a simulation using ANSYS is able to effectively guide tunneling through anhydrite formation.

5. Discussion

The swelling constitutive model developed in this study is in principle capable of reproducing the swelling behavior of anhydrite as observed in swelling tests. As described in the test method, this model was established under the situation that finite rock is subjected to enough water. However, this is

TABLE 6: The basic material parameters for both rock stratums and support structure employed for simulation analysis.

Rock stratum	Elasticity modulus (GPa)	Poisson's ratio	Density (g/cm^3)	Friction angle (°)	Cohesive force (MPa)
Limestone	24.50	0.27	2.70	45.28	9.85
Anhydrite	5.00	0.28	2.70	40.00	0.08
Rock bolt	170.00	0.30	7.80	—	—
Initial liner	31.00	0.17	2.50	54.90	3.18
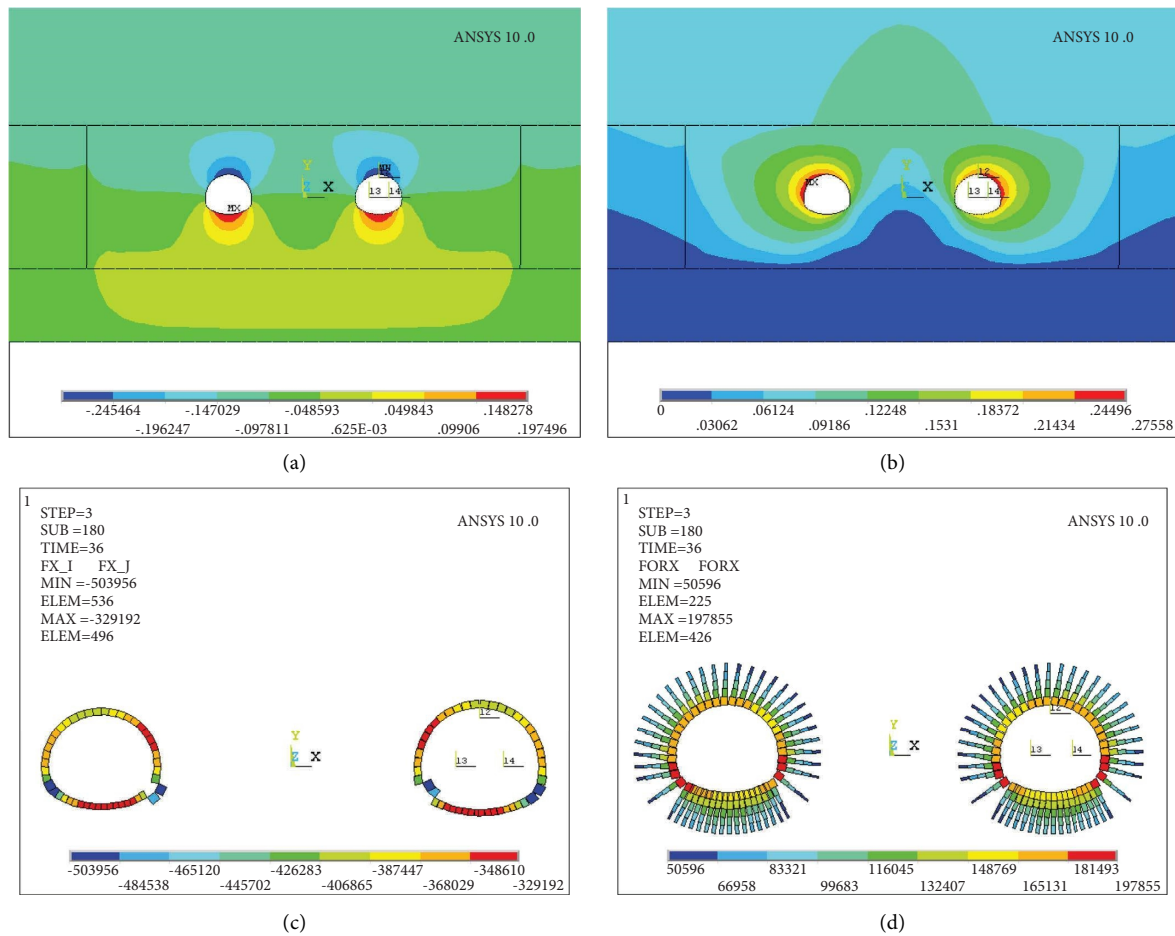
FIGURE 12: The results of numerical simulation. (a) Y direction displacement on day 36 (unit: m). (b) Resultant displacement on day 36 (unit: m). (c) Axial force of first lining on day 36 (unit: m). (d) Axial force of rock bolt on day 36 (unit: m).

TABLE 7: Summary numerical simulation results using ANSYS.

Crown settlement (cm)	Convergence of wall (cm)	Maximal axial force of LE (kN)	Maximal axial force of LE (kN)	Maximal tensile stress of RB (MPa)	Maximal axial force of BE (kN)	Maximal shearing force of BE (N)	Maximal bending moment of BE (N·m)	Maximal compressive stress of FL (MPa)
24.50	54.00	27.60	197.93	100.4	503.96	1.90	0.30	7.40

Note. SR is surrounding rock. LE is the link1 element. RB is the rock bolt. BE is the beam element. FL is the first lining.

different from a realistic situation that the water content of surrounding rock is different at different positions in the tunnel. In other words, our model is unable to consider the water content of rock, so it is unable to reflect the difference in swelling deformation among different positions in the tunnel due to nonuniform distribution of groundwater. For the above problem, we carry out a further discussion for improving the model in this section.

It is worth noting that after the tunnel is excavated, the surrounding rock of the tunnel will produce cracks, and the groundwater will flow into the tunnel floor along the cracks, causing the tunnel floor to expand significantly.

Existing research supports the view that the main mechanics of anhydrite swelling is the growth of the $CaSO_4 \cdot 2H_2O$ crystal, and the volume swelling strain can be expressed as follows [11, 32]:

$$\frac{d\varepsilon_v}{dt} = \frac{\gamma}{\rho_{DH}} \frac{dm_{DH}}{dt}, \tag{8}$$

where ε_v is the volume-swelling strain, γ is the coefficient which reflects the swelling effect caused by crystal growth, m_{DH} is the water consumed by $CaSO_4 \cdot 2H_2O$ crystal growth, and ρ_{DH} is the density of the $CaSO_4 \cdot 2H_2O$ crystal.

Assuming w is the volumetric water content of anhydrite, based on its definition,

$$\omega = \frac{m_\omega}{m_\gamma} \rho_d, \tag{9}$$

where m_ω is the mass of water in anhydrite rock, m_γ is the drying mass of anhydrite rock, and ρ_d is the rock-drying density.

Taking derivative of equation (9) with respect to time t, then the following equation is obtained:

$$\frac{dm_\gamma}{dt} = \frac{d\omega}{dt} \frac{m_\gamma}{\rho_d}. \tag{10}$$

Assuming that mass change of water in rock is only caused by two reasons, one is that water is consumed by $CaSO_4 \cdot 2H_2O$ crystal growth, set as m_{DH}. The other one is that water loss occurs due to evaporation and diffusion, set as m_l, so the following equation can be obtained:

$$\frac{dm_\gamma}{dt} = \frac{dm_{DH}}{dt} + \frac{dm_l}{dt}. \tag{11}$$

Substituting equations (10) to (11), we obtain

$$\frac{dm_{DH}}{dt} = \frac{d\omega}{dt} \frac{m_\gamma}{\rho_d} - \frac{dm_l}{dt}. \tag{12}$$

Then, substituting equations (12) to (8), we obtain

$$\frac{d\varepsilon_\gamma}{dt} = \frac{\gamma}{\rho_{DH}} \left(\frac{d\omega}{dt} \frac{m_\gamma}{\rho_d} - \frac{dm_l}{dt} \right). \tag{13}$$

A new relationship between swelling strain and time can be obtained by taking the integral of both sides of equation (13) with respect to time:

$$\begin{aligned} \varepsilon_v &= \int_0^t \frac{\gamma}{\rho_{DH}} \left(\frac{d\omega}{dt} \frac{m_\gamma}{\rho_d} - \frac{dm_l}{dt} \right) dt \\ &= \frac{\gamma}{\rho_{DH}} \left(W(t) \frac{m_\gamma}{\rho_d} - L(t) \right), \end{aligned} \tag{14}$$

where $W(t)$ is a function employed to describe volumetric water content changing over time during the swelling

process and $L(t)$ is a function employed to describe evaporation and diffusion of water. Equation (14), deduction of which is based on the microcosmic swelling mechanics, considers the mass change of water in rock. However, in this equation, the items $W(t)$ and $L(t)$ are unknown, so we will carry out research on obtaining specific expressions of the two items by using the test method in the follow-up work. After this, a complete expression of ε_v can be obtained. By employing ε_v instead of ε_t in equation (5), a new expression of q is obtained, so that a new swelling constitutive model with consideration of both mass change of water in rock and time is established, and such a model is able to simulate the swelling changing over time at different positions in the tunnel.

Besides, the expansion strain rate of anhydrite is related to the infiltration rate of water in anhydrite for the following reasons: The permeability of anhydrite can not only change the time required for dilatational strain but also affect the stress around gypsum rock, by changing the speed of water immersion in gypsum rock. Thus, the effect of permeability on the expansion stress-strain relationship is a very complex chemical kinetic problem at the mesoscopic level. At this stage, we are committed to solving the tunnel engineering problems related to expansive rock, so from the perspective of phenomenology, we establish a constitutive model whose accuracy meets the requirements of engineering applications. In this constitutive model, the effect of permeability on expansion is attributed and embedded in the change process of the expansion strain with time, which can be embodied by parameters a and b in equation (2).

6. Conclusion

A swelling constitutive model with consideration of the time effect was developed to reproduce the swelling behavior of anhydrite observed in swelling tests. This model is able to describe the dynamic changing of swelling stress-strain of anhydrite in the whole swelling process, so this model can match the construction process of the tunnel with the swelling evolution of surrounding rock, which has practical significance for process simulation and process control of tunnel engineering disaster caused by anhydrite swelling. In addition, by introducing the time effect into the swelling constitutive model, the simulation of swelling can be easily achieved by using the simulation of creep as a reference.

The swelling constitutive model was implemented within ANSYS for the numerical simulation of the Lirang tunnel. This simulation result shows that both the roof and floor of the tunnel are subjected to a larger deformation due to swelling, and arch springing should be paid enough attention. Based on simulation results, some useful measures were proposed and applied to the Lirang tunnel and obtained a satisfactory result according to the feedback information from on-site.

The model developed in this paper is practical enough for solving engineering problems. However, the impossibility of reproducing the swelling deformation difference among different positions in the tunnel reveals that our understanding of swelling influenced by water content is still

incomplete; hence, there is an open field of research in the relationship between water content and swelling of anhydrite.

Data Availability

The data used to support the findings of this study are included within the article.

Disclosure

The manuscript has been submitted as a preprint in the below link [34]: https://www.researchsquare.com/article/rs-1224616/v1.

Conflicts of Interest

The authors declare that they have no conflicts of interest.

Acknowledgments

References

[1] C. Butscher, T. Mutschler, and P. Blum, "Swelling of clay-sulfate rocks: a review of processes and controls," *Rock Mechanics and Rock Engineering*, vol. 49, pp. 1–17.

[2] E. E. Alonso, I. R. Berdugo, and A. Ramon, "Extreme expansive phenomena in anhydritic-gypsiferous claystone: the case of Lilla tunnel," *Géotechnique*, vol. 63, no. 7, pp. 584–612, 2013.

[3] Z. Hou, Y. Liu, Z. Han et al., "Experimental study of the bearing characteristics of a novel energy-saving and environmentally friendly pile: drilling with prestressed concrete pipe cased piles," *International Journal of Geomechanics*, vol. 24, no. 4, pp. 1–16, Article ID 4024035, 2024.

[4] G. Anagnostou, *Untersuchungen zur Statik des Tunnelbaus in quellf?higem Gebirge*, vdf Hochschulverlag AG, Zollikon, Switzerland, 1992.

[5] J. Luo, "Gypsumbearing rock group and its effffect on tunnel engineering," *Journal of Southwest Jiaotong University*, vol. 1, pp. 63–72, 1978.

[6] F. Rauh, G. Spaun, and K. Thuro, "Assessment of the swelling potential of anhydrite in tunnelling projects," in *Proceedings of the Pre-Congress Proceedings 10th IAEG Congress*, Nottingham, UK, September 2006.

[7] F. Rauh and K. Thuro, *Investigations on the Swelling Behavior of Pure anhydrites[C]//1st Canada US Rock Mechanics Symposium*, American Rock Mechanics Association, Alexandria, VA, USA, 2007.

[8] B. Sch¨adlich, T. Marcher, and H. F. Schweiger, "Application of a constitutive model for swelling rock to tunnelling," *Geotechnical Engineering*, vol. 44, pp. 47–54, 2013.

[9] G. Anagnostou, E. Pimentel, and K. Serafeimidis, "Swelling of sulphatic claystones – some fundamental questions and their practical relevance," *Geomechanics and Tunnelling*, vol. 3, no. 5, pp. 567–572, 2010.

[10] A. Ramon Tarragona, *Expansion Mechanisms in Sulphated Rocks and Soils*, Alert Geomaterials, Aix-en-Provence, France, 2014.

[11] L. Oldecop and E. Alonso, "Modelling the degradation and swelling of clayey rocks bearing calcium sulphate," *International Journal of Rock Mechanics and Mining Sciences*, vol. 54, pp. 90–102, 2012.

[12] E. Alonso, A. Gens, I. Berdugo, and E. Romero, "Expansive behaviour of a sulphated clay in a railway tunnel," in *Proceedings Of The International Conference On Soil Mechanics And Geotechnical Engineering*, AA BALKEMA PUBLISHERS, Osaka, Japan, September 2005.

[13] I. R. Berdugo, *Tunnelling in Sulphate-Bearing rocksCexpansive Phenomena*, Department of Geotechnical Engineering and Geosciences, Barcelona, Spain, 2007.

[14] Y. Liu, H. Yu, C. Wang, and C. L. Wang, "Research on mechanism of damage of anhydrock in dolomite layer to tunnel structure," *Rock and Soil Mechanics*, vol. 32, no. 9, Article ID 1000C7598, 2010.

[15] E. Fecker, "Influence of swelling rock on tunnelling," *Bulletin of the International Association of Engineering Geology*, vol. 24, no. 1, pp. 27–32, 1981.

[16] K. Serafeimidis and G. Anagnostou, "On the time-development of sulphate hydration in anhydritic swelling rocks," *Rock Mechanics and Rock Engineering*, vol. 46, no. 3, pp. 619–634, 2013.

[17] F. Zhao, L. Zhang, and M. Zhang, "Experimental study on strength characteristics of expansive rock along kunming-nanning railway," *Subgrade Engineering*, vol. 2, p. 21, 2012.

[18] F. Rauh and K. Thuro, *Why Do Pure Anhydrites Diffffer in Their Swelling Capacity?*, ResearchGate, Berlin, Germany, 2006.

[19] Isrm, "Suggested methods for laboratory testing of argillaceous swelling rocks," *International Journal of Rock Mechanics and Mining Sciences*, vol. 26, pp. 415–426, 1989.

[20] F. T. Madsen and M. Muller-Vonmoos, "The swelling behaviour of clays," *Applied Clay Science*, vol. 4, no. 2, pp. 143–156, 1989.

[21] T. T. Kie, *Swelling Rocks and the Stability of Tunnels*, International Society for Rock Mechanics, Lisbon, Portugal, 1983.

[22] E. Pimentel, "Existing methods for swelling tests-A critical review," *Energy Procedia*, vol. 76, pp. 96–105, 2015.

[23] X. Liu, S. Wang, E. Wang, and Q. Xue, "Study on time-dependent swelling constitutive relation of swelling rock," *Journal of Hydraulic Engineering*, vol. 37, no. 2, pp. 195–199, 2006.

[24] R. H. Becker and L. M. Speltz, "Putting the S-curve concept to work," *Research Management*, vol. 26, no. 5, pp. 31–33, 1983.

[25] M. Wittke, "Design, construction, supervision and long-term behaviour of tunnels in swelling rocks," in *Proceedings of the Eurock*, pp. 211–216, London, UK, June 2006.

[26] H. H. Einstein and N. Bischoffff, "Design of tunnels in swelling rock," in *Proceedings of the The 16th US Symposium*

on Rock Mechanics (USRMS), American Rock Mechanics Association, Minneapolis, MN, USA, September 1975.

[27] P. Wittke-Gattermann, "Dimensioning of tunnels in swelling rock," in *Proceedings of the 10th ISRM Congress*, International Society for Rock Mechanics, Sandton, South Africa, September 2003.

[28] H. Grob, *Schwelldruck am Beispiel des Belchentunnels*, Sitzungsberichte Int. Symposium fr Untertagebau, pp 99–119, Luzern, Switzerland, 1972.

[29] O. J. Pejon and L. V. Zuquette, "Effects of strain on the swelling pressure of mudrocks," *International Journal of Rock Mechanics and Mining Sciences*, vol. 43, no. 5, pp. 817–825, 2006.

[30] K. Kovari, F. T. Madsen, and C. Amstad, "Tunnelling with yielding support in swelling rocks," in *Proceedings of the ISRM International Symposium*, International Society for Rock Mechanics, Tokyo, Japan, September 1981.

[31] Y. Xie, C. Zheng-han, S.-G. Sun, and G. Li, "Test research on three-dimensional swelling pressure of remolded expansive clay," *Rock and Soil Mechanics*, vol. 28, no. 8, pp. 1636–1642, 2007.

[32] A. A. Jeschke, K. Vosbeck, and W. Dreybrodt, "Surface controlled dissolution rates of gypsum in aqueous solutions exhibit nonlinear dissolution kinetics," *Geochimica et Cosmochimica Acta*, vol. 65, no. 1, pp. 27–34, 2001.

[33] X. Miao, "Large deformation analysis of surrounding rock of a tunnel in swelling rock mass based on the humidity stress fifield theory," *Journal of China University of Mining and Technology*, vol. 24, no. 1, pp. 58–63, 1995.

[34] Z. Hou and J. Wu, "A practical swelling constitutive model of anhydrite and its application on tunnel engineering," *Research Square*, 2022.

Research Article

Influence of Mineral Admixtures on the Properties of Magnesium Oxychloride Cement Lean Concrete

Bowen Guan [ID],[1] Wenjin Di,[1] Jiayu Wu [ID],[1,2] Faping Wang,[3] Shuowen Zhang,[1] and Zhenqing He[1]

[1]*School of Materials Science and Engineering, Chang'an University, Xi'an 710061, China*
[2]*School of Civil and Transportation Engineering, Ningbo University of Technology, Ningbo 315016, Zhejiang, China*
[3]*Qinghai Transportation Holding Group Co. Ltd., Xining 810000, China*

Correspondence should be addressed to Jiayu Wu; jy.wu@nbut.edu.cn

This study investigated the effects of light-burned magnesia, fly ash (FA), dolomite powder (DP), and limestone powder (LP) contents on the performance of magnesium oxychloride cement lean concrete (MOCLC). The effects of light-burned magnesia and mineral admixture content on the mechanical properties and durability of MOCLC were tested by the compressive strength test, splitting strength test, water resistance test, shrinkage test, and fatigue test, respectively. The results revealed that the optimum dosage of MgO was 4%. The optimum dosages of FA, DP, and LP were 25%, 20%, and 20% of the cement dosage, respectively. The compressive and splitting strengths of the MOCLC were decreased by the addition of FA and DP. Due to part of the internal pores of MOCLC were filled with FA and DP, the decomposition of the main strength phase $5Mg(OH)_2 \cdot MgCl_2 \cdot 8H_2O$ (phase 5) was suppressed and the water resistance of MOCLC was improved. The addition of FA and DP also improved the shrinkage resistance, and the fatigue resistance of MOCLC was also improved by the addition of FA and DP. The water resistance, shrinkage, and fatigue properties of MOCLC with a FA content of 25% were better than those of MOCLC with DP and LP.

1. Introduction

Lean concrete (LC) has attracted significant attention owing to its low cement content, high strength, and excellent frost resistance [1, 2]. However, previous studies have shown that LC composed of ordinary silicate cement suffers from low early strength and slow strength development [3–5]. The primary reason for this is that ordinary Portland cement has a sluggish hydration rate and a high hydration heat release rate, which results in significant hydration heat release.

Compared with ordinary Portland cement, magnesium oxychloride cement (MOC) has a good availability, simple

preparation [6, 7], low energy consumption, high early strength, and excellent adhesion with a variety of materials [8–10]. MOC is a gas rigid gelled material that was invented by the French chemist Sorel in 1867, and it was made of $MgCl_2$ solution and active magnesium oxide powder [11]. The mixture of active magnesium oxide powder and magnesium chloride solution will produce an exothermic chemical reaction, and MOC with excellent mechanical properties will be rapidly formed [12, 13]. The MOC system is a typical ternary system produced from the reaction of magnesium oxide, magnesium chloride, and water [14, 15]. The chemical expression of the ternary system is MgO-

$MgCl_2$-H_2O. The mechanical properties of MOC depend upon its hydration products [16, 17]. Generally, at ambient condition phases, the main hydration products of MgO-$MgCl_2$-H_2O are $5Mg(OH)_2 \cdot MgCl_2 \cdot 8H_2O$ (phase 5) and $3Mg(OH)_2 \cdot MgCl_2 \cdot 8H_2O$ (phase 3) [18]. The formation of phases 5 and 3 of MOC is summarized in the following equation:

$$5MgO + MgCl_2 \cdot 6H_2O + 7H_2O \longrightarrow 5Mg(OH)_2 \cdot MgCl_2 \cdot 8H_2O,$$
$$3MgO + MgCl_2 \cdot 6H_2O + 5H_2O \longrightarrow 3Mg(OH)_2 \cdot MgCl_2 \cdot 8H_2O,$$

(1)
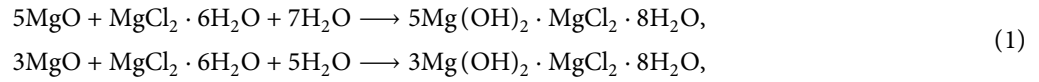
Phases 5 and 3 of MOC occur as well-crystallized needles that developed quickly and have a high material strength. In further detail, phase 5 is almost completed after 96 h and phase 3 is almost completed after 36 h. The crystallized needles can be described as scroll-tubular whiskers. Whiskers intergrow into structures with higher density, which is the key reason for MOC strength growth. Although the thermal stability of phases 5 and 3 is low, and they start to decompose at 145°C and 125°C, respectively, to form H_2O and HCl, they can exist stably at ambient temperature [19, 20]. Therefore, phases 5 and 3 are also called the main strength phases of the MOC system. Reportedly, the mechanical properties and durability of concrete can be effectively improved by adding MOC to concrete materials [21, 22]. As a cementitious material for the preparation of concrete, MOC has a particularly prominent advantage of strength. Zheng et al. investigated the mechanical characteristics of magnesium oxychloride cement concrete (MOCC) using the changing law of the microstructure. The addition of MOC increases the pavement strength of the structure, which was based on X-ray diffraction (XRD) and scanning electron microscopy (SEM) results, as well as the compressive and flexural strengths of MOCC at various ages [23]. Cheng et al. investigated the long-term mechanical properties of MOCC, measured the change in the phase 5 content in MOCC by XRD and SEM, and tested the compressive strength of MOCC at 28, 180, and 270 days. It has been found that the long-term strength of MOCC is significantly higher than that of the ordinary concrete of the same grade [24]. Notably, the early strength properties of MOCC are also excellent. According to Hao and Li, the early strength is higher because MOCC has a greater interfacial adhesion than ordinary concrete [25]. In addition to its mechanical properties, MOCC also exhibits excellent durability. Generally, concrete construction in saline environments can be harmed by salt. However, Gong et al. found that high Mg^{2+} and Cl^- concentrations would enhance the development of phase 5, ensuring the structural integrity and endurance of the MOCC [26]. Although the addition of MOC to concrete buildings can significantly increase their mechanical and durability features, water resistance issues still exist [27, 28]. Phases 5 and 3 are easy to decompose in the water environment, and the strength of MOC decreases gradually [23]. The specific decomposition formula is shown in equations (2) and (3).

$$5Mg(OH)_2 \cdot MgCl_2 \cdot 8H_2O \longrightarrow 5Mg(OH)_2 + Mg^{2+} + 2Cl^- + 8H_2O,$$

(2)

$$3Mg(OH)_2 \cdot MgCl_2 \cdot 8H_2O \longrightarrow 3Mg(OH)_2 + Mg^{2+} + 2Cl^- + 8H_2O.$$

(3)
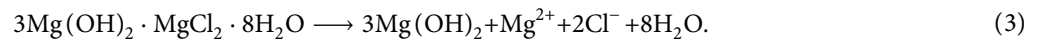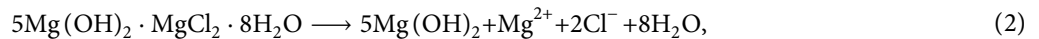
Mineral admixtures have been used to increase the water resistance of MOCC. Qiao et al. studied the effects of phosphoric acid and fly ash (FA) on the water resistance of MOCC by analyzing the water resistance coefficient of MOCC after soaking for 90 days. Combined with different soaking conditions, the study found that water resistance can be effectively improved by phosphoric acid and FA [29]. Furthermore, Deng et al. reported that the coordination of phosphate and magnesium ions increased the water resistance of MOCC [30]. Moreover, the pores and cracks in concrete can also be filled with fibers, which increase the water resistance coefficient, thus improving its water resistance [31].

In summary, existing research studies primarily focus on enhancing the strength and durability of concrete using MOC. Mineral admixtures, such as FA and phosphoric acid, have been used to enhance the mechanical strength and durability of concrete. However, there has currently been little research reporting the application of MOC in lean concrete. In addition, the effects of FA, DP, and LP on the water resistance and durability of MOCLC have not been studied. As lean concrete is mainly used for road bases, its material composition and strength evaluation index are different from ordinary concrete. As a result, the existing conclusions of adding MOC to concrete cannot be directly applied to MOCLC. Based on the above considerations, this paper uses MOC to prepare lean concrete instead of ordinary Portland cement. The effects of different magnesium cement contents and mineral admixtures on the mechanical properties and durability of LC were studied through compression, splitting, immersion, shrinkage and fatigue tests, and microscopic analysis. The addition of MOC can not only improve the early strength of lean concrete but also reduce the cement consumption. The addition of mineral admixtures has little effect on the mechanical properties of MOCLC, but it can effectively improve the water resistance

TABLE 1: Chemical composition of lightly burned magnesium oxide powder.

Oxide	MgO	SiO$_2$	Al$_2$O$_3$	CaO	K$_2$O	Na$_2$O	Fe$_2$O$_3$	P$_2$O$_5$	TiO$_2$
Mass fraction (%)	80.21	6.87	2.01	1.58	0.22	0.15	1.32	0.21	0.02

TABLE 2: Basic properties of lightly burned magnesium oxide powder.

Size		Setting time		Fineness	Stability
Grain size (μm)	Specific surface area (m^2/g)	Initial setting (min)	Final setting (h)	170 mesh screen allowance (%)	
70	30.2	>40	<7	<25	Qualification

TABLE 3: Chemical compositions of magnesium chloride hexahydrate.

Material	MgCl$_2$·6H$_2$O	NaCl	KCl	CaCl$_2$
Mass fraction (%)	96.4	0.3	0.7	0.2

and durability of MOCLC. It can be seen that the application of MOC in lean concrete is expected to achieve an energy-saving green base.

2. Materials and Test Methods

2.1. Raw Materials.
The raw materials used for preparing the magnesium oxychloride cement lean concrete (MOCLC) included light-burned magnesia, magnesium chloride hexahydrate, mineral admixtures, and coarse and fine aggregates. The magnesia employed in this study was 80.3% pure with 57% activity. It was obtained from Yingkou Huiteng refractory material Ltd. (Liaoning Province, China). The chemical compositions and basic properties are shown in Tables 1 and 2. Magnesium chloride hexahydrate (MgCl$_2$·6H$_2$O) was obtained from Yuze Chemical Ltd. (Shandong Province, China). Its chemical composition is shown in Table 3, in which the content of magnesium chloride is 45% and the water content is 50%. Continuously graded limestone rubbles meeting the requirements of Chinese standard GB/T 14685-2011 [32] were applied as coarse aggregate and their size range was from 5 mm to 25 mm. The water absorption and specific gravity of gravel were 0.68% and 2.72, respectively. The crushing value of gravel is 6.8%. Moreover, the water absorption and specific gravity of sand were found to be 1.24% and 2.63, respectively. The sand was the river sand with a fineness modulus of 2.6 while FA, dolomite powder (DP), and limestone powder (LP) were incorporated in the proportions of 10%, 15%, 20%, 25%, and 30%, respectively, by mass of MOC. FA, DP, and LP were obtained from, respectively, Xi'an power plant, Jiangxi Sanbao Industry and Trade Co., Ltd., and Beijing Hongwei Yongjia building materials Co., Ltd. FA with silica and alumina of 87% (Class *F*). The chemical compositions of the FA, DP, and LP are shown in Table 4. In accordance with the Chinese standard JGJ 63–2006 [33], ordinary tap water was used for the tests.

The content of magnesium oxide was divided into 3%, 3.5%, 4%, 4.5%, and 5%, numbered MOCLC$_1$, MOCLC$_2$, MOCLC$_3$, MOCLC$_4$, and MOCLC$_5$ respectively, to study the

effect of lightly burned magnesia content on the performance of MOCLC. The mixing proportions of MOCLC are shown in Table 5. MOCLCs with different mineral admixtures are denoted as MOCLC-FA, MOCLC-DP, and MOCLC-LP.

2.2. Specimen Preparation.
The specimen preparation included seven steps. (1) Preweighed water and magnesium chloride hexahydrate were poured into the glass in turn, and the magnesium chloride solution was prepared by stirring thoroughly for 2 mins using a glass rod. The MOC was prepared by pouring preweighed lightly burnt magnesium powder into magnesium chloride solution and stirring it thoroughly with a glass rod for 5 mins. (2) Then, the preweighed mineral admixture was poured into MOC and was mixed with a glass rod evenly for 5 mins. (3) Preweighed raw materials (sand and gravel) were poured into the basin and mixed evenly with a spatula for 2 mins. (4) The mixtures from (2) and (3) were mixed with a shovel for 5 mins. (5) The slump of the MOCLC was measured according to the Chinese standard JTG 3420-2020 [34]. (6) The MOCLC was cast in 150 mm × 150 mm × 150 mm and 100 mm × 100 mm × 400 mm steel dies, which were cured for 24 h in an indoor natural environment (the temperature and the relative humidity were 22 ± 5°C and 65 ± 5%, respectively). During the curing process, a film was used to cover the steel dies containing the specimen. (7) MOCLC was removed from the steel dies and then cured for 3 days, 7 days, 14 days, 28 days, and 90 days at a temperature of 20 ± 2°C and a relative humidity above 95%, respectively.

2.3. Test Methods

2.3.1. The Strength of MOCLC.
All considered LC mixtures were produced at the optimum moisture content (OMC). The OMC and maximum dry density (MDD) values of the considered LC mixtures were evaluated based on the Chinese standard JTG E51-2009 [35].

A universal testing machine with an accuracy of ±1% was employed to test the strength of MOCLC. First, hardened samples and cubes with a side length of 150 mm were utilized to test the compressive strength and splitting strength of the MOCLC. Second, 12 groups of MOCLC were prepared according to the division criteria in Section 2.1. Accordingly, an average of three specimens was prepared for

TABLE 4: Chemical compositions of considered FA, DP, and LP.

Oxides	SiO_2	MgO	Al_2O_3	CaO	Fe_2O_3	$CaCO_3$	$MgCO_3$	Na_2O
FA (%)	54.8	0.6	33.1	2.24	4.3	—	—	0.25
DP (%)	0.42	21.05	0.28	0.4	0.16	70.5	3.25	0.08
LP (%)	37.2	1.1	12.5	45.8	1.12	0.03	0.06	0.2

TABLE 5: Mixing proportions of MOCLC.

No	Magnesium oxide content (%)	Magnesium oxide (kg/m^3)	Sand (kg/m^3)	Gravel (kg/m^3)	Magnesium chloride (kg/m^3)	Water (kg/m^3)
$MOCLC_1$	3	68	815	1449	31	34
$MOCLC_2$	3.5	77	810	1441	35	37
$MOCLC_3$	4	89	808	1438	37	37
$MOCLC_4$	4.5	98	805	1435	39	39
$MOCLC_5$	5	110	802	1431	45	41

each age. The strength values of different types of MOCLC at each age were then calculated using three groups of parallel test values. Finally, the compressive strength of the MOCLC was determined at the ages of 1, 3, 7, 14, and 28 days. The splitting strength of the MOCLC was determined at 28 days.

2.3.2. Water Resistance of MOCLC. The water resistance of MOCLC was evaluated by the water resistance coefficient [23, 25]. The water resistance coefficient is defined as the ratio of the immersed compressive (splitting) strength to the dry compressive (splitting) strength of the specimen and is calculated using the following formula:

$$K = \frac{f_{\text{imm}}}{f_{\text{dry}}}, \tag{4}$$

where K denotes the water resistance coefficient of MOCLC. f_{imm} and f_{dry} denote the immersion compressive (splitting) strength and dry compressive (splitting) strength of the MOCLC, respectively, for a given period. Evidently, the larger the water resistance coefficient of the specimens, the better the water resistance. The specimens for dry conditioning were placed in a dry conditioning chamber at a room temperature of $20 \pm 1°C$ for 1 day, 3 days, 7 days, 14 days and 28 days, respectively. The specimens were placed in a water tank with a water temperature of $25 \pm 3°C$ for 1 day, 3 days, 7 days, 14 days, and 28 days, respectively. The specimens soaked to the specified age were removed and placed in an oven at $40°C$ for 24 h to dry [36]. After that, the compression test and splitting test were conducted. In addition, the specimens were tested for water absorption and porosity according to standard ASTM C642-06 [37].

2.3.3. Shrinkage Property of MOCLC. The shrinkage coefficient of the MOCLC was obtained by curing a specimen with a molding size of 100 mm × 100 mm × 400 mm by using a box curing for 7 days at a temperature of $20 \pm 1°C$ and a relative humidity of $60 \pm 5\%$, as specified by Chinese standard JTG E51-2009 [35].

Surface moisture was removed from the test piece, and a vernier caliper was used to measure the datum length

before placing the test piece in the shrinkage instrument. The accuracy of the vernier caliper was 0.01 mm. The shrinkage instrument containing the test piece was then placed in a curing box. After curing to the specified age, the test piece was removed, the dial indicator reading $X_{i,j}$ was recorded, and the mass m_i of the standard test piece was weighed. The shrinkage coefficient was calculated using the ratio of shrinkage strain to water loss rate, which was calculated using the following formula:

$$\begin{aligned} \alpha_{di} &= \frac{\varepsilon_i}{w_i}, \\ \varepsilon_i &= \frac{\delta_i}{l}, \\ \delta_i &= \frac{\left(\sum_{j=1}^{4} X_{i,j} - \sum_{j=1}^{4} X_{i+1,j}\right)}{2}, \\ w_i &= \frac{(m_i - m_{i+1})}{m_p}, \end{aligned} \tag{5}$$

where α_{di} corresponds to the shrinkage coefficient of the MOCLC, ε_i represents the shrinkage strain of the MOCLC sample, the value of the dry shrinkage was tested at the ith time, $X_{i,j}$ is the reading of the jth dial indicator at the ith test of the dry shrinkage, l denotes the length of a standard MOCLC sample, w_i is the water loss rate of the test piece, and m_p indicates the constant value for the standard MOCLC sample after drying.

To explore the effect of mineral admixtures on the shrinkage properties of MOCLC, the shrinkage properties of MOCLC were compared by adding FA, DP, and LP. FA and LP were incorporated in a proportion of 25% by a mass of lightly burned magnesia powder in the same proportion. DP replaced 25% of the lightly burned magnesium oxide powder in excess with a mass ratio of 1 : 3.

2.3.4. Fatigue Property of MOCLC. Fatigue is a significant indicator for evaluating the durability of MOCLC [38]. The hardened samples, cuboids of 100 mm × 100 mm × 400 mm, cured at a temperature of $20 \pm 2°C$ and a relative humidity

above 95% for 90 days respectively, were crushed to test the fatigue property, as outlined in the Chinese standard JTG E51-2009 [35]. In the fatigue test, loading was conducted with a continuous sine wave. The loading frequency was set to 10 Hz. In this study, four stress levels were used. Three samples were tested under each stress level. The fatigue equation was calculated using the following formula:

$$\lg N = a + \frac{\sigma}{S},$$

$$\lg N = a + b \lg \sigma,$$

(6)

where N denotes the load action time, σ indicates the action load, and S represents the flexural tensile strength of the beam specimens. Moreover, a and b are the regression coefficients.

3. Results and Discussion

3.1. Fresh Properties of MOCLC. Figure 1 shows the effect of the incorporation of cement content on the MDD and OMC values of MOCLC.

As shown in Figure 1, the optimum moisture content (OMC) of $MOCLC_1$, $MOCLC_2$, $MOCLC_3$, $MOCLC_4$, and $MOCLC_5$ is 3.0%, 3.3%, 3.5%, 3.8%, and 4.2%, respectively, and the maximum dry density (MDD) was 2308 kg/m³, 2313 kg/m³, 2317 kg/m³, 2324 kg/m³, and 2331 kg/m³, respectively. Besides, the OMC and MDD of the ordinary Portland cement lean concrete (OPCLC) were about 6.5% and 2255 kg/m³ respectively [39, 40]. Compared with the OPCLC, the MDD value of MOCLC was higher and the OMC value of MOCLC was lower. It was observed that as the percentage of cement content increased from 3% to 5%, both the MDD and OMC of the MOCLC increased slightly. This phenomenon may be explained by the fact that adding cement to a mixture increases the lubricity between particles and the compatibility of the mixture. An increased proportion of the cement slurry can also help plug the pores in the mixture and can enhance its MDD. Owing to the strong water absorption of cement, with an increase in cement content, the OMC also increases.

3.2. Mechanical Properties of MOCLC

3.2.1. Compressive Strength. The compressive strength of LC is a physical quantity used to express its compressive bearing capacity of LC per unit area. Figure 2 visually describes the change in the compressive strength of MOCLC with different light-burned magnesia contents and ages.

As shown in Figure 2, the compressive strength of MOCLC increased with the increasing magnesium oxide content and age. This is consistent with Wang Dongxing's conclusion [9]. Wang analyzed the change of specimen strength with MOC content and age by XRD. The peak intensity of phase 5 is observed to increase with the curing time thus revealing that more cementitious products are formed. Besides, the peak intensity of phase 5 enhances with the increase of MOC content, leading to the formation of more phase 5, which can fill in the interparticle pores and cement fine particles together."
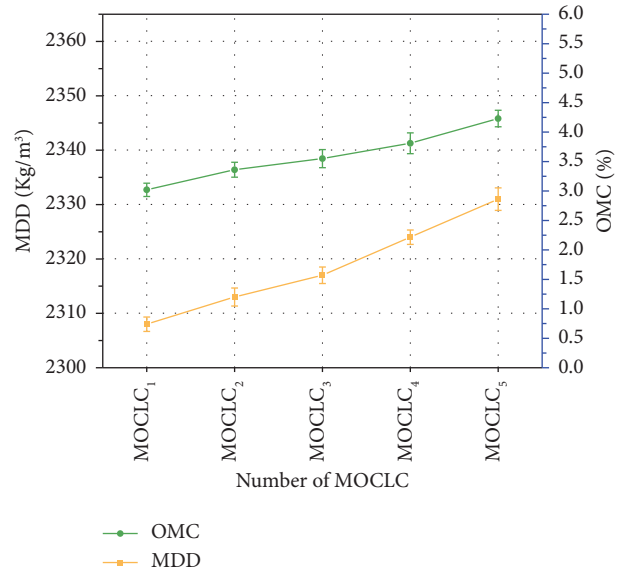
Figure 1: Effect of cement content on fresh properties of MOCLC.
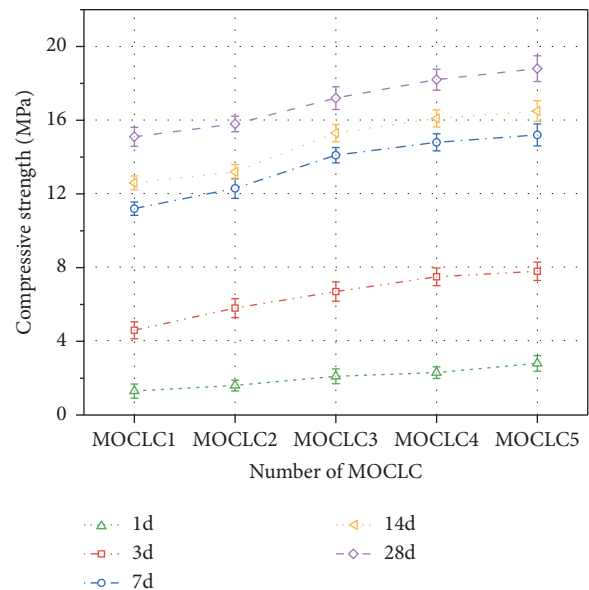
Figure 2: Effect of cement content and age on the compressive strength of MOCLC.

Generally, the compressive strength of MOCLC grew rapidly for the first 7 days and then tended to flatten out. For example, before 7 days, the compressive strength of $MOCLC_3$ increased by approximately 2 MPa/d. However, after seven days, the compressive strength of $MOCLC_3$ only increased by approximately 0.14 MPa/d. Similar patterns in the compressive strength were observed in different contents. Since MOC was used for the preparation of the considered mixes, the rapid increase in the early compressive strength was primarily due to the rapid formation of hydration products, which may have enhanced the chances of strength formation. At 7 days, the compressive strengths of

MOCLC$_3$ were 12 MPa and 7.4 MPa higher than those of MOCLC$_1$ and MOCLC$_2$, respectively. However, compared with MOCLC$_3$, the compressive strengths of MOCLC$_4$ and MOCLC$_5$ did not increase significantly. Obviously, the compressive strength of MOCLC grew the fastest when the magnesium oxide content was 4%.

The effects of mineral admixtures with different types and contents on the compressive strength of MOCLC were investigated using the internal mixing method. The proportion of MgO used in the MOCLC benchmark ratio was 4%. In this study, FA, dolomite powder, and LP were selected to explore the changing trends in the mechanical properties of MOCLC. The content of FA was divided into 10%, 15%, 20%, 25%, and 30%, named as MOCLC-FA$_1$, MOCLC-FA$_2$, MOCLC-FA$_3$, MOCLC-FA$_4$, and MOCLC-FA$_5$, respectively, to study the effect of FA on the performance of MOCLC. Similarly, DP and LP follow this naming rule. The test results are shown in Figure 3.

It can be observed from Figure 3 that the compressive strength of MOCLC decreases with an increase in the mineral admixture content. With an increase in mineral admixture content from 10% to 30%, the compressive strength of MOCLC mixed with FA, DP, and LP decreased by 56%, 77%, and 70%, respectively. The influence of FA on the strength of the MOCLC was minimal.

The compressive strength of the MOCLC by the addition of FA is consistent with Wu's study [41]. For instance, compared with the MOCLC-FA$_1$, the reductions in compressive strength were 9% and 11% for MOCLC-FA$_2$ and MOCLC-FA$_3$, respectively. Ultimately, the compressive strength of MOCLC-FA$_5$ is 16% lower than that of MOCLC-FA$_4$. It can be observed that the optimum proportion of FA is 25%. These findings suggest that the addition of FA to MOCLC does not promote the development of compressive strength. The reason is that FA breaks the bridge between hydration products and weakens the hydration structure. This phenomenon was also suggested by Wu et al. [41]. Moreover, Gong's study [15] also found that FA disrupts the hydration products of MOC, leading to a decrease in the MOCLC-FA intensity.

Figure 3 shows that the compressive strength of MOCLC is reduced by the addition of DP. The compressive strength of the specimen decreased significantly when the DP addition exceeded 20%. Excess DP resulted in a significant decrease in the compressive strength of MOCLC, which is consistent with the results of Nguyen's study [42]. For instance, compared with MOCLC-DP$_1$, the reductions in compressive strength were 3% and 14% for MOCLC-DP$_2$ and MOCLC-DP$_3$, respectively, whereas the reduction was approximately 39% for both MOCLC-DP$_4$ and MOCLC-DP$_5$, respectively. In summary, the optimal content of DP is 20%. The reason is that DP will hinder the contact between lightly burned magnesium powder and magnesium chloride solution, and Liu et al. [43] mentioned a similar theory. Consequently, DP slows the hydration response of the system, resulting in delayed strength development. Moreover, Xu et al. and Yu et al. [44, 45] also suggested that excess DP is equivalent to increasing the proportion of fine
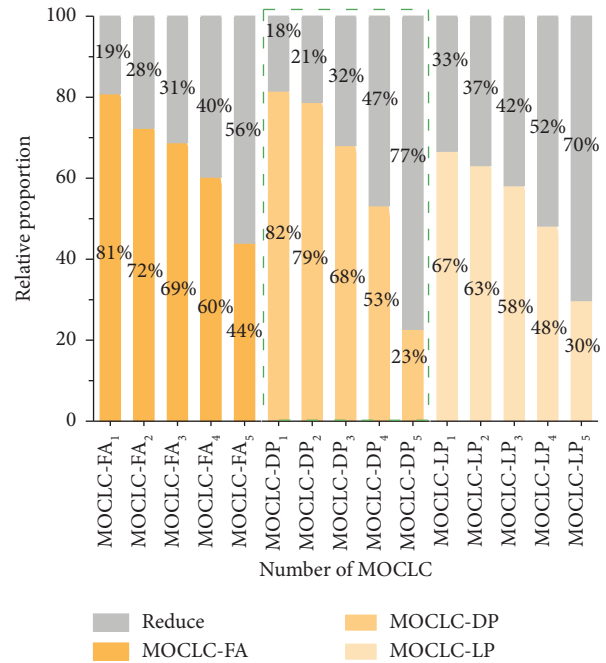
Figure 3: Effect of mineral admixture with different types and contents on compressive strength of MOCLC.

aggregates, which will reduce the coarse and fine aggregate ratio and overall strength.

Compared with MOCLC-LP$_1$, the reductions in compressive strength were 4% and 9% for MOCLC-LP$_2$ and MOCLC-LP$_3$, respectively, whereas the reductions were 19% and 37% for MOCLC-LP$_4$ and MOCLC-LP$_5$. When the LP content of MOCLC exceeded 20%, the compressive strength of the material rapidly declined. Therefore, the optimum content of LP is 20%. The reason for this phenomenon is that LP is present only as a filler, and Ahmad et al. [46] also pointed out that LP is not involved in hydration reactions and does not contribute to the formation of hydration products.

3.2.2. Splitting Strength. To explore the effect of the magnesium oxide content on the splitting strength of the MOCLC, the splitting strength of the MOCLC was observed at an age of 90 days, as shown in Figure 4.

As shown in Figure 4(a), the variation law of the splitting strength of the MOCLC is similar to that of the compressive strength. The splitting strength increased with an increase in the cement content. The splitting strength of MOCLC rose by approximately 0.53 MPa as the cement content increased from 3% to 5%. Compared with MOCLC$_1$, the increase in splitting strength was 11.8% and 30.1% for MOCLC$_2$ and MOCLC$_3$, respectively, whereas the increase was approximately 35.7% for both MOCLC$_4$ and MOCLC$_5$. Clearly, with 4% MgO, MOCLC exhibited the largest increase in splitting strength. Furthermore, the hydration products of MOCLC$_3$ were generally gel-like and leaf-like crystals with thick architectures. The gel-like crystals can characterize the strength of the MOC paste [47]. Besides, these leaf-like

(a)

(b)
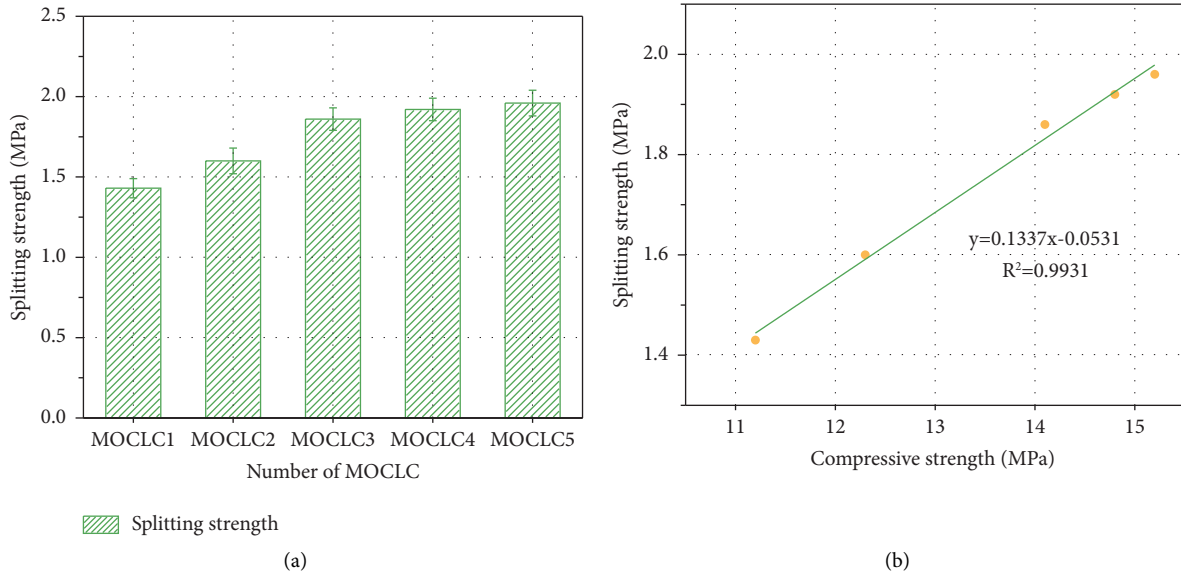
FIGURE 4: Effect of cement content on MOCLC splitting strength.

crystals can also be referred to as "whiskers," and Wu and Tan's study [48, 49] suggests that these "whiskers" are composed of phase 5 and other substances responsible for the reinforcing strength of the MOC paste. These are the reasons for the rapid increase in the mechanical strength of $MOCLC_3$. Therefore, the optimum content of magnesium oxide should be 4%, which is consistent with the conclusion that an optimum amount of MgO is obtained for the compressive strength.

Figure 4(b) shows the regression analysis of the MOCLC's 7-day compressive strength and 90-day splitting strength of the MOCLC. As shown in Figure 4(b), the compressive strength and splitting strength exhibit a good linear relationship. Therefore, the splitting strength can be calculated indirectly from the compressive strength by using a regression formula. Furthermore, this regression analysis method can be used as a strength test.

Figure 5 shows that the splitting strength of the MOCLC decreases with an increase in the mineral admixture content. This is because the hydration product of MOCLC without mineral admixtures appears as leaf-like crystals, as shown in Figure 6(a). However, the incorporation of mineral admixtures can hinder the formation of these leafy crystals, leading to a reduction in splitting strength. With an increase in mineral admixture content from 10% to 30%, the splitting strength of MOCLC mixed with FA, DP, and LP decreased by 26.3%, 59.6%, and 47.5%, respectively. Therefore, in terms of splitting strength, the effect of FA on the strength of the MOCLC is minimal.

The addition of FA lowered the splitting strength of the MOCLC, as shown in Figure 5. For example, compared with $MOCLC-FA_1$, the reduction in splitting strength was 12% and 18% for $MOCLC-FA_2$ and $MOCLC-FA_3$, respectively, whereas the reduction was approximately 21.5% for both $MOCLC-FA_4$ and $MOCLC-FA_5$. Obviously, the incorporation of FA is not conducive to the development of MOCLC splitting strength. In addition, Figure 6(b) shows
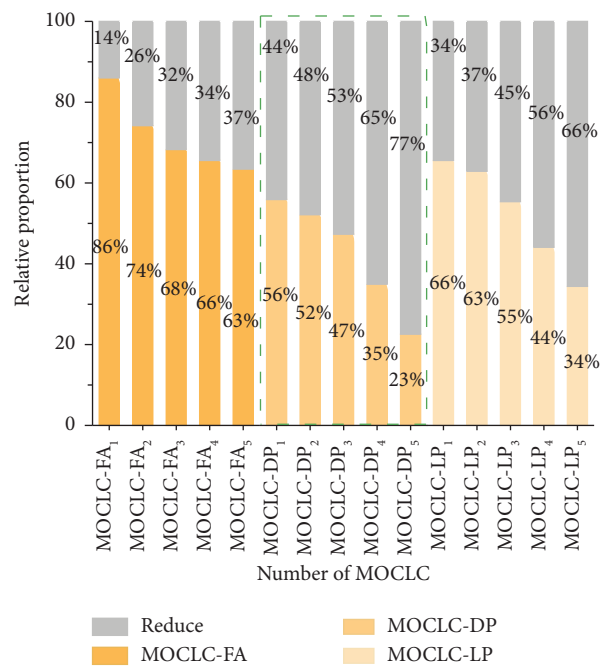
FIGURE 5: Effect of mineral admixture with different types and contents on splitting strength of MOCLC.

that FA is spherically dispersed in the LC system, which hinders the formation of the flaky gel phase, resulting in hydration products that are mostly short rods. This may be the primary reason for the decrease in the splitting strength of MOCLC. Chau et al. [50] also suggested that FA is spherically distributed in the MOC, which is not conducive to its strength formation.

In Figure 5, compared with the $MOCLC-DP_1$, the reductions in the splitting strength were 4% and 9% for $MOCLC-DP_2$ and $MOCLC-DP_3$, respectively, whereas the

(a)

(b)

(c)

(d)
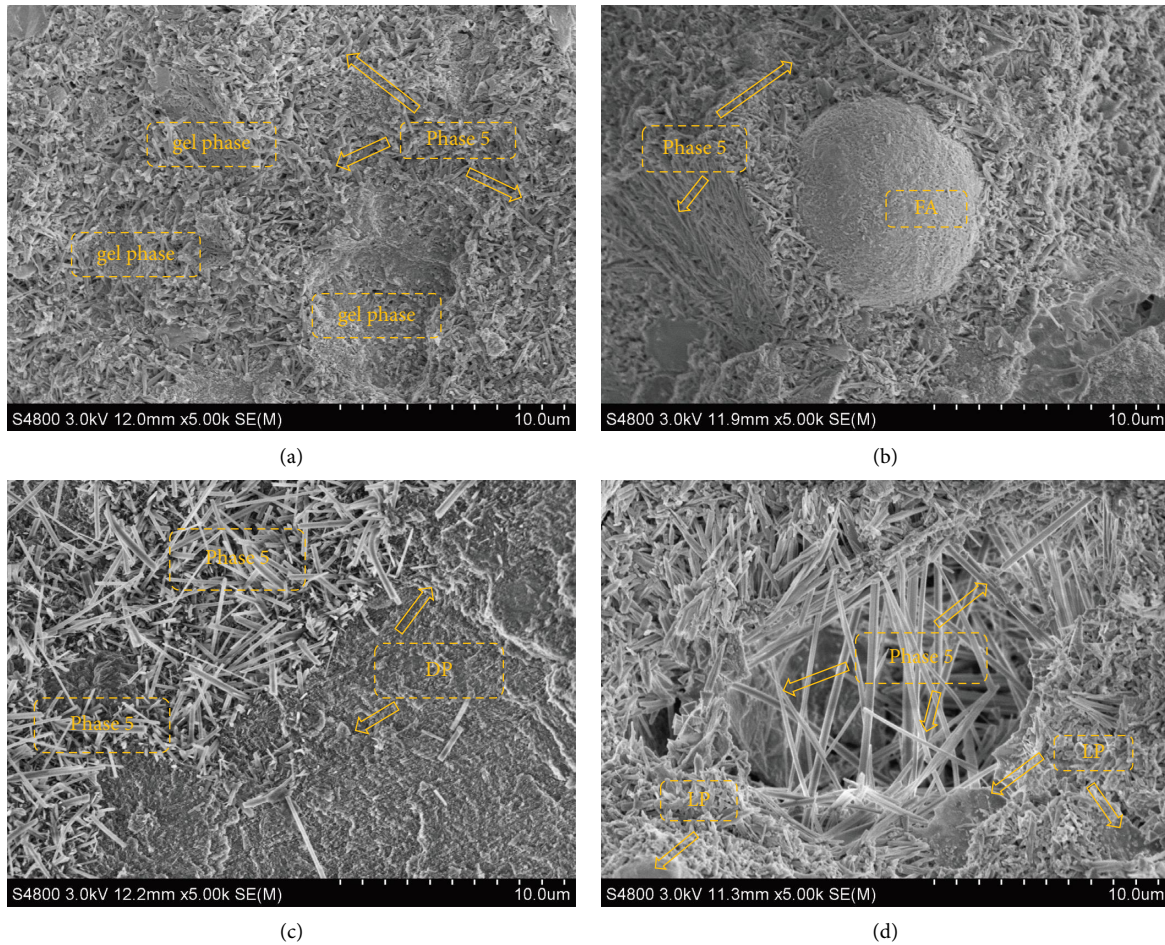
FIGURE 6: SEM image of MOCLC with mineral admixture. (a) SEM image of MOCLC. (b) SEM image of MOCLC-FA. (c) SEM image of MOCLC-DP. (d) SEM image of MOCLC-LP.

reductions were 21% and 33% for MOCLC-DP$_4$ and MOCLC-DP$_5$. Therefore, the addition of DP led to a decrease in the splitting strength of the MOCLC. Figure 6(c) shows the microstructure of the MOCLC-DP. The crystals in the figure primarily exist in the shape of rods. Liu et al. [43] found that the rod-like crystal structure is loose and not conducive to strength formation compared to the flaky gel phase.

Similarly, in Figure 5, compared with MOCLC-LP$_1$, the reductions in splitting strength were 3% and 11% for MOCLC-LP$_2$ and MOCLC-LP$_3$, whereas it was 22% and 32% for MOCLC-LP$_4$ and MOCLC-LP$_5$, respectively. Figure 6(d) shows the microstructure of the MOCLC-LP. Apparently, the presence of LP hinders the formation of the gel phase, making the main strength phase appear needle-rod-like. The low reaction state of LP in the cement paste does not provide mechanical strength, which is consistent with Zeng's study [51]. Therefore, LP reduced the strength of the MOCLC.

3.3. Water Resistance of MOCLC

3.3.1. Water Resistance Coefficient. The water resistance coefficient is a physical quantity used to evaluate the water

resistance. Figure 7 shows the variation in the waterproof coefficient of the MOCLC under different ages and immersion conditions. In this study, two different immersion conditions of the static and flowing water were set, and the compressive strength and splitting strength were used to calculate the water resistance coefficient of MOCLC, respectively. Specifically, the water resistance coefficient calculated by using the compressive strength for static immersion conditions was denoted as MOCLC-SW-C, and the water resistance coefficient calculated using compressive strength for flowing water immersion conditions was denoted as MOCLC-FW-C. The same was performed for the water resistance coefficient calculated using splitting strength.

As shown in Figure 7, the water resistance coefficient of the MOCLC decreased as the age increased. This phenomenon can be attributed to the fact that phase 5 was unstable in water and hence gets easily decomposed into Mg $(OH)_2$, as shown in Figure 8. Figure 8 shows the XRD spectrum of the specimens at different ages under hydrostatic conditions. From Figure 8, it can be seen that the characteristic peak of phase 5 keeps decreasing and the characteristic peak of Mg $(OH)_2$ increases with the increase

(a)

(b)
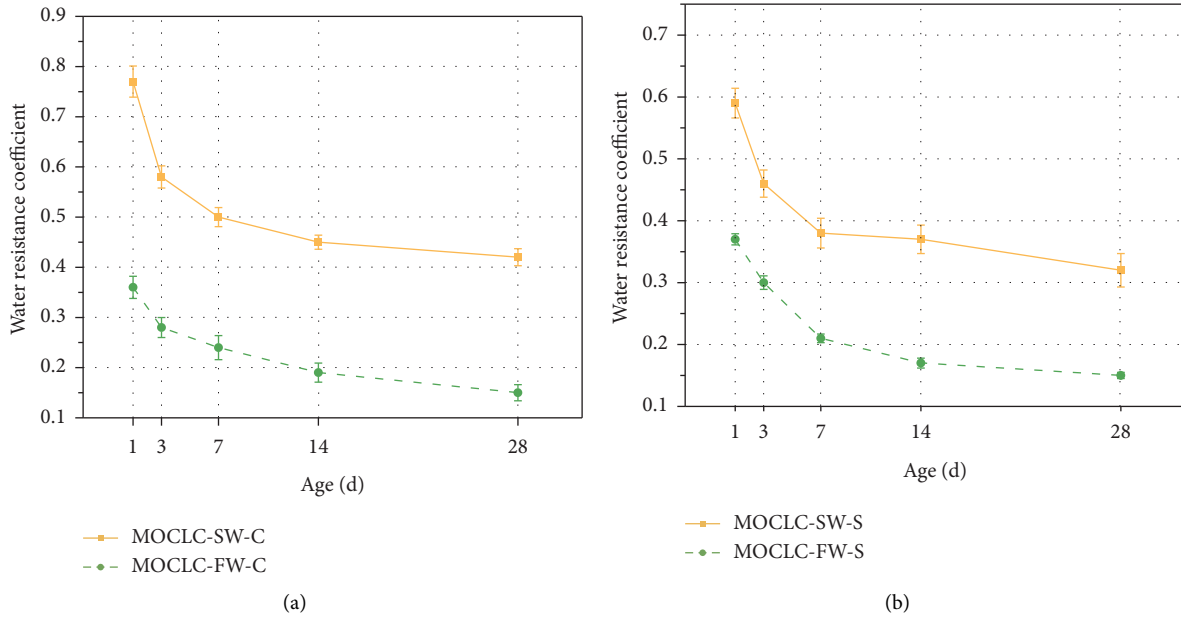
Figure 7: Water resistance coefficient of MOCLC under different water immersion conditions.
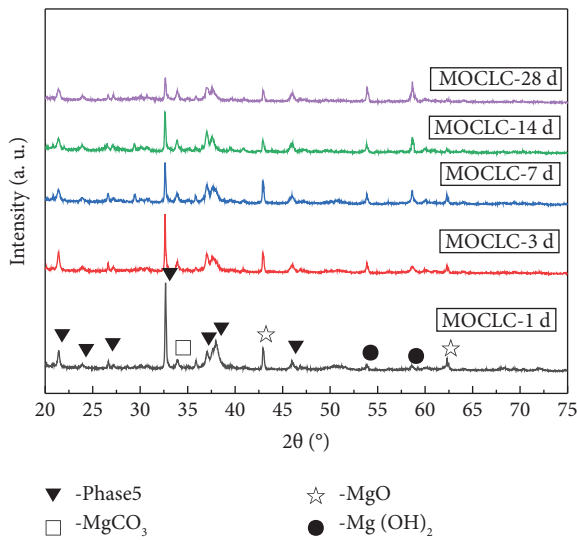
Figure 8: XRD patterns of MOCLC at different immersion ages.

of water immersion age. This is because the hydrolysis product of the phase 5 is mainly Mg (OH)$_2$. The characteristic peak of phase 5 decreased by 65.1% as the age of immersion increased from 1 to 28 days. Phase 5 has a high modulus, which was the main provider of strength for MOCLC, while Mg (OH)$_2$ is a loose layered crystal with a low strength [23]. This indicates that an increase in the number of years of immersion reduces the strength of MOCLC, leading to a decrease in the water resistance coefficient.

In addition, Figure 7(a) shows the change in the water resistance coefficient calculated using the compressive strength. Evidently, at 28 days, the water resistance coefficients of MOCLC-SW-C and MOCLC-FW-C decreased

to 0.42 and 0.15, respectively. Obviously, the water resistance coefficient of the MOCLC has a higher strength loss in flowing water than in still water. Figure 7(b) shows the change in the water resistance coefficient calculated using the splitting strength. At 28 days, the water resistance coefficients of MOCLC-SW-S and MOCLC-FW-S decreased to 0.32 and 0.15, respectively. The result is consistent with the conclusions drawn from the compressive strength measurements. Figure 7 shows the lower softening coefficient of the MOCLC specimens in a flowing water environment. It could be chiefly attributed to the differences in ion concentration caused by the transformation of unstable phase 5 into Mg (OH)$_2$ in water. Under flowing water conditions, the ion concentration remained constant, accelerating the dissolution of phase 5.

Figure 9 shows the variation of the water resistance coefficient of MOCLC with the type and content of mineral admixtures. The test conditions included hydrostatic immersion for 7 days. Generally, the water resistance coefficient of MOCLC increased with the addition of mineral admixtures, except for LP.

Figure 9 shows that the water resistance coefficients of MOCLC-FA and MOCLC-DP were higher than those of MOCLC at all test dosages. For instance, when the dosage was 25%, the water resistance coefficient of MOCLC-FA and MOCLC-DP increased by approximately 0.18 and 0.16 compared with MOCLC, respectively. The results reveal that FA and DP had a positive effect on the water resistance coefficient of the MOCLC, which is in agreement with the results of the XRD analysis in Figure 10. In contrast, the results indicated that LP had a negative effect on the water resistance coefficient of the MOCLC, as shown in Figure 10. Compared to MOCLC, the water resistance coefficient of MOCLC-LP was reduced by an average of 30%.
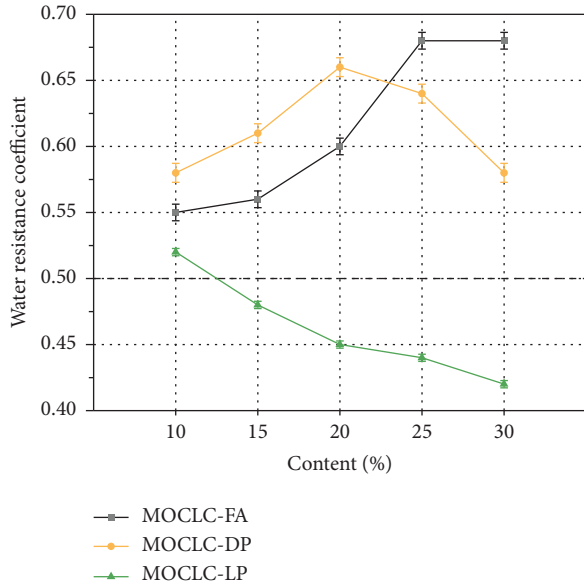
FIGURE 9: Water resistance coefficient of MOCLC varies with the type and content of mineral admixtures.
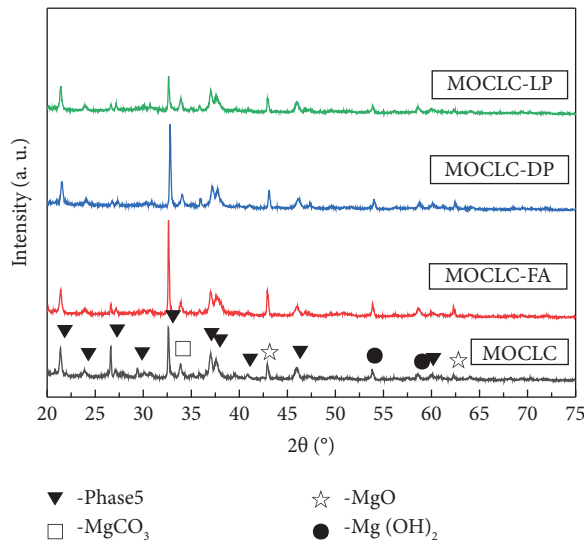
FIGURE 10: XRD patterns of MOCLC with different mineral admixtures.

Figure 10 shows the XRD spectrum of MOCLC, MOCLC-FA, MOCLC-DP, and MOCLC-LP cured for 7 days. It can be observed from Figure 10 that the MOCLC was comprised of phase 5, Mg $(OH)_2$, Mg CO_3, and MgO. Hydration products of MOC primarily included Mg $(OH)_2$ and phase 5. During water immersion, the inclusion of FA and DP raised the characteristic peaks of phase 5 by 36% and 32%, respectively. In addition, the characteristic peak intensity of MgO increased by 25.1% and 19.7%, respectively. However, the characteristic peak intensity of Mg $(OH)_2$ decreased. Chau et al. [50] found that the reason for this phenomenon is that both the degradation of hydration

phases and the formation of Mg $(OH)_2$ were reduced by adding fly ash. Furthermore, this also shows that the addition of FA can reduce the harmful pores of MOC paste and slow down the hydrolysis of the 518 phase. This is consistent with the research study of Guo et al. [36]. Moreover, the study by Averina et al. [52] concluded that DP contributes significantly to the filling of the pores of MOC pastes. Hence, there was an increase in the water resistance coefficient of MOCLC modified by FA and DP.

Apparently, the characteristic peaks of phase 5 appear to diminish with the inclusion of LP in MOCLC, whereas the characteristic peaks of Mg $(OH)_2$ appear to increase slightly. This was principally because the addition of LP reduced the gel material of MOCLC. As the gel material was reduced, the gel phase and crystals in the MOC became more dispersed [53], and the hydrated gel phase was more easily exposed to water because of the inability of the LP to bind the crystal phase together. Therefore, when eroded by water, the gel phase and crystals are more easily hydrolyzed, thus reducing the water resistance of the MOCLC.

3.3.2. Water Absorption and Porosity. The water absorption and porosity of the specimens under different conditions are shown in Figure 11. The water absorption of the specimen under still water conditions was recorded as W-MOCLC-SW, and the porosity of the specimen was recorded as P-MOCLC-SW. Similarly, the water absorption of the specimen under flowing water conditions was recorded as W-MOCLC-FW, and the porosity of the specimen was recorded as P-MOCLC-FW. The water absorption of MOCLC doped with fly ash was recorded as W-MOCLC-FA, and the porosity was recorded as P-MOCLC-FA. The specimens doped with dolomite powder and limestone powder were marked in the same way as mentioned above.

Figure 11(a) shows that water absorption and porosity increase with the increasing age of immersion. This was in line with the results of Wang et al. [7]. The water absorption of the specimens immersed for 7 days and immersed for 28 days in a static water environment increased by 7.1% and 8.2%, respectively. The water absorption of the specimens immersed for 7 days and 28 days increased by 11.4% and 14.2%, respectively, in the flowing water environment. Obviously, the water absorption rate of the specimen in the flowing water environment increased more dramatically. The water absorption rate of the specimens grew rapidly in the first 7 days of immersion. Wang et al. [7] suggested that this is because most of the free water is absorbed and fills the pore space of the cured sample within 2 days, while longer immersion times contribute less to the overall amount of absorbed water. The porosity of the specimens immersed for 7 and 28 days in a static water environment increased by 9.2% and 10.6%, respectively. In the flowing water environment, the water absorption of the specimens immersed for 7 and 28 days increased by 11.5% and 13.8%, respectively. The variation pattern of porosity in Figure 11(a) also confirms Wang's view [7].

Figure 11(b) shows the variation of water absorption and porosity for different contents of MOCLC-FA, MOCLC-DP,

(a)

(b)
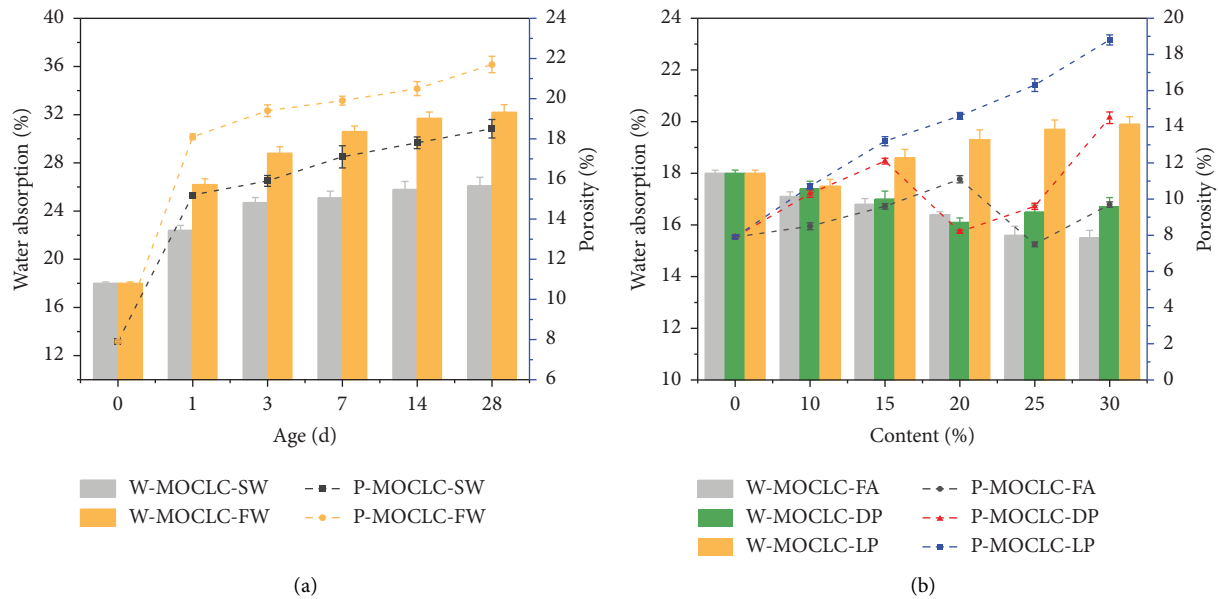
FIGURE 11: Water absorption and porosity of MOCLC.

and MOCLC-LP. The addition of FA and DP reduced the water absorption of the specimens by 2.5% and 1.35, respectively, compared to the reference specimens. However, the addition of LP increased the water absorption of the specimens by 2% and reduced the water resistance of the specimens. This is consistent with the conclusion of the water resistance coefficient in Section 3.3.1. Besides, after doping with FA and DP, the pores of the specimens increased first, then fluctuated, and finally tended to rise again. Guo et al. [36] explained the reason for this phenomenon. This is because the incorporation of FA and DP, while reducing the harmful macropores of the MOC paste, increases the small internal pores with a pore size of less than 50 nm. The increase in small pores was greater than the decrease in large pores, which led to an increase in the overall porosity. When the content of FA and DP is 25% and 20%, respectively, the filling effect on the MOC paste is the best, which densifies the MOC paste, so the porosity curve fluctuates. However, the excess admixture destroys the internal structure of the MOC paste, which leads to another increase in the porosity curve. This was also illustrated by Chau et al. [50]. The doping of LP increased the porosity of the specimens by about 10%, indicating that LP had a negative effect on the water resistance performance of MOCLC. This is in agreement with the study of Mostofinejad et al. [54].

3.4. Shrinkage Properties of MOCLC. Studies have demonstrated that the deterioration in the mechanical properties and durability of LC structures is primarily caused by shrinkage cracking. Furthermore, shrinkage affects MOCLC far more than it affects ordinary Portland cement lean concrete. Figure 12 shows the differences between the shrinkage strains of the MOCLC under the base ratio and mineral admixture conditions. Owing to the rapid hydration
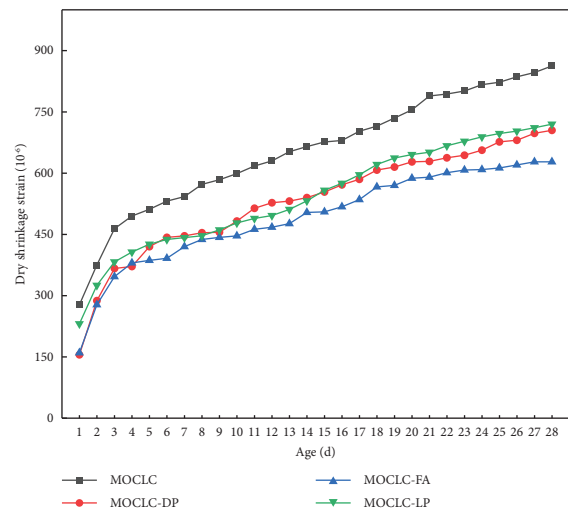
FIGURE 12: Relationship between dry shrinkage strain and time of different admixtures.

of MOC, shrinkage testing was performed in this trial starting on the first day of molding.

Figure 12 shows that the dry shrinkage strain of the MOCLC increased to different degrees with age. According to previous studies, the evaporation of water creates a large number of capillary pores inside the MOCLC [55]. Generally, the dry shrinkage strains of MOCLC-FA, MOCLC-DP, and MOCLC-LP were lower than that of the MOCLC. The dry shrinkage strains of MOCLC-FA, MOCLC-DP, and MOCLC-LP decreased approximately by 27.2%, 18.3%, and 16.5%, respectively. The results exhibited that FA, DP, and LP positively affected the shrinkage performance of the MOCLC. The reasons cited for this declined behaviour were the addition of FA, DP, and LP which reduced the amount of cement in the voids between aggregates. This led to the lesser
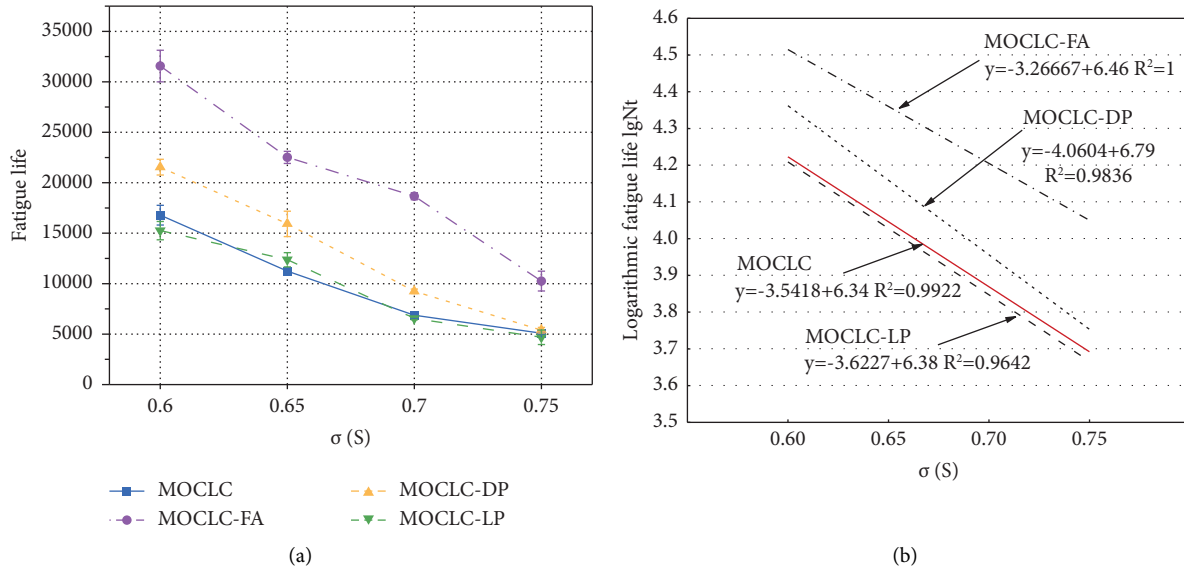
FIGURE 13: Comparison of MOCLC fatigue life under different mineral admixtures.

drying shrinkage [1]. During the drying process, MOCLC samples lost their quality due to the gradual loss of free water and crystal water [23]. With the extension of drying time, the dehydration process can be divided into two steps. Step 1: MOCLC sample gradually loses free water. Step 2: phase 5 in the MOCLC sample loses crystal water. Phase 5 is converted from $5Mg\ (OH)_2 \cdot MgCl_2 \cdot 8H_2O$ to $5Mg\ (OH)_2 \cdot MgCl_2$. The porous and the loose structure of FA has a strong water absorption capacity, which can accelerate the drying of cement interior and can reduce the loss of free water and crystal water [36]. In addition, FA is spherical, with low hydration reaction [56], and can also play a filling role. Therefore, the incorporation of FA reduced the shrinkage strain of the MOCLC. Additionally, DP was finer than ordinary mineral admixtures [57], which could better fill the internal pores of the MOCLC and can improve the pore structure. Additionally, $CaCO_3$ in the DP reacted with calcium aluminate hydrate to form monocarbon aluminate hydrate or tricarbon aluminate hydrate, which could compensate for its volume shrinkage. Additionally, as an inert material, LP is mostly used as a filler for MOCLC to disperse the cementitious phase, thereby reducing its shrinkage strain.

As shown in Figure 12, before 3 days, the shrinkage strain of the MOCLC increased rapidly and flattened after three days. The variation law of the shrinkage strain of the MOCLC with the mineral admixture was the same as that of the standard ratio. On an average, MOCLC-FA exhibited the largest reduction in shrinkage strain of approximately 25% compared to the standard ratio. The reduction in shrinkage strain of MOCLC-DP and MOCLC-LP was similar, approximately 20%. Therefore, adding 25% FA had the best effect in improving the shrinkage properties of MOCLC.

3.5. Fatigue Properties of MOCLC. Figure 13(a) shows the fatigue life of the MOCLC at different stress levels. The logarithmic average fatigue life lgN_t is taken as the ordinate

and the stress level σ/S as the abscissa to perform the linear fitting and regression, as shown in Figure 13(b). Considering the abovementioned shrinkage and mechanical properties of the MOCLC, the stress ratios of the four fatigue tests were considered as 0.6, 0.65, 0.7, and 0.75, respectively.

Figure 13 shows that the increase in the stress level decreased the fatigue life of MOCLC. The fatigue life of MOCLC-FA, MOCLC-DP, and MOCLC-LP increased by 88.0%, 28.4%, and −9.1%, respectively, according to the fitting equation shown in Figure 13. It can be observed that the fatigue curves of MOCLC-FA and MOCLC-DP were located above the fatigue curve of MOCLC, while the fatigue curve of MOCLC-FA was much higher than that of MOCLC-DP. More specifically, the fatigue curves of MOCLC-LP and MOCLC were roughly identical. This implied that the anti-fatigue performance of MOCLC-FA was the best, followed by MOCLC-DP, and MOCLC and MOCLC-LP which were the lowest. Therefore, at the same stress level, MOCLC-FA could bear the most load times, followed by MOCLC-DP, MOCLC, and MOCLC-LP.

Regarding the fatigue curve, the slope of the fatigue curve of MOCLC-FA was the smallest, and the slope of the fatigue curve of MOCLC-DP was the largest. The research of Li et al. and Sun et al. [58, 59] shows that the sensitivity of fatigue life to stress level is reflected by the slope of the fatigue curve. Obviously, the change in stress level had the least effect on the fatigue life of MOCLC-FA. Furthermore, MOCLC-DP exhibited the highest fatigue sensitivity. In summary, FA doping had the best effect on enhancing the fatigue properties of the MOCLC.

4. Conclusions

A comprehensive investigation of the mechanics and durability of MOCLC was conducted using a series of physical mechanical, durability, and microstructural tests. Based on

the obtained data, the following conclusions were drawn regarding the characteristics of the MOCLC:

(1) The addition of MOC improves the compaction characteristics of lean concrete. As the content of light-burned magnesia increased from 3% to 5%, the MDD and OMC of MOCLC increased by 0.96% and 40.1%, respectively.

(2) The compressive and splitting strengths of MOCLC were reduced by the addition of FA, DP and LP, however, its durability was improved. The optimal contents of FA, DP, and LP were 25%, 20% and 20%, respectively.

(3) FA and DP improved the water resistance of MOCLC, but LP was detrimental to the water resistance of MOCLC. The water resistance coefficients of MOCLC-FA and MOCLC-DP were increased by 0.18 and 0.16, respectively, relative to the control sample. And the water resistance coefficient of MOCLC-LP was reduced by an average of 30%.

(4) The shrinkage resistance of MOCLC composites is in the following order: MOCLC-FA > MOCLC-DP > MOCLC-LP > MOCLC. MOCLC-FA has better fatigue properties than DP and LP.

(5) The water resistance, shrinkage, and fatigue properties of MOCLC with a FA content of 25% were better than those of MOCLC with DP and LP.

Data Availability

The data supporting the current study are included in the article.

Conflicts of Interest

The authors declare that they have no conflicts of interest.

Acknowledgments

References

[1] R. K. Khyaliya, K. S. A. Kabeer, and A. K. Vyas, "Evaluation of strength and durability of lean mortar mixes containing marble waste," *Construction and Building Materials*, vol. 147, pp. 598–607, 2017.

[2] S. Lijun and W. Xinwu, "Analysis of load stress for asphalt pavement of lean concrete base," *Physics Procedia*, vol. 24, pp. 404–411, 2012.

[3] M. Singh, R. S. Chhabra, and A. Adhikari, "Feasibility study on use of washed-reclaimed asphalt as a partial replacement of natural aggregate in dry-lean concrete as base course for rigid pavement[J]," *Journal of Materials in Civil Engineering*, vol. 32, no. 9, Article ID 04020266, 2020.

[4] S. Reddy Kasu and S. Patel, "Field experiments and numerical analysis of curling behavior of cast-in-situ short paneled concrete pavement on lean concrete base[J]," *International Journal of Pavement Engineering*, pp. 1–14, 2021.

[5] S. R. Kasu, J. Tangudu, A. K. Chandrappa, and M. Reddy, "Influence of stiffness of dry lean concrete base on load stresses in the plain cement concrete slab of concrete pavements," *Road Materials and Pavement Design*, vol. 23, no. 8, pp. 1942–1955, 2021.

[6] A. Singh, R. Kumar, and P. Goel, "Factors influencing strength of magnesium oxychloride cement," *Construction and Building Materials*, vol. 303, Article ID 124571, 2021.

[7] D. Wang, X. Gao, X. Liu, and G. Zeng, "Strength, durability and microstructure of granulated blast furnace slag-modified magnesium oxychloride cement solidified waste sludge," *Journal of Cleaner Production*, vol. 292, Article ID 126072, 2021.

[8] Q. Ye, Y. Han, T. Liu et al., "Magnesium oxychloride cement reinforced via D-gluconic acid sodium salt for slow-curing, with enhanced compressive strength and water resistance," *Construction and Building Materials*, vol. 280, Article ID 122487, 2021.

[9] D. Wang, S. Di, X. Gao, R. Wang, and Z. Chen, "Strength properties and associated mechanisms of magnesium oxychloride cement-solidified urban river sludge," *Construction and Building Materials*, vol. 250, Article ID 118933, 2020.

[10] Q. Ye, Y. Han, S. Zhang et al., "Bioinspired and biomineralized magnesium oxychloride cement with enhanced compressive strength and water resistance," *Journal of Hazardous Materials*, vol. 383, Article ID 121099, 2020.

[11] D. H. Deng and C. M. Zhang, "The formation mechanism of the hydrate phases in magnesium oxychloride cement," *Cement and Concrete Research*, vol. 29, no. 9, pp. 1365–1371, 1999.

[12] R. M. Andrew, "Global CO2 emissions from cement production[J]," *Earth System Science Data*, vol. 10, no. 1, pp. 1–52, 2018.

[13] H. Qiao, Q. Cheng, and W. Jinlei, "The application review of magnesium oxychloride cement[J]," *Journal of Chemical and Pharmaceutical Research*, vol. 6, no. 5, pp. 180–185, 2014.

[14] H. Bilinski, B. Matkovic, C. Mazuravic, and T. A. Zunic, "The formation of magnesium oxychloride phases in the system of MgO-MgCl2-H2O and NaOH-MgCl2-H2O," *Journal of the American Ceramic Society*, vol. 67, no. 4, pp. 266–269, 1984.

[15] W. Gong, N. Wang, and N. Zhang, "Effect of fly ash and metakaolin on the macroscopic and microscopic characterizations of magnesium oxychloride cement," *Construction and Building Materials*, vol. 267, no. 1, Article ID 120957, 2021.

[16] D. Menetrier-Sorrentino, P. Barret, and S. Saquat, "Investigation in the system mgo-mgcl2-h2o and hydration of sorel cement," in *Proceedings of the 8th ICCC*, pp. 339–343, Rio de Janeiro, Brazil, September 1986.

[17] B. Matkovic, S. Popovic, and V. Rogic, "Reaction products in magnesium oxychloride cement pastes system MgO-MgCl2-H2O," *[J]. Chemischer Informationsdienst*, vol. 9, no. 17, pp. 504–507, 1978.

[18] J. M. Dong, H. F. Yu, and M. J. Wang, "Influence of fly ash on magnesium oxychloride cement deformation," *Materials Science Forum*, vol. 817, pp. 252–256, 2015.

[19] A. Jiříčková, M. Lojka, A. M. Lauermannová et al., "Synthesis, structure, and thermal stability of magnesium oxychloride 5 $Mg (OH)_2 \cdot MgCl_2 \cdot 8H_2O[J]$," *Applied Sciences*, vol. 10, p. 1683, 2020.

[20] M. Lojka, O. Jankovský, A. Jiříčková et al., "Thermal stability and kinetics of formation of magnesium oxychloride phase 3 $Mg (OH)_2 \cdot MgCl_2 \cdot 8H_2O[J]$," *Materials*, vol. 13, no. 3, p. 767, 2020.

[21] P. Wang, H. Qiao, Y. Zhang, Y. Li, Q. Feng, and K. Chen, "Meso-damage evolution analysis of magnesium oxychloride cement concrete based on X-CT and grey-level co-occurrence matrix," *Construction and Building Materials*, vol. 255, Article ID 119373, 2020.

[22] P. Wang, H. Qiao, Y. Li, K. Chen, Q. Feng, and T. Nian, "Durability of organic coated reinforced magnesium oxychloride cement concrete," *Structural Concrete*, vol. 22, no. 5, pp. 2595–2610, 2021.

[23] Q. Huang, W. Zheng, X. Xiao, J. Dong, J. Wen, and C. Chang, "Effects of fly ash, phosphoric acid, and nano-silica on the properties of magnesium oxychloride cement," *Ceramics International*, vol. 47, no. 24, pp. 34341–34351, 2021.

[24] C. Chang, J. Dong, X. Xiao et al., "Long-term mechanical properties and micro mechanism of magnesium oxychloride cement concrete," *Advances in Cement Research*, vol. 32, no. 8, pp. 371–378, 2020.

[25] Y. Hao and Y. Li, "Study on preparation and properties of modified magnesium oxychloride cement foam concrete," *Construction and Building Materials*, vol. 282, Article ID 122708, 2021.

[26] W. Gong, N. Wang, N. Zhang, W. Han, and H. Qiao, "Water resistance and a comprehensive evaluation model of magnesium oxychloride cement concrete based on Taguchi and entropy weight method," *Construction and Building Materials*, vol. 260, Article ID 119817, 2020.

[27] M. Záleská, M. Pavlíková, and Z. Pavlík, "Structural, mechanical and thermal properties of lightweight magnesium oxychloride cement concrete," *AIP Conference Proceedings*, vol. 2170, no. 1, 2019.

[28] H. Qiao, W. Gong, Y. Shi, M. E. Wanjiru, and J. Dong, "Experimental study on magnesium oxychloride cement concrete," *Emerging Materials Research*, vol. 5, no. 2, pp. 248–255, 2016.

[29] P. Wang, H. Qiao, H. Cao, Q. Feng, and K. Chen, "Durability analysis of magnesium oxychloride coated reinforced concrete under the combined effect of carbonization and water loss," *Emerging Materials Research*, vol. 9, no. 2, pp. 1–13, 2020.

[30] T. Huang, Q. Yuan, and D. Deng, "The role of phosphoric acid in improving the strength of magnesium oxychloride cement pastes with large molar ratios of H2O/MgCl2," *Cement and Concrete Composites*, vol. 97, pp. 379–386, 2019.

[31] Y. Wang, L. Wei, J. Yu, and K. Yu, "Mechanical properties of high ductile magnesium oxychloride cement-based composites after water soaking," *Cement and Concrete Composites*, vol. 97, pp. 248–258, 2019.

[32] Gb/T 14685-2011, *Pebble and Gravel for Construction*, Ministry of Transport, Beijing, China, 2011.

[33] Jgj 63-2006, *Standard for Water for Concrete*, Ministry of Construction, Beijing, China, 2006.

[34] Jtg 3420-2020, *Test Specification for Cement and Cement Concrete of Highway Engineering*, Ministry of Construction, Beijing, China, 2020.

[35] J. T. G. E51-2009, *Test Specification for Inorganic Binder Stabilized Materials of Highway Engineering*, Ministry of Construction, Beijing, China, 2009.

[36] Y. Guo, Y. X. Zhang, K. Soe, R. Wuhrer, W. D. Hutchison, and H. Timmers, "Development of magnesium oxychloride cement with enhanced water resistance by adding silica fume and hybrid fly ash-silica fume," *Journal of Cleaner Production*, vol. 313, Article ID 127682, 2021.

[37] Astm C 642, *Standard Test Method for Density, Absorption, and Voids in Hardened Concrete*, Annual Book of ASTM Standards, West Conshohocken, PA, USA, 2006.

[38] J. A. Sainz-Aja, I. A. Carrascal, J. A. Polanco, and C. Thomas, "Effect of temperature on fatigue behaviour of self-compacting recycled aggregate concrete," *Cement and Concrete Composites*, vol. 125, Article ID 104309, 2022.

[39] S. Singh, G. Ransinchung Rn, and K. Monu, "Sustainable lean concrete mixes containing wastes originating from roads and industries," *Construction and Building Materials*, vol. 209, pp. 619–630, 2019.

[40] S. Singh, G. D. R. N. Ransinchung, K. Monu, and P. Kumar, "Laboratory investigation of RAP aggregates for dry lean concrete mixes," *Construction and Building Materials*, vol. 166, no. 30, pp. 808–816, 2018.

[41] J. Wu, H. Chen, and B. Guan, "Effect of fly ash on rheological properties of magnesium oxychloride cement[J]," *Journal of Materials in Civil Engineering*, vol. 31, no. 3, Article ID 04018405, 2019.

[42] H. Nguyen, "Enhancement of engineering properties of slag-cement based self-compacting mortar with dolomite powder," *Journal of Building Engineering*, vol. 24, Article ID 100738, 2019.

[43] Z. Liu, S. Wang, J. Huang, Z. Wei, B. Guan, and J. Fang, "Experimental investigation on the properties and microstructure of magnesium oxychloride cement prepared with caustic magnesite and dolomite," *Construction and Building Materials*, vol. 85, pp. 247–255, 2015.

[44] J. Xu, J. Chen, D. Lu, Z. Xu, and R. Hooton, "Effect of dolomite powder on the hydration and properties of calcium sulfoaluminate cements with different gypsum contents," *Construction and Building Materials*, vol. 225, pp. 302–310, 2019.

[45] J. Yu, J. Qian, F. Wang et al., "Study of using dolomite ores as raw materials to produce magnesium phosphate cement," *Construction and Building Materials*, vol. 253, Article ID 119147, 2020.

[46] S. Ahmad, A. Bahraq, and A. Shaqraa, "Effects of key factors on the compressive strength of metakaolin and limestone powder-based alkali-activated concrete mixtures: an experimental and statistical study," *Case Studies in Construction Materials*, vol. 16, p. e915, 2022.

[47] B. Guan, H. Tian, D. Ding, J. Wu, and R. Xiong, "Effect of citric acid on the time-dependent rheological properties of magnesium oxychloride cement," *Journal of Materials in Civil Engineering*, vol. 30, no. 11, Article ID 04018275, 2018.

[48] J. Wu, B. Guan, H. Chen, H. Tian, J. Liu, and R. Xiong, "Effects of polycarboxylate superplasticiser on the early hydration properties of magnesium oxychloride cement," *Construction and Building Materials*, vol. 259, Article ID 119862, 2020.

[49] Y. Tan, Y. Liu, Z. Zhao, J. Z. Paxton, and L. M. Grover, "Synthesis and *in vitro* degradation of a novel magnesium oxychloride cement: synthesis and *In Vitro* Degradation of

a Novel MOC," *Journal of Biomedical Materials Research Part A*, vol. 103, no. 1, pp. 194–202, 2015.

[50] C. K. Chau, J. Chan, and Z. Li, "Influences of fly ash on magnesium oxychloride mortar," *Cement and Concrete Composites*, vol. 31, no. 4, pp. 250–254, 2009.

[51] H. Zeng, Y. Li, J. Zhang, P. Chong, and K. Zhang, "Effect of limestone powder and fly ash on the pH evolution coefficient of concrete in a sulfate-freeze–thaw environment," *Journal of Materials Research and Technology*, vol. 16, pp. 1889–1903, 2022.

[52] G. F. Averina, T. N. Chernykh, and K. V. Shuldyakov, "Hardening stowing mixture based on technological dolomite," *Procedia Engineering*, vol. 206, pp. 790–794, 2017.

[53] C. Ma, G. Chen, J. Shi, H. Zhou, W. Ren, and Y. Du, "Improvement mechanism of water resistance and volume stability of magnesium oxychloride cement: a comparison study on the influences of various gypsum," *Science of the Total Environment*, vol. 829, Article ID 154546, 2022.

[54] D. Mostofinejad, M. Khademolmomenin, and B. Tayebani, "Evaluating durability parameters of concrete containing limestone powder and slag under bacterial remediation," *Journal of Building Engineering*, vol. 40, Article ID 102312, 2021.

[55] W. Xu, Z. Song, M. Guo, L. Jiang, and H. Chu, "Improvement in water resistance of magnesium oxychloride cement via incorporation of dredged sediment," *Journal of Cleaner Production*, vol. 356, Article ID 131830, 2022.

[56] Y. Li, H. Yu, L. Zheng, J. Wen, C. Wu, and Y. Tan, "Compressive strength of fly ash magnesium oxychloride cement containing granite wastes," *Construction and Building Materials*, vol. 38, pp. 1–7, 2013.

[57] H. A. Nguyen, T. P. Chang, J. Y. Shih, and H. Suryadi Djayaprabha, "Enhancement of low-cement self-compacting concrete with dolomite powder," *Construction and Building Materials*, vol. 161, pp. 539–546, 2018.

[58] L. Li, Q. Zheng, X. Wang, B. Han, and J. Ou, "Modifying fatigue performance of reactive powder concrete through adding pozzolanic nanofillers," *International Journal of Fatigue*, vol. 156, Article ID 106681, 2022.

[59] X. Sun, Y. Tian, W. Yin, and H. Wang, "Effect of free water on fatigue performance of concrete subjected to compressive cyclic load," *Construction and Building Materials*, vol. 318, Article ID 125995, 2022.

Research Article

Research on Rheological Properties by Desulfurized Rubber Powder/SBS Composite-Modified Asphalt and Road Performance of Its Mixture

Ping Guo,[1] Qingwei Ma,[1] Yan Li,[1] Chenguang Yang,[1] Yeji Qiu,[1] Liangyu Sun,[2] Xilun Zhang,[2] and Fayong Yang [1]

[1]Xi'an Highway Research Institute Co., Ltd, Xi'an 710065, China
[2]CCCC Second Highway Engineering Bureau Dongmeng Engineering Co., Ltd, Xi'an 710119, China

Correspondence should be addressed to Fayong Yang; yycc127@163.com

Desulfurized rubber powder and SBS were used as asphalt modifiers to study the rheological properties and performance of desulfurized rubber powder/SBS composite-modified asphalt (DR/SBSCMA). First, the basic performance indicators such as penetration, ductility, softening point, and viscosity were studied. Second, the high-temperature and low-temperature rheological properties of asphalt were evaluated by using a dynamic shear rheometer (DSR) and bending beam rheometer (BBR). Finally, their high-temperature stability, low-temperature crack resistance, and water stability under the gradation of AC-13 and SMA-13 were evaluated. The results show that DR/SBSCMA had great advantages in terms of ductility and softening point, especially the softening point, which reached 90°C. It also demonstrated excellent high-temperature performance and tensile strength, and penetration was slightly lower than that of SBS-modified asphalt. Moreover, after compound modification, high-temperature and low-temperature rheological properties were effectively improved, and DR/SBSCMA adequately met the requirements of PG82-34. In addition, DR/SBSCMA maintained excellent high-temperature stability in both AC-13 and SMA-13 mixtures, coupled with obvious improvements in rutting deformation. Meanwhile, its low-temperature cracking resistance is slightly lower than that of SBS-modified asphalt, but both adequately meet the specification requirements. Ultimately, the water stability of DR/SBSCMA is comparable to that of SBS-modified asphalt, with both reaching more than 90%, proving its excellent water stability.

1. Introduction

In recent years, with increasing traffic, ordinary asphalt pavement is prone to cracking, rutting, loosening, peeling, and other pavement diseases, affecting the quality and life of the pavement. As a means to improve the performance of conventional asphalt at high temperatures and low temperatures, polymer-modified asphalt has developed rapidly [1–3], of which SBS-modified asphalt is the most widely used. Under the stimulus of the circular economy and resource utilization policy, rubber asphalt has launched a new development. Compared with basic asphalt, high-temperature and low-temperature performances of SBS-modified asphalt are effectively improved. However, SBS-modified asphalt is expensive and deteriorates easily, which limits its application [4, 5]. Grinding scrap tires to obtain rubber powder for asphalt modification has become an important way to treat scrap tires in a harmless and resourceful way [6, 7]. However, when using rubberized asphalt, the compatibility and storage stability of rubber powder and asphalt are poor, and segregation occurs easily [8, 9], which limits its further development.

To solve the above difficulties and pain points, road researchers proposed measures such as rubber powder desulfurization and rubber powder/SBS blending and obtained preliminary results [10, 11]. Filippelli et al. [12] used ultrasonic waves to produce desulfurized rubber powder, and produced desulfurized rubber asphalt had better

deformation resistance and fatigue life. Kabir et al. [13] used microbial devulcanization of rubber, and its surface energy was increased three times after devulcanization, which could increase rubber asphalt interaction and reduce segregation. Research by Presti et al. [14] found that the solubility of desulfurized rubber powder is high, the dosage can reach 30%, and the processing time can be shortened. Ibrahim et al. [15] used radiation to pretreat rubber powder and found that its high-temperature and low-temperature properties and antiaging properties were improved. Singh et al. [16] improved the surface activity of rubber crumb after desulfurization, which improves the compatibility of rubber crumb with asphalt and the storage stability of rubber asphalt [17]. Shatanawi et al. [18] found that the desulfurized rubber powder can be melted into asphalt, which enables modified asphalt to have better storage stability. Kim et al. [19, 20] used SBS, SIS, petroleum resin, and tire rubber powder to make composite-modified asphalt. The performance of composite-modified asphalt at high temperature and low temperature was effectively improved, and viscosity was dependent on the content of rubber powder and SIS. Behnood and Olek [21] studied the rheological properties of SBS rubber powder polyphosphoric acid (PPA) composite-modified asphalt, and its rheological properties at high temperatures were improved. Ameri et al. [22] found that adding rubber powder and SBS could improve the fatigue resistance of modified asphalt. Rasool et al. [23, 24] used a twin-screw extruder to desulfurize and degrade rubber powder to improve its dispersing effect on SBS-modified asphalt. The degree of desulfurization and degradation of rubber powder was found to affect its dispersibility and interaction with asphalt. It was then suggested that the components and materials between desulfurized rubber powder, asphalt, and SBS exchange and interact, and the desulfurized rubber powder showed an increase in compatibility with asphalt, thereby improving ductility, softening point, and aging resistance, while reducing viscosity of composite-modified asphalt, which is advantageous for construction workability. The SBS powder and desulfurized rubber powder were also determined to be crosslinked after aging, which further improved ductility and aging resistance. Ma et al. [25] developed modified asphalt with stable rubber powder and found that its storage stability was effectively improved, and after that, the modification mechanism was analyzed.

Desulfurized rubber asphalt is produced after rubber powder is desulfurized, and its storage stability is effectively improved. To a certain extent, the amount of rubber powder can be increased and the construction temperature reduced, but its viscosity and softening point index decrease significantly, which is not conducive to improving high-temperature performance. Rubber powder/SBS composite modification can greatly improve the pavement performance, and the content of SBS is reduced, reducing the cost of use, but the compatibility problem has not been effectively solved.

Based on this, this study extensively uses two solutions of rubber powder desulfurization and rubber powder/SBS compounding, with desulfurized rubber powder and SBS as

asphalt modifier materials to produce composite-modified asphalt and to develop desulfurized rubber powder/SBS composite-modified asphalt. Then, research was conducted on the rheological properties of desulfurized rubber powder/ SBS composite-modified asphalt and its mixture's performance. At the same time, compared to SBS-modified asphalt and rubber asphalt, which are commonly used in pavements, the advantages of composite-modified asphalt in terms of the rheological properties of asphalt and the pavement performance of mixtures are illustrated. Ultimately, the research results can effectively improve the overall performance of modified asphalt, improve the resource utilization of scrap tires in China, and greatly reduce the cost of asphalt pavement construction, which has important economic and environmental significance.

2. Materials and Methods

2.1. Materials

2.1.1. Asphalt

(1) Virgin Asphalt. In this study, base asphalt (SK 90#) was used to prepare rubberized asphalt or SBS-modified asphalt, and the basic performance indicators are shown in Table 1.

(2) Modified asphalt. To compare and analyze the performance of asphalt and the pavement performance of the mixture in this paper, three kinds of modified asphalt commonly used in Shaanxi Province were selected as the control, namely, SBS-modified asphalt, rubber asphalt, and desulfurized rubber asphalt produced by an asphalt plant in Shaanxi Province. The performance indicators are shown in Table 2.

2.1.2. Desulfurized Rubber Powder. Desulfurized rubber powder is produced from rubber powder (Figure 1) after thermal-mechanical shear desulfurization, extrusion, and granulation by using a twin-screw extruder. The appearance and shape are shown in Figure 2, and black particles are uniform in particle size without agglomeration. The technical indicators are shown in Table 3.

2.1.3. SBS Modifiers. SBS modifiers have thermoplastic elastomer properties and are widely used in asphalt modification. An SBS 4303 modifier was selected in this paper, and the performance indicators are shown in Table 4.

2.1.4. Aggregate

(1) AC-13 aggregate. Coarse aggregates are diorite crushed stones from a company in Shaanxi, and the specifications are as follows: 9.5~16 mm, 4.75~9.5 mm, 2.36~4.75 mm. The test results of physical properties of coarse aggregates are shown in Table 5. Machine-made sand and mineral powder were processed by crushed limestone from a company in Shaanxi. The test results of physical properties are shown in Tables 6 and 7.

TABLE 1: The basic properties of SK 90[#] virgin asphalt.

Items		Value	Requirements
Penetration (25°C, 0.1 mm)		89	80~100
Penetration index		−0.6	−1.5~+1.0
Ductility (10°C, cm)		>100	≥20
Softening point (°C)		46.0	≥45
Viscosity (60°C, Pa·s)		162.9	≥160
Flash point (°C)		294.3	≥245
Solubility (%)		99.97	≥99.5
Density (15°C, g/cm^3)		1.032	Measured
	Loss on heating (%)	−0.512	≤±0.8
Aged asphalt (TFOT)	Penetration ratio (%)	59.9	≥57
	Ductility (10°C, cm)	9	≥8

TABLE 2: The performance technical indicators of three kinds of modified asphalt.

Items		Desulfurized rubber asphalt	Rubber asphalt		SBS-modified asphalt	
		Value	Value	Requirements	Value	Requirements
Penetration (25°C, 0.1 mm)		65	53	40~80	63	60~80
Ductility (5°C, cm)		12.6	8.5	≥8	32	≥30
Softening point (°C)		62	68	≥58	79	≥55
Density (15°C, g/cm^3)		—	1.047	Measured	1.030	Measured
Viscosity (135°C, Pa·s)		2.527	8.674	—	1.828	≤3.0
Viscosity (180°C, Pa·s)		0.790	2.142	1.5~4.0	—	—
	Loss on heating (%)	−0.16	−0.182	≤±1.0	−0.229	≤±1.0
Aged asphalt (TFOT)	Penetration ratio (%)	90	89	≥60	81	≥60
	Ductility (5°C, cm)	10.1	5.2	≥5	27.4	≥20

FIGURE 1: Rubber powder.

FIGURE 2: Desulfurized rubber powder.

TABLE 3: The technical indicators of desulfurized rubber powder.

Items	Value	Requirements
Heating loss (80°C) (%)	0.4	≤1.5
Ash (%)	7.2	≤8
Acetone extract (%)	16.4	≤20
Mooney viscosity ML 100°C (1 + 4)	35	≤45
Carbon black content (%)	28.3	≥18
Rubber hydrocarbon content (%)	48	≥40
Iron content (%)	0.028	≤0.03
Particle size (mm)	5	≤10

TABLE 4: The performance indicators of SBS 4303.

Items	Value
Melt index (g/10 min)	11.0
300% tensile stress (MPa)	2.5
Elongation at break (%)	590
Hardness (degree A)	80
Tear-off permanent deformation	12
Volatile	0.50
S/B (mass ratio)	30/70

(2) SMA-13 aggregate. Aggregates and ore powder were produced in a factory in Hainan Province. The specifications of ore materials are 10~15 mm, 5~10 mm, 3~5 mm, and 0~3 mm, respectively. The technical indicators of aggregates and ore powders are shown in Table 8.

TABLE 5: Coarse aggregate quality specification test results.

Items	9.5~16 mm	4.75~9.5 mm	2.36~4.75 mm	Requirements
Volume relative density	2.975	2.952	2.884	—
Apparent relative density	3.026	3.021	2.953	≥2.6
Water absorption (%)	0.57	0.77	0.81	≤2.0
Needle-like particle content (%)	6.1	8.1	—	≤12
Crushing value (%)	10.3	—	—	≤26
Particle content (<0.075 mm, %)	0.1	0.2	0.1	≤1.0
Los Angeles attrition (%)	10.2	—	—	≤28
Polished value (PSV)	43	≥38		
Soft stone content (%)	1.0	—	—	≤3
Firmness (%)	5.0	≤12		
Adhesion to asphalt (grade)	5	—	—	≥4

TABLE 6: Test results of physical properties of manufactured sand.

Items	Value	Requirements
Sand equivalent (%)	70	≥60
Methylene blue value (g/kg)	1.2	≤2.5
Angularity (s)	43	≥30
Robustness (>0.3 mm)	4.5	≤12
Apparent relative density	2.757	≥2.5

TABLE 7: Test results of physical properties of mineral powder.

Items	Value	Requirements
Apparent relative density	2.717	≥2.5
Hydrophilic coefficient	0.70	<1.0
Plasticity index (%)	3	<4
Moisture content (%)	0.1	≤1.0

TABLE 8: Test results of physical properties of SMA-13 aggregates.

Items	10~15 mm	5~10 mm	3~5 mm	0~3 mm	Mineral powder	Requirements
Apparent relative density	2.923	2.913	2.862	—	—	≥2.6
	—	—	—	2.818	2.756	≥2.5
Volume relative density	2.870	2.863	—	—	—	—
Water absorption (%)	0.63	0.60	—	—	—	≤2
Crushing value (%)			10.5			≤20
Wear value (%)			12.4			≤28

2.2. Test Methods

2.2.1. Evaluation Method of Asphalt Physical Properties.
According to the previous research results of composite-modified asphalt under different formulations, the mixing ratio of composite-modified asphalt used in this paper was determined to be 25% desulfurized rubber powder + 2% SBS. We first add SBS and then add rubber powder, the preparation temperature is 175°C, and the shearing time is 50 min. Conventional indexes such as penetration, softening point, ductility, and Brookfield rotational viscosity of composite-modified asphalt were tested according to the Standard Test Methods of Bitumen and Bituminous Mixtures for Highway Engineering (JTG E20-2011).

2.2.2. Rheological Property Test.
The high-temperature and low-temperature rheological properties of asphalt were evaluated by using a dynamic shear rheometer (DSR) and bending beam rheometer (BBR). The DSR strain control is 12%, the angular frequency is 10 rad/s, the temperature sweep range is 34~88°C, and the temperature range is 6°C. Parameters such as complex modulus G^*, phase angle δ, and rutting factor were tested. The BBR test temperature range was $-6\sim-24$°C, the temperature interval is 6°C, and the parameters such as stiffness modulus S and creep rate m were also tested.

In the Superpave asphalt binder specification, the original asphalt rutting factor $G^*/\sin\delta$ is required to be no less than 1.00 kPa. The corresponding rutting factor critical temperature can be obtained by fitting the rutting factor change curve, which corresponds to the temperature when the rutting factor is 1.00 kPa. The rutting factor is further improved, and $G^*/(\sin\delta)^9$ is used as the improved rutting factor [26]. The critical temperature was determined by exponential regression, and then, high-temperature rheological properties were evaluated. In this paper, formulas (1)
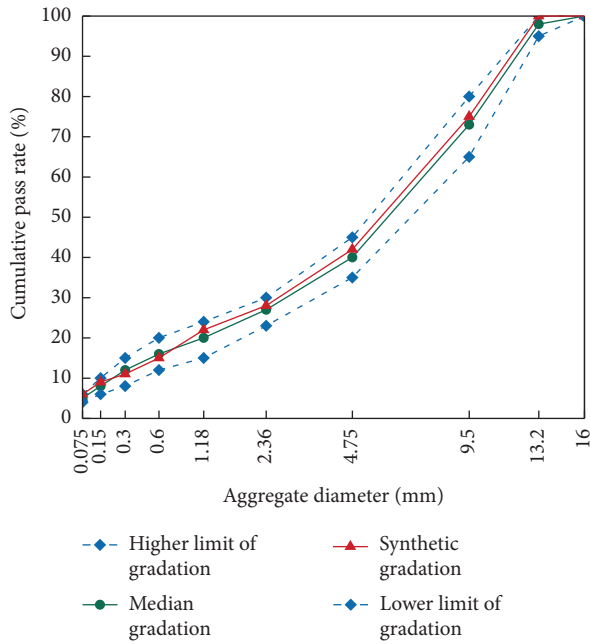
FIGURE 3: Synthetic gradation diagram of AC-13 asphalt mixture.

and (2) were used to perform exponential regression fitting on the rutting factor $G*/\sin\delta$ and the improved rutting factor $G*/(\sin\delta)^9$, as well as to further obtain the critical temperature, and determine its PG classification.

$$y = \exp(a + b*x + c*x\hat{2}), \tag{1}$$

$$y = d * \exp(e*x), \tag{2}$$

where a–e are regression coefficients.

2.2.3. Mixture Mix Ratio Design and Pavement Performance Test

(1) Mix ratio design. According to the grading requirements of AC-13 and SMA-13 asphalt mixture in the Technical Specifications for Construction of Highway Asphalt Pavement (JTG F40-2004), the design of mineral material gradation was carried out. The synthetic gradation diagram of the mixture is shown in Figures 3 and 4.

The optimum asphalt dosage of desulfurized rubber powder/SBS composite-modified asphalt in AC-13 mixture grading was determined to be 4.7%. According to the same method, the optimum amounts of rubber asphalt, desulfurized rubber asphalt, and SBS-modified asphalt were determined to be 6.0%, 5.7%, and 4.8%, respectively. In the gradation of SMA-13 asphalt mixture, the optimum asphalt dosage of desulfurized rubber powder/SBS composite-modified asphalt and SBS-modified asphalt was 6.0%. The optimum asphalt dosage was then applied to the road asphalt pavement mixture, and after that, test pieces were moulded for performance testing.

(2) Pavement performance test. According to the Standard Test Methods of Bitumen and Bituminous Mixtures for Highway Engineering (JTG E20-2011), the rutting test, low-

FIGURE 4: Synthetic gradation diagram of SMA-13 asphalt mixture.
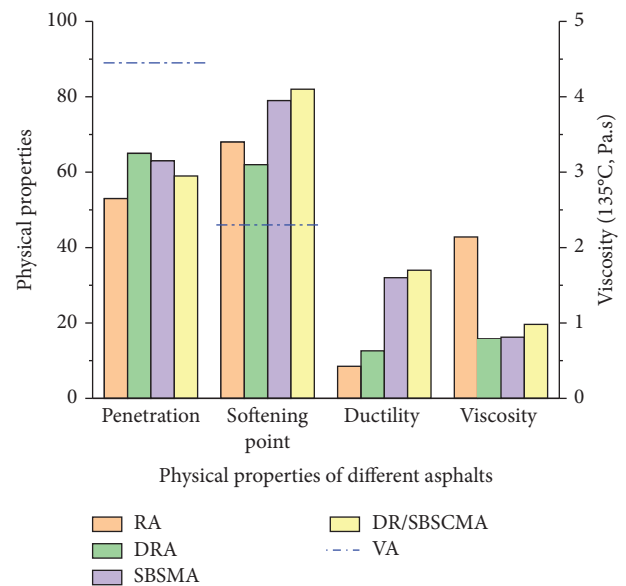
FIGURE 5: Test results of different basic performance indexes of asphalt.

temperature trabecular bending test, immersion Marshall test, and freeze-thaw splitting test were used to evaluate high-temperature stability, low-temperature cracking resistance, and water stability of asphalt mixture, respectively.

3. Results and Analysis

3.1. Basic Performance Analysis. Penetration, ductility, softening point, and viscosity of virgin asphalt (VA), rubber asphalt (RA), desulfurized rubber asphalt (DRA), SBS-modified asphalt (SBSMA), and desulfurized rubber

powder/SBS composite-modified asphalt (DR/SBSCMA) were tested. The test results are shown in Figure 5. In the follow-up research, each type of asphalt is represented by the corresponding letter code.

From Figure 5, it can be seen that the four types of modified asphalt have some improvement over the conventional performance of virgin asphalt and that the penetration, softening point, ductility, and viscosity of DR/SBSCMA could all meet the performance requirements of composite-modified asphalt in the specification. It is superior to SBSMA, RA, and DRA in ductility and softening point, especially the softening point, which reached whopping 90°C, indicating that DR/SBSCMA has excellent high-temperature performance and tensile strength. It also proves the stability of the crosslinked lattice structure, which is formed by rubber powder and SBS is higher than that of the a single modified asphalt system. The penetration of DR/SBSCMA is slightly lower than that of SBSMA and DRA but higher than that of RA. This is due to swelling and dispersion of rubber powder particles, which absorb a large amount of light oil, and composite-modified asphalt becomes hard to some extent, resulting in a decrease in penetration. With rubber-modified asphalt, the viscosity at 180°C is crucial to ensure that construction can be carried out smoothly. The viscosity of DR/SBSCMA is slightly higher than that of SBSMA and DRA but much lower than that of RA, indicating that composite-modified asphalt can fully meet construction requirements and does not affect construction workability.

3.2. Research on Rheological Properties

3.2.1. Dynamic Shear Rheological Test. The American SHRP program proposes to use the DSR test to evaluate the high-temperature stability of asphalt, test the complex shear modulus $G*$ and phase angle δ, and calculate the rutting factor $G*/\sin\delta$. In this paper, the temperature sweep was used, and the $G*$ and δ test results of the five types of asphalt at a test temperature of 34~88°C are shown in Figures 6 and 7.

From Figure 6, it can be seen that the complex shear modulus $G*$ of some asphalt gradually decreases with increasing temperature. Compared to virgin asphalt, the removal of modified asphalt is somewhat slower. In the temperature range, $G*$ of asphalt ranking from large to small goes as follows: DR/SBSCMA, SBSMA, RA, DRA, and VA, indicating that composite-modified asphalt has higher rigidity and greater resistance to deformation under load. Modifiers such as rubber powder and SBS have good resilience and strength, and their incorporation improves the viscoelastic properties of asphalt and improves the asphalt system's ability to resist deformation. Compared with the single modification, the compound modification shows greater improvement in asphalt viscoelasticity.

It can be seen from Figure 7 that the phase angle of virgin asphalt gradually increases with increasing temperature and gradually tends to 90°, thereby losing elastic deformability and entering a viscous flow state. Unlike virgin asphalt, the
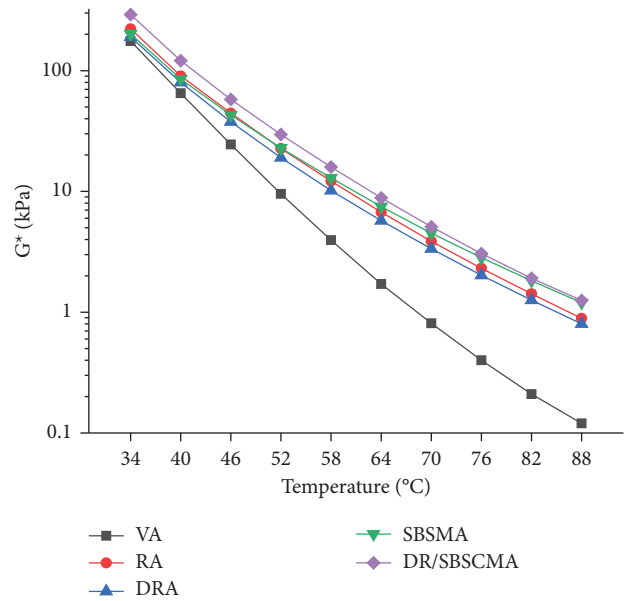
Figure 6: Relationship between complex shear modulus and temperature.
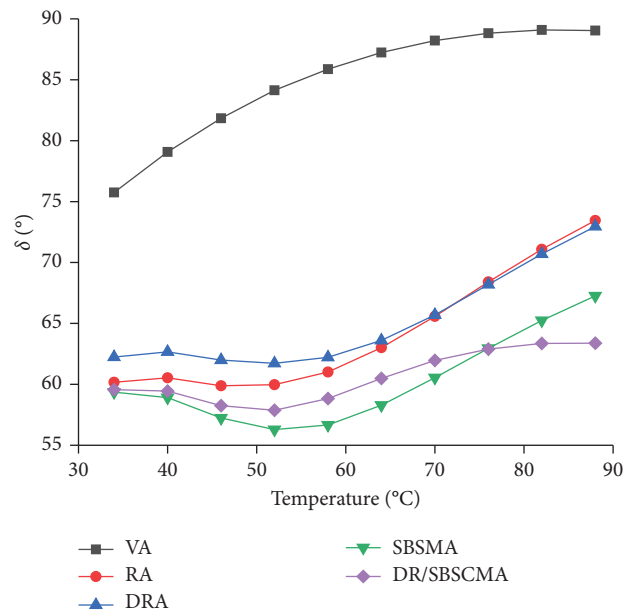
Figure 7: Relationship between the phase angle and temperature.

phase angles of four types of modified asphalt became significantly smaller at the same temperature, indicating that the addition of the modifier improved the elastic properties of the asphalt system, and showed a trend of first decreasing and then increasing with an increase in temperature. In the lower temperature range, the change in the phase angle was relatively gentle. At this time, the phase angle trend was VA > DRA > RA > DR/SBSCMA > SBSMA; when temperature exceeded 70°C, SBSMA, RA, and DRA had similar growth trends, while DR/SBSCMA was still growing slowly, and the phase angle trend at this stage was VA > RA > DRA > SBSMA > DR/SBSCMA. In the test

temperature range, high-temperature performance of DR/SBSCMA and SBSMA was better and temperature sensitivity was reduced.

The rutting factor $G*/\sin\delta$ is calculated, and the results are shown in Figure 8.

It can be seen from Figure 8 that the rutting factor gradually decreased exponentially with increasing temperature, and the rutting factor, also called high-temperature stiffness, characterizes the resistance of asphalt to rutting at high temperature. It can be intuitively seen that in the temperature range of 30–50°C, the rutting resistance of the five types of asphalt is DR/SBSCMA > RA > SBSMA > DRA > VA. When it exceeds 50°C, asphalt rutting resistance is DR/SBSCMA > SBSMA > RA > DRA > VA, with DR/SBSCMA having the strongest high temperature performance, followed by SBSMA and RA. As the temperature rises, the performance difference of four types of modified asphalt gradually decreased, and it was also shown that the improvement in high-temperature performance by the composite modification method was better than that in the single modification.

The rutting factor $G*/\sin\delta$ and the improved rutting factor $G*/(\sin\delta)^9$ were further fitted by exponential regression, respectively. The regression curves are shown in Figures 9 and 10, and it can be seen that equations (1) and (2) achieved good fitting results. On this basis, the corresponding critical temperatures of the rutting factor and the improved rutting factor were obtained, respectively, as shown in Table 9.

It can be seen from Table 9 that the difference between the critical temperature of the rutting factor determined by the regression fitting of equations (1) and (2) is not large. Overall, the fitting results of the critical temperature of formula (2) were slightly lower than those of formula (1), and the difference was basically within 3°C. DR/SBSCMA had the highest critical temperature, the strongest antirutting ability, and met the requirements of high temperature classification PG-82, followed by SBSMA, RA, and DRA, which all had the same trend as the softening point index.

The critical temperature of the improved rutting factor is higher than that of the rutting factor, indicating that the improved rutting factor is more sensitive to the phase angle, and the improved rutting factor can be selected when analyzing the difference in the high-temperature performance of modified asphalt. If high-temperature performance requirements are more stringent or the results are more conservative, the rutting factor can be selected and fitted with (2).

3.2.2. Bending Beam Rheometer Test. The creep stiffness modulus S represents the ability of asphalt to resist permanent deformation under low temperature load, and the creep rate m is the rate of change of the stiffness modulus. SHRP stipulates that $S \leq 300.0$ MPa, $m \geq 0.300$, if stiffness is too high, asphalt is brittle and prone to cracks; the thermal stress of asphalt accumulates during the process of temperature reduction, and stiffness changes. The faster the
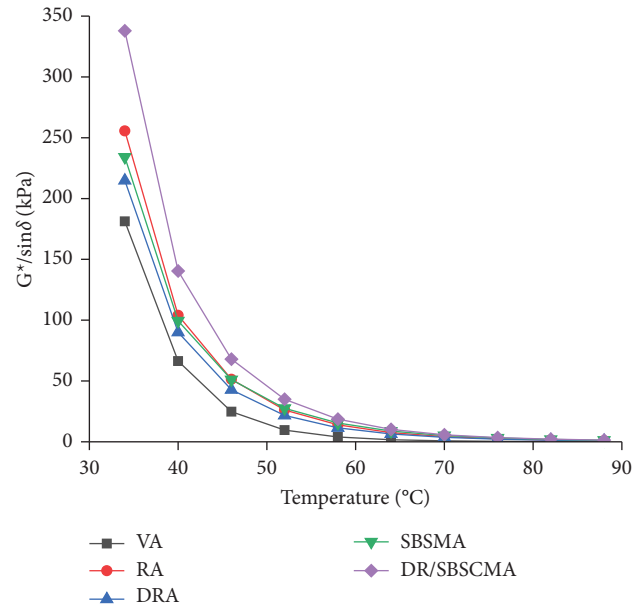
Figure 8: Test results of the rutting factor.

change, the stronger the relaxation stress. Therefore, a high m value and low S value can effectively reduce low-temperature cracking, and both are indispensable.

The creep stiffness modulus and creep rate test results are shown in Figures 11 and 12.

It can be seen from Figure 11 that in the temperature range of $-12\sim-24$°C, except for virgin asphalt, the creep stiffness modulus of four types of modified asphalt all meets the requirements of the specification (less than 300 MPa). Meanwhile, with the decrease in temperature, the stiffness modulus shows a gradual upward trend, and the increase range is quite different. DR/SBSCMA and SBSMA have the same growth trend. When temperature is higher than -18°C, the growth rate of the stiffness modulus is relatively slow, and after temperature is lower than -18°C, the amplitude increases greatly. DRA and RA are completely opposite and gradually tend to be flat when temperature is lower than -18°C. After compound modification, DR/SBSCMA did not show obvious rubber-like asphalt properties in terms of low-temperature rheological properties, which further indicated that there was more than physical swelling reaction between desulfurized rubber powder, SBS, and asphalt.

It can be seen from Figure 12 that with the decrease of temperature, the creep rate gradually decreases. At -18°C, several types of asphalt meet specification requirements. At -24°C, only DRA and DR/SBSCMA meet specification requirements. The creep rate from large to small is DRA > DR/SBSCMA > RA > SBSMA > VA. The addition of the rubber powder modifier significantly improved the elasticity of the asphalt system, enabling it to respond quickly and relax the stress in the face of thermal stress concentration, thereby reducing the possibility of cracking.

Based on the test results of the creep stiffness modulus and creep rate, low-temperature rheological properties from best to worst are DRA > DR/SBSCMA > RA > SBSMA > VA.
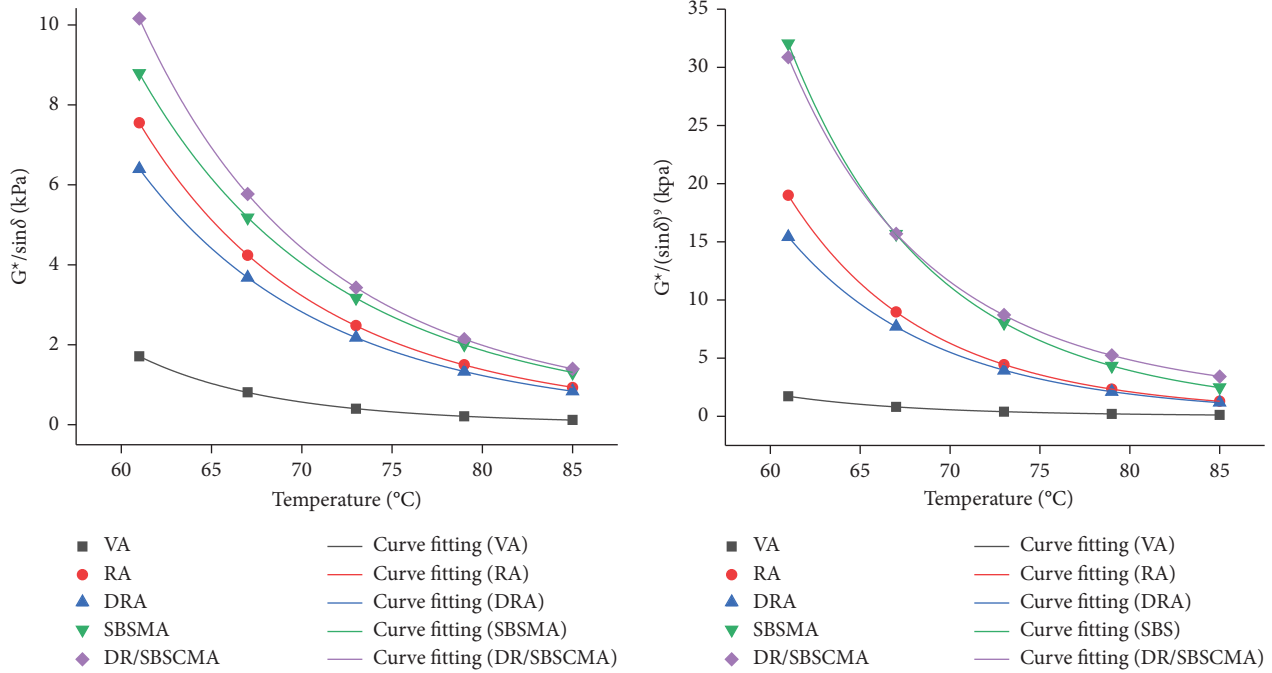
Figure 9: Equation (1) fitting regression curve.
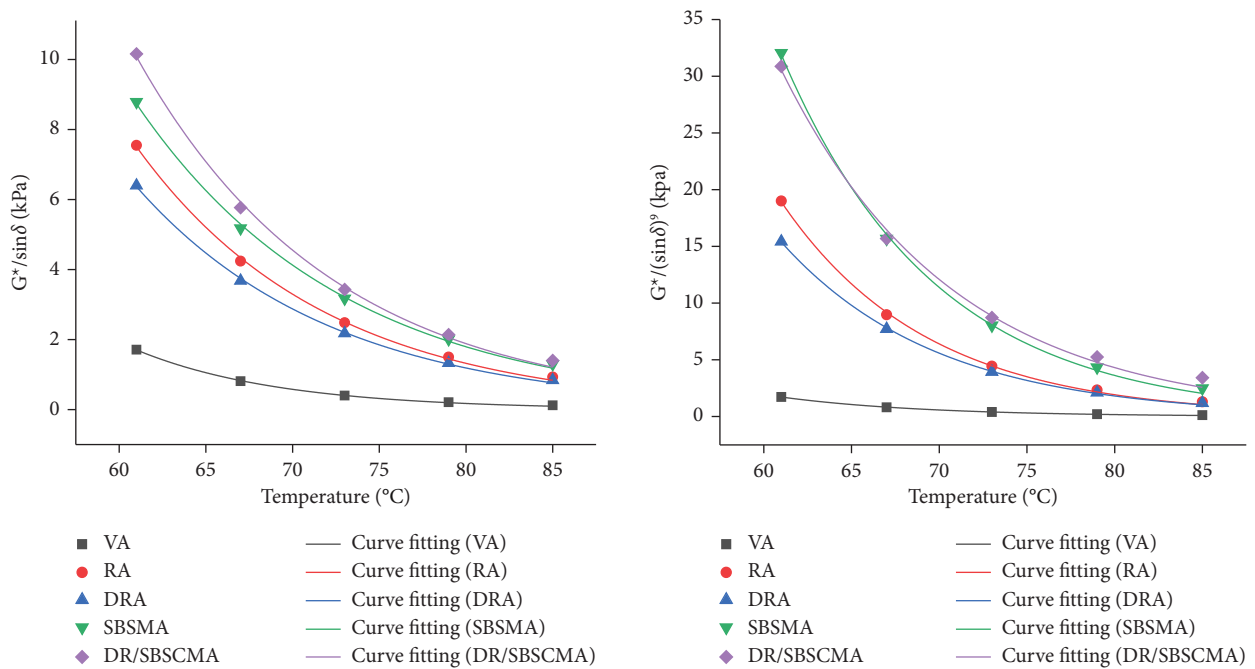
Figure 10: Equation (2) fitting regression curve.

Combined with the dynamic shear rheological test, PG grades were carried out, and DR/SBSCMA was PG82-34, DRA was PG76-34, SBSMA was PG82-28, RA was PG82-28, and VA was PG64-22.

3.3. Research on the Pavement Performance of Mixture

3.3.1. High-Temperature Stability. The high-temperature stability of asphalt mixture is mainly reflected in the ability of the pavement to resist rutting when the pavement is subjected to traffic loads during the high-temperature process in summer. The rutting test results are shown in Figure 13.

From Figure 13 it can be seen that the dynamic rut stability of four modified asphalt mixes far exceeds the requirements of more than 3000 or 5000 times/mm in the specification. Moreover, DR/SBSCMA had excellent high temperature stability for both AC-13 and SMA-13 compounds, as they both improved to varying degrees compared

TABLE 9: Test results of critical temperature.

Type	$G * /\sin\delta$ critical temperature (°C)		$G * /(\sin\delta)^9$ critical temperature (°C)	
	Equation (1)	Equation (2)	Equation (1)	Equation (2)
VA	65.25	65.43	65.30	65.49
RA	84.12	83.05	87.81	85.43
DRA	82.67	81.95	86.71	85.29
SBSMA	89.06	87.02	95.99	91.25
DR/SBSCMA	90.29	87.17	111.44	94.19
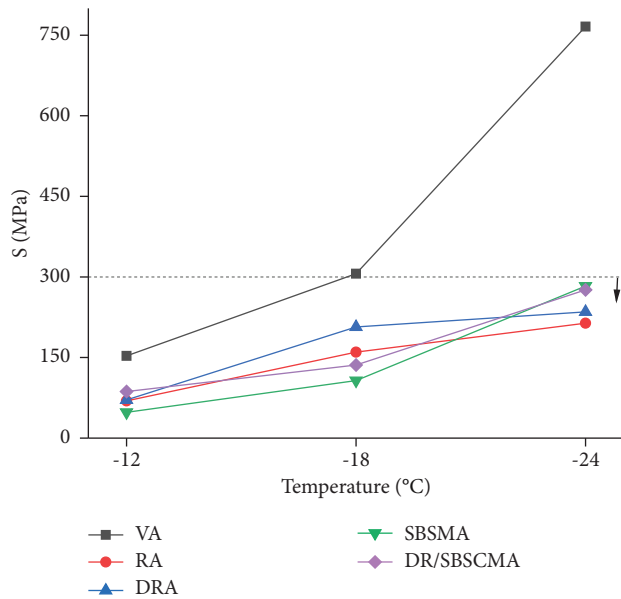
FIGURE 11: Creep stiffness modulus test results.

to other types of modified asphalt, and rut deformation was also effectively improved, indicating that the composite modification of desulfurized rubber powder and SBS can effectively improve mixtures' resistance to high temperature and load capacity. When continuously rated to AC-13, the dynamic stability of composite-modified asphalt was 24.3%, 7.0%, and 5.0% higher than that of RA, DRA, and SBSMA, respectively. With SMA-13 discontinuous grading, the dynamic stability of composite-modified asphalt mixture reaches 8664 times/mm, which is 5.2% higher than that of SBS-modified asphalt mixture. This shows that composite-modified asphalt has a more obvious effect on improving high-temperature stability in batch sorting and has more performance advantages. At the same time, it can be noted that under the same type of asphalt, the dynamic stability of the SMA-13 compound is significantly higher than that of the AC-13 compound. This is because the gradation composition of the SMA-13 mixture is different, and the aggregate contains coarse aggregates. During the moulding process, aggregates are embedded into a skeletal structure and pores are filled with mastic, which consists of fine aggregates, mineral powder, and asphalt. This special structure has stronger integrity and more strength, showing that SMA-13 connection has better high-temperature stability. In addition, because of high viscosity properties of composite-modified asphalt, there is no need to add lignin fibers into the composite-modified asphalt SMA mixture. When fibers are added, they affect mixing difficulty of mixture and increase production costs.

3.3.2. Low-Temperature Crack Resistance. The low-temperature cracking of asphalt pavements is prone to occur in areas with large temperature difference, and temperature drops, the volume shrinkage of mixture is limited, and temperature stress is generated. The results of the trabecular bending test are shown in Figure 14.

It can be seen from Figure 14 that the elongations at break of four types of modified asphalt in the mixed bending tests AC-13 and SMA-13 all meet the technical requirements. In the AC-13 mixture, rubber asphalt has the highest elongation at break, followed by DR/SBSCMA and SBSMA, and DRA has the lowest elongation at break, indicating that rubber asphalt has the best low-temperature crack resistance. On the other hand, in the SMA-13 mix, the low-temperature crack resistance of SBS-modified asphalt has more performance advantages than that of composite-modified asphalt. For the same type of asphalt, the crack resistance of the SMA-13 compound proved to be better than that of the AC-13 mixture.

Without considering aggregate forces, there are a large number of rubber powder particles due to the special system structure of rubber asphalt. When loaded, the load is mainly concentrated on rubber powder particles, because rubber powder has its own elastic properties, and it can absorb and consume external energy, so it can store a large amount of elastic strain energy, thereby improving the low-temperature crack resistance of rubber asphalt. Since the modified material for composite-modified asphalt and desulfurized rubber asphalt is mainly desulfurized rubber powder, desulfurized rubber powder is easier to swell and decompose into asphalt, different from ordinary rubber powder. The reaction in asphalt is more complete and forms a more stable overall structure with asphalt. At the same time, desulfurized rubber asphalt and composite-modified asphalt are manufactured by the shearing method, considering that different manufacturing methods have a certain influence on it, there are fewer and smaller rubber powder particles in asphalt. Meanwhile, rubber asphalt is produced by agitation methods, and the incompatibility of rubber powder and asphalt leads to a large number of large rubber powder particles in asphalt, which has a positive effect on low-temperature cracking resistance.
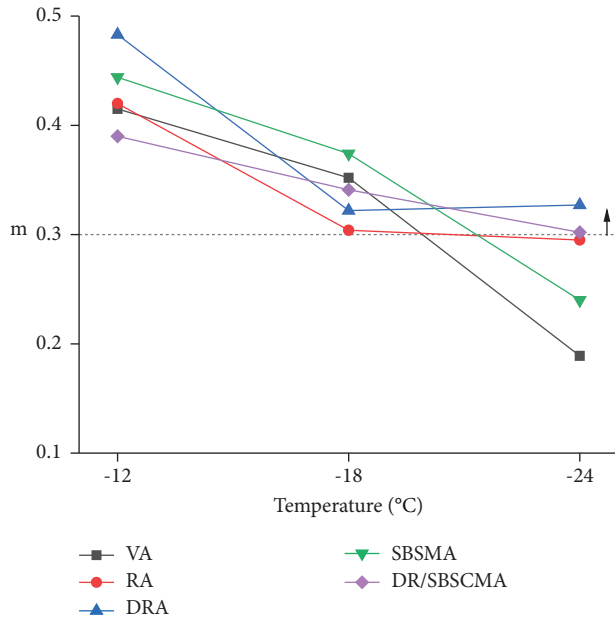
FIGURE 12: Creep rate test results.

FIGURE 14: Results of the bending test of mixture.

FIGURE 13: Results of the mixture rutting test.

In the low-temperature flexural test, rubber-modified asphalt has higher fracture stress than SBS-modified asphalt, indicating that the addition of the rubber-based modifier has a positive effect on stress absorption and is used in the asphalt pavement with high cold crack resistance requirements. When planning, it is recommended that rubber-modified asphalt be used. In addition, rubber asphalt has a better effect on reducing road noise.

3.3.3. Water Stability. Water damage usually means that under the action of rainwater and seasonal freeze-thaw cycles, road surface water enters the interior of the pavement structure through cracks or the dynamic water pressure of the load. Under the action of water and load, the adhesion between asphalt and aggregate is gradually weakened. Then, they are separated from each other and damaged. The results of immersion Marshall and freeze-thaw split tests are shown in Figure 15.

From Figure 15, it can be seen that the residual stability ratios in water immersion from large to small are DR/SBSCMA > SBSMA > DRA > RA. The residual stability of four types of modified asphalts meets the specification requirements. In AC-13 and SMA-13 mixtures, the residual stability of the composite-modified asphalt mixture exceeded 95%, and especially, in the AC-13 mixture, the residual stability of composite-modified asphalt reached 98%. This shows that it has excellent water damage resistance and that the compound modification of desulfurized rubber powder and SBS can improve the water stability of the compound. The strength of the mix depends on the cohesiveness of asphalt and the internal friction between minerals. The addition of desulfurized rubber powder and SBS increases the viscosity of asphalt, which improves the interfacial strength between asphalt and aggregates, effectively reducing oil scale detachment, and further improves adhesion and resistance to water damage, ultimately improving the water stability of the mixture.

The improvement of compound-modified asphalt by desulfurized rubber powder and SBS contrasts with other related research on rubber-asphalt mixtures. Usually, water stability is affected by the addition of rubber powder. This is because ordinary rubber powder cannot completely react with asphalt and there are a large number of incompletely dissolved rubber powder particles. As a stress concentration point, it is easy to generate stress concentration and damage. On the other hand, the addition of rubber powder to absorb the light oil and part of paraffin in asphalt increases asphaltic acid and acid anhydride in asphalt, which is beneficial for the adhesion of stone and asphalt. The two effects have a mutually weakening and strengthening effect on water stability.
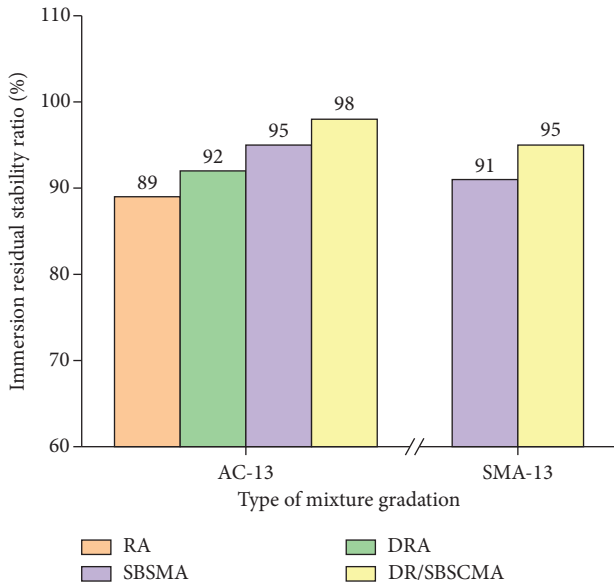
FIGURE 15: Marshall test results of mixture immersion in water.
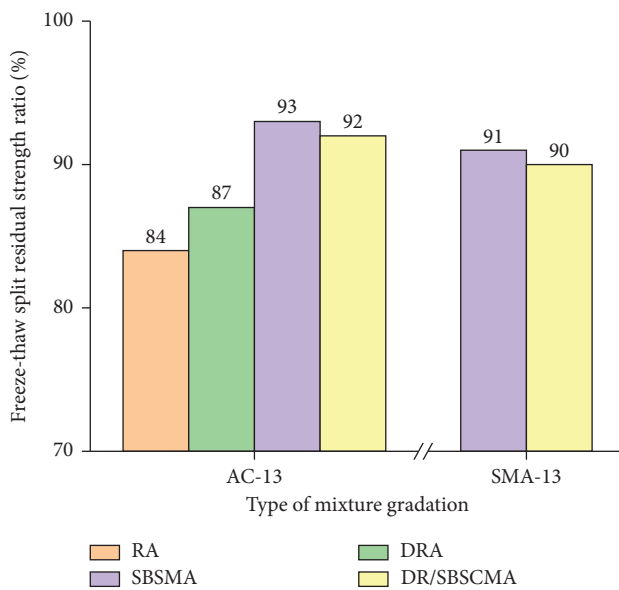
FIGURE 16: Results of the freeze-thaw splitting test of mixture.

The composite-modified asphalt in this study is different from conventional rubber asphalt. The modification process is no longer simple physical swelling but a compatible and stable modification of the coexistence of physical mixing and chemical reaction, forming a more stable three-dimensional network structure, and there is not a large amount of undissolved rubber powder particles. Under the compatible and stable system, mutual flow between molecules is impeded, viscosity increases, cohesion is increased, aggregate encapsulation is stronger, and cohesion is improved, and it has a greater positive effect on water stability.

The freeze-thaw splitting test results are shown in Figure 16.

It can be seen from Figure 16 that the residual strength ratio of freeze-thaw splitting is SBSMA > DR/

SBSCMA > DRA > RA. In the AC-13 and SMA-13 mixtures, the residual strength ratio of the composite-modified asphalt mixture reached more than 90%, which was slightly lower than that of SBS-modified asphalt. The reason for the above results may be that rubber powder particles made asphalt hard at low temperature and viscoelastic properties decreased, thus affecting its water stability.

On the other hand, considering that the curing temperature of the specimens in the immersion Marshall test and the freeze-thaw split test were 60°C and −18°C, respectively, combined with the properties of composite-modified asphalt and SBS-modified asphalt. Composite-modified asphalt had stronger adhesion at a temperature of 60°C; SBS-modified asphalt had stronger rheological and low-temperature properties at −18°C, which are reflected in Sections 3.1 and 3.2. Thus, the different performance trends of composite-modified asphalt and SBS-modified asphalt in the two tests appeared.

Under the same asphalt conditions, the residual stability ratio and the strength ratio of AC-13 mixture are larger than those of SMA-13 mixture, indicating that AC-13 mixture has stronger resistance to water damage, which is closely related to gradation. AC-13 is a continuous dense gradation, which contains more fine aggregates, the flatness and the depth of the surface structure are small, and it is not easy for the surface water to enter the interior of the mixture structure, which reduces the impact of water damage on it. The SMA-13 mixture contains more coarse aggregates, has larger structural depth, and is more likely to accumulate and store water. Under the action of load, small molecular water easily enters the structure and affects water stability.

Based on the above analysis, composite-modified asphalt has water stability equivalent to that of SBS and even surpassed SBS-modified asphalt in the water immersion Marshall test, indicating that the composite modification improved the water damage resistance of the asphalt mixture to a certain extent, and the improvement was more obvious in the AC-13 mixture.

4. Conclusions

In this paper, the rheological properties of desulfurized rubber powder/SBS composite-modified asphalt and the properties of its mixture were studied. The main conclusions are as follows:

(1) DR/SBSCMA is superior to SBSMA, RA, and DRA in terms of ductility and softening point, especially the softening point which reached 90°C, with excellent high temperature performance and tensile strength. In addition, the penetration ofDR/SBSCMA is slightly lower than that of SBSMA, and the viscosity ofDR/SBSCMA is slightly higher than that of SBSMA and DRA but much lower than that of RA.

(2) DR/SBSCMA has higher stiffness and greater deformation resistance under load and has the strongest high-temperature performance, followed by SBSMA and RA. With the increase in temperature, the performance difference of four types of modified

asphalt gradually narrows, showing that the improvement of rheological properties by composite modification is better than that of a single modifier. Low-temperature rheological properties were as follows: DRA > DR/SBSCMA > RA > SBSMA > VA. The comprehensive high- temperature and low-temperature rheological tests were carried out for PG classification, and DR/SBSCMA was found to be PG82-34, DRA was PG76-34, SBSMA was PG82-28, RA was PG82-28, and VA was PG64-22.

(3) DR/SBSCMA maintains excellent high-temperature stability in both AC-13 and SMA-13 mixtures, which is improved to varying degrees compared with other modified asphalt, and rutting deformation is also effectively improved. It has the advantage of high-temperature performance in intermittent grading. The low-temperature cracking resistance of DR/SBSCMA is slightly lower than that of SBS-modified asphalt, but both meet the requirements of the specification. The water stability of DR/SBSCMA is comparable to that of SBS-modified asphalt, reaching more than 90%, which is better than that of RA and DRA, thereby proving its excellent water stability.

Data Availability

No data were used to support this study.

Conflicts of Interest

The authors declare that they have no conflicts of interest.

Acknowledgments

References

[1] I. Rodríguez-Fernández, T. B. Farrokh, M. Chiara Cavalli, L. D. Poulikakos, and M. Bueno, "Microstructure analysis and mechanical performance of crumb rubber modified asphalt concrete using the dry process," *Construction and Building Materials*, vol. 259, 2020.

[2] K.-D. Jeong, S.-J. Lee, S. N. Amirkhanian, and K. W. Kim, "Interaction effects of crumb rubber modified asphalt binders," *Construction and Building Materials*, vol. 24, no. 5, pp. 824–831, 2010.

[3] A. Ghavibazoo, M. Abdelrahman, and M. Ragab, "Effect of crumb rubber modifier dissolution on storage stability of crumb rubber–modified asphalt," *Transportation Research Record*, vol. 2370, no. 1, pp. 109–115, 2013.

[4] F. J. Navarro, P. Partal, F. Martınez-Boza, and C. Gallegos, "Thermo-rheological behaviour and storage stability of ground tire rubber-modified bitumens," *Fuel*, vol. 83, no. 14-15, pp. 2041–2049, 2004.

[5] H. Wang, P. Apostolidis, and J. Zhu, "The role of thermodynamics and kinetics in rubber–bitumen systems: a theoretical overview," *International Journal of Pavement Engineering*, pp. 1–16, 2020.

[6] D. Ge, K. Yan, Z. You, and H. Xu, "Modification mechanism of asphalt binder with waste tire rubber and recycled polyethylene," *Construction and Building Materials*, vol. 126, pp. 66–76, 2016.

[7] S. Kedarisetty, K. P. Biligiri, and J. B. Sousa, "Advanced rheological characterization of Reacted and Activated Rubber (RAR) modified asphalt binders," *Construction and Building Materials*, vol. 122, pp. 12–22, 2016.

[8] M. Xu, J. Liu, W. Li, and W. Duan, "Novel method to prepare activated crumb rubber used for synthesis of activated crumb rubber modified asphalt," *Journal of Materials in Civil Engineering*, vol. 27, no. 5, Article ID 04014173, 2015.

[9] R. Yu, Z. Gong, W. Guo, H. Zhang, and C. Liu, "A novel grafting-modified waste rubber powder as filler in natural rubber vulcanizates," *Journal of Applied Polymer Science*, vol. 133, no. 6, 2016.

[10] V. Tatangelo, I. Mangili, P. Caracino et al., "Microbial desulfurization of ground tire rubber (GTR): characterization of microbial communities and rheological and mechanical properties of GTR and natural rubber composites (GTR/NR)," *Polymer Degradation and Stability*, vol. 160, pp. 102–109, 2019.

[11] L. Asaro, M. Gratton, N. Poirot, S. Seghar, and N. Ait Hocine, "Devulcanization of natural rubber industry waste in supercritical carbon dioxide combined with diphenyl disulfide," *Waste Management*, vol. 118, pp. 647–654, 2020.

[12] L. Filippelli, F. E. Antunes, and L. Gentile, "Rheological performance and NMR structure investigation of ultrasound crumb rubber modified bitumen," *Technical Proceedings of the*, vol. 2014, pp. 214–217, 2014.

[13] S. F. Kabir, R. Zheng, A. G. Delgado, and E. H. Fini, "Use of microbially desulfurized rubber to produce sustainable rubberized bitumen," *Resources, Conservation and Recycling*, vol. 164, Article ID 105144, 2021.

[14] D. L. Presti, M. A. Izquierdo, and A. J. del Barco Carrión, "Towards storage-stable high-content recycled tyre rubber modified bitumen," *Construction and Building Materials*, vol. 172, pp. 106–111, 2018.

[15] I. M. Ibrahim, E. S. Fathy, M. El-Shafie, and M. Y. Elnaggar, "Impact of incorporated gamma irradiated crumb rubber on the short-term aging resistance and rheological properties of asphalt binder," *Construction and Building Materials*, vol. 81, pp. 42–46, 2015.

[16] B. Singh, L. Kumar, M. Gupta, M. Chauhan, and G. Chauhan, "Effect of activated crumb rubber on the properties of crumb rubber-modified bitumen," *Journal of Applied Polymer Science*, vol. 129, no. 5, pp. 2821–2831, 2013.

[17] Y. Sheng, H. Li, J. Geng, Y. Tian, Z. Li, and R Xiong, "Production and performance of desulfurized rubber asphalt binder," *International Journal of Pavement Research and Technology*, vol. 10, no. 3, pp. 262–273, 2017.

[18] K. Shatanawi, S. Biro, C. Thodesen, and S. Amirkhanian, "Effects of water activation of crumb rubber on the properties of crumb rubber-modified binders," *International Journal of Pavement Engineering*, vol. 10, no. 4, pp. 289–297, 2009.

[19] H. H. Kim, M. Mazumder, M. S. Lee, and S. J. Lee, "Evaluation of high-performance asphalt binders modified with SBS, SIS, and GTR," *Advances in Civil Engineering*, vol. 2019, Article ID 2035954, 11 pages, 2019.

[20] H. H. Kim, M. Mazumder, and M. S. Lee, "Laboratory evaluation of SBS modified asphalt binder containing GTR, SIS, and PE," *Advances in Civil Engineering*, p. 2020, 2020.

[21] A. Behnood and J. Olek, "Rheological Properties of Asphalt Binders Modified with Styrene-Butadiene-Styrene (SBS), Ground Tire Rubber (GTR), or Polyphosphoric Acid (PPA)," *Construction and Building Materials*, vol. 151, pp. 464–478, 2017.

[22] M. Ameri, M. Reza Seif, M. Abbasi, and A. Khavandi Khiavi, "Viscoelastic fatigue resistance of asphalt binders modified with crumb rubber and styrene butadiene polymer," *Petroleum Science and Technology*, vol. 35, no. 1, pp. 30–36, 2017.

[23] R. T. Rasool, S. Wang, and Y. Zhang, "Improving the aging resistance of SBS modified asphalt with the addition of highly reclaimed rubber," *Construction and Building Materials*, vol. 145, no. AUG.1, pp. 126–134, 2017.

[24] R. T. Rasool, P. Song, and S. Wang, "Thermal analysis on the interactions among asphalt modified with SBS and different degraded tire rubber," *Construction and Building Materials*, vol. 182, no. SEP.10, pp. 134–143, 2018.

[25] Q. Ma, Z. Guo, P. Guo, F. Yang, and H. Li, "Research on the viscosity-temperature properties and thermal stability of stabilized rubber powder modified asphalt," *Sustainability*, vol. 13, no. 24, Article ID 13536, 2021.

[26] H. Chen and B. Wang, "Modification of rutting factor of styrene butadiene styrene block copolymer modified-asphalt," *Journal of Tongji University*, no. 10, pp. 1384–1387+1403, 2008.

Research Article

Repeated Uniaxial Compression Test of Permeable Friction Courses Mixtures under Seepage Field and Stress Field Coupling

Zhang Xingmei,[1,2] Li Yarui,[1] and Yang Datian (ID)[1]

[1]*College of Civil Engnieering, Chongqing Jiaotong University, Chongqing 400074, China*
[2]*Chongqing Radio and TV University, Chongqing 400052, China*

Correspondence should be addressed to Yang Datian; tywoyangda@cqjtu.edu.cn

In order to study the variations of the non-Darcy flow permeability coefficient and the porosity of permeable friction courses (PFCs), as well as the effects of the coupled seepage and stress fields on them, repeated uniaxial compression tests were carried out under the coupled action of water and a load. A set of water and load coupling tests were conducted, and a non-Darcy flow permeability coefficient tester was also made. After the PFC-13 specimen was carried out by the repeated uniaxial compression test under the water and load coupling, the total air void ratio and effective air void ratio were measured by the vacuum sealing method, and the non-Darcy flow permeability coefficients were obtained by a non-Darcy flow permeability coefficient tester. It was found that the coupled action of water and a load caused the total air void ratio, effective air void ratio, and permeability coefficient to sharply increase and reduced the number of repeated uniaxial compression cycles. These results are helpful for the design, construction, and maintenance of PFC mixtures.

1. Introduction

Permeable friction courses (PFCs) [1] are a new generation of open-graded friction courses (OGFCs). PFCs typically contain at least 20% more asphalt binder (by volume) than conventional OGFC mixtures. PFCs contain 18%–22% air voids, whereas conventional OGFC mixtures only contain 10%–15% air voids [2]. Unlike conventional OGFCs, PFCs typically contain polymer fibers [1].

PFCs have many advantages, but durability is a critical issue. The existing standard methods to evaluate the durability of PFCs typically only include the Cantabro loss [3, 4], the indirect tensile (IDT) strength [3, 4], and the Hamburg wheel tracking test (HWTT) [5].

Poulikakos et al. used a coaxial shear test and wheel tracking tests to investigate the mechanical properties of porous asphalt mixtures [6]. Because PFC mixtures have large air voids, the freeze-thaw process cannot cause internal damage, and therefore, the indirect tensile strength is less

likely to decrease. At the same time, there is water in the voids, which influences the Cantabro loss in the Cantabro test. Huang et al. [7] used fracture energy to evaluate the durability of porous asphalt mixture.

The coaxial shear test and Hamburg wheel tracking test can simulate a load and the influence of water and temperature. However, water does not flow in the pores, and thus, the test cannot reflect the seepage process of rainwater in the pores. Yang and Zhou [8] investigated the immersion fatigue of a dense asphalt mixture and found that the effect of static and dynamic water on the fatigue lives of asphalt mixtures was not significant.

The main causes of asphalt pavement damage are a heavy load and repeated rolling. In addition, excess-pressure pore water is also an important factor causing asphalt pavement damage. The existence of moisture significantly affects the material properties of the asphalt mixture, and it changes the mechanical response of the asphalt mixture under a load. In the process of water seepage, the change of the seepage field
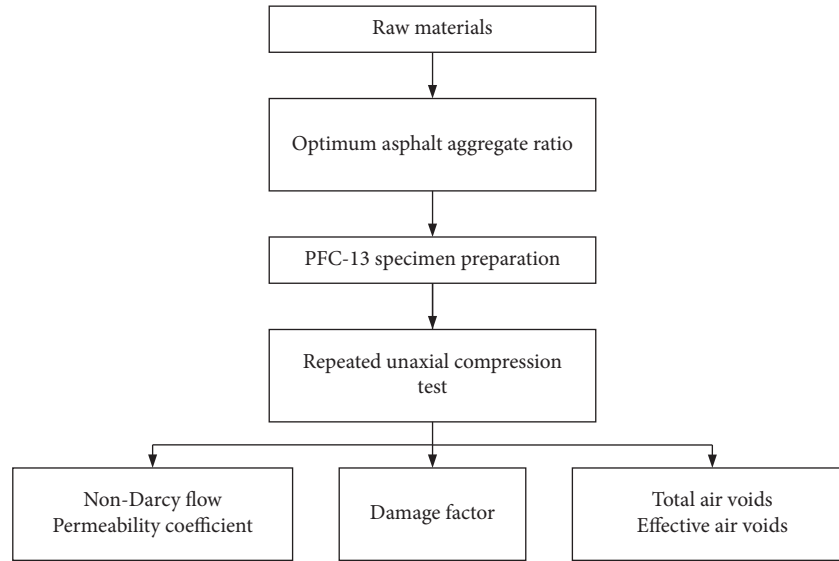
FIGURE 1: Flowchart of study materials and corresponding test methods.

leads to the redistribution of stress in the mixture. At the same time, due to the change in stress, the void ratio and void volume will also be affected.

Kringosn et al. [9] believed that water intruded into the gaps between the asphalt and aggregate and produced a pumping effect under a load, resulting in water damage, and they established a fluid-solid coupling model based on this. Si et al. [10] established a viscoelastic constitutive equation of asphalt and a finite element model of asphalt pavement, deduced the stress seepage coupling equation of asphalt pavement, and verified the effectiveness of the model. Ding and Wang [11] analyzed the mechanical response of saturated asphalt pavement under the coupling of a seepage field and a stress field.

Sun et al. [12] studied the dynamic response of unsaturated permeable asphalt pavement under a moving load with a three-dimensional finite element model with the coupling of water, air, and forces based on unsaturated seepage theory. Si et al. [13] computed the mechanical response of asphalt pavement under rainfall with the finite element method.

From above the papers, it was found that the variations of non-Darcy flow permeability coefficient and the porosity of permeable asphalt mixture samples, as well as the effects of the coupled seepage and stress fields on them, have been less studied after repeated uniaxial compression tests.

In this paper, first, the optimal asphalt-aggregate ratio was determined by a draindown loss test. Second, PFC-13 specimens were formed by a gyratory compactor. Water and load coupling tests were conducted, and non-Darcy flow permeability tests were also conducted. After the specimens underwent repeated uniaxial compression tests under the coupled action of water and a load, the total air void and effective air void ratios were measured by a vacuum sealing method, and the non-Darcy flow permeability coefficients were obtained by a non-Darcy flow permeability tester. The materials and corresponding test methods used in this study are summarized as a flowchart in Figure 1.

2. Materials

2.1. High-Viscosity Polymer-Modified Asphalt. The high-viscosity polymer-modified asphalt composed of a high-viscosity polymer modifier and styrene-butadiene-styrene (SBS) polymer-modified asphalt, and they were mixed together and sheared for 30 min at 4000–5000 r/min and 180°C [14]. The technical properties [15] are shown in Table 1.

2.2. Aggregate

2.2.1. Coarse Aggregate. Hard sandstone aggregate was used to form a skeleton contact structure of the coarse aggregate. The technical properties [2] are shown in Table 2.

2.2.2. Fine Aggregate. The fine aggregate used was limestone-manufactured sand. The technical properties [2] are shown in Table 3.

2.3. Filler. The filler was limestone powder, which could significantly enhance the adhesion between the aggregate particles [2]. The technical properties are shown in Table 4.

2.4. Fiber Stabilizer. Polyester fiber does not absorb water, which is helpful in improving the moisture stability of PFC mixtures. At the same time, the polyester fiber was easily dispersed during the mixing process. Hence, polyester fibers with lengths of 9 mm and diameters of 15 μm were used.

3. Aggregate Gradation and Optimal Asphalt-Aggregate Ratio

3.1. Aggregate Gradation. The 10–15 mm coarse aggregate, 0–5 mm fine aggregate, and the filler were sieved. Their results are shown in Table 5. According to the technical

TABLE 1: Technical properties of high-viscosity polymer-modified asphalt.

No.	Item	Unit	Requirements	Results
1	Penetration degree (25°C, 100 g, 5 s)	0.1 mm	40–60	48
2	Ductility (5°C, 5 cm/min)	cm	≥ 35	47
3	Softening point $T_{R\&B}$	°C	≥ 85	97
4	Capillary dynamic viscosity, 60°C	kPa·s	400–800	509.6
5	Viscosity, 25°C	N·m	≥ 25	53.3
6	Toughness, 25°C	N·m	≥ 20	35.0
7	Elastic recovery, 25°C	%	≥ 90	99.3

TABLE 2: Technical properties of hard sandstone aggregate.

No.	Item	Unit	Requirements	Results
1	Stone crushing value	%	≤ 24	9.5
2	Los Angeles abrasion loss	%	≤ 26	10.4
3	Apparent relative density	—	≥ 2.60	2.912
4	Water absorption	%	≤ 2.0	0.8
5	Robustness	%	≤ 12	1.3
6	Flatness, elongated particles	%	≤ 10	9.0
7	Particle content smaller than 0.075 mm	%	≤ 1	0.6
8	Soft stone content	%	≤ 1.0	0
9	Polishing value	PSV	≥ 42	52
10	Adhesion level for asphalt	—	Level 5	Level 5

TABLE 3: Technical properties of limestone machine-made sand.

No.	Items	Unit	Requirements	Results
1	Apparent relative density	—	≥ 2.60	2.912
2	Particle content smaller than 0.075 mm	%	≤ 1	0.6

TABLE 4: Technical properties of limestone filler.

No.	Item	Unit	Requirements	Results
1	Apparent relative density	—	≥ 2.60	2.723
	Particle size range	—	—	—
	< 0.6 mm	%	100	100
2	< 0.3 mm	%	95–100	99.8
	< 0.15 mm.	%	90–100	95.4
	< 0.075 mm	%	75–100	79.9

requirements [15], the combined aggregate gradation of PFC-13 is shown in Table 6.

3.2. Optimal Asphalt-Aggregate Ratio.

First, five groups of PFC-13 mixtures were prepared according to the suggested asphalt-aggregate ratio of ±0.5%. Second, the draindown losses of the PFC-13 mixtures were measured. Finally, fitted power function curves were obtained. Two tangent lines, labeled l and m, were drawn, which intersected at point A. The straight line labeled o bisected the angle φ and intersected the fitted curve at point B. Through point B, the vertical straight line n of the horizontal axis (asphalt-stone ratio) was drawn and intersected at point D. The value corresponding to point D was the optimal asphalt-stone ratio [15], as shown in Figure 2. According to Figure 2, the optimal asphalt-aggregate ratio was 5.1%.

4. Repeated Uniaxial Compression Test of Seepage and Stress Field Coupling

A seepage field is a water flow field in which water with a certain flow velocity flows from a porous medium. If there is no other load coupled with it, the water seepage field is a hydrostatic seepage field, and hydrostatic pressure is applied to the pore walls [16]. The stress field is due to an applied external load on the top surface of the sample, which acts on the sample and generates a stress field in the porous medium. For a porous medium similar to a permeable asphalt mixture, this stress field is borne by the particle skeleton around the pores.

When a seepage field and a stress field are generated simultaneously in the porous medium, the seepage-stress coupled field is formed in the porous medium. In order to simulate the damage of the permeable asphalt mixture specimen caused by the coupling of seepage and stress fields, a system for performing repeated uniaxial compression tests under the coupling of a seepage field and a stress field was designed and fabricated, as shown in Figure 3. The water flow volume, which was coupled with the stress field, was about 5 L/h [17]. This simulated the non-Darcy flow seepage of a rainstorm in permeable asphalt mixture pavement, forming a seepage field.

As shown in Figure 3, the seepage field was established with a water pump, transparent rubber pipe, flowmeter, loading permeable plate, and water tank. The red circle

TABLE 5: Aggregate sieving analysis.

| Aggregate size | Sieve size | | | | | | | | | |
| | 16 | 13.2 | 9.5 | 4.75 | 2.36 | 1.18 | 0.6 | 0.3 | 0.15 | 0.075 |
	Percentage of weight passing (%)									
10–15	100.0	93.0	14.5	1.2	1.2	1.0	1.0	1.0	1.0	1.0
0–5	100.0	100.0	100.0	100.0	84.2	59.3	40.3	25.5	18.3	14.5
Filler	100.0	100.0	100.0	100.0	100.0	100.0	100.0	99.8	95.4	79.9

TABLE 6: Combined aggregate gradation of PFC-13.

| Gradation | Percentage of weight passing (%) | | | | | | | | | |
	16	13.2	9.5	4.75	2.36	1.18	0.6	0.3	0.15	0.075
Gradation two	100.0	94.1	27.3	16.0	13.9	10.6	8.1	6.2	5.2	4.4
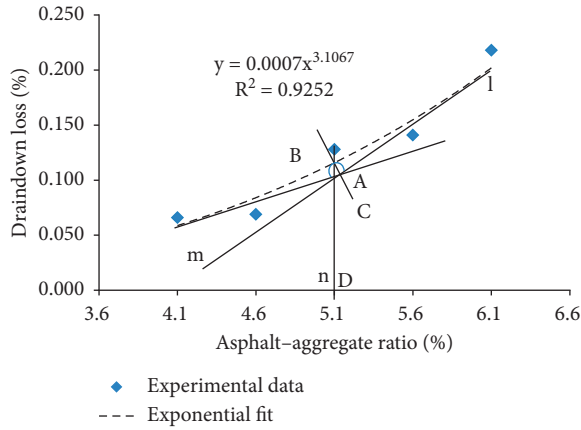
FIGURE 2: Draindown loss vs. asphalt-aggregate ratio.

highlights the water flowmeter. Water seeped into the permeable asphalt mixture specimen through the water flowmeter and a loading plate to simulate the seepage process of rainwater in the permeable asphalt mixture pavement. To describe the process of the seepage and stress field coupling, a schematic diagram of the coupling test is shown in Figure 4.

As shown in Figure 4, water percolated into the permeable asphalt mixture specimen at a certain flow rate, and a seepage-stress coupled field was formed in the permeable asphalt mixture specimen together with the load on the top of the specimen to jointly load the permeable asphalt mixture specimen. The impermeable metal floor simulated the impermeable layer. Water seeped out from the side wall of the permeable asphalt mixture specimen and the top part of the impermeable metal base plate.

5. Non-Darcy Flow Permeability Coefficient of Compacted Permeable Asphalt Mixture

In order to obtain the non-Darcy flow permeability coefficient (or hydraulic conductivity) of the compacted permeable asphalt mixture, a non-Darcy flow permeability tester was designed and fabricated. Its design sketch is shown in Figure 5, and Figure 6 shows a photograph of the actual system.

Based on Figure 5, the water heads at ϕ_1 and ϕ_2 can be expressed as

$$\phi_1 = z_1 + \frac{P_1}{\rho g}, \tag{1}$$

$$\phi_2 = z_2 + \frac{P_2}{\rho g}, \tag{2}$$

where Z_1 is the water head at the position of the inlet section of the sample with respect to the reference plane 0–0, Z_2 is the water head at the position of the outlet section of the sample with respect to the reference plane 0–0, P_1 is the water pressure on the inlet section of the sample, whose value is equal to the water head of the water column $\phi_1 - Z_1$, P_2 is the water pressure on the outlet section of the sample, whose value is equal to the water column $\phi_2 - Z_2$, ρ is the density of water, generally taken as $1.0 \times 10^3 \text{ kg/m}^3$, and g is the gravitational acceleration, generally taken as 9.81 m/s^2.

The rate of water flow Q (volume per unit time) is equal to the product of the average seepage velocity u and the constant cross-sectional area A, i.e.,

$$u = \frac{Q}{A}, \tag{3}$$

where u is the average seepage velocity of water in the porous medium (m/s), Q is the rate of water flow (volume per unit time) through the porous medium sample (m³/s), and A is the cross-sectional area of the porous medium sample (m²).

Considering the effective porosity φ of the porous media sample [16], (3) is rewritten as

$$u = \varphi \frac{Q}{A}. \tag{4}$$

When water is in a laminar flow state in the porous medium, i.e., Darcy's flow, the permeability coefficient of Darcy's flow [18] is calculated through Darcy's law, as follows:

$$-\frac{\partial P}{\partial X} = \frac{1}{k}\mu u, \tag{5}$$

where P is the pressure (Pa), X is the seepage length of water in the porous medium (m), μ is the dynamic viscosity (the dynamic viscosity of water is 1.01×10^{-3} Pa s at 20°C), u is the
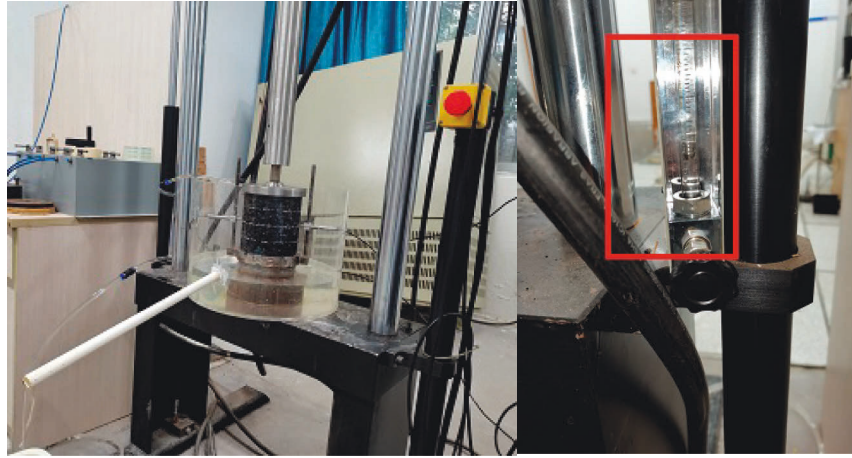
Figure 3: Seepage field-stress field coupling test.
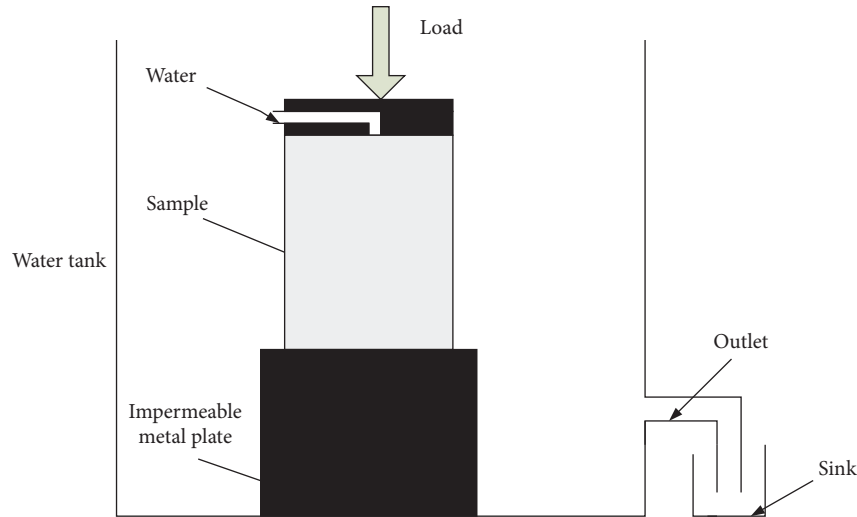
Figure 4: Schematic diagram of the seepage field-stress field coupling test.

average seepage velocity of water in the porous medium (m/s), and k is the hydraulic conductivity (m^2).

Therefore, it is necessary to convert k into a permeability coefficient K (m/s), as follows:

$$K = k\frac{\rho g}{\mu}. \tag{6}$$

According to Figure 5 and equation (6), equation (5) is changed to an expression of the head gradient:

$$-\frac{\Delta\phi}{\Delta X} = \frac{u}{K}. \tag{7}$$

When the effective porosity of the porous medium is large, it is generally considered that the seepage of water in the porous medium is non-Darcy flow and satisfies the Forchheimer equation, which can be expressed using either of the following forms [19, 20]:

$$-\frac{\partial P}{\Delta X} = \frac{\mu u}{k} + \beta\rho u^2, \tag{8}$$

$$-\frac{\partial\phi}{\Delta X} = \frac{u}{K} + \frac{\beta}{g}u^2, \tag{9}$$

where β is the Forchheimer coefficient (1/m). The meanings of the other parameters are the same as above.

The permeability coefficient (or hydraulic conductivity) of the compacted permeable asphalt mixture is obtained based on Figures 5 and 6, equations (1)–(9), and the following test steps:

(1) After the permeable asphalt mixture specimen underwent the repeated uniaxial compression test under seepage and stress field coupling, according to the non-Darcy flow permeability coefficient tester described above, the water drainage volume M at
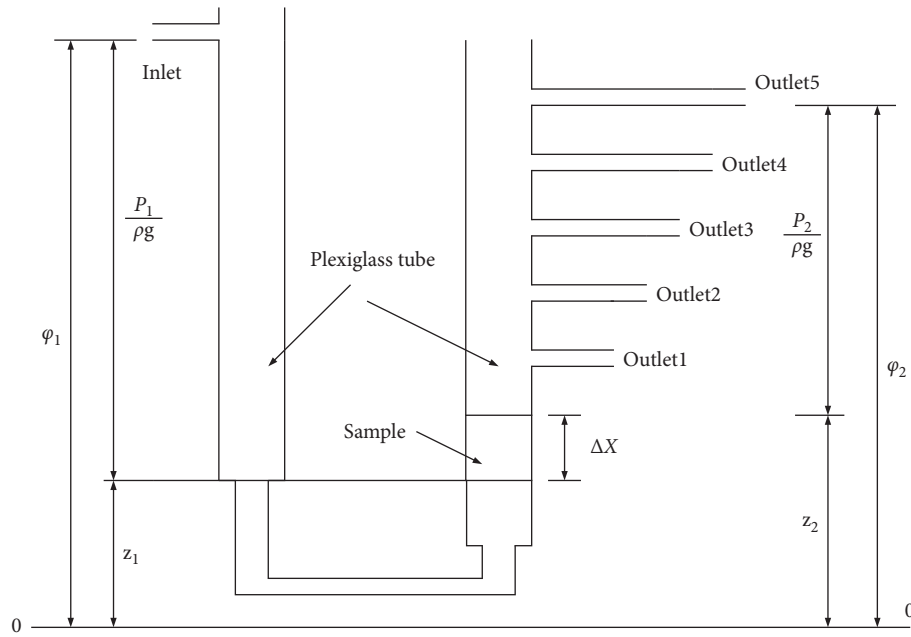
FIGURE 5: Schematic diagram of non-Darcy flow permeability coefficient tester.

FIGURE 6: Non-Darcy flow permeability coefficient tester for compacted PFC-13 specimen.

time t was measured five times. The maximum and minimum values among the five values were removed, whereupon the average value $\overline{M}$ of the remaining three values was calculated.

(2) Q was calculated as follows:

$$Q = \frac{\overline{M}}{t}. \tag{10}$$

(3) The average seepage velocity was calculated using equation (3) or (4)

(4) The water pressure gradient was calculated

(5) The water outlet height was changed, which in turn changed the water pressure gradient

FIGURE 7: Flow velocity vs. water head gradient.

(6) According to steps (1)–(4), five groups of seepage velocities and their corresponding pressure gradients were obtained

(7) Based on equation (8) or (9), the above five sets of data were fitted with a one-variable quadratic equation, as shown in Figure 7

(8) Based on equation (8) or (9), the coefficients of the first-order and second-order terms of the one-variable quadratic fitting equation were converted into a k or K value and a β value.

Based on the fit shown in Figure 7, $\beta\rho = 627.76$ and $\mu/k = 352.87$. The β and k values were calculated according to the density and dynamic viscosity of water: β was 0.628 and k was 2.862×10^{-6}. Based on the k values and (6), k was transformed into K, and K was 27.801 m/s. The test procedure from Step (1) to Step (8) is shown in Figure 8.

From the non-Darcy flow permeability coefficient test, the relationship between the permeability coefficient and
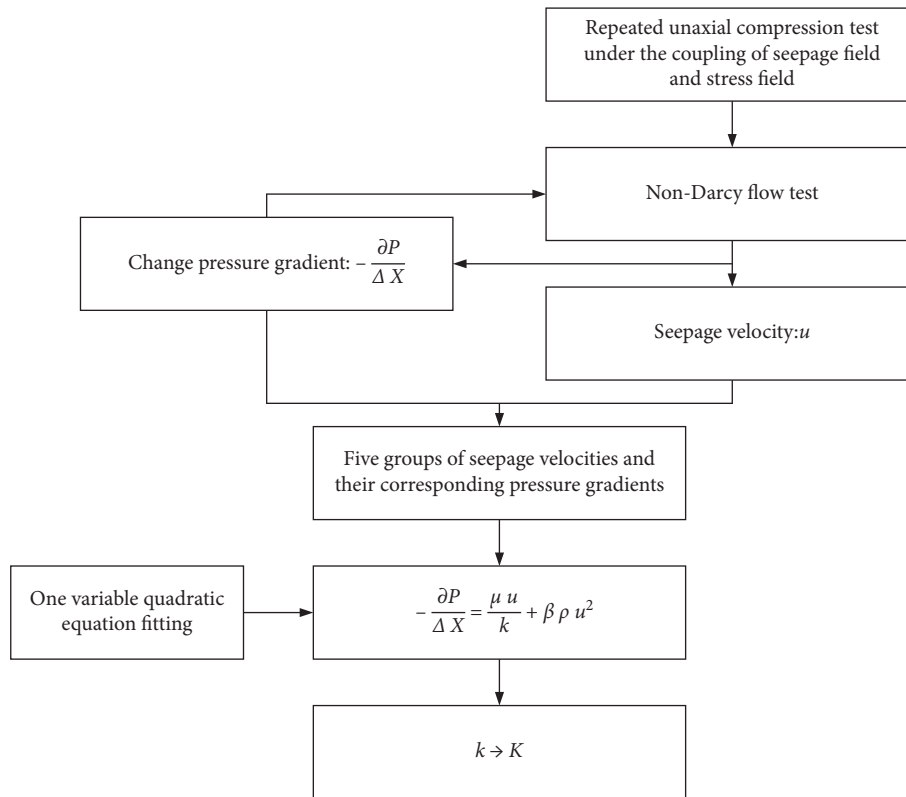
Figure 8: Test process of non-Darcy flow permeability coefficient.
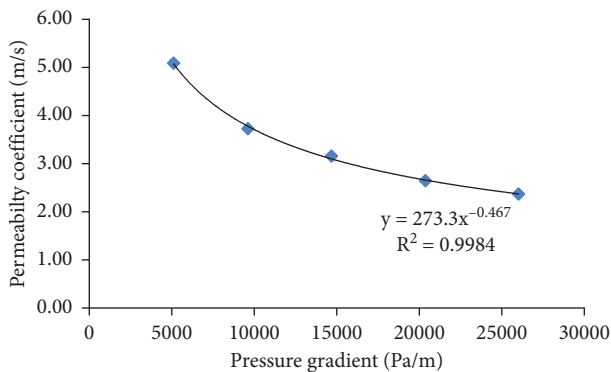
Figure 9: Permeability coefficient vs. pressure gradient.

Figure 10: PFC-13 specimens prepared with a gyratory compactor.

pressure gradient was determined, as shown in Figure 9. The water flow in the permeable asphalt mixture specimen was a typical non-Darcy flow, and the permeability coefficient had a nonlinear relationship with the pressure gradient.

6. Testing Plan

6.1. Preparation of PFC-13 Specimen. According to the combined aggregate gradation and the optimal asphalt-aggregate ratio of the PFC-13 mixture, PFC-13 specimens with 150 mm diameters and 150 mm heights were prepared with a gyratory compactor, as shown in Figure 10.

In this study, the vacuum sealing method was used to measure the bulk-specific densities of the PFC-13 specimens and to calculate the total air void and effective air void ratios, as shown in Figure 11. The results are shown in Table 7. The effective air void ratio was about 5% smaller than the total air void ratio, which fully indicated that there were partially closed pores in the compacted PFC-13 sample, which would not affect its permeability.

6.2. Test Load. The test load of this study was set as a contact pressure between a rubber tire and asphalt pavement of 700 kPa, i.e., a standard contact load. Under the action of the above three contact loads, the variation characteristics of the permeability of the compacted permeable asphalt mixture samples were studied. The load waveform was half a sine wave with a frequency of 10 Hz. After the PFC-13 specimens underwent repeated uniaxial compression under water and
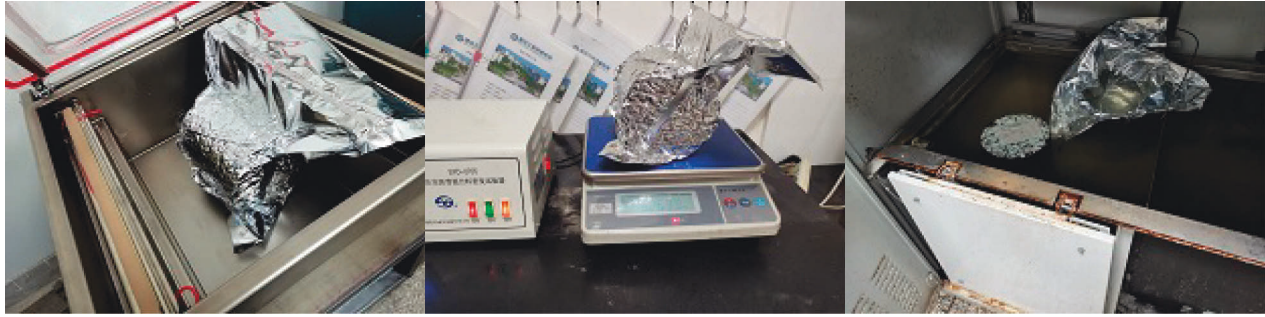
FIGURE 11: Total air void and effective air void ratios determined using the vacuum sealing method.

TABLE 7: Total air void and effective air void ratios of PFC-13 specimens.

No.	Bulk-specific relative density	Theoretical maximum relative density	Total air voids (%)	Effective air voids (%)
1	1.971	2.450	19.6	14.6
2	1.911	2.450	22.0	18.5

load coupling, the total air void ratio, effective air void ratio, sample height, and permeability coefficient were measured.

7. Results and Discussion

In order to reduce the influence of water in the pores on the total air void ratio and especially on the effective air void ratio, after repeated uniaxial compression tests, the samples were first dried by fans. During the drying process, the water in the pores basically flowed out under the dual effects of self-weight and wind. In the process of drying, the sample mass was determined by weighing. If the weight difference between two consecutive times was less than 0.1%, it indicated that the water in the sample flowed out completely.

7.1. Effect of Seepage Field on Damage Factors. In order to compare the influence of the seepage field on the damage factor, the damage factor was calculated as follows:

$$H = \frac{h_0 - h_n}{h_0}, \tag{11}$$

where H is the damage factor, h_0 is the original height of the sample (mm), and h_n is the height of the sample after n cycles of repeated uniaxial compression testing (mm).

Repeated uniaxial compression tests were carried out on PFC-13 specimens under a nonseepage field and a seepage field. Based on (10), the damage factors were calculated, as shown in Figure 12. For the same number of repeated uniaxial compression cycles, namely, 2 million cycles, the damage factor was about 0.006 for the nonseepage field, but the damage factor was about 0.025 for the seepage field. The ratio of 0.025–0.006 was 4.2, indicating that the seepage field along with the stress field heavily accelerated the damage of the PFC-13 specimens.

7.2. Effect of Seepage Flow Field on Total Air Void and Effective Air Void Ratios. In order to eliminate the influence of the initial air voids on the number of repeated uniaxial
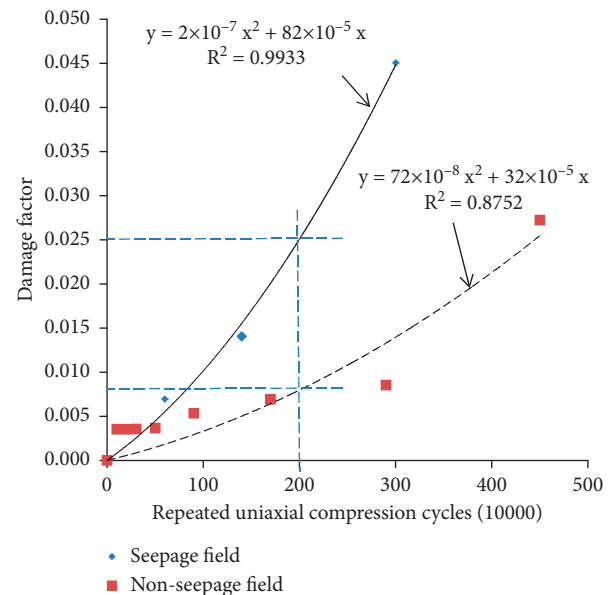
FIGURE 12: Relationship between the number of uniaxial loading cycles and the damage factor.

compression cycles, the total air void and effective air void ratios were measured after each repeated uniaxial compression test and were divided by the initial total air void and effective air void ratios. The ratio of these two sets of data was used to express the change in voids. Then, the relationships between the ratios and the number of repeated uniaxial compression cycles are shown in Figures 13 and 14. It can be seen from Figure 13 that when the total air void ratio was 1%, the number of repeated uniaxial compression cycles for the nonseepage field was about 1.5 times that for the seepage field. It can be seen from Figure 14 that when the effective void ratio was about 1%, the number of repeated uniaxial compression cycles for the nonseepage field was about 1.3 times that of the seepage field.

Therefore, under the coupled action of the seepage field and the stress field, the changes in total air void and effective
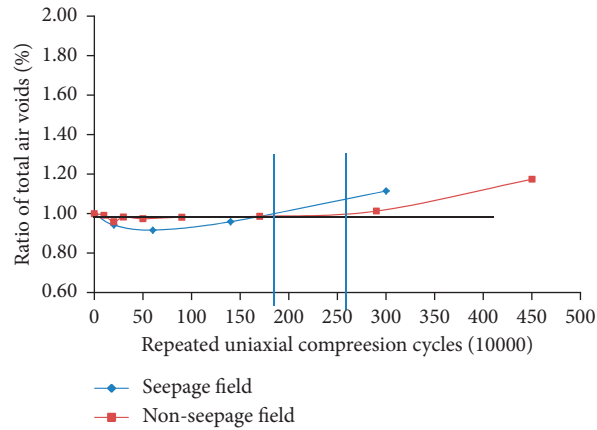
FIGURE 13: Relationship between repeated uniaxial compression cycles and ratio of total air voids.
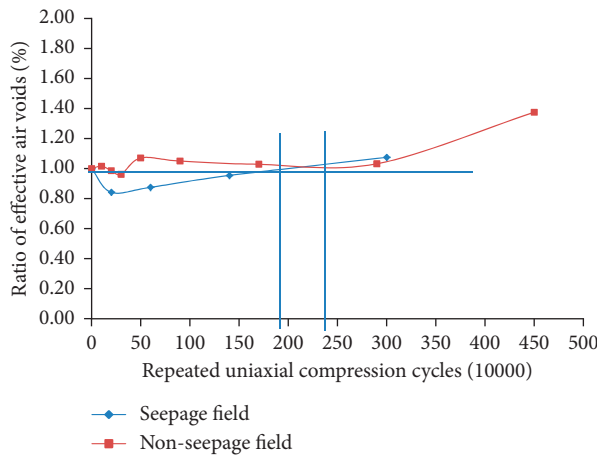
FIGURE 14: Relationship between repeated uniaxial compression cycles and ratio of effective air voids.

air void ratios of PFC-13 were accelerated. At the same time, the total air void and effective air void ratios decreased first and then increased with the increase in the number of repeated uniaxial compression cycles. This showed that the PFC-13 specimen was compacted first and then cracks appeared in the specimen. Then, changes in the displacement of the aggregates began to occur, and the specimen was damaged.

7.3. Effect of Seepage Field on Permeability Coefficient. Figure 15 shows the relationship between the number of repeated uniaxial compression cycles and the non-Darcy flow permeability coefficient. When the permeability coefficients were the same, the seepage field had a great impact on the number of repeated uniaxial compression cycles, and this effect was more significant with the increase in the number of repeated uniaxial compression cycles. When the permeability coefficient was 500 m/s, the number of repeated uniaxial compression cycles with the nonseepage field was about 1-2 times that with the seepage field. Therefore, the coupled effect of the seepage field and the stress field accelerated the water damage of the PFC-13 specimen.
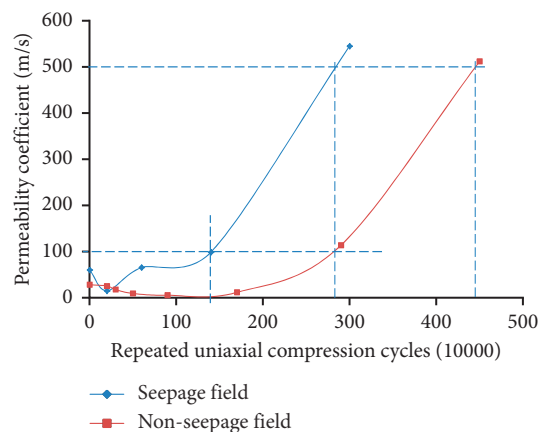
FIGURE 15: Relationship between repeated uniaxial compression cycles and permeability coefficient.

Furthermore, it was found that the non-Darcy flow permeability coefficient decreased first and then increased with the increase in the number of repeated uniaxial compression cycles, which fully showed that the PFC-13 specimen was further compacted first and then gradually

TABLE 8: Repeated uniaxial compression test results with non-seepage field.

Repeated uniaxial compression cycles (10000)	Total air voids (%)	Effective air voids (%)	Damage factor	Permeability coefficient (m/s)
450	23.0	20.1	0.0272	512.243
290	19.8	15.1	0.00855	113.884
170	19.3	15.0	0.00693	11.883
90	19.2	15.3	0.00535	5.525
50	19.1	15.6	0.00367	9.418
30	19.2	14.1	0.00356	17.828
20	18.8	14.4	0.00355	25.648
10	19.4	14.85	0.00355	—
0	19.6	14.6	0	28.339

TABLE 9: Repeated uniaxial compression test results with seepage field.

Repeated uniaxial compression cycles (10000)	Total air voids (%)	Effective air voids (%)	Damage factor	Permeability coefficient (m/s)
300	23.8	19.9	0.0456	545.256
140	20.5	17.7	0.0141	99.128
60	19.6	16.2	0.00698	65.716
20	20.2	15.6	0.00375	15.537
0	22.0	18.5	0	60.310
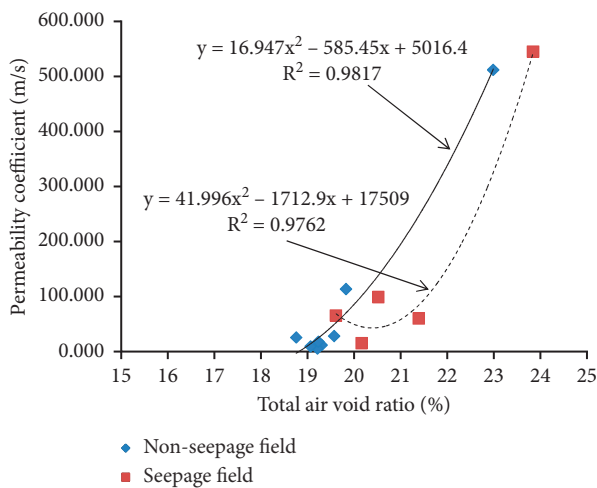
FIGURE 16: Relationship between total void ratio and non-Darcy flow permeability coefficient.
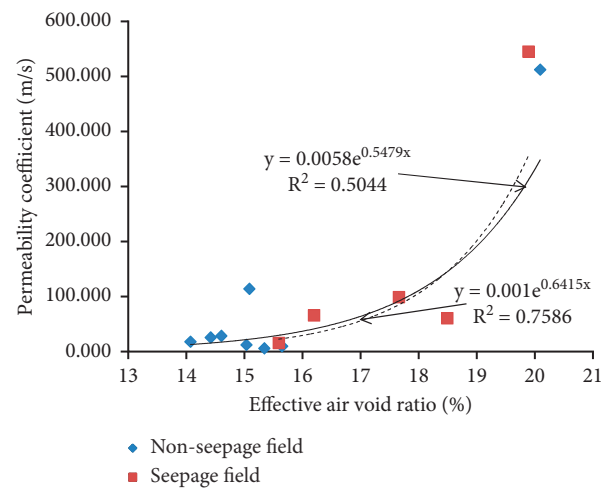
FIGURE 17: Relationship between effective void ratio and non-Darcy flow permeability coefficient.

developed cracks during the repeated uniaxial compression test.

7.4. Relationship between Non-Darcy Flow Permeability Coefficient and Air Voids.

Curves relating the total air void and effective air void ratios to the non-Darcy flow permeability coefficient (Tables 8 and 9) are shown in Figures 16 and 17, respectively. According to Figure 16, the non-Darcy flow permeability coefficient followed a one-dimensional quadratic relation with the total air void percentage. When the total air void percentage exceeded 21.4%, the permeability coefficient increased sharply. Figure 17 shows that the correlation between the permeability coefficient and the effective air voids was adequate, which could be described by an exponential function. The overall variation trend was that the non-Darcy flow permeability coefficient increased with the increase in the effective air void ratio. Similarly, when the

effective air void ratio was about 18.1%, the non-Darcy flow permeability coefficient increased significantly.

8. Conclusions

In this paper, a draindown loss test and power function fitting were used to determine the optimal asphalt-aggregate ratio of a PFC-13 mixture. The coupled action of water and a repeated compression load on PFC-13 specimens was examined. The vacuum sealing method was used to measure the total air void and effective air void ratios. A non-Darcy flow test device was made to measure the permeability coefficients of the PFC-13 specimens. It was found that the damage factor, total air void ratio, effective air void ratio, and permeability coefficient were influenced by the seepage and stress fields under repeated uniaxial compression conditions. The conclusions were as follows:

(1) Under the same number of repeated uniaxial compression cycles, namely, 2 million cycles, the damage factor for the seepage field was about 4.2 times that for the nonseepage field

(2) When the total air void ratio was 1%, the number of repeated uniaxial compression cycles for the specimen without the seepage field was about 1.5 times that of the specimen with the seepage field. When the effective void ratio was about 1%, the number of repeated uniaxial compression cycles of the specimen with the nonseepage field was about 1.3 times that of the sample with the seepage field.

(3) When the permeability coefficient was 500 m/s, the number of repeated uniaxial compression cycles for the specimen with the nonseepage field was about 1-2 times that of the specimen with the seepage field. Furthermore, the non-Darcy flow permeability coefficient decreased first and then increased with the increase in the number of repeated uniaxial compression cycles.

(4) When the total void ratio exceeded 21.4%, the permeability coefficient increased significantly. The effective void ratio was about 18.1%, and the permeability coefficient changed significantly. Therefore, the coupled effect of seepage and stress fields accelerated the water damage of the permeable asphalt pavement. In the permeable asphalt mixture, the water flow was non-Darcy flow.

In the future, after the coupling of the seepage and stress fields, the aggregate structure changes in permeable asphalt mixtures will be studied. The permeability properties and the crack evolutionary process will be explored under the coupled action of multiple factors, namely, seepage, stress, and temperature fields.

Data Availability

The data used to support the findings of this study are included within the article.

Conflicts of Interest

The authors declare that they have no conflicts of interest.

Authors' Contributions

The work presented herein was carried out in collaboration between all the authors. Zhang Xingmei was responsible for the study conception and design. Li Yaru was responsible for data collection and writing. Yang Datian was responsible for the analysis and interpretation of the data. All the authors reviewed the results and approved the final version of the manuscript.

Acknowledgments

Supplementary Materials

In the manuscript, the manuscript was copyedited for English language by LetPub (www.letpub.com), with regard to grammar, punctuation, spelling, and clarity. All of language editors are native English speakers with long-term experience in editing scientific and technical manuscripts. (*Supplementary Materials*)

References

[1] National Academies of Sciences, "Engineering, and medicine," *Constructionand Maintenance Practices for Permeable Friction Courses*, TheNational Academies Press, Washington, DC, 2009.

[2] Ministry of Communications of the People's Republic of China and JTG E20-2011, *Technical Specification for Construction of Highway Asphalt Pavement*China Communications Press Co. LTD., Beijing, China, 2005.

[3] Ministry of Communications of the People's Republic of China and JTG E20-2011, *Standard Test Methods of Bitumen and Bituminous Mixtures for Highway Engineering*China Communications Press Co. LTD., Beijing, China, 2011.

[4] A. Eduardo Alvarez, A. Epps-Martin, C. Estakhri, and R. Izzo, "Evaluation of Durability tests for permeable friction course mixtures," *International Journal of Pavement Engineering*, vol. 11, no. 1, pp. 49–60, 2010.

[5] T. Aashto, *324 Standard Method of Test for Hamburg Wheel-Track Testing of Compacted Asphalt Mixtures*, p. 324, AASHTO Designation, Washington, D.C, 2019.

[6] L. Poulikakos, S. Takahashi, and M. N. Partl, "Coaxial shear test and wheel tracking tests for determining porous asphalt mechanical properties," *Road Materials and Pavement Design*, vol. 8, no. 3, pp. 579–594, 2007.

[7] W. Huang, H. Yu, Yi Lin et al., "Energy analysis for evaluating durability of porous asphalt mixture," *Construction and Building Materials*, vol. 326, no. 4, Article ID 126819, 2022.

[8] D. Yang and Q. Zhou, "Effect of immersion conditions on fatigue life of asphalt concrete," *Road construction machinery and construction mechanization*, vol. 35, no. 3, pp. 54–59+64, 2018.

[9] N. Kringos, T. Scarpas, C. Kasbergen, and P. Selvadurai, "Modelling of combined physical mechanical moisture-induced damage in asphaltic mixes, Part 1: governing processes and formulations," *International Journal of Pavement Engineering*, vol. 9, no. 2, pp. 115–128, 2008.

[10] C. D. Si, E. L. Chen, Z. You, R. Zhang, P. Qiao, and Y. Feng, "Dynamic response of temperature-seepage-stress coupling in asphalt pavement," *Construction and Building Materials*, vol. 211, pp. 824–836, 2019.

[11] Y. M. Ding and H. Wang, "Evaluation of hydroplaning risk of permeable friction course using 3-D grooved tire-water-pavement interaction model," *Int. Assoc. Chin. Infrastruct. Professionals*, vol. 2672, 2018.

[12] Y. Sun, R. Guo, X. Wang, and X. Ning, "Dynamic response characteristics of permeable asphalt pavement based on unsaturated seepage," *International Journal of Transportation Science and Technology*, vol. 8, no. 4, pp. 403–417, 2019.

[13] C. Si, C. Si, F. Yang, and Y. Wang, "Finite element analysis of asphalt pavement on account of stress-seepage coupling field," *Metallurgical and Mining Industry*, vol. 6, pp. 259–266, 2015.

[14] Ministry of Communications of the People's Republic of China and JT/T 860.2-2013, *Modifier for Asphalt Mixture Part 2: High Viscosity Additive*China Communications Press CO. LTD., Beijing, China, 2013.

[15] Chongqing Municipal Commission of Municipal and Rural Construction and DBJ50/T-241-2016, *Technical Specification for Porous Asphalt Pavement*, Chongqing Municipal Commission of Municipal and Rural Construction, Chongqing, China, 2016.

[16] I. Tsvankin, "Handbook of geophysical exploration," *Seismic Exploration*, vol. 31, no. 2, pp. 219–293, 2001.

[17] Q. Li, Q. Zhu, J. Zheng, K. Liao, and G. Yang, "Soil moisture response to rainfall in forestland and vegetable plot in taihu lake basin, China," *Chinese Geographical Science*, vol. 25, no. 4, pp. 426–437, 2015.

[18] B. Jacob, *Dynamics of Fluids in Porous media*, America Elsevier Publishing Company, Inc, New York, NY, 1972.

[19] Z. Zeng and G. Reid, "A Criterion for Non-Darcy Flow in Porous," *Media Transport in Porous Media*, vol. 63, no. 1, pp. 57–69, 2006.

[20] J. S. Wu, H. U. DeZhi, L. I. Wenjun, and C. A. I. Xin, "A review on non-Darcy flow-forcheimer equation, hydraulic radius model, fractal model and experiment," *Fractals*, vol. 24, no. No. 2, p. 13, Article ID 1630001, 2016.

Research Article

Investigation on the Feasibility of Different Semicircular Bend Methods for Asphalt Concrete

Xijie An,[1] Yangpeng Zhang [ID],[2,3,4] Lili Li,[5] and Qinglin Guo [ID][5]

[1]*Inner Mongolia Vocational and Technical College of Communications, Chifeng, Inner Mongolia 024005, China*
[2]*Guangxi Transportation Science & Technology Group Co. Ltd., Nanning 530007, China*
[3]*Guangxi Key Lab of Road Structure and Materials, Nanning 530007, China*
[4]*School of Traffic & Transportation Engineering, Changsha University of Science and Technology, Changsha, China*
[5]*School of Civil Engineering, Hebei University of Engineering, Handan, Hebei 056038, China*

Correspondence should be addressed to Yangpeng Zhang; zhangypgxjk@163.com

Cracking of asphalt pavement is mostly caused by the mixed fracture of asphalt concrete. Determining a simple, repeatable, and accurate method is necessary for evaluating the fracture resistance of asphalt concrete. To explore the mixed fracture performance of asphalt concrete and determine the feasibility of different semicircular bend methods, the mixed fracture performances of asphalt concrete at medium and low temperatures were measured. The mixed fracture modes were realized through changing the position of the support and notch or changing the notch angle. After that, the crack propagating characteristics, crack initiation angle, and fracture toughness were analyzed. Results show that temperature has a significant impact on the fracture path, and crack initiation angle at low temperature follows the generalized maximum tangential stress (GMTS) theory. The measured fracture toughness ratios are lower than the theoretical value of GMTS criterion, but the established empirical model has higher accuracy. In the semicircular bend method, changing the positions of the support and notch is stable and repeatable. Therefore, this method may be preferred to evaluate the mixed fracture performance of asphalt concrete in the future.

1. Introduction

As a major concern of asphalt pavement, cracks seriously affect the service life of the pavement. Accurately evaluating and improving the crack resistance of asphalt concrete is one of the important topics to reduce pavement cracking [1]. Based on the theory of fracture mechanics, the cracking of asphalt concrete is divided into pure tensile failure (mode I), pure shear failure (mode II), and mixed fracture [2].

In the 1980s, Chong and Kuruppu [3] used the semicircular bend test to explore the fracture toughness of rocks in mixed modes for the first time, which provided a new method for studying the mixed fracture properties of materials. The load-displacement curve of the semicircular bend test is stable. The semicircular bend method can be used not only to determine the fracture and fatigue properties of asphalt concrete [4–6] but also to evaluate the low-temperature fracture resistance of asphalt cores from the construction site [7]. The good applicability of this method makes it rapidly popularized in road engineering research. In order to measure the mixed fracture toughness of asphalt concrete, mixed fracture mode is often achieved by adjusting the position of the support and notch or the angle of the notch [8–10]. The fracture characteristics of the specimens through moving the positions of the notch and the support were in good agreement with the theoretical values [11–13].

However, Ameri and Primohammad [14] found that changing the notch angle could easily lead to premature failure at the location around acute angles, and the crack propagation path was inconsistent with the theoretical results while only changing the position of the support, and this phenomenon was more prominent in mode II. It can be seen that, although the semicircular bend test has a good application prospect in the analysis of the fracture

performance of asphalt concrete, the feasibility of different methods is not consistent. Therefore, this work conducts experimental tests on different semicircular bend methods. The applicability and accuracy of different semicircular bend methods were compared, so as to clarify the applicability of various methods to asphalt materials. It will provide a reference for the comprehensive evaluation of asphalt concrete mixed fracture performance.

2. Materials and Methods

2.1. Materials. The asphalt with a penetration grade 70, which is called AH-70#, and basalt aggregate are used to prepare asphalt mixture, and their properties are listed in Tables 1 and 2. The filler is limestone powder. The gradation AC-13, which is recommended by China technical specifications JTG D50-2017, is adopted in this paper, and the gradation curve is shown in Figure 1. According to the Marshall test, the optimal asphalt content is 4.6%, the apparent density of the mixture is 2.43 g/cm^3, and the air void in asphalt mixture is 3.62%. The Marshall specimens with a diameter of 152.4 mm and a height of 95.3 mm were formed by the Marshall method, and then the Marshall specimens were cut to make four semicircular specimens with a thickness of about 45 mm for use according to the work of Guo et al. [15].

2.2. Semicircular Bend Test. In order to realize the mixed fracture of asphalt concrete, this paper designs different fracture modes by adjusting the position, notch angle, and support span. In the field of fracture mechanics, the mixed mode parameter M^e ($0 \leq M^e \leq 1$) is generally used to characterize different fracture modes: $M^e = 1$, it is the pure mode I fracture; $M^e = 0$, it is the pure mode II fracture, and M^e is obtained using the following formula.

$$M^e = \frac{2}{\pi} \arctan\left(\frac{K_I}{K_{II}}\right). \tag{1}$$

In equation (1), K_I is the stress intensity factor of mode I fracture, MPa·m$^{0.5}$, and K_{II} is the stress intensity factor of mode II fracture, MPa·m$^{0.5}$. K_I and K_{II} are calculated using the following equations.

$$\begin{cases} K_I = \frac{P}{2Rt}\sqrt{\pi a}\, Y_I, \\ \\ K_{II} = \frac{P}{2Rt}\sqrt{\pi a}\, Y_{II.} \end{cases} \tag{2}$$

In equation (2), P is the peak load; R is the radius of the specimen; t is the thickness of the specimen; a is the notch length; and Y_I and Y_{II} are geometric parameters, which are only related to the size and can be determined by the finite element method. Based on the existing research results [13], this paper uses the plane stress model to determine Y_I and Y_{II}. The thickness of the model is set to 1 mm, the radius of the semicircular model is 76 mm, the length of the notch is 20 mm, and the elastic modulus in FE analysis is 2000 Mpa. On the basis of studies [12, 14], the influence of Poisson's

TABLE 1: Properties of AH-70# asphalt.

Items	Values	Test methods
Penetration (25°C, 0.1 mm)	68	ASTM D5
Softening point (°C)	48.0	ASTM D36
Ductility (15°C, cm)	>100	ASTM D113
Flashing point (°C)	285	ASTM D92
Mass loss after TFOT, 163°C, 5 hours (%)	0.15	ASTM D6
Penetration ratio after TFOT (%)	78.8	ASTM D5
Ductility after TFOT (cm)	6.5	ASTM D113
Density (g/cm^3)	1.034	ASTM D70

ratio is modest, so this paper uses Poisson's ratio of 0.35 for FEM analysis. The load is set to 1N. After FE analysis, the geometric parameters of different modes are determined and listed in Table 3. Considering the different test methods for mixed mode fracture, 10 typical conditions were selected in this paper.

After determining the position of the notch, a diamond cutting machine was used to make the notch with a width of 2 mm. Before test, the semicircular specimens were kept in a chamber at −10°C and 20°C for more than 24 hours to keep the temperature of specimens stable. Afterwards, the bend test was carried out in 5 minutes using an electrical universal testing machine without environmental box. According to the recommendation of the Chinese specification JTG E20-2011, a loading rate of 1 mm/min is often used in the low-temperature test, so the loading rate was 1 mm/min in this paper, and the diameter of the roller support was 25 mm. An industrial camera was used to capture the photos of specimen surface in real time to analyze the crack propagation characteristics. The test procedure is shown in Figure 2.

2.3. GMTS Criterion. To accurately predict the material fracture properties using the fracture test results, the maximum tensile stress (MTS) criterion was often employed to predict the mixed fracture parameters, but this theory does not consider the effect of the T stress at the notch tip, which may result in large errors sometimes [16]. Considering the T stress, the MTS criterion evolves into the generalized tangential tensile stress (GMTS) criterion, which is widely used in the analysis of mixed fracture properties [17]. T stress can be expressed as follows:

$$T = \frac{P}{2Rt}T^*, \tag{3}$$

where T^* is the normalized form of T stress and can be obtained with finite element analysis, and T^* for different fracture modes are listed in Table 2. The GMTS criterion indicates that the crack occurs within the region, which can be controlled by the critical radius r_c of the notch tip, and the propagating direction of the crack is perpendicular to the direction of maximum tangential stress. When the crack length exceeds the critical radius r_c, the crack begins to expand in further. According to existing results [18], the critical radius r_c changes with temperature. The values were 0.0084 m and 0.0056 m at −10°C and 20°C, respectively. The tangential stress at the notch tip can be calculated using equation (4).

TABLE 2: Properties of aggregates.

Sieve size (mm)	16	13.2	9.5	4.75	2.36	1.18	0.6	0.3	0.15	0.075
Apparent gravity (g/cm^3)	2.716	2.723	2.681	2.679	2.694	2.708	2.713	2.713	2.712	2.712
Moisture uptake ratio (%)	0.49	0.57	0.63	0.52	—	—	—	—	—	—
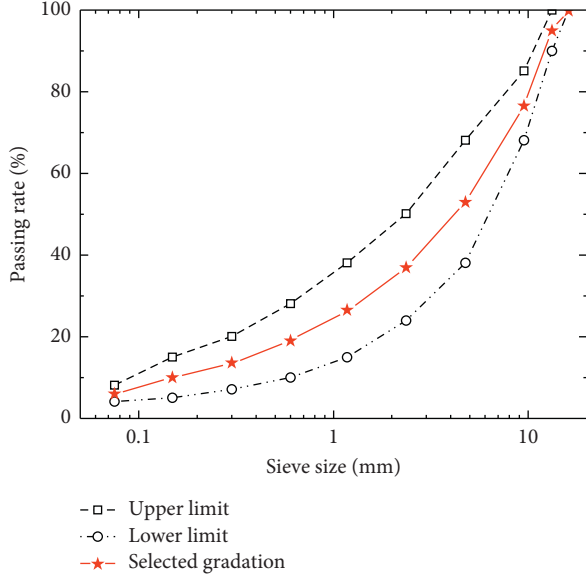
FIGURE 1: Experimental gradation.

$$\frac{1}{\sqrt{2\pi r}}\cos\frac{\theta}{2}\left[K_I\cos^2\frac{\theta}{2} - \frac{3}{2}K_{II}\sin\theta\right] + T\sin^2\theta + O\left(r^{1/2}\right). \quad (4)$$

In equation (4), r is the notch tip extension radius; θ is the notch tip extension angle; and $O(r^{1/2})$ is the high-order term, which can be ignored. According to the GMTS criterion, the crack initiation angle can be determined when $\partial\sigma_{\theta\theta}/\partial\theta|_{\theta=\theta_0} = 0$, namely,

$$\left[K_I\sin\theta_0 + K_{II}(3\cos\theta_0 - 1)\right] - \frac{16}{3}T\sqrt{2\pi r_c}\cos\theta_0\sin\frac{\theta_0}{2} = 0. \quad (5)$$

Substituting (2) and (3) into equation (5), the crack initiation angle can be obtained by using the following equation:

$$\left[Y_I\sin\theta_0 + Y_{II}(3\cos\theta_0 - 1)\right] - \frac{16}{3}T^*\sqrt{\frac{2r_c}{a}}\cos\theta_0\sin\frac{\theta_0}{2} = 0. \quad (6)$$

The GMTS criterion shows that when the stress reaches a critical value, the crack starts to propagate in the direction of θ_0. According to (4), the critical stress can be expressed as follows:

$$\sigma_{\theta\theta_0} = \frac{1}{\sqrt{2\pi r_c}}\cos\frac{\theta_0}{2}\left[K_I\cos^2\frac{\theta_0}{2} - \frac{3}{2}K_{II}\sin\theta_0\right] + T\sin^2\theta_0. \quad (7)$$

For mode I fracture, K_{IC} can be expressed as

$$K_{IC} = \sigma_{\theta\theta_0}\sqrt{2\pi r_c}. \quad (8)$$

While the critical stress intensity factor for the mode I is equal to the fracture toughness, i.e., $K_I = K_{IC}$, at the same

time $K_{II} = 0$ and $\theta_0 = 0$. Therefore, the fracture toughness K_{IC} for mode I also can be expressed as follows:

$$K_{IC} = \cos\frac{\theta_0}{2}\left[K_I\cos^2\frac{\theta_0}{2} - \frac{3}{2}K_{II}\sin\theta_0\right] + \sqrt{2\pi r_c}T\sin^2\theta_0. \quad (9)$$

Generally, the mode I fracture toughness of materials is often measured in the experiment. The ratios of stress intensity factor to fracture toughness (K_I/K_{IC}, K_{II}/K_{IC}) are often analyzed in order to utilize K_{IC} to evaluate the mixed fracture properties of materials. After the transformation of (9), we can get (10) and (11).

$$\frac{K_I}{K_{IC}} = \left[\cos\frac{\theta_0}{2}\left(\cos^2\frac{\theta_0}{2} - \frac{3}{2}\frac{Y_{II}}{Y_I}\sin\theta_0\right) + \sqrt{\frac{2r_c}{a}}\frac{T^*}{Y_I}\sin^2\theta_0\right]^{-1}, \quad (10)$$

$$\frac{K_{II}}{K_{IC}} = \left[\cos\frac{\theta_0}{2}\left(\frac{Y_I}{Y_{II}}\cos^2\frac{\theta_0}{2} - \frac{3}{2}\sin\theta_0\right) + \sqrt{\frac{2r_c}{a}}\frac{T^*}{Y_{II}}\sin^2\theta_0\right]^{-1} \quad (11)$$

Once the K_{IC} is determined through experiment, the stress intensity factors K_I, K_{II} and the crack initiation angle of any mixed mode will be determined by using the GMTS theory.

3. Results and Discussion

3.1. Crack Propagation Characteristics. An industrial camera was utilized to take real-time photos in the loading procedure and then analyze the crack propagation characteristics of different modes. Crack propagation characteristics were marked in yellow line, as shown in Table 4.

On the basis of the crack propagation characteristics of typical specimens listed in Table 4, it can be seen that the crack development at 20°C shows a dispersed distribution due to the influence of coarse aggregate under the same loading mode, and the influence of coarse aggregate is not obvious at −10°C. The cracks are concentrated and expanded along the direction of the main crack at low temperature. Herein, the coarse aggregate has a significant influence on the fracture path at medium temperature.

For the case of mixed mode $M^e = 0.7$ (condition 6#), changing the notch angle can realize the mixed fracture of asphalt concrete, which is in line with the designed experimental expectation. For the cases of $M^e = 0.5$, the crack initiation position of conditions 2#, 7#, and 8# occurred near the support, which deviates from the designed fracture expectation. It proves that only moving the support position or changing the notch angle could not ensure the crack initiation firstly occurs at the notch tip. Although the stress concentration caused by the roller support cannot be ignored, Ameri and Primohammad [14] showed that even if the diameter of the roller support was adjusted, the fracture of condition 2# still

TABLE 3: Parameters of mixed fracture modes.

No.	M^e	S_1 (mm)	S_2 (mm)	b (mm)	α (°)	Y_I	Y_{II}	T^*	Schematic
1#	1	50	50	—	—	3.66	0	−0.58	
2#	0.5	50	16	—	—	0.99	0.99	−1.72	
3#	0	50	9	—	—	0	1.79	−3.91	
4#	0.5	50	50	38	—	1.45	1.36	−1.47	
5#	0	50	50	47	—	0	2.24	−3.92	
6#	0.7	50	50	—	40	2.14	1.10	1.8	
7#	0.5	50	50	—	70	0.81	0.73	2.72	
8#	0.5	33	33	—	40	0.71	0.74	1.99	
9#	0.5	50	25	11	—	1.22	1.29	−1.9	
10#	0	50	25	22	—	0	2.46	−4.74	

S_1 represents the distance from the left support to the mid-span, S_2 represents the distance from the right support to the mid-span, b is the distance from the notch to the mid-span, and T^* represents the tangential stress in the area near the notch tip.
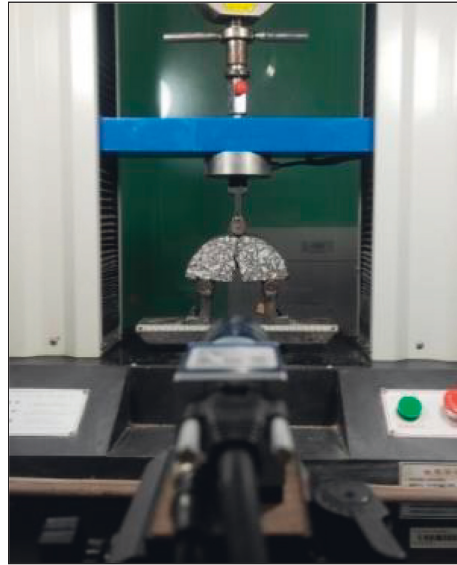
Figure 2: Process of semicircular bend test.

Table 4: Typical crack propagation characteristics of different modes.
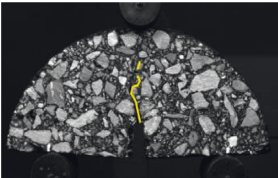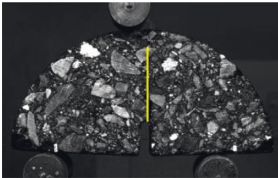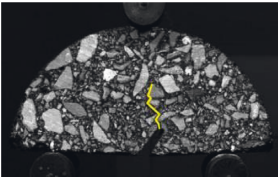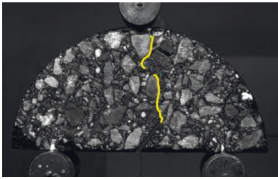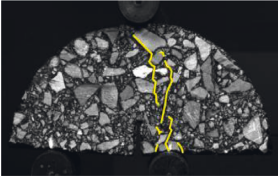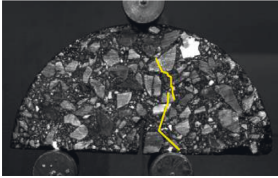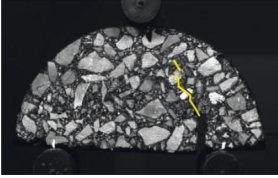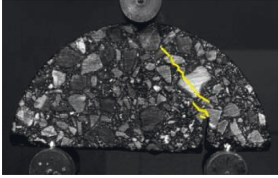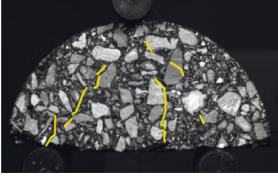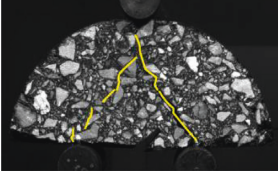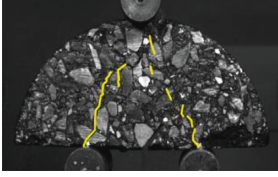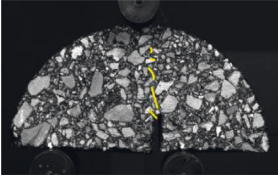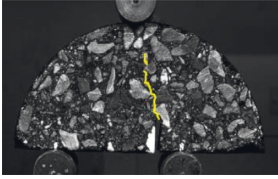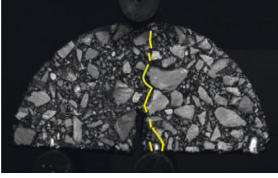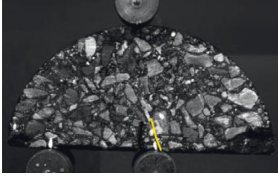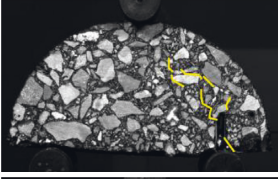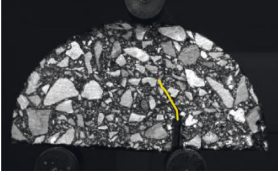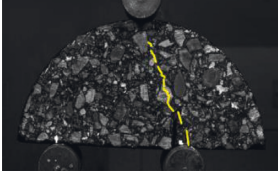
No.	M^e	20°C	−10°C
1#	1		
6#	0.7		
2#	0.5		
4#	0.5		
7#	0.5		Specimen fabrication failed
8#	0.5		

Table 4: Continued.

No.	M^e	20°C	−10°C
9#	0.5		
3#	0		
5#	0		
10#	0		

generated at the supporting position, and one possible way was to set steel gaskets on the support [19]. The methods that only change the notch position or synchronously adjust the positions of support and the notch (i.e., 4# and 9#) can effectively prevent the fracture in the vicinity of the support, which can achieve the designed experimental expectation. Therefore, these two methods have better feasibility for investigating the mixed fracture performance of asphalt concrete.

In addition, it can also be observed from condition 7# that it is difficult to ensure the processing quality of the specimen by changing the notch angle when the span is 100 mm. There is no guarantee that every specimen can be prepared successfully. If the span is shorten (such as condition 8#), the cracks also first generate near the support position during the loading process even though the notch angle and the quality of specimen can be guaranteed. Hence, when M^e is large and the proportion of tensile stress is high, changing the notch angle is feasible. It should be noted that the feasibility of changing the notch angle is inadequate when M^e is less than 0.5.

For the pure mode II fracture characteristics of 3#, 5#, and 10#, changing the support position and the notch angle induced the crack initiation near the support, and the crack initiation direction was almost along the mixed fracture path. It can be inferred that the stress concentration is significant, and the stress transmission path in the vicinity of the notch is blocked by notch when it is close to the support, which leads to the crack initiation at the support. So, there is a damage risk near the support for the pure shear fracture mode in the semicircular bend test.

3.2. Comparative Analysis of Crack Initiation Angle.

In order to accurately predict the fracture path of asphalt concrete, the crack initiation angle was determined by using (6) based on the GMTS theory, and the difference between the theoretical angle and the measured one was analyzed. To eliminate the errors from the specimen processing, the results of the remaining 9 conditions in addition to 7# were selected for comparison, as shown in Figure 3. The negative angle in Figure 3 means counterclockwise rotation direction.

As shown in Figure 3(a), the measured fracture initiation angle through changing notch angle is almost consistent with the theoretical value of GMTS at medium temperature, but the discreteness of the angle is large, and the standard deviation is about 10°. The fracture initiation angles measured through the other means are all less than the theoretical value of GMTS. When M^e is lower than 0.5, the growth of fracture initiation angle becomes slow. Although the measured angles are lower than the theoretical ones, their changing trends are similar. It can be inferred that the GMTS criterion cannot accurately predict the fracture path of asphalt concrete at medium temperature.

It can be seen from Figure 3(b) that the tensile action occupies the main proportion when M^e is higher than 0.5, and the measured fracture initiation angles of these four bend means are almost consistent with the theoretical results of GMTS at −10°C. With the increase of shearing action, the fracture initiation angle gradually deviates from the theoretical value of GMTS when M^e is less than 0.5. In addition, the measured angles by changing the positions of support and notch are the closest to the theoretical value of GMTS.

(a)

(b)
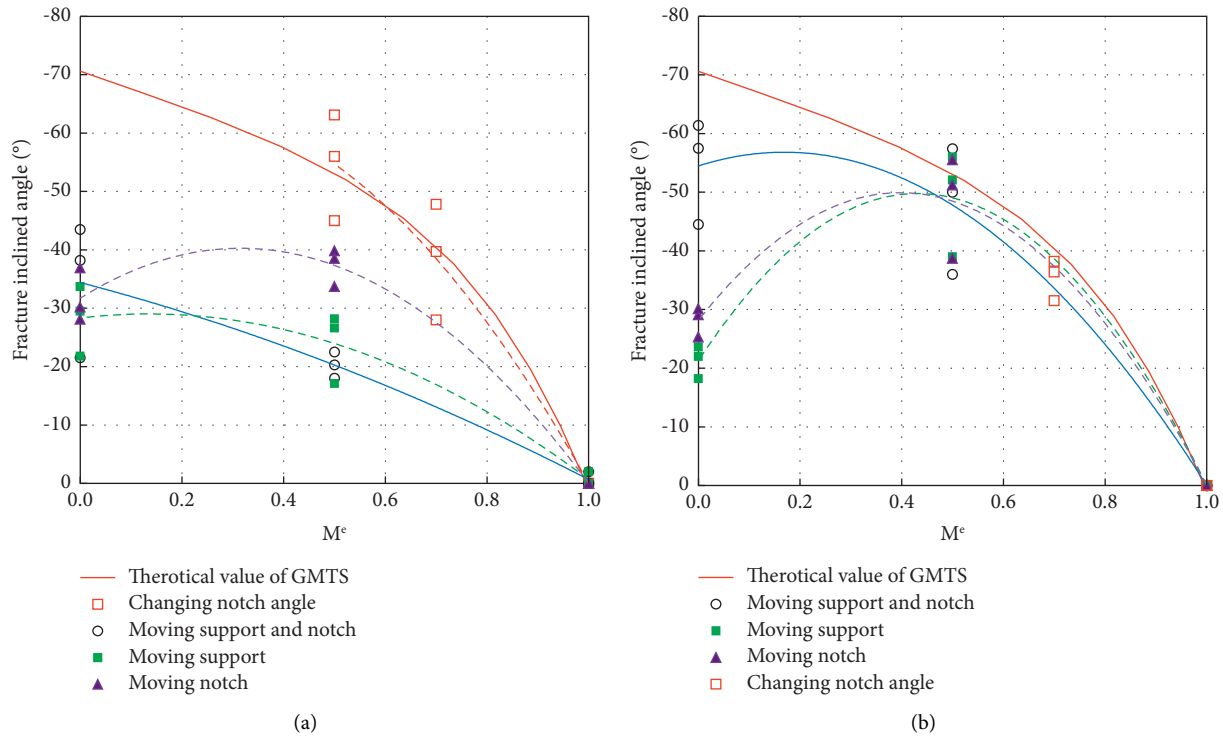
FIGURE 3: Comparison of fracture initiation angles at different temperatures: (a) 20°C and (b) −10°C.

For the pure shear mode, the deviations between the measured angles and the theoretical values are the largest by changing the support position or the notch position. Based on the angles at medium and low temperatures, it is proved that temperature has a significant effect on the fracture path of asphalt concrete. The GMTS criterion is suitable for describing the low-temperature fracture performance of asphalt concrete. At medium temperature, a large error would generate if one uses the GMTS criterion to predict the fracture path.

3.3. Comparative Analysis of Fracture Toughness Ratio. It can be seen from the above analysis that the notch is close to the support, which causes the area in the vicinity of support to crack first in the pure shearing fracture test. The larger the M^e is, the lower the differences between the measured and the theoretical values are. Fortunately, the critical fracture toughness K_{IC} of mode I is easy to measure, the fracture toughness K_{IIC} for pure shear mode II can be estimated using the mixed fracture criterion, which had been widely applied in the field of fracture mechanics. Therefore, this paper discusses the applicability of GMTS criterion based on K_I/K_{IC} and K_{II}/K_{IC}. Based on the results as shown in Table 2, the fracture initiation angle is determined and substituted in (10) and (11) to obtain the theoretical values of K_I/K_{IC} and K_{II}/K_{IC}, the ratios of stress intensity factor to fracture toughness. The experimental K_I/K_{IC} and K_{II}/K_{IC} can be calculated by using (2). These ratios are shown in Figure 4.

It can be seen from Figure 4 that the measured K_{II}/K_{IC} at medium and low temperatures is all lower than the theoretical values, and the measured K_{II}/K_{IC} is about 0.3 lower than the theoretical value. This may be caused by the
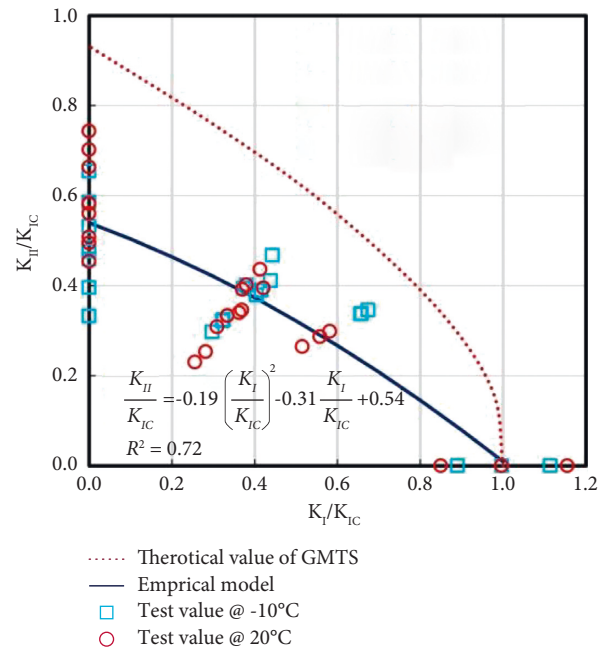
FIGURE 4: Comparison on the ratios of fracture toughness.

experimental control precision and the influence of coarse aggregate inside the asphalt concrete [20–23]. The critical shear fracture toughness K_{IIC} would be overestimated when it was estimated by using the GMTS criterion and the critical fracture toughness K_{IC} of mode I. The empirical model established in Figure 4 has a good correlation with the experimental values, and this empirical model effectively reduces the prediction error. In order to verify the validity of
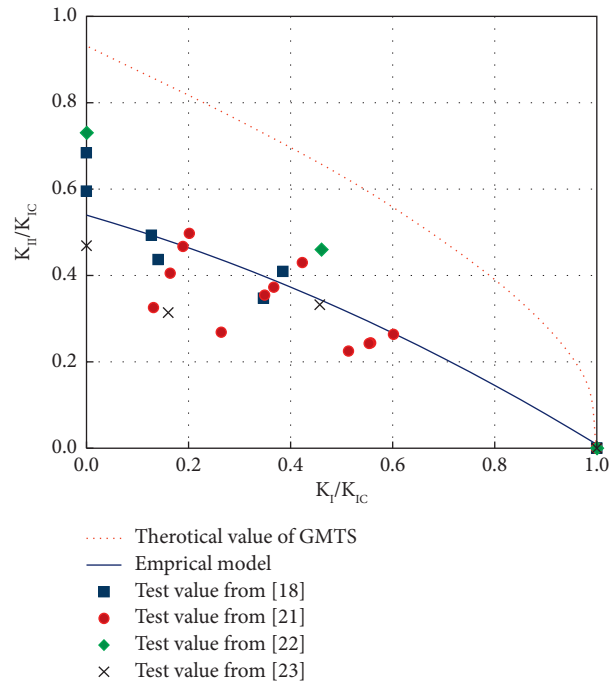
FIGURE 5: Verification on the empirical model.

TABLE 5: Feasibility analysis of different methods.

Test method	Advantages	Drawbacks	Priority
Moving support only	Notch remains in the mid-span, easy preparation	Cracks generate and propagate from the support, and the fracture initiation angle is discrete	4
Moving notch only	Easy preparation, cracks first generate and propagate from notch tip.	The vicinity of support is severely damaged in the pure shear mode	2
Changing notch angle only	Cracks propagate at the notch tip	The angle control requirements are high, and when the span is small, it will be destroyed first near the support, and it is difficult to measure in the pure shear mode	3
Moving support and notch synchronously	Notch is easy to be cut, cracks propagate along the notch tip, and good repeatability	High accuracy requirement for notch position	1

the empirical model in this paper, the experimental data from the existing literature were also taken in this part, and their results were collected and are shown in Figure 5.

It can be seen from Figure 5 that the predicted ratios using the empirical model are closer to the experimental data than that using the GMTS criterion, and the prediction deviation of the empirical model is smaller than that of GMTS. It can also be seen that the empirical model established in this paper has good universality for different mixtures.

3.4. Feasibility of Different Methods. It can be determined from the previous analysis that different test methods have significant influences on the low-temperature fracture performance of asphalt concrete. Taking into account the difficulty of preparing procedure and the discreteness of test results, the four methods selected in this paper are comprehensively evaluated, as shown in Table 5.

It can be seen from Table 5 that different methods have their own advantages and disadvantages. In addition to the method of moving support only, the other three methods can ensure that the crack propagates along the notch tip. Although the position of the notch remains unchanged, it is beneficial to the processing of the specimen, but it still cannot avoid the fracture in the vicinity of support, which is particularly serious in the pure shear fracture mode. Changing the notch angle can realize the crack propagation along the notch tip. For semicircular specimens, it is difficult to realize the pure shear mode by changing the notch angle due to the limitation of the size of the notch. However, changing the support position and the notch position has good repeatability for asphalt mixture and can ensure that the crack generates and propagates along the notch tip. It can also be determined that cracking near the support easily leads to the failure of the pure shear fracture test due to the limitation of processing, and it is difficult to control the pure shear fracture test.

4. Conclusions

(1) Temperature and fracture mode have significant influences on the crack propagation path of asphalt concrete. At medium temperature, the crack initiation and propagation path are affected by the coarse aggregate, while asphalt concrete mostly exhibits elastic fracture at low temperature, and the coarse aggregate has no influence on the fracture path. For the pure shear mode, asphalt concrete is prone to first fracture near the supports.

(2) In addition to the method of changing the notch angle, the crack initiation angle obtained from other methods is quite different from the theoretical value of GMTS at medium temperature. The crack initiation is closely related to the semicircular bend method at low temperature, and this difference is more prominent in mode II fracture. The measured ratios of fracture toughness are lower than the theoretical value of GMTS, but the empirical model can be used to exactly describe the relationship of fracture toughness ratios.

(3) For the selected bend methods in this work, changing the positions of the support and notch synchronously is stable and repeatable; this method is suggested to be popularized and applied on the mixed fracture behavior of materials in the future, but attention should be paid to controlling the positioning accuracy of the notch [21–23].

Data Availability

All the data obtained from several experiments are included in the paper.

Conflicts of Interest

The authors declare that there are no conflicts of interest regarding the publication of this paper.

Acknowledgments

References

[1] H. Ban, S. Im, and Y. R. Kim, "Mixed-mode fracture characterization of fine aggregate mixtures using semicircular bend fracture test and extended finite element modeling," *Construction and Building Materials*, vol. 101, pp. 721–729, 2015.

[2] G. Feng, Y. Kang, F. Chen et al., "The influence of temperatures on mixed-mode (I+II) and mode-II fracture toughness of sandstone," *Engineering Fracture Mechanics*, vol. 189, no. 5, pp. 51–63, 2018.

[3] K P. Chong and M. D. Kuruppu, "New specimen for fracture toughness determination for rock and other materials," *International Journal of Fracture*, vol. 26, no. 2, pp. R59–R62, 1984.

[4] Y. Cui, X. Li, and H. Wu, "Multi-scale evaluation of asphalt mixture damage healing performance," *Journal of Building Materials*, vol. 24, no. 02, pp. 432–439, 2021.

[5] J. Yan, J. Zheng, and N. Li, "Study on crack resistance of basalt fiber asphalt mortar," *Journal of Building Materials*, vol. 22, no. 05, pp. 800–804, 2019.

[6] J. Xie and W. Luo, "Comparative analysis of three fatigue test methods for asphalt mixture," *China Foreign Highway*, vol. 38, no. 02, pp. 197–202, 2018.

[7] D. Feng, S. Cui, and J. Yi, "Research on low temperature performance evaluation index of asphalt mixture based on SCB test," *China Journal of Highway and Transport*, vol. 33, no. 07, pp. 50–57, 2020, (in Chinese).

[8] J. Ren, *Macro and Meso Analysis of Fracture Characteristics of Asphalt Mixture at Low Temperature Based on DEM*, Southeast University, Nanjing, 2017.

[9] M. Fakhri, S. A. Siyadati, and M. R. M. Aliha, "Impact of freeze–thaw cycles on low temperature mixed mode I/II cracking properties of water saturated hot mix asphalt: an experimental study," *Construction and Building Materials*, vol. 261, Article ID 119939, 2020.

[10] B. Ameri, F. Taheri-Behrooz, and M. R. M. Aliha, "Fracture loads prediction of the modified 3D-printed ABS specimens under mixed-mode I/II loading," *Engineering Fracture Mechanics*, vol. 235, Article ID 107181, 2020.

[11] S. Pirmohammad and M. R. Ayatollahi, "Asphalt concrete resistance against fracture at low temperatures under different modes of loading," *Cold Regions Science and Technology*, vol. 110, pp. 149–159, 2015.

[12] S. Pirmohammad, Y. M. Shokorlou, and B. Amani, "Influence of natural fibers (kenaf and goat wool) on mixed mode I/II fracture strength of asphalt mixtures," *Construction and Building Materials*, vol. 239, no. 5, 2020.

[13] X. Tian, H. Han, and X. Li, "Fracture performance of asphalt concrete under different loading modes," *Journal of Building Materials*, vol. 53, no. 4, pp. 758–761, 2016.

[14] M. Ameri and S. Primohammad, "Mixed mode fracture resistance of asphalt concrete mixtures," *Engineering Fracture Mechanics*, vol. 93, pp. 153–167, 2012.

[15] Q. Guo, Z. Chen, and P. Liu, "Influence of basalt fiber on mode I and II fracture properties of asphalt mixture at medium and low temperatures," *Theoretical and Applied Fracture Mechanics*, vol. 112, no. 7, Article ID 102884, 2020.

[16] J. Ewing, "Fracture under complex stress -The angled crack problem," *International Journal of Fracture Mechanics*, vol. 26, no. 4, pp. 346–351, 1984.

[17] D. J. Smith, M. R. Ayatollahi, and M. J. Pavier, "The role of T-stress in brittle fracture for linear elastic materials under mixed-mode loading," *Fatigue and Fracture of Engineering Materials and Structures*, vol. 24, no. 2, pp. 137–150, 2000.

[18] P. Liu, *Analysis of the Influence of Dry-Wetting Cycle on the Fracture Mode of Asphalt Mixture*Hebei University of Engineering, Handan, 2020.

[19] M. Fakhri, K. E. Haghighat, and M. R. M. Aliha, "Mixed mode tensile – in plane shear fracture energy determination for hot mix asphalt mixtures under intermediate temperature conditions," *Engineering Fracture Mechanics*, vol. 192, pp. 98–113, 2018.

[20] M. Aliha, H. Ziarib, and B. Mojaradic, "Modes I and II stress intensity factors of semi-circular bend specimen computed for

two-phase aggregate/mastic asphalt mixtures," *Theoretical and Applied Fracture Mechanics*, vol. 106, Article ID 102437, 2020.

[21] D. Taylor, M. Merlo, and R. Pegley, "The effect of stress concentrations on the fracture strength of Polymethylmethacrylate," *Materials Science and Engineering*, vol. 382, pp. 288–294, 2004.

[22] A. Mansourian, R. Ali, and R. Mahmoud, "Evaluation of fracture resistance of warm mix asphalt containing jute fibers," *Construction and Building Materials*, vol. 117, pp. 37–46, 2016.

[23] M. Aliha and S. Shaker, "Effect of bitumen type, temperature and aging on mixed I/II fracture toughness of asphalt binders-experimental and theoretical assessment," *Theoretical and Applied Fracture Mechanics*, vol. 110, no. 4, Article ID 102801, 2020.

Research Article

Study on Properties of Magnesium Oxychloride Cement Solidified Soil

Haoyu Wang,[1] Jinbao Zhang,[2] Xiaohui Yan,[1] and Rui Xiong [1]

[1]School of Materials Science and Engineering, Chang'an University, Xi'an 710061, China
[2]Qinghai Transportation Holding Group Co., Ltd., Xining 810001, China

Correspondence should be addressed to Rui Xiong; xiongrui@chd.edu.cn

Due to the poor performance of ordinary Portland cement (OPC) as a solidified soil road and the large pollution in the production process, environment-friendly magnesium oxychloride cement (MOC) was used as the soil curing agent to prepare the solidified soil, exploring the optimal ratio of various raw materials when MOC is used as a curing agent. Analyzing the properties of MOC solidified soil in the application of road subgrade. This paper tests compaction, mechanical properties, and durability of the MOC solidified soil, simulates the development trend of 7 days unconfined compressive strength of MOC solidified soil, and then analyzes the hydration process and strengthens the formation mechanism of MOC in solidified soil. The study found that the addition of MOC as a curing agent to the soil can effectively improve the compaction and mechanical properties of the soil. Matlab simulation found that when the MgO content is 5.5% to 6% and the ratio of raw materials MgO, MgCl$_2$, and H$_2$O is 2.45 : 1 : 14 to 6.3 : 1 : 14, the performance of MOC solidified soil is excellent. Fitting UCS data, it is found that MOC solidified soil has early strength characteristics. The excellent compaction and mechanical properties of MOC solidified soil are due to the formation of a small amount of phase 5 and layered Mg(OH)$_2$ by the hydration of MOC, and the formation of amorphous gel with SiO$_2$ in the soil. This reaction improves soil compaction and reduces internal porosity from a microscopic perspective. The strength loss rate of MOC solidified soil is higher after immersion in water at the initial stage of curing, but it is still better than that of traditional cement-based solidified soil. Poor performance after immersion in water is associated with disruption of the network-like structure. As an environment-friendly soil curing agent, MOC can be used in engineering practice with low environmental humidity.

1. Introduction

Soft soil can lead to potential safety hazards caused by poor bearing capacity during construction; high soil expansion will generate subgrade shrinkage, resulting in pavement cracking and reduced service life [1–3]. Soil stabilization is one of the soil improvement methods in geotechnical engineering. In addition, cement and lime stabilizations are two of the most commonly used methods in recent years [4, 5]. The addition of traditional curing agents such as ordinary Portland cement (OPC) and lime can improve soil mechanical properties and durability [6–8]. Further, the study found that after adding MgO to the OPC stabilized soil, the pH of the soil increased with the increase of

magnesium slag. During the hydration process, calcium aluminate hydrate (C-A-H) and calcium silicate hydrate gel (C-S-H) were produced, which improved soil conditions [9, 10]. However, traditional OPC curing agents have problems such as limited mechanical strength, poor durability, poor volume stability, high pollution in the production process, and high CO$_2$ emissions [11–14].

Magnesium oxychloride cement (MOC) is an environment-friendly magnesia cementitious material prepared by lightly burning magnesium oxide, magnesium chloride and water [15]. Due to its fast-setting speed, high mechanical strength, good wear resistance, salt resistance and halogen corrosion, simple production process, and low cost, it is widely used in construction materials, biological materials,

TABLE 1: Technical indexes of fine-grained soil.

Nominal maximum particle size (mm)	Maximum particle size (mm)	Moisture content (%)	Liquid limit (%)	Plastic limit (%)	Plasticity index
2.36	4.75	8.7	23.8	14.7	9.1

TABLE 2: Physical properties and chemical composition of raw materials.

Raw materials	Chemical composition (%)				
	MgO	SiO_2	Al_2O_3	CaO	Fe_2O_3
Light burned magnesite	80.21	6.87	2.01	1.58	1.32
Industrial magnesium chloride	85.43	6.65	1.82	1.33	1.31

and other fields [16–18]. The salt lakes in the Qinghai area of China have sufficient reserves of magnesium salts and high grades [19]. Part of the waste MOC can be reused after recycling and processing, such as superhydrophobic magnesium oxychloride cement [20]. Waste building materials and industrial residues can also be used to prepare MOC or improve the performance of MOC, such as waste gypsum, ammonia alkali residue, and fly ash [21–23]. Studies have shown that when MOC is used as a soil stabilizer, it can form an amorphous gel product covering the surface of soil particles, effectively cementing soil particles and filling interparticle voids. It also greatly improves soil mechanical properties and reduces harmful ion leakage. The optimum dosage of MOC as a soil stabilizer is 10% [24–26]. At present, the environment-friendly soil stabilizer MOC has not attracted enough attention, and there are few related researches and experiments. The optimal raw material ratio and maintenance method of MOC as a soil stabilizer still need to be studied. Various properties of soil after curing with MOC have yet to be tested, and the microscopic mechanism remains to be explored.

This paper analyzes and simulates the optimal raw material ratio of MOC as a curing agent through a macro compaction test, mechanical test, durability test, and MATLAB software. Scanning electron microscope (SEM) and X-ray diffractometer (XRD) are used to observe the microstructure of MOC solidified soil. The microscopic mechanism of MOC reinforced fine-grained soil has been explored. It is hoped that this study can provide a valuable reference for the subsequent use of MOCs as soil stabilizers.

2. Materials and Methods

2.1. Materials. The test soil was fine-grained soil with a plasticity index of 9.1, which has low liquid limit clay. Technical indexes are shown in Table 1. The raw materials for the preparation of MOC were lightly burned magnesia and industrial magnesium chloride. MgO was a light-burned magnesite powder produced in Haicheng, Liaoning Province. The content of MgO was more than 85%, and the content of active MgO was 60%. The specific surface area of the light-burned magnesia powder was 340 m^2/kg. The physical properties and chemical composition are shown in Table 2. The particle size distribution of MgO is shown in
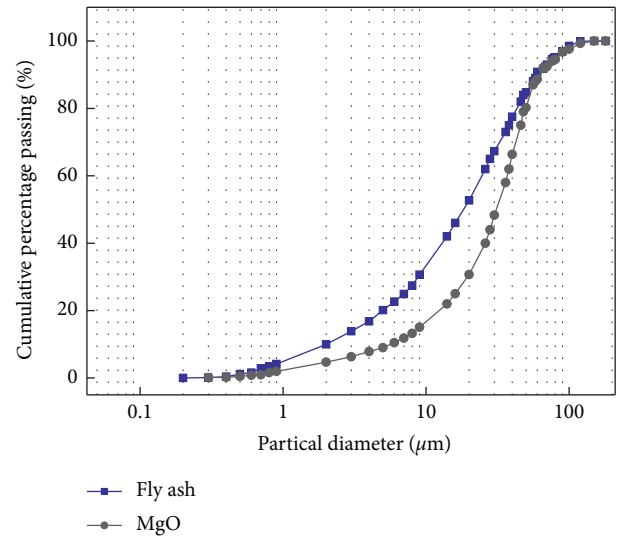
FIGURE 1: Particle size distribution of MgO.

Figure 1. MgCl2 was produced by Qinghai Golmud. The content of magnesium chloride was more than 45%.

2.2. Experimental Methods. Mechanical properties and durability tests were used to evaluate the performance of MOC stabilized soil. Test flow is shown in Figure 2. The following is a detailed description of the mechanical properties and durability tests.

2.2.1. Compaction Test. The compaction test (Method A) was adopted JTG-E51-2009. The size of the tube used in the test was 10.0 cm × 12.7 cm (inner diameter × height) and the volume was 997 cm^3. Five different water contents were set, with a difference of 2.0% in sequence. The ratio of the compaction test is shown in Table 3.

2.2.2. Mechanical Property Analysis. The differences in mechanical properties of OPC and MOC solidified soils were compared. OPC consisted of 5% 42.5 cement and 11% water content. The effects of different ratios of raw materials on the mechanical strength of MOC solidified soil were discussed. The MOC raw material ratio is shown in Table 4. The
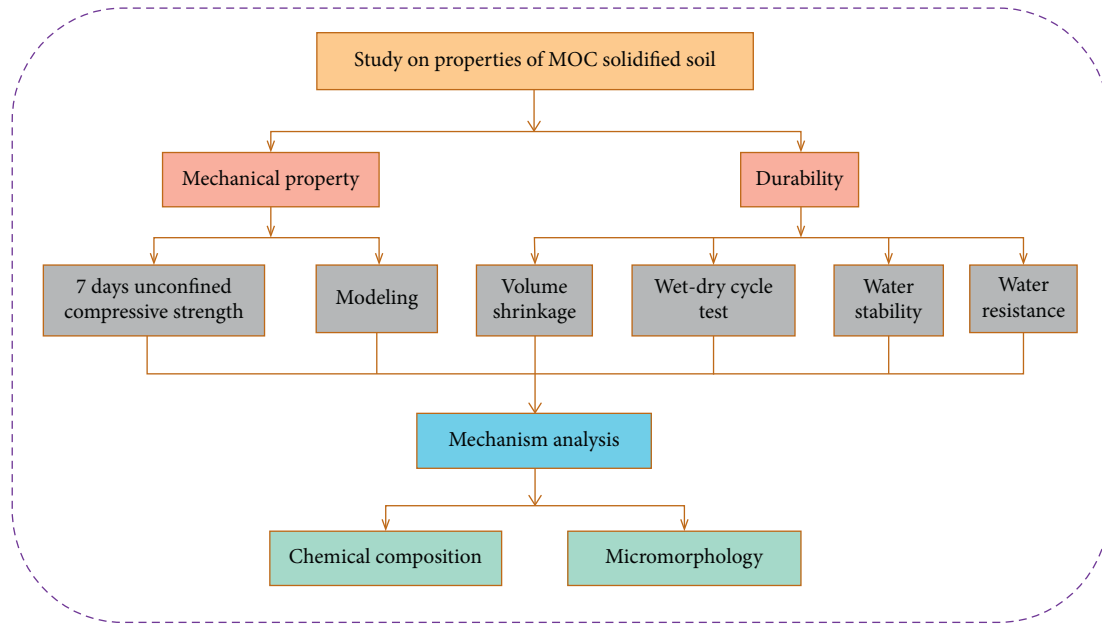
FIGURE 2: Test flow chart.

TABLE 3: Compaction test ratios.

Number	MgO (%)	MgCl$_2$:H$_2$O	Water content
1	3	1:15	7%, 9%, 11%, 13%, 15%
2	4	1:15	7%, 9%, 11%, 13%, 15%
3	5	1:15	7%, 9%, 11%, 13%, 15%
4	4	1:10	7%, 9%, 11%, 13%, 15%
5	4	1:15	7%, 9%, 11%, 13%, 15%
6	4	1:20	7%, 9%, 11%, 13%, 15%

TABLE 4: MOC raw material ratios.

Number	MgO (%)	MgCl$_2$:H$_2$O	MgO:MgCl$_2$:H$_2$O	Moisture content (%)
A1	3	1:10	1.42:1:10	9.5
A2	3	1:15	2.13:1:15	9.5
A3	3	1:20	2.84:1:20	9.5
B1	4	1:10	1.80:1:10	10
B2	4	1:15	2.70:1:15	10
B3	4	1:20	3.60:1:20	10
C1	5	1:10	2.14:1:10	10.5
C2	5	1:15	3.21:1:15	10.5
C3	5	1:20	4.29:1:20	10.5
D1	6	1:10	2.45:1:10	11
D2	6	1:15	3.68:1:15	11
D3	6	1:20	4.91:1:20	11
E1	7	1:10	2.63:1:10	12
E2	7	1:15	3.94:1:15	12
E3	7	1:20	4.25:1:20	12

specimens were prepared and cured in an indoor environment for 7 days, and the unconfined compressive strength (UCS) was tested. The variation trend of 7 days UCS of MOC solidified soil was simulated by MATLAB.

2.2.3. Durability Analysis. The durability of MOC solidified soil was evaluated by volume shrinkage test, wet-dry cycle test, water stability test, and infiltration conductivity test. The specimen size was Φ50 × 50 mm cylindrical specimens.

FIGURE 3: Digital conductivity meter.

The volume shrinkage test adopted the ratio of B2, C2, and D2, and the curing temperature was $20 \pm 2°C$. The original height and diameter of specimens were measured with a vernier caliper, then continued to test the data for 1 to 7 days of curing, and calculated the volume change.

The wet-dry cycle test was prepared according to the C2 ratio, the static pressure method was compacted and the demoulding curing was carried out for 7 days. The number of wet-dry cycles was set to 0, 1, 3, and 5 times.

The water stability test applied C2 ratio and the specimen standard curing for 48 h in $20 \pm 2°C$. After the specimen had been formed, the UCS was measured after immersing in water for 24 h on the third and seventh day, respectively. Water stability coefficient of the specimens was calculated according to

$$\text{water stability coefficient} = \frac{\text{UCS of immersing water } 24h}{\text{UCS of standard care}}. \quad (1)$$

The ratio of B2, C2, and D2 were set for the water resistance test, and the curing temperature was $20 \pm 2°C$. After curing for 7 days, the specimens were completely immersed in water, and the amount of water in each group was strictly controlled to be exactly the same. After immersing for 6 h, the conductivity changes of water were measured. The instrument used is a DDS-11A digital conductivity meter as shown in Figure 3.

2.2.4. Micro Tests.
Scanning electron microscope was used to observe the microscopic morphology of MOC solidified soil, and X-ray diffractometer was used to test the chemical composition of MOC solidified soil. The sample design scheme of the microscopic analysis test is shown in Table 5.

3. Results and Discussion

3.1. MOC Solidified Soil Compaction.
Figure 4 shows the effect of different raw material ratios on the maximum dry density of MOC solidified soil. The maximum dry density can reflect the compaction of MOC solidified soil well. As shown in Figure 4, the change of MgO content has a great influence on the maximum dry density of MOC solidified soil. In Figure 4(a), when the content of MgO is 5%, the maximum dry density reaches 2.008 g/cm^3 compared with 3% MgO, which is increased by 15.33%. The curing effect improved continuously with the increase of MgO content. In Figure 4(b), the curing effect has little correlation with the ratio of $MgCl_2$ to H_2O.

3.2. Mechanical Properties of MOC Solidified Soil.
Figure 5 illustrates 7 days UCS of MOC solidified soil specimens with different ratios. The strength of C2, D1, D2, E1, and E2 samples are higher than OPC solidified soil. The strength of D2 reaches 1.76 MPa, which is composed of 6% MgO and the ratio of $MgCl_2$ to H_2O is 1:15. Compared with OPC solidified soil, D2 is increased by 30.4%. Compared with traditional cement-based soil stabilizers [27, 28], such as OPC and calcium sulfoaluminate cement (CSA), 7 days UCS value of MOC stabilized soil is the highest. Therefore, in order to make the strength of the MOC solidified soil higher, MgO should not be less than 5% and the ratio of $MgCl_2$ to H_2O is about 1 to 10~15.

In order to explore the effect of the raw material ratio on the 7 days UCS of MOC solidified soil, MATLAB was used to fit the ratio of MgO, $MgCl_2$, and H_2O on the surface. Three fitting surfaces are shown in Figure 6. The x-axis is the content of MgO (a%). The y-axis is the molar ratio of $MgCl_2$ to H_2O (1:b), and z-axis is the 7 days UCS.

The functional equations obtained by the fitting of Models I, II, and III are sequentially shown in

$$\sigma_1 = -1.876 + 43.87x + 0.293y - 252.4x^2 \\ - 0.009y^2 - 0.58xy, \quad (2)$$

$$\sigma_2 = 5.03 - 239.6x - 0.253y + 3955x^2 + 0.008y^2 \\ + 11.03xy - 2.72ex^2 - 5.714x^2y - 0.368xy^2, \quad (3)$$

$$\sigma_3 = -1.45 + 19.17x + 0.312y - 0.58xy - 0.1y^2. \quad (4)$$

The statistical parameter lists of the three models were compared, as shown in Table 6. Statistical parameters include error term degrees of freedom (f), error sum of squares (SSE), root mean square (RMSE), coefficient of determination R-square, and adjusted R-square.

The SSE and RMSE of Model II tend to be closer to 0 and the R-square is closer to 1. It can be seen that the fitting degree of Model II for MOC solidified soil is better. In addition, from the models in Figure 6 and Table 6, it can be seen that Model II is matched only when the MgO content is greater than 5%, and the fitting degree of the data is better under the same condition. When the MgO content is lower, the strength predicted in Model II increases, but the actual strength decreases. Model II is the opposite of the actual situation, so it is not adopted. Taking into account comprehensively, Model I is suitable for characterizing the 7 days UCS of MOC solidified soil with different proportions.

The shaded part of Figure 7(b) indicates that 7 days UCS of MOC solidified soil is higher than that of OPC solidified soil. It can be seen from Figure 7 that the optimum content of MgO is 5.5%~6% and the ratio of $MgCl_2$ to H_2O is 1:14. At this dosage range, the strength reaches more than 1.6 MPa, and the effect of constantly increasing the dosage of MgO on improving the strength is not significant. Combined with the experimental data, 7 days UCS of C2, D1, D2, E1, and E2 are better than that of OPC solidified soil, and the strength of D2 reaches 1.76 MPa, which is 30.4% higher than that of OPC solidified soil. 7 days UCS of MOC solidified soil is more

TABLE 5: Microscopic test sample design scheme.

Number	MgO (%)	MgCl$_2$: H$_2$O	Maintenance method
1	5	1 : 15	Standard curing 7 d
2	5	1 : 15	Standard curing for 7 d, last day soaked in water
3	6	1 : 10	Standard curing 7 d
4	5	1 : 15	Standard curing 6 h

(a)

(b)
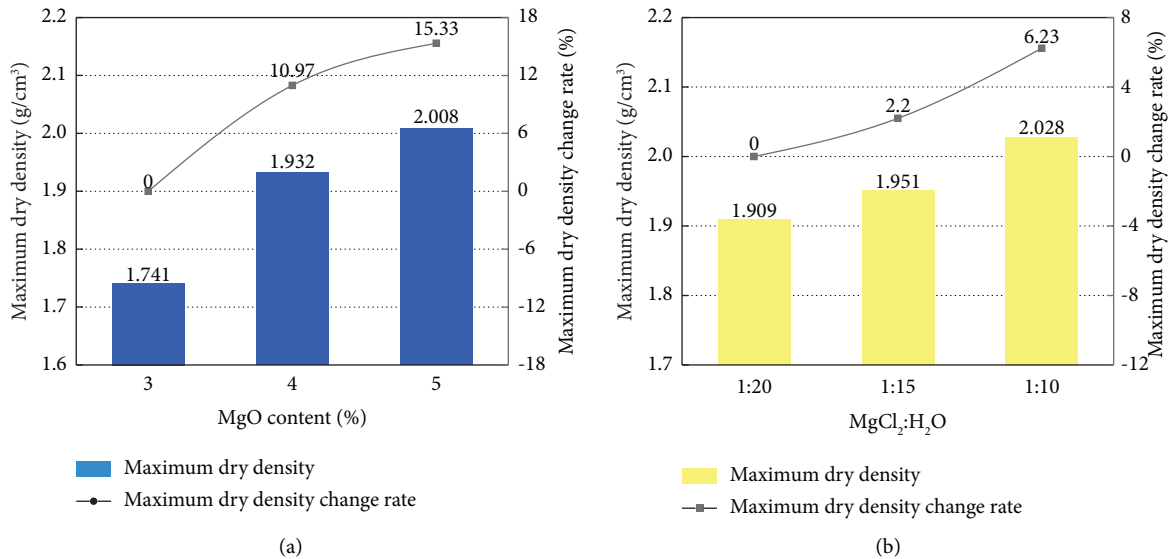
FIGURE 4: Influence of raw material ratio on the maximum dry density of MOC solidified soil. (a) Different MgO contents. (b) Different ratios of MgCl$_2$ to H$_2$O.
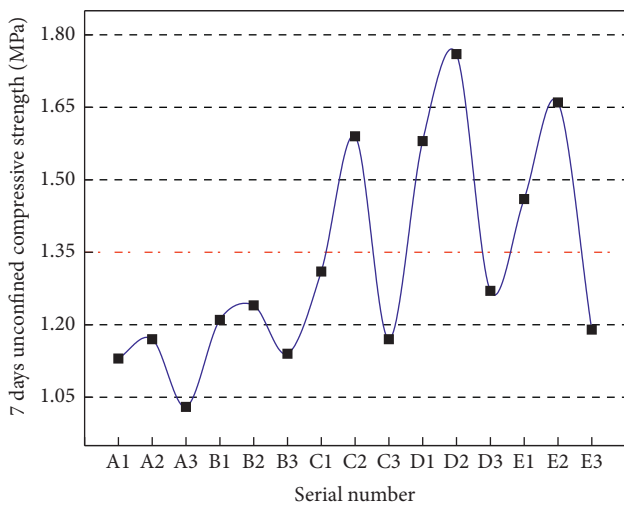
FIGURE 5: Unconfined compressive strength of specimen for 7 days.

than 1.0 MPa. Combining with Table 7, it can be seen that it meets the requirements of the sub-base of secondary and lower highways under medium and light traffic loads.

In order to study the effect of curing age on UCS of MOC solidified soil, different curing times were taken and UCS tests were carried out. Figure 8 shows the UCS change rate of specimens after different curing aging. UCS development trends of MOC solidified soil and OPC solidified soil are shown in Figure 9.

Figures 8 and 9 demonstrate that the UCS of MOC solidified soil develops faster than that of OPC solidified soil. 3 days strength reaches 90% of 7 days strength and the 28 days strength is significantly higher than that of the OPC solidified soil. It shows that MOC added to fine-grained soil as a curing agent can effectively improve the mechanical properties of the solidified soil.

3.3. *Durability of MOC Solidified Soil.* Figure 10 represents the volume shrinkage of MOC solidified soil as the ratio change of MgCl$_2$ and H$_2$O. After the MOC solidified soil was formed, a slight volume expansion occurred on the first day, then a certain degree of shrinkage came up. When MgO content is 4%, 7 days change rate is 2.3%. When MgO content is 6%, the change rate is 1.27%. Overall, the volume change rate of MOC solidified soil was slight.

Under the natural environment, the early soil is easy to absorb water and swell. With the extension of time, the water in the soil gradually volatizes and shrinks in volume, which is easy to produce a large volume change rate. Nevertheless, MOC can play a role in consolidating and MgO has a certain expansion, which offsets part of the soil autogenous shrinkage and reduces the volume change rate of MOC solidified soil.

After the wet-dry cycle test, the strength loss rate and volume shrinkage rate of MOC solidified soil (C2) are shown in Figure 11. Wet-dry cycles have little effect on the volume shrinkage of MOC solidified soil, but have a greater effect on

(a)

(b)

(c)
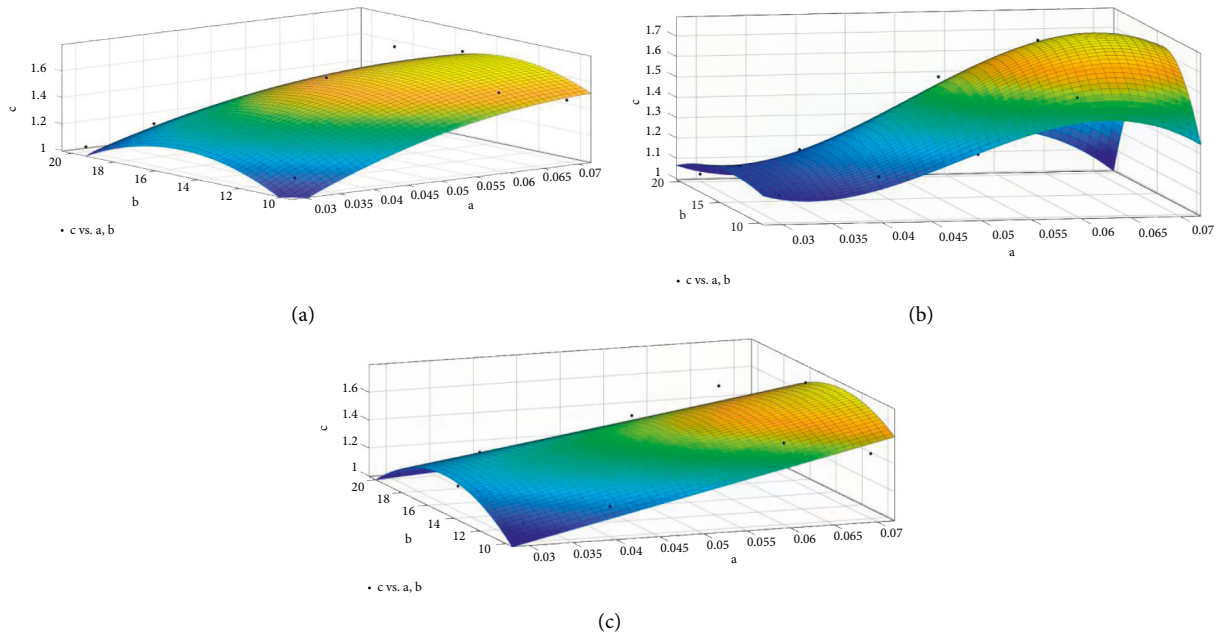
FIGURE 6: Three fitting surfaces. (a) Fitting surface of model I. (b) Fitting surface of model II. (c) Fitting surface of model III.

TABLE 6: Statistical parameters of different models.

Models	f	SSE	RMSE	R-square	Adjusted R-square
I	9	0.1093	0.1102	0.8568	0.7772
II	6	0.0207	0.0587	0.9729	0.9369
III	10	0.1286	0.1134	0.8315	0.7641

(a)

(b)
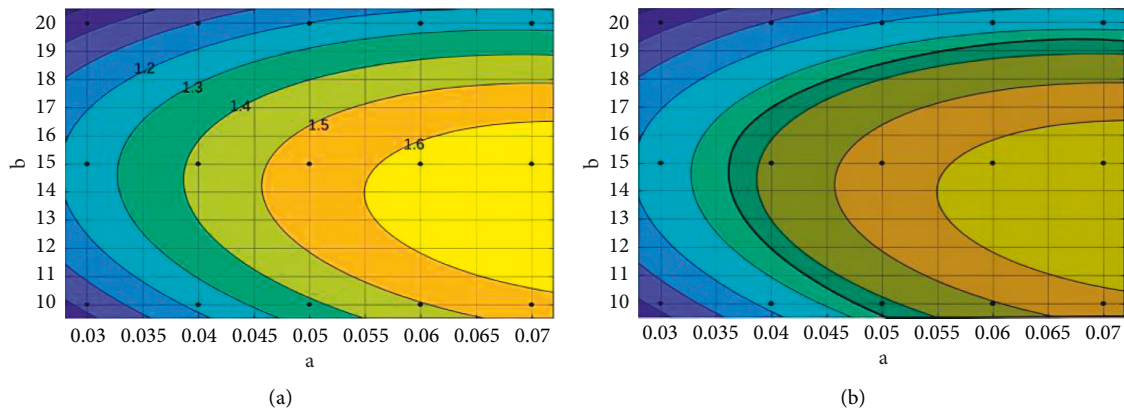
FIGURE 7: 7 days UCS contour map of MOC and OPC solidified soils. (a) Contour map of MOC solidified soil. (b) Comparison of MOC and OPC solidified soil contour map.

UCS. After 5 cycles, the volume change rate of MOC solidified soil is only 1.98%, and the strength loss rate is as high as 41.92%. By simply fitting the data, it can be seen that the strength loss rate decreases significantly before the 6th time, and becomes flat at the 9th time. The volume shrinkage rate of C2 fluctuates sharply only before 3 times, and fluctuates in a small range since then.

Figure 12 shows the strength change rate of the MOC solidified soil specimens before and after immersion in

water. After curing for 48 hours, improving with the age, the UCS of the immersed specimens decreased by 80.4% and 36.5% compared with the unimmersed specimens. After immersion in water for 24 h on the seventh day, the strength of the CSA solidified soil was only 0.6 MPa [27]. The strength of the MOC solidified soil is still as high as 1.26 MPa.

To sum up, MOC solidified soil has poor water stability and is sensitive to moisture and environmental humidity. With the increase of age, the strength loss rate of the

TABLE 7: Chinese cement-based material 7 days UCS standard (MPa).

Structural layer	Highway grade	Extremely heavy traffic	Heavy traffic	Medium and light heavy traffic
Subbase	Class 1 and above highways	3.0~5.0	2.5~4.5	2.0~4.0
	Secondary and lower highways	2.5~4.5	2.0~4.0	1.0~3.0
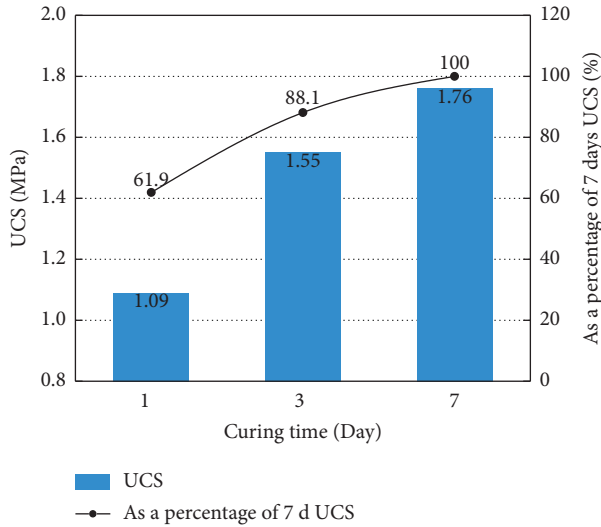
FIGURE 8: UCS of MOC solidified soil with different curing time.
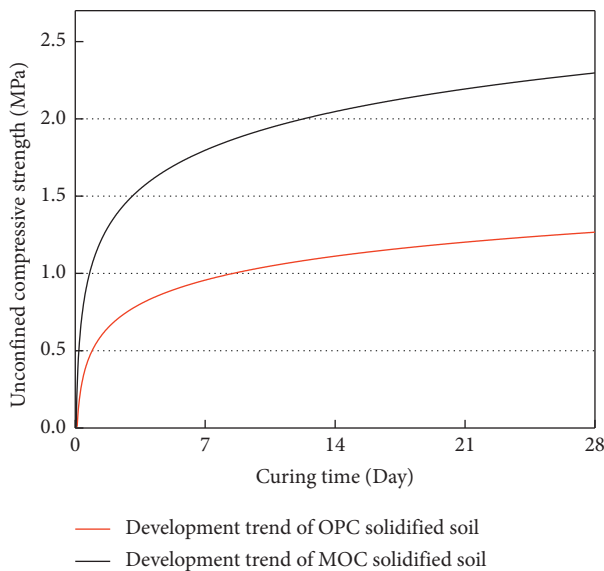
FIGURE 9: Strength prediction curve of OPC and MOC solidified soil.

FIGURE 10: Volume shrinkage rate of MOC solidified soil with different ratios.

specimens after immersing in water gradually decreases. In particular, during the initial maintenance, contacting with water should be avoided or the ambient humidity should be reduced. However, compared with other cement-based solidified soils, it still has better water resistance.

As illustrated in Figure 13, the electrical conductivity of the samples with different ratios in the infiltration solution is compared. As the ratio of $MgCl_2$ to H_2O increases, the electrical conductivity gradually decreases, and it enhances continuity with the increase of MgO content. The change of conductivity is more correlated with the ratio of $MgCl_2$ to H_2O, and the effect of MgO content is less. When the MOC solidified soil was soaked in water, free Cl^- ions played a conductive role, and Mg^{2+} ions might be transformed into $Mg(OH)_2$ and $MgCO_3$.

Because MOC is an unsaturated porous, multiphase material, its main strength phase (phase 5) is an unstable crystalline phase, which is prone to hydrolysis in water environment. After immersing in water, the needle-like dense structure was transformed into a loosely structured $Mg(OH)_2$. Therefore, the density of MOC decreases and the internal voids increase, which led to poor water resistance and mechanical properties.

3.4. Microstructure. The XRD patterns of the four samples are shown in Figure 14. Sample 1 contained more phase 5, a small amount of MgO and SiO_2 phases. It indicated that the reaction of active MgO was relatively complete, and it reacted with SiO_2 in the soil to form an amorphous gelling substance. Calcium was derived from fine-grained soils and impurities in raw materials.

After sample 2 absorbed water, the Mg^{2+} concentration in the system decreased. This phenomenon led to the instability of the presence of alkaline hydrates on the surface, and phase 5 hydrolysis reaction occurred to generate $Mg(OH)_2$. In addition, free Mg^{2+} was carbonized to form $MgCO_3$ and $MgCO_3ClOH \cdot 2H_2O$. $MgCO_3ClOH \cdot 2H_2O$ was
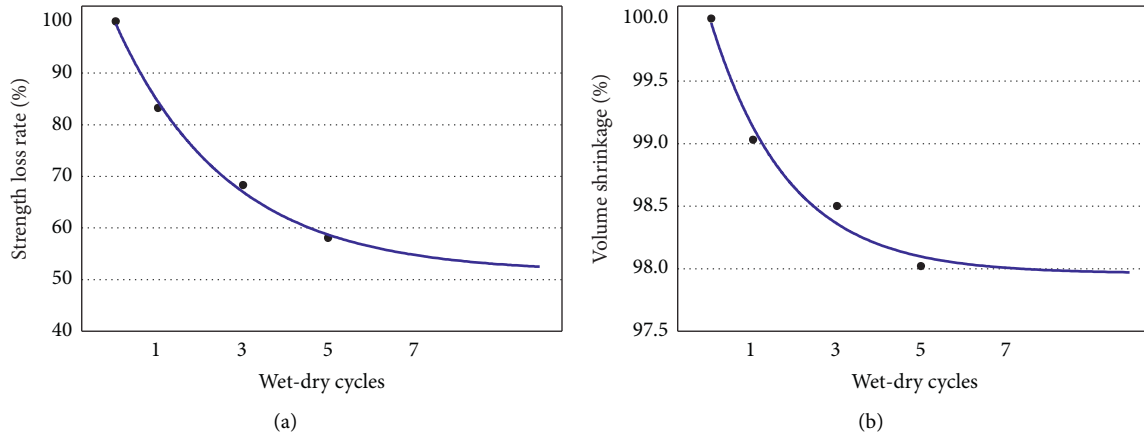
FIGURE 11: Effects of different wet-dry cycles on strength and volume. (a) Strength loss rate. (b) Volume shrinkage.
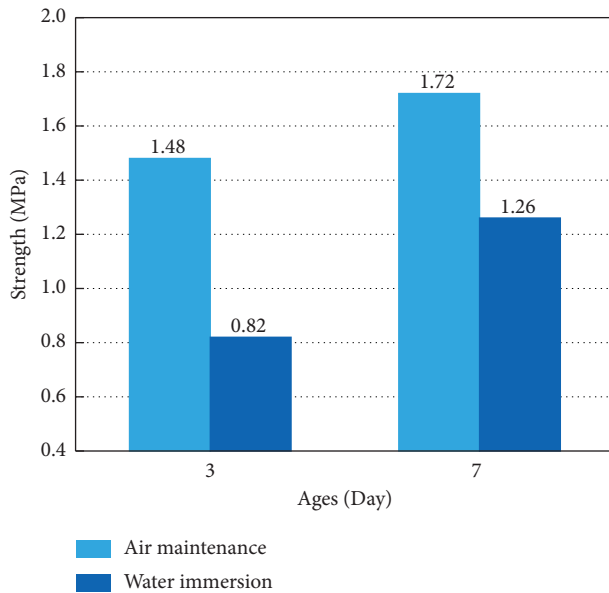
FIGURE 12: Changes in strength of MOC solidified soil after water immersion.
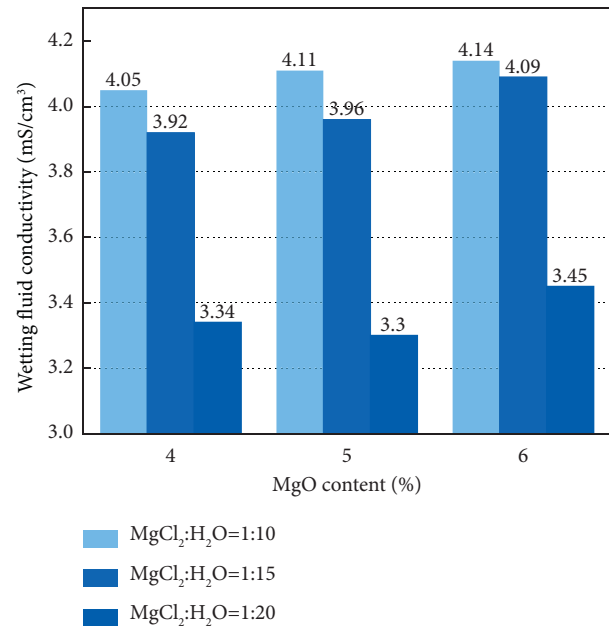
FIGURE 13: Infiltration conductivity of MOC solidified soil with different proportions.

not stable, and would continue to react in the solidified soil under the condition of sufficient water to generate $Mg(ClO_2)_2 \cdot (H_2O)_6$ [29]. The hydrolysis reaction is indicated in formula (5), and the carbonization reaction is presented in

$$5Mg(OH)_2MgCl_28H_2O \longrightarrow 5Mg(OH)_2 + Mg^{2+} + 2Cl^- + 8H_2O, \quad (5)$$

$$MgO + CO_2 + H_2O \longrightarrow MgCO_3 + H_2O, \quad (6)$$

$$MgO + CO_2 + MgCl_2 + H_2O \longrightarrow MgCO_3ClOH2H_2O. \quad (7)$$
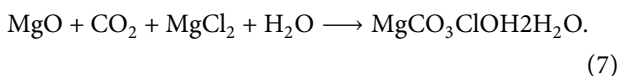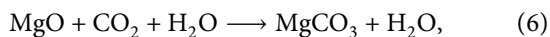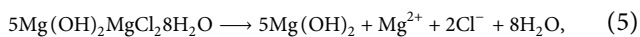
The spectrum of sample 3 was similar to that of sample 1. Sample 3 has a higher content of phase 5 and less SiO_2. It showed that the curing reaction of sample 3 was more complete. The SiO_2 content of sample 4 was very high, and

phase 5 began to appear. A small amount of MgO could still be seen in the sample. It illustrated that the curing reaction was still continuing when curing under standard conditions for 6 h.

Figure 15 indicates the SEM of the four samples. In sample 1, it can be observed that the surface of soil particles is covered with a large number of amorphous gelling products, lamellar $Mg(OH)_2$, and a few needle-like phase 5. The gelling product and the lamellar $Mg(OH)_2$ are closely connected, and a small amount of phase 5 fills the voids in the soil to form a network structure and improve the compaction and mechanical properties of the soil.

Sample 2 was soaked in water after the hydration product was formed. On the one hand, phase 5 hydrolysis reaction occurred to produce loosely packed triangular pyramid $Mg(OH)_2$, which distributed along the soil voids.
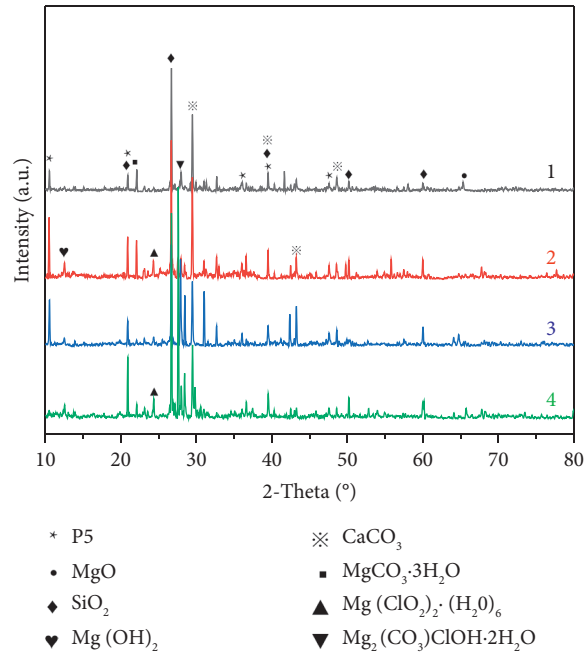
Figure 14: XRD analysis.

(a)

(b)

(c)

(d)
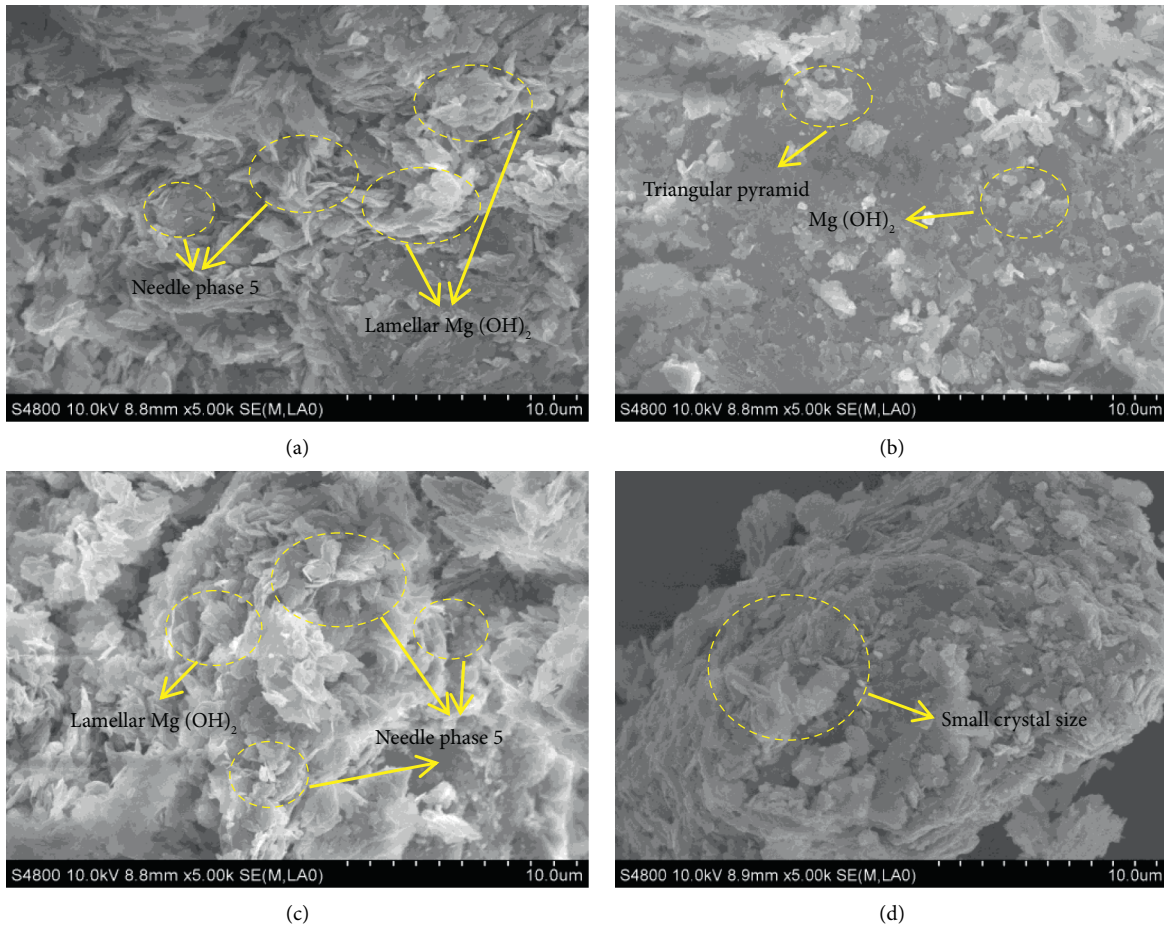
Figure 15: SEM analysis. (a) Sample 1, (b) Sample 2. (c) Sample 3, and (d) Sample 4.

And part of $Mg(OH)_2$ reacted with CO_2 dissolved in water to form $MgCO_3$, attaching to the unhydrolyzed hydration product in the form of massive grains. On the other hand, the soil expands after the flood, causing the network structure to be destroyed. Therefore, larger voids could be seen, and the density of MOC solidified soil decreased.

After increasing the active MgO content and the ratio of $MgCl_2$, the amorphous gel, lamellar $Mg(OH)_2$, and needle-like phase 5 were superimposed on each other to form a network structure, and soil particles could hardly be seen. The reaction greatly increases soil density, it is consistent with the above compaction degree and mechanical property analysis.

For sample 4 had smaller size amorphous gels as well as layered $Mg(OH)_2$. Because of the short curing time, the activated magnesium oxide had not fully reacted, the strength mainly depended on the consolidation of soil particles by the gel tissue produced by the previous hydration. At the same time, it also reflects that a small amount of the phase 5 appeared in MOC solidified soil at the beginning of curing for 6 h, which is consistent with the fast-setting characteristics of MOC.

Through the above microscopic experiments, it can be concluded that the process of using MOC as a curing agent to solidified soil includes: active MgO, H_2O, and silicon in soil form M-S-H gel, which is wrapped on the surface of soil; then Cl^- in dissolved $MgCl_2$ reacted with the gel layer to form the main strength phase (phase 5). Phase 5 continued to grow to fill the gaps between soil particles and cross-linked to form a network structure to consolidate the soil particles. The reason for the poor performance of MOC solidified soil after immersing is that the phase 5 was hydrolyzed to form layered $Mg(OH)_2$, and part of the $Mg(OH)_2$ was carbonized to form $MgCO_3$, which destroys the network structure formed by the phase 5 and soil particles.

4. Conclusions

In this paper, MOC stabilized soil was studied through laboratory experiments and mathematical modeling, and the feasibility of MOC as an environmentally friendly soil-stabilizing agent was described and discussed. Through a series of mechanical properties, durability and microstructure test, engineering properties, main hydration products and microstructure characteristics of MOC stabilized soil were explored, and the optimal raw material ratio of MOC as a soil curing agent was proposed. The precautions and application fields of MOC as a soil stabilizer in engineering practice are given. According to the experimental data and model, the following conclusions are drawn:

(1) Compared with existing cement-based soil stabilizers, such as OPC and CSA, the MOC curing agent can effectively improve soil compaction and mechanical properties. Combined with the specification requirements under the action of different grades of highways and traffic loads, MOC solidified soil is suitable for the sub-base of secondary and lower highways under light traffic load.

(2) In-depth research was carried out on the strength development law of MOC solidified soil with different ratios of raw materials. The test found that when the content of MgO is 6% and the ratio of MgO, $MgCl_2$, and H_2O is $3.68 : 1 : 15$, the properties of MOC solidified soil are the best. Then the relevant mathematical model was established according to the test data, and the optimal ratio of raw materials was obtained as MgO content in $5.5\% \sim 6\%$ and the ratio of $MgCl_2$ to H_2O is 1:14. After the test data was fitted to analyze the strength change trend, it was found that the MOC solidified soil had the characteristics of early strength, and the construction time should be controlled in practice.

(3) The strength loss rate of MOC solidified soil after water immersion in the initial stage of curing is higher, but it is still better than that of traditional cement-based solidified soil. MOC solidified soil should be avoided in coastal areas, areas with sufficient rainfall, and the sub-base of permeable pavement. Water erosion should be minimized in the initial stage of maintenance.

(4) According to mechanical test and durability test combined with microscopic morphology, the hydration process of MOC in soil was analyzed, and the strength formation mechanism of MOC that used as a soil stabilizer was explained: MgO, H_2O, and SiO_2 formed M-S-H gel to wrap soil particles. It further reacts with $MgCl_2$ to form the main strength phase (phase 5) and lamellar $Mg(OH)_2$, and the soil particles form a cross-linked network structure with phase 5 and lamellar $Mg(OH)_2$, thereby forming a high-strength solidification soil. The poor water resistance is due to the destruction of the network structure, resulting in the formation of loose triangular pyramid-shaped $Mg(OH)_2$ and $MgCO_3$.

(5) In this paper, optimal raw material ratio range of MOC curing agent is given. Experiments and microscopic analysis are conducted to investigate the process that MOC enhanced soil. Subsequent experiments can be refined with reference to the given ratio range and mathematical model. Moreover, the test found that the water stability and water resistance of MOC solidified soil were poor. Follow-up research could focus on improving the water resistance of MOC solidified soil.

Data Availability

The data used to support the findings of this study are included within the article.

Conflicts of Interest

The authors declare that they have no conflicts of interest.

Acknowledgments

References

[1] Y. M. Zheng, H. Sun, M. X. Hou, and G. Xiurun, "Microstructure Evolution of Soft clay under Consolidation Loading," *Engineering Geology*, vol. 293, Article ID 106284, 2021.

[2] B. Apinun, H. Suksun, U. Artit et al., "Durability improvement of cement stabilized pavement base using natural rubber latex," *Transportation Geotechnics*, vol. 28, Article ID 100518, 2021.

[3] S. Li, J. Yang, Y. Wu, and M. Wang, "Study on tensile properties of cement-solid soft soil," *Journal of Central South University*, vol. 53, no. 07, pp. 2619–2632, 2022.

[4] S. Jahandari, M. Saberian, Z. Tao et al., "Effects of saturation degrees, freezing-thawing, and curing on geotechnical properties of lime and lime-cement concretes," *Cold Regions Science and Technology*, vol. 160, pp. 242–251, 2019.

[5] M. Saberian, S. Jahandari, J. Li, and F. Zivari, "Effect of curing, capillary action, and groundwater level increment on geotechnical properties of lime concrete: experimental and prediction studies," *Journal of Rock Mechanics and Geotechnical Engineering*, vol. 9, no. 4, pp. 638–647, 2017.

[6] F. D. S. J. Tennison, S. H. Karla, F. Silva Cezar, and R. Dalla, "Mechanical Behavior and Durability of a Typical Frictional Cohesive Soil from Rio Grande Do Sul/Brazil Improved with Portland cement," *Transportation Geotechnics*, vol. 34, 2022.

[7] A. Pivák, M. Pavlíková, M. Záleská et al., "Foam glass lightened sorel's cement composites doped with coal fly ash," *Materials*, vol. 14, no. 5, p. 1103, 2021.

[8] A. Pham Tuan, K. Junichi, and D. Daniel, "Optimum Material Ratio for Improving the Performance of Cement-Mixed soils," *Transportation Geotechnics*, vol. 28, 2021.

[9] J. F. Zhu, R. Q. Xu, Z. Y. Luo, B. Pan, and C. Rao, "Nonlinear constitutive model of magnesia cement-solidified soil considering the effect of curing agent dosage," *Rock and Soil Mechanics*, vol. 41, no. 7, pp. 2224–2232, 2020.

[10] L. C. Yu, C. Yan, S. L. Guo, C. Yan, and X. Lin, "Effect of organic matter content on the properties of magnesium phosphate cement-solidified soil," *Chinese Journal of Engineering Geology*, vol. 28, no. 2, pp. 335–343, 2020.

[11] R. Rintu, R. Dilan, S. Sujeeva, C. Susanga, and M. Abbas, "Optimization of fly ash based soil stabilization using secondary admixtures for sustainable road construction," *Journal of Cleaner Production*, vol. 294, Article ID 126264, 2021.

[12] C. Hu, X. Z. Weng, C. Liu, L. Jiang, J. Liu, and W. Li, "Performance of polypropylene fiber-reinforced solidified soil," *Advances in Civil Engineering*, vol. 2021, Article ID 8859358, 16 pages, 2021.

[13] T. Zhang, Y. L. Yang, and S. Y. Liu, "Application of biomass by-product lignin stabilized soils as sustainable Geomaterials: a review," *Science of the Total Environment*, vol. 728, Article ID 138830, 2020.

[14] Ta Zhang, S. Y. Liu, H. B. Zhan, M. Chong, and C. Guojun, "Durability of silty soil stabilized with recycled lignin for

[15] sustainable engineering materials," *Journal of Cleaner Production*, vol. 248, no. C, Article ID 11293, 2020.

[15] T. A. Aiken, M. Russell, D. McPolin, B. Gavin, L. Nugent, and L. Bagnall, "Effect of molar ratios and curing conditions on the moisture resistance of magnesium oxychloride cement," *Journal of Materials in Civil Engineering*, vol. 34, no. 2, 2022.

[16] Q. Huang, W. X. Zheng, X. Y. Xiao, J. Dong, J. Wen, and C. Chang, "A study on the salt attack performance of magnesium oxychloride cement in different salt environments," *Construction and Building Materials*, vol. 320, Article ID 126224, 2022.

[17] A. Maier and D. L. Manea, "Perspective of using magnesium oxychloride cement (MOC) and wood as a composite building material: a bibliometric literature review," *Materials*, vol. 15, no. 5, p. 1772, 2022.

[18] A. Singh, R. Kumar, and P. Goel, "Factors influencing strength of magnesium oxychloride cement," *Construction and Building Materials*, vol. 303, Article ID 124571, 2021.

[19] A. Pivák, M. Pavlíková, M. Záleská et al., "Low-Carbon composite based on MOC, silica sand and ground porcelain insulator waste," *Processes*, vol. 8, no. 7, p. 829, 2020.

[20] K. Li, Y. S. Wang, X. Wang et al., "Superhydrophobic magnesium oxychloride cement based composites with integral stability and recyclability," *Cement and Concrete Composites*, vol. 118, Article ID 103973, 2021.

[21] K. Gu, B. Chen, W. L. Bi, and Y. Guan, "Recycling of waste gypsum in preparation of magnesium oxychloride cement (MOC)," *Journal of Cleaner Production*, vol. 313, Article ID 127958, 2021.

[22] A. Pivák, M. Pavlíková, M. Záleská, M. Lojka, O. Jankovsky, and Z. Pavlik, "Magnesium oxychloride cement composites with silica filler and coal fly ash admixture," *Materials*, vol. 13, no. 11, p. 2537, 2020.

[23] Y. Y. Guo, Y. X. Zhang, K. Soe, R. Wuhrer, W. D. Hutchison, and H Timmers, "Development of magnesium oxychloride cement with enhanced water resistance by adding silica fume and hybrid fly ash-silica fume," *Journal of Cleaner Production*, vol. 313, Article ID 127682, 2021.

[24] D. X. Wang, S. J. Di, X. Y. Gao, R. Wang, and Z. Chen, "Strength properties and associated mechanisms of magnesium oxychloride cement-solidified urban river sludge," *Construction and Building Materials*, vol. 250, Article ID 118933, 2020.

[25] D. X. Wang, X. Y. Gao, X. Q. Liu, and G. Zeng, "Strength, durability and microstructure of granulated blast furnace slag-modified magnesium oxychloride cement solidified waste sludge," *Journal of Cleaner Production*, vol. 292, Article ID 126072, 2021.

[26] D. X. Wang and Z. G. Chen, "Mechanical properties and microscopic mechanism of sludge solidified by magnesium oxychloride cement," *Geotechnical Mechanics*, vol. 42, no. 01, pp. 77–85+92, 2021.

[27] F. T. Wang, K. Q. Li, and Y. Liu, "Optimal water-cement ratio of cement-stabilized soil," *Construction and Building Materials*, vol. 320, 2022.

[28] J. Pooni, D. Robert, F. Giustozzi, S. Setunge, Y. M. Xie, and J. Xia, "Novel use of calcium sulfoaluminate (CSA) cement for treating problematic soils," *Construction and Building Materials*, vol. 260, 2020.

[29] I. M. Power, G. M. Dipple, and P. S. Francis, "Assessing the carbon sequestration potential of magnesium oxychloride cement building materials," *Cement and Concrete Composites*, vol. 78, pp. 97–107, 2017.

Research Article

Effect of Recycled Bagasse on Cracking Behavior of Clay Materials

Wenlong Ma ⓘ**, Wenbo Liu** ⓘ**, Yuanhang Wang** ⓘ**, and Binbin Yang** ⓘ

School of Civil Engineering, Xuchang University, Xuchang, Henan 461000, China

Correspondence should be addressed to Binbin Yang; yangbinbin@xcu.edu.cn

Bagasse is the residue after juicing sugarcane, and bagasse is a recyclable biological resource that can be used in many ways. Under arid climatic conditions, the clay material shrinks and loses water. Many crisscross drying shrinkage cracks formed on the surface and inside the soil will affect the stability of the soil. In this article, the cracking characteristics of clays with different bagasse contents during the evaporation process have been studied. The cracks were extracted and calculated by digital image processing technology, and the crack characteristics of samples with different bagasse contents were studied by fractal dimension and crack entropy. The results show that when moisture content maintains 34%, the clay material forms only one main crack without bagasse, forms no crack with bagasse content of 9%, and forms a crack network with the bagasse content of 3%. Adding bagasse to the clay can advance the cracking time of the clay, and different contents of bagasse have different effects on the cracking time of the clay. Among these five experimental groups, the clay was affected the most with 3% bagasse content, while the least effect happened with 6% bagasse content. The time can be advanced when the clay crack entropy appears and increases the size of the crack entropy.

1. Introduction

Sugarcane is a kind of sugar cash crop. As a renewable biological resource, bagasse is the residue of sugarcane juice, which is mainly composed of cellulose, hemicellulose, and lignin [1, 2]. Hemicellulose is bound between cellulose. As a molecular adhesive, lignin has a network structure, which surrounds and strengthens cellulose and hemicellulose as a supporting framework [3]. After bagasse is recycled, it can be mixed with urea, fermented, dried, and ground into powder, which can be used as feed for cattle, sheep, pigs, etc. Bagasse contains high sugar and nutrients. The cellulose in bagasse can be converted into sugar, which can be used as alcohol and fuel. As the raw material for making paper cups, mulching films, and paper tableware, wood can be replaced by bagasse to reduce tree felling and protect the environment. It can also make disposable tableware green.

Bagasse used to improve soil is often processed into biochar first. Biochar is a carbon-rich material formed by pyrolysis and carbonization of biomass under the conditions of low oxygen, hypoxia, and relatively low temperature [4]. The biochar is generally alkaline, with large porosity and specific surface area, and rich in ash, which can improve soil

pH, improve soil structure, and increase soil nutrient content. Therefore, biochar is often used as a soil improvement material [5, 6]. But converting bagasse into biochar requires additional energy. Bagasse is widely used in concrete building materials. The characteristics of concrete produced with bagasse ash as a substitute by substituting bagasse ash for some components of concrete mixtures, such as cement and pozzolan materials, have been analyzed by many scholars [7, 8]. By summarizing the articles about replacing cement with bagasse ash in the Scopus database from 2007 to 2021, it is found that replacing cement with bagasse ash in cement composites is a sustainable method [9].

In recent years, as a new type of slope protection and treatment technology, vegetation slope protection and greening technology have been widely used in engineering practice. It can not only improve the stability of the slope to a certain extent and prevent geological disasters, but also improve the ecological environment and promote green development [10, 11]. As major slope protection and greening technology in China, the main soil base material (clay) is prone to water loss and cracking under dry climate conditions, which has a serious impact on the protection effect of actual slope engineering [12]. The crack

characteristics of soil are related to a series of processes such as soil structure, permeability, and water evaporation. The existence of cracks destroys the integrity of soil, makes the cementation between soil particles loose, reduces the cohesion and internal friction angle of soil, reduces the strength of soil, and thus causes a series of engineering problems. Geological disasters caused by soil shrinkage cracking and other problems continue to occur, posing a great threat to human living environment and property safety [13–15]. At present, domestic and foreign scholars have conducted a lot of research on the influencing factors of cohesive soil cracking and quantitative analysis of crack networks [16, 17]. In the process of soil shrinkage and expansion, the content of water and clay has a very important impact on cracks, and wind speed has the greatest impact on the evaporation of cracked soil [18–20].

Cracked clay is a geological body with multiple cracks and significant expansion and contraction produced during the formation of natural geology. Its main components are strongly hydrophilic minerals like montmorillonite, illite, and their mixed-layer clay minerals [21]. In an arid climate, the soil loses water due to dry shrinkage. Crisscross dry shrinkage cracks will develop on the surface and inside the soil. This phenomenon is particularly common and typical in expansive soils with high clay content [22, 23]. Clay shrinkage cracks are a common phenomenon in nature. The crack will accelerate the evaporation of water in the soil, greatly change the movement of nutrients, water and microorganisms in the soil, affect the development of crop roots, and even lead to yield reduction [24]. It not only destroys the integrity of soil, but also provides a good channel for rainfall infiltration, thus reducing the strength of soil, which is an important factor affecting the engineering properties of clay [25, 26]. Cracks will also increase the weathering depth of soil mass, aggravate soil erosion on slope surfaces, and damage the ecological environment. The dry-wet cycle will lengthen the cracks on the surface of the weak argillaceous interlayer, and the dry-wet cycle will increase the crack degree of the weak argillaceous interlayer and reduce the shear strength [27].

In this article, bagasse was recovered and crushed. The cracking characteristics of clay with different bagasse content during evaporation were investigated by an evaporation drying test. The change of water content in the process of evaporation cracking of different samples was monitored, and the development characteristics of cracks of samples in the process of evaporation cracking were recorded by a digital camera. The crack was extracted and calculated by digital image processing technology, and the complexity of cracking was studied by fractal dimension. We observe the degree of chaos in the direction of crack development is determined by the crack entropy.

2. Materials and Testing Methods

2.1. Materials.
The clay used in the experiment is mainly from Xuchang City, Henan Province, China. The weather here is a typical temperate monsoon climate. The annual sunshine duration is about 2280 hours, with sufficient

sunshine and abundant heat resources. Xuchang is mainly affected by seasonal climate, with less precipitation and dry weather in spring. Summer is the season with the most precipitation in a year, and the weather is hot. Normal rainfall in autumn is mild and comfortable. Winter is cold with less rain and snow. The average annual precipitation can generally reach 650 mm. The annual average temperature is $13°C$-$16°C$, and the average temperature in January is about $0.7°C$. The average temperature in July is about $27.5°C$. The physical and mechanical properties of clay samples are listed in Table 1.

In the past five years, the global sugarcane planting industry has developed steadily. Due to its strong adaptability, sugarcane has been planted in most parts of the world. Therefore, the global sugarcane resources can be said to be very rich. However, our utilization of sugarcane only stays at its sugar-making value and edible value. There are two kinds of sugarcane produced in the world, most of which are used to make sugar and most of which are used for our daily consumption. According to my investigation and research, 80% of the raw materials of sugar in the world are cane sugar and 20% is beet sugar, as shown in Figure 1. According to the experimental results, it is found that both the sugarcane used for sugar production and the fruit cane we eat daily contain rich lignocellulose in the remaining bagasse after use. Lignocellulose can not only improve the strength, stiffness, and ductility of the soil, but also play a good role in strengthening the soil. It can also reduce the crack width of the clay, delay the cracking time of the clay, and improve the drying shrinkage of the clay to a certain extent. Therefore, if we can recycle the unused bagasse, we can not only increase the utilization rate of natural resources, but also promote the development of the sugarcane industry chain to a certain extent, so that we can promote common economic progress while making green development. The bagasse used in this experiment is 5 mm bagasse particles dried and screened after mixing the bagasse collected from the sugar factory with the bagasse after juice extraction and consumption. The sugarcane treatment process is shown in Figure 2. The purpose of adding bagasse to the soil is to explore the influence of bagasse as a micro-additive on the drying shrinkage of the clay. The content of chemical components in bagasse is listed in Table 2, and the comparison of mechanical properties between bagasse and other fibrous materials is listed in Table 3. In this article, the experimental results were obtained by comparing the evaporation rate of water and the rupture rate and rupture morphology of soil between normal clay and clay with bagasse in a controlled laboratory environment.

2.2. Methods

2.2.1. Sample Preparation and Experimental Procedures.
After obtaining soil samples from the surrounding areas of Xuchang, the retrieved original soil was dried, crushed with a wooden hammer, and screened to remove large particles in the soil through a 2 mm sieve. The screened small granular soil was poured into 15 open round glassware with a

TABLE 1: Physical and mechanical properties of clay samples.

Density (g·cm^{-3})	Liquid limit (%)	Plastic limit (%)	Plasticity index	Cohesion	Internal friction angle (°)	Compression factor
1.88	60.34	37.71	22.63	58.13	23.31	0.223
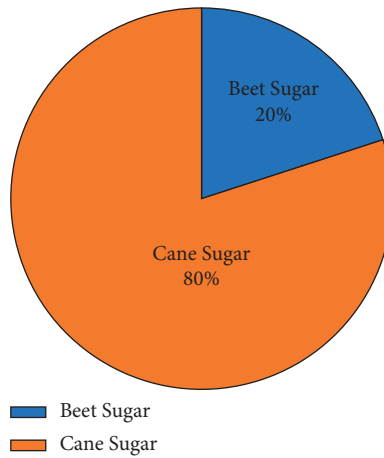
FIGURE 1: Composition of global sugar raw materials.
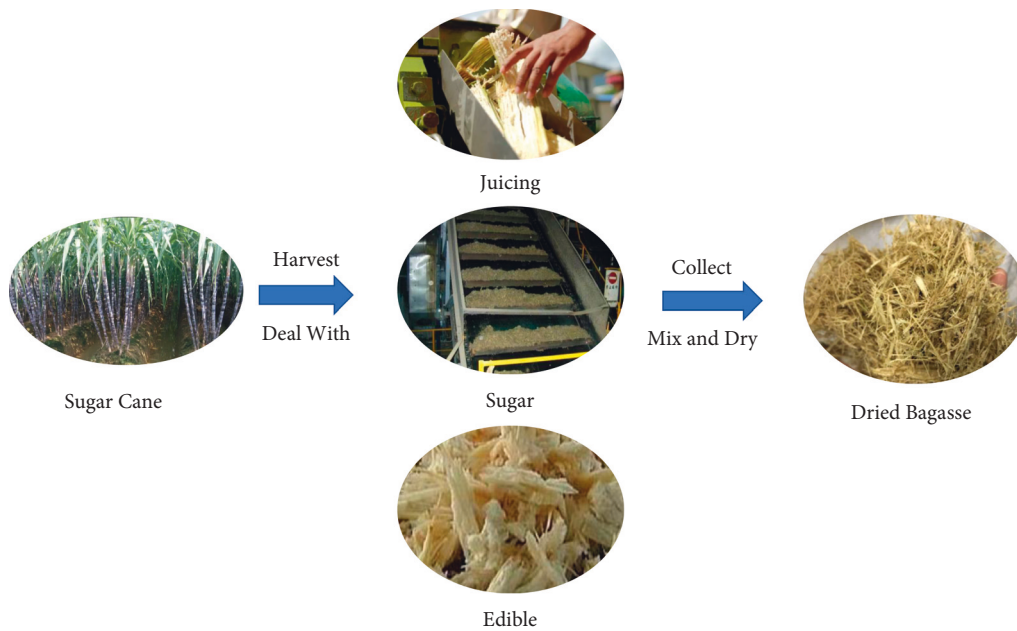
FIGURE 2: Sugarcane treatment process.

TABLE 2: Contents of chemical components in bagasse.

Ingredient name	Cellulose (%)	Hemicellulose (%)	Lignin (%)	Ash (%)	Wax (%)
Composition ratio	49	24	23.6	2.8	0.6

TABLE 3: Comparison of mechanical properties between bagasse and other fibrous materials.

Type of material	Density (g·cm^{-3})	Elastic modulus (GPa)	Tensile strength (MPa)
Bagasse	1.5	6.38	92

diameter of 18 cm and a height of 5 cm. Each glassware contained 150 g of dry soil and different contents of bagasse of different contents, which were mixed evenly. Then, water was added to the material to make it reach the saturation state. After the material reaches the saturation state, it can be observed that the material changes from solid state to slurry state. The treated slurry sample was sealed, placed at a constant temperature and humidity box with a constant temperature of 30°C and relative humidity of 40%, and solidified for 170 h under the condition of weight. In the process of weight consolidation, in order to ensure the accuracy of the test results, the test samples should be strictly controlled in a constant temperature and humidity environment of 30°C and 40% relative humidity, and an electronic balance with an accuracy of 0.01 g should be used to record the real-time weight changes of the test samples. The specific operation steps are shown in Figure 3. A total of 15 samples with the same initial thickness were prepared for the test, including 5 bagasse test samples with different proportions. Three samples were set for each test sample to avoid special data in the test, and to ensure the accuracy of the test results.

2.2.2. Image Processing of Drying Experiment. The development of cracks in clay with or without bagasse was monitored with a digital camera. First, a fixed platform was selected and the platform was connected to the computer through the wireless network. The digital camera was installed on the fixed platform selected, with the orientation directly above the test sample and 75 cm away from the test sample. The lens direction of the digital camera was adjusted perpendicular to the surface of the glass container of the test sample. The electronic balance was placed for measuring the weight of the test sample under the circular glass container containing the test sample and the projection range of the camera lens was adjusted to 200 mm × 200 mm, making it the same size as the electronic scale. After adjustment, in the process of test monitoring, we can directly observe the changes of test samples in each round glass container by observing the imaging of the projection center of the digital camera. In order to observe the center change of the image more intuitively and eliminate the influence of the boundary, the image collected by the digital camera is cropped to 15 cm × 15 cm, and then the cropped image is processed according to the process in Figure 4. First, all the collected images are color images in RGB mode, as shown in Figure 4(a). The gamma correction graying method can be used to process the image after we remove the noise, as shown in Figure 4(b). The principle is as follows:

$$\text{Gray} = \sqrt[2.2]{\frac{R^{2.2} + (1.5G)^{2.2} + (0.6B)^{2.2}}{1 + 1.5^{2.2} + 0.6^{2.2}}}. \tag{1}$$

Second, the binary image which can clearly reflect the local and overall characteristics of the image is obtained by selecting the appropriate binary threshold for the gray image with 256 brightness levels after processing. After calculating the binarization threshold of different gray values in the gray

histogram, the gray image can be divided into two parts: crack and clay. The binary image after the assignment is shown in Figure 4(c).

Finally, the image without past noise processing is very blurred, and even isolated pixel points or pixel blocks will be formed. There are some denoising methods: mean filter, median filter, and Gaussian filter. Because the mean filter can easily lead to the blurring of image edges, and since the premise of using the median filter is to select an appropriate sliding window, a Gaussian filter is used to remove noise in this experiment. The denoised image is shown in Figure 4(d).

2.2.3. Calculation of Crack Fractal Dimension and Crack Entropy. In order to better analyze the length, shape, crack length, and other characteristics of clay cracks, fractal dimension is used to quantify the sample crack network. The commonly used fractal dimension algorithms mainly include the size method, the island method, and the box-counting dimension method. The sizing method is often used to measure the tortuosity of a curve. It mainly uses a selected size r to measure along the measured curve by dividing rules. The precondition for the use of the island method is the closed curve. The crack change map extracted is the closed curve, which meets the requirements. However, because it is not a regular figure, it cannot be calculated by assuming that the perimeter is directly proportional to the power of the measurement unit, and the area is directly proportional to the power of the measurement unit. The original smooth perimeter was replaced by the fractal perimeter curve according to the calculation method of the fractal dimension of irregular graphics, which was proposed by Blumen and Mandelbort [28]. The box-counting dimension method covers the fractal curve by taking a small box with side length l and uses the least square method to fit the curve in the double logarithmic coordinates through the number of boxes $N(l)$. The slope of the curve is the fractal dimension, as shown in the following formula:

$$D = -\lim_{l \to 0} \frac{\log N(l)}{\log (1/l)}, \tag{2}$$

where D is the fractal dimension. The box-counting dimension method is similar to the size method, which is suitable for fractal dimension calculation in this test.

Information entropy is related to the number of possible results of events. Under the condition of equal probability, the more possibilities exist, the greater the information entropy, that is, the greater the uncertainty of events. Information entropy is related to the probability distribution of events. The more uniform the probability distribution, the greater the information entropy [29]. When all probabilities are equal, the larger the information entropy is. Based on the information entropy, the probability entropy of a crack can be constructed. The larger the crack entropy is, the more uniform the crack distribution is.

$$K_c = -\sum_{i=1}^{n} p_i \log p_i, \tag{3}$$

where K_c is the fractal dimension and pi is the probability of crack occurrence in a certain direction.
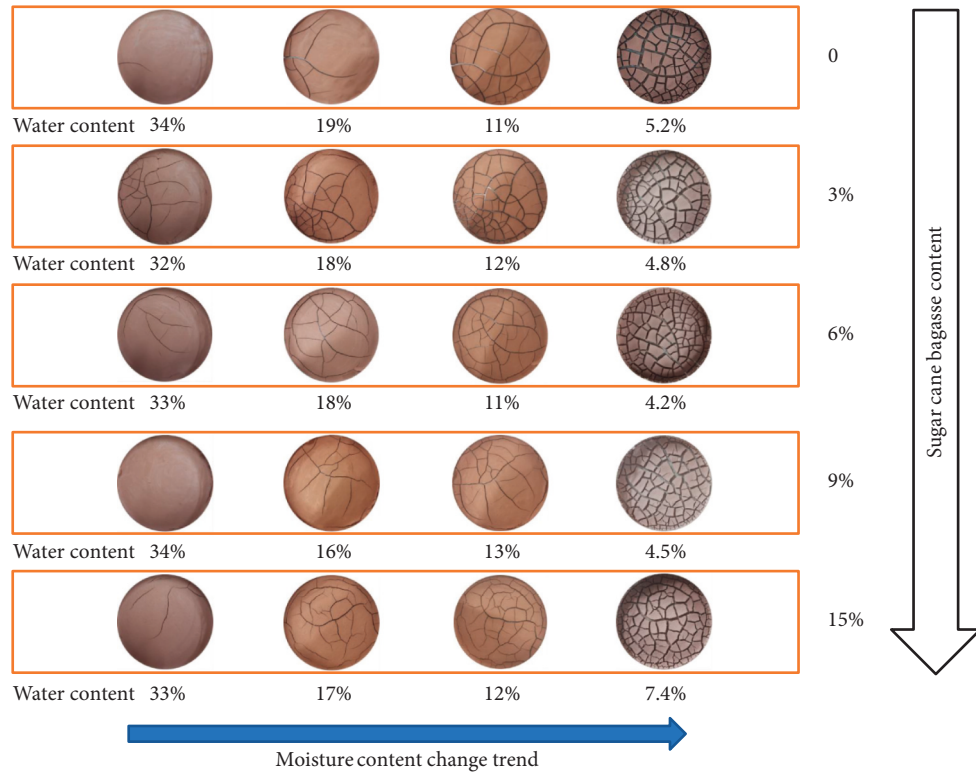
Figure 3: Change image of clay crack network with different bagasse content.

(a) Original Image

(b) Grayscale Image

(c) Binary Image

(d) Denoised Image
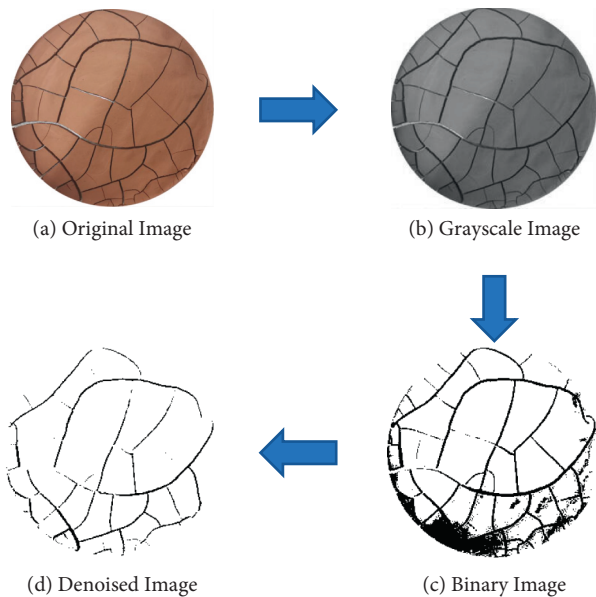
Figure 4: Image processing process.

3. Result

3.1. Fractal Characteristics of Crack Network. By observing the changing image of the clay crack network with different bagasse content in Figure 3, it can be found that the cracking degree of clay increases with the decrease of water content when the bagasse content is 0, 3%, 6%, 9%, and 15%, but the cracking degree of bagasse clay with similar water content is different under different bagasse content. There is only one main crack in the clay without bagasse when the water content is 34%, and there is no crack in the clay with bagasse content of 9% when the water content is 34%. However, secondary cracks appear in the clay with a bagasse content of 3%, 6%, and 15% when the water content is approximately 33%, and the clay with bagasse content of 3% has initially formed a crack network. The clay with a bagasse content of 6% and 15% initially formed its crack network when the water content was about 18%, while the clay without bagasse and with a bagasse content of 9% initially formed its crack network when the water content was about 12%. When the water content is 5.2%, the clay without bagasse is completely cracked. When the clay with bagasse content of 3%, 4.2%, 6%, 9%, and 15% is completely cracked, the water content is 4.8%, 4.2%, 4.5%, and 7.4%, respectively. Through simple data analysis, we can find that different bagasse content can affect the cracking degree of clay under the same water content.

As shown in Figure 5, the change characteristics of the fractal dimension of clay crack with different bagasse content, the lines with different colors represent the clay with different bagasse content, and the starting points of the lines represent the occurrence time and stability time of the fractal dimension of the clay with different bagasse content. The slope of the line represents the relationship between the fractal dimension of clay with different bagasse content and time. The observation shows that when the bagasse content of clay is 3%, its fractal dimension begins to increase at 112 h,
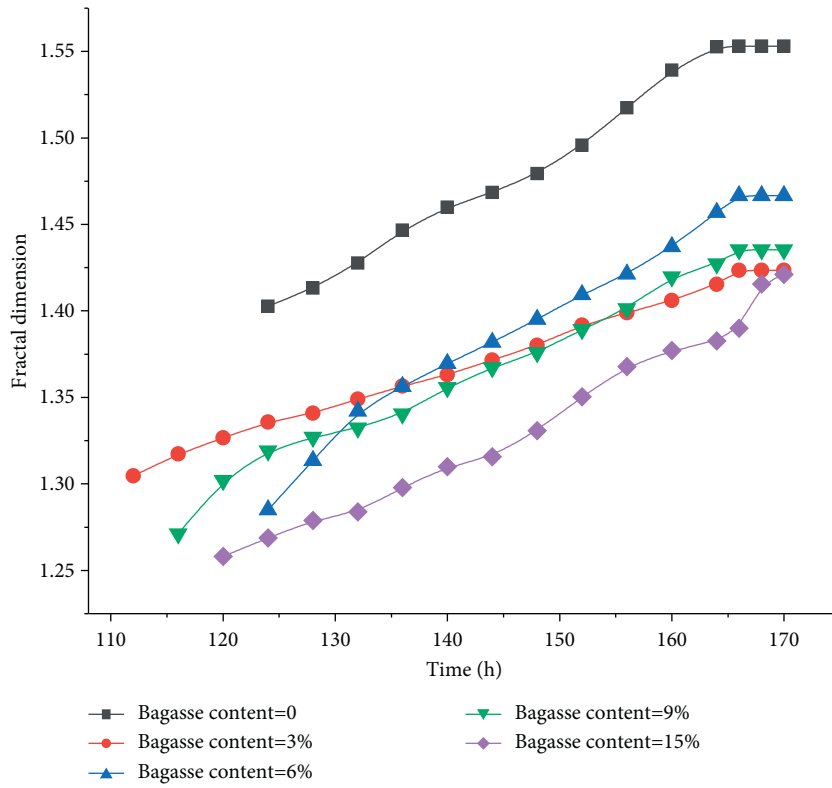
Figure 5: Change characteristics of clay crack fractal dimension with different bagasse content.
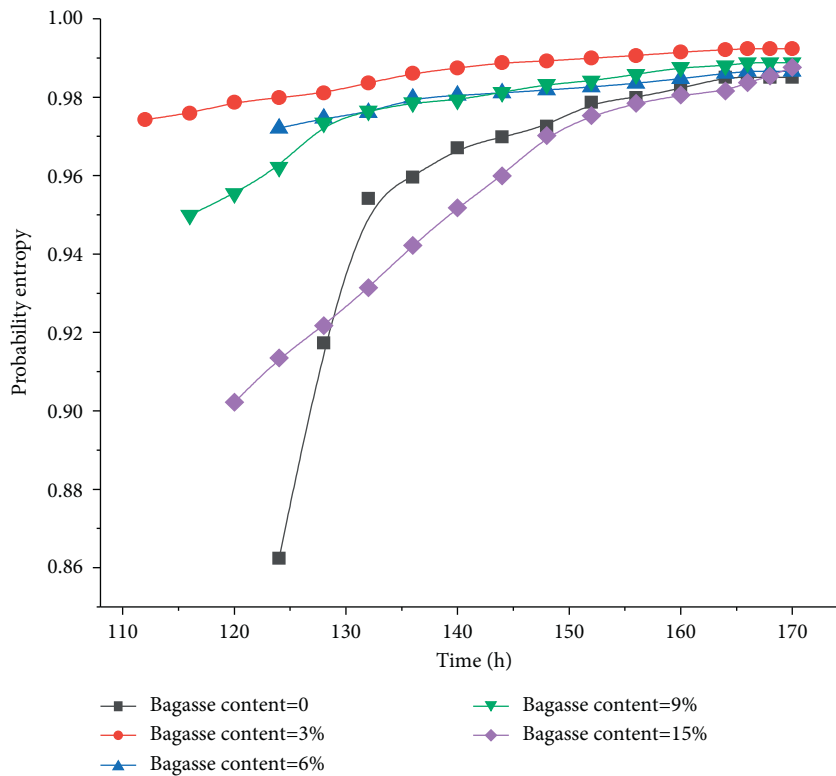
Figure 6: Change characteristics of clay crack entropy with different bagasse content.
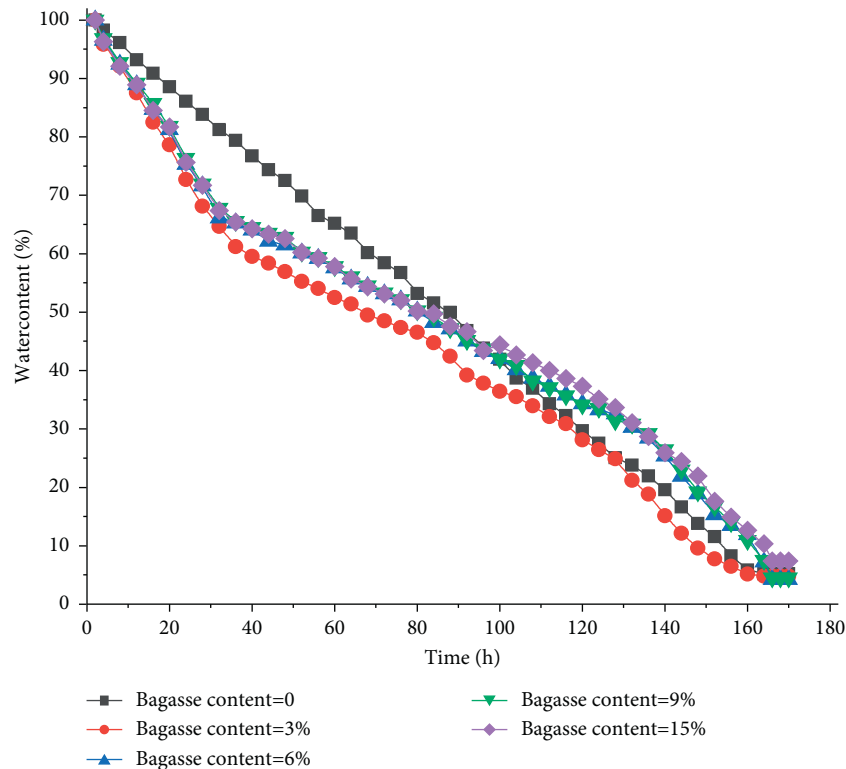
Figure 7: Variation characteristics of clay water content with different bagasse content.

indicating that the clay with a bagasse content of 3% cracks first and its fractal dimension is 1.304. Then, the fractal dimension of clay with a bagasse content of 9% was 1.271 at 116 h. The fractal dimension of clay with 15% bagasse is 1.258 at 120 h. The fractal dimension values of clay with bagasse content of 6% and clay without bagasse at 124 h are 1.285 and 1.402, respectively. The cracking time of clay varies with the different contents of bagasse. Adding bagasse to the clay can advance the cracking time of the clay, and different bagasse contents have different effects on the cracking time of the clay. Among our five experimental groups, the clay with 3% bagasse content has the greatest impact, and the clay with 6% bagasse content has the least impact. We can advance the cracking of clay by adding different content of bagasse to the clay.

As shown in Figure 6, the change characteristics of clay crack entropy with different bagasse content, different bagasse content in clay will change the time and size of clay crack entropy. By observing the data changes in the figure, the crack entropy of clay with a bagasse content of 3% first appeared at 112 h, with a size of 0.974. Compared with the clay with a bagasse content of 9% and a bagasse entropy of 0.950 at 116 h, the clay with a bagasse content of 3% obviously cracks earlier and has a greater impact on the clay crack entropy than the clay with a bagasse content of 9%. By observing the change curves of the other three contents, the earliest crack entropy of the clay with a bagasse content of 15% has first appeared at 120 h, and the size of the crack entropy is 0.902. The clay without bagasse and the clay with bagasse content of 6% both appeared at 124 h, but the clay without bagasse had a crack entropy of 0.862 at 124 h, and

the clay with bagasse content of 6% had a crack entropy of 0.972 at 124 h. Finally, the crack entropy of the clay with and without bagasse tends to be about 0.980 at 170 h. The crack entropy of clay with bagasse appeared earlier than the clay without bagasse, and the value is large. The effect of bagasse with different content on the change characteristics of clay crack entropy is also different. The addition of bagasse to the clay can advance the time of clay crack entropy and increase the current size of crack entropy.

Variation characteristics of clay water content with different bagasse content are shown in Figure 7. The variation characteristics of clay water content with and without bagasse are different. The water content of the clay without bagasse decreased from 100% to 5.2% in 170 h, and the water content basically showed a linear change with time. The water content of the clay with different content of bagasse decreased from 100% to about 65% in 0–30 h, while the water content of the clay without bagasse decreased from 100% to about 80% in 0–30 h, indicating that the addition of bagasse can make the water content of the clay decrease rapidly in the early stage. The water content of clay with different content of bagasse slows down at 30–170 h. The water content of clay with different content of bagasse is basically the same as that of clay without bagasse at about 100 h. The water content of clay with 6%, 9%, and 15% bagasse at 100–170 h is greater than that of clay without bagasse. Only the water content of clay with 3% bagasse is less than that of clay without bagasse at 100–170 h, Finally, at 164 h, the water content of the clay without bagasse and the clay with bagasse content of 3% completely cracked did not change and decreased to 5.2% and 4.8%, respectively. The
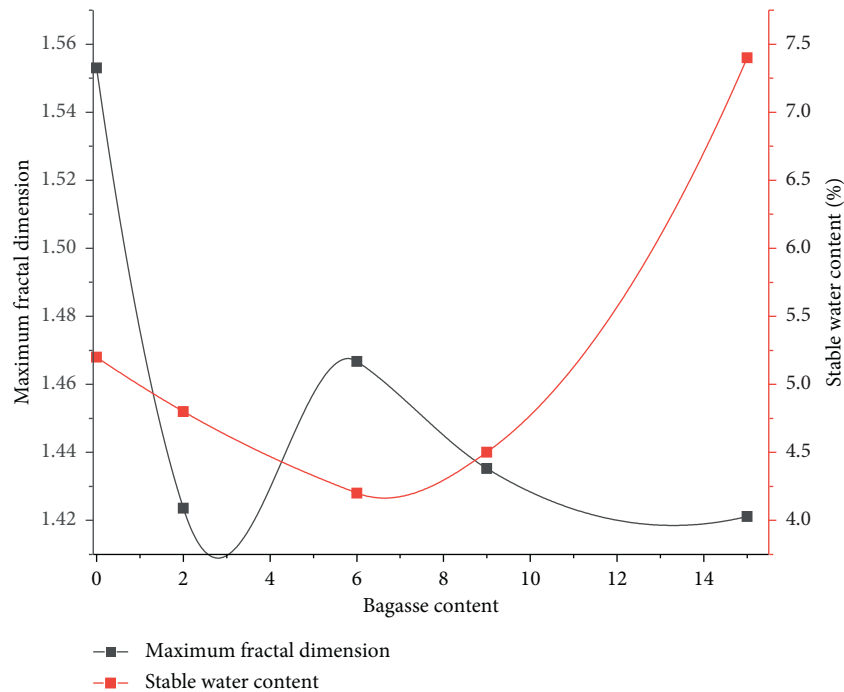
FIGURE 8: Relationship between water content and crack fractal dimension of clay with different bagasse content.

clay with a bagasse content of 6%, 9%, and 15% completely cracked at 166 h, and the water content decreased to 4.2%, 4.5%, and 7.4%, respectively. It shows that the appropriate addition of bagasse to the clay can make the water content of the clay with bagasse higher than that of the clay without bagasse at the same time in the later stage, and enhance the water retention capacity of the clay in the later stage.

4. Discussion

Bagasse fiber contains many polar hydroxyl groups, and its compatibility with hydrophobic polymer matrix is very poor; at the same time, hydroxyl groups generate strong hydrogen bonds between bagasse fibers, which makes bagasse easy to agglomerate in the polymer matrix, and the dispersion is not ideal. As shown in Figure 8, for the sample without bagasse, the final fractal dimension of the sample crack network is the largest, with a value of 1.553. The final fractal dimension of the sample crack network decreases with the addition of bagasse. The final fractal dimension of the sample with 15% bagasse content is the smallest, which is 1.421, which is decreased by 8.4% compared with the sample without bagasse. The final fractal dimension of the sample with bagasse content of 3% was 1.423, which decreased by 8.3% compared with the sample without bagasse. The final fractal dimension of the crack network of the sample with bagasse content of 6% was 1.466, which decreased by 5.6% compared with the sample without bagasse. The final fractal dimension of the crack network of the samples with bagasse content of 9% was 1.435, which decreased by 7.5% compared with the samples without bagasse. The stable water content of the sample decreased first and then increased with the addition of different amount of bagasse. For the sample without bagasse, the

stable water content of the sample is 5.2%. The stable water content of the sample with bagasse content of 3% was 4.8%, which decreased by 7.6% compared with the sample without bagasse. The sample with a bagasse content of 6% had the lowest stable water content, which was 4.2%, and decreased by 19.2% compared with the sample without bagasse. For the samples with a bagasse content of 9%, the stable water content of the samples began to rise, and the value was 4.5%. However, compared with the samples without bagasse, the stable water content of the samples still decreased, with a decreasing percentage of 13.4%. The stable water content of the sample with 15% bagasse was the highest, which was 7.4%, and increased by 42.3% compared with the sample without bagasse.

5. Conclusions

There are many polar hydroxyl groups in the bagasse fiber, and its compatibility with the hydrophobic polymer matrix is very poor. In this article, the cracking characteristics of clay materials with different bagasse contents during evaporation were studied by recycling bagasse. The digital image processing technology is used to extract and calculate the crack. The fractal dimension and entropy of cracks are used to quantitatively analyze the crack characteristics of the samples.

When the content of bagasse in the clay is different, the cracking time of the clay is also different. The clay with a bagasse content of 9% has no cracks when the water content is 34%, and the clay with a bagasse content of 3% has initially formed a crack network.

The clay with 3% bagasse content has the greatest impact, and the clay with 6% bagasse content has the least impact. By adding a certain amount of bagasse to the clay, the time of

clay crack entropy and the size of clay crack entropy can be increased.

The final fractal dimension of the sample crack network decreases with the addition of bagasse. The final fractal dimension of the sample with 15% bagasse content is the smallest, which is 1.421, which is decreased by 8.4% compared with the sample without bagasse.

Data Availability

The datasets generated during the current study are available from the corresponding author upon reasonable request.

Conflicts of Interest

No conflicts of interest exit in the submission of this manuscript.

Authors' Contributions

All authors approved the manuscript for publication.

Acknowledgments

References

[1] Y. R. Loh, D. Sujan, M. E. Rahman, and C. A. Das, "Sugarcane bagasse—the future composite material: a literature review," *Resources, Conservation and Recycling*, vol. 75, pp. 14–22, 2013.

[2] A. Kumar, V. Kumar, A. Kumar, V. Kumar, and B. Singh, "Cellulosic and hemicellulosic fractions of sugarcane bagasse: potential, challenges and future perspective," *International Journal of Biological Macromolecules*, vol. 169, pp. 564–582, 2021.

[3] P. Khatri and A. B. Pandit, "Systematic review of life cycle assessments applied to sugarcane bagasse utilization alternatives," *Biomass and Bioenergy*, vol. 158, Article ID 106365, 2022.

[4] M. Inyang, B. Gao, P. Pullammanappallil, W. Ding, and A. R. Zimmerman, "Biochar from anaerobically digested sugarcane bagasse," *Bioresource Technology*, vol. 101, no. 22, pp. 8868–8872, 2010.

[5] L. R. Bento, A. J. R. Castro, A. B. Moreira, O. P. Ferreira, M. C. Bisinoti, and C. A. Melo, "Release of nutrients and organic carbon in different soil types from hydrochar obtained using sugarcane bagasse and vinasse," *Geoderma*, vol. 334, pp. 24–32, 2019.

[6] B. S. Q. Alves, K. P. S. Zelaya, F. Colen et al., "Effect of sewage sludge and sugarcane bagasse biochar on soil properties and sugar beet production," *Pedosphere*, vol. 31, no. 4, pp. 572–582, 2021.

[7] S. Rukzon and P. Chindaprasirt, "Utilization of bagasse ash in high-strength concrete," *Materials & Design*, vol. 34, pp. 45–50, 2012.

[8] K. Ganesan, K. Rajagopal, and K. Thangavel, "Evaluation of bagasse ash as supplementary cementitious material," *Cement and Concrete Composites*, vol. 29, no. 6, pp. 515–524, 2007.

[9] W. Ahmad, A. Ahmad, K. A. Ostrowski, F. Aslam, P. Joyklad, and P. Zajdel, "Sustainable approach of using sugarcane bagasse ash in cement-based composites: a systematic review," *Case Studies in Construction Materials*, vol. 15, Article ID e00698, 2021.

[10] M. Suhatril, N. Osman, P. Azura Sari, M. Shariati, and A. Marto, "Significance of surface eco-protection techniques for cohesive soils slope in Selangor, Malaysia," *Geotechnical & Geological Engineering*, vol. 37, no. 3, pp. 2007–2014, 2019.

[11] B. Yuan, Z. Li, Y. Chen et al., "Mechanical and microstructural properties of recycling granite residual soil reinforced with glass fiber and liquid-modified polyvinyl alcohol polymer," *Chemosphere*, vol. 286, Article ID 131652, 2022.

[12] X. Tong, M. Brandt, Y. Yue et al., "Increased vegetation growth and carbon stock in China karst via ecological engineering," *Nature Sustainability*, vol. 1, no. 1, pp. 44–50, 2018.

[13] B. Yuan, W. Chen, J. Zhao, F. Yang, Q. Luo, and T. Chen, "The effect of organic and inorganic modifiers on the physical properties of granite residual soil," *Advances in Materials Science and Engineering*, vol. 2022, Article ID 9542258, , 2022.

[14] Z. Huang, B. Wei, L. Zhang, W. Chen, and Z. Peng, "Surface crack development rules and shear strength of compacted expansive soil due to dry–wet cycles," *Geotechnical & Geological Engineering*, vol. 37, no. 4, pp. 2647–2657, 2019.

[15] B. Yuan, M. Chen, W. Chen, Q. Luo, and H. Li, "Effect of pile-soil relative stiffness on deformation characteristics of the laterally loaded pile," *Advances in Materials Science and Engineering*, vol. 2022, Article ID 4913887, 2022.

[16] J. J. Xu, H. Zhang, C. S. Tang, Q. Cheng, B. Liu, and B. Shi, "Automatic soil desiccation crack recognition using deep learning," *Géotechnique*, vol. 72, no. 4, pp. 337–349, 2022.

[17] B. Yuan, Z. Li, W. Chen, J. Zhao, J. Lv, J. Song, and X. Cao, Influence of groundwater depth on pile–soil mechanical properties and fractal characteristics under cyclic loading," *Fractal and Fractional*, vol. 6, no. 4, p. 198, 2022.

[18] F. Favre, P. Boivin, and M. C. S. Wopereis, "Water movement and soil swelling in a dry, cracked Vertisol," *Geoderma*, vol. 78, no. 1-2, pp. 113–123, 1997.

[19] P. D. Hallett and T. A. Newson, "Describing soil crack formation using elastic–plastic fracture mechanics," *European Journal of Soil Science*, vol. 56, no. 1, pp. 31–38, 2005.

[20] T. G. Poulsen, W. Cai, and A. Garg, "Water evaporation from cracked soil under moist conditions as related to crack properties and near-surface wind speed," *European Journal of Soil Science*, vol. 71, no. 4, pp. 627–640, 2020.

[21] W. Zhu, G. Feng, and J. Du, "Restricted effect of two plant root systems on the crack expansion of China yunnan laterite under dry-wet cycle," *Design Engineering*, pp. 1–10, 2020.

[22] B. Yuan, Z. Li, Z. Zhao, H. Ni, Z. Su, and Z. Li, "Experimental study of displacement field of layered soils surrounding laterally loaded pile based on Transparent Soil," *Journal of Soils and Sediments*, vol. 21, no. 9, pp. 3072–3083, 2021.

[23] H. Zhu, Y. Zhang, Z. Li, and X. Xue, "Study on crack development and micro-pore mechanism of expansive soil improved by coal gangue under drying–wetting cycles," *Materials*, vol. 14, no. 21, p. 6546, 2021.

[24] T. Colombi, N. Kirchgessner, D. Iseskog, S. Alexandersson, M. Larsbo, and T. Keller, "A time-lapse imaging platform for quantification of soil crack development due to simulated root water uptake," *Soil and Tillage Research*, vol. 205, Article ID 104769, 2021.

[25] M. Z. Izzo and M. Miletić, "Sustainable improvement of the crack resistance of cohesive soils," *Sustainability*, vol. 11, no. 20, p. 5806, 2019.

[26] C. Liu, C. Tang, K. Sun, H. Li, S. Xu, and T. Leng, "Review on the mechanism and theoretical model of desiccation cracking

in clay soil," *Journal of Engineering Geology*, vol. 26, no. 2, pp. 296–308, 2018.

[27] L. P. He, J. Y. Yu, Q. J. Hu, Q. J. Cai, M. F. Qu, and T. J. He, "Study on crack propagation and shear behavior of weak muddy intercalations submitted to wetting-drying cycles," *Bulletin of Engineering Geology and the Environment*, vol. 79, no. 9, pp. 4873–4889, 2020.

[28] A. Blumen and B. B. Mandelbort, "Fractals, geometry: what is it, and what does it do?: discussion," *Proceedings of the Royal Society of London Series A*, vol. 423, no. 1864, p. 16, 1989.

[29] Y. M. Omar and P. Plapper, "A survey of information entropy metrics for complex networks," *Entropy*, vol. 22, no. 12, p. 1417, 2020.

Research Article

Effects of Commercial Antioxidants on Aging Resistances of Asphalt Binders

Xijie An,[1] **Ying Gao,**[2] **Zizhen Dong,**[2] **Qinglin Guo** ⬦,[2] **Lili Li,**[2] **and Yancang Li** ⬦[2]

[1]*Inner Mongolia Vocational and Technical College of Communications, Chifeng, Inner Mongolia 024005, China*
[2]*School of Civil Engineering, Hebei University of Engineering, Handan, Hebei 056038, China*

Correspondence should be addressed to Qinglin Guo; guoql@hebeu.edu.cn

Asphalt aging has a direct influence on the durability of asphalt mixture. In order to improve thermal oxidizing aging resistance of asphalt, the commercial antioxidants including Irganox 1010 and Irgafos 168 were selected to modify base asphalt and SBR asphalt. The basic properties of modified asphalt before and after the rolling thin film oven test (RTFOT) are evaluated by penetration, softening point, ductility, and viscosity. The Fourier transform infrared spectroscopy (FTIR) test was applied to determine the antiaging mechanism of modified and unmodified asphalt. According to the test result, Irganox 1010 not only reduces the aging degree of asphalt but also has little adverse effect on other properties. Irgafos 168 with a content of 1% improves the low temperature ductility of asphalt and improves the antiaging performance of asphalt significantly. After RTFOT, the content of oxygen-containing functional groups (carbonyl group and sulfoxide group) declines significantly in antioxidation modified asphalt, and Irganox 1010 and Irgafos 168 inhibit oxidizing reaction in the aging procedure. This study can provide a useful reference for improving the aging property of asphalt in highway construction.

1. Introduction

Asphalt pavement with a good performance has been widely used around the world since the 1850s [1–6]. In the mixing and paving stage of asphalt mixture, the oxidation reaction of asphalt with oxygen occurs at high temperature, which leads to the rapid aging of asphalt. In the service stage, a slow oxidation reaction gradually occurs between asphalt and oxygen in the air [7–9]. Asphalt aging causes the binder to become hard and brittle, with a severe decline in relaxation properties, eventually leads to pavement cracking and other diseases. Therefore, research efforts on asphalt aging research and discussion had never terminated until now [10–14]. Adding additives to asphalt to improve the antiaging performance of asphalt is the most commonly used method [15–18]. Therefore, more and more attention has been paid to the addition of antiaging agents, which can inhibit the thermal and oxygen aging reaction process to improve the antiaging property of asphalt.

The antioxidant was used as antiaging agents frequently. Previous studies have shown that antioxidants can effectively improve the aging resistance of asphalt. Williams et al. [19] have evaluated the antioxidant effects of lignin-containing ethanol coproducts on asphalt binders. They proved that lignin-containing ethanol coproducts can effectively reduce the aging degree of asphalt binders. Reyes et al. [20] have studied the antiaging effect of VE for the base and modified asphalt binders, and the results showed that the viscosity of asphalt decreases and fatigue crack resistance increases. Ouyang et al. [21] have investigated the impacts of anti-oxidants including zinc dialkyl dithiophosphate (ZDDP) and zinc dibutyl dithiocarbamate (ZDBC) on SBS-modified asphalt, and they suggested that ZDDP and ZDBC can retard the oxidation of asphalt through the inhibition of peroxides and radical scavenging. Li et al. [22] researched the antiaging effect of three antioxidants in asphalt, evaluated antiaging performance using the aging index, and analyzed the antiaging mechanism with FTIR. The result shows that the antioxidants make the aging chain reaction terminated so

that the aging resistance had been effectively improved. The composite antioxidant was more stable for aging resistance improvement of asphalt due to its good synergistic effect. Different kinds of antioxidants in asphalt binders have different effects on resistance oxidation [22, 23].

Among the antioxidants, Irganox 1010 and Irgafos 168 were the common antioxidants. Irganox 1010 was characterized by low volatilization, extraction resistance, nontoxic and high thermal stability, and melting temperature similar to asphalt, and Irgafos 168 has good high temperature resistance, color resistance, strong extraction resistance, and stable hydrolysis. Both of them have significant antiaging effects on polymer materials. Apeagyei et al. [9] used Irganox 1010 and its different combinations with other antioxidants to explore the antiaging effect of antioxidants on asphalt through the dynamic shear rheological (DSR) test and the bending beam rheometer (BBR). Their result shows that the hardness of asphalt after short-term aging did not decrease significantly when the content was less than 1%, but the effect was significant when it is above 5%. The reduction in hardness after aging of asphalt was related to the content of Irganox 1010. Irganox 1010 in combination with carbon black has a good antiaging effect for asphalt binders when its content reaches 3%. Thus, it can be found that Irganox 1010 is beneficial for the improvement of asphalt properties. However, only the rheological properties and antiaging properties of asphalt under the influence of Irganox 1010 were studied, but the impact of different contents on the physical properties of asphalt is required to be researched in the future, and the interaction mechanism between Irganox 1010 and asphalt also should be revealed. Furthermore, Feng et al. [24] studied the effects of Irganox 1010, Irgafos 168 and their different combinations on the physical properties and antiaging properties of asphalt, and the result shows that Irganox 1010 can improve the thermal oxidative aging resistance of asphalt; the oxidative aging resistance of asphalt can also be improved when the content of Irganox 1010 was not more than 0.6 by a total weight of bitumen. Irgafos 168 did not improve the thermal oxidative aging resistance when the content was less than 0.6 by a total weight of bitumen. A notable improvement can be found when the content exceeds 0.6 by a total weight of bitumen. However, the range of antioxidant content was on a small scale and lacked Irganox 1010 and Irgafos 168 in the thermal oxidative aging mechanism of asphalt. Li et al. [25] studied that the reaction mechanism of Irganox 1010 and Irgafos 168 in asphalt, indicating that Irganox 1010 was one of hindered phenols, and it can effectively prevent SBS from oxidation via scavenging free radical; Irgafos 168 can decompose hydroperoxides as phosphite. It can be inferred that the antiaging properties of polymers were improved by adding Irganox 1010 and Irgafos 168; therefore, the antiaging performance of asphalt can also be modified by Irganox1010 and Irgafos168.

Herein, the aging reaction can be reduced by Irganox1010 and Irgafos 168. Though above research studies have studied the effects of Irganox 1010 and Irgafos 168 on

asphalt, but the effect of Irganox 1010 and Irgafos 168 on thermal oxidative aging properties of asphalt has not been studied systematically. It is meaningful to investigate the effect of Irganox 1010 and Irgafos 168 on the aging performance of asphalt in order to reduce the aging during the service process of pavement. This will also provide a reference for the application of antiaging asphalt mixture.

The aging of asphalt is closely related to the change in the asphalt structure and the molecular structure, and the chemical composition of asphalt can be studied by Fourier transform infrared spectroscopy. Wu [26] indicated that the antiaging effect of Irganox 1010 on asphalt was improved using FTIR, and Irganox 1010 inhibited gelatinization of asphalt in the thermal oxidation aging process. Lmontagne et al. [27] used the sum of the peak areas at $4000 \, cm^{-1}$-$700 \, cm^{-1}$ as a benchmark to evaluate the effect of thermal oxidative aging on different asphalt and different functional groups. Studies have shown that the main reason for asphalt aging is that it reacts with oxygen to produce carbonyl polar macromolecules during the aging process. Zhang et al. [28] studied the structure characteristics of asphalt based on FTIR and used five analytical benchmarks in different ranges to study the functional group indexes before and after the aging. The results showed that the peak area at $4000 \, cm^{-1}$~$700 \, cm^{-1}$ was the most stable.

In this paper, the rolling thin film oven test was used to simulate the short-term aging process in order to study the impact of Irganox 1010 and Irgafos 168 on the thermal oxidative aging property of asphalt. The modified antiaging asphalt was homogenized using a high-speed shearing method. The impacts of both antioxidants on properties were evaluated through penetration, softening point, ductility, and viscosity tests before and after RTFOT. FTIR analysis was conducted to reveal the antiaging reaction mechanism of Irganox 1010 and Irgafos 168.

2. Materials and Experiment

2.1. Raw Materials. Asphalt called AH-70# and SBR-II-A and modified asphalt were selected for experiment, and physical properties of asphalt binders are summarized in Table 1. It should be noted that SBR-modified asphalt was the standard product from an asphalt plant. The antioxidant includes Irganox 1010[pentaerythritol tetrakis 3-(3,5-di-tert-butyl 4-hydroxyphenyl)propionate] and Irgafos168 [tris-(2,4-di-tert-butyl)phosphite]. The common properties of Irganox 1010 and Irgafos 168 are summarized in Table 2.

2.2. Preparation of Modified Asphalt. A high-speed shearing machine was used to prepare modified asphalt in this paper. Base asphalt AH-70# and SBR-modified asphalt were selected for experiment. The contents of Irganox 1010 and Irgafos 168 were 0wt.%,1wt.%,5wt.%, and 10wt.%. In preparing the procedure, asphalt is placed in an oven at 135 °C for 1 hour in order to ensure the fluidity of asphalt and reduce aging of the thermal insulation process, and then, the

TABLE 1: Physical properties of the asphalt binder.

Physical properties	AH-70#	SBR asphalt	Standard
Penetration (25°C, 0.1 mm)	75	140	ASTM-D5
Ductility (10°C, cm)	38.9	144	ASTM-D113
Ductility (15°C, cm)	>100	>150	ASTM-D113
Softening point (°C)	49.2	49.6	ASTM-D36
Viscosity (135°C, Pa·s)	0.306	0.528	JTG E20-2011

TABLE 2: The common indexes of antioxidants.

Physical properties	Irganox 1010	Irgafos 168
Color	White	White
Melting point (°C)	110~125	182~186
Content (%)	≥98	≥99
Density (g·cm^{-3})	1.15	1.03
Ash (%)	≤0.1	≤0.3
Transmittance (425 nm%)	≥95	≥93
Transmittance (500 nm%)	≥97	≥95
Volatile (%)	≤0.5	≤0.5

TABLE 3: Preparation conditions of modified asphalt.

No	Antioxidant	Asphalt	Temperature (°C)	Shearing speed (rad/s)
1#	Irganox 1010	AH-70	150	4500
2#	Irgafos 168	AH-70	180	4500
3#	Irganox 1010	SBR-II-A	150	4500
4#	Irgafos 168	SBR-II-A	180	4500

antiaging asphalt in Table 3 is obtained after mixing for 15 minutes. AH-70# asphalt and SBR-modified asphalt should be mixed under the same conditions related to the speed, temperature, and time in order to eliminate the adverse effect caused by operation.

2.3. Experimental Methods.

According to the standard JTG E20-2011, oxidative aging of antioxidation aging asphalt binders was performed using the rolling thin film oven test (RTFOT). The penetration test, softening point test, ductility test, and viscosity test before and after RTFOT were performed according to the standard JTG E20-2011. The test temperature of the penetration test was 25°C. The softening point test (ring-and-ball Apparatus) had adopted a standard test. The test temperature of the ductility test was 10°C, and the speed was 5 cm/min because the ductility of SBR modified asphalt at 15°C was overrange, and at 5°C, the 70# binder was easy to fracture. The viscosity was determined by the Brookfield viscometer method, and the test temperatures of the viscosity test were 90°C, 100°C, 110°C, 120°C, and 135°C. Three replicates were prepared for each test.

2.4. Characterization Method.

The asphalt aging degree was evaluated by the penetration retention rate (PRR), the ductility retention rate (DRR), the softening point increment (SPI), and the viscosity aging index (VAI).

2.4.1. Penetration Retention Rate (PRR)

$$PRR(\%) = \frac{P}{P_0} \times 100\%, \tag{1}$$

where P_0 indicates the unaged penetration of asphalt, 0.1 mm; P indicates the aged penetration of asphalt, 0.1 mm. The lower the PPR, the more severe the aging.

2.4.2. Ductility Retention Rate (DRR)

$$DRR(\%) = \frac{D}{D_0} \times 100\%, \tag{2}$$

where D_0 indicates the unaged ductility of asphalt, cm; D indicates the aged ductility of asphalt, cm. The lower the DRR, the more severe the aging.

2.4.3. Softening Point Increment (SPI)

$$SPI = SP - SP_0, \tag{3}$$

where SP indicates the aged softening point of asphalt, °C; SP_0 indicates the unaged softening point of asphalt, °C. The greater the SPI, the more severe the aging.

2.4.4. Viscosity Aging Index (VAI)

$$VAI = \frac{V_{aged} - V_{unaged}}{V_{unaged}} \times 100\%, \tag{4}$$

where V_{aged} indicates the aged viscosity of asphalt, Pa·s; V_{unaged} indicates the unaged viscosity of asphalt, Pa·s. The greater the VAI, the more severe the aging.

2.5. FTIR Test.

The asphalt sample for FTIR analysis was prepared by the KBr disc method. In the narrow-mouthed bottle, the asphalt sample was dissolved in a toluene solvent to prepare a 5% asphalt/toluene solvent. In order to avoid the water in the air entering into the narrow-mouthed bottle, we put the narrow-mouthed bottle in the desiccator waiting for the test. For the Irganox 1010 and Irgafos 168 sample, the spectra samples were obtained by blending Irganox 1010 and Irgafos 168 with the KBr powder, respectively. FTIR was measured by FTIR-1500 series. The spectra were recorded from 4000 to 400 cm^{-1} averaging 120 scans for each measurement. The testing process is shown in Figure 1. The FTIR data were analyzed and processed by OMNIC.

3. Results and Discussions

3.1. Effects of the Mixing Procedure and Aging on the Properties of Asphalt.

Influence of Irganox1010 and Irgafos168 contents on antiaging performances of modified asphalt for virgin bitumen and RTFOT aged one is shown in Table 4. The coefficients of variation of parallel experiments were all within 10%.

As listed in Table 4, it can be seen that both Irganox 1010 and Irgafos 168 have significant effects on asphalt physical properties. For Irganox 1010, with the increase of
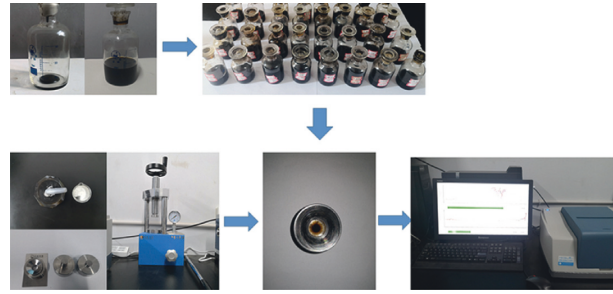
FIGURE 1: Fourier infrared spectroscopy (FTIR) sample preparation and test.

TABLE 4: Influence of matrix asphalt on three indexes before and after mixing and aging.

Name	Property	Before aging				After aging			
		0	1	5	10	0	1	5	10
1#	Penetration (0.1 mm)	81	79	76	60	49	49	47	37
	Softening point (°C)	48.9	48.6	48.8	48.4	54.4	53.6	53.9	53.3
	Ductility (10 °C, cm)	39.0	44.8	33.6	—	6.6	7.9	7.2	—
2#	Penetration (0.1 mm)	81	77	80	87	49	49	53	56
	Softening point (°C)	48.9	48.8	48.2	48.0	54.4	54.1	53.0	52.3
	Ductility (10 °C, cm)	39.0	41.6	35.8	50.3	6.6	7.3	7.5	10.0
3#	Penetration (0.1 mm)	145	144	138	117	89	94	88	77
	Softening point (°C)	49.2	48.5	48.8	50.0	49.9	48.9	49.3	50.3
	Ductility (10 °C, cm)	150.0	150.0	142.5	117.1	52.7	53.1	52.6	44.3
4#	Penetration (0.1 mm)	145	145	141	142	89	97	101	98
	Softening point (°C)	49.2	49.0	48.4	48.3	49.9	49.6	48.7	48.5
	Ductility (10 °C, cm)	150.0	150.0	150.0	144.5	52.7	58.5	68.7	70.7

antioxidant contents, the penetration of asphalt gradually decreased and the range of change gradually increased. However, Irganox 1010 has little effect on the softening point of both types of asphalt and will not influence the thermal stability of asphalt. At the same time, it is clearly found that Irganox 1010 has a similar impact on the ductility of both types of asphalt, and adding 1% antioxidant can improve the low temperature performance. Low temperature ductility will be greatly declined with the increase of antioxidants. In particular, the ductility of asphalt 1# dropped significantly when Irganox 1010 content reached 10%. After RTFOT, the ductility of asphalt was optimal when its content was 1%. The addition of Irganox 1010 to asphalt forms an ester-based substance, which causes asphalt to become hard. Thus, the penetration and ductility of the aged asphalt declined when Irganox 1010 is more than 1%.

For Irgafos 168, when the antioxidant content is 1%, the penetration and softening point of asphalt changed slightly. The regularity is also observed in the paper of Feng et al. [24]. With the increase of Irganox 168, the most drastic changes existed in the penetration and ductility, but the softening point changed a little. In particular, the penetration of asphalt 4# decreased but is still greater than original SBR asphalt. The ductility is greater than 150 cm when the content is not more than 5%, but it dropped a little when the content reached 10%. After RTFOT, the penetration and ductility of asphalt had risen notably, and

the softening point decreased. It can be seen that large content of Irgafos 168 has a notable improvement on the property after aging.

Influence of Irganox 1010 and Irgafos 168 on the Brookfield viscosity of antiaging modified asphalt is shown in Figure 2.

As shown in Figure 2, it can be seen that Irganox 1010 and Irgafos 168 have similar effects on the viscosity of asphalt. The antioxidants reduced the viscosity, and with the increase of Irganox 1010 and Irgafos 168, the viscosity decreased gradually. In the case of a small content, the effect of antioxidants on base and SBR asphalt is not consistent. Antioxidants have little effect on the viscosity of base asphalt, which made the viscosity of SBR asphalt decrease significantly. The higher the test temperature, the less the effect of antioxidants.

3.2. Evaluation of Antiaging Effects

3.2.1. Mass Loss. During the aging process, the light molecular structure of volatilization reduces the mass of the sample, but the oxidation reaction also occurs during aging, which increases the mass of asphalt. The positive value of mass loss meant that oxygen reacts during the aging process to increase the mass, while a negative value of the mass loss is due to the volatilization of light oils, and the influence of Irganox 1010 and Irgafos 168 on the mass loss is shown in Figure 3.
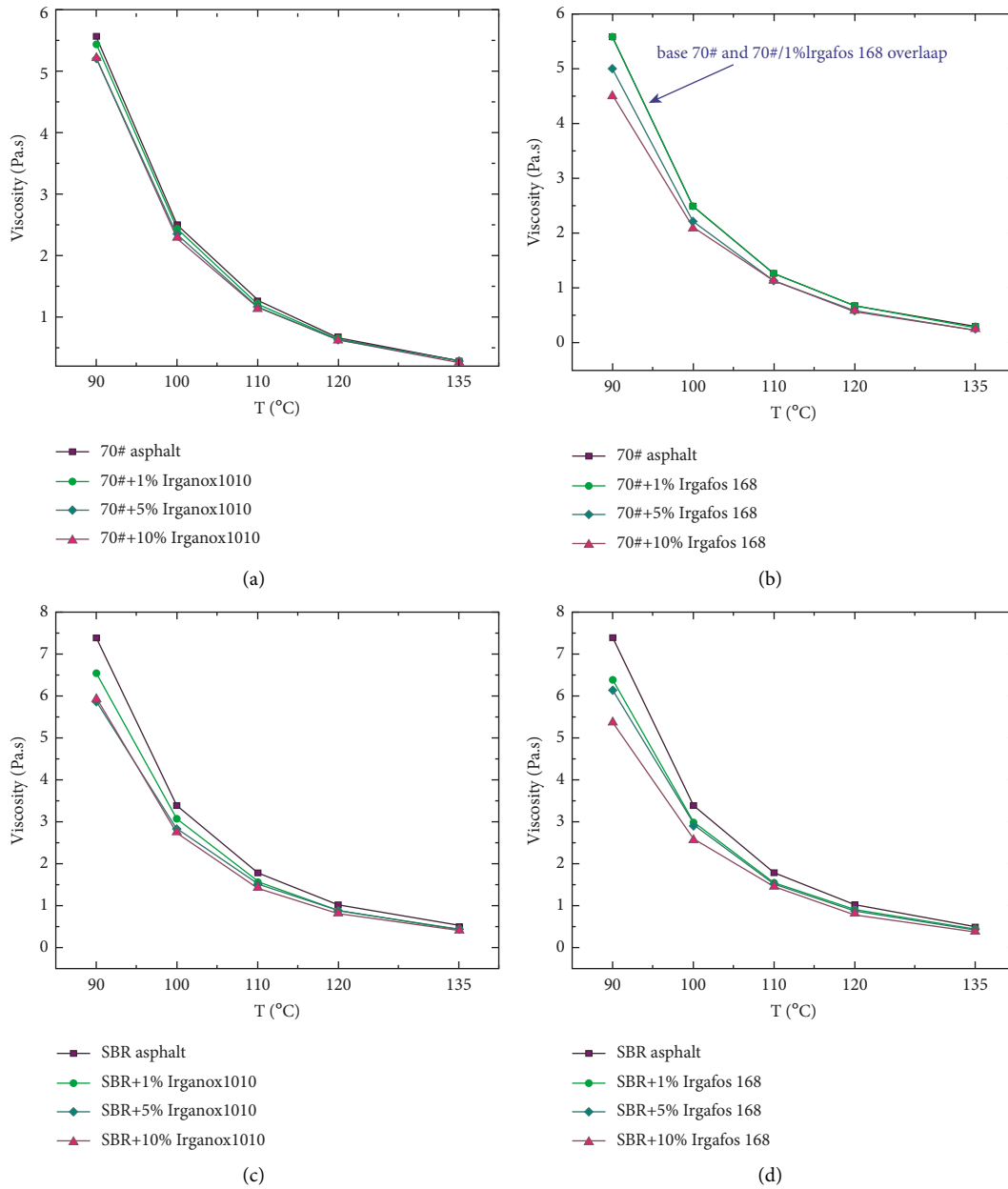
FIGURE 2: Viscosities of virgin and modified asphalt.

As shown in Figure 3, it could be seen that the mass loss of modified antiaging asphalt decreased after adding Irganox 1010 and Irgafos 168, and with the increase of the content, the mass loss tended to be stable. SBR asphalt generated more mass loss after aging. The antiaging capacity was improved after adding the antioxidants, which weakened the volatilization of light components and also inhibited the aging of SBR asphalt.

3.2.2. Aging Index. The influence of RTFOT aging on the penetration is shown in Figure 4.

The penetration retention rate (PPR) can be used to evaluate the antiaging performance, Yu et al. [18] indicated that the lower the PPR was, the more severe the aging was.

As described in Figure 4, it was easy to find that the PPR of base asphalt increased, but its improvement was limited. So, Irganox 1010 has slight influence on the PPR of asphalt 1# when the content of Irganox 1010 was not more than 5%. Although the PPR substantially increased when the content of Irganox 1010 reached 10%, Irganox 1010 would produce adverse effects on the penetration. Therefore, considering the antiaging action and the adverse effect for the penetration, the optimal content of Irganox 1010 is 1% for base asphalt. The PPR of SBR asphalt increased significantly with the increase of Irgafos 168, the PPR was at its peak when the content reached 5%. Therefore, Irgafos 168 effectively reduces the decrease of penetration caused by aging and improves the antiaging performance. From the PPR, the antiaging action of Irgafos 168 is better than that of
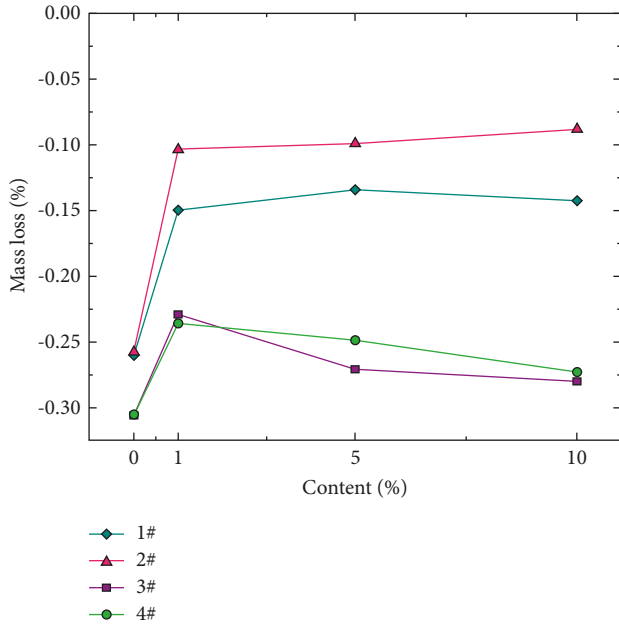
Figure 3: Mass loss of different types of asphalt.
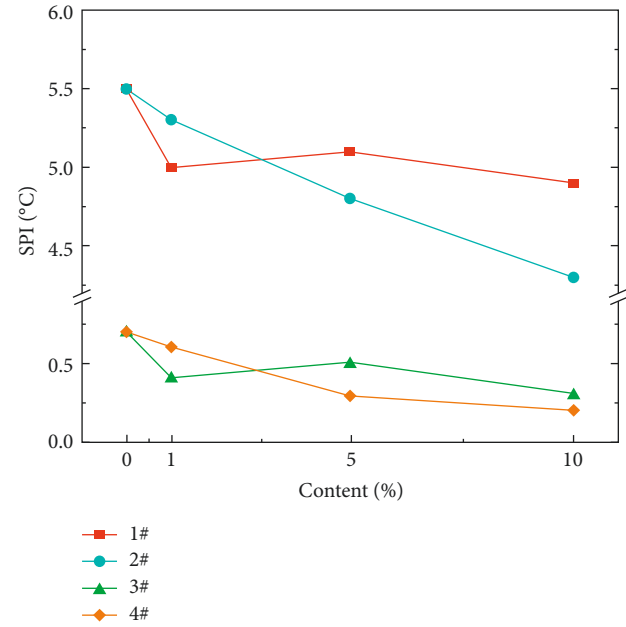
Figure 5: SPI of different binders.
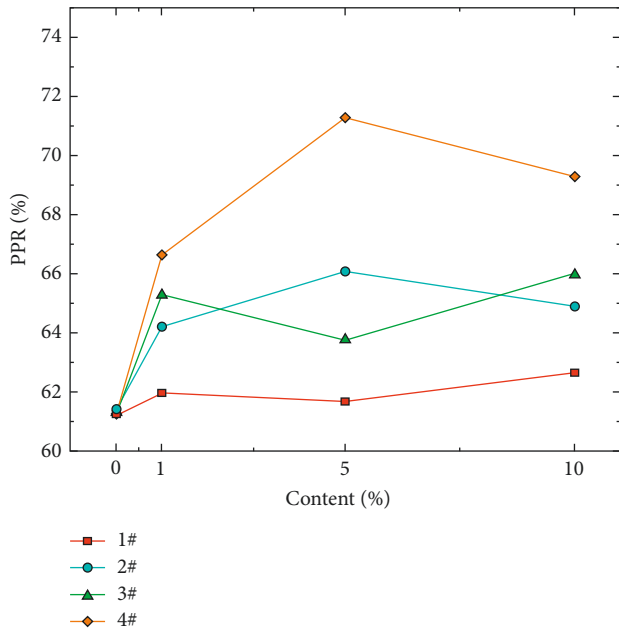
Figure 4: PPR of different types of asphalt.

Irganox1010. The PPR of SBR is higher than that of base asphalt. This is because the antioxidant and SBR have a synergistic effect, and the composite modification has a better antiaging action.

As described in Figure 5, the softening point increment (SPI) can be used to evaluate the antiaging performance, and the larger the SPI, the more severe the aging. The SPI of antioxidant-modified SBR binders is always smaller than that of base asphalt. The SPI dropped with the increase of both antioxidants. The SPIs of modified base and SBR as-phalt gradually decreased with the increase of Irgafos 168.

When the content is small, the change in the SPI was rel-atively small. It can be inferred that the addition of two antioxidants can reduce the oxidative aging degree of modified asphalt. Among them, Irganox 1010 showed a better aging resistance when the content was 1%, and a better antiaging performance was observed when Irgafos 168 was more than 1%.

The ductility retention rate (DRR) can be used to evaluate the antiaging performance, and the lower the DRR was, the more severe the aging was . From Figure 6, it can be seen that DRRs of the modified asphalt with Irganox 1010 and Irgafos 168 are higher than those of the unmodified ones. When the amount of antioxidants is small, the DRR of base asphalt slightly changed. The DRR significantly rose after the amount exceeded 1%. For asphalt 1#, when Irga-nox1010 reached 10%, the asphalt generated brittle failure before and after aging. Therefore, the DDR of the modified group containing 10% Irganox 1010 was unavailable. The DRR of Irgafos 168 modified SBR asphalt increases with the increase of antioxidants. However, the DDR of asphalt 4# showed a good improvement, while the DDR of asphalt 3# had no significant change.

The viscosity aging index (VAI) can be used to eval-uate the antiaging performance, and the higher the VAI was, the more severe the aging was. As shown in Figure 7, the VAI of modified asphalt shows an overall downward trend, especially when the antioxidant content is 10%, the decline is the largest. Among them, Irganox 1010 has a complex effect on the VAI of base asphalt. With the in-crease of antioxidant content, the VAI of base asphalt first decreased then gradually increased and finally dropped to the lowest value. At the same content, the VAI decline amplitude of modified SBR is obviously larger than that of base asphalt. The antiaging effect of antioxidants on SBR is better.
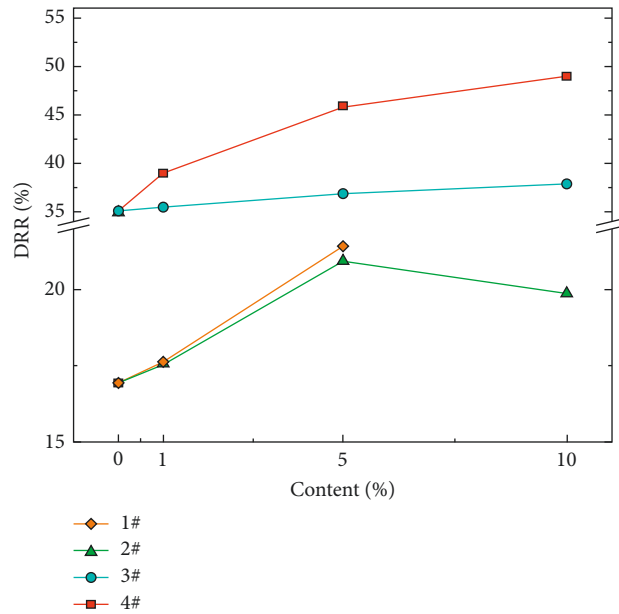
FIGURE 6: Ductility retention rate of different binders.

3.3. FTIR Analysis of the Antioxidant Mechanism.

FTIR tests were performed on the samples of 70# asphalt, SBR asphalt, Irganox 1010, Irgafos 168, and modified asphalt before and after aging. The main absorption peaks in modified asphalt were analyzed , as shown in Table 5. The FTIR analysis of Irganox 1010, Irgafos 168, unmodified asphalt, and modified asphalt is shown in Figures 8–11.

As shown in Figures 8 and 10, for Irganox 1010, it is not difficult to find two peaks in Irganox 1010 spectra observed at $3645\,cm^{-1}$ and $1750\,cm^{-1}$. From Table 5, it can be found that the corresponding functional group at $3645\,cm^{-1}$ is a phenolic hydroxyl group (O–H) and at $1750\,cm^{-1}$ is an ester group (C=O). Therefore, Irganox 1010 is fused with 70# and SBR asphalt mainly through physical adsorption without chemical reaction.

As shown in Figures 9 and 11, for Irgafos 168, the characteristic peak is located at $856\,cm^{-1}$ and $1083\,cm^{-1}$. The corresponding functional group at $856\,cm^{-1}$ is a " = CH" nonplanar variable angle vibration on the benzene ring and at $1083\,cm^{-1}$ is a P–H in-plane vibration in phosphorous acid. In particular, the groups of 2# + 10% Irgafos 168 and 4# asphalt+10%Irgafos 168 contain a peak at $970\,cm^{-1}$. Irgafos 168 and 70# asphalt did not have this peak as shown in Figure 9. So, the difference between the peak at $970\,cm^{-1}$ is trans-butyl, and the peak intensity also increased. Therefore, Irgafos 168 is fused with 70# asphalt and SBR asphalt mainly through chemical reaction.

It is found in Figure 12(a) and Figure 13(a) that the sulfoxide group appeared at $1030\,cm^{-1}$, but no obvious carbonyl group is found at $1700\,cm^{-1}$, indicating that the content of the carbonyl group is very low before aging, but there is still a small amount of the sulfoxide group, and this finding is consistent with previous research [29, 30]. The peak intensity of the phenolic hydroxyl group at $3645\,cm^{-1}$ and the ester group at $1750\,cm^{-1}$ is increased with the increase of Irganox 1010. The increase

of the ester group is the main cause of hardening of asphalt 1# and 3#. Because the ester group can connect different molecules to produce higher relative molecular weight substances, resulting in the increase of asphaltenes, so that the colloidal structure, chemical composition and properties of asphalt would be changed. As the core of the micelles, the increase of asphaltenes leads to the decrease of the solubility of the micelles, the development of the network structure, and the gelation of the asphaltenes. By comparing the FTIR of 1# and 3#, it can be found that Irganox 1010 has a greater impact on 70# asphalt.

As can be seen in Figures 14 and 15, when Irganox 1010 was not added, the absorption peaks of carbonyl groups at $1700\,cm^{-1}$ and sulfoxide groups at $1030\,cm^{-1}$ were significantly enhanced after aging by RTFOT, indicating that the content of oxygen-containing functional groups in asphalt increased during aging. With the addition of Irganox 1010, the absorption peak strength of carbonyl and sulfoxide groups gradually decreased, indicating that the hydroxyl (-OH) functional groups in Irganox 1010 were relatively easy to release hydrogen atoms, which destroys the reaction of free radical automatic oxidation chains, thus inhibiting the generation of oxygen-containing functional groups in asphalt and delaying the aging process. For asphalt 3# after aging, the absorption peak of trans-butadiene at $970\,cm^{-1}$ is also significantly reduced, which was due to the cleavage reaction of the SBR modifier during aging. The synergistic effect of the Irganox 1010 and SBR modifier increases the antiaging capability of asphalt 3#, which is also the reason why 3# has better antiaging capability than 1#.

It is not difficult to see in Figure 14(a) and Figure 15(a), with the increase of Irgafos 168, the absorption peaks of 2# and 4# at $1083\,cm^{-1}$, $970\,cm^{-1}$, and $875\,cm^{-1}$ were significantly enhanced, and sulfoxide group absorption peaks appeared at

(a)

(b)

(c)

(d)
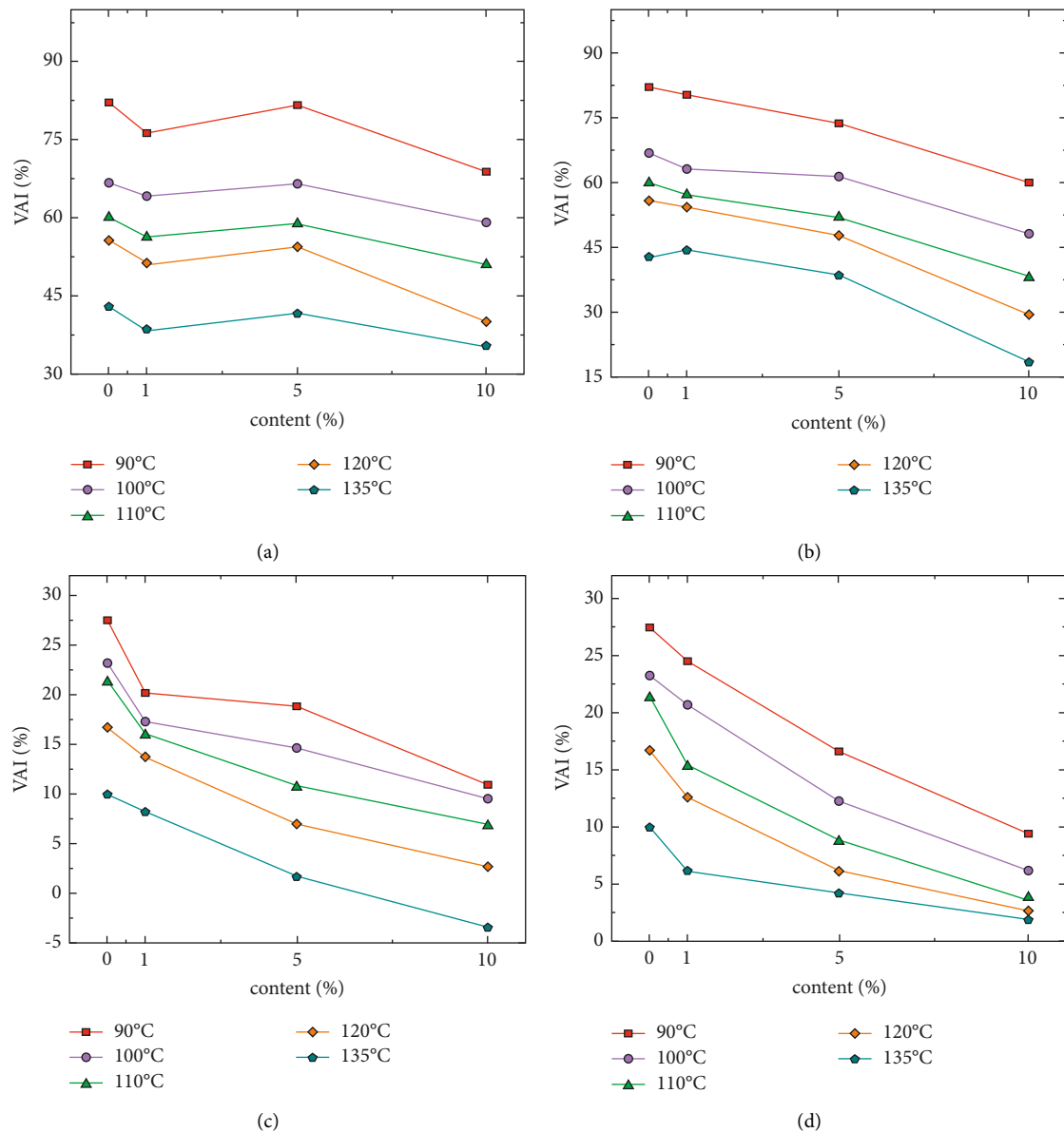
Figure 7: Viscosity aging index of different binders.

$1030\,cm^{-1}$, but no obvious carbonyl absorption peaks were found at $1700\,cm^{-1}$. The peak at $970\,cm^{-1}$ generated by the chemical reaction in 2# was the alkene functional group, which had the same peak position as the transbutadiene in SBR, and the absorption peak at $970\,cm^{-1}$ in 4# is also significantly enhanced. As shown in Figure 14(b) and Figure 15(b), the content of carbonyl and sulfoxide functional groups in 2# and 4# decreased with the increase of Irgafos 168 after aging by RTFOT. After aging, the absorption peak intensity of 2# and 4# decreased significantly at $970\,cm^{-1}$, indicating that butadiene can improve the antiaging performance. Therefore, Irgafos 168 can significantly improve the aging resistance of asphalt.

In order to avoid the influence of experimental errors, it is often suggested that we select a part of a peak area and use it as a reference to calculate the functional group index. The change in the relative intensity of functional groups was analyzed by using the functional group index, and the antiaging properties of asphalt were studied by using the change rate of the functional group index before and after aging. In the FTIR analysis of asphalt, the carbonyl index, sulfoxide group index, aromatic index, and aliphatic index are often used as the analysis indexes. Therefore, according to Lmontagne's study [29], the sum of different peak areas within the range of $4\,000\,cm^{-1}{\sim}700\,cm^{-1}$ is adopted as the benchmark. The functional group index is calculated based on equations (5)–(8). The exponential change rates of functional groups before and after aging are calculated based on equation (9).

Table 5: Spectral analysis of main absorption peaks in modified asphalt.

Wavenumber (cm)	Functional groups
3645^{-1}	vO-H
2925^{-1}	vC-H aliphatic
2852^{-1}	vC-H aliphatic
1750^{-1}	$vC = O$
1700^{-1}	$vC = O$ conjugated
1600^{-1}	$vC = C$ aromatic
1460^{-1}	δC-H of -(CH 2)n- (aliphatic index)
1377^{-1}	δC-H of CH3 (aliphatic branched)
1083^{-1}	P–H in-plane vibration in δ phosphite
1031^{-1}	$vS = O$ sulfoxide
965^{-1}	δC-H trans disubstituted –CH=CH- (butadiene block)
856^{-1}	= CH nonplanar variable angle vibration on benzene ring
747^{-1}	δC-H aromatic monosubstituted (styrene block)
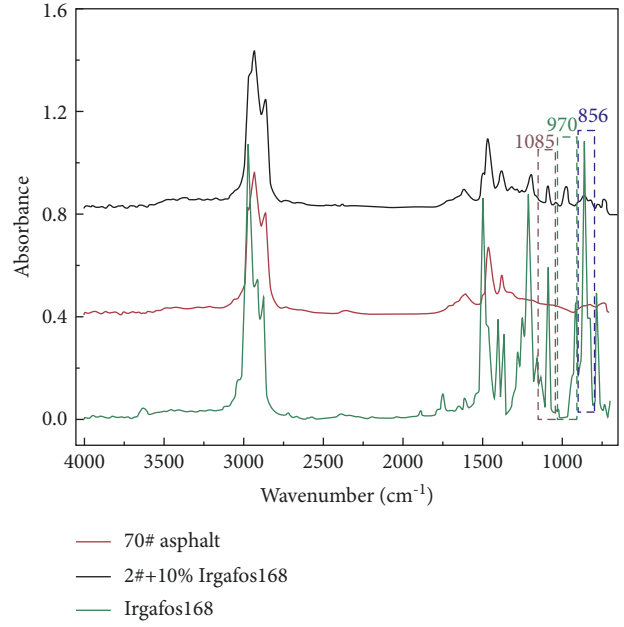
Figure 9: Spectra of Irgafos 168, 70# asphalt, and 2# + 10%Irgafos 168.
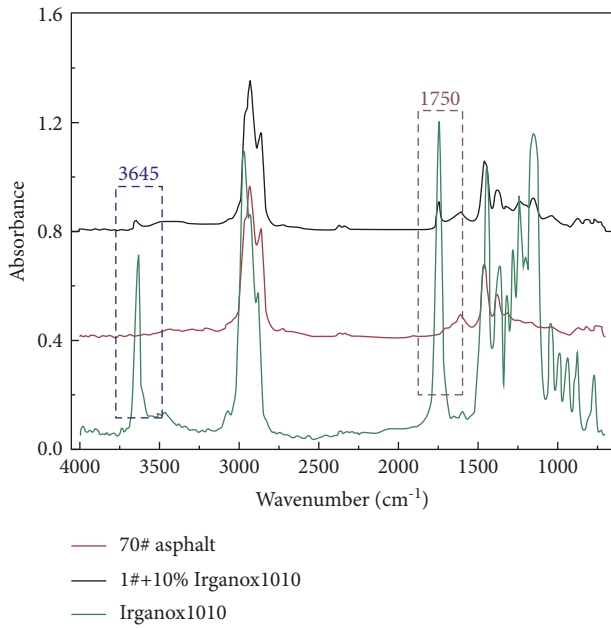
Figure 8: Spectra of Irganox 1010, base asphalt, and 1# + 10% Irganox 1010.
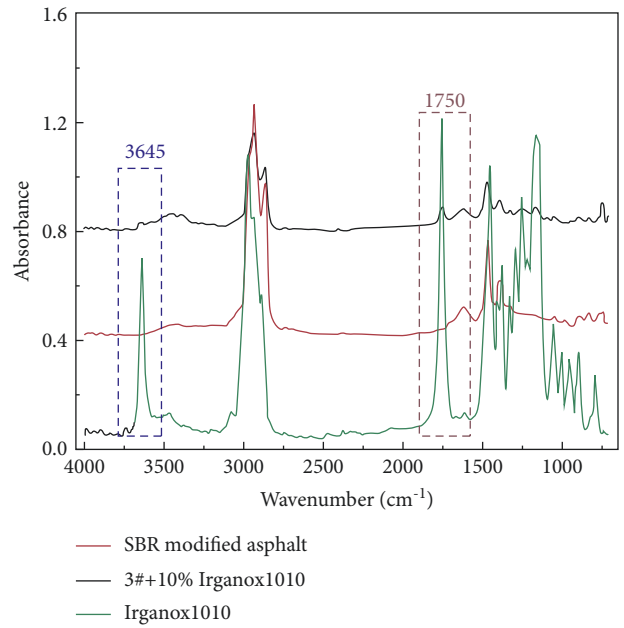
Figure 10: Spectra of Irganox 1010, SBR-modified asphalt, and 3# + 10%Irganox 1010.

$$I_{C=O} = \frac{Area\,of\,the\,carbonyl\,band\,centered\,around\,1700\,cm^{-1}}{\sum Area\,of\,the\,spectral\,bands\,between\,4000\,cm^{-1}\,and\,700\,cm^{-1}}, \tag{5}$$

$$I_{Ar} = \frac{Area\,of\,the\,aromatic\,band\,centere\,daround\,1600\,cm^{-1}}{\sum Area\,of\,the\,spectral\,bands\,between\,4000\,cm^{-1}\,and\,700\,cm^{-1}}, \tag{6}$$
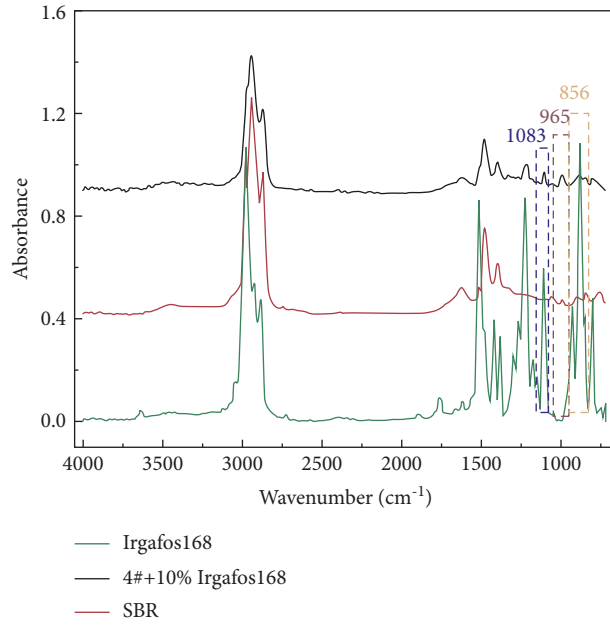
Figure 11: Spectra of Irgafos 168, SBR-modified asphalt, and 4# + 10%Irgafos 168.
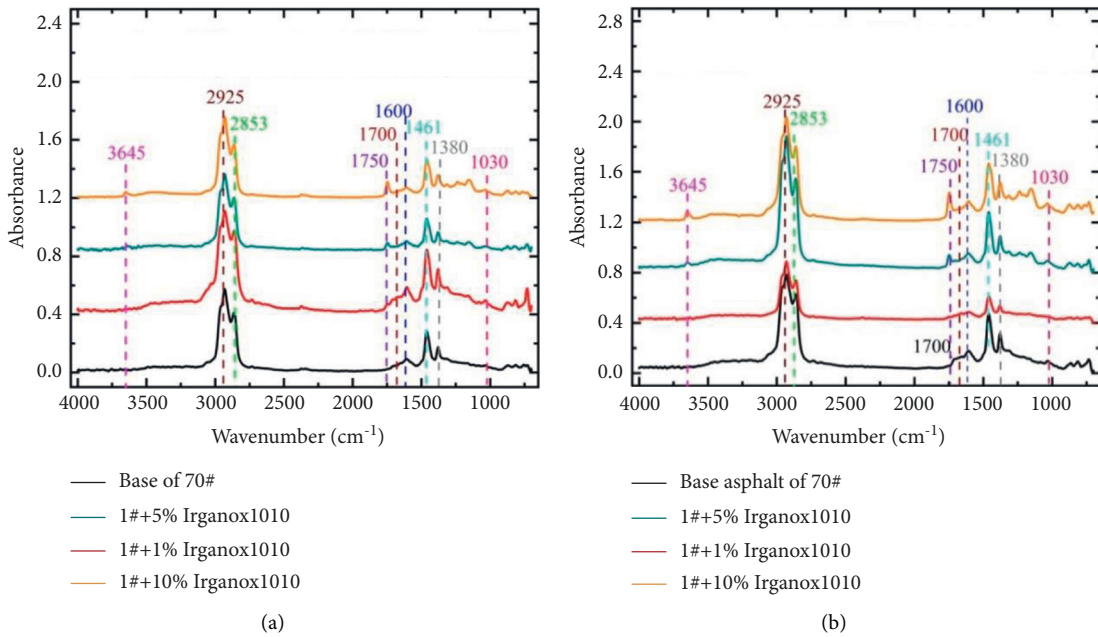
Figure 12: FTIR spectra of asphalt 1# (a) before aging (b) after aging.

$$\begin{cases} I_B = \dfrac{I_{C-H\,of\,CH_3}}{I_{C-H\,of\,CH_3} + I_{C-H\,of-(CH_2)_n}}, \\[2mm] I_{C-H\,of\,CH_3} = \dfrac{Area\,of\,the\,aromatic\,band\,centered\,around\,1600\,cm^{-1}}{\sum Area\,of\,the\,spectral\,bands\,between\,4000\,cm^{-1}\,and\,700\,cm^{-1}}, \\[2mm] I_{C-H\,of-(CH_2)_n} = \dfrac{Area\,of\,the\,aromatic\,band\,centered\,around\,1600\,cm^{-1}}{\sum Area\,of\,the\,spectral\,bands\,between\,4000\,cm^{-1}\,and\,700\,cm^{-1}}, \end{cases} \qquad (7)$$
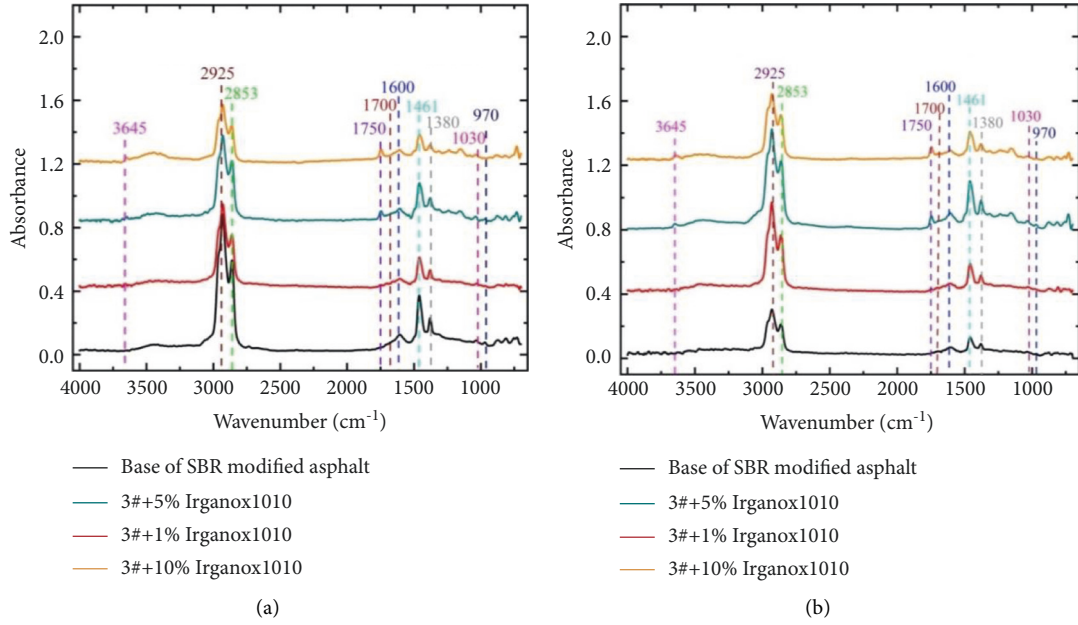
FIGURE 13: FTIR spectra of asphalt 3# (a) before aging (b) after aging.
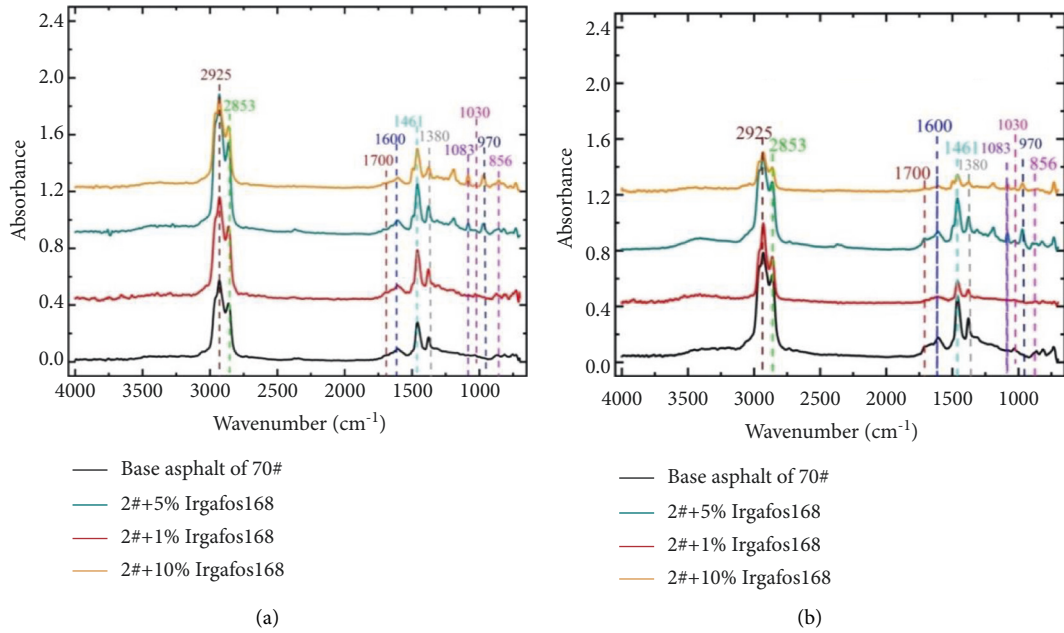
FIGURE 14: FTIR spectra of asphalt 2# (a) before aging (b) after aging.

$$I_{S=O} = \frac{Area\ of\ the\ sulfoxide\ band\ centered\ around\ 1031\ cm^{-1}}{\sum Area\ of\ the\ spectral\ bands\ between\ 4000\ cm^{-1}\ and\ 700\ cm^{-1}}, \quad (8)$$

$$W = \frac{I_{afteraging} - I_{beforeaging}}{I_{beforeaging}}. \quad (9)$$

Where $I_{C=O}$ is the carbonyl functional group index, I_{Ar} is the aromatic functional group index, I_B is the aliphatic functional group index, sulfoxide functional group index, $A_{1700\text{cm}}^{-1}$ is the peak area of carbonyl at $1700\ \text{cm}^{-1}$, $A_{1030\text{cm}}^{-1}$ is the peak area of the sulfoxide group at $1030\ \text{cm}^{-1}$, $\sum A_{4000\ \text{cm}^{-1}\sim700\ \text{cm}^{-1}}$ is the peak area in the range

(a)

(b)
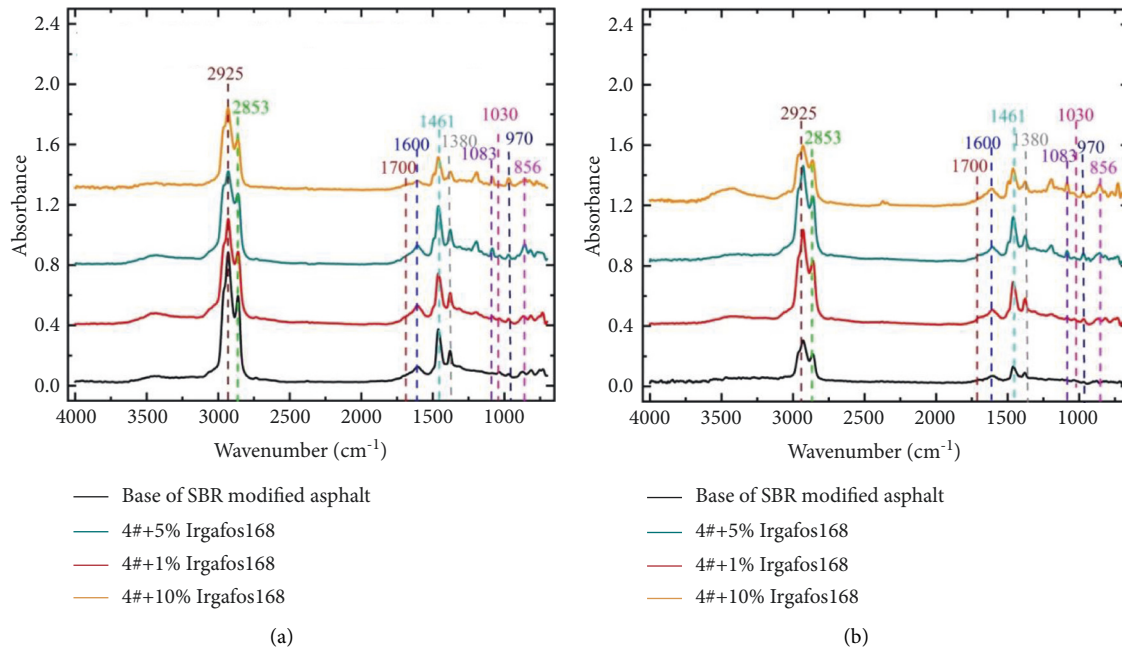
Figure 15: FTIR spectra of asphalt 4# (a) before aging (b) after aging.

of $4000 \, \text{cm}^{-1} \sim 700 \, \text{cm}^{-1}$, W is the functional group change rate, $I_{\text{beforeaging}}$ is the functional group index before aging, and $I_{\text{afteraging}}$ is the functional group index after aging.

Irganox 1010 has different effects on 1# and 3# asphalt. It can be seen from Table 6 that the carbonyl functional group index, sulfoxide functional group index, and aromatic functional group index decrease with the increase of Irganox1010 content, while the aliphatic functional group index remains almost unchanged. As can be seen from the change in the functional group index in Table 7, the carbonyl functional group index and the aromatic functional group index first increase and then decrease, while the contents of the sulfoxide functional group index and the aliphatic functional group index increase, indicating that the Irganox 1010 content has different influences on the functional group index of different asphalt. When studying the chemical structure changes of asphalt in the aging process, the content of carbonyl and sulfoxide functional groups is often used to evaluate the oxidation of asphalt. The functional group index is greater, and the content of carbonyl and sulfoxide functional groups in asphalt is higher [35–39]. The contents of the carbonyl group and the sulfoxide group decrease in 1# and 3# asphalt, and this is because of the oxidation reaction between asphalt and oxygen during the preparation process; thus, the content of the carbonyl and sulfoxide group increased. Therefore, the addition of Irganox 1010 inhibited the oxidation reaction between asphalt and oxygen in the preparation process, and the contents of carbonyl and sulfoxide groups were reduced. The carbonyl functional group index and the sulfoxide functional group index in 3# are lower than that in 1#, indicating that Irganox 1010 has a good synergistic effect on SBR.

After aging by RTFOT, the carbonyl functional group index, sulfoxide functional group index, and aromatic

functional group index of 1# and 3# increased. During the short-term aging of asphalt, carbon, sulfur, nitrogen, and other elements in asphalt will be oxidized with the presence of oxygen in the air; thus, the content of a series of oxygen-containing functional group compounds such as carbonyl and sulfoxide increased. The carbonyl and sulfoxide groups of base and SBR asphalt significantly increased after aging, which proves that aging leads to the increase of carbohydrate and sulfur-oxygen groups in asphalt. The functional group index change rate (W) is used to evaluate the aging resistance of asphalt from the perspective of the functional group intensity, as shown in Figure 16(a) and 16(b). After adding Irganox 1010, $W_{C=O}$ and $W_{S=O}$ in asphalt significantly decrease, and with the increase of Irganox 1010, the change in carbonyl and sulfoxide functional groups first decrease, then increase, and lastly decrease, which is consistent with other aging index regularity. After aging, W_{Ar} and W_B of base asphalt and SBR-modified asphalt are both positive, and the aromatic and aliphatic content increased after RTFOT. After adding Irganox 1010, W_{Ar} and W_B tend to decrease gradually. This is because Irganox 1010 improves the antiaging performance, and aging causes polymerization and chain scission of asphalt, thus producing more aromatic groups after aging. Therefore, Irganox 1010 slows down chain scission and polycondensation of asphalt in the aging process, thus reducing the aromatic content in asphalt. W_B close to zero indicates that the chain scission of normal paraffin hydrocarbon in saturated fragrance is effectively inhibited. To sum up, Irganox 1010 produces positive effects during asphalt aging. Irganox 1010 prevents oxidative chain reactions and weakens the aging process of asphalt by capturing the active radicals generated during asphalt aging, and it was found that 3# had better antiaging effects when

TABLE 6: Effect of Irganox 1010 on the functional group index of 1#.

Content/%	Before aging				After aging			
	$I_{C=O}$	$I_{S=O}$	I_{Ar}	I_B	$I_{C=O}$	$I_{S=O}$	I_{Ar}	I_B
0	0.0055	0.0125	0.0372	0.2106	0.0155	0.0171	0.0561	0.2062
1	0.0048	0.0119	0.0336	0.1909	0.0087	0.0153	0.0368	0.1820
5	0.0030	0.0081	0.0271	0.20634	0.0077	0.0158	0.0272	0.2067
10	0.0015	0.0106	0.0247	0.2229	0.0021	0.0151	0.0268	0.2270

TABLE 7: Effect of Irganox 1010 on the functional group index of 3#.

Content/%	Before aging				After aging			
	$I_{C=O}$	$I_{S=O}$	I_{Ar}	I_B	$I_{C=O}$	$I_{S=O}$	I_{Ar}	I_B
0	0.0036	0.0043	0.0477	0.1820	0.0065	0.0064	0.1463	0.1790
1	0.0056	0.0036	0.0508	0.1940	0.0054	0.0043	0.078	0.1945
5	0.0027	0.0030	0.0462	0.1942	0.0037	0.0042	0.0840	0.1981
10	0.0032	0.0025	0.0412	0.2030	0.0014	0.0016	0.0811	0.1963
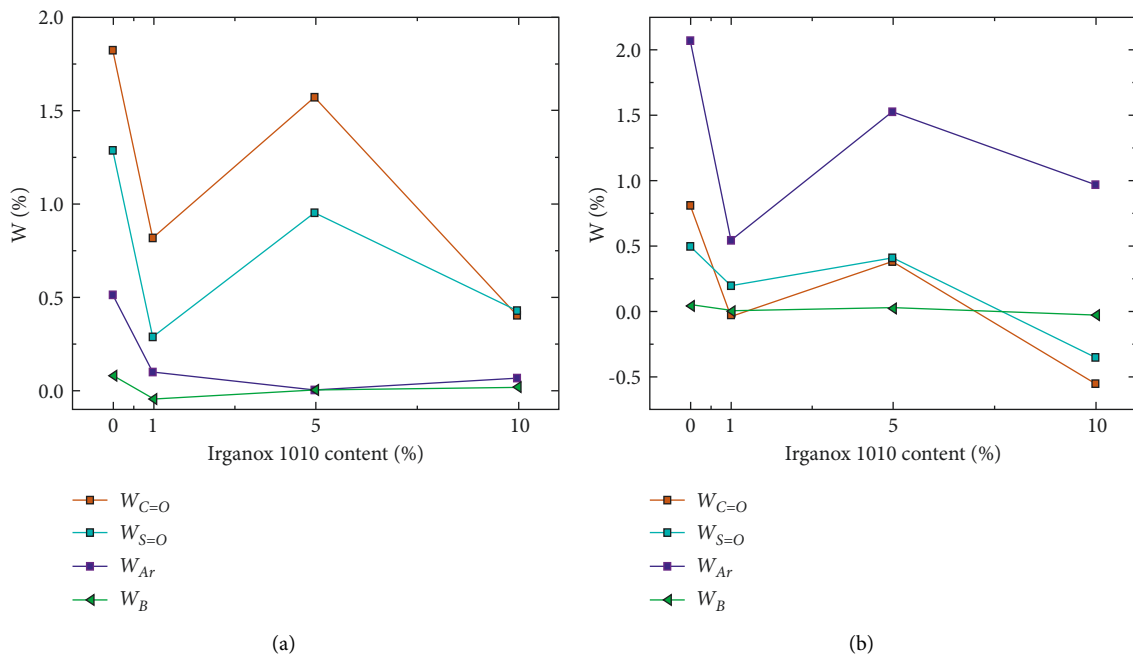
FIGURE 16: Effect of Irganox 1010 on (W) (a) 1# (b) 3#.

the Irganox1010 content is 1%, which is consistent with the previous conclusion in this paper.

It can be seen from Table 8 that after adding Irgafos 168, the carbonyl functional group index decreased, while the sulfoxide functional group index changed a little. It proved that Irgafos 168 had inhibited the oxidation of asphalt in the preparation and test process but had little influence on the sulfoxide group. It can be found that the carbonyl functional group indexes show a downward trend in different asphalt from Table 9, while the sulfoxide functional group indexes have different changes, indicating that the carbonyl functional group indexes can represent the weak oxidation reaction in asphalt.

As shown in Figure 17, after aging by RTFOT, the carbonyl functional group index, sulfoxide functional group index, and aromatic functional group index all increased, while the aliphatic functional group index decreased. It can be found from Figure 17(a) that adding Irgafos 168 makes $W_{C=O}$ and $W_{S=O}$ in 2# significantly lower, W_{Ar} changes slightly, and W_B first reduced and then gradually flattened. From Figure 17(b), it can be found that adding Irgafos 168 reduces $W_{C=O}$ and $W_{S=O}$ in 4#, while W_{Ar} and W_B first reduced and then gradually flattened. $W_{C=O}$, $W_{S=O}$, and W_{Ar} in 2# and 4# asphalt are due to Irgafos 168 inhibiting the oxidation reaction, and thus the antiaging performance of asphalt is improved. W_B below 0 indicates that W_B not only effectively inhibits the chain scission of normal paraffin hydrocarbon in saturated fractions but also promotes the saturated fraction production. In one word, Irgafos 168 also has a positive effect on the asphalt aging. Irgafos 168 weakens

TABLE 8: Effect of Irgafos 168 on the functional group index of 2#.

Content/%	Before aging				After aging			
	$I_{C=O}$	$I_{S=O}$	I_{Ar}	I_B	$I_{C=O}$	$I_{S=O}$	I_{Ar}	I_B
0	0.0055	0.0075	0.0372	0.2106	0.0155	0.0171	0.0561	0.2062
1	0.0034	0.0072	0.0516	0.2306	0.0075	0.0068	0.0747	0.1963
5	0.0037	0.0080	0.0577	0.3081	0.0055	0.0106	0.0808	0.1771
10	0.0028	0.0082	0.0731	0.3272	0.0033	0.0085	0.0962	0.1886

TABLE 9: Effect of Irgafos168 on the functional group index of 4#.

Content/%	Before aging				After aging			
	$I_{C=O}$	$I_{S=O}$	I_{Ar}	I_B	$I_{C=O}$	$I_{S=O}$	I_{Ar}	I_B
0	0.0036	0.0043	0.0477	0.1820	0.0065	0.0064	0.1463	0.1790
1	0.0029	0.0043	0.0879	0.2306	0.0047	0.0070	0.1523	0.1966
5	0.0027	0.0050	0.0984	0.3244	0.0039	0.0074	0.1565	0.2593
10	0.0031	0.0040	0.1042	0.3476	0.0040	0.0046	0.162	0.3228
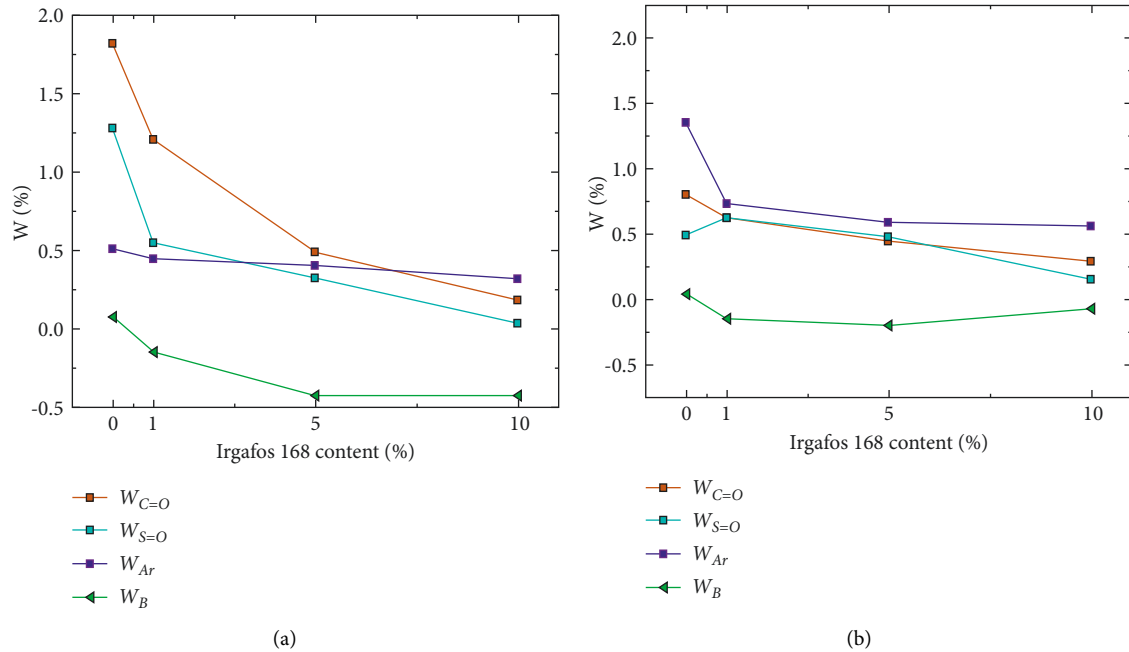
FIGURE 17: Effect of different Irgafos 168 contents on W of modified antiaging asphalt. (a) 2#. 4#.

the aging degree of asphalt, and Irgafos 168 decomposes hydroperoxides from thermally oxidized aging chain reactions into inactive products. For asphalt 2# and 4#, a higher Irgafos168 content has the better the antiaging effect.

4. Conclusions

From the result discussed above, the conclusions can be drawn as follows:

(1) Commercial antioxidants including Irganox1010 and Irgafos168 improve the aging resistance of base and SBR-modified asphalt. Based on the basic indexes of asphalt binders and their antiaging performance, 1% Irganox 1010 can improve the antiaging performance of asphalt and has little negative influence on the original properties. Asphalt including 1% Irgafos 168 possesses good aging resistance and low temperature ductility. Due to the synergistic effect between SBR and antioxidants such as Irganox 1010 and Irgafos 168, the antiaging effect on SBR is more significant.

(2) FTIR analysis showed that there was physical adsorption between Irganox 1010 and asphalt, while there was a chemical reaction between Irgafos 168 and asphalt. According to the qualitative and quantitative analysis, the main reason for the performance degradation of Irganox 1010 is the ester group. Irganox 1010 and Irgafos 168 effectively

prevented the oxidation reaction during aging and reduced the content of carbonyl and sulfoxide groups after asphalt aging. [31–39].

Data Availability

All the data obtained from several experiments are included in the paper.

Conflicts of Interest

The authors declare that there are no conflicts of interest regarding the publication of this paper.

Acknowledgments

References

[1] D. Lesueur, "The colloidal structure of bitumen: consequences on the rheology and on the mechanisms of bitumen modification," *Advances in Colloid and Interface Science*, vol. 145, no. 1-2, pp. 42–82, 2009.

[2] Q. Guo, Z. Chen, P. Liu et al., "Influence of basalt fiber on mode I and II fracture properties of asphalt mixture at medium and low temperatures," *Theoretical and Applied Fracture Mechanics*, vol. 112, p. 102884, 2021.

[3] Q. Guo, L. Li, Y. Cheng, Y. Jiao, and C. Xu, "Laboratory evaluation on performance of diatomite and glass fiber compound modified asphalt mixture," *Materials & Design*, vol. 66, pp. 51–59, 2015.

[4] H. Wei, J. Li, B. Hu, F. Wang, and J. Zheng, "Influence of temperature on deformation failure and acoustic emission characterisation of asphalt concrete under uniaxial compression. International Journal of Pavement Engineering," vol. 44, pp. 1–10, 2022.

[5] Z. Junhui, Z. Anshun, H. Chao, Yu Huayang, and Z. Chao, "Characterising the resilient behaviour of pavement subgrade with construction and demolition waste under FreezeeThaw cycles," *Journal of Cleaner Production*, vol. 300, Article ID 126702, 2021.

[6] J. Li, J. Zhang, G. Qian, J. Zheng, and Y. Zhang, "Three-dimensional simulation of aggregate and asphalt mixture using parameterized shape and size gradation," *Journal of Materials in Civil Engineering*, vol. 31, no. 3, p. 31, Article ID 04019004, 2019.

[7] F. R. Adolfo, L. E. Claussen, R. S. Cargnin et al., "Influence of thermal aging and long term-aging on Ni and V content in asphalt fractions and their determination in air particulate matter from asphalt mixing plants," *Fuel*, vol. 324, p. 124289, 2022.

[8] G. Airey, "State of the art report on ageing test methods for bituminous pavement materials," *International Journal of Pavement Engineering*, vol. 4, pp. 165–176, 2003.

[9] A. K. Apeagyei, "Laboratory evaluation of antioxidants for asphalt binders," *Construction and Building Materials*, vol. 25, pp. 47–53, 2011.

[10] W. N. Houston, M. W. Mirza, C. E. Zapata, and S. Raghavendra, "Environmental effects in pavement mix and structural design systems," *Part 1 of Contractor's Final Report for NCHRP Project*, pp. 9–23, Arizona State University, Phoenix, AZ, USA, 2005.

[11] R. B. Mallick and E. R. Brown, "An evaluation of superpave binder aging methods," *International Journal of Pavement Engineering*, vol. 5, pp. 9–18, 2004.

[12] H. L. Zhang, J. Y. Yu, Z. G. Feng, L. H. Xue, and S. P. Wu, ""Effect of aging on the morphology of bitumen by atomic force microscopy: effect of aging on morphology of bi- tumen, " Journal of Microscopy, vol," *Journal of Microscopy*, vol. 246, pp. 11–19, 2012.

[13] R. G. Allen, D. N. Little, A. Bhasin, and R. L. Lytton, "Identification of the composite relaxation modulus of asphalt binder using AFM nanoindentation," *Journal of Materials in Civil Engineering*, vol. 25, pp. 530–539, 2013.

[14] L. M. Rebelo, J. S. de Sousa, A. S. Abreu et al., "Aging of asphaltic binders investigated with atomic force microscopy," *Fuel*, vol. 117, pp. 15–25, 2014.

[15] X. Lu and U. Isacsson, "Chemical and rheological evaluation of ageing properties of SBS polymer modified bitumens," *Fuel*, vol. 77, no. 9-10, pp. 961–972, 1998.

[16] F. Zhang and C. Hu, "Influence of aging on thermal behavior and characterization of SBR compound-modified asphalt," *Journal of Thermal Analysis and Calorimetry*, vol. 115, pp. 1211–1218, 2014.

[17] F. Zhang, C. Hu, and Y. Zhang, "Influence of montmorillonite on ageing resistance of styrene–ethylene/butylene–styrene-modified asphalt," *Journal of Thermal Analysis and Calorimetry*, vol. 133, 2018.

[18] Y. C. Cheng, J. Tao, Y. Jiao, Q. Guo, and C. Li, "Influence of diatomite and mineral powder on thermal oxidative ageing properties of asphalt," *Advances in Materials Science and Engineering*, vol. 2015, pp. 1–10, Article ID 947834, 2015.

[19] R. C. Williams, *Using Lignin as an Asphalt Antioxidant*, Iowa State University, USA, 2008.

[20] C. M. Reyes, "Influence of anti-oxidant modifications in asphalt binder phesio-chemical properties and mixes per-formance, M.S. Thesis," *Department of Civil Engineering*, The University of Texas at San Antonio, San Antonio, TX, USA, 2012.

[21] C. Ouyang, S. Wang, Y. Zhang, and Y. Zhang, "Improving the aging resistance of styrene–butadiene–styrene tri-block copolymer modified asphalt by addition of antioxidants," *Polymer Degradation and Stability*, vol. 91, no. 4, pp. 795–804, 2006.

[22] B. H. Li, Q. C. Liu, Y. J. Yu, and D. M. Gong, "Influence of composite antioxidants to asphalt anti-aging performance," *Advanced Materials Research*, vol. 562-564, pp. 380–384, 2012.

[23] T. Pan, L. Sun, and Q. Yu, "Retracted article: an atomistic-based chemophysical environment for evaluating asphalt oxidation and antioxidants," *Journal of Molecular Modeling*, vol. 18, no. 12, pp. 5113–5126, 2012.

[24] Z. G. Feng, J. Y. Yu, H. L. Zhang, and D. L. Kuang, "Preparation and properties of ageing resistant asphalt binder with various anti-ageing additives," *Applied Mechanics and Materials*, vol. 71-78, pp. 1062–1067, 2011.

[25] Y. Li, L. Li, Y. Zhang, and S. Zhao, "Improving the aging resistance of styrene-butadiene-styrene tri-block copolymer and application in polymer-modified asphalt," *Journal of Applied Polymer ence 116*, vol. 2, pp. 754–761, 2010.

[26] W. Wu, L. Li, J. Yu, S. Xu, C. Zhang, and L. Xue, "Investigation on thermo-oxidative aging properties of asphalt binder with

hindered phenolic antioxidant," *Journal of Testing and Evaluation*, vol. 46, no. 2, pp. 624–630, 2018.

[27] J. Lmontagne, P. Dumas, V. Mouillet, and J. Kister, "Comparison by Fourier transform infrared (FTIR) spectroscopy of different ageing techniques: application to road bitumens," *Fuel*, vol. 80, no. 4, pp. 483–488, 2001.

[28] B. L. Zhang, "Characterization of bitumen structure based on fourier transform infrared," Wuhan University of Technology, Wuhan, 2014.

[29] Z. G. Feng, H. J. Bian, X. J. Li, and J. Y. Yu, "FTIR analysis of UV aging on bitumen and its fractions," *Materials and Structures*, vol. 49, no. 4, pp. 1381–1389, 2016.

[30] Wu S-p, L. Pang, Mo L-t, C. Y-c, and Z. G-j, "Influence of aging on the evolution of structure, morphology and rheology of base and SBS modified bitumen," *Construction and Building Materials*, vol. 23, no. 2, pp. 1005–1010, 2009.

[31] R. M. Januszke, "Paving asphalt. Additives in durability determination," *Product R&D*, vol. 10, pp. 209–214, 1971.

[32] B. Singh, N. Saboo, and P. Kumar, "Use of Fourier transform infrared spectroscopy to study ageing characteristics of asphalt binders," *Petroleum Science and Technology*, vol. 35, no. 16, pp. 1648–1654, 2017.

[33] J. Li, Y. Liu, and X. N. Zhang, "Microscopic analysis on the aging mechanism of asphalt," *Bull. Chin. Ceram. Soc.,* vol. 33, pp. 1275–1281, 2014.

[34] Z. G. Feng, J. Y. Yu, H. L. Zhang, D. L. Kuang, and L. H. Xue, "Effect of ultraviolet aging on rheology, chemistry and morphology of ultraviolet absorber modified bitumen," *Materials and Structures*, vol. 46, no. 7, pp. 1123–1132, 2013.

[35] F. Zhang, J. Yu, and J. Han, "Effects of thermal oxidative ageing on dynamic viscosity, TG/DTG, DTA and FTIR of SBS- and SBS/sulfur-modified asphalts," *Construction and Building Materials*, vol. 25, no. 1, pp. 129–137, 2011.

[36] D. O. Larsen, J. L. Alessandrini, A. Bosch, and M. S. Cortizo, "Micro-structural and rheological characteristics of SBS-asphalt blends during their manufacturing," *Construction and Building Materials*, vol. 23, no. 8, pp. 2769–2774, 2009.

[37] V. Bellitto, "Atomic force microscopy–imaging," *Measuring and Manipulating Surfaces at the Atomic Scale, InTech, Rijeka, Croatia*, vol. 63, 2012.

[38] P. K. Das, H. Baaj, S. Tighe, and N. Kringos, "Atomic force microscopy to investigate asphalt binders: a state-of-the-art review," *Road Materials and Pavement Design*, vol. 17, pp. 693–718, 2016.

[39] J. F. Masson, V. Leblond, and J. Margeson, "Bitumen morphologies by phase-detection atomic force microscopy," *Journal of Microscopy*, vol. 221, no. 1, pp. 17–29, 2006.

Research Article

Comparative Investigation on the Properties and Molecular Mechanisms of Natural Phenolic Compounds and Rubber Polymers to Inhibit Oxidative Aging of Asphalt Binders

Fenghua Yang [ID],[1] Zhuang Hu,[2,3] and Hongyi Xi[4]

[1]*School of Engineering Management and Logistics, Shaanxi Railway Institute, Weinan, Shaanxi 714000, China*
[2]*National Engineering and Research Center for Mountainous Highways, Chongqing 400067, China*
[3]*China Merchants Chongqing Transportation Technology Research & Design Institute Co.,Ltd., Chongqing 400067, China*
[4]*School of High-Speed Rail Engineering, Shaanxi Railway Institute, Weinan, Shaanxi 714000, China*

Correspondence should be addressed to Fenghua Yang; yangfenghua@chd.edu.cn

Using bio-based antioxidants and industrial wastes to inhibit asphalt aging is a sustainable practice in the pavement industry. To investigate the inhibitory effects and potential mechanisms of phenolic compounds and crumb tire rubber on the aging deterioration of asphalt binders, the aging characteristics of base asphalt, catechin modified asphalt, and crumb rubber modified asphalt were evaluated using Fourier transform infrared spectroscopy and reactive molecular dynamics simulations. The results showed that both catechins and crumb rubber exerted resistance to asphalt aging and that the former performed better. Specifically, catechins block asphalt aging at the chemical level by providing active H atoms to react with O_2 and free radicals, thus preventing them from oxidizing asphalt molecules. In contrast, crumb rubber exerts its antiaging properties mainly in physical aspects, firstly by limiting the movement of asphalt molecules to reduce the contact and reaction of asphalt with O_2 and secondly by counteracting the aging-induced asphalt hardening through its own degradation, thus partially restoring the mechanical properties of aged asphalt. This study provides molecular insight into the antiaging mechanisms of natural phenolic compounds and rubber polymers and is expected to provide theoretical guidance for the development of targeted antiaging technologies for asphalt binders.

1. Introduction

Asphalt is the residue of petroleum fractionation and is widely used as a pavement bonding material due to its unique viscoelastic property and mineral adhesion [1, 2]. According to the Corbett component separation test, asphalt molecules are divided into four components, namely, saturates, aromatics, resins, and asphaltenes (SARA), depending on their polarity and solubility in different solvents [3]. In the natural state, SARA components of asphalt are in thermodynamic equilibrium with the effect of intermolecular interactions, thus maintaining its satisfactory fluidity and functionality [4].

However, asphalt is susceptible to aging during service by reacting with oxygen [5–7]. At high altitude areas, aging of asphalt becomes faster and more severe under UV radiation [8]. Studies based on Fourier transform infrared (FTIR) spectroscopy indicate that a large number of polar oxygen-containing groups, such as carbonyl (mainly ketones and aldehydes) and sulfoxide groups, as well as small amounts of carboxylic acids, dicarboxylic anhydrides, and hydroxyl groups, are produced during asphalt aging [9, 10]. As a result, the molecular polarity and intermolecular agglomeration of aged asphalt increases and the thermodynamic equilibrium between SARA components is irreversibly disrupted, which makes asphalt hard, brittle, and

difficult to flow, resulting in asphalt pavement cracking more easily under load [11–13].

Governments and contractors typically address pavement cracking caused by asphalt aging through preventive maintenance, but it reduces the operational efficiency of the transportation system [14]. Therefore, taking measures to actively inhibit the aging of asphalt is a better choice for building tough and durable road facilities. Current asphalt antiaging technologies, such as the incorporation of layered silicates and layered double hydroxides (LDHs) compounds, face the challenges of high cost and poor compatibility with asphalt, making them difficult to apply in engineering practice on a large scale [15, 16]. In contrast, phenolic antioxidants from natural sources such as catechin, gallic acid, and lignin are widely available and have a similar molecular structure to asphalt, thus avoiding these disadvantages and becoming a promising raw material for the development of efficient asphalt antiaging technology [17].

At the atomic level, the aging of asphalt can be explained by the theory of free radical chain reactions with the steps equations (1)–(3). In the free radical chain reaction, one or more steps are repeated multiple times until the chain is terminated or until one of the reactants is exhausted.

$$R_aH \xrightarrow{h} eat, UV \ R_a\cdot, \tag{1}$$

$$R_a \cdot + O_2 \longrightarrow R_aOO., \tag{2}$$

$$R_aOO \cdot + R_bH \longrightarrow R_aOOH + R_b.. \tag{3}$$
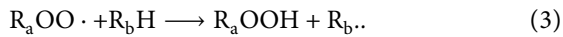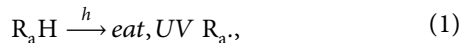
The asphalt molecule (RaH) is dehydrogenated under environmental conditions of heat and UV light to generate an unstable asphalt molecular radical (Ra•). Ra• adsorbs an O_2 molecule to produce the highly reactive RaOO• radical, which further attacks another asphalt molecule (RbH) to generate RaOOH and an Rb• radical. Then, RaOOH undergoes isomerization to produce ketones, aldehydes, and other groups, while Rb• drives the reactions equations (2) and (3) to keep repeating, resulting in the continuous aging of asphalt. This process of asphalt aging is supported by the experimental study of Petersen et al. [9].

Fortunately, phenolic hydroxyl groups can capture R• and ROO• and block the radical chain reactions by providing protons to transform them to RH and ROOH [18], as shown in reactions equations (4) and (5):

$$R \cdot + ArOH \longrightarrow RH + ArO., \tag{4}$$

$$ROO \cdot + ArOH \longrightarrow ROOH + ArO.. \tag{5}$$

The generated ArO• is also a free radical, but its unpaired electron is conjugated to the delocalized π bond on the neighboring aromatic ring and thus remains stable in the subsequent reactions. Therefore, the addition of phenolic compounds theoretically prevents the asphalt molecules from being attacked by free radicals and aging.

In addition, adding crumb rubber into asphalt binders is also an antiaging technology widely used in engineering practice [19]. This is because the carbon black in the rubber

has antioxidant properties, and the crumb rubber can absorb aromatic components of asphalt to prevent them from evaporating during aging. Furthermore, the crumb rubber can limit the physical hardening of asphalt during aging by reducing the bulk viscosity of asphalt [20]. The crumb rubber is usually recycled from used automobile tires, and its utilization not only improves the performance of asphalt materials but also exerts environmental benefits [21, 22]. The use of crumb rubber modified asphalt (RMA) is mainly used to improve the rutting resistance of asphalt mixtures at high temperatures and cracking resistance at low temperatures, but some studies suggest that the addition of rubber powder also enhances the aging resistance of asphalt, although the mechanism is unclear [23–25]. The main component of crumb rubber from tires is styrene-butadiene rubber (SBR) polymer, which is produced by polymerizing styrene with butadiene and does not contain phenolic structures [26]. This fact suggests that crumb rubber enhances the aging resistance of the asphalt binder by a different mechanism than phenolic compounds.

Understanding the mechanisms by which phenolic compounds and rubber crumbs inhibit asphalt aging is important for the development of targeted antiaging technologies for asphalt but is challenged by the inability to experimentally observe the aging behavior of asphalt molecules and their blocking process at the nanoscale as well as the inability to predict aging-related chemical reactions by classical molecular simulation methods [27]. To address this issue, molecular dynamics (MD) simulations based on the reactive force field (ReaxFF) were carried out in this study to investigate the chemical reaction information of asphalt aging and to comprehensively analyze the inhibition mechanism of phenolic compounds and crumb rubber on asphalt aging in combination with classical MD methods [28]. The specific research steps were as follows:

(i) conducting attenuated total reflection (ATR)-FTIR tests to evaluate and compare the aging resistance of base asphalt with phenolic compound-modified and crumb rubber-modified asphalt samples;

(ii) modeling the aging behaviors of various asphalt samples by ReaxFF MD simulations to analyze the potential inhibition mechanisms of phenolic compounds and crumb rubber on asphalt aging from a chemical perspective;

(iii) determining the molecular diffusion and thermodynamic properties of various asphalt samples by classical MD simulations to analyze the potential antiaging mechanisms of phenolic compounds and crumb rubber from a physical perspective.

2. Background on Classical and ReaxFF MD Simulations

MD simulation is a numerical method to predict the state of motion of molecular and atomic systems at a given time by solving Newton's equations of motion by computer [29]. MD simulations can overcome the scale limitations of experimental methods and thus analyze the molecular

mechanisms by which material systems exert their properties. MD was originally conducted in 1957 by Alder and Wainwright to simulate elastic collisions between hard spheres [30]. In 1964, Rahman simulated the system properties of liquid argon using a Lennard-Jones potential and compared them with experimental results [31]. His computer code provided the basic framework for many subsequent MD computing programs. In 2007, Zhang and Greenfield were the first to introduce MD methods to asphalt research, and they proposed a three-component molecular model of asphalt, with each asphalt component represented by a single molecule [32]. Many years later, Li and Greenfield proposed another four-component molecular model of asphalt by summarizing previous studies, in which each asphalt component is represented by multiple molecules [33]. Compared with the three-component model, the simulation results of asphalt properties such as density, polarity, and solubility parameters using the four-component model are closer to the experimental data, so the four-component model was widely accepted as soon as it was proposed.

Subsequently, researchers have conducted numerous studies on the physical and thermodynamic properties of asphalt materials using MD methods [34]. Bhasin et al. and Sun et al. investigated the self-healing mechanism of asphalt based on the diffusion principle and cohesion theory and demonstrated the correlation between the chemical composition and the healing properties of asphalt binders [35, 36]. Xu and Wang et al. performed comprehensive mechanistic analyses of asphalt cohesion and adhesion behaviors based on the interfacial energy theory and considered the effects brought by humidity and oxidation [37, 38]. Guo et al. and Xu et al. investigated the strength formation and debonding mechanisms at the asphalt-aggregate interface, providing theoretical guidance for understanding the cracking resistance of asphalt mixtures [39, 40]. These studies demonstrate that the MD method provides an effective tool for obtaining insight into the microscopic characteristics and mechanical properties of asphalt materials.

However, in these MD methods based on classical force fields (e.g., COMPASS, PCFF, and OLPS), the connectivity between atoms is predefined and remains constant during simulation [27]. In other words, the chemical bonds of the molecule will not be broken or newly generated. Therefore, classical MD simulations cannot be used to study the aging and antiaging behaviors of asphalt related to chemical reactions. Quantum chemistry methods, such as ab initio molecular dynamics (AIMD), are able to accurately predict chemical reactions between substances because they calculate electron behaviors based on quantum mechanics (QM), but AIMD is much more computationally expensive than classical MD due to the cost of dealing with electronic degrees of freedom and is typically limited to shorter times and smaller systems [41, 42].

Fortunately, the ReaxFF force field proposed by Senftle et al. bridges this gap [28]. ReaxFF is a bond-order-based force field that can predict the chemical reactions of a system by determining the breakage and formation of chemical

bonds based on the bond-order size. Bond-order refers to the number of chemical bonds that exist between two atoms and determines the type and stability of covalent bonds. If the bond-order is zero, there is no covalent bond between the two atoms. The bond-order is calculated empirically from the interatomic distances and is used to determine the bond connectivity. The model parameters of the ReaxFF force field are obtained by QM calculations, so the accuracy of ReaxFF MD simulations is close to that of quantum chemistry calculations, but its computational cost is only comparable to that of classical MD methods.

The potential energy of the ReaxFF force field is given by

$$E_{\text{system}} = E_{\text{bond}} + E_{\text{over}} + E_{\text{under}} + E_{\text{val}} + E_{\text{pen}} + E_{\text{tors}} \\ + E_{\text{conj}} + E_{\text{vdW}} + E_{\text{Coulomb}}, \tag{6}$$

where Ebond is the bond energy describing the energy associated with bond stretching; Eover and Eunder are overcoordination and undercoordination energy corrections according to the valence bond theory; Eval is the valence angle energy corresponding to valence angle strain; Epen is the penalty energy, Etors is the torsion angle energy corresponding to torsional angle strain; EvdW and ECoulomb are van der Waals energy and coulomb energy between atoms that are not connected with covalent bonds.

ReaxFF MD has been successfully applied to the study of oxidation and thermal decomposition of complex organic compounds such as hydrocarbons, coal, and lignin [28]. As for asphalt materials, Pan and Hu et al. performed ReaxFF MD simulations to analyze the thermodynamic and kinetic properties of oxidative aging of asphalt, and the simulated results were well compared with experimental data [11, 43]. Their studies demonstrate that ReaxFF MD is feasible for investigating the aging behavior of asphalt binders and their aging blocking mechanisms.

3. Experimental and Modeling Methods

3.1. Preparation of Crumb Rubber-Modified and Phenolic Compound-Modified Asphalt. The base asphalt used was a Performance Grade (PG) 64–22 asphalt produced by SK Company (Korea). The crumb rubber was produced by Huangshi Rubber Factory (China), and its size was 40–80 mesh. Catechin purchased from Sigma–Aldrich (Shanghai, China) was selected to represent phenolic compounds for this study. Catechin is a natural phenol and antioxidant widely found in tea leaves and other plants. It is rich in phenolic hydroxyl groups and is therefore expected to have strong antiaging properties. It has a small molecular size, which ensures uniform dispersion when added to asphalt.

First, the base asphalt was heated to a flowing state in an oven at 160°C, and then placed in an oil bath at 180°C to maintain the flowing state. Next, 9 wt.% of crumb rubber and catechin were added to base asphalt, respectively, and stirred manually to make them well dispersed, and then sheared by a high-speed rotary shear at 6000 r/min for 60 min to obtain the RMA sample and the catechin modified asphalt (CMA) sample.
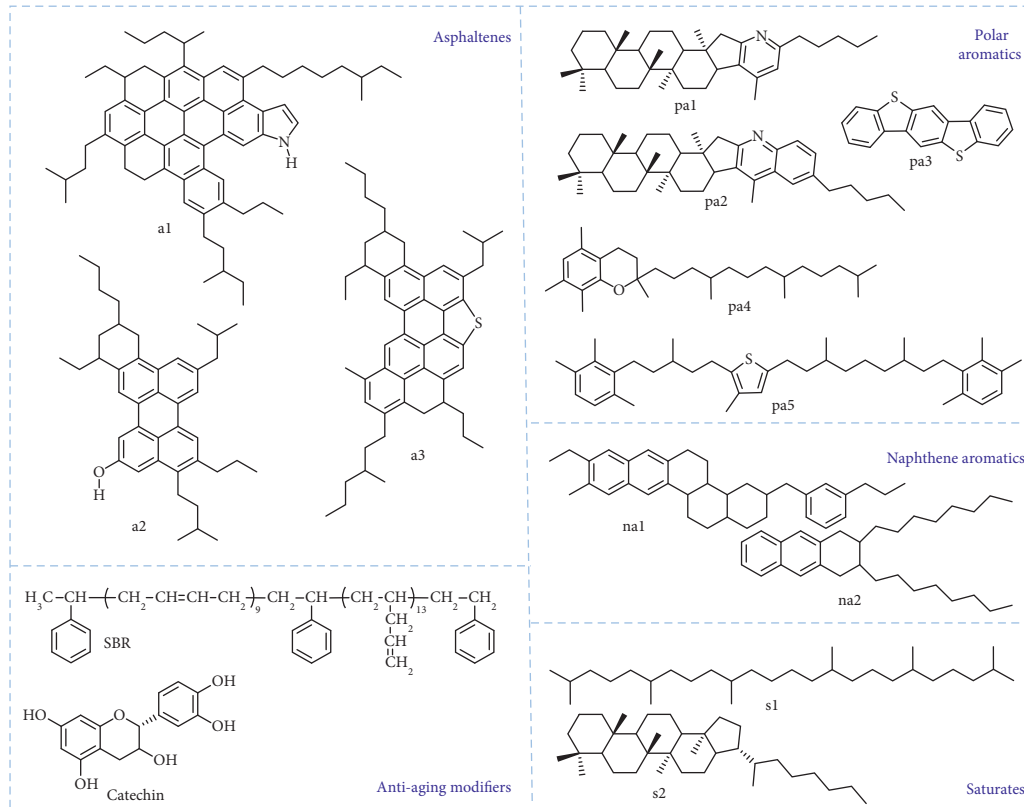
Figure 1: Representative molecules of asphalt components and antiaging modifiers.

3.2. Aging Tests and ATR-FTIR Spectroscopy.

Base asphalt and modified asphalt were subjected to a rolling thin-film oven (RTFO) test according to the AASHTO T240 standard to produce short-term aged samples [44], followed by another pressure aging vessel (PAV) test following the AASHTO R 28 standard to produce long-term aged samples [45]. ATR-FTIR spectroscopy was performed on virgin and long-term aged asphalt samples to assess changes in the characteristics of their oxygen-containing functional groups [46]. The ATR-FTIR tests were conducted on a Thermo Nicolet iS10 spectrometer in the spectral range of $4000-400 \, \text{cm}^{-1}$.

The carbonyl index (CI) and sulfoxide index (SI) of asphalt samples before and after aging were calculated according to equations (7) and (8) to quantify the abundance of carbonyl and sulfoxide groups and to evaluate the aging degree of asphalt samples.

$$CI = \frac{A(1700)}{A(1460) + A(1375)}, \quad (7)$$

$$SI = \frac{A(1030)}{A(1460) + A(1375)}, \quad (8)$$

where $A(1460)$, $A(1375)$, $A(1700)$, and $A(1030)$ are integrated absorption peak areas of methylene, methyl, carbonyl, and sulfoxide groups, respectively. It is generally assumed that the amount of methylene and methyl groups remains constant during asphalt aging, and thus their

integral areas are used as references in the calculation of CI and SI indexes.

3.3. Modeling Details for MD Simulations

3.3.1. Molecular Models of Asphalt and Modifiers.
Asphalt is composed of a large number of complex hydrocarbons and their nonmetallic derivatives. It is not possible to separate all asphalt molecules and to determine their chemical structures through experimental methods. Therefore, asphalt is usually modeled with a certain proportion of representative molecules in the MD simulation. The asphalt model used in this study was proposed by Li and Greenfield in 2014 by modifying and integrating earlier developed molecular structures [33]. In this model, asphalt was divided into four fractions, namely, asphaltenes, polar aromatics, naphthene aromatics, and saturates, as shown in Figure 1. Each fraction contains multiple representative molecules and is combined into a bulk asphalt model according to the ratios in Table 1.

An SBR polymer chain composed of 13-unit monomers of 1, 2-butadiene, 9-unit monomers of 1, 4-butadiene, and 3-unit monomers of styrene was used to represent the crumb rubber by reference to the literature [47]. Catechin is a small-sized compound with a clear chemical structure. The molecular models of SBR and catechin are shown in Figure 1 [18]. The number of SBR chain and catechin molecule added to the modified asphalt model was 2 and 10, respectively,

TABLE 1: Chemical information for molecular IDs in Figure 1 and their proportion in the asphalt model.

Component	Molecular ID	Chemical name	Number in the asphalt model
Asphaltenes	a1	1-pyrrole	2
	a2	2-phenol	3
	a3	3-thiophene	3
Polar aromatics	pa1	1-pyridinohopane	4
	pa2	2-quinolinohopane	4
	pa3	3-benzobisbenzothiophe	15
	pa4	4-trimethylbenzeneoxane	5
	pa5	5-thioisorenieratane	4
Naphthene aromatics	na1	1-PHPN	11
	na2	2-DOCHN	13
Saturates	s1	1-squalane	4
	s2	2-hopane	4
Antiaging modifiers	SBR	—	2
	Catechin	—	10
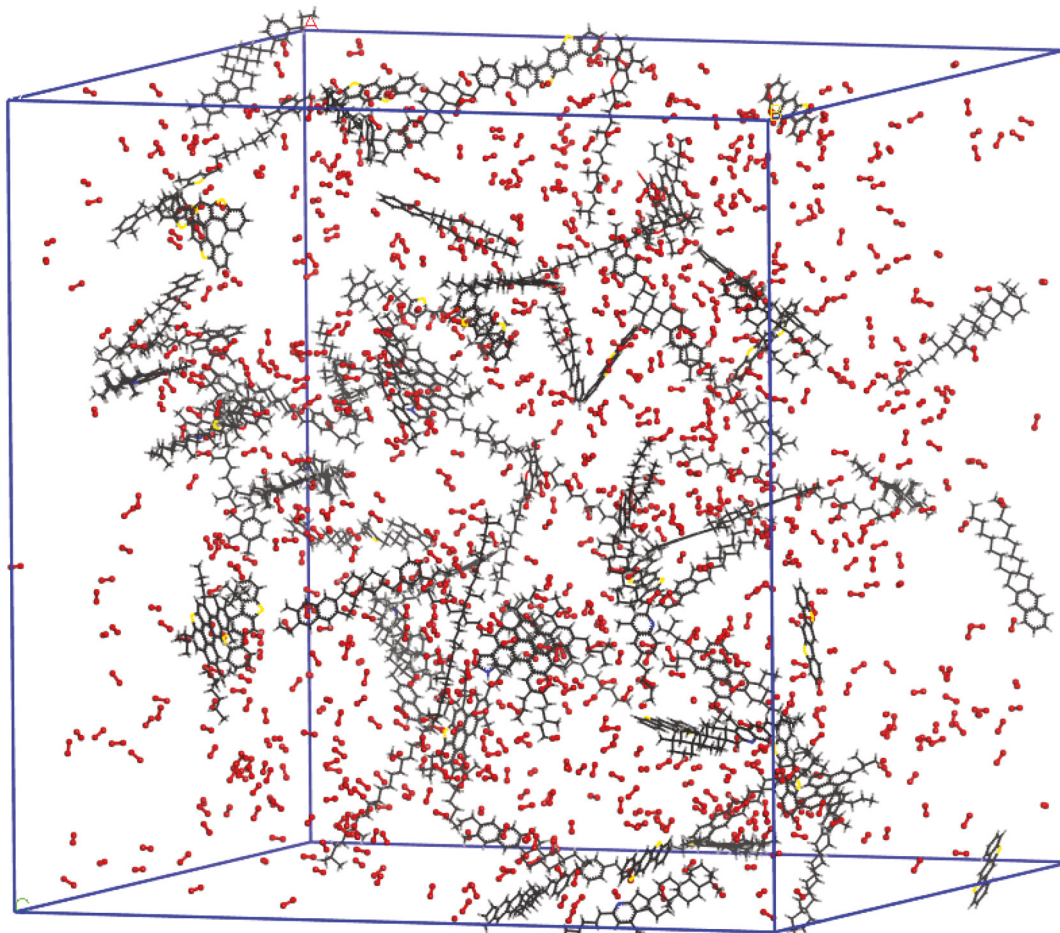
FIGURE 2: Reaction system of base asphalt for ReaxFF simulations (102.4 Å × 102.4 Å × 102.4 Å, black molecules are asphalt, red molecules are O_2).

which was calculated based on a modifier dosage of 9 wt.% of base asphalt.

3.3.2. ReaxFF MD Simulation of Asphalt Aging Behavior.

ReaxFF MD simulations were carried out in this study using LAMMPS software to predict the chemical reactions that occur during asphalt aging [48]. The VMD procedure was used to postprocess the simulation results for visualization [49]. According to the molecular structures and ratios presented in Figure 1 and Table 1, cubic periodic reaction systems of base asphalt, RMA, and CMA mixed with 1000 O_2 molecules were established, respectively, as shown in Figure 2. The number of O_2 molecules ensures that the asphalt molecules can be seriously oxidized. The reaction system first underwent energy minimization. After that, a 1 ns thermodynamic equilibrium was performed at a canonical ensemble (NVT) and a temperature of 298 K, followed by a 2 ns oxidation simulation at the NVT-ensemble and target temperature.

To accelerate the aging reaction of asphalt in the ReaxFF MD simulation, the simulation temperature should be set higher than the ambient temperature at which the asphalt binder is exposed to in engineering practice. Meanwhile, it should not be set too high, otherwise the oxidation reaction will be too intense and incompatible with the mild aging process of asphalt. To determine the proper temperature condition, aging simulations of base asphalt were performed at different temperatures (1000 K, 1200 K, 1400 K, and 1600 K) in this study. Asphalt is transformed from the solid to gas phase at these simulated temperatures, and its density is much smaller than the real density of around 1.0 g/cm^3; therefore, the density of the reaction system was set to 0.1 g/cm^3. The time step of the ReaxFF MD simulation was set to 1 fs, and the cut-off of bond-order used to identify the reaction products was set to 0.3. The ReaxFF parameters used in this study were determined according to the C/H/O/N/S description developed by Van Duin's group [50].

3.3.3. Classical MD Simulation of Asphalt Molecular Diffusion.

In addition to inhibiting the oxidation reaction activity of asphalt at the chemical level, modifiers may also reduce asphalt aging at the physical level by inhibiting the free diffusion of asphalt molecules and reducing their exposure to oxygen. This is particularly true for polymers such as rubber. Therefore, we simulated the diffusion behavior of asphalt binders and calculated the self-diffusion coefficient of asphalt molecules to evaluate the effect of rubber polymers and catechins on the diffusion property of asphalt molecules. The self-diffusion coefficient (D) is calculated as follows [36]:

$$D = \frac{1}{6N} \lim_{t \longrightarrow \infty} \frac{d}{dt} \sum_{n=1}^{N} \left[x_n(t) - x_n(0) \right]^2, \qquad (9)$$

where N is the number of particles of the system; $x_n(0)$ and $x_n(t)$ are the initial and current positions of the particles. D is difficult to obtain directly, but it can be calculated from mean square displacement (MSD) of the system particles using the following equation:

$$D = \frac{Slope \ of \ the \ MSD \ curve \ with \ respect \ to \ time}{6}, \qquad (10)$$

$$MSD = \frac{1}{N} \sum_{n=1}^{N} \left[x_n(t) - x_n(0) \right]^2. \qquad (11)$$

MD simulations based on the COMPASS II force field were carried out using Materials Studio software to obtain the MSD data of asphalt molecules [51]. COMPASS II is a universal ab initio force field suitable for analyzing the physical and thermodynamic properties of organic materials and polymers. Firstly, cubic periodicity simulation systems of base asphalt and modified asphalt were established according to Figure 1 and Table 1, and the initial density of each system was set to 1.0 g/cm^3, which was consistent with the real density of asphalt at ambient temperature. Then, a 1 ns thermodynamic equilibrium was performed at NVT ensemble and a temperature of 180°C to simulate the mixing of asphalt in engineering practice with a time step of 1 fs and a cut-off of 15.5 Å. After that, a 1 ns isothermal isobaric (NPT) equilibrium was performed at 25°C and the atmospheric (atm) pressure to bring the system density to its true value at ambient temperature. Finally, another 1 ns NPT equilibrium was performed under the same conditions, and the MSD and self-diffusivity coefficients were calculated based on the trajectory of this phase.

3.3.4. Classical MD Simulation of Hardening-Related Parameters.

The main adverse effect caused by asphalt aging is the hardening of the asphalt binder, namely, an increase in its viscosity and modulus and a decrease in molecular mobility and intermolecular compatibility. Modifiers may enhance the aging resistance of asphalt by reducing the susceptibility of asphalt to aging. Therefore, hardening-related parameters were calculated for aged asphalt models with and without modifiers to analyze whether there is such a potential effect. The molecular structures of the aged asphalt used was obtained according to the ReaxFF simulation in Section 3.3.2. The component ratio of the aged asphalt models was the same as that of the virgin models.

The hardening-related parameters of the asphalt samples were also obtained by conducting MD simulations based on COMPASS II force fields using Materials Studio software. Cubic periodic systems with a density of 1.0 g/cm^3 were first established for various asphalt samples. Then, a 1 ns NVT equilibrium was performed at 180°C to simulate the mixing of asphalt with a time step of 1 fs and a cut-off of 15.5 Å, followed by a 1 ns NPT equilibrium at 25°C and a pressure of 1 atm. The bulk modulus and compatibility parameters were calculated for the obtained system configurations, and the diffusion coefficients related to molecular mobility were calculated according to the procedure in Section 3.3.3. The obtained system configurations were subsequently subjected to another 1 ns NPT equilibrium at 60°C and 1 atm to calculate the shear viscosity. The shear viscosity (η) was calculated according to the Green–Kubo equation (11) from the

trajectory data of a 10 ns NVT-shear simulation at 60°C and a shear rate of 0.00005/ps [52].

$$\eta = \frac{V}{kT} \int_0^\infty \langle P_{\alpha\beta}(t) P_{\alpha\beta}(0) \rangle dt, \tag{12}$$

where V is the system volume, k is the Boltzmann constant, T is the temperature in thermodynamic scale, $P_{\alpha\beta}$ is the three off-diagonal elements of the instantaneous pressure tensor, and t is the time.

4. Results and Discussion

4.1. ATR-FTIR Spectroscopy of Asphalt Samples before and after Aging. Figure 3(a) displays the ATR-FTIR spectra of base asphalt and modified asphalt before and after aging. The spectra have undergone baseline correction and normalization (by peak height) based on OMSNIC software. The sharp peaks at 1375 and 1460 cm^{-1} are assigned to methyl and methylene groups, respectively. The moderate peaks at 1700 and 1030 cm^{-1} correspond to stretching absorption of carbonyl (C=O) and sulfoxide (S=O) groups, respectively. The virgin base asphalt, RMA, and CMA were close in intensity at the peaks corresponding to C=O and S=O, demonstrating the absence of these oxygen-containing groups in the crumb rubber and catechin.

Figure 3(b) shows a significant increase in both CI and SI indices for the aged asphalt samples, manifesting that a large amount of C=O and S=O groups were generated in asphalt during aging, which is consistent with the observation of previous studies [53, 54]. However, the increase in both CI and SI indices of the aged CMA sample is significantly smaller than that of aged base asphalt, indicating that catechins exert considerable antiaging properties. The aged RMA sample also shows less increase in CI and SI indices than base asphalt, although not as significant as the CMA sample.

The FTIR spectroscopy demonstrate that both crumb rubber and catechin can inhibit the degree of aging of asphalt binders, but there are differences in their antiaging ability, which may be attributed to their different antiaging mechanisms. Therefore, the potential antiaging mechanisms of these two modifiers were investigated based on ReaxFF and classical MD simulations.

4.2. ReaxFF MD Simulations of Asphalt Aging Behaviors

4.2.1. Aging Characteristics of Base Asphalt. FTIR spectra showed that the oxygen-containing groups produced during asphalt aging are mainly carbonyl and sulfoxide, and their corresponding chemical bonds in ReaxFF MD simulations are C–O and S–O bonds (note: the ReaxFF MD simulation cannot distinguish whether the chemical bond is a single or a double bond), respectively. Therefore, based on the results of ReaxFF MD simulations, the number of C–O and S–O bonds in the base asphalt reaction system at each temperature was calculated, and then the oxygen content of base asphalt with time was obtained accordingly, as shown in

Figure 4. Due to the presence of oxygen atoms in the virgin asphalt molecules, the oxygen content in Figure 4 is an increment relative to virgin asphalt rather than an absolute value.

It can be seen that the dependence of the degree of asphalt aging on temperature is very significant. The oxygen content of asphalt at the end of the simulation increases from 8% at 1000 K to 85% at 1600 K. For every 200 K increase in temperature, the oxygen content of asphalt more than doubles. However, the oxygen content of aged asphalt measured in the experiments generally does not exceed 8% [55]. Therefore, the excessive oxygen content observed in the ReaxFF MD simulations at high temperatures (1200, 1400, and 1600 K) suggests that asphalt may have undergone an intense combustion reaction rather than a mild aging process. Consequently, the aging characteristics of asphalt and its influence by rubber polymers and catechins were analyzed hereafter only at a temperature of 1000 K.

The molecular structures of asphalt components at the end of the ReaxFF MD simulation under 1000 K were identified using VMD software to determine the aging products of asphalt. For example, Figure 5 displays the molecular structures of asphaltene-pyrrole (i.e., a1 in Figure 1 and Table 1) before and after aging. It can be seen that the most prominent change on this asphaltene molecule during aging is the production of many carbonyl groups, and most of them are generated on the benzyl C atom (the C atom directly attached to the benzene ring), which is in agreement with the experimental results of Dorrence et al. [56]. This is because the bond dissociation energy of the benzyl C–H bond is relatively small, and the H atom can be easily abstracted from the benzyl C atom by O$_2$ and initiate the subsequent oxidation reaction. In addition, a carboxyl (–COOH) group is generated on the asphaltene molecule, which is supported by Petersen's research [9].

The formation of these polar groups leads to an increase in intermolecular binding energy and molecular agglomeration of aged asphalt, increasing the hardness and decreasing the fluidity of the asphalt binder. Another change on the asphaltene molecule is the conversion of two cycloalkanes into benzene rings due to the loss of H atoms. In this process, the bond-order between the carbon atoms on the cycloalkane increases, and the originally distorted carbon ring becomes flat, so aromatization is considered to have occurred. This aromatization reaction was also confirmed by the experimental characterization of Petersen [9]. The well comparison of the simulation results with experimental studies demonstrates that ReaxFF MD is feasible for simulating the aging behavior of asphalt materials.

Figure 6 displays the molecular structures of the various asphalt components at the end of the ReaxFF MD simulation. It can be seen that the main product of asphalt aging is carbonyl, followed by sulfoxide, and a small amount of carboxyl and hydroxyl groups. Because the saturate molecules do not contain benzene rings and thus do not have benzyl groups that are susceptible to oxidation reactions, the saturate molecules (s1 and s2) were generally unreacted at the end of the ReaxFF MD simulation. This is consistent with the observation from the asphalt fraction separation

(a)

(b)
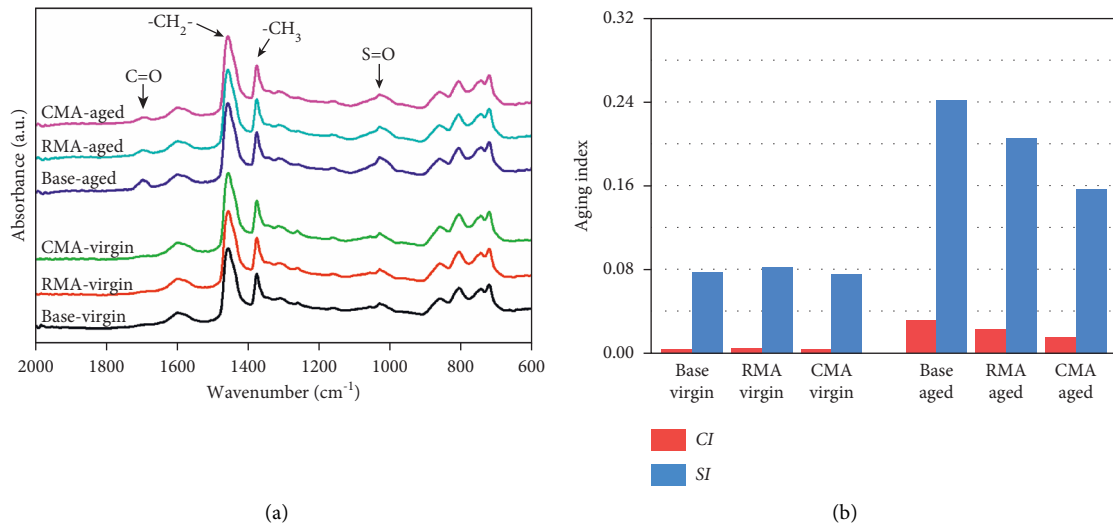
FIGURE 3: ATR-FTIR spectra of virgin and aged asphalt samples.
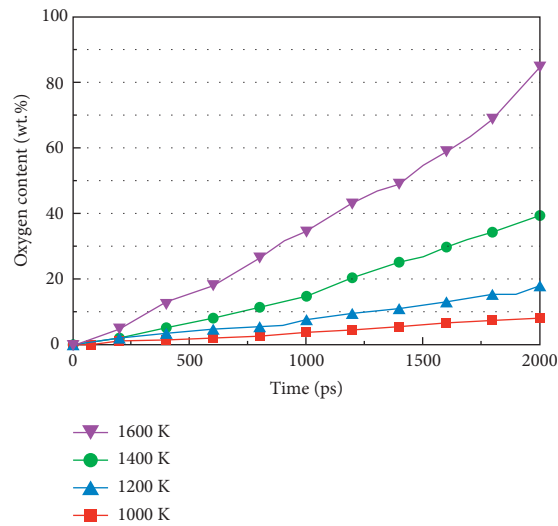
FIGURE 4: Oxygen content of base asphalt at various temperatures observed from ReaxFF MD simulations.
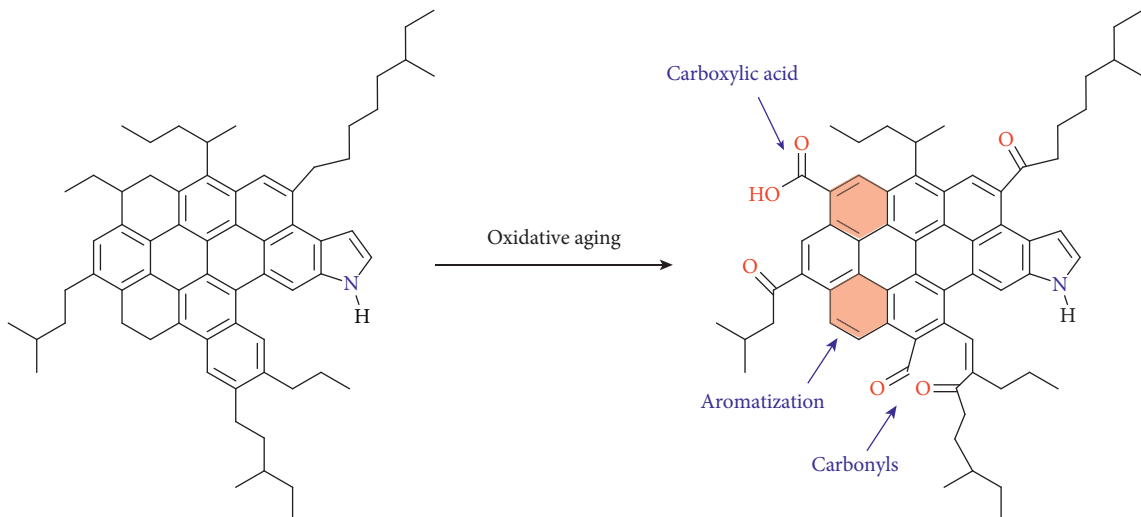
FIGURE 5: Molecular structures of asphaltene-pyrrole before and after aging.
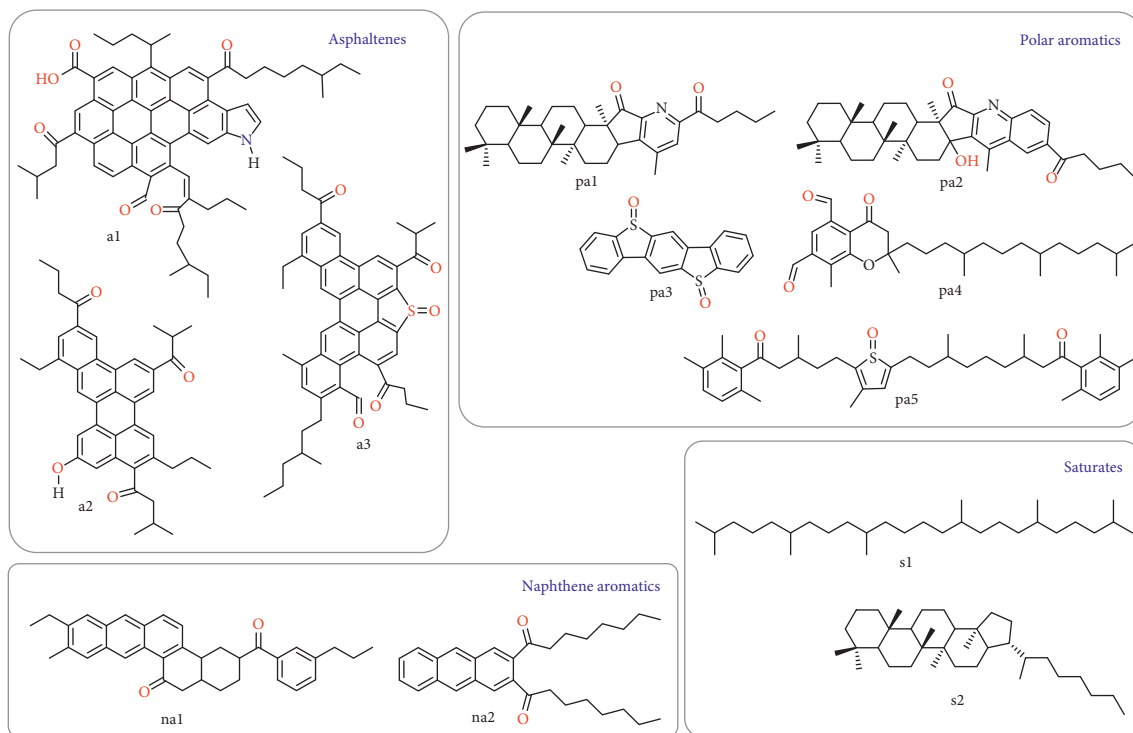
FIGURE 6: Molecular structures of various asphalt components at the end of the ReaxFF MD simulation.

experiments that the percentage of saturate fractions remained essentially unchanged before and after aging [57].

It should be noted that Figure 6 shows representative simulation results of the molecular structures of asphalt after aging; due to the stochastic nature of the chemical reactions, not every simulation will yield the same aging results. For example, there are two asphaltene-a1 molecules in the system, and at the end of the ReaxFF MD simulation, the structure of one molecule is shown in Figure 5, while the carbonyl groups on the other molecule are in different positions, and no carboxyl group is produced. This difference suggests that the aging pathway is not fixed for multiple replicates of the same asphalt molecule. Nevertheless, since these replicates have a similar aging process, the typical representation in Figure 6 was subsequently applied to represent the molecular structures of aged asphalt.

4.2.2. Antiaging Properties of Rubber Polymers and Catechins. Figure 7 displays the number of C–O and S–O bonds in the base and modified asphalt with time obtained from the ReaxFF MD simulations. Due to the presence of C–O bonds in the virgin asphalt molecules, the bond amounts in Figure 7(a) are increments relative to the virgin samples rather than absolute values. As shown in Figure 7(a), there is no significant difference in the growth trend of C–O bonds in RMA compared to base asphalt, indicating that rubber polymers cannot inhibit asphalt aging at the chemical level. However, the amount of C–O bond produced in LMA was significantly reduced relative to base asphalt, suggesting that catechins chemically mitigate asphalt aging. This is due to the abundant phenolic hydroxyl

groups on catechins that attract and react with O_2 and free radicals, thus reducing the attack of the latter on asphalt molecules. Figure 7(b) shows that the number of S–O bonds generated during asphalt aging is much smaller than the number of C–O bonds due to the fact that the number of S atoms in the asphalt molecule is much smaller than the number of C atoms. Nevertheless, it can still be observed that rubber polymers cannot but catechins can inhibit the generation of S–O bonds.

Figure 8 displays the changes in chemical structures of rubber polymers and catechins during aging. As can be seen in Figure 8(a), two rubber chains underwent different aging reactions, but they both decomposed into four segments and reacted at the ends of the segments, including the formation of carbonyl, hydroxyl, and unsaturated olefin bonds. For these small-size segments, their molecular structures are similar to that of the saturate molecules of asphalt, except for the oxygen-containing groups at the ends. Therefore, the decomposition of the rubber polymer may exert properties that counteract the degradation of the mechanical performance of aged asphalt, as will be discussed in Section 4.4.

Figure 8(b) shows that the catechin molecule loses the H atoms on its hydroxyl groups after aging, which is the underlying mechanism by which phenolic compounds exert their antiaging properties: phenolic compounds provide active H atoms to consume O_2 and free radicals in the reaction system, thus preventing them from attacking asphalt molecules. Although the catechin molecule exists as a free radical after the loss of H atoms, it remains unreactive due to the conjugation of the phenoxy group to the delocalized π bond of the aromatic ring and therefore does not react with the asphalt molecules.
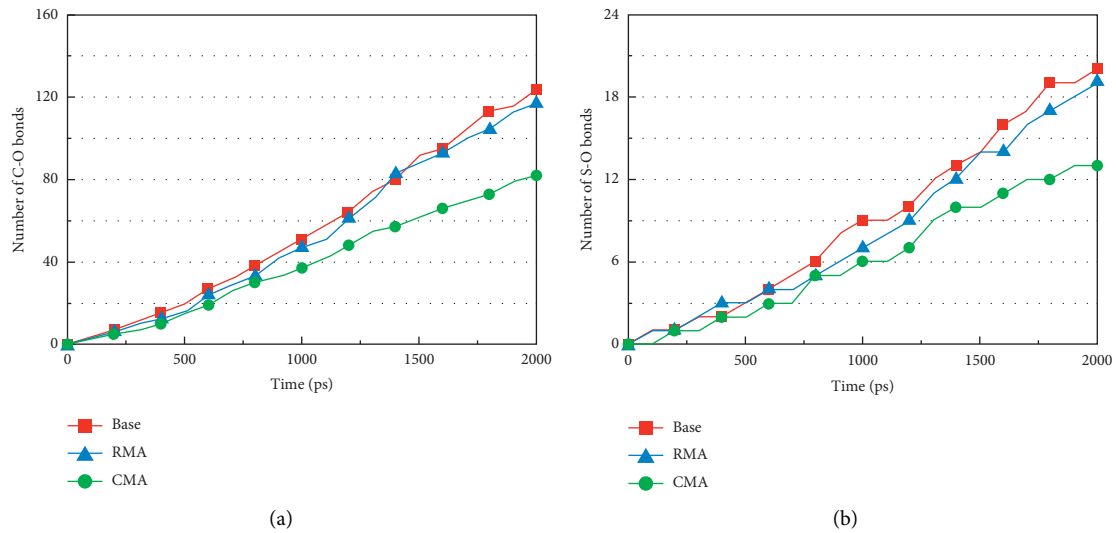
FIGURE 7: Number of C–O and S–O bonds in the base and modified asphalt samples with aging time obtained from ReaxFF MD simulations.
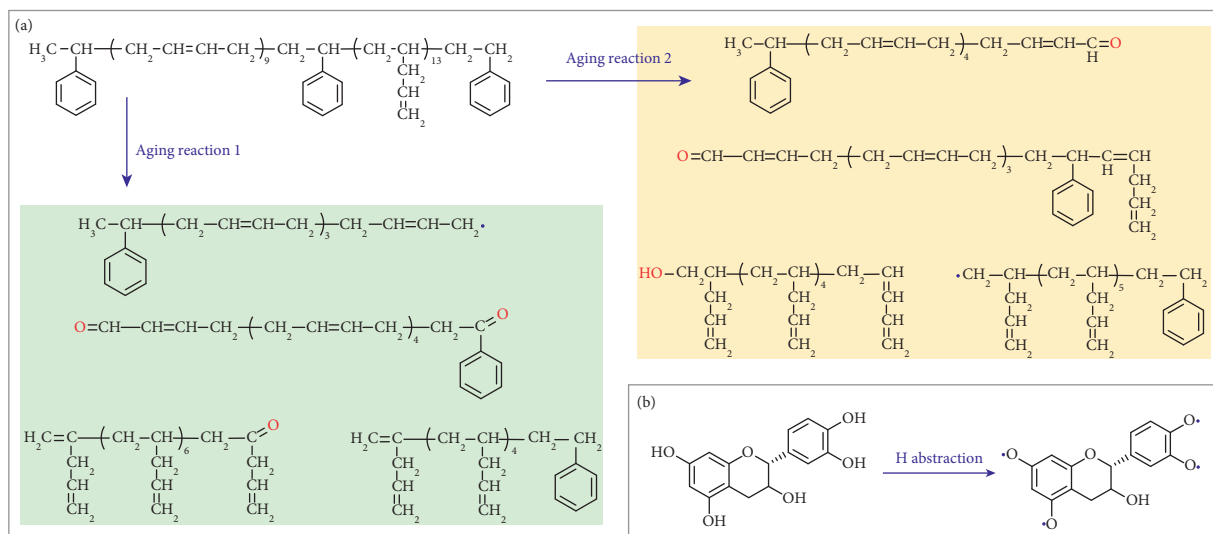
FIGURE 8: Changes in molecular structures of the rubber polymer and catechin during aging.

4.3. Effects of Rubber Polymers and Catechins on the Diffusivity of Asphalt. To investigate whether rubber polymers and catechins reduce the contact of asphalt with oxygen and inhibit asphalt aging by restricting the diffusion of asphalt molecules, we calculated and analyzed the diffusivity of base and modified asphalt samples. As described earlier, the self-diffusion coefficient is numerically 1/6 of the slope of the MSD curve. Since the MSD curve is not linearly related to the simulation time in the initial stage of the MD simulation, the first 50 ps of data are not used in the linear fitting of the MSD curve, as shown in Figure 9(a). The self-diffusion coefficients calculated from the MSD curves are shown in Figure 9(b), and they are the average of three replicate simulations.

The self-diffusion coefficient of RMA decreases from 0.021 Å2/ps to 0.015 Å2/ps compared to base asphalt, indicating that the addition of rubber polymers inhibits the

diffusion of asphalt molecules, which is attributed to the embedding locking effect of the styrene block in the SBR polymer on the asphalt molecules. In contrast, the addition of small-sized catechins does not significantly affect the diffusivity of asphalt molecules. By comparing Figures 7 and 9, it can be seen that both catechins and rubber polymers can exert the property of inhibiting asphalt aging, but their antiaging mechanisms are different: catechins prevent oxidative aging of asphalt by competitively consuming O_2 and free radicals, while rubber polymers exert an antiaging effect by reducing the contact of asphalt molecules with O_2.

4.4. Effects of Rubber Polymers and Catechins on the Hardening of Aged Asphalt. Figure 8(a) reveals that the rubber polymers decompose during aging into small fragments with
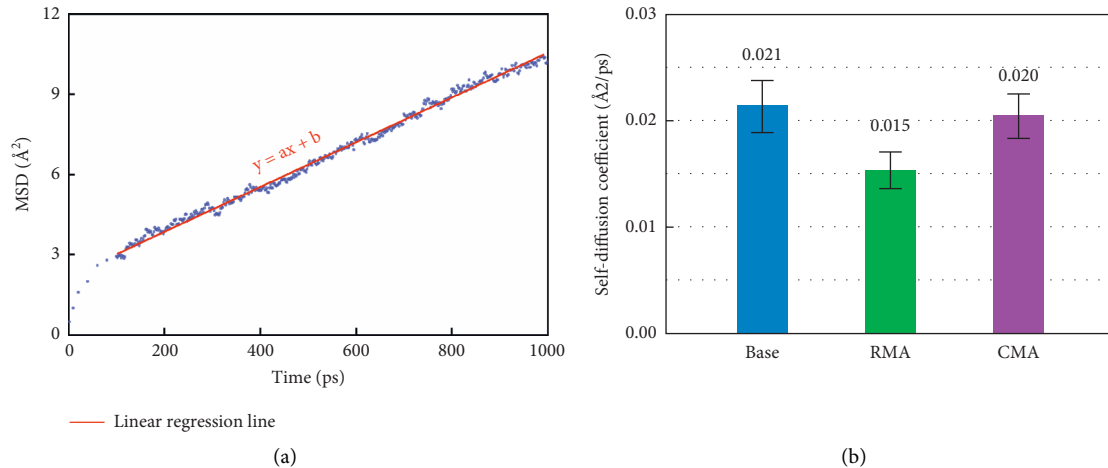
FIGURE 9: Effect of modifiers on the diffusivity of asphalt: (a) linear fitting of the MSD data; (b) self-diffusion coefficients of base and modified asphalt.

similar molecular structures to the saturates of the asphalt binder, which may counteract the hardening caused by asphalt aging to some extent. Therefore, we further analyzed the effect of aging-induced changes in the molecular structures of the modifiers on the hardening-related parameters of the aged asphalt, as shown in Figure 10. The molecular structures of aged asphalt and modifiers presented in Figures 6 and 8 were used here to construct MD models.

Figure 10(a) shows that the shear viscosity of RMA under the virgin condition doubles compared to base asphalt, which is attributed to the enhanced intermolecular friction of the asphalt binder caused by the embedding locking effect of the rubber polymer. The shear viscosity of CMA also increases slightly compared to base asphalt, which may be attributed to the numerous polar hydroxyl groups in catechins that increase the agglomeration of asphalt molecules. After aging, the viscosity of all three asphalt samples increases significantly due to the generation of polar oxygen-containing groups on the asphalt molecules. However, the viscosity of RMA under the aging condition is lower than that of base asphalt due to the breakage of rubber chains into fragments similar to the saturate fraction of asphalt binders. The viscosity of aged CMA also decreases slightly compared to base asphalt, probably because the molecular structure of the catechins was disrupted and their molecular polarity decreased, thus serving to dilute the highly polar aged asphalt molecules.

As displayed in Figure 10(b), the bulk modulus of each sample increases substantially after aging compared to that before aging, which is also attributed to the generation of polar groups that bind the asphalt molecules more tightly and make it difficult for deformation to occur. Compared to base asphalt, the bulk modulus of RMA increases slightly before aging and decreases after aging by the same mechanism as the viscosity change. However, there was no statistical difference in the modulus of CMA before or after aging compared to the matrix asphalt, suggesting that the polar hydroxyl groups of catechins have a different effect on the modulus of asphalt than on the shear viscosity.

The solubility parameter shown in Figure 10(c) is a measure of intermolecular compatibility of the binder samples. The larger the solubility parameter of modified or aged asphalt, the more difficult it is for their respective internal molecules to be compatible, thus exhibiting unfavorable local hardening. In the virgin state, the solubility parameter of RMA increases slightly compared to base asphalt, indicating that the addition of rubber polymers reduced the compatibility of the asphalt components, which is consistent with the lack of storage stability of CRMA in engineering practice [58, 59]. However, the solubility parameter of RMA after aging is smaller than that of base asphalt, indicating that the decomposition products of the rubber polymer become more compatible with the asphalt molecules. The solubility parameters of CMA are not statistically different compared to base asphalt both before and after aging.

Figure 10(d) displays the effects of modification and aging on the diffusivity of the asphalt binder. The lower diffusivity indicates that the asphalt binder is more difficult to flow and is therefore also related to the hardening properties of the asphalt material. The effects of rubber polymers and catechins on the diffusivity of virgin asphalt have been discussed in Section 4. The diffusivity of all samples decreases significantly after aging, indicating that the polar groups produced during aging restricted the movement of asphalt molecules. Compared to aged base asphalt, the diffusivity of RMA increases slightly while that of CMA remains unchanged, suggesting that the cleaved rubber polymers act as a lubricant for the aged asphalt molecules, thus increasing their movement, while catechins do not exert this effect.

According to Figures 9 and 10, it can be concluded that rubber polymers can not only reduce the asphalt aging reaction by limiting the contact of asphalt molecules with oxygen but also restore the mechanical properties of aged asphalt by partially offsetting the aging-induced hardening of the asphalt binder through its own degradation. Therefore, crumb rubber is widely used as antiaging
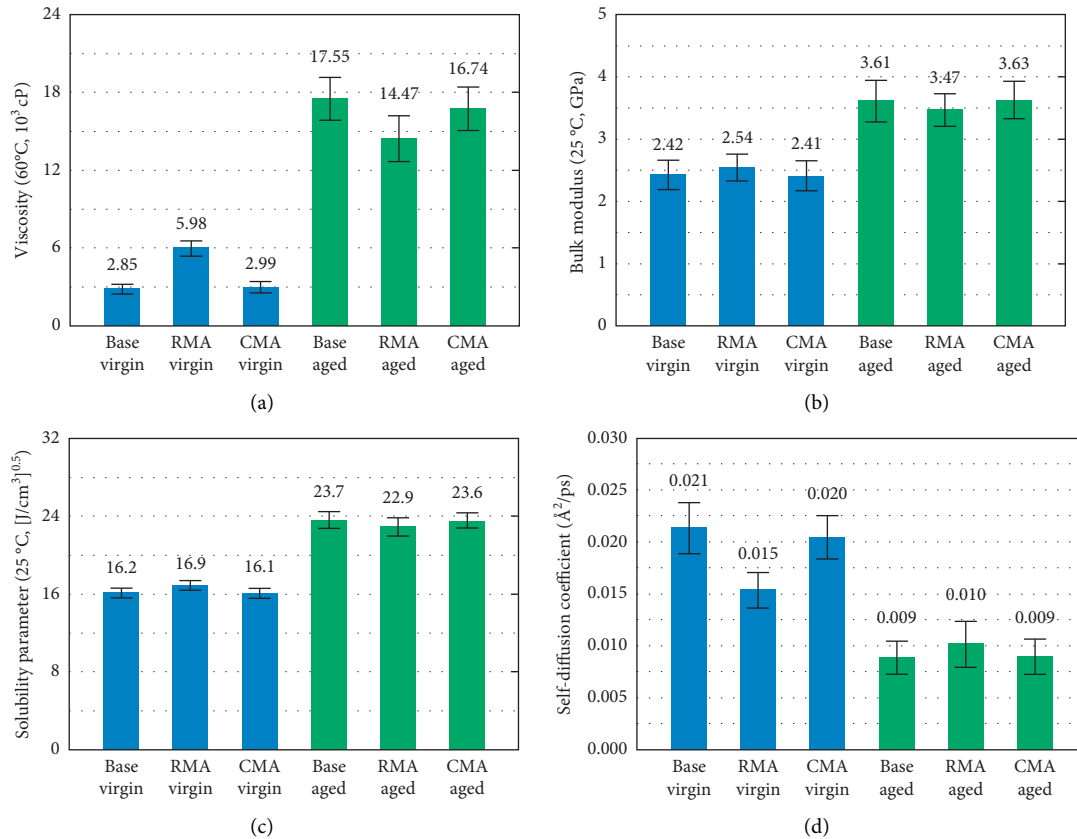
Figure 10: Effects of modifiers on the hardening-related parameters of aged asphalt: (a) viscosity; (b) bulk modulus; (c) solubility parameter; (d) self-diffusion coefficient.

agents for asphalt binders, even though it cannot directly block the oxidation reaction of asphalt molecules at the chemical level.

5. Conclusions

ATR-FTIR spectroscopy and ReaxFF with classical MD simulations were performed in this study to investigate the inhibitory effects of catechins and crumb rubber on asphalt aging and their potential mechanisms. The following conclusions can be drawn:

(1) ATR-FTIR analysis showed that both catechins and crumb rubber can inhibit the aging of the asphalt binder to some extent, and catechins have better antiaging properties than crumb rubber.

(2) ReaxFF MD simulations of asphalt aging behavior demonstrated that catechins can prevent asphalt aging at the chemical level, leading to a reduction of generated S–O and C–O bonds by the mechanism that catechins provide H atoms to react with O_2 and free radicals, thus preventing them from attacking asphalt molecules.

(3) Classical MD simulations of diffusion behavior suggested that the addition of rubber polymers

restricts the movement of asphalt molecules, thus reducing their contact and reaction frequency with O_2 at the physical level.

(4) MD calculations of the hardening parameters of the aged asphalt binder show that the aging degraded rubber polymer acts as a diluting and lubricating agent, thus partially restoring the aging-induced asphalt hardening.

In conclusion, this study demonstrates that phenolic compounds and rubber polymers enhance the aging resistance of asphalt binders through their respective mechanisms at the molecular scale and is expected to provide theoretical guidance for the development of targeted antiaging technologies for asphalt. In future studies, we will further analyze the correspondence between the chemical structures of polymers and phenolic compounds and their antiaging properties to guide the selection and development of antiaging agents for asphalt.

Data Availability

Some or all data that support the findings of this study are available from the corresponding author upon reasonable request.

Conflicts of Interest

Acknowledgments

References

[1] W. Xia, S. Wang, H. Wang, and T. Xu, "Thermal effects of asphalt SARA fractions, kinetic parameter calculation using isoconversional method and distribution models," *Journal of Thermal Analysis and Calorimetry*, vol. 146, no. 4, pp. 1577–1592, 2021.

[2] D. Wang, A. Cannone Falchetto, C. Riccardi, and M. P. Wistuba, "Investigation on the low temperature properties of asphalt binder: glass transition temperature and modulus shift factor," *Construction and Building Materials*, vol. 245, Article ID 118351, 2020.

[3] L. W. Corbett, "Composition of asphalt based on generic fractionation, using solvent deasphaltening, elution-adsorption chromatography, and densimetric characterization," *Analytical Chemistry*, vol. 41, no. 4, pp. 576–579, 1969.

[4] O. C. Mullins, "The modified Yen model," *Energy & Fuels*, vol. 24, no. 4, pp. 2179–2207, 2010.

[5] B. Guan, J. Liu, J. Wu et al., "Investigation of the performance of the ecofriendly fiber-reinforced asphalt mixture as a sustainable pavement material," *Advances in Materials Science and Engineering*, vol. 2019, Article ID 6361032, 11 pages, 2019.

[6] Y. Wang, X. Wang, X. Zhou, G. Yang, and L. Zhang, "Evaluation of the physical and adhesive properties of natural weathering asphalt," *Advances in Materials Science and Engineering*, vol. 2021, Article ID 5783256, 10 pages, 2021.

[7] X. Sun, J. Yuan, Z. Liu, X. Qin, and Y. Yin, "Evaluation and characterization on the segregation and dispersion of anti-UV aging modifying agent in asphalt binder," *Construction and Building Materials*, vol. 289, Article ID 123204, 2021.

[8] D. Zheng, Z.-d Qian, P. Li, and L.-b Wang, "Performance evaluation of high-elasticity asphalt mixture containing inorganic nano-titanium dioxide for applications in high altitude regions," *Construction and Building Materials*, vol. 199, pp. 594–600, 2019.

[9] J. C. Petersen, "A Review of the Fundamentals of Asphalt Oxidation: Chemical, Physicochemical, Physical Property, and durability Relationships," *Transportation Research Circular*, vol. E-C140, 2009.

[10] X. Sun, X. Qin, Z. Liu, Y. Yin, C. Zou, and S. Jiang, "New preparation method of bitumen samples for UV aging behavior investigation," *Construction and Building Materials*, vol. 233, Article ID 117278, 2020.

[11] D. Hu, X. Gu, B. Cui, J. Pei, and Q. Zhang, "Modeling the oxidative aging kinetics and pathways of asphalt: a ReaxFF molecular dynamics study," *Energy & Fuels*, vol. 34, no. 3, pp. 3601–3613, 2020.

[12] L. Lyu, D. Li, Y. Chen, Y. Tian, and J. Pei, "Dynamic chemistry based self-healing of asphalt modified by diselenide-crosslinked polyurethane elastomer," *Construction and Building Materials*, vol. 293, Article ID 123480, 2021.

[13] D. Wang, C. Riccardi, B. Jafari, A. Cannone Falchetto, and M. P. Wistuba, "Investigation on the effect of high amount of Re-recycled RAP with Warm mix asphalt (WMA) technology," *Construction and Building Materials*, vol. 312, Article ID 125395, 2021.

[14] M. Zheng, W. Chen, X. Ding, W. Zhang, and S. Yu, "Comprehensive life cycle environmental assessment of preventive maintenance techniques for asphalt pavement," *Sustainability*, vol. 13, no. 9, p. 4887, 2021.

[15] P. Apostolidis, X. Liu, C. Kasbergen, and A. T. Scarpas, "Synthesis of asphalt binder aging and the state of the art of antiaging technologies," *Transportation Research Record: Journal of the Transportation Research Board*, vol. 2633, no. 1, pp. 147–153, 2017.

[16] H. Zhang, H. Duan, C. Zhu, Z. Chen, and H. Luo, "Mini-review on the application of nanomaterials in improving antiaging properties of asphalt," *Energy & Fuels*, vol. 35, no. 14, pp. 11017–11036, 2021.

[17] M. Leopoldini, N. Russo, and M. Toscano, "The molecular basis of working mechanism of natural polyphenolic antioxidants," *Food Chemistry*, vol. 125, no. 2, pp. 288–306, 2011.

[18] M. Brewer, "Natural antioxidants: sources, compounds, mechanisms of action, and potential applications," *Comprehensive Reviews in Food Science and Food Safety*, vol. 10, no. 4, pp. 221–247, 2011.

[19] S. Wang, Q. Wang, and S. Li, "Thermooxidative aging mechanism of crumb-rubber-modified asphalt," *Journal of Applied Polymer Science*, vol. 133, no. 16, 2016.

[20] Y. Ma, S. Wang, H. Zhou, W. Hu, P. Polaczyk, and B. Huang, "Recycled polyethylene and crumb rubber composites modified asphalt with improved aging resistance and thermal stability," *Journal of Cleaner Production*, vol. 334, Article ID 130102, 2022.

[21] F. Guo, J. Zhang, J. Pei, B. Zhou, and Z. Hu, "Study on the mechanical properties of rubber asphalt by molecular dynamics simulation," *Journal of Molecular Modeling*, vol. 25, no. 12, pp. 365–368, 2019.

[22] L. Lyu, J. Pei, D. Hu, G. Sun, and E. H. Fini, "Bio-modified rubberized asphalt binder: a clean, sustainable approach to recycle rubber into construction," *Journal of Cleaner Production*, vol. 345, Article ID 131151, 2022.

[23] N. S. Mashaan, A. H. Ali, M. R. Karim, and M. Abdelaziz, "An overview of crumb rubber modified asphalt," *International Journal of the Physical Sciences*, vol. 7, no. 2, pp. 166–170, 2012.

[24] K.-D. Jeong, S.-J. Lee, S. N. Amirkhanian, and K. W. Kim, "Interaction effects of crumb rubber modified asphalt binders," *Construction and Building Materials*, vol. 24, no. 5, pp. 824–831, 2010.

[25] Q. Li, H. Zhang, and Z. Chen, "Improvement of short-term aging resistance of styrene-butadiene rubber modified asphalt by sasobit and epoxidized soybean oil," *Construction and Building Materials*, vol. 271, Article ID 121870, 2021.

[26] F. Khabaz and R. Khare, "Glass transition and molecular mobility in styrene-butadiene rubber modified asphalt," *The Journal of Physical Chemistry B*, vol. 119, no. 44, pp. 14261–14269, 2015.

[27] H. Yao, J. Liu, M. Xu, J. Ji, Q. Dai, and Z. You, "Discussion on molecular dynamics (MD) simulations of the asphalt materials," *Advances in Colloid and Interface Science*, vol. 299, Article ID 102565, 2022.

[28] T. P. Senftle, S. Hong, M. M. Islam et al., "The ReaxFF reactive force-field: development, applications and future directions," *Npj Computational Materials*, vol. 2, no. 1, pp. 15011–15014, 2016.

[29] K. Zhou and B. Liu, *Molecular Dynamics Simulation: Fundamentals and Applications*, Elsevier, Amsterdam, Netherlands, 2022.

[30] B. J. Alder and T. E. Wainwright, "Phase transition for a hard sphere system," *The Journal of Chemical Physics*, vol. 27, no. 5, pp. 1208-1209, 1957.

[31] A. Rahman, "Correlations in the motion of atoms in liquid argon," *Physical Review*, vol. 136, no. 2A, pp. A405–A411, 1964.

[32] L. Zhang and M. L. Greenfield, "Analyzing properties of model asphalts using molecular simulation," *Energy & Fuels*, vol. 21, no. 3, pp. 1712–1716, 2007.

[33] D. D. Li and M. L. Greenfield, "Chemical compositions of improved model asphalt systems for molecular simulations," *Fuel*, vol. 115, pp. 347–356, 2014.

[34] Z. Chen, J. Pei, R. Li, and F. Xiao, "Performance characteristics of asphalt materials based on molecular dynamics simulation - a review," *Construction and Building Materials*, vol. 189, pp. 695–710, 2018.

[35] A. Bhasin, R. Bommavaram, M. L. Greenfield, and D. N. Little, "Use of molecular dynamics to investigate self-healing mechanisms in asphalt binders," *Journal of Materials in Civil Engineering*, vol. 23, no. 4, pp. 485–492, 2011.

[36] D. Sun, T. Lin, X. Zhu, Y. Tian, and F. Liu, "Indices for self-healing performance assessments based on molecular dynamics simulation of asphalt binders," *Computational Materials Science*, vol. 114, pp. 86–93, 2016.

[37] G. Xu and H. Wang, "Study of cohesion and adhesion properties of asphalt concrete with molecular dynamics simulation," *Computational Materials Science*, vol. 112, pp. 161–169, 2016.

[38] G. Xu and H. Wang, "Molecular dynamics study of oxidative aging effect on asphalt binder properties," *Fuel*, vol. 188, pp. 1–10, 2017.

[39] M. Guo, Y. Tan, and J. Wei, "Using molecular dynamics simulation to study concentration distribution of asphalt binder on aggregate surface," *Journal of Materials in Civil Engineering*, vol. 30, no. 5, Article ID 04018075, 2018.

[40] M. Xu, J. Yi, D. Feng, Y. Huang, and D. Wang, "Analysis of adhesive characteristics of asphalt based on atomic force microscopy and molecular dynamics simulation," *ACS Applied Materials & Interfaces*, vol. 8, no. 19, pp. 12393–12403, 2016.

[41] B. Li, P. Ou, Y. Wei, X. Zhang, and J. Song, "Polycyclic aromatic hydrocarbons adsorption onto graphene: a DFT and AIMD study," *Materials*, vol. 11, no. 5, p. 726, 2018.

[42] D. Hu, X. Gu, Q. Dong, L. Lyu, B. Cui, and J. Pei, "Investigating the bio-rejuvenator effects on aged asphalt through exploring molecular evolution and chemical transformation of asphalt components during oxidative aging and regeneration," *Journal of Cleaner Production*, vol. 329, Article ID 129711, 2021.

[43] T. Pan, "A first-principles based chemophysical environment for studying lignins as an asphalt antioxidant," *Construction and Building Materials*, vol. 36, pp. 654–664, 2012.

[44] Astm D1754, *Standard Test Method for Effect of Heat and Air on Asphaltic Materials (Thin-Film Oven Test)*, ASTM International, West Conshohocken, PA, USA, 2009.

[45] M. Frisch, G. Trucks, H. B. Schlegel, G. E. Scuseria, M. A. Robb, and J. R. Cheeseman, *Gaussian 09, Revision d. 01*, p. 201, Gaussian. Inc, Wallingford CT, UK, 2009.

[46] B. Guan, J. Wu, H. Tian et al., "Investigation of adhesion properties between asphalt and calcined bauxite aggregate," *Journal of Materials in Civil Engineering*, vol. 32, no. 7, Article ID 04020168, 2020.

[47] M. Zhou, J. Liu, G. Hou, H. Yang, and L. Zhang, "Study on structures, dynamics and mechanical properties of styrene butadiene rubber (SBR)/silica interfaces: a fully atomistic molecular dynamics," *Polymer*, vol. 218, Article ID 123523, 2021.

[48] S. Plimpton, "Fast parallel algorithms for short-range molecular dynamics," *Journal of Computational Physics*, vol. 117, no. 1, pp. 1–19, 1995.

[49] W. Humphrey, A. Dalke, and K. Schulten, "VMD: visual molecular dynamics," *Journal of Molecular Graphics*, vol. 14, no. 1, pp. 33–38, 1996.

[50] F. Castro-Marcano, A. M. Kamat, M. F. Russo Jr, A. C. van Duin, and J. P. Mathews, "Combustion of an Illinois No. 6 coal char simulated using an atomistic char representation and the ReaxFF reactive force field," *Combustion and Flame*, vol. 159, no. 3, pp. 1272–1285, 2012.

[51] D. Systèmes, *Materials Studio, Release 8.0*, Dassault Systèmes BIOVIA Corp, San Diego, CA, USA, 2014.

[52] W. G. Hoover, D. J. Evans, R. B. Hickman, A. J. C. Ladd, W. T. Ashurst, and B. Moran, "Lennard-Jones triple-point bulk and shear viscosities. Green-Kubo theory, Hamiltonian mechanics, and nonequilibrium molecular dynamics," *Physical Review A*, vol. 22, no. 4, pp. 1690–1697, 1980.

[53] Z.-g Feng, H.-j Bian, X.-j Li, and J.-y Yu, "FTIR analysis of UV aging on bitumen and its fractions," *Materials and Structures*, vol. 49, no. 4, pp. 1381–1389, 2016.

[54] N. C. L. Madeira, PdS. Ferreira, J. F. Allochio Filho et al., "Study of thermal aging of model compounds present in asphalt cement by GC/MS, ESI-MS, NMR, and FTIR," *Energy & Fuels*, vol. 35, no. 18, pp. 14553–14568, 2021.

[55] M. Liu, M. A. Ferry, R. R. Davison, C. J. Glover, and J. A. Bullin, "Oxygen uptake as correlated to carbonyl growth in aged asphalts and asphalt Corbett fractions," *Industrial & Engineering Chemistry Research*, vol. 37, no. 12, pp. 4669–4674, 1998.

[56] S. M. Dorrence, F. A. Barbour, and J. C. Petersen, "Direct evidence of ketones in oxidized asphalts," *Analytical Chemistry*, vol. 46, no. 14, pp. 2242–2244, 1974.

[57] F. Fallah, F. Khabaz, Y.-R. Kim, S. R. Kommidi, and H. F. Haghshenas, "Molecular dynamics modeling and simulation of bituminous binder chemical aging due to variation of oxidation level and saturate-aromatic-resin-asphaltene fraction," *Fuel*, vol. 237, pp. 71–80, 2019.

[58] G. Cheng, B. Shen, and J. Zhang, "A study on the performance and storage stability of crumb rubber-modified asphalts," *Petroleum Science and Technology*, vol. 29, no. 2, pp. 192–200, 2011.

[59] A. Ghavibazoo, M. Abdelrahman, and M. Ragab, "Effect of crumb rubber modifier dissolution on storage stability of crumb rubber-modified asphalt," *Transportation Research Record: Journal of the Transportation Research Board*, vol. 2370, no. 1, pp. 109–115, 2013.

Research Article

Experimental Research on Mix Ratio of Construction Waste Cemented Filling Material Based on Response Surface Methodology

Weixin Chen ⓘ**, Guohua Zhang** ⓘ**, Qin Tao** ⓘ**, Liangliang Yu** ⓘ**, Tao Li** ⓘ**, and Xianhua Guan** ⓘ

School of Mining Engineering, Heilongjiang University of Science and Technology, D2468 Puyuan Road, Harbin 150022, China

Correspondence should be addressed to Weixin Chen; cwxkygcxy@163.com

In order to solve the problem of insufficient supply of aggregate for cemented filling material, the experimental research on the mix ratio of cemented filling material using construction waste as recycled coarse aggregate was carried out. A ternary quadratic regression model was created using the Box-Behnken design (BBD) based on the response surface methodology (RSM), using slump, bleeding ratio, and 28 d uniaxial compressive strength of the filling material as response variables, and the model's accuracy and reliability were confirmed. The findings of the regression model reveal that the response value is influenced by a single component as well as the interaction between the two factors. Finally, based on filling material cost optimization model, an optimal mix ratio is given, in which the wet fly ash/aggregate ratio, Talbol gradation index of recycled aggregate, and dosage of water reducing agent to cement are 0.507, 0.5, and 0.678%, respectively. The filling material which adopted the optimal mix ratio exhibited a good performance with slump of 215 mm and bleeding ratio of 4.00%, uniaxial compressive strength increased significantly within 3 d, and 28 d uniaxial compressive strength was 4.08 MPa, which meet the requirements of field construction.

1. Introduction

Coal, as an important natural resource, plays a significant role in industrial production and daily life. However, coal mining activities give rise to a series of environmental problems, such as ecological environment destruction, stratum instability, surface subsidence, and groundwater loss. In order to address these issues, abundant studies and practices have been conducted, yielding many effective solutions. In recent years, the development of human society has been calling for the environmental, safe, and harmless technologies and methods [1, 2]. It has been proved in practice that filling mining is an effective way to achieve this goal in coal mining [3–5].

Currently, the common filling materials for coal mining include waste gangue, paste, and high water material. Beside the expensive prices, the insufficient supply of these raw materials for filling is also a key factor restricting the large-scale application of filling mining [6–10]. In the process of urban construction, huge amount of construction waste has been produced. Specifically, the construction waste accounts for 30~40% of the total amount of urban waste in China, which is relatively large [11, 12]. Since 2012, the amount of new construction waste in China reached over 1 billion tons per year, though its reutilization rate was no more than 10% [13, 14]. Undoubtedly, this construction waste, in such a large amount, will cause harmful impacts on the ecological environment if without proper handling. In view of this, the reutilization of construction waste is an effective way to solve the problems. Therefore, construction waste is made into recycled aggregates and mixed with cemented materials to form new cemented filling material, so as to meet the needs of the industry, which can effectively save the cost and solve the raw material shortage for mine filling, as well as realizing resource conservation and ecological environment protection.

In recent years, the research about filling material containing construction waste recycled aggregate has been a hot topic. Based on the orthogonal experiment, Liu et al. [15] took construction waste, quick lime, gypsum, and the coarse fly ash as cemented material to analyze the influence of various factors on property indexes of filling mortar and derived the optimal ratio of construction waste to filling material. The result exhibited that mortar mass concentration and cement-aggregate ratio are the main influential factors for the delamination degree and compressive strength of the filling body. Zhang et al. [16] studied three kinds of construction waste; ordinary silicate cement and fly ash formulated into paste materials basically meet the requirements of filling, among which the frame structure construction waste paste material has better performance. Jiang et al. [17] determined the optimal mixture proportion of mortar filling material composed of construction waste, natural sand, ordinary Portland cement, and fly ash through the orthogonal test. Qiu et al. [18] studied the preparation of cementitious filling material with construction waste, silicate cement, water ash, and additives and analyzed the strength and microstructural changes of the filling material with different particle sizes of construction waste. Li et al. [19] used quicklime, gypsum, compound early strength agent, coarse fly ash, and construction waste as the raw materials for the filling material and used orthogonal tests to determine the optimum ratio of the filling material and to analyze the mechanical properties of the construction waste-coarse fly ash-based binder filling body. Liu et al. [20] analyzed the aggregate particle size distribution, compressive strength, and fine structure of cementitious paste fillings prepared from construction waste and ordinary silicate cement. Yang et al. [21] established the regression models by using the RSM optimization method to explore the effects of the concentration and suspension agent on the properties of coal gangue and silicate cement based cementitious filling material and finally obtained an optimal mix ratio. Tang et al. [22] used the RSM-DDC (the central-composite design based on the response surface methodology) method to study the mechanical properties of the filling material ratio with coal gangue as aggregate and Portland cement as cementitious materials, assessed the influence of each component on the properties, and got the optimal ratio with the coal-based solid waste consumption of 91.5%.

Although there has been much research on construction waste filling material, few papers have focused on experimental investigation of construction waste filling material utilizing the RSM-BBD (the Box-Behnken design based on the response surface methodology) approach. In addition, in previous studies, the main cementitious materials for filling material were silicate cement, lime, gypsum, and so forth. This paper makes an attempt to prepare filling material from tiny quantities of sulphate aluminium cement and silicate cement as cementitious materials with construction waste, fly ash, water reducing agents, and water and to use the response method implemented by the Box-Behnken module of the Design-Expert software. This work can improve the early strength of filling material as much as possible under the premise of meeting the performance requirements of filling material, considering the cost factor, and finally obtaining the final mix ratio of construction waste cemented filling material. The research can reference the field application of construction waste cemented filling material.

2. Materials and Methods

2.1. Materials

2.1.1. Construction Waste. The construction waste (Figure 1), mainly composed of fragment concrete, mortar, bricks, and tiles, was used as recycled aggregate, whose density is 2.62 g/cm³. Clear construction waste was collected by two stages of crush at Harbin Jinlu Renewable Resources Co., Ltd, and it was sieved into five particle size ranges: 0~2.5 mm, 2.5~5 mm, 5~10 mm, 10~16 mm, and 16~20 mm. The Talbol continuous gradation equation was used to calculate the mass ratio of the construction waste in each particle size range of samples, with the following expression:

$$P = 100 \times \left(\frac{d}{D}\right)^n, \tag{1}$$

where n is Talbol grading index; d is the particle size of crushed construction waste, mm; D is the maximum particle size of crushed construction waste, mm; P is the mass percentage of crushed construction waste with the particle size less than D, %.

Talbol gradation index (n) of the broken construction waste is 0.65 (Figure 2). When Talbol gradation index (n) of the aggregate ranges between 0.3 and 0.5, the materials mixed will be more uniform, with high bulk density and strength [23]. So the aggregates with Talbol gradation indexes (n) of 0.3, 0.4, and 0.5 were taken as experimental objects. Aggregates with various Talbol gradation indexes are listed in Table 1.

2.1.2. Wet Fly Ash. The abandoned wet fly ash of Qitaihe Gangue Thermal Power Plant has moisture content of 42%. The chemical composition of fly ash [24] is shown in Table 2. The SEM photos show that the fly ash has major irregular shape, massive block granules, and rare spherical glass beads (Figure 3). The Talbol gradation index n of fly ash is 0.47 (less than 0.5, Figure 4), indicating good gradation and high bulk density.

2.1.3. Cement. The cement used in the experiments was 42.5[#] sulphate aluminate cement and 42.5[#] Portland cement mixed at a mass ratio of 3 : 10, with density of 3.1 g/cm³. The fineness of mixed cement measured by specific surface area is 3100–3300 cm²/g. The initial setting time of mixed cement is more than 30 minutes, and the final setting time is less than 5 hours.

2.1.4. Water Reducing Agent. Polycarboxylic acid water reducing agent with density of 2.1 cm³/g can reduce 35% of water, and gas increase is less than 6%. The 28-day strength of cement can be increased by more than 30%.

FIGURE 1: Appearance of construction waste.
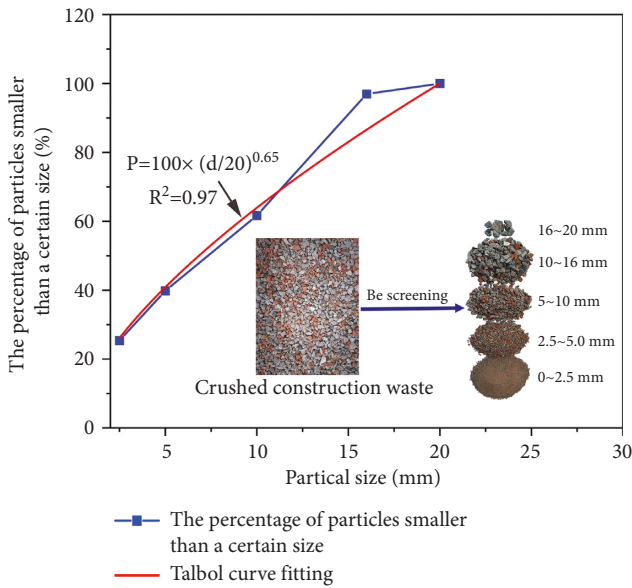
FIGURE 2: Particle size grading curve of crushed construction waste.

2.2. Experimental Design Method.

In this paper, Box-Behnken design (BBD) based on the response surface methodology (RSM) was conducted by using Design-Expert 10.0.3 software [21]. In the Box-Behnken design, wet fly ash/construction waste ratio, Talbol gradation index of construction waste, and usage of water reducing agent were taken as independent variables. Table 3 shows different levels in the form of actual and coded values. The slump, bleeding ratio, and uniaxial compressive strength of filling material were taken as dependent variables. The multivariate nonlinear regression fitting of these data was performed by the Design-Expert 10.0.3 software. The established regression model is

$$Y_n = a + \sum_{j=1}^{m} b_j x_j + \sum_{j=1}^{m} b_{kj} x_j^2 + \sum_{k<j} b_{jj} x_k x_j + e(X_1, X_2, \ldots X_3), \quad (2)$$

where Y_n represents the dependent variable; a is constant; b_j, b_{kj}, and b_{jj} are the linear, quadratic, and interaction coefficients, respectively; x_j and x_k are the coded values of independent parameters; e denotes the error caused by test and regression.

2.3. Mix Ratios.

In this paper, on the basis of the filling mining practice of Longhu mine in Qitaihe, the approximate proportion range of the experimental level of raw materials is determined. When the solid mass concentration is 75% and the cement content is 8% of the total weight, the 28 d uniaxial compressive strength of the material is greater than 3 MPa, which can meet the strength requirements of Longhu mine for filling material. The horizontal selection of the mass ratio of wet fly ash to construction waste x_1, Talbol grading index x_2 of construction waste, and the mass percentage of water reducing agent in cement x_3 are shown in Table 3. During the experiment, 17 mix ratios were tested, as listed in Table 4.

2.4. Testing and Evaluation Methodology

2.4.1. Slump Test.

Filling slurry was added to a moist slump cone by three times, and a third amount of slurry was added each time. Each layer was rammed 25 times with a ramming bar. When adding the top layer, the filling slurry should be higher than the top of the slump cone, and the excess filling slurry was scraped off with a spatula. Then the slump cone was lifted vertically and smoothly. The level difference between the height of slump cone and the highest point of the filling slurry tested is the slump value of filling slurry (Figure 5).

2.4.2. Bleeding Ratio Test.

Firstly, filling slurry was added to a 5 L covered barrel (inner diameter of 185 mm and height of 200 mm) and vibrated on the vibration table for 20 s, of which surface was wiped gently with a spatula and covered to prevent moisture evaporation. The surface level of the slurry was 20 mm lower than the edge of the barrel. After the filling slurry was smoothed, bleeding water was pumped out by a straw every 10 mins once for the first 60 mins and every 20 mins once later until there was no bleeding water for three times (Figure 6). The water pumped out was injected in a measuring cylinder with a plug, and the total amount of water was accumulated. The bleeding ratio is calculated by the following formula:

$$B = \frac{W_W}{(w/m) \times (m1 - m0)} \times 100\%, \quad (3)$$

where B is the bleeding ratio (%); W_W is the accumulated amount of water (g); m is the total weight of filling slurry (g); w is the total weight of water (g); m_1 is the initial total weight of barrel and loaded filling slurry (g); m_0 is the weight of barrel (g).

2.4.3. Uniaxial Compressive Strength Test.

Three $10 \times 10 \times 10$ cm^3 cube specimens of filling material were made as a group. The filling slurry was loaded into the mold and vibrated for 20 s. Then excess filling slurry at the top of mold was scraped off, and the surface of specimen was smoothed. These specimens were put into the standard curing box for 28 d (Figure 7). After that, these specimens were taken out and the mold was removed for uniaxial

TABLE 1: Particle size distribution of construction waste for different Talbol gradation indexes (wt. %).

n	Particle size range (mm)				
	<2.5	2.5~5	5~10	10~16	16~20
$n = 0.3$	53.59	12.39	15.25	12.30	6.48
$n = 0.4$	43.53	13.91	18.35	15.68	8.54
$n = 0.5$	35.36	14.64	20.71	18.73	10.56

TABLE 2: Chemical composition and physical properties of fly ash.

	SiO_2	Al_2O_3	Fe_2O_3	CaO	MgO	K_2O	Na_2O	SO_3	Loss	Total	Fineness (m^2/kg)	Density (kg/m^3)
Fly ash	37.2	24.5	8.4	8.3	1.6	1.2	1.6	12.2	2.7	97.7	119.0	2.2

(a)   (b)
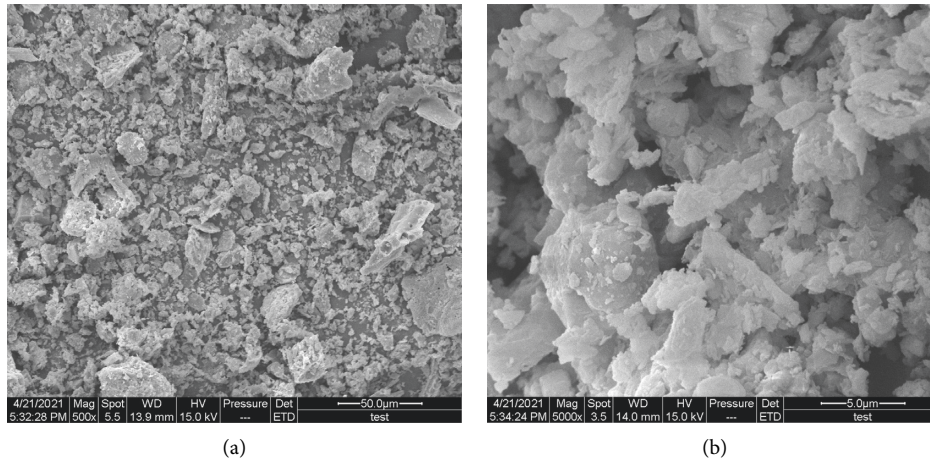
FIGURE 3: SEM photos of fly ash. (a) 500 times of SEM photo. (b) 5000 times of SEM photo.
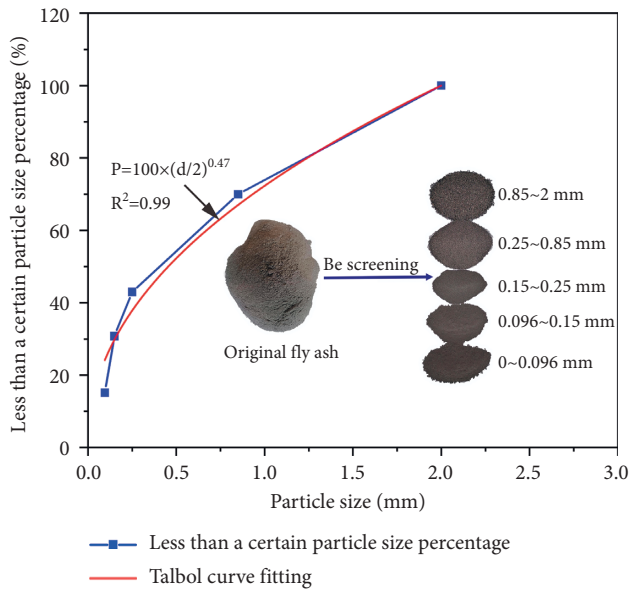
FIGURE 4: Particle size gradation curve of fly ash.

compressive strength test. YAW-300 microcomputer controlled automatic concrete pressure testing machine was used for test. In test process, the bearing surface of the specimen should be vertical to the top surface of the specimen, and the center of specimen was aligned with the center of the pressing plate. The press was boosted continuously at the loading speed of 0.002 mm/s until yield failure occurred in the specimen, and the maximum was recorded as the failure load (Figure 7(b)). The compressive strength (σ_c) of specimen was calculated according to the following formula:

$$\sigma_c = \frac{F}{A}, \tag{4}$$

where F is failure load (N) and A is compression area (mm^2).

3. Results and Discussion

3.1. Model Fitting and Analysis. The results of tests are listed in Table 5.

In this study, the acceptance probability of coefficients (P) was less than 0.05. To ensure the accuracy of the model, the insignificant terms with P value of the independent variable coefficient greater than 0.05 were eliminated. The response surface functions of slump, bleeding ratio, and 28 d uniaxial compressive strength were obtained. The final equations in terms of the coded factors are listed as follows.

TABLE 3: Actual and coded values of the experimental factors.

Wet fly ash/construction waste ratio	Talbol gradation index of construction waste	The percentage of water reducing agent in cement (%)	Coded value
x_1	x_2	x_3	
0.45	0.3	0.6	1
0.50	0.4	0.7	0
0.55	0.5	0.8	−1

TABLE 4: Mix ratios of filling material for orthogonal test.

Samples	Wet fly ash (wt. %)	Construction waste (wt. %)	Talbol gradation index	Sulphate aluminate cement (wt. %)	Portland cement (wt. %)	Water reducing agent (wt. %)	Water (wt. %)
1[#]	20.78	46.17	0.5	2.4	5.6	0.56	25.0
2[#]	22.31	44.63	0.4	2.4	5.6	0.56	25.0
3[#]	23.76	43.19	0.4	2.4	5.6	0.48	25.0
4[#]	22.31	44.63	0.4	2.4	5.6	0.56	25.0
5[#]	22.32	44.63	0.5	2.4	5.6	0.48	25.0
6[#]	22.31	44.62	0.5	2.4	5.6	0.64	25.0
7[#]	23.75	43.19	0.3	2.4	5.6	0.56	25.0
8[#]	20.78	46.17	0.4	2.4	5.6	0.48	25.0
9[#]	22.32	44.63	0.3	2.4	5.6	0.48	25.0
10[#]	23.75	43.18	0.4	2.4	5.6	0.64	25.0
11[#]	22.31	44.63	0.4	2.4	5.6	0.56	25.0
12[#]	22.31	44.63	0.4	2.4	5.6	0.56	25.0
13[#]	20.77	46.16	0.4	2.4	5.6	0.64	25.0
14[#]	23.75	43.19	0.5	2.4	5.6	0.56	25.0
15[#]	20.78	46.17	0.3	2.4	5.6	0.56	25.0
16[#]	22.31	44.63	0.4	2.4	5.6	0.56	25.0
17[#]	22.31	44.62	0.3	2.4	5.6	0.64	25.0

Slump:

$$Y_1 = 211.89 - 3.25x_1 + 3.63x_2 + 5.63x_3 \\ + 1.75x_1x_2 - 20.01x_1^2 - 3.76x_2^2. \quad (5)$$

Bleeding ratio:

$$Y_2 = 4.30 - 0.81x_1 + 0.27x_2 + 0.30x_3 \\ - 0.094x_1x_2 - 0.48x_1^2 - 0.38x_2^2. \quad (6)$$

28 d compressive strength:

$$Y_3 = 3.66 + 0.063x_1 + 0.25x_2 \\ - 0.088x_3 + 0.1x_1x_2 - 0.17x_1x_3 \quad (7) \\ - 0.12x_1^2 + 0.16x_2^2 - 0.17x_3^2.$$

To investigate the interaction influence between factors based on the response surface regression model and the response values, variance analysis was conducted on the error sources of the regression equation, as shown in Table 6. The significance of the model is determined by F value and P value: the higher F value and lower P value indicate a significant influence. The F values of the regression model are 180.35, 197.19, and 70.72, respectively, with the P values far less than 0.0001, indicating a significant influence of the regression model. The orders of significance of the single factors on response values (Y_1, Y_2, and Y_3) are $x_3 > x_2 > x_1$, $x_1 > x_3 > x_2$, and $x_2 > x_3 > x_1$, respectively. The order of

significance of interaction effect on 28 d compressive strength is $x_1x_3 > x_1x_2$. The determination coefficient determined by the model can explain the degree of difference between the response surface and the real value. Therefore, the determination coefficient determined by the model is used to evaluate the accuracy and reliability of the regression model [25], as shown in Table 7. If the determination coefficient (R^2) and coefficient of variation (CV) are close to 1 and 0, respectively, the model is of high reliability. For the three models, the determination coefficient (R^2), adjusted determination coefficient (R^2_{Adj}), and predictive determination coefficient (R^2_{pred}) are greater than 0.93, and all the coefficients of variation (CV) are less than 5%, indicating that the models are reliable and accurate (Table 7).

In order to directly express the accuracy of the model, a three-dimensional error coordinate system was constructed, in which the relative differences between the measured value Y and the calculated value Y' of x_1, x_2, and x_3 are plotted (Figure 8). As shown in Figure 8, the relative errors of slump, bleeding ratio, and 28 d compressive strength, are less than 1.5%, 4%, and 1.5%, respectively [26], which means calculated values of the models are close to the actual values, indicating a high accuracy of the models.

3.2. Properties Analysis of Filling Material.
In this study, the established model was used to explain the influence of various independent variables and their binary interactions

(a)   (b)
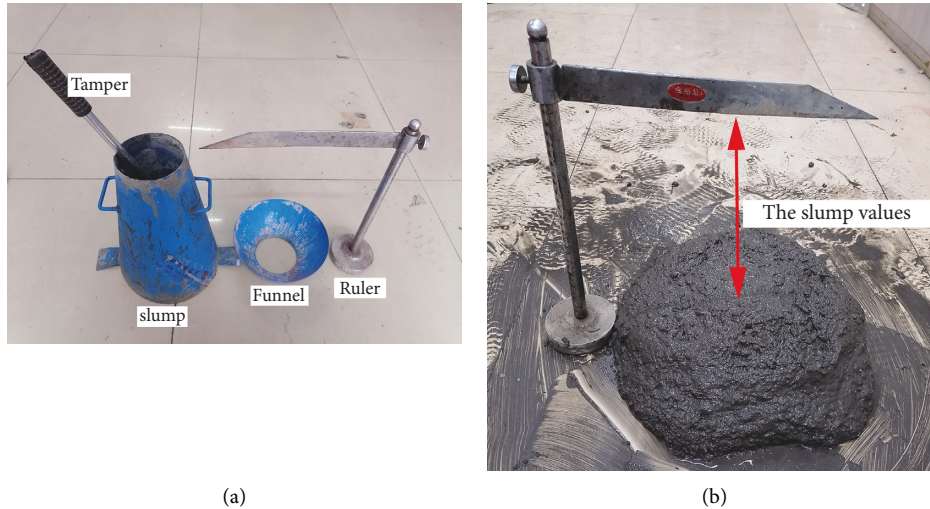
FIGURE 5: Photos of slumps test. (a) Measuring device. (b) Slump measurement.

(a)   (b)
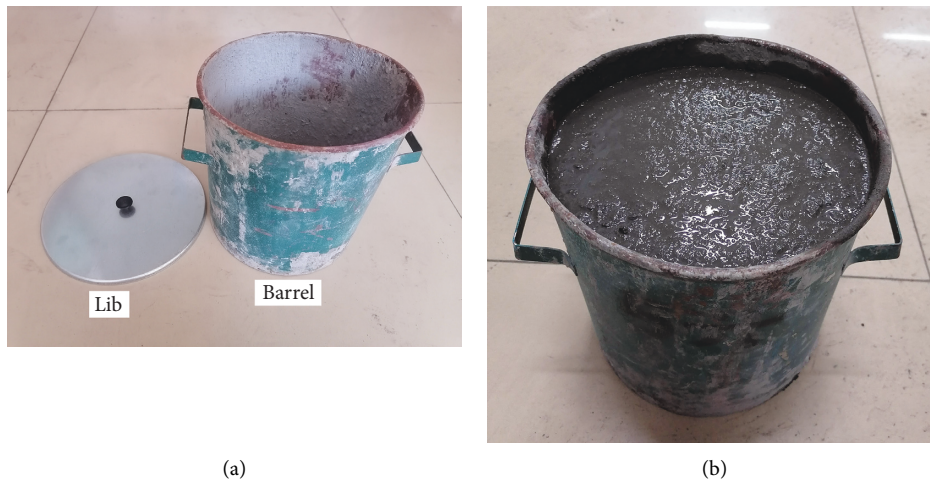
FIGURE 6: Photos of bleeding ratio test. (a) Measuring device. (b) Bleeding ratio measurement.

on the response values, namely, properties of filling material. The details are discussed as follows.

3.2.1. Analysis of Single Factor Influence on Response Value

(1) Analysis of Factors Influencing Slump. In response surface methodology regression model, according to the results of ANOVA, slump is significantly influenced by single factors. The influence of each factor on slump is shown in Figure 9(a). When analyzing the influence of a single factor on slump, the other two factors are fixed at the code level of 0 (i.e., wet fly ash/aggregate ratio of 0.5 or Talbol gradation index of 0.4 or water reducing agent of 0.7, the same as follows). With the increase of wet fly ash content, slump value increases at the beginning and then decreases. In relevant literature [27], there is a similar rule, but the threshold value is 30%, which may be increased due to the coarse particle size of wet fly ash. With the increase of Talbol gradation index of construction waste (N), the slump first

obviously increases and then slightly decreases or remains as is. Water reducing agent can increase the fluidity of filling material. Therefore, with the increase of water reducing agent proportion, slump would increase continuously, but the increase rate of slump shows a decreasing trend. It proves that the water reducing agent accounts for a lasting impact on the fluidity of filling material within the permissible amount.

(2) Analysis of Factors Influencing Bleeding Ratio. The influence of each factor on bleeding ratio is shown in Figure 9(b). With the increase of wet fly ash/aggregate ratio, the bleeding ratio remains as is at first and then decreases. When the code value of wet fly ash/aggregate ratio exceeds −0.50, the decreasing range of bleeding becomes more obvious. Wet fly ash can make up for the shortage of fine aggregate in cement and construction waste, so as to reduce the water usage and block the bleeding channel, thus decreasing the bleeding ratio and improving the antiseepage ability of filling material [27, 28]. When the proportion of

| (a) | (b) |
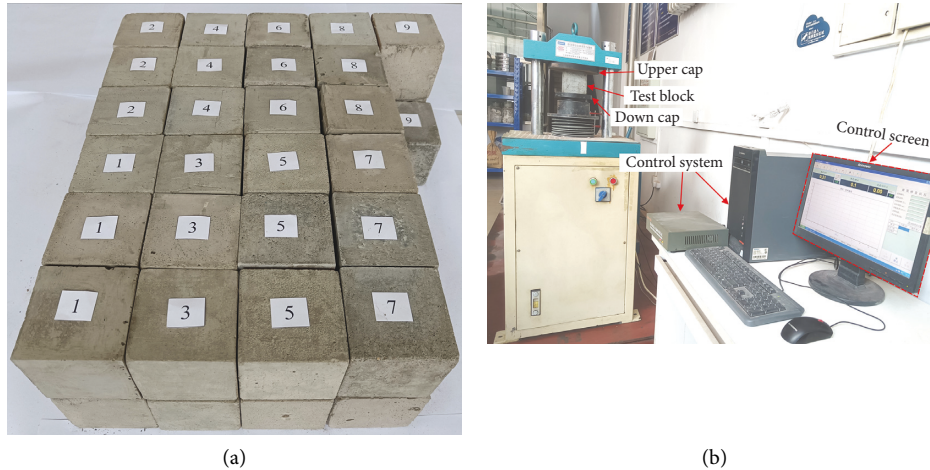
FIGURE 7: Photos of stress resistance test. (a) The test specimens. (b) Compressive strength measurement.

TABLE 5: The results of tests.

Samples	Slump (mm)	Bleeding ratio (%)	28 d compressive strength (MPa)
1[#]	193	4.63	3.8
2[#]	213	4.38	3.7
3[#]	183	2.63	3.7
4[#]	212	4.25	3.7
5[#]	206	3.75	4
6[#]	217	4.50	3.8
7[#]	181	2.50	3.4
8[#]	190	4.38	3.2
9[#]	196	3.38	3.5
10[#]	192	3.25	3.2
11[#]	212	4.38	3.7
12[#]	213	4.38	3.6
13[#]	200	4.88	3.4
14[#]	191	2.88	4.1
15[#]	190	3.88	3.5
16[#]	212	4.25	3.6
17[#]	211	3.88	3.3

water reducing agent increases, the bleeding ratio increase continuously, showing a linear correlation between them. The water reducing agent changes the ratio of bound water, adsorption water, and free water and improves the free water content. Therefore, the excess free water bleeds at first, thus increasing the rate of bleeding. There are both positive and negative effects of gradation on bleeding ratio. When the code value of Talbol gradation index is 0.425, the bleeding ratio reaches the maximum; when the index is less than 0.025, the bleeding ratio increases with the increase of the index; when the index is above 0.025, the bleeding ratio decreases with the increase of the index, but the increment is more obvious than the decrement.

(3) 28 d Compressive Strength. The influence of various factors on 28 d compressive strength is shown in Figure 9(c). With the increase of wet fly ash/aggregate ratio, the 28 d compressive strength of filling material increases first and then basically remains constant and finally decreases. When the code of wet fly ash/aggregate ratio is between 0.21 and 0.23, the 28 d compressive strength remains basically stable.

Before that, the compressive strength increases with the increase of the ratio. After the maximum value, the compressive strength declines as the ratio increases. The effect of gradation on compressive strength exhibits a fixed value when the Talbol gradation index code is below −0.178. Subsequently, with the increase of Talbol grading index, the compressive strength increases. It indicates that the coarse aggregate content is conducive to the increase of compressive strength. When the water reducing agent usage is less than 0.071, the compressive strength increases with the increase of water reducing agent content. After that, the compressive strength decreases with the increase of the proportion of water reducing agent. It proves that the rational use of polycarboxylic acid water reducing agent will increase the compressive strength of filling material, but too much water reducing agent will decrease the compressive strength of filling material.

3.2.2. Analysis of Interaction Influence on Response Value. According to the test results and variance analyses, it can be seen that the response values are affected not only by a single

TABLE 6: Results of ANOVA.

Source	Sum of squares	d_f	Mean square	F value	P value prob $> F$	
Slump						
Model	2246.77	6	374.46	180.35	<0.0001	Significant
x_1	84.50	1	84.50	40.70	<0.0001	
x_2	105.13	1	105.13	50.63	<0.0001	
x_3	253.13	1	253.13	121.91	<0.0001	
$x_1 x_2$	12.25	1	12.25	5.90	0.0355	
x_1^2	1691.11	1	1691.11	814.48	<0.0001	
x_2^2	59.79	1	59.79	28.80	0.0003	
Bleeding rate						
Model	5.29	6	0.8822	197.19	<0.0001	Significant
x_1	3.38	1	3.38	755.53	<0.0001	
x_2	0.3613	1	0.3613	80.75	<0.0001	
x_3	0.4512	1	0.4512	100.87	<0.0001	
$x_1 x_2$	0.0225	1	0.0225	5.03	0.0488	
x_1^2	0.6190	1	0.6190	138.37	<0.0001	
x_2^2	0.4003	1	0.4003	89.47	<0.0001	
28 d compressive strength						
Model	1.03	8	0.1282	70.72	<0.0001	Significant
x_1	0.0313	1	0.0313	17.24	0.0032	
x_2	0.5000	1	0.5000	275.86	<0.0001	
x_3	0.0613	1	0.0613	33.79	0.0004	
$x_1 x_2$	0.0400	1	0.0400	22.07	0.0015	
$x_1 x_3$	0.1225	1	0.1225	67.59	<0.0001	
x_1^2	0.0581	1	0.0581	32.07	0.0005	
x_2^2	0.1044	1	0.1044	57.63	<0.0001	
x_3^2	0.1181	1	0.1181	65.18	<0.0001	

TABLE 7: Model correlation evaluation.

Evaluation index	Y_1	Y_2	Y_3
Determination coefficient (R^2)	0.995	0.992	0.986
Adjusted determination coefficient (R_{Adj}^2)	0.990	0.987	0.972
Predictive determination coefficient (R_{pred}^2)	0.930	0.970	0.951
Coefficient of variation (CV)	0.610%	2.150%	1.18%
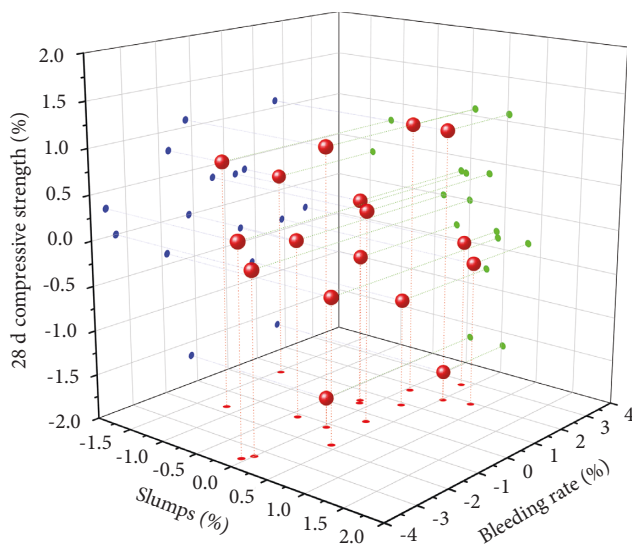
FIGURE 8: Three-dimensional error coordinate system of the regression model.

factor but also by the interaction between factors, which is discussed in detail as follows.

In Figure 10, when the percentage of water reducing agent is 0.7%, the slump shows a trend of gradual increase with the increase of wet fly ash/aggregate ratio before 0.49 at the aggregate gradation of 0.3. When wet fly ash/aggregate ratio is 0.49, it reaches the maximum and then presents a declining trend, with the rate of decline slightly higher than the increase rate. When the wet fly ash/aggregate ratio is fixed, the slump obviously increases at first and then decreases with the increase of gradation. The effect of gradation on slump is lower than that of the wet fly ash/aggregate ratio, which is consistent with the result of variance analysis. In addition, the contour map is oval, indicating a strong interaction between mass and cement dosage [29]. In a word, when the gradation and wet fly ash/aggregate ratio vary, slump values show a parabolic regularity on the coordinate axes. Suitable aggregate gradation and wet fly ash/aggregate ratio can adjust the slump of filling material to reach a reasonable engineering range.

(a)

(b)

(c)
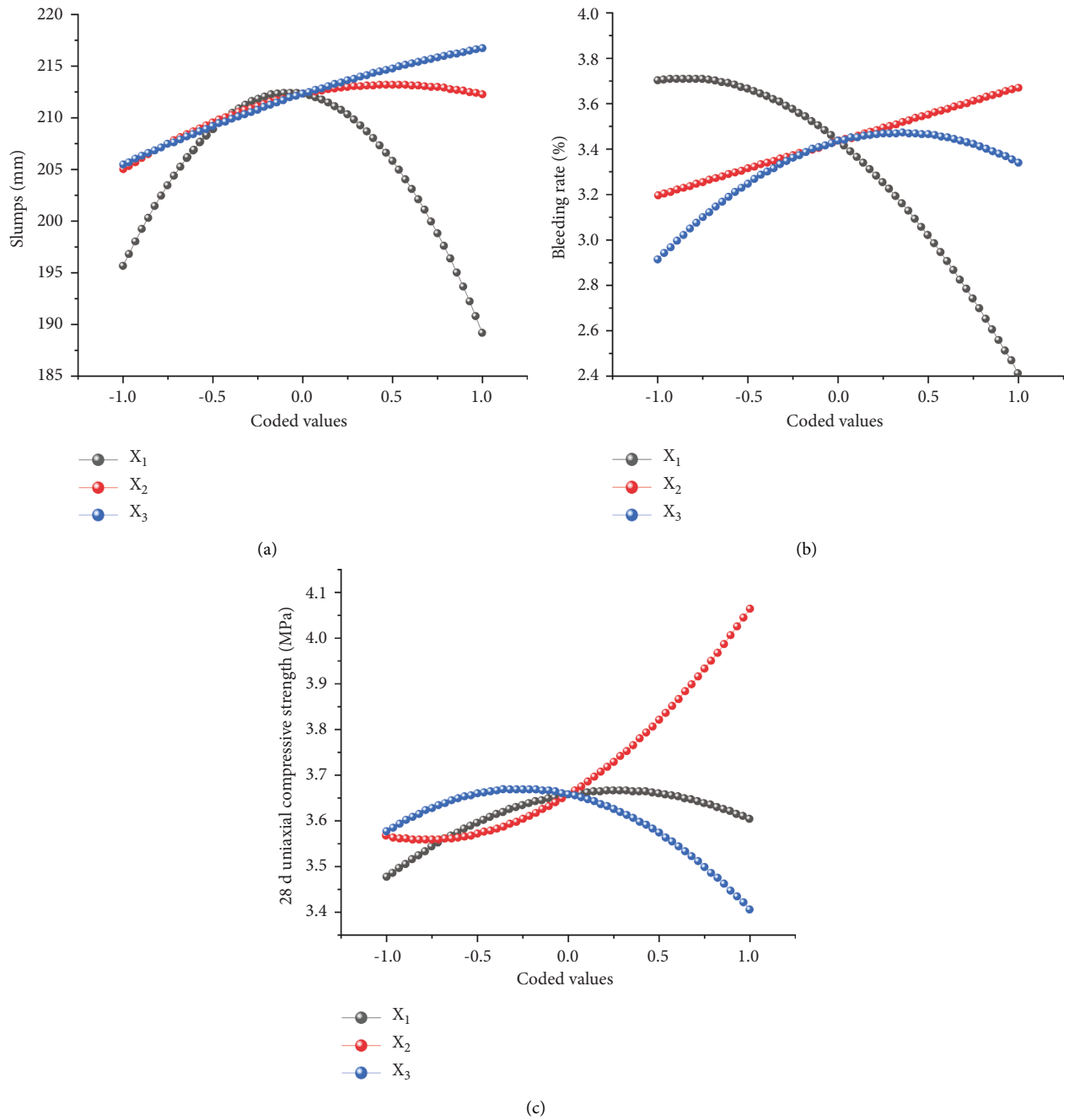
FIGURE 9: Influence curve of single factors on each response value. (a) Slump. (b) Bleeding ratio. (c) 28 d compressive strength.

In Figure 11, when the percentage of water reducing agent is 0.7%, the bleeding ratio of filling material shows a slight increase with the increase of wet fly ash/aggregate ratio and reaches the maximum of 3.9% at the wet fly ash/aggregate ratio of 0.46. After that, the bleeding ratio declines to 2.45% at last, indicating a significant influence of wet fly ash/aggregate ratio on the bleeding ratio. When Talbol gradation index of construction waste is 0.5, with the increase of wet fly ash/aggregate ratio, the bleeding ratio decreases sharply, from 4.63% to 2.79%, reaching a variation of 40%. At a low wet fly ash/aggregate ratio, with the increase of the index, the bleeding ratio increases from 3.88% to 4.72% and then

remains as is. When the wet fly ash/aggregate ratio is 0.55, with the increase of gradation, the bleeding rate increases from 2.45% to 3.02% and then decreases to 2.79%, indicating that the influence of gradation on bleeding rate can be reduced with the increase of wet fly ash/aggregate ratio. In addition, according to the contour diagram (Figure 11(a)), when the Talbol grading index of construction waste and wet fly ash/aggregate ratio are in the ranges of 0.3 to 0.39 and 0.53 to 0.55, respectively, the bleeding ratio is low.

In Figure 12, when the percentage of water reducing agent is 0.7% with the gradation of construction waste fixed, 28 d compressive strength increases first and then decreases

(a)

(b)
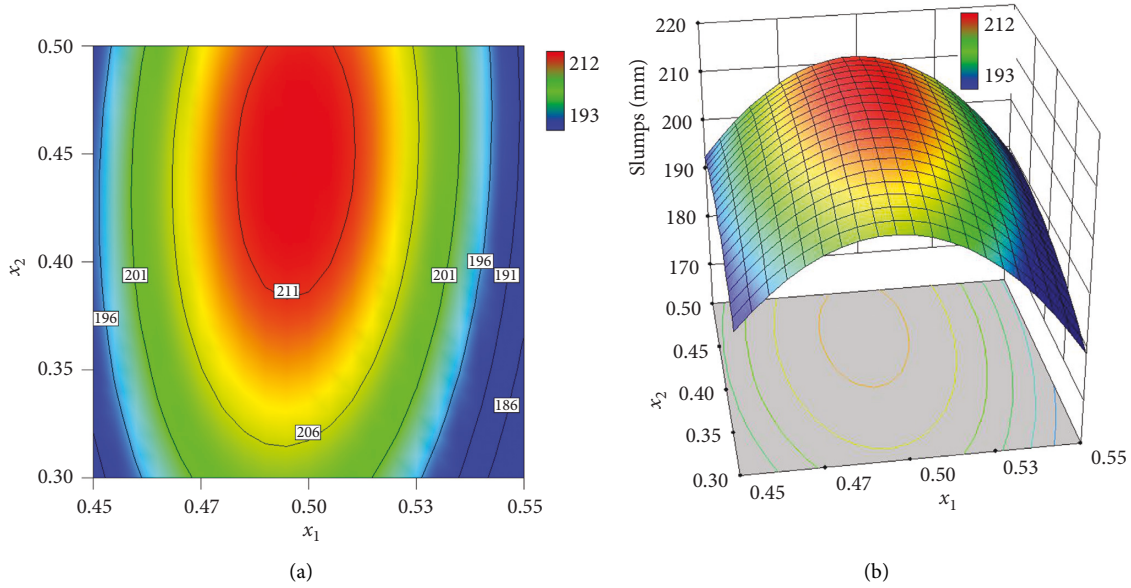
FIGURE 10: Interaction influence of x_1 and x_2 on slump. (a) Two-dimensional diagram. (b) Three-dimensional diagram.

(a)

(b)
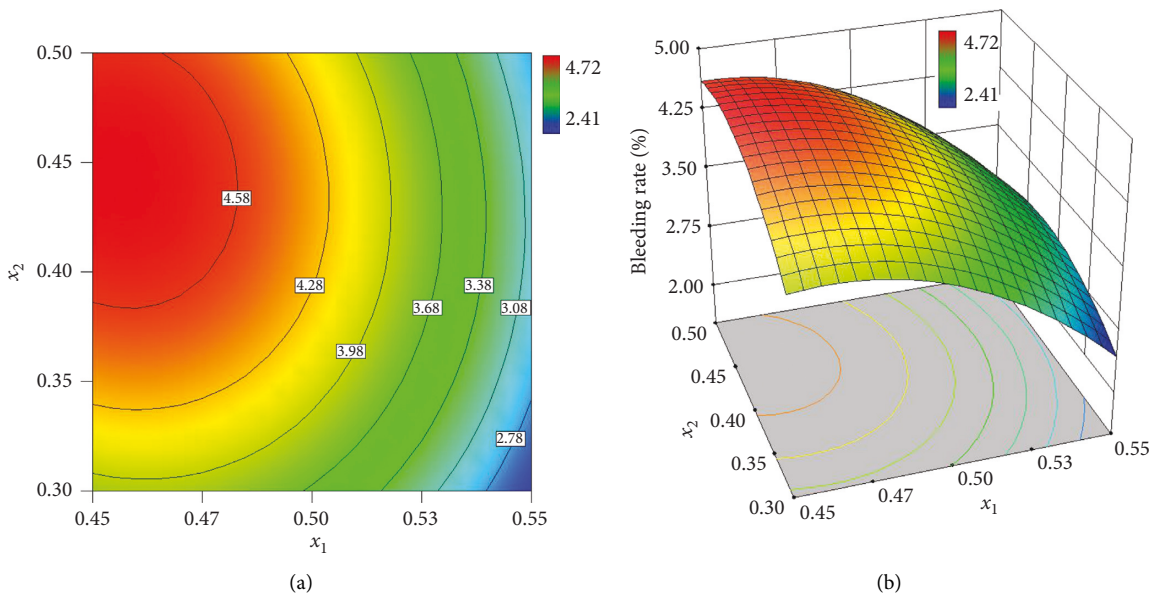
FIGURE 11: Interaction influence of x_1 and x_2 on bleeding ratio. (a) Two-dimensional diagram. (b) Three-dimensional diagram.

with the increase of the wet fly ash/aggregate ratio. For example, when Talbol gradation index and wet fly ash/aggregate ratio are 0.3 and 0.49, respectively, the maximum of 28 d strength is 3.58 MPa. Moreover, with the increase of gradation, the maximum of 28 d strength increases gradually, and the maximum of wet fly ash/aggregate ratio increases accordingly. For example, when Talbol gradation index and wet fly ash/aggregate ratio are 0.45 and 0.52, respectively, the maximum of 28 d compressive strength reaches 3.85 MPa, which is significantly higher than that with the Talbol gradation of 0.3. In addition, the contour diagram demonstrates that when the gradation and wet fly ash/aggregate ratios are 0.48 to 0.50 and 0.48 to 0.55, respectively, high compressive strength can be obtained.

In Figure 13, the interaction influences of wet fly ash/aggregate ratio and the percentage of water reducing agent on 28 d compressive strength are depicted, in which Talbol gradation index of construction waste is fixed at 0.4. When the dosage of water reducing agent is small, the strength increases gradually with the increase of wet fly ash/aggregate ratio. When the dosage of water reducing agent is 0.60 and the wet fly ash/aggregate ratio is 0.55, the 28 d strength is 3.70 MPa. If the percentage of water reducing agent in cement exceeds 0.63%, with the increase of wet fly ash/aggregate ratio, the strength increases at first and then decreases, and the increase or decrease rate gets smaller around the peak. When the dosage of water reducing agent and the wet fly ash/aggregate ratio are 0.8 and 0.55,
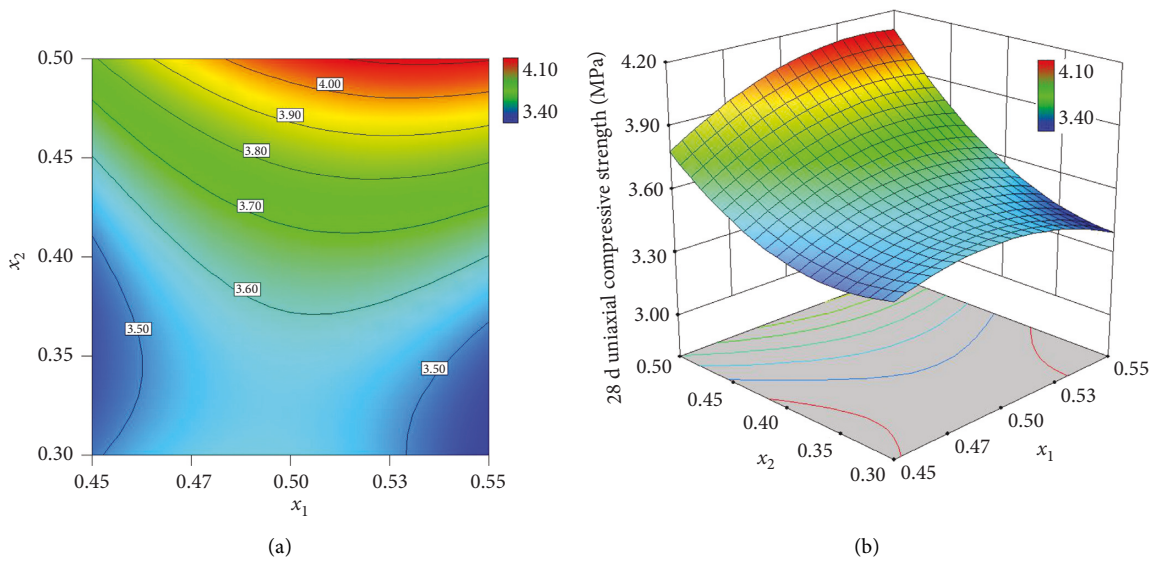
FIGURE 12: Interaction influence of x_1 and x_2 on 28 d compressive strength. (a) Two-dimensional diagram. (b) Three-dimensional diagram.
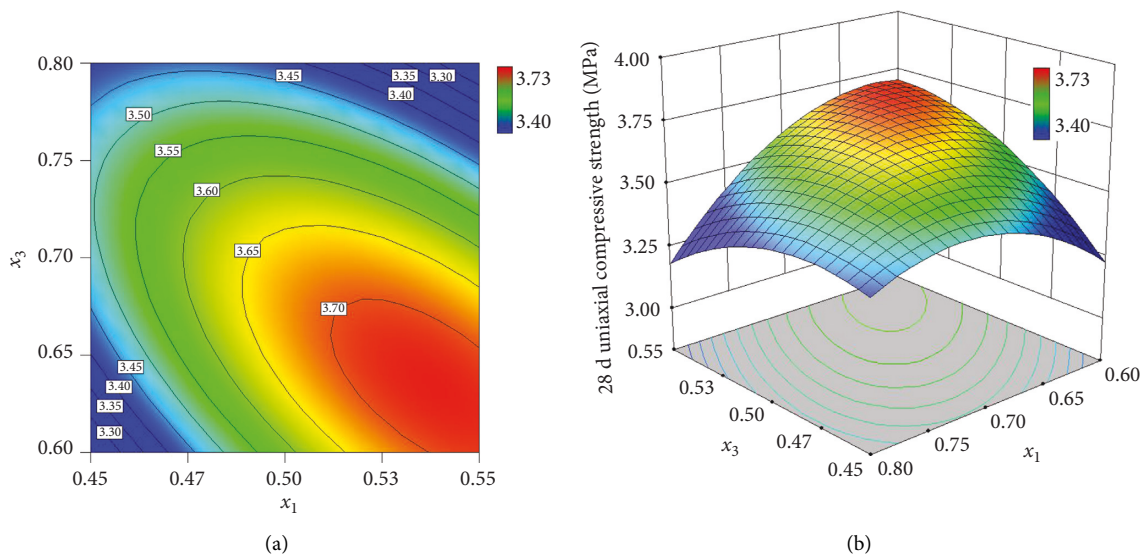
FIGURE 13: Interaction influence of x_1 and x_3 on 28 d compressive strength. (a) Two-dimensional diagram. (b) Three-dimensional diagram.

respectively, the 28 d strength is 3.17 MPa. At a low wet fly ash/aggregate ratio, the strength increases at first and then decreases slightly with the increase of water reducing agent. However, when the wet fly ash/aggregate ratio increases gradually, the increase gets smaller, followed by an increasingly obvious decrease. As shown in the contour diagram, when the wet fly ash/aggregate ratio and dosage of water reducing agent are in the ranges of 0.52 to 0.55 and 0.60 to 0.67, respectively, the maximum of compressive strength can be derived.

3.3. Multiobjective Optimization and Model Verification.
The cost of filling material is an important factor affecting the economic benefit of mine. As long as the physical property of filling material is ensured, reducing the cost of filling material is an important way to improve the benefit of mining.

At present, Longhu Mine of Qitaihe Co., Ltd. of Longmei Group is using the filling mining method to mine the coal below buildings. The filling material used must satisfy certain performance specifications, specifically, with slump, bleeding ratio, and the 28 d compressive strength being 210–220 mm, less than 5%, and greater than 3 MPa, respectively. If taking the Longhu Mine as the case to demonstrate the economic optimization of filling material, the following planning equation can be established:

$$220 \geq Y_1 \geq, Y_2 = \min, Y_3 = \max. \qquad (8)$$

TABLE 8: Price of partial filling material mix ratio.

No.	x_1	x_2	x_3 (%)	M_c	M_f	M_w	M_s	Slump (mm)	Bleeding ratio (%)	28 d compressive strength (MPa)	Price (yuan/m^3)
1[#]	0.507	0.500	0.678	0.817	0.414	0.460	0.147	210	3.99	4.10	103.7
2[#]	0.509	0.500	0.686	0.816	0.415	0.460	0.147	210	3.95	4.11	104.0
3[#]	0.513	0.498	0.697	0.814	0.418	0.460	0.147	210	3.92	4.09	104.5
4[#]	0.506	0.488	0.670	0.818	0.414	0.460	0.147	210	4.03	4.04	105.0
5[#]	0.511	0.478	0.680	0.815	0.416	0.460	0.147	210	4.00	3.99	106.5
6[#]	0.517	0.448	0.709	0.812	0.420	0.460	0.147	210	4.01	3.83	110.9
7[#]	0.505	0.401	0.675	0.818	0.413	0.460	0.147	210	4.14	3.68	115.8
8[#]	0.504	0.369	0.700	0.819	0.413	0.460	0.147	210	4.11	3.60	120.5
9[#]	0.501	0.352	0.714	0.821	0.411	0.460	0.147	210	4.11	3.56	123.1
10[#]	0.497	0.314	0.766	0.823	0.409	0.460	0.147	210	4.03	3.44	129.4

In the optimization module of Design-Expert 10.0.3 software, 77 groups of solutions satisfying the equation can be obtained by setting the value range of response value according to the above planning equation. The minimum cost of filling material per unit volume is taken as the optimization objective, namely, $f_{\min}$ (yuan/m^3), and the optimization model is established as shown in the following formula:

$$
\begin{cases}
\dfrac{M_c}{2.62} + \dfrac{M_f}{2.3} + \dfrac{M_w}{1} + \dfrac{M_s}{3.1} + \dfrac{M_s x_3}{2.1} = 1, \\[2mm]
\dfrac{M_s}{M_c + M_f + M_s + M_w + M_s x_3} \times 100\% = 8\%, \\[2mm]
\dfrac{M_w}{M_c + M_f + M_s + M_w + M_s x_3} \times 100\% = 25\%, \\[2mm]
\dfrac{M_f}{M_c} = x_1, \\[2mm]
x_4 = -150 x_2 + 95, \\[2mm]
f_{\min} = x_4 M_c + 10 M_f + 3.2 M_w + 420 M_s + 20000 M_s x_3,
\end{cases}
\tag{9}
$$

where x_1 is the ratio of wet fly ash versus construction waste; x_2 is Talbol gradation index of construction waste; x_3 is the mass percentage of water reducing agent versus cement; x_4 is the price of construction waste; M_c, M_f, M_w, and M_s, are the masses of construction waste, wet fly ash, water, and cement per cubic metre of filling material. The mass concentration of solid material in the filling material is 75%. The masses of water and cement account for 25% and 8%, respectively, of filling material.

Based on current raw material prices, cement, water reducing agent, wet fly ash, and industrial water are 420, 20000, 10, and 3.2 yuan/t, respectively. The prices of construction waste with n of 0.5 and 0.3 are 20 and 50 yuan/t, respectively, and the price of construction waste of other Talbol gradation indexes can be obtained by interpolation formula ($x_4 = -150 x_2 + 95$). The 77 groups of solutions were substituted into the optimization model (formula (8)), and the results were calculated using Matlab (see Table 8 for
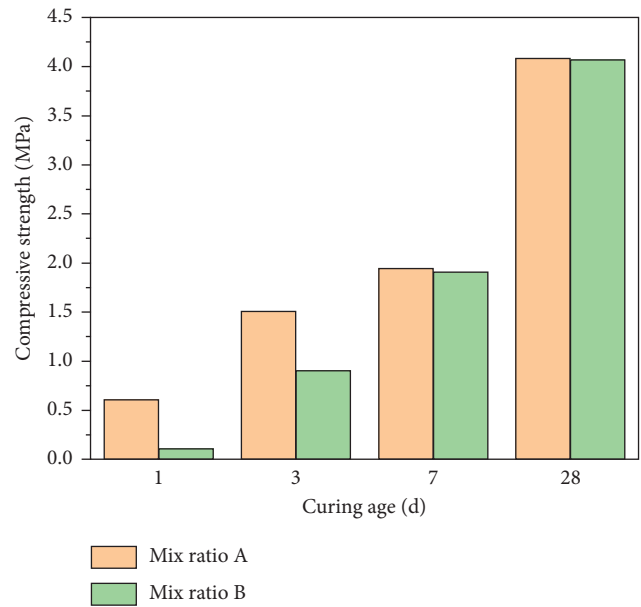
FIGURE 14: Compressive strength of various curing ages of the optimal mix ratio of filling material.

some of the results). From the results, it can be seen that the lowest price ($f_{\min}$) per cubic metre of filling material is 103.7 yuan for $x_1 = 0.507$, $x_2 = 0.5$, and $x_3 = 0.678\%$. The model predicts that the slump, bleeding ratio, and 28 d compressive strength are 210 mm, 3.99%, and 4.10 MPa, respectively. Indeed, the filling materials with these mix ratios were tested experimentally, and the slump, bleeding ratio, and 1 d, 7 d, and 28 d compressive strength are 215 mm, 4.00%, and 4.08 MPa, respectively, indicating that the results addicted by the model highly match the actual results and can meet requirements of field construction.

3.4. Analysis of Filling Material at Different Curing Ages.
In Figure 14, mix ratio A shows the compressive strength at the curing ages for the optimum mix ratio of filling material. Mix ratio B is the compressive strength at each curing age after replacing 42.5[#] sulphate aluminate cement with 42.5[#] Portland cement in the optimum mix ratio of filling material. Figure 14 shows that the one-day compressive strength of mix ratio A is 6 times that of mix ratio B, and the three-day
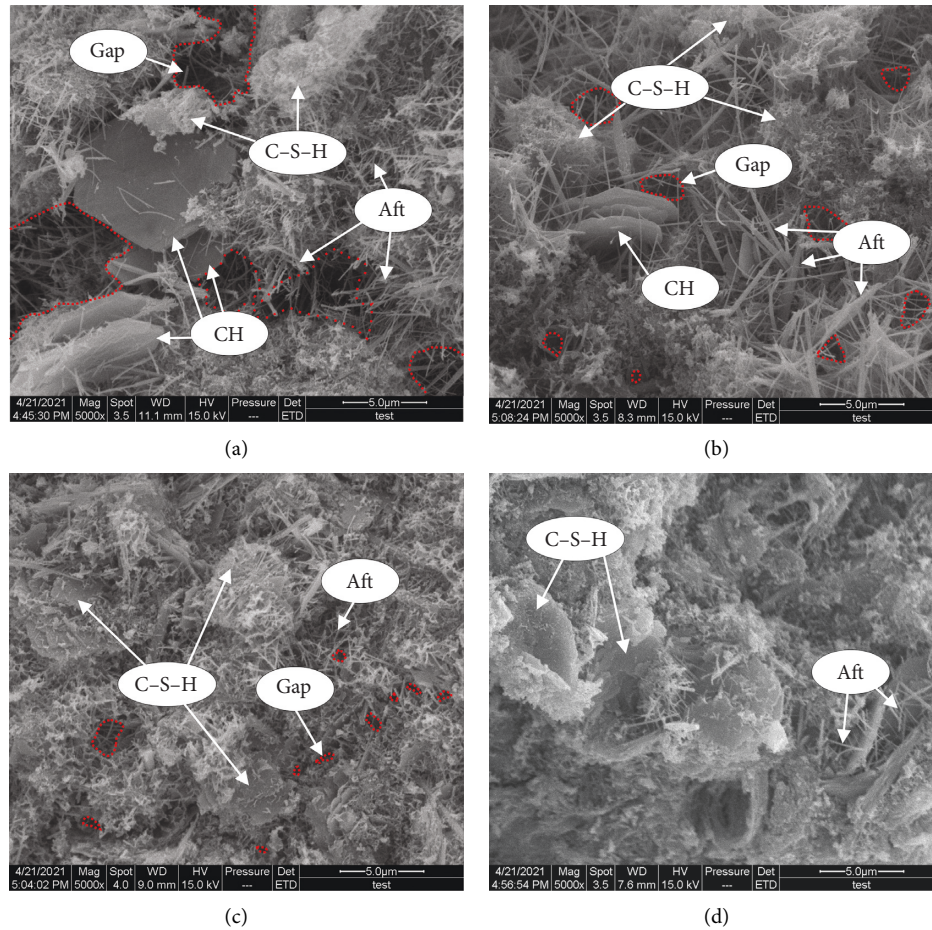
Figure 15: SEM photos of the hydration products of the optimum mix ratio of filling material at different curing ages. (a) 1 d curing age. (b) 3 d curing age. (c) 7 d curing age. (d) 28 d curing age.

compressive strength of mix ratio A is 1.67 times that of mix ratio B; after that, the compressive strengths of the two mix ratios are basically the same.

The SEM photos of the hydration products of the optimum mix ratio of filling material at curing ages of 1 d, 3 d, 7 d, and 28 d are shown in Figure 15. The sulphate aluminate cement mainly produces calcium vanadate (Aft), and the Portland cement hydrates mainly produce hydrated calcium silicate (C-S-H) gelation, both of which precipitate calcium hydroxide (CH). When the curing age of the filling material is 1 d (Figure 15(a)), the gaps between the hydration products are significant, a large number of needle-like Aft appear, and there is a small amount of C-S-H gelation, while a large number of CH can be seen, and the morphology of CH is a regular plate hexahedron, the surface of which has a crystal luster and good crystallinity. When the age of the filling material is 3 d (Figure 15(b)), the gaps between the hydration products become smaller; the size of the Aft increases significantly and becomes "rod" shaped; the hydration of Portland cement produces a certain amount of C-S-H gelation; CH becomes less, because CH reacts chemically with the active SiO_2, Al_2O_3, and so forth in fly ash. As shown from Figures 15(a) and 15(b), the increase in compressive strength of the filling material within 3 d of the curing age is mainly due

to the hydration of the sulphate aluminate cement to produce a large amount of Aft. At the curing age of 7 d for the filling material (Figure 15(c)), the gaps between the mid-hydration products are smaller, a significant number of filamentous C-S-H encapsulates the Aft, and the shape of CH hexahedron is not obvious, and the crystallinity of CH is worse than that in Figure 15(b). At the curing age of 28 d (Figure 15(d)), the filling material is dense and the needle stick Aft is largely encapsulated by the gel. Only a small amount of Aft can be seen, and CH crystals are basically invisible. From Figures 15(a) and 15(b), it can be seen that the compressive strength of the filling material at the curing age of 7 d to 28 d is mainly due to the large amount of C-S-H gelation which is produced by the hydration of Portland cement.

4. Conclusions

The response surface methodology (RSM) is using slump, bleeding ratio, and 28 d uniaxial compressive strength of the filling material as response variables, as well as using wet fly ash/aggregate ratio, Talbol gradation index of recycled aggregate, and dosage of water reducing agent as factors, which has optimized the mix ratio of construction waste cemented filling material. The main conclusions are as follows:

(1) The reliable and accurate response surface model of slump, bleeding ratio, and 28 d compressive strength was established, with the determination coefficient greater than 0.93 and the coefficient of variation (CV) less than 5%. The relative errors between the response surface model and the experimental results were within 4%, indicating a good fitting.

(2) The wet fly ash/construction waste ratio, Talbol gradation index of recycled aggregate, and dosage of water reducing agent had the most significant effects on bleeding ratio, 28 d compressive strength, and slump, respectively. The interaction of wet fly ash/construction waste ratio and Talbol gradation index of recycled aggregate had an obvious effect on the three response values, and the interaction of wet fly ash/construction waste ratio and water reducing agent proportion significantly influenced the 28 d compressive strength.

(3) The optimal mix ratio of filling material was obtained: the wet fly ash/construction waste ratio was 0.507, Talbol gradation index of recycled aggregate was 0.5, and dosage of water reducing agent was 0.678%. Experimentally, the filling material with the optimal mix ratio yielded slump of 215 mm, bleeding ratio of 4.00%, and 28 d compressive strength of 4.08 MPa, which meet the actual needs of mining.

(4) The hydration of sulphate aluminate cement produces a large amount of Aft, which can obviously improve the compressive strength of the filling material in 3 d. The hydration of Portland cement produces a large amount of C-S-H gelation, which is the main source of the compressive strength of the filling material from 7 d to 28 d.

Data Availability

The data used to support the findings of this study are available from the corresponding author upon request or change this to the fixed mode of journals.

Conflicts of Interest

The authors declare that they have no conflicts of interest.

Acknowledgments

References

[1] S. G. Wang, Q. Sun, J. W. Qiao, and H. H. Schobert, "Discussion on the geological guarantee of green coal mining," *Journal of China Coal Society*, vol. 45, no. 1, pp. 8–15, 2020.

[2] H. P. Kang, G. Xu, B. M. Wang, and S. Li, "Forty years development and prospects of underground coal mining and strata control technologies in China," *Journal of Mining and Strata Control Engineering*, vol. 1, no. 1, pp. 232–237, 2019.

[3] G. F. Wang, "Innovation and development of safe, high-efficiency and green coal mining technology and equipments," *Coal Mining Technology*, vol. 18, no. 5, pp. 1–5, 2013.

[4] J. G. Liu, X. W. Li, and T. He, "Application status and development of filling mining in coal mine in China," *Journal of China Coal Society*, vol. 45, no. 1, pp. 141–150, 2020.

[5] J. L. Xu, "Research and progress of green mining in coal mine in 20 years," *Coal Science and Technology*, vol. 48, no. 9, pp. 1–15, 2020.

[6] B. N. Hu, "Backfill mining technology and development tendency in China coal mine," *Coal Science and Technology*, vol. 40, no. 11, pp. 1–5, 2012.

[7] K. J. Jia and G. M. Feng, "Backfill mining technology with ultra high water material in coal mine and outlook," *Coal Science and Technology*, vol. 40, no. 11, pp. 6–9, 2012.

[8] B. G. Yang and J. Yang, "Development and selection on filling technology of coal mine," *Mining Research and Development*, vol. 35, no. 5, pp. 11–15, 2015.

[9] K. Cheng, B. G. Yang, B. G. Zhang, D. Li, J. Yang, and R. Zhang, "Present situation and development direction of filling mining technology in coal mines in China," *Coal Technology*, vol. 37, no. 3, pp. 73–76, 2018.

[10] X. K. Sun, "Present situation and prospect of green backfill mining in mines," *Coal Science and Technology*, vol. 46, no. 9, pp. 48–54, 2020.

[11] Z. H. Li, "Discussion on the present situation and development suggestions of the utilization of construction waste resources in China," *China Resources Comprehensive Utilization*, vol. 36, no. 10, pp. 74–77, 2018.

[12] J. Zhou, "Present situation and treatment process of construction and demolition waste at home and abroad," *Guangdong chemical*, vol. 48, no. 20, pp. 193-194, 2021.

[13] H. L. Lu, "Analysis of the problem and outlet of China's construction waste," *Environment and Sustainable Development*, vol. 43, no. 3, pp. 45–48, 2018.

[14] Y. B. Xu, Y. Li, and B. Fan, "The current situation, problems and suggestions of construction waste recycling industry in China," *Wall Materials Innovation and Energy Saving in Building*, vol. 12, no. 1, pp. 56–59, 2019.

[15] Y. Liu, H. Guo, W. Chen, and Y. Huang, "Experimental study on proportion optimization of construction waste paste filling materials," *Safety In Coal Mines*, vol. 48, no. 6, pp. 65–68, 2017.

[16] H. Q. Zhang, Y. Liu, and Q. F. Wang, "Study on performance of paste filling with urban construction waste," *Mining Research and Development*, vol. 34, no. 4, pp. 37–39, 2014.

[17] M. Y. Jiang, T. C. Li, Z. Li, H. Y. Wang, and Y. Z. Sun, "Orthogonal test study on the preparation of filling paste with construction waste aggregate," *Bulletin of the Chinese Ceramic Society*, vol. 34, no. 10, pp. 2948–2953, 2015.

[18] W. C. Qiu, F. G. Wang, S. J. Liu, and W. Jie, "Effect of particle size on the strength of construction waste slurry backfill material," *Journal of Shandong University of Technology*, vol. 30, no. 6, pp. 40–43, 2016.

[19] H. Li, Y. Liu, K. Wang, and R. Raghavan, "Experimental study on physical properties of construction waste aggregate-coarse fly ash-based cement filling," *Safety In Coal Mines*, vol. 50, no. 12, pp. 60–63, 2019.

[20] H. F. Liu, J. X. Zhang, N. Zhou et al., "Investigation of spatial stratified heterogeneity of cemented paste backfill characteristics in construction demolition waste recycled

aggregates," *Journal of Cleaner Production*, vol. 249, Article ID 119332, 2020.

[21] B. G. Yang, J. Y. Jin, X. D. Yin, and H. Yang, "Effect of concentration and suspension agent (HPMC) on Properties of coal gangue and fly ash cemented filling material," *Shock and Vibration*, vol. 2021, Article ID 6643773, , 2021.

[22] Y. S. Tang, L. F. Zhang, and H. Y. Lu, "Study on proportion optimization of coal-based solid wastes filling materials," *Journal of Mining Science and Technology*, vol. 4, no. 4, pp. 328–336, 2019.

[23] A. P. Cheng, F. S. Dong, P. F. Shu, and X. Fu, "Mechanical properties and acoustic emission characteristics of continuous graded cemented backfill," *Journal of Huazhong University of Science and Technology (Nature Science Edition)*, vol. 49, no. 8, pp. 47-48, 2021.

[24] W. X. Chen, F. Y. Li, and Q. Y. Shan, "Rheological properties behind fly-ash-based cement filling material," *Journal of Heilongjiang University of Science* & *Technology*, vol. 29, no. 1, pp. 105–109, 2019.

[25] S. L. Shu, G. C. Li, G. L. Liu et al., "Ratio Optimization of Slag-Based Solid Waste Cementitious Material Based on response surface method," *Bulletin of the Chinese Ceramic Society*, vol. 40, no. 1, pp. 187–192, 2021.

[26] S. H. Yin, S. Hao, L. Zhou, Y. Z. Kou, X. W. Li, and A. Belibi, "Research on strength regression and slurry optimization of cemented backfill based on response surface method," *Journal of Central South University (Science and Technology)*, vol. 51, no. 6, pp. 1596–1600, 2020.

[27] S. H. Liu, K. H. Fang, H. L. Shen, and X. Y. Wang, "Influence of fly ash on water requirement, landslide degree and workability of concrete," *Fly Ash Comprehensive Utilization*, vol. 2, no. 3, pp. 47-48, 2005.

[28] T. Li, X. L. Wang, M. Li, D. Y. Nan, Q. Y. Shan, and W. X. Chen, "Synergy between suspending agent and air entraning agent in cement slurry," *Revista Romana de Materiale*, vol. 41, pp. 344–353, 2020.

[29] Z. G. Fu, D. P. Qiao, Z. L. Guo, X. Jincheng, H. Fei, and W. Jiaxin, "Experimental research on mixture proportion and strength of cemented hydraulic fill with waste rock and eolian sand based on RSM-BBD," *Journal of China Coal Society*, vol. 43, no. 43, pp. 695–700, 2018.

Hindawi

Research Article

Design and Performance Evaluation of Dry-Mixed Cement Recycled Aggregate Pile

Boming Shang [ID],[1,2] Feng Jin,[1,2] Xuewen Rong,[1,2] Shanjun Wang,[1,2] Qi Zhang,[1,2] Zhen Wang,[1,2] and Kang Yao[1,2]

[1]*Shaanxi Zhengcheng Road and Bridge Engineering Research Institute Co. LTD, Xi'an 710065, China*
[2]*Shaanxi Huashan Road and Bridge Group Co. LTD, Xi'an 710065, China*

Correspondence should be addressed to Boming Shang; bomingshang@163.com

In this paper, dry-mixed recycled cement concrete gravel (CCG) piles and dry-mixed cement macadam gravel (CMG) piles were analyzed. CCG and CMG were prepared by using recycled concrete aggregate (RCA) with different substitution rates, recycled macadam aggregate (RMA) from waste bricks and tiles, and fly ash, respectively. Mechanical properties, hydration heat release performance, and frost resistance were used as evaluation factors. The compressive strength, hydration heat, relative dynamic elastic modulus, and mass loss rate were tested. Based on the requirements of subgrade reinforcement on the material strength, hydration heat release, and frost resistance of dry-mixed CRA piles, TOPSIS analysis method was used to conduct a comprehensive evaluation. The results show that the mechanical properties and frost resistance of CCG and CMG gradually deteriorate with the increase of RCA and RMA replacement rates. At the same time, the hydration heat release of CCG and CMG increases with the increase of the replacement rate. The fly ash instead of cement can improve the compressive strength and frost resistance of CCG and CMG and reduce the hydration heat and material cost. When the CCG replacement rate reaches 20%, the CCG composite score of 20% fly ash is higher than that of traditional dry-mixed cement gravel pile and has better comprehensive performance.

1. Introduction

In recent years, with the large-scale construction of high-grade highway, the problems encountered in the project have become more frequent and complex. Soft soil foundation has the characteristics of high compressibility, large settlement, and poor stability of drainage consolidation. Before building high-grade highway on such foundations, if the foundations are not treated or improper treatment, the quality of the highway will be reduced or even destroyed [1]. As a result, a series of problems such as pavement subsidence, muddying, pulping, bridge jumping, and roadbed slippage appear [2]. Dry-mixed cement gravel pile is a new trenchless rapid reinforcement technology for highway subgrade developed based on gravel pile and cement fly-ash gravel (CFG) pile [3]. This technology has the advantages of simple process, low equipment requirements, local materials for raw materials, high overall strength formed with the original topography,

and effective suppression of the unstable settlement of roadbed. Along with the rapid development of highway traffic construction, construction engineering, water conservancy, and other infrastructure construction industry, the rapid development of engineering construction in the aggregate supply gap is gradually expanding [4]. However, a series of environmental problems will be caused in the process of large-scale construction. In order to solve the problem of environmental pollution caused by aggregates shortage in engineering construction, waste aggregates recycling has become an effective solution [5].

The research on recycled waste concrete materials has become a hot topic for scholars in related fields. Many scholars have studied the properties of recycled aggregate (RA) and recycled concrete. Bai et al. investigated the characteristics of RA and the mechanical properties of recycled concrete [6]. Some scholars have conducted comparative studies on the mechanical properties of

(a)   (b)

FIGURE 1: Macroscopic view of RA. (a) RCA, (b) RMA.

ordinary concrete and recycled concrete [7]. The research results generally show that the properties of RA are often somewhat degraded compared with natural aggregate. The improvement of the physical and mechanical strength of recycled concrete has become a hot issue in the research of recycled concrete. Accelerated carbonation can effectively improve the strength of concrete, and steam curing can improve the impermeability of recycled concrete [8, 9]. Deng et al. applied recycled coarse aggregate to cement stabilized base and studied the influence of RA homogeneity on cement stabilized base [10]. Many scholars have also carried out corresponding studies on the application and reinforcement of RA. Among them, fly ash as industrial waste is also a concern by many scholars. Some scholars have found that fly ash pore refinement is beneficial to offset the higher porosity of RA by means of microscopic tests. In addition, fly ash has a positive effect on the erosion resistance of recycled concrete [11, 12]. The research of most scholars has shown that the appropriate addition of fly ash is helpful for the application of RA in engineering. To sum up, although there are many related researches on the application of RA in China, these researches are mainly focused on non-load-bearing concrete and semirigid base materials. The characteristics of different road engineering materials are quite different. Although the existing research results have certain reference significance, it is difficult to directly apply to roadbed reinforcement projects.

Several production technologies capable of manufacturing high-quality RA have been developed, and the recycled coarse aggregate concrete were applied to the upper structure of buildings on a trial basis particularly in Japan [13, 14]. In some Southern European countries, most RA are used in road construction and unpaved rural roads [15]. These uses have little added value but are a good alternative for RA with medium or low quality [16]. High-quality RA with high recycling potential can be obtained using selective dismantling techniques [17]. The use of these high-quality aggregates in the manufacture of concrete and mortar gives more added value to these recycled materials. In addition, the TOPSIS analysis method can comprehensively analyze the optimal solution of each parameter under multifactor conditions [18].

TABLE 1: Physical properties of RCA and RMA.

Aggregate type	Apparent density (kg/m^3)	Micro powder content (%)	Needle-like content (%)	Crush value (%)	Water absorption (%)
RCA	2.59	1.5	5.3	27.3	5.8
RMA	2.39	2.1	6.1	40.8	11.2

In this paper, recycled concrete aggregate (RCA) and recycled macadam aggregate (RMA) are the research objects. The compressive strength, hydration characteristics, and frost resistance were used as evaluation indexes to analyze the influence of RA content on the material properties of dry-mixed cement RA pile. At the same time, based on the characteristics of low hydration heat and durability improvement of fly ash, this paper systematically studied the influence of different fly ash content on compressive strength, hydration characteristics, and frost resistance of dry-mixed cement RA pile. Based on the requirements of roadbed reinforcement on the material strength, hydration heat release, and freezing resistance of dry-mixed cement RA piles, TOPSIS analysis method was used to comprehensively evaluate dry-mixed cement recycled piles prepared from different types of RA, and to explore the regeneration of dry-mixed cement. The optimal composition of aggregate piles provides corresponding reference for its engineering application.

2. Materials and Test Methods

2.1. Raw Materials. The raw materials used for preparing the CCG and CMG included ordinary Portland cement, mineral admixture, fine aggregates, RCA, and RMA. The morphology of RCA and RMA is shown in Figure 1, and the physical performance indicators of RCA and RMA are shown in Table 1. The physical properties of Portland cement are shown in Table 2. The chemical composition of industrial-grade fly ash (FA) is shown in Table 3. The fineness modulus of fine aggregate is 3.3, and its performance indicators are shown in Table 4.

In order to study the effect of RA content on the performance of CCG and CMG, the content of RCA and RMA

TABLE 2: Physical properties of cement.

Cement fineness (%)	Setting time		Compressive strength (MPa)		Flexural strength (MPa)		Stability (mm)
	Initial setting (min)	Final setting (h)	3 d	28 d	3 d	28 d	
2.3	165	5.5	12.6	35.0	2.9	6.1	1.5

TABLE 3: Chemical composition of considered FA (wt. %).

Al_2O_3	SiO_2	MgO	K_2O	CaO	Fe_2O_3	P_2O_5	SO_3	Na_2O
22.0	52.68	0.6	1.98	8.53	11.8	0.94	1.12	0.35

TABLE 4: Physical properties of fine aggregate.

Fineness modulus	Bulk density (kg/m^3)	Apparent density (kg/m^3)	Void ratio (%)	Stone powder content (%)	Crush indicator (%)
3.3	1447	2700	40	4.1	13

was 0, 20%, 40%, 60%, 80%, and 100%, numbered NC, RCA-20, RCA-40, RCA-60, RCA-80, RCA-100, RMA-20, RMA-40, RMA-60, RMA-80, and RMA-100, respectively. The mixing proportion of CCG and CMG is shown in Table 5. In order to study the effect of FA content on the performance of CCG and CMG, the content of FA was 0, 10%, 20%, and 30%, numbered RCA20F10, RCA20F20, RCA20F30, RMA20F10, RMA20F20, and RMA20F30, respectively. The mixing proportion of CCG and CMG is shown in Table 6.

2.2. Specimen Preparation. The test process includes the following steps: (1) the suitable amount coarse and fine aggregates are placed in a rectangular pan with a size of 400 mm × 600 mm × 70 mm; (2) the dry materials are mixed evenly for 3 min; (3) the water is poured into the dry ingredients and whisk quickly for 5 min; (4) add the suitable amount cement to the stuffed mixture and mix well for 6 min; (5) put the wet material into a square test mould with a side length of 100 mm; (6) according to the specification "*Testing Methods of Cement and Concrete for Highway Engineering*" [19], cure for 1 d and then demould.

2.3. Test Methods

2.3.1. Compressive Strength. According to the specification "*Standard for Test Method of Concrete Physical and Mechanical Properties*" [20], the compressive strength test was carried out on the samples of standard curing 7 d, 28 d, and 90 d respectively, and each sample was tested 3 times, and the average value was calculated as the final result.

2.3.2. Heat of Hydration. The heat of hydration of CCG and CMG was obtained by curing a specimen with a moulding size of 100 mm × 100 mm × 100 mm using box curing for 24 d, under the temperature of 20°C ± 2°C and a relative humidity of 90% ± 5%, according to the standard "*Test*

Methods for Heat of Hydration of Cement" [21]. The PTS-12S hydration heat tester was used in the experiment.

2.3.3. Mass Loss Rate. Cubes with a side length of 150 mm were subjected to freeze-thaw cycles according to the specification "*Standard for Test Methods of Long-term Performance and Durability of Ordinary Concrete*" [22]. The mass of exfoliation (m_s) and the mass loss rate (γ) of the specimen are computed using the formula below for the specimen after freeze-thaw cycles.

$$m_s = m_b - m_f \tag{1}$$

$$\gamma = \frac{m_s}{m} \tag{2}$$

where m_s is mass of exfoliation of specimen. m_b is the total mass of filter paper and peel after drying; m_f is the filter paper quality; m is the mass of the dried specimen.

2.3.4. Relative Dynamic Elastic Modulus. The relative dynamic elastic modulus of the samples was tested according to specification "Test Methods of Cement and Concrete for Highway Engineering" [19]. The test was carried out with a cuboid specimen of 100 mm × 100 mm × 400 mm, and the frequency was set to 100 Hz.

3. Results and Discussion

3.1. Effects of RA Substitution Rate on Material Properties

3.1.1. Compressive Strength. The test results of different substitution rates on the compressive strength of CCG and CMG are shown in Figure 2. It can be seen from Figure 2 that, with the increase of the replacement rate, the strength of the dry-mixed cement aggregate pile decreases gradually. This may be related to the old mortar in the outer layer of RA [13, 14]. There are a lot of micro-cracks in the old mortar, and the internal structure is more easily damaged when it is subjected to external pressure. It can be seen from Table 4 that the crushing value of RCA is 27.3%; the crushing value of MCA is 40.8%. The aggregate acts as a scaffold in the dry-mixed cement aggregate pile, and the destruction of the aggregate reduces the overall compressive strength [15]. Therefore, the compressive strength of the dry-mixed

TABLE 5: The mixing proportion of CCG and CMG.

No.	Cement (kg/m^3)	Effective water (kg/m^3)	Additional water (kg/m^3)	W/C	Stone chips (kg/m^3)	Gravel kg/m^3
NC		240.0	0	0.5		
RCA-20		259.2	6.65	0.54		
RCA-40		273.3	13.31	0.57		
RCA-60		292.8	19.96	0.61		
RCA-80		312.0	26.61	0.65		
RCA-100	480	331.2	33.26	0.69	1297	1584
RMA-20		259.2	6.65	0.54		
RMA-40		273.3	13.31	0.57		
RMA-60		292.8	19.96	0.61		
RMA-80		312.0	26.61	0.65		
RMA-100		331.2	33.26	0.69		

TABLE 6: The mixing proportion of CCG and CMG.

No.	FA content (%)	Cement (kg/m^3)	Sand (kg/m^3)	Gravel (kg/m^3)	Additional water (kg/m^3)	Free water (kg/m^3)
RCA20F10	26	228				
RCA20F20	52	202				
RCA20F30	77	177	595	1103	113	194
RMA20F10	26	228				
RMA20F20	52	202				
RMA20F30	77	177				
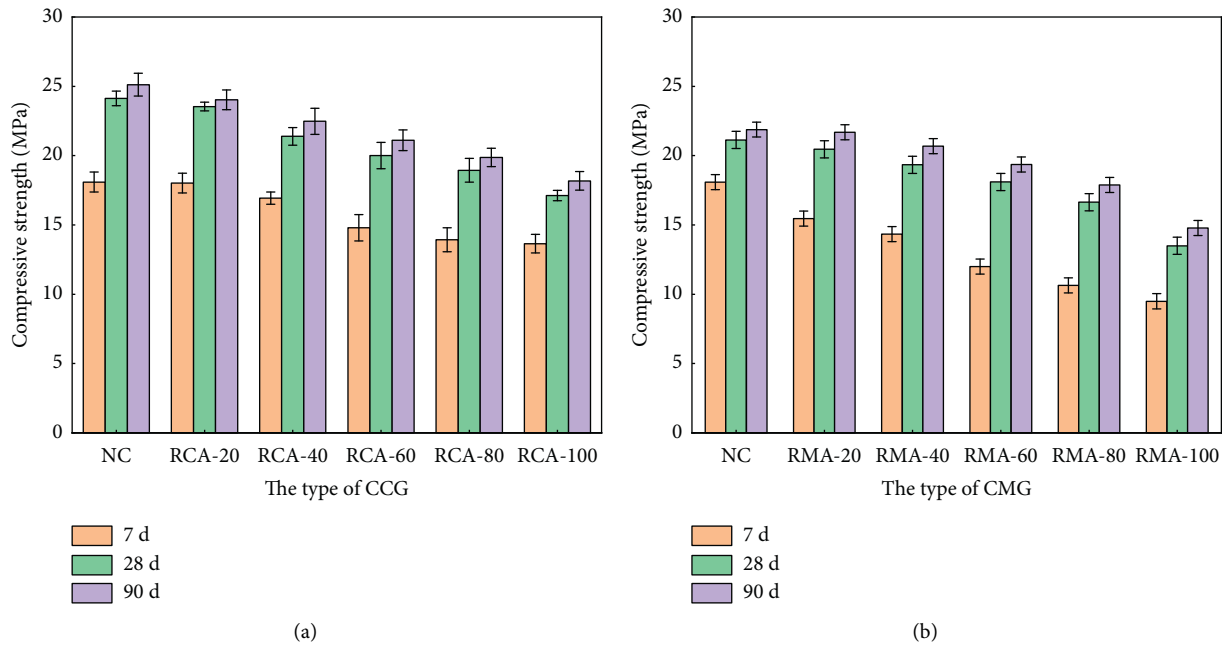
FIGURE 2: The effect of RCA and RMA with different dosages on compressive strength of CCG and CMG. (a) CCG, (b) CMG.

cement recycled aggregate pile gradually decreases with the increase of the amount of recycled aggregate. In contrast, the compressive strength of CMG is lower than that of CCG due to the lower crush value of RMA and the higher water absorption of RMA, which is about two times that of RCA.

3.1.2. Heat of Hydration. The experimental results of the heat of hydration of CCG and CMG with different substitution rates are shown in Figure 3. According to Figure 3, with the increase of the replacement rate of RA, the heat of hydration of CCG and CMG also increases. It can be found from Table 5 that, due to the high water absorption of RA, a part of additional water is required for prewetting treatment [16]. Besides, with the increase of the replacement rate of RA, the required water consumption is also increasing, resulting in an increasing water-cement ratio. The cement paste with low water-cement ratio has smaller porosity and smaller pore size, so the cement paste is denser. In order for cement to be

(a)

(b)
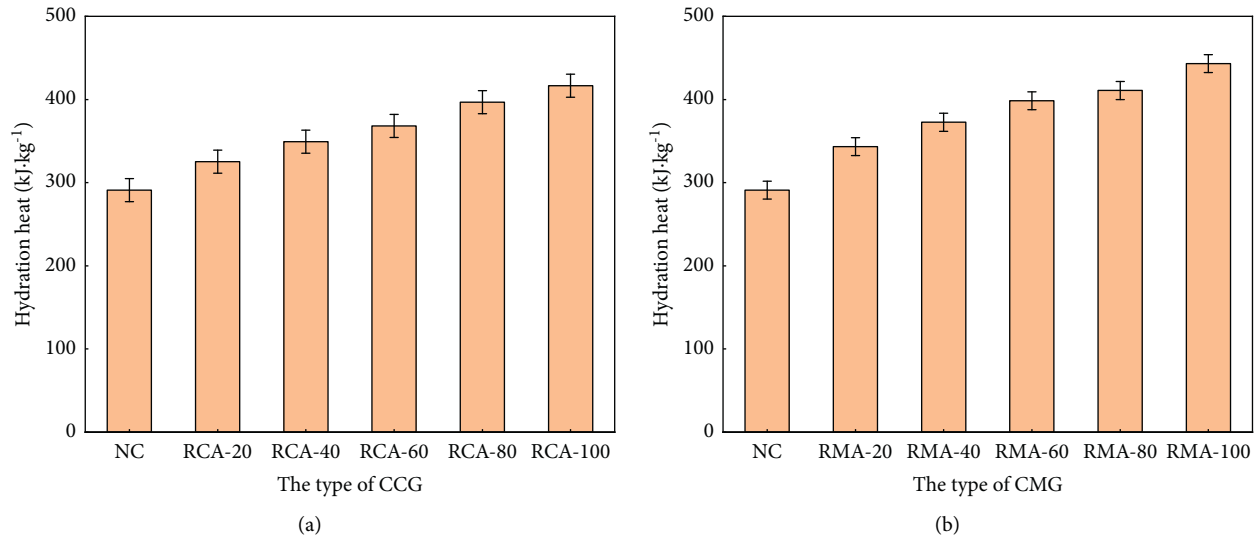
FIGURE 3: The effect of RCA and RMA with different dosages on hydration heat of CCG and CMG. (a) CCG, (b) CMG.

(a)

(b)
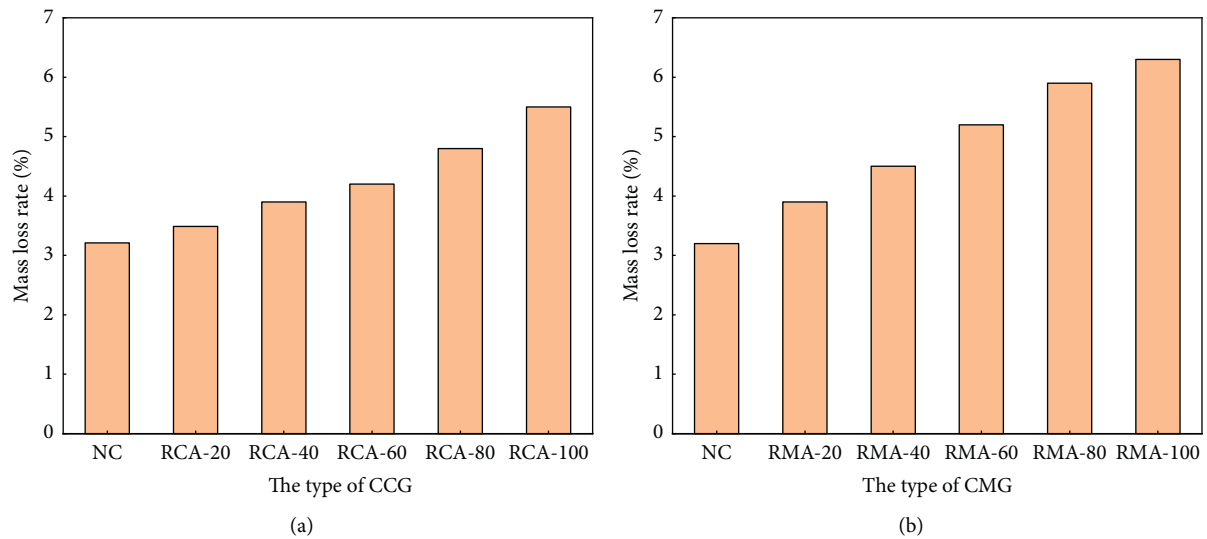
FIGURE 4: The effect of RCA and RMA with different dosages on mass loss rate of CCG and CMG. (a) CCG, (b) CMG.

fully hydrated, sufficient water diffusion in the slurry is required [17]. Therefore, the heat of hydration of the sample with a smaller water-cement ratio is also smaller; in other words, the heat of hydration of the sample with a higher replacement rate of recycled aggregate is also larger. Compared to CCG, CMG has a higher heat of hydration. The hydration exotherm is not only affected by the degree of hydration, but also closely related to the initial water content [18]. It can be seen from Table 4 that the water absorption rate of RCA is 5.8%, and that of RMA is 11.2%. Due to the high water absorption, the additional water gives the CMG a higher initial water content, resulting in a higher heat of hydration for the CMG. In conclusion, CCG shows better performance in terms of heat of hydration.

3.1.3. Frost Resistance. The test results of different RA substitution rates on the mass loss rate of CCG and CMG are shown in Figure 4. Figure 4 shows that when the replacement rate of recycled aggregate increases, the mass loss rate increases as well. This is owing to recycled aggregates' high crushing value and low apparent density, which makes them more prone to damage [23, 24]. On the one hand, the high water absorption rate of RA causes it to absorb part of the water, and frost heave occurs during the freezing and thawing process, resulting in structural damage and loss. On the other hand, the bonding strength of RA is weaker than that of natural aggregate, and it is not easy to bond with old and new mortar, so the frost resistance is worse [25].

The experimental results of the relative dynamic elastic modulus of RCA and RMA with different RA substitution rates are shown in Figure 5. The relative dynamic elastic modulus

(a)

(b)
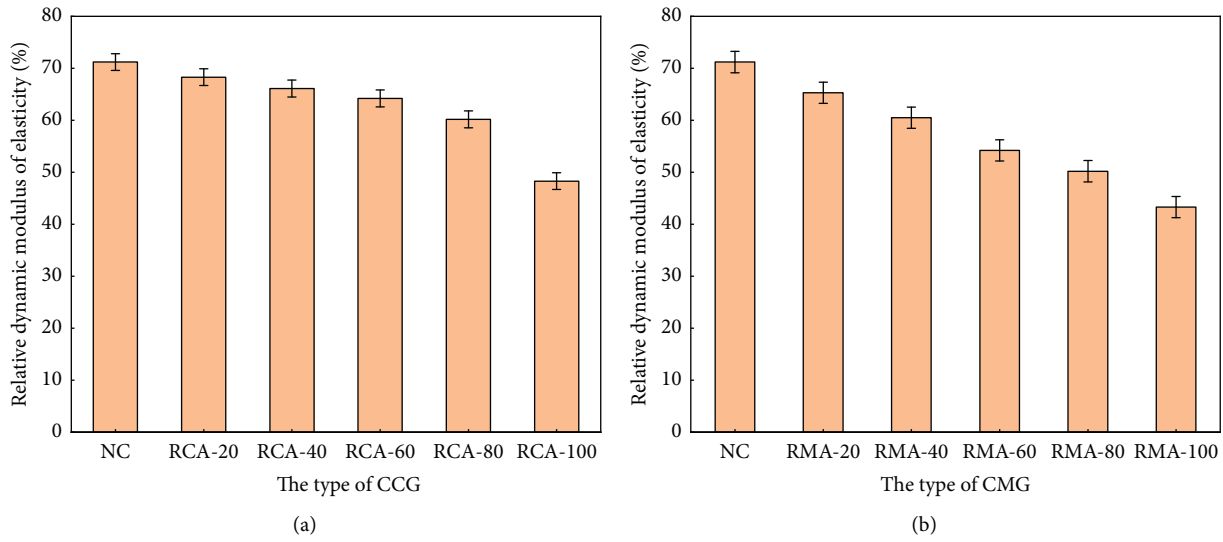
Figure 5: The effect of RCA and RMA with different dosages on relative dynamic elastic modulus of CCG and CMG. (a) CCG, (b) CMG.
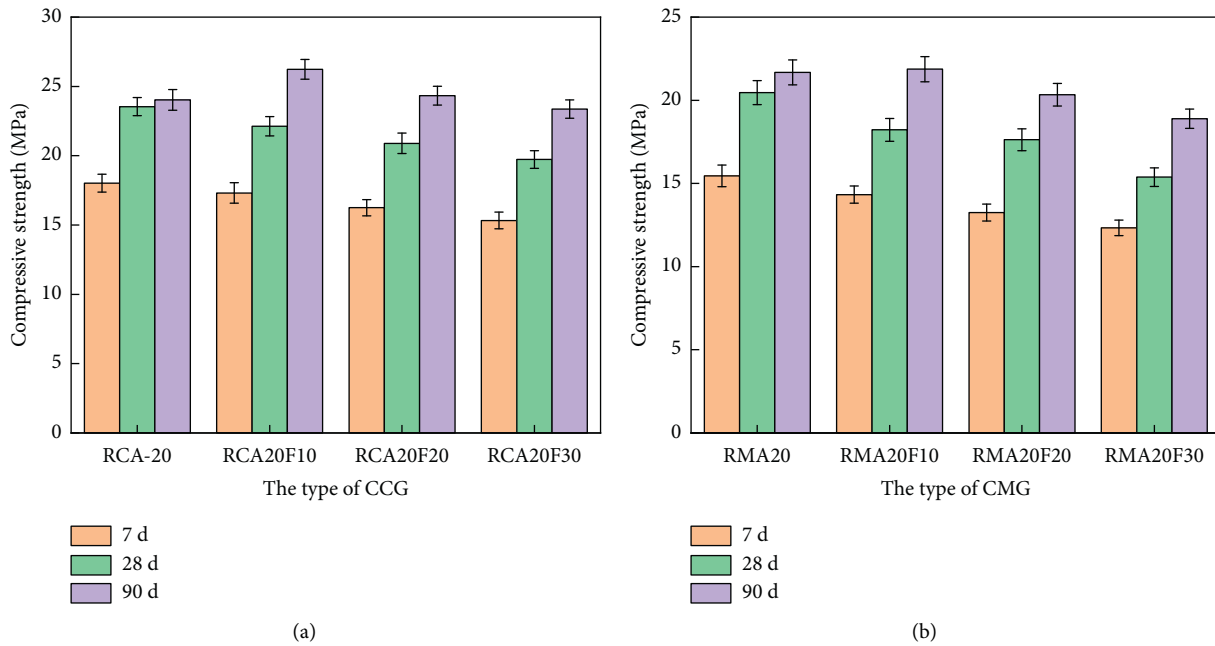
(a)

(b)

Figure 6: The compressive strength of CCG and CMG with different content of fly ash. (a) CCG, (b) CMG.

rapidly falls as the RA content increases, as seen in Figure 5. The high crushing value and low apparent density of RA, like the mass loss rate, render the interior structure of CCG and CMG prone to destruction. RMA has a rougher surface and more pores than RCA, as seen in Figure 1. Table 4 shows that RCA has a higher apparent density than RMA, as well as a lower crush value and water absorption. In conclusion, CCG has a higher relative dynamic elastic modulus than CMG.

3.2. Effect of fly Ash Content on the Performance of Dry Mix Cement RA Pile

3.2.1. Compressive Strength. The compressive strength of CCG and CMG with different content of fly ash is shown in

Figure 6. From Figure 6, the compressive strength of CCG and CMG decreases at 7 d and 28 d due to the slow hydration of fly ash in the early stages, which cannot provide enough strength for CCG and CMG [26]. However, the AFt crystals and CH crystals are generated after the secondary hydration reaction of fly ash, contributing to an increase in compressive strength at 90 d [27]. Furthermore, with the increase of fly ash, the compressive strength of CCG and CMG at 90 d shows a trend of first increasing and then declining. The high fly ash content can cause problems such as low strength and carbonation of concrete at an early stage [28]. Meanwhile, excessive amounts of fly ash can decrease the workability and compressive strength of concrete (Temesge et al.) [29]. The reason for this phenomenon is the excessive water requirement of fly ash in large content, and the secondary
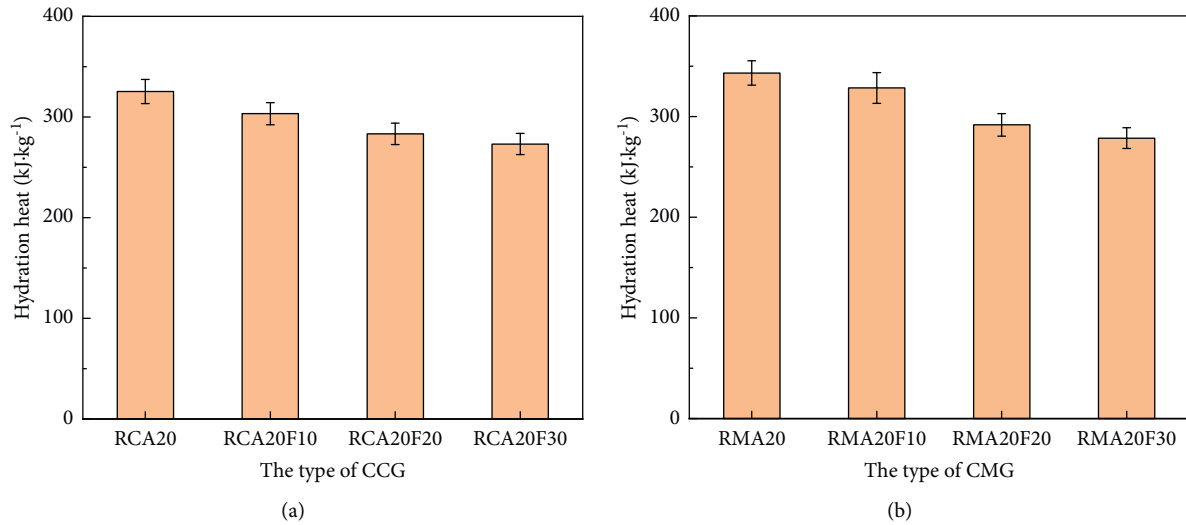
FIGURE 7: The hydration heat of CCG and CMG with different content of fly ash. (a) CCG, (b) CMG.
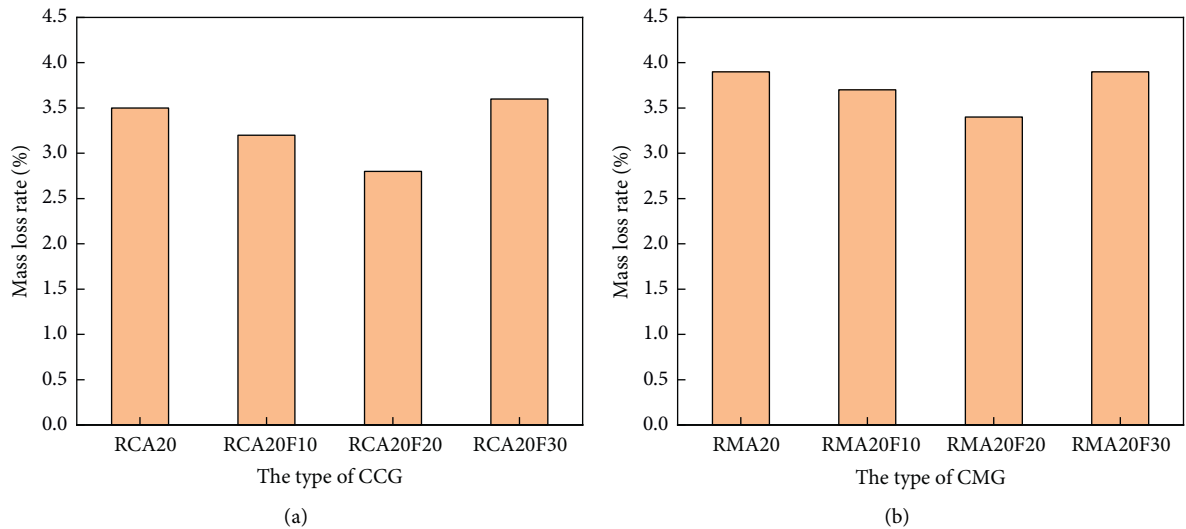
FIGURE 8: The mass loss rate of CCG and CMG with different content of fly ash. (a) CCG, (b) CMG.

hydration is incomplete. It can be found that the compressive strength is higher when the CCG replacement rate is 20%, and the fly ash content is 10%.

3.2.2. Hydration Heat. The results of fly ash content on the hydration heat of CCG and CMG are shown in Figure 7. The hydration heat of CCG and CMG will gradually decrease with the increase of fly ash [30]. The generation of hydration heat mainly comes from the heat release from the cement hydration reaction. The cement content of the hydration reaction in the early stage and the hydration heat is reduced by using fly ash instead of cement, and this result is consistent with the conclusion of other studies [27, 31].

3.2.3. Frost Resistance. Figures 8 and 9 show the test results of fly ash content on the frost resistance of CCG and CMG. According to Figures 8 and 9, the mass loss rate decreases and

then increases with the increase of fly ash content, and the relative dynamic elastic modulus exhibited a trend of rising and then falling. Moreover, using fly ash as the filler will help fill gaps in the dry-mixed cement recycled aggregate pile, improving structural compactness and providing frost resistance [32, 33]. As a result, too much fly ash will reduce the strength of CCG and CMG in the early stage, resulting in higher water demands and a more vulnerable internal structure to freeze-thaw damage. The internal structure is not tight enough, and the frost resistance is reduced. RCA with 20% fly ash content has a lower mass loss rate and a higher relative dynamic elastic modulus.

3.3. The Comprehensive Performance Evaluation of Dry-Mixed RA Piles

3.3.1. The Analysis of TOPSIS. TOPSIS analysis method first normalizes the original data matrix and then determines the
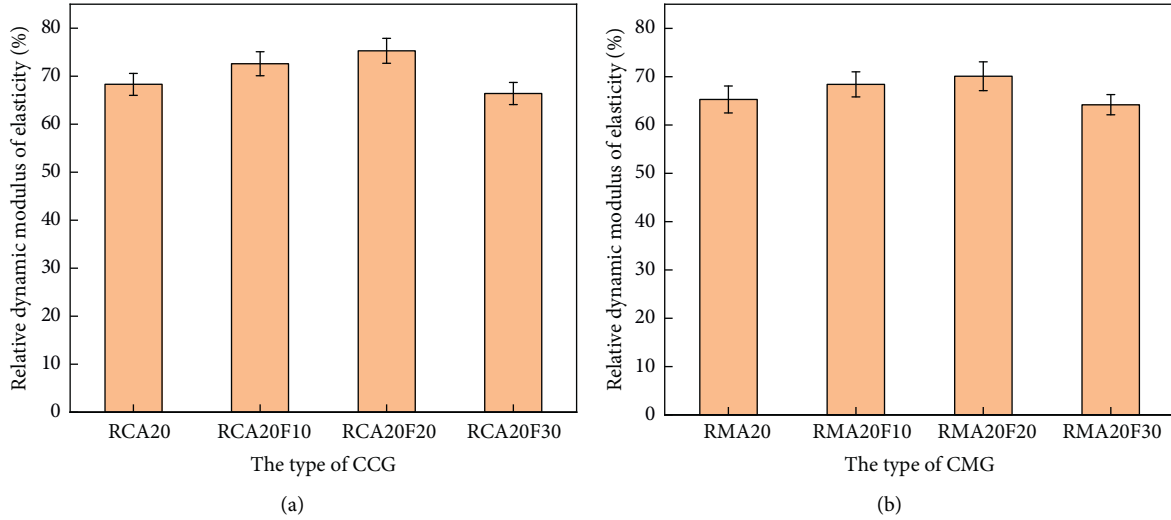
FIGURE 9: The relative dynamic modulus of elasticity of CCG and CMG with different content of fly ash. (a) CCG, (b) CMG.

optimal and inferior solutions among a finite number of solutions through the optimal vector and inferior vector. Then, it determines the closeness of each study factor of the object of investigation relative to the optimal solution by comparing the object of investigation with the optimal and inferior solutions and then evaluates the superiority and inferiority of the object of investigation [34, 35]. The specific steps are as follows.

In the first step, a decision matrix needs to be constructed, and the raw data can be represented by matrix $X = (X_{ij})_{n \times m}$, where n and m represent the number of evaluation objects and evaluation indicators, respectively. The resulting raw data are matrixed by

$$Z_{ij} = \frac{X_{ij}}{\sqrt{\sum_{i=1}^{m} X_{ij}^2}} \tag{3}$$

In the second step, the above obtained matrix is normalized by Eq. (4) and Eq. (5); then, determine the optimal vector and the worst vector.

$$Y^+ = (Y_{\max 1}, Y_{\max 2}, \cdots, Y_{\max m}) \tag{4}$$

$$Y^- = (Y_{\min 1}, Y_{\min 2}, \cdots, Y_{\min m}) \tag{5}$$

In the third step, the difference distance between the ith examined object and the optimal solution and the worst solution is then determined by Eq. (6) and Eq. (7).

$$D_i^+ = \sqrt{\sum_{j=1}^{m} (X_{\max j} - Y_{ij})^2} \tag{6}$$

$$D_i^- = \sqrt{\sum_{j=1}^{m} (X_{\min j} - Y_{ij})^2} \tag{7}$$

In the fourth step, the similarity between each examined object and the optimal solution is calculated by Eq. (8) and ranked for comparison to determine the optimal solution.

$$CI = D_i^- / (D_i^+ + D_i^-) 1 \leq i \leq n \tag{8}$$

3.3.2. Analysis of Calculation Results. Compressive strength, hydration heat, and frost resistance are used as the investigating factors to achieve a comprehensive evaluation of CCG and CMG. The results of experimental values of compressive strength, the heat of hydration, mass loss, and relative dynamic modulus of elasticity are shown in Table 7.

(1) The above experimental data are matrixed by Eq. (3), and the resulting standard matrix is as follows:

$$\begin{pmatrix}
0.2850 & 0.3466 & 0.3241 & 0.2715 \\
0.2726 & 0.2687 & 0.2927 & 0.2605 \\
0.2550 & 0.2140 & 0.2614 & 0.2521 \\
0.2390 & 0.1707 & 0.2300 & 0.2448 \\
0.2254 & 0.1060 & 0.1568 & 0.2296 \\
0.2062 & 0.0604 & 0.0523 & 0.1842 \\
0.2460 & 0.2277 & 0.2509 & 0.2490 \\
0.2347 & 0.1609 & 0.1882 & 0.2307 \\
0.2196 & 0.1019 & 0.1150 & 0.2067 \\
0.2028 & 0.0738 & 0.0418 & 0.1914 \\
0.1677 & 0 & 0 & 0.1651 \\
0.2976 & 0.3188 & 0.3241 & 0.2605 \\
0.2760 & 0.3646 & 0.3659 & 0.2769 \\
0.2650 & 0.3877 & 0.2823 & 0.2872 \\
0.2481 & 0.2277 & 0.2718 & 0.2609 \\
0.2306 & 0.2616 & 0.3032 & 0.2673 \\
0.2143 & 0.3450 & 0.2509 & 0.2448
\end{pmatrix} \tag{9}$$

(2) The optimal vector and the worst vector obtained by Eq. (4) and Eq. (5) are as follows:

TABLE 7: Factor values for CCG and CMG.

Number	90 d compressive strength (MPa)	The heat of hydration (kJ/kg)	Mass loss (%)	Relative dynamic modulus of elasticity (%)
NC	25.12	291.1	3.2	71.2
RCA20	24.03	325.3	3.5	68.3
RCA40	22.48	349.3	3.8	66.1
RCA60	21.11	368.3	4.1	64.2
RCA80	19.87	396.7	4.8	60.2
RCA100	18.18	416.7	5.8	48.3
RMA20	21.68	343.3	3.9	65.3
RMA40	20.69	372.6	4.5	60.5
RMA60	19.36	398.5	5.2	54.2
RMA80	17.88	410.8	5.9	50.2
RMA100	14.78	443.2	6.3	43.3
RCA20F10	26.23	303.3	3.2	68.3
RCA20F20	24.33	283.2	2.8	72.6
RCA20F30	23.36	273.1	3.6	75.3
RMA20F10	21.87	343.3	3.7	68.4
RMA20F20	20.33	328.4	3.4	70.1
RMA20F30	18.89	291.8	3.9	64.2

TABLE 8: Sorting index values for different types of recycled aggregate materials.

Aggregate type	D^+	D^-	Similarity CI
NC	0.0619	0.5003	0.8899
RCA20	0.1444	0.4219	0.7450
RCA40	0.2101	0.3596	0.6312
RCA60	0.2659	0.3059	0.5349
RCA80	0.3628	0.2081	0.3646
RCA100	0.4737	0.0907	0.1607
RMA20	0.2072	0.3577	0.6332
RMA40	0.3002	0.2648	0.4686
RMA60	0.3965	0.1674	0.2969
RMA80	0.4708	0.0956	0.1687
RMA100	0.5621	0	0
RCA20F10	0.0848	0.4823	0.8504
RCA20F20	0.0332	0.5395	0.9421
RCA20F30	0.0898	0.5043	0.8489
RMA20F10	0.1939	0.3760	0.6598
RMA20F20	0.1571	0.4181	0.7268
RMA20F30	0.1542	0.4365	0.7390

$$Y^+ = (0.2976, 0.3877, 0.3659, 0.2872) \qquad (10)$$

$$Y^- = (0.1677, 0, 0, 0.1651) \qquad (11)$$

The difference distance and similarity between each examined object and the optimal solution are obtained by Eq. (7) and Eq. (8). The obtained results are shown in Table 8.

Table 8 shows that, through the TOPSIS analysis method, the piles with 20% fly ash added scored the highest, even exceeding the score of natural aggregates after a comprehensive analysis of compressive strength, exothermic hydration, and frost resistance indexes. In comparing the properties of recycled materials, it is concluded that RCA > RMA considering the compressive strength, exothermic hydration, and frost resistance.

4. Conclusion

(1) The mechanical properties and freezing resistance of CCG and CMG gradually deteriorate with RCA and RMA substitution rates. Meanwhile, the exothermic hydration of CCG and CMG increases continuously with the increase of the substitution rate.

(2) RCA has a higher crushing value and lower water absorption than RMA. CCG prepared by RCA has higher compressive strength, frost resistance and lower hydration heat than CMG prepared by CMG.

(3) The use of fly ash to replace part of cement improves the late compressive strength and frost resistance of CCG and CMG and lowers the hydration heat and material cost.

(4) TOPSIS analysis of dry-mix cement recycled aggregate piles based on mechanical properties, frost resistance, and exothermic hydration capacity demonstrated that the comprehensive score initially increases and then decreases with fly ash. When the CCG substitution rate reaches 20%, the composite score of CCG mixed with 20% fly ash is higher than that of the conventional dry-mix cement aggregate pile material, which has better performance.

Data Availability

The data used to support the findings of this study are included within the article.

Conflicts of Interest

The authors declare no conflicts of interest.

Acknowledgments

References

[1] E. M. B. De Guzman and M. C. Alfaro, "Laboratory-scale model studies on corduroy-reinforced road embankments on peat foundations using transparent soil," *Transportation Geotechnics*, vol. 16, pp. 1–10, 2018.

[2] J. Liu, T. Zhang, H. Guo, Z. Wang, and X. Wang, "Evaluation of self-healing properties of asphalt mixture containing steel slag under microwave heating: mechanical, thermal transfer and voids microstructural characteristics," *Journal of Cleaner Production*, vol. 342, p. 130932, 2022.

[3] J. Zhang, "Numerical Simulation of soft roadbed reinforced by dry cement gravel pile," *Highway*, vol. 66, no. 04, pp. 18–22, 2021, (in Chinese).

[4] S. Li, Y. Fang, and X. Wu, "A systematic review of lean construction in Mainland China," *Journal of Cleaner Production*, vol. 257, p. 120581, 2020.

[5] G. Bai, C. Zhu, C. Liu, and B. Liu, "An evaluation of the recycled aggregate characteristics and the recycled aggregate concrete mechanical properties," *Construction and Building Materials*, vol. 240, no. 240, p. 117978, 2020.

[6] M. S. Bidabadi, M. Akbari, and O. Panahi, "Optimum mix design of recycled concrete based on the fresh and hardened properties of concrete," *Journal of Building Engineering*, vol. 32, p. 101483, 2020.

[7] Q. Liu, J. Xiao, Z. Pan, and L. Li, "Modeling of recycled concrete with waste Concrete aggregate and waste brick Aggregate," *Journal of Building Structures*, vol. 41, no. 12, pp. 133–140, 2020, (in Chinese).

[8] J. Park, J. Lee, C.-W. Chung, S. Wang, and M. Lee, "Accelerated carbonation of recycled aggregates using the pressurized supercritical carbon dioxide sparging process," *Minerals*, vol. 10, no. 6, p. 486, 2020.

[9] S. Zhuang and J. Sun, "The feasibility of properly raising temperature for preparing high-volume fly ash or slag steam-cured concrete: an evaluation on DEF, 4-year strength and durability," *Construction and Building Materials*, vol. 242, p. 118094, 2020.

[10] C. Deng, Y. Chen, H. Chen, B. Guan, and Z. Sun, "Research on homogeneity evaluation and control technology of reclaimed coarse aggregate for cement stabilized base," *Highway*, vol. 65, no. 09, pp. 251–255, 2020, (in Chinese).

[11] B. Ali, S. S. Raza, R. Kurda, and R. Alyousef, "Synergistic effects of fly ash and hooked steel fibers on strength and durability properties of high strength recycled aggregate concrete," *Resources, Conservation and Recycling*, vol. 168, p. 105444, 2021.

[12] S. Sunayana and S. V. Barai, "Partially fly ash incorporated recycled coarse aggregate based concrete: microstructure perspectives and critical analysis," *Construction and Building Materials*, vol. 278, p. 122322, 2021.

[13] A. Shintani, K. Yoda, T. Onodera, and Y. Kawanishi, "On-site application of two types of recycled course aggregate concrete," *Annual report of JCI*, vol. 28, no. 1, pp. 1463–1468, 2006, (in Japanese).

[14] E. Kawai, K. Yanagibashi, T. Iwashimizu, and H. Takiguchi, "Application of recycled aggregate concrete to building project: example of Shin-Senri Sakuragaoka renovation project," *Concrete J*, vol. 44, no. 2, pp. 46–53, 2006, (in Japanese).

[15] F. Agrela, A. Barbudo, A. Ramírez, J. Ayuso, M. D. Carvajal, and J. R. Jiménez, "Construction of road sections using mixed recycled aggregates treated with cement in Malaga, Spain," *Resources, Conservation and Recycling*, vol. 58, pp. 98–106, 2012.

[16] J. R. Jiménez, J. Ayuso, F. Agrela, M. López, and A. P. Galvín, "Utilisation of unbound recycled aggregates from selected CDW in unpaved rural roads," *Resources, Conservation and Recycling*, vol. 58, pp. 88–97, 2012.

[17] J. Jiménez, J. Ayuso, A. Galvín, M. López, and F. Agrela, "Use of mixed recycled aggregates with a low embodied energy from non-selected CDW in unpaved rural roads," *Construction and Building Materials*, vol. 34, pp. 34–43, 2012.

[18] H. Shen, L. Hu, and K. K. Lai, "A mathematical programming model to determine objective weights for the interval extension of TOPSIS," *Mathematical Problems in Engineering*, vol. 2018, pp. 1–6, 2018.

[19] Ministry of Transport 2020, *Testing Methods of Cement and Concrete for Highway Engineering*, Ministry of Transport of the People's Republic of China, 2020.

[20] Gb/T 50081-2019, *Standard for Test Method of concrete Physical and Mechanical Properties*, Ministry of Housing and Urban-Rural Development of the People's Republic of China, 2019.

[21] Gb/T 18046-2008, *Test Methods for Heat of Hydration of Cement*, General Administration of Quality Supervision and Quarantine of the People's Republic of China, 2008.

[22] Gb/T 50082-2009, *Standard for Test Methdos of Long-Term Performance and Durability of Ordinary Concrete*, Ministry of Housing and Urban-Rural Development of the People's Republic of China, 2009.

[23] H. Dabiri, M. Kioumarsi, A. Kheyroddin, A. Kandiri, and F. Sartipi, "Compressive strength of concrete with recycled aggregate; a machine learning-based evaluation," *Cleaner Materials*, vol. 3, p. 100044, 2022.

[24] Q. Zhu, Y. X. Yuan, J. H. Chen, L. Fan, and H. Yang, "Research on the high-temperature resistance of recycled aggregate concrete with iron tailing sand," *Construction and Building Materials*, vol. 327, p. 126889, 2022.

[25] A. İ. Uğurlu, M. B. Karakoç, and A. Özcan, "Effect of binder content and recycled concrete aggregate on freeze-thaw and sulfate resistance of GGBFS based geopolymer concretes," *Construction and Building Materials*, vol. 301, p. 124246, 2021.

[26] H. Li, Z. Ban, H. Qin, L. Ma, and G KingWang, "A heteromeric membrane-bound prenyltransferase complex from hop catalyzes three sequential aromatic prenylations in the bitter acid pathway," *Plant physiology*, vol. 167, no. 3, pp. 650–659, 2015, (in Chinese).

[27] M. Farzad, S. Vute, and V. Kirk, "The effect of fly ash fineness on heat of hydration, microstructure, flow and compressive strength of blended cement pastes," *Case Studies in Construction Materials*, vol. 10, pp. 152–159, 2019.

[28] D. Florian, W. Frank, L. Barbara et al., "Hydration of Portland cement with high replacement by siliceous fly ash[J]," *Cement and Concrete Research*, vol. 42, no. 10, pp. 1389–1400, 2012.

[29] T. Fantu, G. Alemayehu, G. Kebede, Y. Abebe, S. K. Selvaraj, and V. Paramasivam, "Experimental investigation of compressive strength for fly ash on high strength concrete C-55 grade," *Materials Today Proceedings*, vol. 46, pp. 7507–7517, 2021.

[30] W. Chen, Y. Zhou, S. Li, and P. Yan, "Impact of temperature rising inhibitor on hydration of cement-fly ash cementitious materials and performance of concrete," *Journal of the Chinese Ceramic Society*, vol. 49, no. 08, pp. 1609–1618, 2021.

[31] Z. Giergiczny, "Fly ash and slag," *Cement and Concrete Research*, vol. 124, p. 105826, 2019.

[32] L. Xiao and J. Li, "Study on the effect of straw fiber, fly ash and diatomite on mechanical property and frost resistance of straw cement-based material," *New Chemical Materials*, vol. 49, no. 06, pp. 236–239, 2021, (in Chinese).

[33] J. Liu, L. Qi, X. Wang, M. Li, and Z. Wang, "Influence of aging induced by mutation in temperature on property and microstructure development of asphalt binders," *Construction and Building Materials*, vol. 319, p. 126083, 2022.

[34] I. Basheleishvili, "Developing the expert decision-making algorithm using the methods of multi-criteria analysis," *Cybernetics and Information Technologies*, vol. 20, no. 2, pp. 22–29, 2020.

[35] S. Hasnain, M. K. Ali, J. Akhter, B. Ahmed, and N. Abbas, "Selection of an industrial boiler for a soda-ash production plant using analytical hierarchy process and TOPSIS approaches," *Case Studies in Thermal Engineering*, vol. 19, p. 100636, 2020.

Research Article

Moisture Stability of Hard Sandstone Asphalt Mixture Based on APT with MMLS3

Zhang Ermao,[1] Yang Liming,[2] and Yang Datian [3]

[1]*Nanning Expressway Construction & Development Co., Ltd., Nanning 530023, China*
[2]*Guangxi Communication Design Group Co., Ltd, Nanning 530029, China*
[3]*College of Civil Engnieering, Chongqing Jiaotong University, Chongqing 400074, China*

Correspondence should be addressed to Yang Datian; tywoyangda@126.com

To evaluate the moisture stability of a hard sandstone asphalt mixture, a testing section of a hard sandstone asphalt mixture was prepared in the laboratory. The accelerated pavement testing (APT) with the one-third-scale model mobile load simulator (MMLS3) was conducted in this testing section under temperature and water-coupled conditions. As the APT number increased, the elastic modulus of the hard sandstone asphalt mixture pavement gradually decreased. The average elastic modulus was 22.99 GPa after 160000 APT cycles. The bulk specific density of the sample rolled by the MMLS3 increased, and the residual indirect tensile strength ratio was 88.7%. Therefore, the hard sandstone asphalt mixture had good resistance to moisture damage, and hard sandstone aggregates can be used in a hot mix of asphalt.

1. Introduction

Moisture damage is one of the diseases of asphalt mixture pavement [1]. The main external cause of moisture damage in asphalt pavement is the coupled effect of water, temperature, and vehicle loads. The main internal causes of water damage in asphalt pavement are the properties of the aggregate and asphalt [2]. High temperatures reduce the asphalt viscosity, water erodes the asphalt film on the aggregates, and repeated loads accelerate the moisture damage of asphalt mixtures.

The indirect tensile strength ratio is used to evaluate the moisture stability of asphalt mixtures in the standard method [3, 4]. Based on a certain sinusoidal waveform [5–9], water moves in the core in a compacted asphalt mixture sample, which simulates hydraulic scouring. After this moisture conditioning, the indirect tensile strength or dynamic modulus of the asphalt mixture sample is measured [10].

An immersion rutting test is a procedure in which a rolling tire compacts asphalt mixture specimens in the presence of water and measures the rutting depth after each rolling cycle. The rutting depth curves versus rolling cycles are then processed to determine the asphalt mixture's moisture stability. For this immersion rutting test, the Hamburg wheel-track test (HWTT) and an asphalt pavement analyzer (APA) are used to evaluate the moisture susceptibility of asphalt mixtures [11–14]. Twagira and Jenkins [15] used a one-third-scale model mobile load simulator (MMLS3) and tensile strength retention to evaluate the moisture damage and reveal the performances of bitumen stabilized materials.

The aggregate used in the hot mix asphalt is a nonrenewable resource, especially for individual aggregate types that are gradually becoming scarce, such as basalt aggregate and diabase aggregate. To solve the shortage problem of aggregate in asphalt mixtures, hard sandstone aggregate is being used in asphalt mixture pavement. Ouyang et al. [16] used sandstone aggregate to study the highway performances of sandstone asphalt mixtures. Metcalf and Goetz [17] found that sandstone as an aggregate type can be satisfactorily used in asphalt pavement. Zhang and Li [18] used sandstone aggregate to produce sandstone concrete as the road base.

In this study, hard sandstone aggregate from an aggregate plant in Guangxi was used. To examine the moisture stability of the hard sandstone asphalt mixture, a testing section of the hard sandstone asphalt mixture pavement with a length of 4.2 m, a width of 1.4 m, and a thickness of 0.04 m was paved in the laboratory. Then, accelerated pavement testing (APT) with the MMLS3 under hot-water conditions was performed on the hard sandstone asphalt mixture pavement. The elastic modulus of the asphalt mixture pavement was measured with a portable seismic property analyzer (PSPA) after the APT. Finally, some core samples at the wheel and nonwheel track locations were drilled, and their indirect tensile strengths and bulk specific densities were measured. Then, their indirect tensile strength ratios were computed to evaluate their moisture stability. The materials and corresponding test methods used in this study are summarized as a flow chart, as shown in Figure 1.

2. Materials

2.1. Coarse Aggregate. In this study, the coarse aggregate was a type of hard sandstone aggregate that has been rarely used in asphalt mixtures. Its properties were measured by the Test Methods of Aggregate for Highway Engineering (JTG E42-2005) [19], as shown in Table 1.

2.2. Fine Aggregate. The fine aggregate was a limestone manufactured sand, whose properties are shown in Table 2.

2.3. Filler. The filler was a limestone grinding powder, whose properties are shown in Table 3.

2.4. Asphalt. Styrene-butadiene-styrene (SBS) modified asphalt was used, whose properties are shown in Table 4.

3. Aggregate Gradation and Optimal Asphalt Aggregate Ratio

In this paper, the optimal asphalt aggregate ratio was determined by the Marshall mix design method [20].

According to the Technical Specifications for Construction of Highway Asphalt Pavement (JTG F40-2004) [20], for hot areas in the summer with heavy traffic, the air void content (AV) of an AC-13C asphalt mixture ranges from 4% to 6%.

In this paper, the coarse aggregate with three size ranges (3–5 mm, 5–10 mm, and 10–15 mm) was used. The coarse aggregate of 3–5 mm was a limestone aggregate. Through aggregate sieve analysis and the specification requirements, the aggregate gradation was optimized as shown in Table 5 and Figure 2. Hence, the combined gradation is composed of 5% filler, 29% fine aggregate, 16% coarse aggregate of 3–5 mm, 26% coarse aggregate of 5–10 mm, and 24% coarse aggregate of 10–15 mm, whose percentages are the ratio of the mass of various aggregates to the mass of blended aggregates.

The bulk specific density, Marshall stability (MS), flow value (FL), air void content (AV), voids in the mineral

aggregate (VMA), and voids filled with asphalt (VFA) were determined and are shown in Table 6 and Figure 3. In Figure 3, the horizontal axis corresponds to the asphalt aggregate ratio.

First, from Figure 3, the following points were determined:

(a) asphalt aggregate ratio, a_1, at the maximum bulk specific density

(b) asphalt aggregate ratio, a_2, at the maximum MS

(c) asphalt aggregate ratio, a_3, at the midpoint of the specified AV range (4%–6%)

(d) The asphalt aggregate ratio, a_4, at the midpoint of the specified VFA range (65%–75%)

Second, the average of the four asphalt aggregate ratios was computed, as follows:

$$\begin{aligned} \mathrm{OAC}_1 &= \frac{(a_1 + a_2 + a_3 + a_4)}{4} \\ &= \frac{(4.7\% + 4.5\% + 5.0\% + 5.1\%)}{4} = 4.83\%. \end{aligned} \tag{1}$$

Third, the range of the asphalt aggregate ratio, $C_{\min}–C_{\max}$, was determined, based on the Technical Specifications for Construction of Highway Asphalt Pavement (JTG F40-2004) [20] (excluding VMA). The average of the minimum and maximum values were computed, as follows:

$$\mathrm{OAC}_2 = \frac{(\mathrm{OAC}_{\min} + \mathrm{OAC}_{\max})}{2} = \frac{(3.8\% + 5.0\%)}{2} = 4.40\%. \tag{2}$$

Finally, the average of C_1 and C_2 were calculated, as follows:

$$\mathrm{OAC} = \frac{(\mathrm{OAC}_1 + \mathrm{OAC}_2)}{2} = \frac{(4.83\% + 4.40\%)}{2} = 4.6\%. \tag{3}$$

The optimal asphalt aggregate ratio was 4.6%.

4. Construction of Hard Sandstone Asphalt Mixture Pavement

To study the moisture stability of the hard sandstone asphalt mixture, a pavement sample of the hard sandstone asphalt mixture was constructed in the laboratory. This hard sandstone asphalt mixture pavement had a thickness of 0.04 m, length of 4.2 m, and width of 1.4 m. The construction procedure of the pavement sample is shown in Figure 4.

In the laboratory, workers removed the old asphalt mixture layer, then sprayed a seal coat, and finally, sprinkled the hot asphalt as the binder on the base. Because the mixing pot used in the laboratory only mixed 30 L of asphalt mixture at a time, about 500 kg of the hard sandstone asphalt mixture was mixed several times. The asphalt mixtures mixed each time were packed in a white iron bucket, which were then stored in an oven at 180°C, as shown in Figure 5.

Based on previous construction experience for AC-13C, the loose paving coefficient for AC-13C was 1.2. The hard
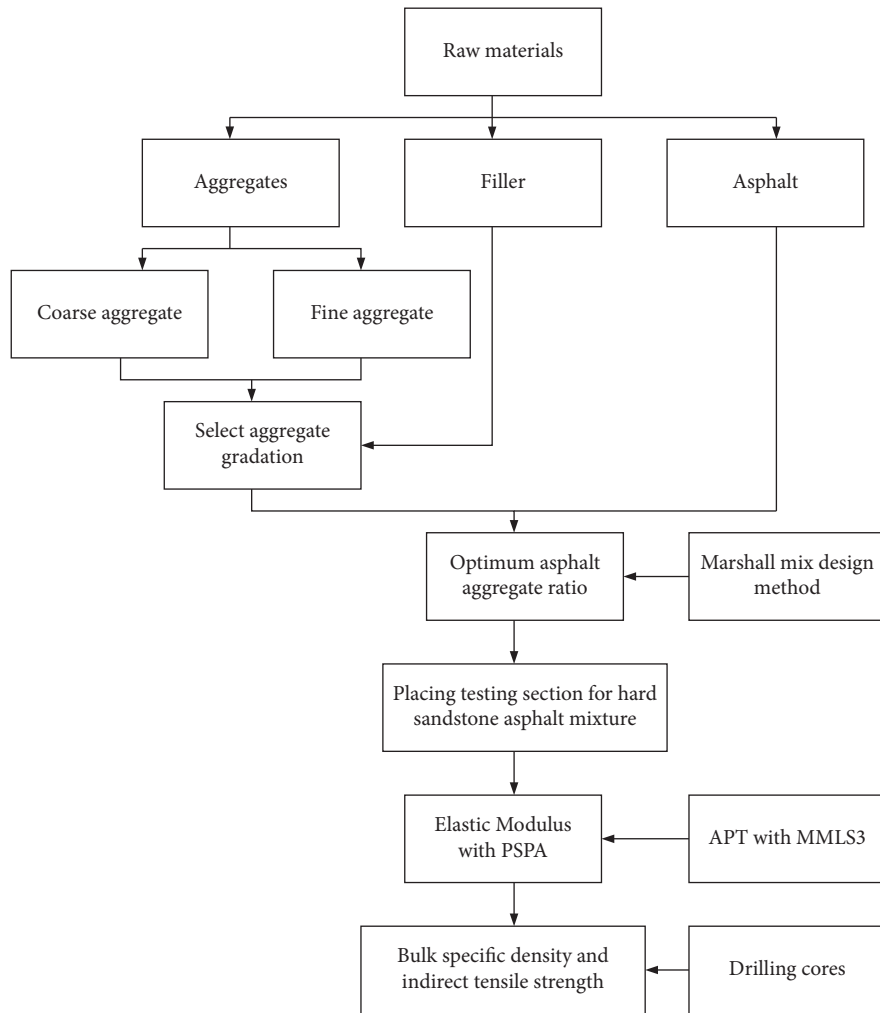
FIGURE 1: Flow chart of study materials and corresponding test methods.

TABLE 1: Properties of coarse aggregate.

Properties		Unit	Requirements	Results
Crushing value		%	≤26	23.4
Los Angeles abrasion		%	≤28	25.0
Bulk relative density	5–10 mm	—	≥2.60	2.715
	10–15 mm			2.714
Water absorption	5–10 mm	%	≤2.0	0.45
	10–15 mm			0.43
Flat and elongated particles (%)	>9.5	%	≤12	11.1
	<9.5		≤18	12.8
Washing method <0.075 mm		%	<1	0.9
Durability/soundness		%	≤12	6

sandstone asphalt mixtures were placed on the binding layer, as shown in Figure 6. After the hard sandstone asphalt mixtures were placed, about a 5-ton road roller-compacted them to a 40-mm thickness, as shown in Figure 7.

5. Accelerated Pavement Testing

5.1. One-Third Scale MMLS3. APT refers to "the controlled application of a prototype wheel loading, at or above the appropriate legal load limit to a prototype or actual, layered, structural pavement system to determine pavement response and performance under a controlled, accelerated accumulation of damage in a compressed time period. The acceleration of damage is achieved by means of increased repetitions, modified loading conditions, imposed climatic conditions, the use of thinner pavements with a decreased structural capacity and thus shorter design lives, or a combination of these factors. Full-scale construction by

Table 2: Properties of fine aggregate.

Properties	Unit	Technical requirements	Results
Apparent relative density	—	≥2.50	2.62
Durability/soundness	%	≤12	0.9
Mud content	%	≤3	1.8
Methylene blue value	g/kg	≤25	16
Angularity	s	≥30	45

Table 3: Technical properties of filler.

Properties		Unit	Technical requirements	Results
Apparent density		g/cm^3	≥2.50	2.679
Water content		%	≤1	0.3
Hydrophilic coefficient		—	<1	0.75
	<0.6 mm	%	100	100
Particle size	<0.15 mm	%	90–100	98.8
	<0.075 mm	%	75–100	87.4

Table 4: Technical properties of SBS modified asphalt.

Properties		Unit	Technical requirements	Results
Penetration depth at 25°C, 100 g, 5 s		0.1 mm	40–60	50
Penetration index		—	≥0	1.152
Softening point (ring and ball method)		°C	≥60	85.0
Ductility at 5 cm/min, 5°C		cm	≥20	39
Specific relative density at 15°C		—	—	1.060
Kinematic viscosity at 135°C		Pa·s	≤3	1.2
Flash point temperature		°C	≥230	303
Solubility in trichloroethylene		%	≥99	99.54
Elasticity recovery at 25°C		%	≥75	81
	Weight change	%	±1.0	−0.105
Rolling thin-film oven test at 163°C	Retained penetration	%	≥65	67
	Ductility at 5°C	cm	≥15	19

Table 5: Combined gradation.

Sieve size (mm)	Mass percentage passing through the sieve (%)									
Gradation	0.075	0.15	0.3	0.6	1.18	2.36	4.75	9.5	13.2	16
Upper limit of gradation	8	15	20	28	38	50	68	85	100	100
Lower limit of gradation	4	5	7	10	15	24	38	68	90	100
Middle limit of gradation	6	10	13.5	19	26.5	37	53	76.5	95	100
Combined gradation	5	8	11	16	24	34	50	76	95	100
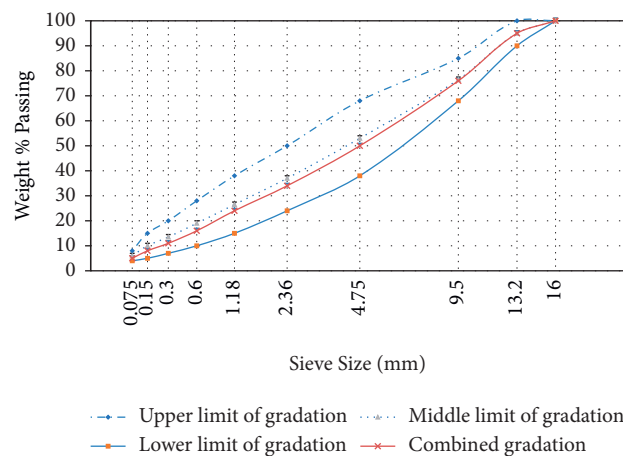
Figure 2: Aggregate gradation curve.

TABLE 6: Marshall testing results.

Asphalt aggregate ratio (%)	Bulk specific density	AV (%)	VMA (%)	VFA (%)	MS (kN)	FL (mm)
3.5	2.380	6.42	16.29	60.58	21.71	2.01
4.0	2.398	5.70	16.05	64.47	23.93	2.97
4.5	2.413	5.28	15.97	66.94	24.33	3.57
5.0	2.412	5.00	16.54	69.77	22.91	4.09
5.5	2.382	4.76	16.84	71.73	19.94	4.56
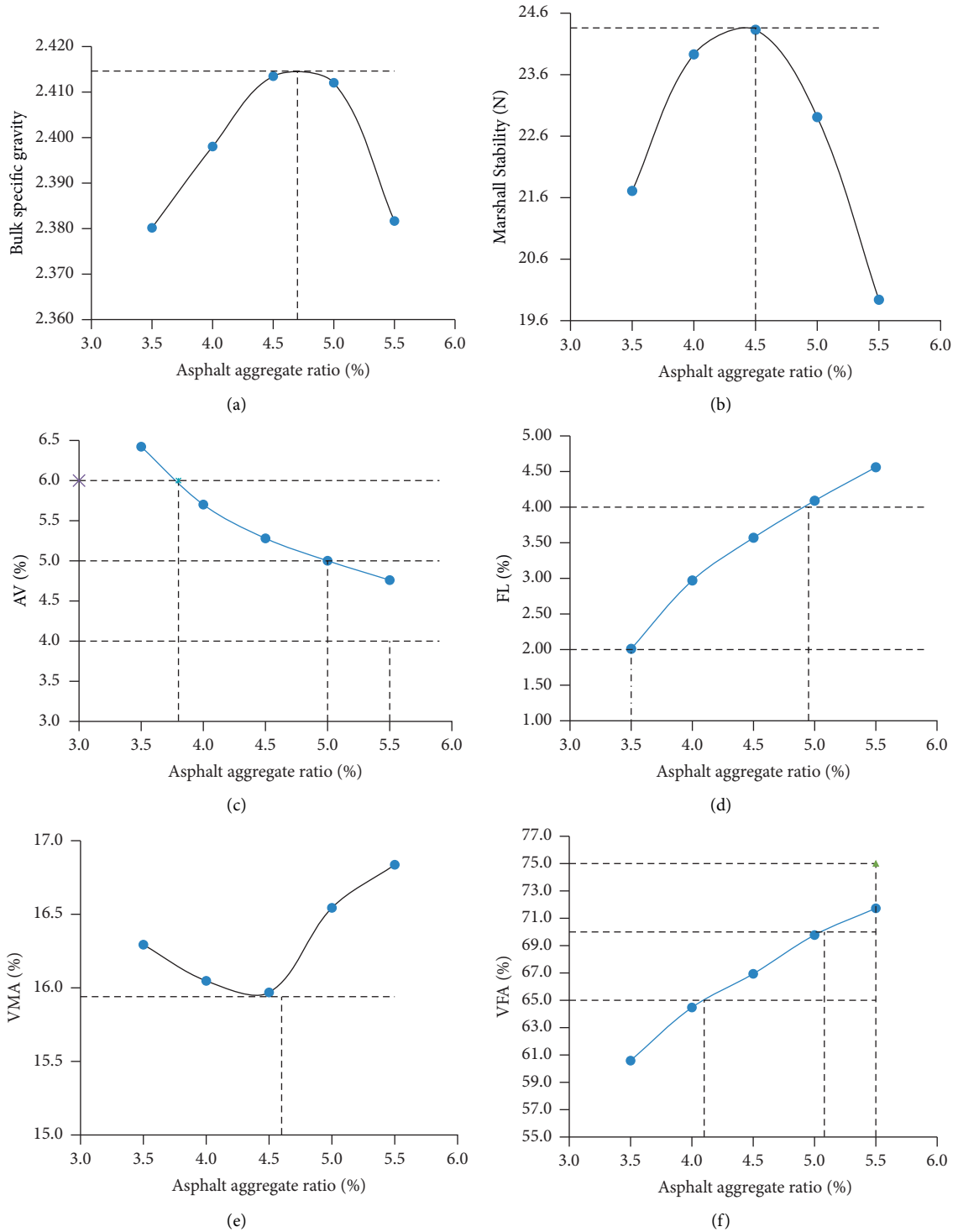
FIGURE 3: Design plots for Marshall mix design.

```
┌──────────────────┐      ┌──────────────────────┐      ┌──────────────────────┐
│ Heat the asphalt │      │ Heat 11.3793 kg per  │◄─────│ 0-3 =3.4737 kg       │
│ to 170-180°C     │      │ blended aggregates   │      │ 3-5 =1.9165 kg       │
│                  │      │ to 180-190°C         │      │ 5-10 =3.1143 kg      │
└────────┬─────────┘      └──────────┬───────────┘      │ 10-15=2.8748 kg      │
         │                           │                  └──────────────────────┘
         ▼                           ▼
┌──────────────────┐      ┌──────────────────────┐      ┌──────────────────────┐
│ Per asphalt      │─────►│ Mix the asphalt      │◄─────│ Per filler =0.5989 kg│
│ 0.5510 kg        │      │ mixtures at 180°C    │      │                      │
└──────────────────┘      └──────────┬───────────┘      └──────────────────────┘
                                     │
                                     ▼
                          ┌──────────────────────┐      ┌──────────────────────┐
                          │ Store the asphalt    │◄─────│ 479.1 kg asphalt     │
                          │ mixtures in the      │      │ mixtures             │
                          │ oven 180°C           │      │                      │
                          └──────────┬───────────┘      └──────────────────────┘
                                     │
                                     ▼
                          ┌──────────────────────┐
                          │ Pave the asphalt     │
                          │ mixtures             │
                          └──────────┬───────────┘
                                     │
                                     ▼
                          ┌──────────────────────┐
                          │ Compact the asphalt  │
                          │ mixtures             │
                          └──────────────────────┘
```
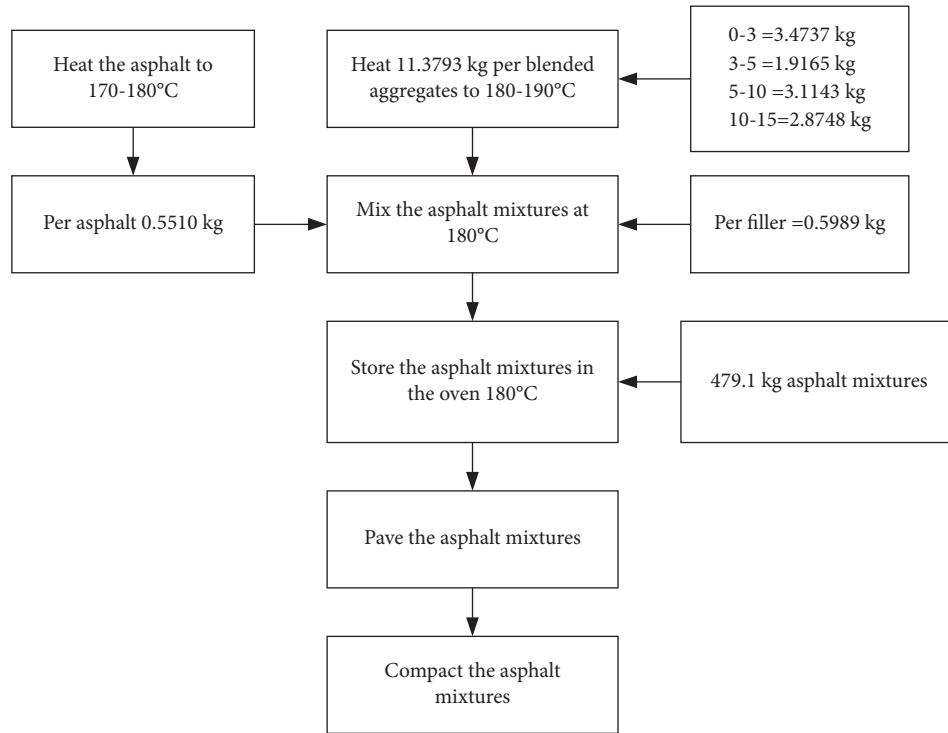
FIGURE 4: Construction flow chart for the hard sandstone asphalt mixture testing section.

FIGURE 5: Mixing the hard sandstone asphalt mixture.

FIGURE 6: Paving the hard sandstone asphalt mixture.

FIGURE 7: Compacting the hard sandstone asphalt mixture.

periods) on the 300-mm-diameter pneumatic tire wheels. The maximum tire pressure was 700 kPa (800 kPa for short periods). The MMLS3 included an electronic wheel load calibration unit, one spare load wheel, eight spare guide wheels, spare drive belts, a tool kit, and a canvas cover, as shown in Figure 8.

5.2. Wet Heater System. The water heater unit was used to circulate and heat the water to be applied onto the material to be tested. It can be used in conjunction with a set of spray nozzles to spray hot water onto the pavement in the field or a slab in the laboratory while it is being trafficked by the

conventional plant and processes is necessary so that real-world conditions are modeled" [21].

The MMLS3 [22] can apply 7200 wheel loads per hour. The maximum wheel load was 2.7 kN (2.9 kN for short
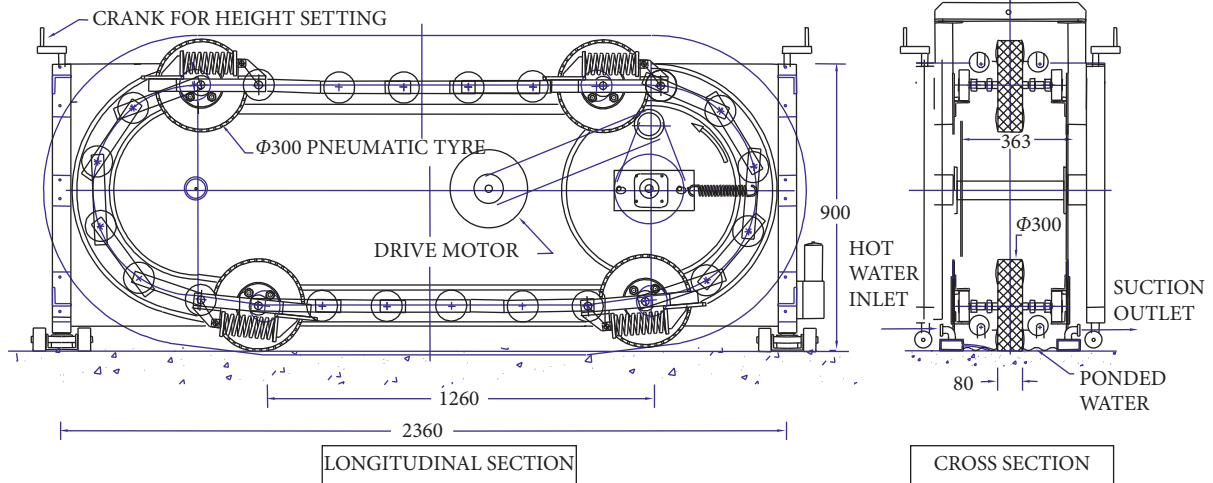
FIGURE 8: Schematic diagram of MMLS3.

FIGURE 9: MMLS3 and water heater unit.

MMLS3. In this study, the hard sandstone asphalt mixture pavement was mainly heated by spraying hot water at 80°C, which resulted in hot and humid environmental conditions, as shown in Figure 9.

5.3. *Testing Locations.* The testing pavement was divided into four segments to measure their elastic moduli separately, as shown in Figure 10.

5.4. *PSPA.* The elastic moduli of the hard sandstone asphalt mixture pavement were measured by the seismic wave method, namely using a PSPA [23], as shown in Figures 11 and 12. Because the hard sandstone asphalt mixture pavement was heated by hot water, the elastic moduli measured by the PSPA were transformed into the elastic moduli at 25°C using the following equation [24]:

$$E_{25} = \frac{E_t}{1.35 - 0.01404t},$$ (4)

where E_{25} and E_t are the modulus at 25°C and temperature t (°C), respectively.

5.5. *Experimental Plan.* The numbers of passes during the APT were 0, 5000, 10000, 20000, 40000, 80000, and 160000. After the APT, the elastic moduli of four testing segments
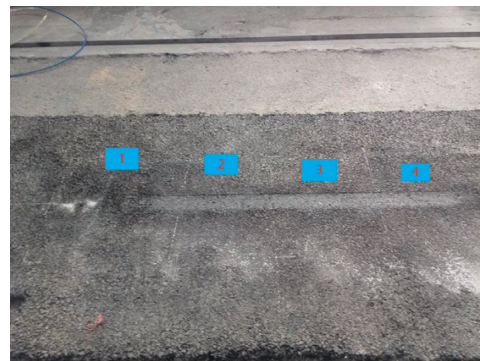
FIGURE 10: Measurement locations for PSPA.

FIGURE 11: PSPA.
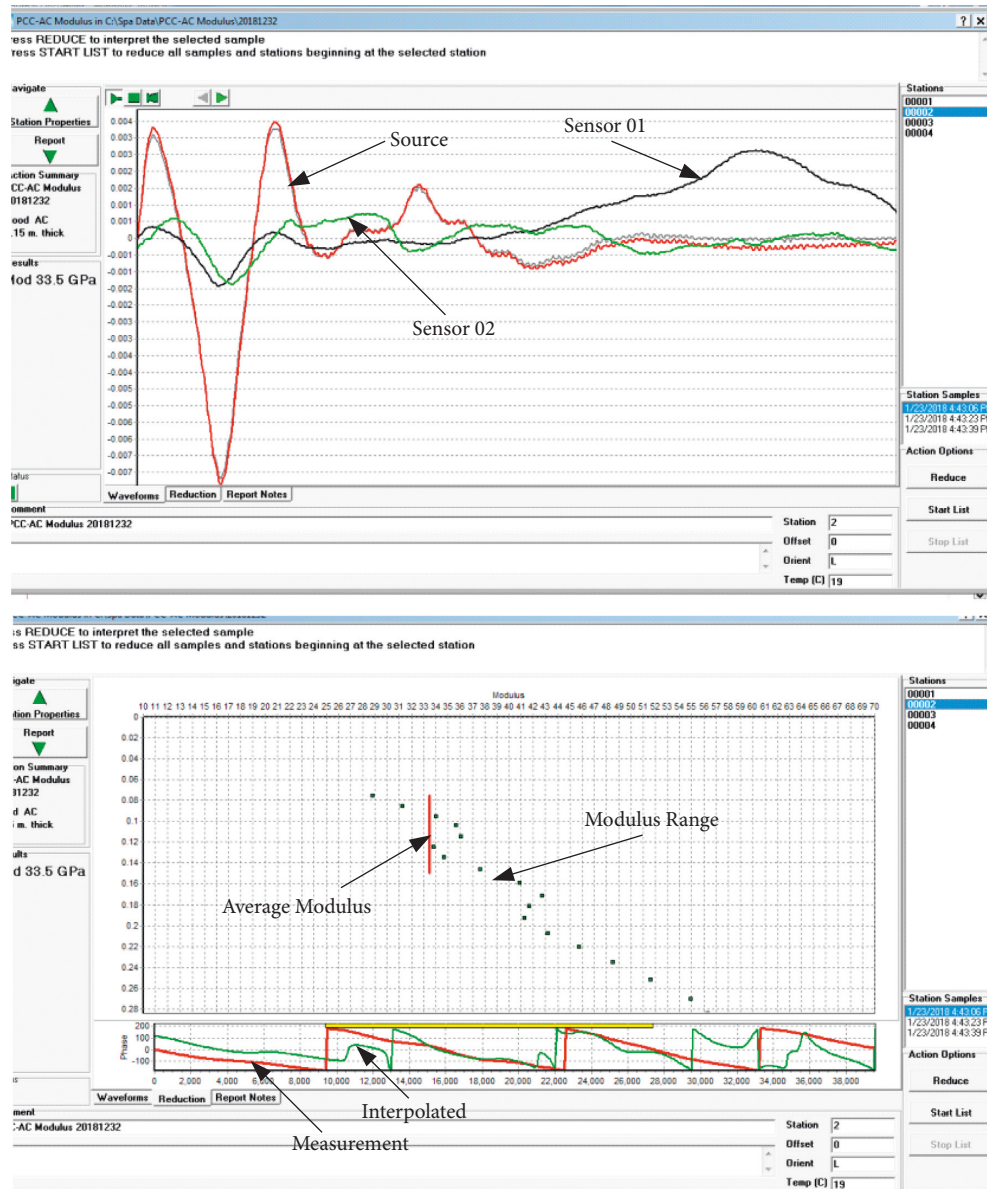
Figure 12: PSPA time records and dispersion curves.

were measured. Finally, the core specimens were drilled at the wheel track and nonwheel track. Their bulk specific density and the indirect tensile strength were measured in the laboratory.

6. Results and Discussion

6.1. Elastic Modulus of Hard Sandstone Asphalt Mixture.
As shown in Figure 10, there were two segments completely rolled by the MMLS3. The first and fourth segments were only partially rolled. Hence, the elastic moduli of the second and third segments are discussed here. The elastic moduli of the hard sandstone asphalt mixture pavement segments are shown in Table 7.

According to Grubbs' statistical method [25], the elastic modulus of 117.13 GPa in Segment 2 was an outlier. This outlier was excluded, and the elastic modulus of the hard

sandstone asphalt mixture pavement ranged from 11.13 to 57.1 GPa and decreased to 22.60–23.37 GPa after 160000 loading cycles, as shown in Figure 13.

From Figure 13, as the number of loading cycles increased, the elastic moduli gradually decreased.

6.2. Bulk Specific Density and Indirect Tensile Strength.
After the hard sandstone asphalt mixture pavement was rolled repeatedly by the MMLS3, some core specimens were drilled from the wheel track of the MMLS3, as shown in Figure 13. In addition, other core specimens were drilled from sites that were not rolled by the MMLS3, as shown in Figure 14.

The bulk specific densities and the indirect tensile strengths of these core specimens were measured in the laboratory. These results are shown in Table 8. The bulk

TABLE 7: Elastic moduli of the hard sandstone asphalt mixture pavement segments.

APT cycles	0	5000	10000	20000	40000	80000	160000
Segment 2	117.13	57.10	30.4	21.40	35.37	25.50	22.60
Segment 3	44.10	14.53	58.95	11.13	30.67	25.87	23.37

FIGURE 13: Relationships between the elastic moduli and the number of APT cycles for two segments.

FIGURE 14: Core specimens.

TABLE 8: Bulk specific densities and indirect tensile strengths of two types of core specimens.

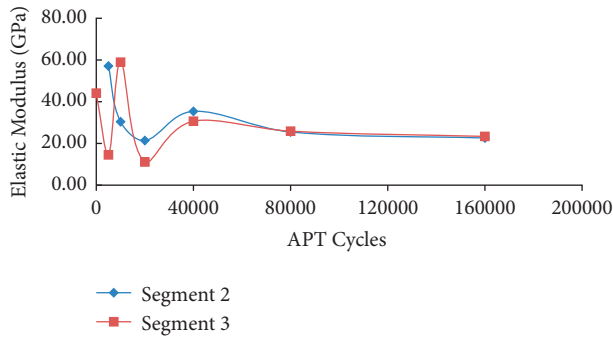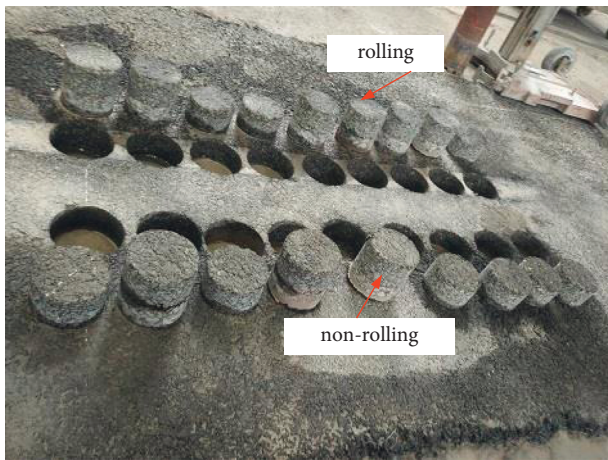| Number	Bulk specific density		Indirect tensile strength (MPa)	
	Rolled specimens	Nonrolled specimens	Rolled specimens	Nonrolled specimens
1	2.369	2.341	1.307	1.417
2	2.356	2.335	1.230	1.297
3	2.351	2.326	1.243	1.408
4	2.334	2.337	1.126	1.403
5	2.342	2.324	1.179	1.283
6	2.349	2.334	1.108	1.399
7	2.364	2.333	1.319	1.394
8	2.372	2.329	1.249	1.501
9	2.364	2.324	1.427	1.518
Average value	2.356	2.331	1.243	1.402

TABLE 9: t-test for the bulk specific densities of two types of core specimens.

t-test: paired two sample for means		
Sample	Sample 1	Sample 2
Mean	2.356	2.3314
Variance	0.0001633	3.628×10−05
Observations	9	9
Pearson correlation coefficient	0.04765	
Hypothesized mean difference	0	
df	8	
t Stat	5.242	
P ($T \leq t$) one-tailed	0.0003909	
t critical one-tailed	1.860	
P ($T \leq t$) two-tailed	0.0007818	
t critical two-tailed	2.306	

TABLE 10: t-test for the indirect tensile strengths of two types of core specimens.

t-test: paired two sample for means		
Sample	Sample 1	Sample 2
Mean	1.243	1.402
Variance	0.01004	6.112×10−03
Observations	9	9
Pearson correlation coefficient	0.5053	
Hypothesized mean difference	0	
df	8	
t Stat	−5.263	
P ($T \leq t$) one-tailed	0.0003807	
t critical one-tailed	1.860	
P ($T \leq t$) two-tailed	0.0007614	
t critical two-tailed	2.306	

specific density increased and the indirect tensile strength decreased after the APT. The cause of the bulk specific density increase was that the air void content was smaller in the hard sandstone asphalt mixture pavement rolled repeatedly by the MMLS3. Under conditions with water, temperature, and load coupling, microdamage could occur in the hard sandstone asphalt mixture, which made the indirect tensile strength smaller. However, the residual indirect strength ratio was still 88.7%, which fully meets the technical requirements of the moisture stability of hot mix asphalt [17].

To verify the significance of the effect of the wet-heated APT with the MMLS3 on the bulk density and the indirect tensile strength, the bulk specific density and the indirect tensile strengths of the two types of core samples were analyzed by the t-test method, as shown in Tables 9 and 10. According to the Pearson correlation coefficient of 0.04764 shown in Table 9, the linear correlation between the two types of samples was good. The one-tailed and two-tailed P ($T \leq t$) values were both smaller than the significance level of 0.05, which verified that there was a significant difference between them. Hence, the APT with the MMLS3 further compacted the hard sandstone asphalt mixture.

According to the Pearson correlation coefficient of 0.5052 shown in Table 10, the linear correlation between the two types of samples was a subpositive correlation. The one-

tailed and two-tailed $P\,(T \leq t)$ values were both smaller than the significance level of 0.05, which verified that there was a significant difference between them. Hence, under conditions with water, temperature, and load coupling, the APT with the MMLS3 could accelerate the damage to the hard sandstone asphalt mixture.

7. Conclusion

In this study, the moisture damage of a hard sandstone asphalt mixture was investigated using APT with an MMLS3. The elastic modulus of the hard sandstone asphalt mixture pavement as well as the bulk specific densities and indirect strengths of the specimens drilled from rolled and nonrolled sites were analyzed by the t-test method. The elastic modulus initially increased and then gradually decreased. The average elastic modulus was 22.99 GPa after 160000 APT cycles.

It was also found that the bulk specific density increased and the indirect tensile strength decreased after the APT with the MMLS3. The bulk specific density increased by 1.1%. The indirect tensile strength ratio of the two types of core samples was 88.7%. Based on a paired t-test, the bulk specific densities and indirect tensile strengths of the two types of core samples were significantly different at the significance level of 0.05. Hence, the hard sandstone asphalt mixture had a good ability to resist moisture damage.

In the future, it would be necessary to further track the changes in the highway performance of hard sandstone asphalt mixture pavement in the field and further carry out fatigue tests of hard sandstone asphalt mixtures. In addition, the differences between the hard sandstone aggregate, limestone aggregate, basalt aggregate, and diabase aggregate will be investigated. These results will be presented in successive publications.

Data Availability

The data in the manuscript were obtained by experiments, and the data were effectively collected and correctly presented. The data used to support the findings of this study are included in the article.

Disclosure

The authors would like to declare that the work described is original research and has not been publicly published previously.

Conflicts of Interest

The authors declare no conflicts of interest.

Authors' Contributions

The work presented herein was carried out in collaboration between all the authors. ZE was responsible for study conception and design. YL was responsible for the data collection. YD was responsible for the analysis and interpretation of the data. All the authors reviewed the results and approved the final version of the manuscript for publication.

References

[1] J. S. Miller and W. Y. Bellinger, "Distress identification manual for the long-term pavement performance program (5 revised edition)," Report No. FHWA-HRT-13-092, Federal U.S. Department of Transportation Highway Administration, Washington, DC, USA, 2014.

[2] H. Soenen, S. Vansteenkiste, and K. De Maeijer, "Fundamental approaches to predict moisture damage in asphalt mixtures: state-of-the-art review," *Infrastructure*, vol. 5, no. 2, p. 20, 2020.

[3] Aashto T 283-2014, *Standard Method of Test for Resistance of Compacted Hot Mix Asphalt (HMA) to Moisture-Induced Damage*, AASHTO, Washington, DC, USA, 2014.

[4] JTG E20-2011, *Standard Test Methods of Bitumen and Bituminous Mixtures for Highway Engineering*, Ministry of Communications of the People's Republic of China, Beijing, China, 2011, in Chinese.

[5] J Wang-heng, X. N. Zhang, and Z. Li, "Mechanical mechanism of moisture-induced damage of asphalt mixture based on simulation test of dynamic water pressure," *China Journal of Highway and Transport*, vol. 24, no. 4, pp. 21–25, 2011.

[6] R. A. Tarefder, M. T. Weldegiorgis, and M. Ahmad, "Assessment of the effect of pore pressure cycles on moist ure sensitivity of hot mix asphalt using MIST conditioning and dynamic modulus," *Journal of Testing and Evaluation*, vol. 42, no. 6, pp. 1530–1540, Article ID JTE20130095, 2014.

[7] W. Wang, L. Wang, G. Yan, and B. Zhou, "Evaluation on moisture sensitivity of asphalt mixture induced by dynamic pore water pressure," *International Journal of Pavement Research and Technology*, vol. 13, no. 5, pp. 489–496, 2020.

[8] S. Dhakal and R. Ashtiani, "Effect of Different Levels of Moisture Intrusion on the Dynamic Modulus and Tensile Properties of Dense Graded Hot Mix Asphalt Using a Cyclic Moisture Induced Stress Tester," in *Proceedings of the International Conference on Transportation and Development 2016*, Houston, TX, USA, June 2016.

[9] P. Sulejmani, S. Said, S. Agardh, and A. Ahmed, "Moisture sensitivity of asphalt mixtures using cycling pore pressure conditioning," *Transportation Research Record: Journal of the Transportation Research Board*, vol. 2673, no. 2, pp. 294–303, 2019.

[10] R. A. Tarefder and M. Ahmad, "Evaluating the relationship between permeability and moisture damage of asphalt concrete pavements," *Journal of Materials in Civil Engineering*, vol. 27, no. 5, pp. 1–10, Article ID 04014172, 2015.

[11] J. Xie, L. I. Yu-zhi, and L. G. Shao, "Laboratory evaluation on the moisture susceptibility of hot asphalt mixtures by asphalt pavement analyze," *Journal of Hunan University of Science &*

Technology (Natural Science Edition), vol. 20, no. 2, pp. 53–57, 2005, in Chinese.

[12] F. Yin, E. Arambula, R. Lytton, A. E. Martin, and L. G. Cucalon, "Novel method for moisture susceptibility and rutting evaluation using Hamburg wheel tracking test," *Transportation Research Record: Journal of the Transportation Research Board*, vol. 2446, no. 1, pp. 1–7, 2014.

[13] R. P. Izzo and M. Tahmoressi, "Use of the Hamburg wheel-tracking device for evaluating moisture susceptibility of hot-mix asphalt," *Transportation Research Record: Journal of the Transportation Research Board*, vol. 1681, no. 1, pp. 76–85, 1999.

[14] P. Chaturabong and U. Hussain, "The evaluation of relative effect of moisture in Hamburg wheel tracking test," *Construction and Building Materials*, vol. 153, no. 30, pp. 337–345, 2017.

[15] E. M. Twagira and K. J. Jenkins, "Application of MMLS3 in laboratory conditions for moisture damage classification of bitumen stabilised materials," *Road Materials and Pavement Design*, vol. 13, no. 4, pp. 642–659, 2012.

[16] X. Ouyang, C. Zhao, P. Gao, and X. Wang, "Analysis of influencing factors of performance for sandstone asphalt mixture," *IOP Conference Series: Earth and Environmental Science*, IOP Publishing, Bristol, UK, Article ID 012088, 2020.

[17] C. T. Metcalf, W. H. Goetz, Bituminous sandstone mixtures, https://docs.lib.purdue.edu/cgi/viewcontent.cgi?article=2573&context=roadschool.

[18] H. Zhang and H. Li, "Optimization of sandstone concrete pavement materials based on finite element method," *Arabian Journal for Science and Engineering*, vol. 46, no. 11, pp. 10835–10845, 2021.

[19] JTG E42-2005, *Highway Engineering Aggregate Test Regulations*, Ministry of Communications of the People's Republic of China, Beijing, China, 2005, in Chinese.

[20] JTG F40-2004, *Technical Specification for Construction of Highway Asphalt Pavement*, Ministry of Communications of the People's Republic of China, Beijing, China, 2005, in Chinese.

[21] J. B. Metcalf, *NCHRP Synthesis of Highway Practice 235: Application of Full-Scale Accelerated Pavement Testing. TRB*, National Research Council, Washington, DC, USA, 1996.

[22] Mlstestsystems, *MMLS3 Operator's Mannual*, MLS Test Systems Pty Ltd, Stellenbosch, South Africahttps://www.mlstestsystems.com.

[23] Geomedia Research & Development, *SPA Manager Manual*, Geomedia Research & Development, El Paso, TX, USA, 2007.

[24] M. Jurado, N. Gibson, M. Celaya, and S. Nazarian, "Evaluation of asphalt damage and cracking development with seismic pavement analyzer," *Journal of the Transportation Research Board*, vol. 1, no. 2304, pp. 47–54, 2012.

[25] P. He, "Some methods of deleting inordinate values from measuring data," *Aviation Metrology& Measurement Technology*, vol. 15, no. 1, pp. 19-20, 1995.

Research Article

Evaluation of the Effects of Tunnel Lighting Environment on Energy Consumption and Drivers' Reaction Time

Long Zhao,[1] Song Hu,[2] Dongwei Wang,[1] Yujin Guo,[1] and Chaoliang Fu [ID][3]

[1]*China Railway Siyuan Survey and Design Group Co. Ltd., Heping Avenue No. 745, Wuhan 430063, China*
[2]*Guangzhou Highway Engineering Company, Erheng Road No. 6, Guangzhou 510030, China*
[3]*Institute of Highway Engineering, RWTH Aachen University, Aachen North Rhine-Westphalia, Aachen 52074, Germany*

Correspondence should be addressed to Chaoliang Fu; fu@isac.rwth-aachen.de

The 24-hour artificial lighting of the tunnels consumes a large amount of electricity, which means increased environmental damage and carbon footprint for China, which is dominated by thermal power. In order to alleviate the above problems, the effects of the tunnel lighting environment on energy consumption and drivers' reaction time were evaluated by the finite element method and laboratory test to optimize the lighting environments. In this study, based on the Wanxichong extra-long tunnel in Yunnan Province, a 3D tunnel model using DIALux software is established first. Then, the effects of climate conditions, layout method of the lamps, and layout height and reflection of the sidewall material on the average luminance and uniformity on the pavement, the efficiency ratio per unit length, and the actual energy efficiency value were investigated. Finally, the indoor lighting environment simulation experiments were conducted to examine the effect of the type of sidewall materials, contrast, background luminance, and eccentricity on drivers' reaction time. Simulation results show that, under the same climate condition and layout method of lamps, the average luminance and luminance uniformity on the road surface are positively correlated with the reflectivity of the sidewall material. On the clear days, the efficiency ratio per unit length corresponding to the 2 m high sidewall material is the largest, while the efficiency ratio per unit length on cloudy days and mixed days corresponding to the 2.5 m high sidewall material is the largest. In addition, the staggered layout of the lamps at the entrance of the tunnel consumes less power, which is more conducive to energy saving. Experimental results show that, with the increase of background luminance, the reaction time of drivers decreases. Meanwhile, applying energy-storage reflective coating on the sidewalls of the tunnel has a better visual performance than using light yellow ceramic tiles and cement mortar on the sidewalls. This conclusion would provide a lower energy consumption lighting design method and higher drive comfortable for highway tunnels.

1. Introduction

The sustainable development of infrastructure is an important development goal in the future [1–4]. With the development of China's transportation industry, the mileage of tunnels in China has increased rapidly [5–7]. Compared with the open road, the tunnel is a semiclosed tubular structure, resulting in a great difference in luminance inside and outside the tunnel. According to the Rules of Highway Tunnel Lighting Design (JTG/T D70/2-01-2014), the tunnel should be installed in the lighting facilities when the length of the tunnel is higher than 100 m. Therefore, due to the closed characteristics of the tunnel, the

tunnel needs to provide a 24-hour artificial light source to ensure driving safety in the tunnel [8–10]. For this reason, the tunnel lighting system will bear overloading energy consumption and management costs. This means increased environmental damage and carbon footprint for China, which is dominated by thermal power. In addition, although lighting is installed inside the tunnel to reduce the luminance difference, the luminance difference between inside and outside of the tunnel is still largely due to the excessive natural light outside the tunnel. As a result, unique visual phenomena, such as "black hole" and "white hole," still appear in the tunnel entrance and exit section [11–15]. Therefore, it is necessary to optimize the luminance and

energy consumption of the tunnel from the perspective of environmental sustainability.

In order to better solve the above phenomenon in tunnels, researchers have carried out a lot of research on the luminance at the tunnel entrance [16–18]. Guo et al. studied the relationship between the external environment surrounding the tunnel entrance and the driving behavior, and they concluded that driving safety would be influenced by the luminance at the entrance and exit of the tunnel. In this case, they proposed a safety design plan for the tunnel based on the vehicle speed [19]. Angel Pachamanov and Dessislava Pachamanova proposed an optimization method to design the lighting distribution of luminaries for tunnels based on the International Commission on Luminance, and they found that the optimization model can significantly improve the lighting parameters of luminaries, thus resulting in the lowest energy consumption for lighting installations [20]. Liu et al. investigated the effect of light source color on tunnel lighting based on the experiment of reaction times, and they concluded that the appropriate light sources in different sections of tunnel lighting were selected in terms of the influence of light source color on visual performance [21]. Xie et al. used the DIALux software to compare the average luminance of different lamps forms and spacing, and they found that the luminance of staggered sides arraignment of the lamp is the highest when the layout spacing of lamps was the same, while the luminance of the lamps with centerline sideways is the worst [22]. Na et al. explored the effects of the different combinations of lighting power and the installation space on surface luminance and uniformity on the road, and they concluded that when the power is small and the installation space is large, the surface luminance becomes smaller, but uniformity is better [23]. Zhang et al. optimized the lighting environment at the entrance of highway tunnels by using the simulation method and found that the change of natural luminance is the strongest within 5 m from the tunnel entrance, while when the distance is larger than 5 m, the change of natural luminance decreases significantly [24]. Yang et al. investigated the effect of white LED and high-pressure sodium lamp on the reaction time of drivers under different background luminance, and they concluded that the white LED can provide a shorter reaction time for drivers [25]. Cai et al. studied the optimal values of contrast revealing coefficient under different lighting systems, and they found that the optimal value under symmetric lighting was 0.2 and the optimal value under counter-beam lighting was 0.85 [26].

In summary, the tunnel lighting environment design, including climate condition, sidewall, pavement, and the layout of the lamp and vault, is different from the road lighting and has obvious particularity and importance. On the one hand, the energy efficiency of artificial light sources and the luminance and luminance uniformity on the pavement are influenced by the lighting environment. On the other hand, the drivers' reaction time also has a close relationship with the lighting environment. In this case, to investigate and optimize the complex and changeable lighting environment in the tunnel, based on the Wanxichong extra-long tunnel in Yunnan Province, the simulation

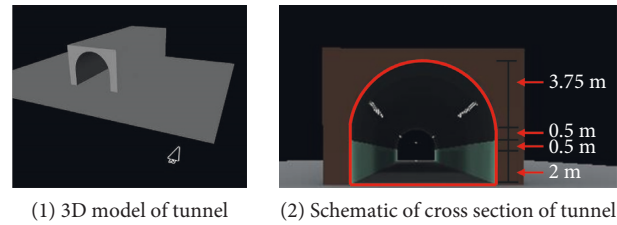|	
(1) 3D model of tunnel	(2) Schematic of cross section of tunnel

FIGURE 1: The three-dimensional simulation model of the tunnel: (a) 3D model of tunnel and (b) schematic of cross section of tunnel.

and experimental research will be conducted at the entrance section, middle section, and exit section of the tunnel. Firstly, a 3D tunnel model using DIALux software is established. The 30 m long pavement surface with both sides inside the tunnel is set as the measurement area, and the effects of different climate conditions, layout methods of lamps, and the reflectivity of sidewall materials on the tunnel lighting quality and energy-saving effect at the entrance and exit are investigated. Based on the simulation results, the optimal lighting parameters at the entrance and exit of the tunnel with the different conditions will be discussed. Finally, the indoor lighting environment simulation system of the highway tunnel is established, and the test parameters such as type of sidewall materials, contrast, background luminance, and eccentricity are selected to investigate the reaction time of the participants.

2. Simulation Research

2.1. 3D Model Establishment of the Tunnel. The purpose of the lighting simulation is to optimize the lighting conditions at the entrance of the Wanxichong extra-long tunnel in Yunnan. The DIALux simulation software was selected to carry out a 3D simulation analysis of the tunnel with different climate conditions (clear, cloudy, and mixed) combined with lamps and reflections from the inner wall of the tunnel. The actual tunnel geometry at the tunnel entrance is complex, and it is difficult to directly establish a tunnel model using the space module of the DIALux software. However, the tunnel can be disassembled according to its geometric size. As shown in Figure 1, the cross section of the three-dimensional simulation model of the tunnel can be composed of a circular arch and multiple cubes. The length, width, and height of the tunnel model are 200 m, 8 m, and 6.75 m, respectively. In addition, according to the characteristics of the tunnel sidewalls in Chongqing, the geometric dimensions of the bottom of the model were divided into three heights from bottom to top during the model building process, which were 2 m, 0.5 m, and 0.5 m, respectively. In this case, the reflectivity of the inner side material at different heights can be adjusted.

Compared with the open section of the road, the tunnel is a semiclosed tubular structure, resulting in a great difference in luminance inside and outside the tunnel. Although a lamp is installed inside the tunnel to reduce the luminance difference, due to the excessive natural light outside the tunnel and the requirement of energy saving in tunnel operation, the luminance difference between inside and outside of the tunnel is still large. As a result, unique

TABLE 1: The layout parameters of the lamps.

Type	Spacing	Height	Installed angle
Staggered lighting	1.5	5	30°
Middle lighting	0.75	6.75	90°

(1) Schematic of lamp layout

(2) Schematic of layout height of reflective materials of the side walls
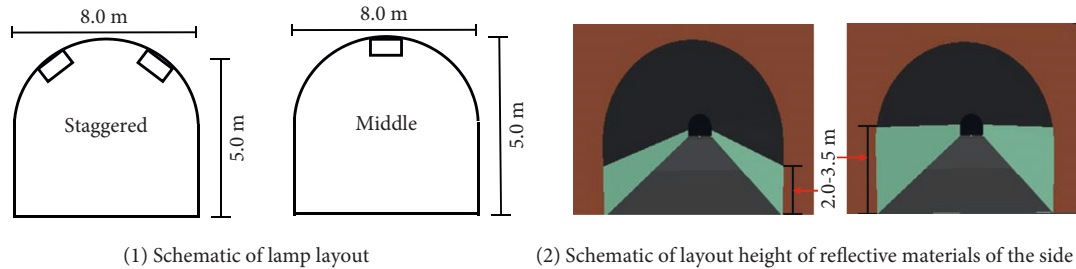
FIGURE 2: The schematic of lamp layout and layout height of reflective materials of the sidewall. (a) Schematic of lamp layout. (b) Schematic of layout height of reflective materials of the sidewall.

visual phenomena such as "black holes" and "white holes" will appear in the tunnel entrance and exit section. Therefore, in this simulation, the 30 m long road surface with the opening on both sides of the tunnel is set as the measurement area, and the luminance on the road surface under different working conditions is calculated. The entrance is the southward tunnel, and the exit is the northward tunnel.

2.2. Scheme Design of the Simulation.

The luminance at the entrance of the tunnel is affected by many factors, such as the natural light outside the tunnel, the light source of lamps in the tunnel, and the materials of the sidewall. Therefore, in this section, these above factors will be considered in the 3D simulation analysis of the tunnel, including the different climate conditions (clear, cloudy, and mixed days), layout arrangement of lamps, and reflectivity of the material of the sidewall of the tunnel.

2.2.1. Climate Conditions.

The Wanxichong extra-long tunnel is located in the northern hemisphere. On December 22 of each year, the sun shines directly on the tropic of Capricorn, and the northern hemisphere gets the least amount of sunlight at this time. Therefore, in this study, the different climate conditions (clear, cloudy, and mixed days) were considered. The noon with the highest sunlight intensity and the smallest sun elevation angle on December 22 is selected as the natural light environment for simulation analysis. At this moment, the sunlight can directly enter the entrance of the southward tunnel on clear days. In addition, there is little direct sunlight at the entrance of the southward tunnel and exit of the northward tunnel when the climate condition is cloudy and mixed days.

2.2.2. Layout Method of the Lamps.

In this study, the LED lights for tunnels with a color temperature of 4500 K and a power of 160 W produced by Yaming Company, Shanghai, were selected. The layout of the lamps has a great influence on the lighting quality of the tunnel. For the same type and quantity of lamps, the average luminance and uniformity on the road surface in the tunnel will vary greatly due to the layout method of the lamps. When the average luminance on the road surface is large and the uniformity is low, the zebra effect is likely to occur, which endangers driving safety. In this case, this study intends to adopt two common layouts of lamps in tunnels: double-sided staggered lighting and middle lighting. The detailed layout methods of the lamps are shown in Table 1 and Figure 2(a).

2.2.3. Layout Height and Reflectivity of the Sidewall Material.

The inner sidewall material of the tunnel has a reflective synergistic effect on the luminance on the road surface in the tunnel, and the greater the reflectivity, the better the material's reflection performance. Therefore, in order to investigate the effects of reflectivity on the luminance quality, the reflection coefficients of the inner sidewall material were taken as 0.75, 0.80, and 0.85. In addition, the sidewall without sidewall materials and vault shall be sprayed with a dark gray fire-retardant coating with a reflectivity of 0.1. The asphalt pavement was selected as the surface material of the road in the tunnel, and the reflection coefficient was taken as 0.2. Based on the actual situation of the tunnel, 2 m, 2.5 m, 3 m, and 3.5 m are, respectively, taken as the layout heights of the sidewall materials, as shown in Figure 2.

In summary, with the climate conditions (clear, cloudy, and mixed days), the reflectivity (0.75, 0.80, and 0.85) of the sidewall material, the layout height of lamps (2 m, 2.5 m, 3 m, and 3.5 m), the layout method of lamps (staggered and middle) as the independent variables, and the average luminance, uniformity, and energy efficiency value as the dependent variables, the lighting at the entrance and exit of the tunnel is optimized. Combined with these above factors, the simulation schemes of the 3D model of the tunnel are shown in Table 2.

3. Experimental Research

The lighting luminance in the tunnel will have an impact on the driver's reaction time. According to the calculation formula of the stopping sight distance, the length of the

TABLE 2: The simulation schemes of the 3D model of the tunnel.

No.	Reflectivity of sidewall	Climate condition	Layout method	Layout height of sidewall (m)
1	0.75	Clear	Staggered	2
2	0.75	Clear	Staggered	2.5
3	0.75	Clear	Staggered	3
4	0.75	Clear	Staggered	3.5
5	0.75	Clear	Middle	2
6	0.75	Clear	Middle	2.5
7	0.75	Clear	Middle	3
8	0.75	Clear	Middle	3.5
9	0.75	Cloudy	Staggered	2
10	0.75	Cloudy	Staggered	2.5
11	0.75	Cloudy	Staggered	3
12	0.75	Cloudy	Staggered	3.5
13	0.75	Cloudy	Middle	2
14	0.75	Cloudy	Middle	2.5
15	0.75	Cloudy	Middle	3
16	0.75	Cloudy	Middle	3.5
17	0.75	Mixed	Staggered	2
18	0.75	Mixed	Staggered	2.5
19	0.75	Mixed	Staggered	3
20	0.75	Mixed	Staggered	3.5
21	0.75	Mixed	Middle	2
22	0.75	Mixed	Middle	2.5
23	0.75	Mixed	Middle	3
24	0.75	Mixed	Middle	3.5
25	0.8	Clear	Staggered	2
26	0.8	Clear	Staggered	2.5
27	0.8	Clear	Staggered	3
28	0.8	Clear	Staggered	3.5
29	0.8	Clear	Middle	2
30	0.8	Clear	Middle	2.5
31	0.8	Clear	Middle	3
32	0.8	Clear	Middle	3.5
33	0.8	Cloudy	Staggered	2
34	0.8	Cloudy	Staggered	2.5
35	0.8	Cloudy	Staggered	3
36	0.8	Cloudy	Staggered	3.5
37	0.8	Cloudy	Middle	2
38	0.8	Cloudy	Middle	2.5
39	0.8	Cloudy	Middle	3
40	0.8	Cloudy	Middle	3.5
41	0.8	Mixed	Staggered	2
42	0.8	Mixed	Staggered	2.5
43	0.8	Mixed	Staggered	3
44	0.8	Mixed	Staggered	3.5
45	0.8	Mixed	Middle	2
46	0.8	Mixed	Middle	2.5
47	0.8	Mixed	Middle	3
48	0.85	Mixed	Middle	3.5
49	0.85	Clear	Staggered	2
50	0.85	Clear	Staggered	2.5
51	0.85	Clear	Staggered	3
52	0.85	Clear	Staggered	3.5
53	0.85	Clear	Middle	2
54	0.85	Clear	Middle	2.5
55	0.85	Clear	Middle	3
56	0.85	Clear	Middle	3.5
57	0.85	Cloudy	Staggered	2
58	0.85	Cloudy	Staggered	2.5
59	0.85	Cloudy	Staggered	3
60	0.85	Cloudy	Staggered	3.5

Table 2: Continued.

No.	Reflectivity of sidewall	Climate condition	Layout method	Layout height of sidewall (m)
61	0.85	Cloudy	Middle	2
62	0.85	Cloudy	Middle	2.5
63	0.85	Cloudy	Middle	3
64	0.85	Cloudy	Middle	3.5
65	0.85	Mixed	Staggered	2
66	0.85	Mixed	Staggered	2.5
67	0.85	Mixed	Staggered	3
68	0.85	Mixed	Staggered	3.5
69	0.85	Mixed	Middle	2
70	0.85	Mixed	Middle	2.5
71	0.85	Mixed	Middle	3
72	0.85	Mixed	Middle	3.5

(1) lighting environment system of the highway tunnel

(2) Data acquisition

Figure 3: The lighting environment system and data acquisition. (a) Lightning environment system of highway tunnel. (b) Data acquisition.

reaction time has a direct impact on the stopping sight distance. Therefore, the value of the lighting luminance in the tunnel will indirectly affect the stopping sight distance in the tunnel. In this study, the purpose of the experiments is to measure the reaction time of the participants to observe small objects under different luminance levels by simulating the lighting environment system of the highway tunnel.

The lighting environment simulation system of a highway tunnel consists of three parts: observation box, optical system, and light box, as shown in Figure 3. The ratio of the simulated device to the actual tunnel size is 1 : 10. The width of the pavement inside the tunnel is 1 m, the height of the sidewall is 0.6 m, and the vault is made of a 1/3 circle with an approximate diameter of 0.57 m. The entire observation box is made of the wood skeleton and filled with plywood. The current main-stream light source (80W LED light) was selected, and its luminance range (1–15 cd/m2) can be adjusted to simulate the luminance level of the middle section of the tunnel. A random light spot is used to simulate the obstacles that may appear when driving through the tunnel. The diameter of the light spot is 25 mm, which can completely fall in the fovea of the participants' eyes. The luminance of the light spot and the luminance of the background are provided by the same light source to ensure that their luminance has the same spectral distribution. In addition, the luminance of the light spot can be adjusted arbitrarily to form a different contrast with the background. Reaction time refers to the time difference between the light spot appearing and the participants pressing the button under each test condition.

To investigate the reaction time of the participants, the test parameters such as type of sidewall materials, contrast, background luminance, and eccentricity were selected for the experiments, as shown in Table 3. In this experiment, three kinds of sidewall materials were selected, including cement mortar, light yellow ceramic tile, and energy-storage reflective coating. These kinds of background luminance, including 2 cd/ m2, 6 cd/m2, and 10 cd/m2, were used. Three kinds of eccentricity were selected, including 0°, 10°, and 20°. In addition, two kinds of contrast (0.2 and 0.5) were used. Ten people were selected as test subjects, and their ages ranged from 24 to 30 years. All participants had normal color vision and corrected visual acuity. In addition, all participants understood the purpose of the experiments. Test procedures were as follows:

(1) Before starting each group of experiments, a luminance meter was used to calibrate the luminance of the background and light spot of the two-contrast ratio. All participants spent 30 minutes to adapt to the darker experimental environment. Both eyes of the participants were used to observe the objects during the experiment, and they needed to ensure that both eyes were always looking at the cross mark in front of them.

(2) The observer holds the reaction time trigger button for testing and records the reaction time. If the subject does not respond or the reaction time exceeds a certain interval when the light spot appears, it will be regarded as invalid data.

TABLE 3: Value of the test parameters.

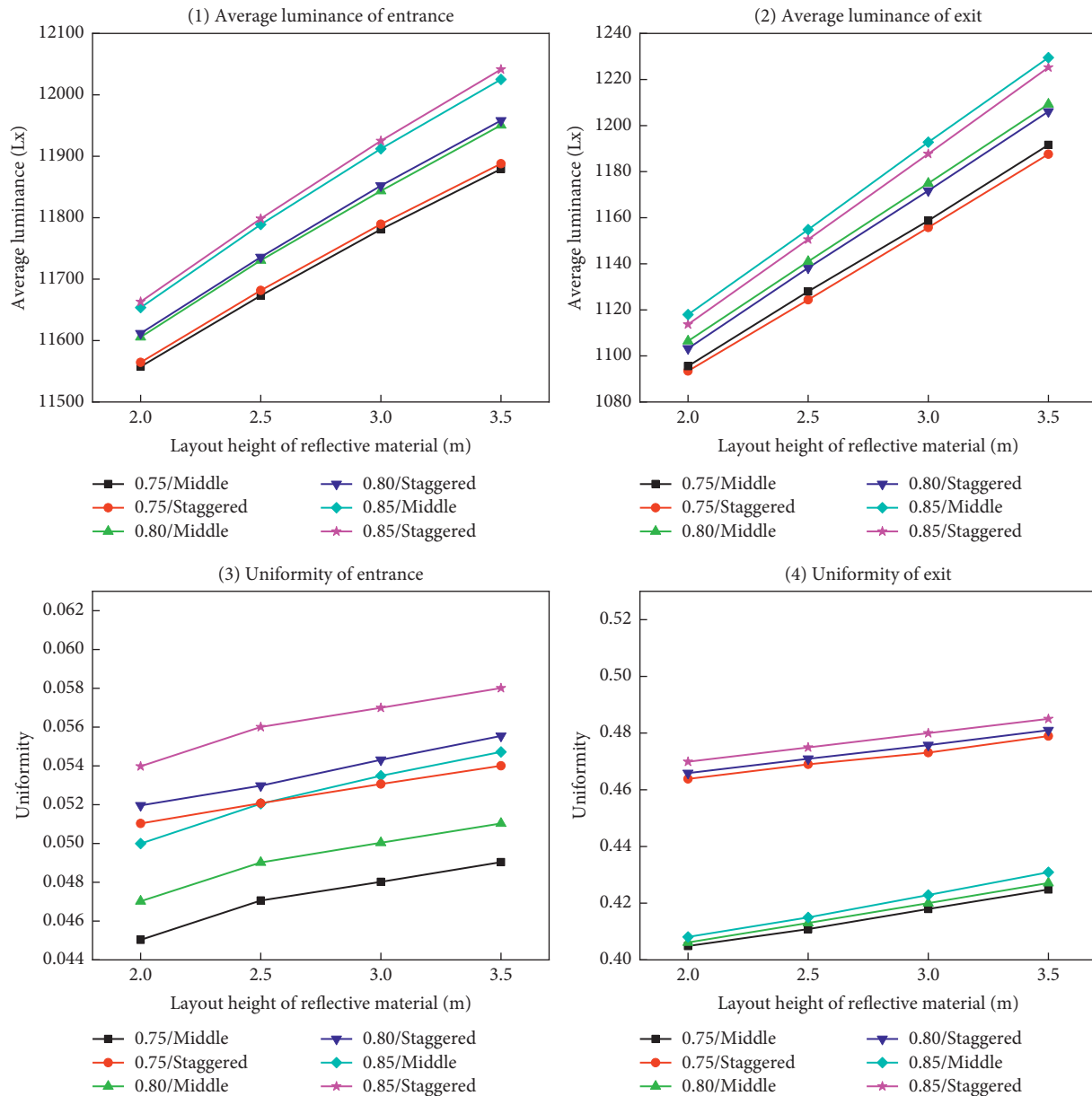| Test parameters	Value		
Sidewall materials	Cement mortar	Light yellow ceramic tile	Energy-storage reflective coating
Contrast (C)	0.2		0.4
Background luminance	2	6	10
Eccentricity (θ)	0°	10°	20°

FIGURE 4: The average luminance and uniformity on the road surface on the clear days. (a) Average luminance of entrance. (b) Average luminance of exit. (c) Uniformity of entrance. (d) Uniformity of exit.

(3) The tests are performed in order of sidewall material type. Namely, after testing all the experimental schemes of a certain sidewall material, the experiment of the next material is conducted. In addition, in order to ensure the mental state of the participants, the duration of each experiment should not exceed two hours.
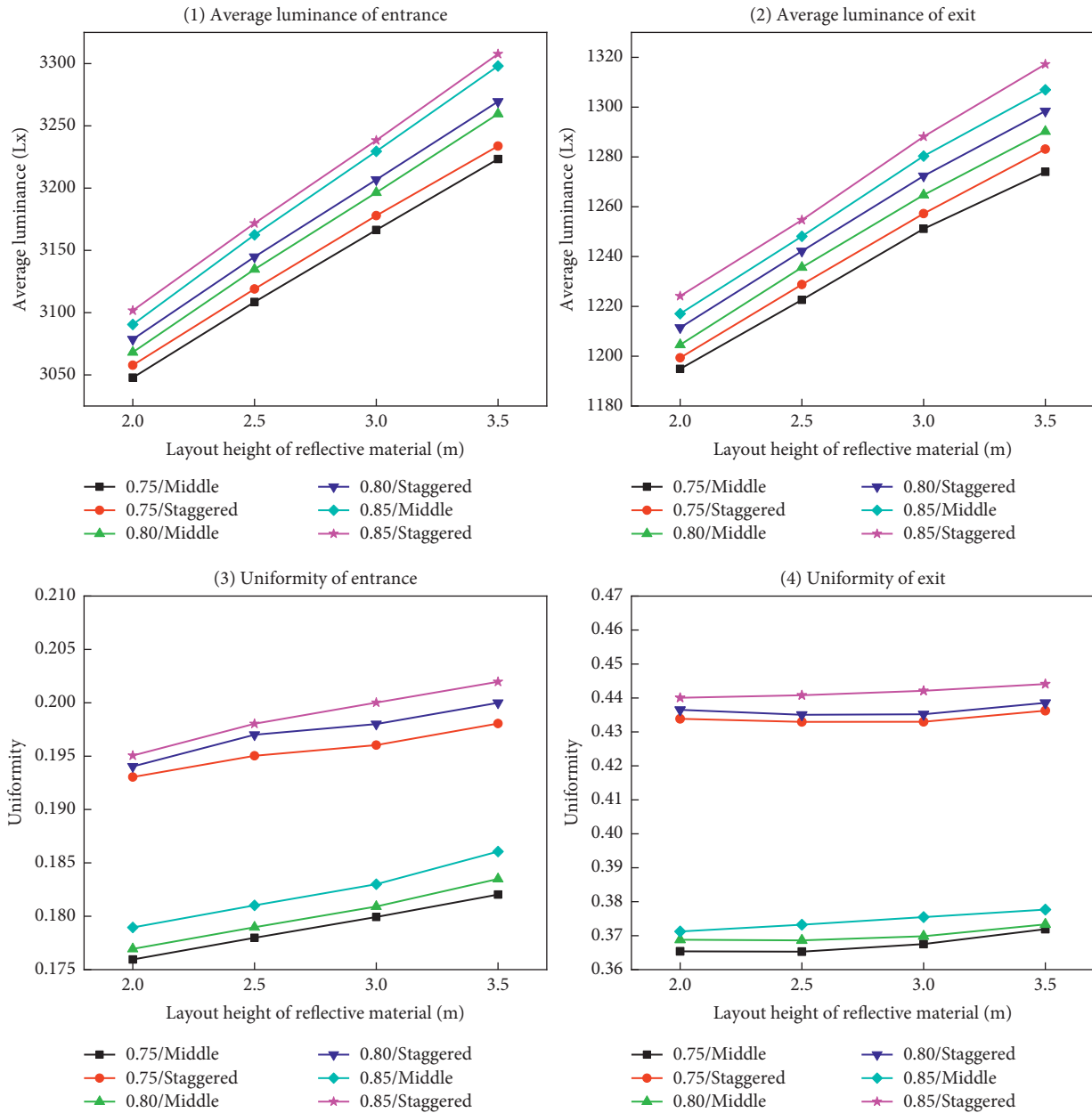
FIGURE 5: The average luminance and uniformity on the road surface on cloudy days. (a) Average luminance of entrance. (b) Average luminance of exit. (c) Uniformity of entrance. (d) Uniformity of exit.

(4) Finally, the reaction times of each participant were obtained under different conditions through the procedures of the experiment. The mean reaction time of the 10 participants was calculated.

4. Results and Discussion

4.1. Simulation Results and Discussion

4.1.1. Effect of Climate Condition on Average Luminance and Uniformity. The average luminance and luminance uniformity at the entrance and exit of the tunnel on clear days are shown in Figure 4. It can be seen that inner sidewall materials with high reflectivity at the entrance and exit sections of the

tunnel can improve the average luminance on the road surface. When the layout method of lamps and the layout height of sidewall material is the same, as the reflectivity of the sidewall material increases from 0.75 to 0.85, the average luminance on the road surface at the entrance of the tunnel increases by 99 lx, 117 lx, 136 lx, and 149 lx, while the average luminance at the exit of the tunnel increases by 20 lx, 26 lx, 32 lx, and 36 lx. In addition, the sidewall material with high reflectivity is also beneficial in improving the luminance uniformity on the road surface. Another interesting phenomenon is that the average luminance at the entrance is larger, but the luminance uniformity is lower than that at the tunnel exit. This is because the entrance of the southward tunnel is directly irradiated by sunlight, which makes the
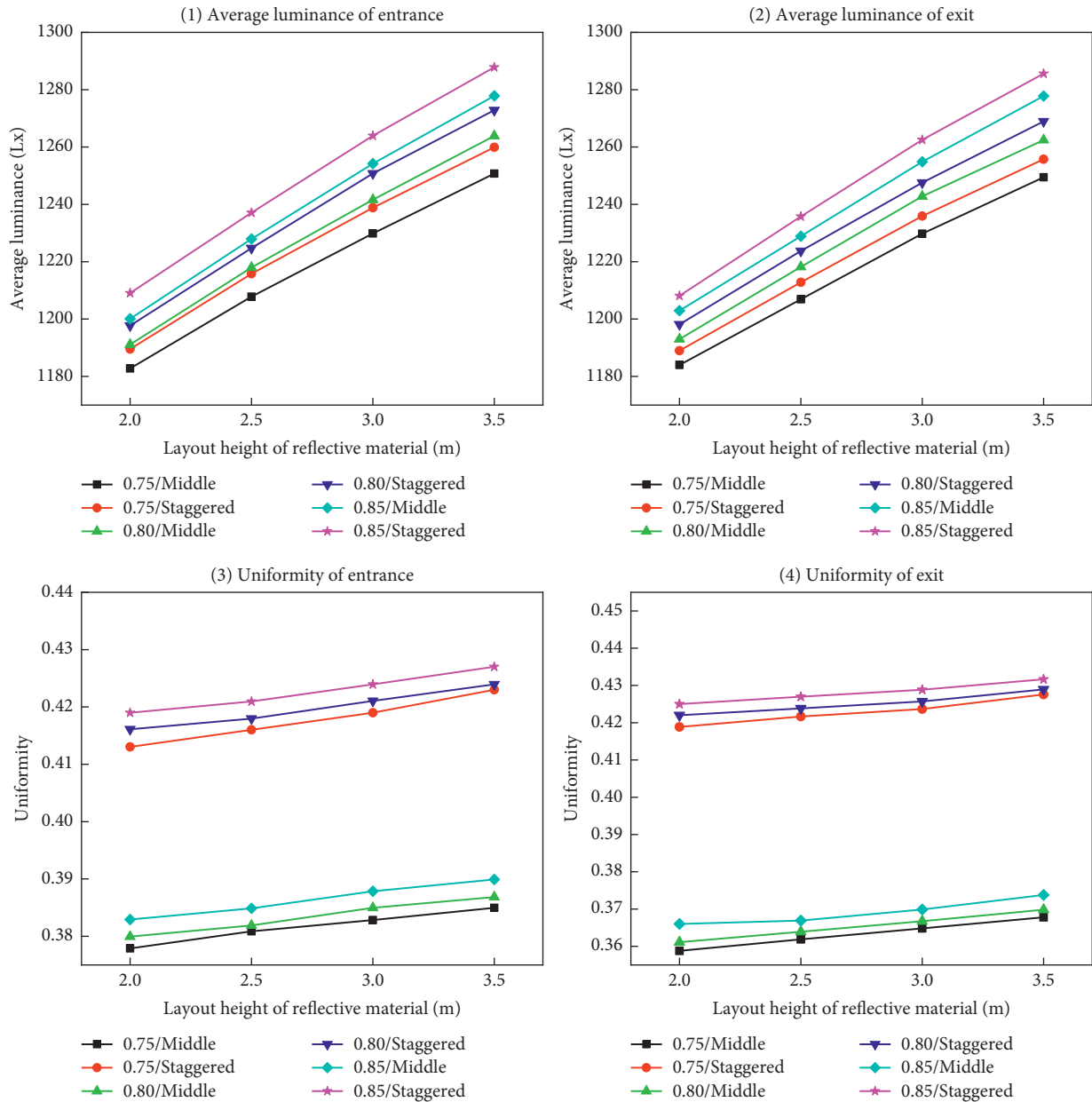
FIGURE 6: The average luminance and uniformity on the road surface on mixed days. (a) Average luminance of entrance. (b) Average luminance of exit. (c) Uniformity of entrance. (d) Uniformity of exit.

luminance distribution of the southward tunnel entrance extremely uneven, which seriously affects the driver's ability to distinguish the front target. Therefore, the arrangement of high-reflectivity sidewall materials at the tunnel entrance is a measure to improve the luminance uniformity, which is conducive to safe driving.

In addition, it can be observed that, on cloudy days, the average luminance and luminance uniformity at the exit and entrance of the tunnel are similar, as shown in Figure 5. When the layout method of lamps and the layout height of sidewall material are the same, as the reflectivity of the sidewall material increases from 0.75 to 0.85, the average luminance on the road surface at the entrance of the tunnel increases by 18 lx, 20 lx, 25 lx, and 28 lx. Also, the luminance

conditions of the mixed days are similar to those of clear days, as shown in Figure 6. Namely, the average luminance on the road at the entrance to the south is higher than that of the entrance to the north, while the luminance uniformity at the entrance to the south is relatively low compared with the exit to the north. When the layout method of lamps and the layout height of sidewall material are the same, as the reflectivity of the sidewall material increases from 0.75 to 0.85, the average luminance on the road surface at the entrance of the tunnel increases by 44 lx, 53 lx, 63 lx, and 75 lx, while the average luminance at the exit of the tunnel increases by 22 lx, 25 lx, 31 lx, and 35 lx. The uniformity at the entrance and exit of the tunnel increases with the reflectivity of the sidewall material, but the improvement at

TABLE 4: Efficiency ratio per unit length of sidewall material at tunnel entrance.

Climate condition	Reflectivity	Layout height			
		2	2.5	3	3.5
Clear days	0.75	2.72%	2.58%	2.48%	2.37%
	0.80	2.94%	2.81%	2.67%	2.58%
	0.85	3.15%	3.04%	2.91%	2.78%
Cloudy days	0.75	4.35%	4.64%	4.59%	4.55%
	0.80	5.06%	5.22%	5.07%	4.76%
	0.85	5.07%	5.28%	5.21%	4.97%
Mixed days	0.75	5.22%	5.24%	4.92%	4.79%
	0.80	5.47%	5.51%	5.30%	5.19%
	0.85	5.87%	5.92%	5.68%	5.60%

TABLE 5: Efficiency ratio per unit length of sidewall material at tunnel exit.

Climate condition	Reflectivity	Layout height			
		2	2.5 (%)	3	3.5 (%)
Clear days	0.75	7.35%	7.21	7.10%	7.03
	0.80	7.41%	7.28	7.65%	7.49
	0.85	8.20%	7.87	8.25%	7.96
Cloudy days	0.75	5.15%	4.71	4.90%	5.04
	0.80	5.88%	5.29	5.39%	5.46
	0.85	6.62%	5.88	5.85%	5.90
Mixed days	0.75	5.07%	5.22	5.31%	4.97
	0.80	5.80%	5.80	6.28%	5.79
	0.85	6.52%	6.38	6.76%	6.21

the exit is relatively small. Therefore, the sidewall material with high reflectivity can improve the average luminance and luminance uniformity on the road at the entrance and exit when the climate condition is mixed days.

4.1.2. Effect of Layout Height of Sidewall Material on Efficiency Ratio per Unit Length.

The layout height of the sidewall material has a significant impact on the improvement of the luminance of the road surface, thus affecting its energy-saving effect. In order to get the optimal layout height, the efficiency ratio per unit length was used as the evaluation index. This evaluation index is to first calculate the percentage of luminance improvement caused by the arrangement of sidewall materials with different heights in the tunnel relative to the whole sidewall sprayed with gray fire-retardant coating and then divide the above percentage by the height of the sidewall material under the corresponding working conditions to obtain the efficiency ratio per unit length.

The efficiency ratio per unit length with different layout heights of sidewall material is shown in Tables 4 and 5. According to the data in the table, the efficiency ratio per unit length at the tunnel entrance under different climate conditions is compared. It can be seen that, on the clear days, the efficiency ratio per unit length corresponding to the 2 m high sidewall material at the tunnel entrance is the largest. When the reflectivity of the sidewall material is 0.75, 0.80, and 0.85, the efficiency ratio per unit length is 2.72%, 2.94%, and 3.15%, respectively. On the cloudy days and mixed days, the efficiency ratio per unit length corresponding to the

2.5 m high sidewall material at the tunnel entrance is the largest. When the reflectivity of the sidewall material is 0.75, 0.80, and 0.85, the unit length efficiency ratios for cloudy days are 4.64%, 5.22%, and 5.28%, respectively, and as the reflectivity increases, the unit length efficiency ratio for mixed days also increases from 5.24% to 5.92%.

The efficiency ratio per unit length at the tunnel exit under different climate conditions is compared. It can be observed that, on clear days, the efficiency ratio per unit length corresponding to the 2 m high sidewall material at the tunnel exit is the largest when the reflectivity of the sidewall material is 0.75. However, the efficiency ratio per unit length corresponding to the 3 m high sidewall material at the tunnel exit is the largest when the reflectivity of the sidewall material is 0.80 and 0.85. On cloudy days, the efficiency ratio per unit length corresponding to the 2 m high sidewall material at the tunnel exit is the largest. When the reflectivity of the sidewall material is 0.75, 0.80, and 0.85, the efficiency ratio per unit length on cloudy days is 5.15%, 5.88%, and 6.62%, respectively. When the climate condition is mixed days, the efficiency ratio per unit length corresponding to the 3 m high sidewall material at the tunnel exit is the largest. When the reflectivity is 0.75, 0.80, and 0.85, the efficiency ratio per unit length in mixed days is 5.31%, 6.28%, and 6.76%, respectively.

4.1.3. Effect of Layout Method of Lamps on Actual Energy Efficiency Value.

The actual energy efficiency value refers to the power consumption of lamps when the luminance value reaches 100lx per square meter on the road surface. In other
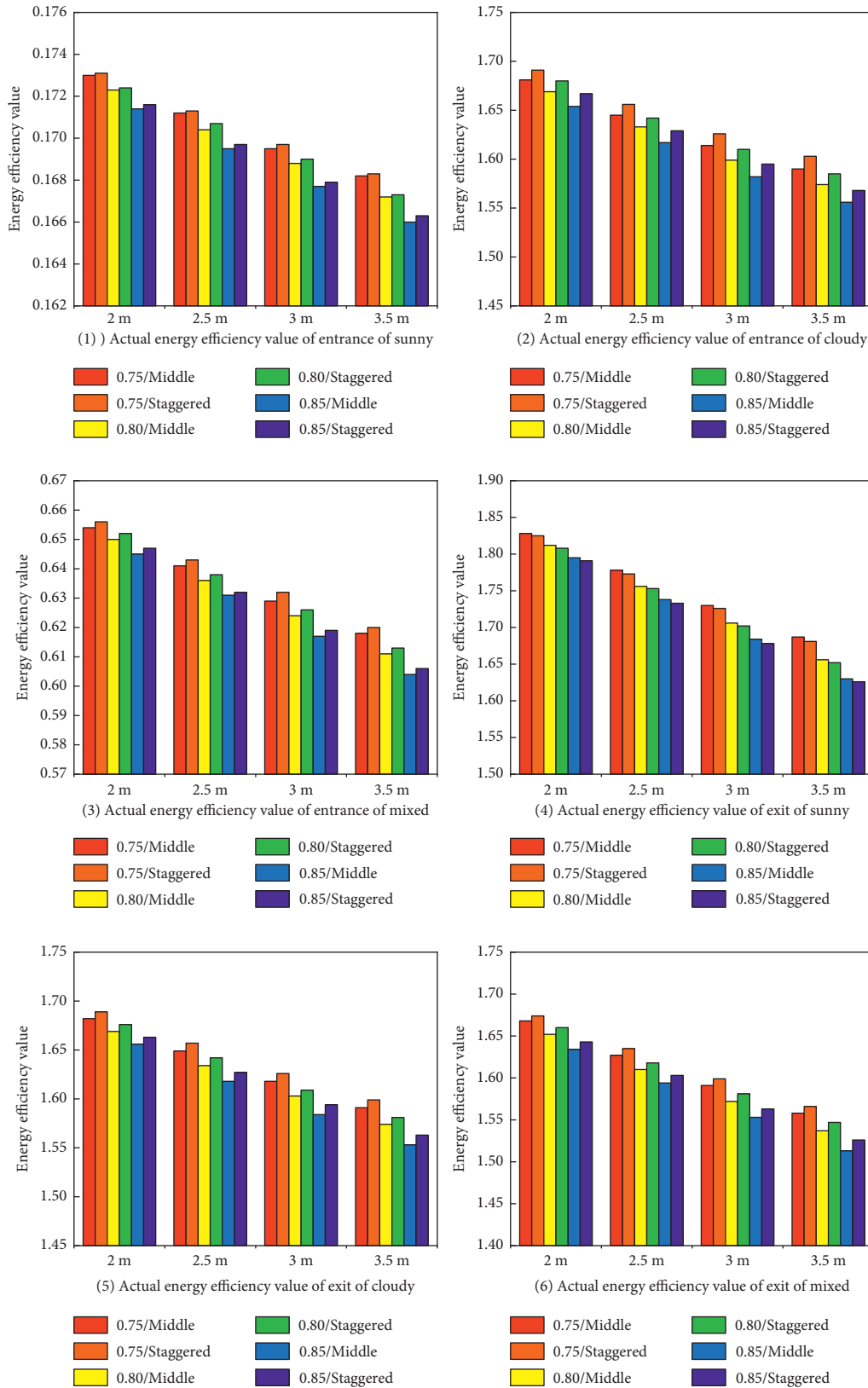
FIGURE 7: The actual energy efficiency value with different layout methods of lamps. (a) Actual energy efficiency value of entrance of sunny. (b) Actual energy efficiency value of entrance of cloudy. (c) Actual energy efficiency value of entrance of mixed. (d) Actual energy efficiency value of exit of sunny. (e) Actual energy efficiency value of exit of cloudy. (f) Actual energy efficiency value of exit of mixed.
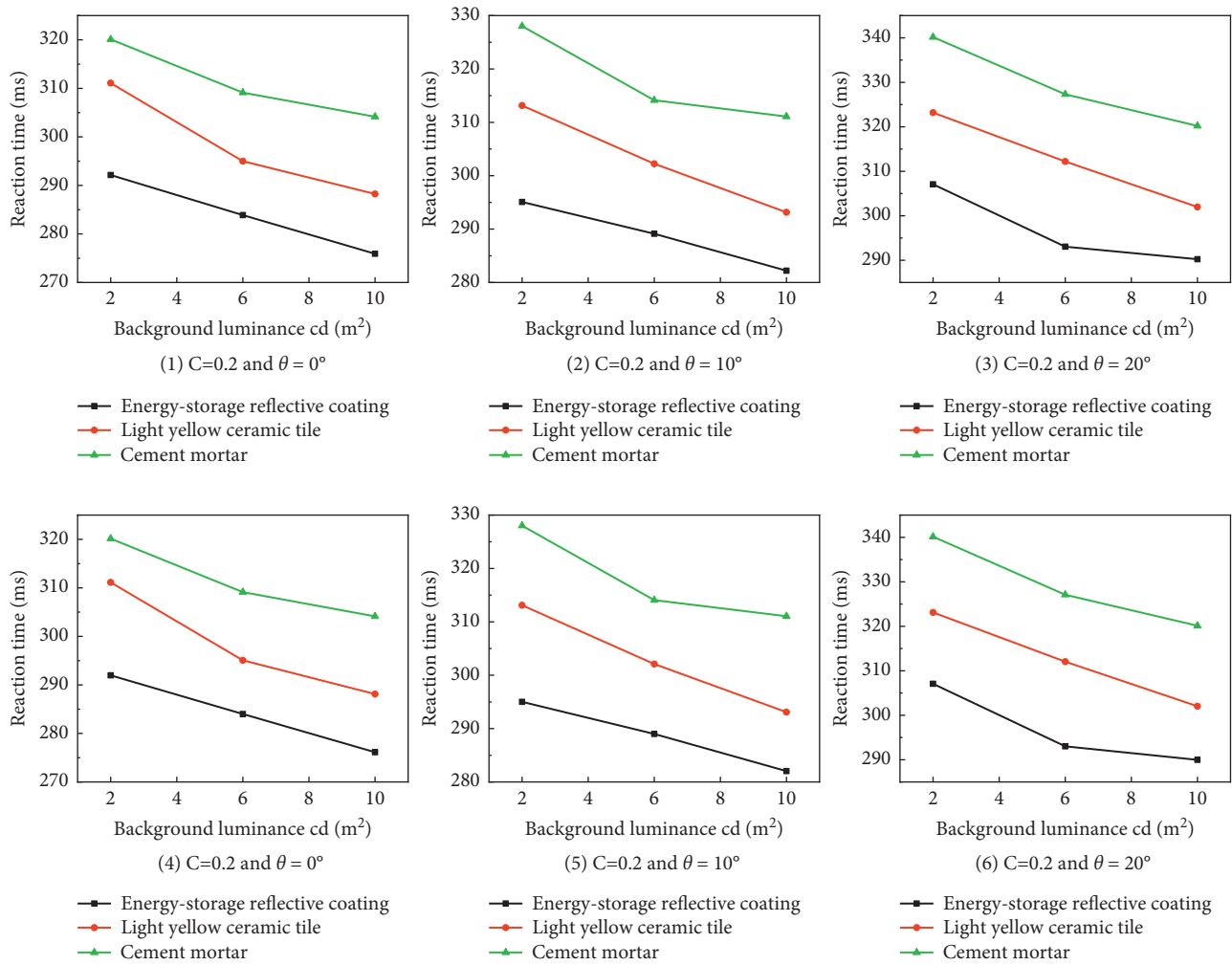
FIGURE 8: The mean value of reaction time of participants at different conditions. (a) $C = 0.2$ and $\theta = 0°$. (b) $C = 0.2$ and $\theta = 10°$. (c) $C = 0.2$ and $\theta = 20°$. (d) $C = 0.2$ and $\theta = 0°$. (e) $C = 0.2$ and $\theta = 10°$. (f) $C = 0.2$ and $\theta = 20°$.

words, the smaller the actual energy efficiency value is, the less electric energy consumed is. The actual energy efficiency value corresponding to the entrance and exit of the tunnel under the two layout forms is shown in Figure 7. When the climate condition is clear days and the reflectivity of the sidewall is constant since the entrance of the tunnel is greatly affected by the direct sunlight, the actual energy efficiency value of the lamp is small at this time, and the difference in the actual energy efficiency values corresponding to the two layout forms is only 0.06%~0.18%. When the climate condition is cloudy and mixed days, the difference in the actual energy efficiency values of the two layout forms is 1%. In other words, the staggered layout of the lamps at the entrance of the tunnel consumes less power, which is more conducive to energy saving. In addition, when the climate condition is clear days, the actual energy efficiency value with the middle layout at the exit of the tunnel is 0.16%~ 0.35% lower than that of the staggered layout. When the climate condition is cloudy and mixed days, the actual energy efficiency value with a staggered layout at the entrance of the tunnel is 0.42%~0.64% lower than that of staggered layout.

4.2. Experimental Results and Discussion. The relationship between the reaction time of participants and background luminance under two kinds of contrast is described in Figure 8. As shown in Figures 8(a)–8(c), it can be seen that the reaction time of the participants decreases with the increase of background luminance. When the background luminance is 2 cd/m2, the reaction time is the longest. When the background luminance reaches 10 cd/m2, the reaction time under the action of three kinds of sidewall materials all reached the minimum, and the reduction speed of the reaction time slowed down with the increase of background luminance. When the background luminance is within the range of 2 cd/m2–10 cd/m2, the response time corresponding to the energy-storage reflective coating is shorter than that of the other two materials. When the contrast is 0.2, the eccentricity is 0°, and the background luminance is 10 cd/m2, the minimum response time can be obtained as 276 ms. In addition, the response time corresponding to the energy-storage reflective coating on the sidewalls decreases slightly less than the other two materials with the increase of the background luminance.

In addition, when the contrast is 0.5, the eccentricity is 0°, and the sidewall materials of the tunnel are energy-storage reflective coating, the driver's reaction time decreased from 271 ms to 256 ms as the background luminance increased from 2 cd/m2 to 10 cd/m2. When the contrast is 0.5, the eccentricity is 10°, and the sidewall materials of the tunnel are energy-storage reflective coating, the driver's reaction time decreased from 282 ms to 263 ms as the background luminance increased from 2 cd/m2 to 10 cd/m2. When the contrast is 0.5, the eccentricity is 20°, the sidewall materials of the tunnel are energy-storage reflective coating, and the driver's reaction time decreases from 296 ms to 277 ms as the background luminance increases from 2 cd/m2 to 10 cd/m2. The change law of reaction time corresponding to the other two materials is similar. In summary, with the increase of background luminance, the reaction time of drivers decreases. Meanwhile, applying energy-storage reflective coating on the sidewalls of the tunnel has a better effect than using light yellow ceramic tiles and cement mortar on the sidewalls.

5. Conclusion

The 24-hour artificial lighting of the tunnels consumes a large amount of electricity, which means increased environmental damage and carbon footprint for China, which is dominated by thermal power. In this study, based on the Wanxichong extra-long tunnel in Yunnan Province, the simulation and experimental research were conducted at the entrance section, middle section, and exit section of the tunnel to evaluate the energy consumption of the tunnel from the perspective of environmental sustainability. The effects of different climate conditions, layout methods of lamps, and the reflectivity of sidewall materials on the tunnel lighting quality and energy-saving effect at entrance and exit are investigated by using the simulation method. At the same time, the test parameters such as type of sidewall materials, contrast, background luminance, and eccentricity are selected to investigate the reaction time of the participants by using the indoor lighting environment simulation system of a highway tunnel. The main conclusions are summarized as follows:

(1) The greater the brightness of natural light, the more obvious the improvement effect of the sidewall material on the lighting quality at the entrance and exit of the tunnel. When the reflectivity is constant, the improvement of the luminance and luminance uniformity on the road surface by the sidewall material is much greater on clear days than on cloudy days, while the mixed days are between the both. With the same climate condition and layout method of lamps, the average luminance and luminance uniformity are positively correlated with the reflectivity of the sidewall material. Therefore, the high-reflectivity sidewall material on the sidewall is beneficial to improving the lighting quality and achieving the purpose of energy-saving lighting. For the same climate condition and sidewall material reflectivity, the higher the height of the sidewall material, the greater the average luminance and luminance uniformity at the entrance and exit of the tunnel. When the reflectivity of the sidewall material is constant, the use of staggered lights in the tunnel can greatly improve the luminance uniformity on the road, which is more conducive to safe driving.

(2) Firstly, the efficiency ratio per unit length at the tunnel entrance under different climate conditions is compared. It can be seen that, on the clear days, the efficiency ratio per unit length corresponding to the 2 m high sidewall material at the tunnel entrance is the largest, but on the cloudy days and mixed days, the efficiency ratio per unit length corresponding to the 2.5 m high sidewall material at the tunnel entrance is the largest. The efficiency ratios per unit length at the tunnel exit under different climate conditions are compared. It can be observed that, on clear days, the efficiency ratio per unit length corresponding to the 2 m high sidewall material at the tunnel exit is the largest when the reflectivity of the sidewall material is 0.75. However, the efficiency ratio per unit length corresponding to the 3 m high sidewall material at the tunnel exit is the largest when the reflectivity of the sidewall material is 0.80 and 0.85. On cloudy days, the efficiency ratio per unit length corresponding to the 2 m high sidewall material at the tunnel exit is the largest. When the climate condition is mixed days, the efficiency ratio per unit length corresponding to the 3 m high sidewall material at the tunnel exit is the largest.

(3) On cloudy and mixed days, double-sides staggered lighting should be used for the entrance and exit of the tunnel, which can achieve the maximum actual energy efficiency value, and this layout method also can improve the lighting quality of the tunnel. On clear days, it is greatly affected by natural light, and the actual energy efficiency values of the two layout methods are a little different, but double-side staggered lighting can improve the luminance uniformity, so it is advisable to use double-side staggered lighting on clear days.

(4) The reaction time of the participants decreases with the increase of background luminance, and the reduction speed of the reaction time slowed down with the increase of background luminance. Applying energy-storage reflective coating on the sidewalls of the tunnel has a shorter reaction time than using light yellow ceramic tiles and cement mortar on the sidewalls.

Data Availability

All the data obtained from several experiments are included in the article.

Conflicts of Interest

The authors declare that they have no conflicts of interest.

Acknowledgments

References

[1] H. Wang, X. Liu, A. Varveri et al., "Thermal aging behaviors of the waste tire rubber used in bitumen modification," *Progress in Rubber, Plastics and Recycling Technology*, vol. 38, no. 1, pp. 56–69, 2022.

[2] Y. Gao, Y. Zhang, F. Gu, T. Xu, and H. Wang, "Impact of minerals and water on bitumen-mineral adhesion and debonding behaviours using molecular dynamics simulations," *Construction and Building Materials*, vol. 171, pp. 214–222, 2018.

[3] W. G. Qiu, Y. Liu, F. Lu, and G. Huang, "Establishing a sustainable evaluation indicator system for railway tunnel in China," *Journal of Cleaner Production*, vol. 268, Article ID 122150, 2020.

[4] Q. Yang, Y. Yang, Z. Fan et al., "Exploiting the synergetic effects of graphene and carbon nanotubes on the mechanical properties of bitumen composites," *Carbon*, vol. 172, pp. 402–413, 2021.

[5] L. Wang, S. Q. Li, and B. Hui, "Simulation analysis of the distance between tunnels at the bridge-tunnel junction of mountainous expressway on driving safety under crosswinds," *IEEE Access*, vol. 9, pp. 28514–28524, 2021.

[6] Y. Y. Liu, L. Peng, L. Y. Lin, Z. L. Chen, J. Weng, and Q. W. Zhang, "The impact of LED spectrum and correlated color temperature on driving safety in long tunnel lighting," *Tunnelling and Underground Space Technology*, vol. 112, Article ID 103867, 2021.

[7] H. Lu, T. Shang, Y. Wei, and P. Wu, "Safety assessment of exit advance guide signs in mountainous highway tunnel based on eye-tracking technology," *IEEE Access*, vol. 9, pp. 111315–111325, 2021.

[8] S. Y. He, B. Liang, G. B. Pan, F. Wang, and L. L. Cui, "Influence of dynamic highway tunnel lighting environment on driving safety based on eye movement parameters of the driver," *Tunnelling and Underground Space Technology*, vol. 67, pp. 52–60, 2017.

[9] J. Hu, X. J. Gao, R. H. Wang, P. F. Xu, and G. Y. Miao, "Safety evaluation index on daytime lighting of tunnel entrances," *Advances in Mechanical Engineering*, vol. 11, no. 5, Article ID 168781401985456, 2019.

[10] L. Domenichini, F. La Torre, D. Vangi, A. Virga, and V. Branzi, "Influence of the lighting system on the driver's behavior in road tunnels: a driving simulator study," *Journal of Transportation Safety & Security*, vol. 9, no. 2, pp. 216–238, 2017.

[11] L. Zhao, S. C. Qu, W. G. Zhang, and Z. L. Xiong, "An energy-saving fuzzy control system for highway tunnel lighting," *Optik*, vol. 180, pp. 419–432, 2019.

[12] J. Hu and X. J. Gao, "Mechanism of the "white hole" phenomenon and relative security technology in the tunnel," *International Conference on Transportation and Development*, pp. 265–274, 2018.

[13] T. Shang, P. Wu, G. Lian, and Q. J. Sheng, "Influences of Exit advance Guide Signs on the Trajectory and Speed of Passenger Cars in Highway Tunnels," *Journal of Advanced Transportation*, vol. 2021, Article ID 8453439, 2021.

[14] S. Y. Liang and C. Y. Yang, "Study of the lighting of entrance/exit segments of urban tunnels and outside-tunnel roads based on visual efficiency theory," *Applied Mechanics and Materials*, vol. 470, pp. 871–875, 2013.

[15] A. Mehri, R. Hajizadeh, S. Farhang Dehghan et al., "Safety evaluation of the lighting at the entrance of a very long road tunnel: a case study in Ilam," *Safety and Health at Work*, vol. 8, no. 2, pp. 151–155, 2017.

[16] S. Fotios and C. Cheal, "Correction: lighting for subsidiary streets: investigation of lamps of different SPD. Part 2 — Brightness," *Lighting Research and Technology*, vol. 41, no. 4, pp. 381–383, 2009.

[17] S. A. Fotios and C. Cheal, "Lighting for subsidiary streets: investigation of lamps of different SPD. Part 1––Visual Performance," *Lighting Research and Technology*, vol. 39, no. 3, pp. 215–232, 2007.

[18] C. L. B. McCloughan, P. A. Aspinall, and R. S. Webb, "The impact of lighting on mood," *Lighting Research and Technology*, vol. 31, no. 3, pp. 81–88, 1999.

[19] Z. Y. Guo, D. L. Su, G. Q. Liu, and H. Lu, "Tunnel entrance and exit safety design based on driving speed," *Highway Engineer*, vol. 38, pp. 146–150, 2013.

[20] A. Pachamanov and D. Pachamanova, "Optimization of the light distribution of luminaries for tunnel and street lighting," *Engineering Optimization*, vol. 40, pp. 47–65, 2008.

[21] Y. Y. Liu, J. Weng, J. Z. Chen, and Z. L. Chen, "Influence of light sources color on tunnel lighting," *Journal of Civil, Architectural and Environmental Engineering*, vol. 35, pp. 162–166, 2013.

[22] W. J. Xie, Y. Wu, M. Y. Chen, Q. Li, and Q Wang, "Research on lamp distribution parameters of interior zone of high altitude highway tunnel based on lighting energy saving," *IOP Conference Series: Earth and Environmental Science*, vol. 510, no. 5, Article ID 052051, 2020.

[23] S. Na, L. L. Dong, Q. Li, and W. H. Xu, "Study on lamp-layout scheme of highway tunnel lighting based on DIALux," in *Proceedings of the International Conference on Energy and Environmental Protection*, Sanya, China, November 2016.

[24] Y. Q. Zhang, X. Zhuo, W. Guo, X. Y. Wang, and Z. L. Zhao, "Lighting environment optimization of highway tunnel entrance based on simulation research," *International Journal of Environmental Research and Public Health*, vol. 16, no. 12, p. 2195, 2019.

[25] Y. Yang, C. Z. Zhu, and L. Wang, "Highway tunnel lighting research based on mesopic vision," *Applied Mechanics and Materials*, vol. 71-78, pp. 4061–4064, 2011.

[26] X. Y. Cai, J. Weng, Y. K. Hu, and F. Du, "Research on optimal values of contrast revealing coefficient in road tunnel lighting," *Sādhanā*, vol. 45, no. 1, p. 170, 2020.

Research Article

Mesoscopic Fracture Model of Coarse Aggregate Interlocking Concrete

Ben Li [1,2] **Ying Yu,** [2] **Chen Zhang,** [2] **and Yu Zhang** [2]

[1]*Opening Funding Supported by the Key Laboratory of Transport Industry of Road Structure and Material, (Research Institute of Highway Ministry of Transport), Beijing, China*
[2]*Advanced and Sustainable Infrastructure Materials Group, School of Transportation, Civil Engineering and Architecture, Foshan University, Foshan 528000, Guangdong, China*

Correspondence should be addressed to Ben Li; sktm1@163.com

The skeleton formed by coarse aggregate has an important influence on the macroscopic mechanical properties of concrete, especially the fracture properties. Based on mesomechanics and fracture mechanics, this paper conducts theoretical simulations and experimental studies on the mechanical and fracture properties of coarse aggregate interlocking concrete through the theory of mesomechanics homogenization as well as compressive strength tests, flexural strength tests, axial compressive strength tests, elastic modulus tests, and fracture toughness tests. The results show that when the coarse aggregate is within a certain volume increase, the fracture energy and ultimate strength of concrete are significantly improved. At the same time, the proposed mesomechanics calculation model has high accuracy for calculating the fracture characteristics of concrete when the coarse aggregate increment is less than 20%.

1. Introduction

The mechanical strength and fracture toughness of concrete are material parameters that characterize the crack resistance and failure criteria of the material and are extremely important for the safe design of concrete members [1–3]. Concrete can be considered as a two-phase composite material containing mortar and aggregate [4–6], and its crack tips will form irregular intermittent cracks or crack extension zones during fracture. In recent years, relevant studies have shown that material property parameters such as fracture toughness and fracture energy of concrete are affected by significant size effects, and to obtain material parameters independent of the size of the concrete material, sufficiently large specimens must be cast [7–9]. In the concrete single-sided incised beam (SENB) specimen proposed by the International Federation for Research in Structures and Materials (RILEM) [5], the fracture parameters of concrete independent of size will not be obtained directly from this test because the concrete specimen size

relative to the maximum particle size of the aggregate is not sufficiently large (W/dmax = 5∼30). For this reason, revealing the effect of size on the fracture performance of concrete has become a hot spot for domestic and international research.

Cement paste forms a large component in conventional concrete, while the coarse aggregate content is very small. Coarse aggregates are the strength framework of concrete and are usually the strongest, most durable, and volumetrically stable structural units of concrete materials [10, 11]. As a composite material, the mechanical properties of the aggregate improve with increasing aggregate volume fraction as long as the aggregate is well integrated with the cement paste [12–14]. However, the mechanical behavior of concrete is not an absolute property and it is influenced by many factors. Traditional concrete has some problems in its mechanical design [15–17]: (1) The large amount of cement and cementitious materials leads to significant cracks in the concrete at an early stage, which in turn affects its mechanical and durability properties at a later stage. (2) The

low- or high-volume content of coarse aggregates not only fails to give full play to the strength contribution of aggregates but also causes adverse effects such as increased concrete cost, waste of resources, and increased environmental load. (3) In the process of concrete fracture, the initial crack tip between the aggregate and the cementitious material fails the cementitious occlusion leading to crack expansion. Therefore, the content of coarse aggregates in concrete will directly affect the mechanical properties of concrete. Hillerborg [18] proposed earlier that the development of the fracture process zone (FPZ) of concrete is essential in the development of aggregate bond bite cracking and proposed a virtual cracking model, which was widely used and became the basis for the study of quasi-brittle fracture of concrete. The influence of aggregate content on fracture energy and fracture process zone was analyzed; Zollinger et al. [19] showed through tests that the FPZ will increase with the increase in average aggregate size during concrete fracture. Currently, many studies have been conducted to construct high-performance, high-volume stability aggregate interlocking concrete by increasing the amount of coarse aggregates in order to greatly optimize the comprehensive performance and application of concrete materials [20, 21].

Among them, cast-in-place aggregate concrete, a newly proposed and promising coarse aggregate interlocking concrete, is considered as a new component to improve the service life of concrete by maximizing the material performance and reducing the incidence of diseases [22, 23]. Compared with conventional concrete, aggregate interlocking concrete has some significant advantages in terms of mechanical, durability, and stability properties [24–27]. In addition, the establishment of fracture models for aggregate interlocking concrete is basically based on three-point loading tests, and equally important mechanical tests such as compressive strength and modulus of elasticity and their mechanical mechanisms, especially fracture theory, have not been systematically studied. Fracture or cracking characteristics are the most required engineering and material properties of concrete, which are necessary signs to ensure the stability of concrete. Also, based on the influence of coarse aggregates, the internal nanostructure and hydration products of aggregate interlocking concrete are redistributed. Traditional mechanical models are not comprehensive in characterizing its fracture mechanism, and a multiscale model is needed for theoretical analysis.

Based on these backgrounds, the main objective of this paper is to investigate the fracture mechanism and theoretical calculation model of aggregate interlocking concrete. Based on the integration of fine-scale mechanics and fine-scale structural changes of concrete, a fine-scale transport model based on description, theoretical calculation, and numerical analysis is established and determined and its reliability is verified by macroscopic mechanical tests to provide a theoretical supplement and support for the mechanical mechanism of aggregate interlocking concrete.

2. Theoretical Analysis

The theory of fracture and damage of traditional concrete materials is established based on the energy law, crack development law, and other factors. However, it does not consider the changes in mechanical response caused by the increase in coarse aggregate and the interlocking shape. Considering the influence of coarse aggregate on the microstructure of concrete interface, a new fracture mechanism of aggregate interlocking concrete based on the theory of mesomechanics homogenization (RVE model) was established.

2.1. The RVE Model of Coarse Aggregate Interlocking Concrete. Suppose there is an elastic solid with a volume of V in the concrete matrix at the mesoscale and an inclusion subdomain in the inclusion and disturbance caused by coarse aggregate in elastic solids. The base domain and the inclusion domain have different elastic tensors and flexibility tensors. The inhomogeneity caused by the existence of pore structure inclusions due to the interaction of coarse aggregates will produce stress and strain field disturbances in a uniform solid. Therefore, the stress and strain equations of an elastic solid with pore structure inclusions can be expressed as

$$\sigma(X, x) = \sigma^0(X) + \sigma^d(x),$$
$$\varepsilon(X, x) = \varepsilon^0(X) + \varepsilon^d(x), \tag{1}$$

where $\sigma(X, x)$ is the stress of a cement-based elastic solid with pore structure inclusions, $\varepsilon(X, x)$ is the strain of a cement-based elastic solid with pore structure inclusions, $\sigma^0(X)$ is the stress of the cement-based elastic solid, $\varepsilon^0(X)$ is the strain of the cement-based elastic solid, $\sigma^d(x)$ is the disturbance stress of the pore structure with inhomogeneous bodies, and $\varepsilon^d(x)$ is the disturbance strain of the pore structure with inhomogeneous bodies.

Through the superposition of the characteristic strain field and the actual strain field, the relationship between the equivalent uniform solid stress field and the original nonuniform stress field can be obtained:

$$\sigma(X, x) = \mathbb{C} : [\varepsilon(X) - \varepsilon^*(x)],$$
$$= \begin{cases} \mathbb{C} : [\varepsilon^0(X) + \varepsilon^d(x)] & x, X \subset M, \\ \mathbb{C} : [\varepsilon^0(X) + \varepsilon^d(x) - \varepsilon^*(x)] & x, X \subset \Omega, \end{cases} \tag{2}$$

where $\mathbb{C}$ is the elasticity tensor of nonuniform solids, $\varepsilon^*(x)$ is the characteristic strain for simulating material mismatch, defect, pore structure, or inhomogeneity mismatch, M is the characteristic domain at the mesoscale of solids, and Ω is the inclusion subdomains in solids.

Therefore, the characteristic stress field of the pore structure in the hardened concrete due to the interaction of the coarse aggregate can be obtained:

$$\sigma^*_{\text{pore}}(x) = \mathbb{C}^I : \left[\varepsilon^*_{ij}(x)\right]_{\text{pore}} = \mathbb{C}^I : \left[\varepsilon^0(X) + \varepsilon^d(x)\right] - \sigma(X, x),$$

$$(3)$$

where $\mathbb{C}^I$ is the elastic tensor of the inclusion field.

In an infinite space, the induced displacement field caused by the characteristic strain field in the hole structure is determined as

$$\left[u_i(x)\right]^{\text{pore}} = -\int_{\mathbb{R}^3} C_{jlmn}\varepsilon^*_{mn}(y)G^\infty_{ij,l}(x-y)d\Omega_y,$$

$$= -\varepsilon^*_{mn}\int_\Omega C_{jlmn}G^\infty_{ij,l}(x-y)d\Omega_y,$$

$$= \frac{\varepsilon^*_{mn}}{8\pi(1-v)}\left\{\frac{\partial^3\psi}{\partial x_i \partial x_m \partial x_n}\right.$$

$$\left. -2(1-v)\left[\delta_{mi}\frac{\partial\phi}{\partial x_n} + \delta_{ni}\frac{\partial\phi}{\partial x_m}\right] - 2v\delta_{mn}\frac{\partial\phi}{\partial x_i}\right\},$$

$$(4)$$

where $[u_i(x)]^{\text{pore}}$ is the induced displacement field caused by characteristic strain, $C_{jlmn}G^\infty_{ij,l}(x-y)$ is the Green transformation formula, and $\mathbb{R}^3$ is the unlimited space domain.

For the coarse aggregate lock concrete, the elastic strain field can be expressed as

$$\varepsilon_{ij}(x) = \left\{\frac{1}{2}\left[u_{i,j}(x) + u_{j,i}(x)\right]\right\}$$

$$= \frac{\varepsilon^*(x)}{8\pi(1-v)}\left[\psi_{,mnij} - 2v\delta_{mn}\phi_{,ij}\right.$$

$$\left. -(1-v)\left(\delta_{mi}\phi_{,nj} + \delta_{ni}\phi_{,mj} + \delta_{mj}\phi_{,ni} + \delta_{nj}\phi_{,mi}\right)\right].$$

$$(5)$$

2.2. The Elastic-Plastic Constitutive Relationship of Aggregate Interlocking Concrete.

According to Hooke's law, the relationship between elastic strain and Cauchy stress is

$$\sigma'_{ij}(x) = C^{\text{concrete}}_{ijkl}\varepsilon^{*\text{concrete}}_{ij}(x)$$

$$+ C_{ijkl}\left(\varepsilon^{*\text{concrete}}_{ij}(x) - \left[\varepsilon^*_{ij}(x)\right]_{\text{pore}} - \left[\varepsilon_{ij}(x)\right]^{\text{pore}}\right),$$

$$= C^{\text{concrete}}_{ijkl}u^{\text{concrete}}_{i,j}(x)$$

$$+ C_{ijkl}\left(u^{\text{concrete}}_{i,j}(x) - \left[\varepsilon^*_{ij}(x)\right]_{\text{pore}} - \left[\varepsilon_{ij}(x)\right]^{\text{pore}}\right).$$

$$(6)$$

The theoretical solution of the elastic-plastic constitutive relationship of coarse aggregate lock-type concrete is determined as

$$[\sigma_{FAC}]_{ij} = \sigma'_{ij}(x) = \underbrace{\overline{[C_{FAC}]}_{ijkl} \otimes [\varepsilon_{FAC}]^{kl}}_{\text{elastic}} + \underbrace{\overline{[C_{FAC}']}_{ijkl} \otimes [\varepsilon_{FAC}']^{kl}}_{\text{plastic}},$$

$$(7)$$

where $\overline{[C_{FAC}]}_{ijkl}$ is the effective modulus of the concrete in the elastic stage, $\overline{[C_{FAC}']}_{ijkl}$ is the effective modulus of the concrete in the plastic stage, $[\varepsilon_{FAC}]^{kl}$ and $[\varepsilon_{FAC}']^{kl}$ is the strain of concrete in the elastic-plastic stage, and $[\sigma_{FAC}]_{ij}$ is the loading stress.

The effective modulus of concrete in the elastic stage is deduced based on the theory of generalized self-consistent method, which is the mechanical behaviour influenced by the interlocking of coarse aggregate and the mortar between the interface:

$$C^{pq}_{FAC} = \left[1 + \frac{16}{9}\frac{1-\vartheta_1^2}{1-2\vartheta}f\left(V_{\text{Coarse aggregate interlocking}}\right) + \frac{4.35 - 2.06(1+\vartheta_1)}{1-2\vartheta}f^{2/5}\left(V_{\text{Coarse aggregate interlocking}}\right)\right]C^{pq}_{f\left(V_{\text{Coarse aggregate interlocking}}\right)}$$

$$+ \left[1 + \frac{16}{9}\frac{1-\vartheta_2^2}{1-2\vartheta}f\left(\phi_{\text{pore}}\right) + \frac{4.35 - 2.06(1+\vartheta_2)}{1-2\vartheta}f^{2/5}\left(\phi_{\text{pore}}\right)\right]C^{pq}_{ITZ},$$

$$(8)$$

where C^{pq}_{FAC} is the effective modulus of concrete, $C^{pq}_{f(V_{\text{Coarse aggregate interlocking}})}$ is the modulus of coarse aggregate under the interlocking action, C^{pq}_{ITZ} is the modulus of ITZ, ϑ_1 is Poisson's ratio of coarse aggregate under the interlocking action, ϑ_2 is Poisson's ratio of ITZ, $f(V_{\text{Coarse aggregate interlocking}})$ is the density distribution of coarse aggregate, and $f(\phi_{\text{pore}})$ is the distribution characterization function of pore structure.

2.3. The Fracture Toughness Equation of Aggregate Interlocking Concrete.

The fracture process of materials is predicted by the yield function during the plastic development.

Therefore, the fracture yield equation of concrete is established based on the Gurson model as

$$\Phi\left(\sigma_{ij}'(x), \sigma_e, f^*(\phi_{\text{pore}})\right) = \left(\frac{\sum_{eq}}{\sigma_e}\right)^2 + 2f^*(\phi_{\text{pore}})\cosh\frac{\overline{C_{FAC}} \cdot \overline{\overline{C_{FAC}'}}}{\overline{C_{FAC}} - \overline{C_{FAC}'}}\left(\frac{3\sum_m}{2\sigma_e}\right) - 1 - f^*(\phi_{\text{pore}})^2 = 0,$$

$$f^*(\phi_{\text{pore}}) = f_c(\phi_{\text{pore}}) + \frac{0.53 - f_c(\phi_{\text{pore}})}{f_{fra}(\phi_{\text{pore}}) - f_c(\phi_{\text{pore}})}\left(f(\phi_{\text{pore}}) - f_c(\phi_{\text{pore}})\right),$$

$$\overline{C_{FAC}^{pq}} = \left[1 + \frac{16}{9}\frac{1-\vartheta^2}{1-2\vartheta}f(V_{\text{Coarse aggregate interlocking}}) + \frac{4.35 - 2.06(1+t\vartheta)}{1-2\vartheta}f^{2/5}(V_{\text{Coarse aggregate interlocking}})\right]C_{f(V_{\text{Coarse aggregate interlocking}})}^{pq} +$$

$$(1 - D')\left[1 + \frac{16}{9}\frac{1-\vartheta^2}{1-2\vartheta}f^*(\phi_{\text{pore}}) + \frac{4.35 - 2.06(1+t\vartheta)}{1-2\vartheta}f^{*,2/5}(\phi_{\text{pore}})\right]C_{ITZ}^{pq}$$

$$= \left[1 + \frac{16}{9}\frac{1-\vartheta^2}{1-2\vartheta}f(V_{\text{Coarse aggregate interlocking}}) + \frac{4.35 - 2.06(1+\vartheta)}{1-2\vartheta}f^{2/5}(V_{\text{Coarse aggregate interlocking}})\right]C_{f(V_{\text{Coarse aggregate interlocking}})}^{pq}$$

$$+ \left(1 - \frac{\Delta R}{R_N}\right)\left[1 + \frac{16}{9}\frac{1-\vartheta^2}{1-2\vartheta}f^*(\phi_{\text{pore}}) + \frac{4.35 - 2.06(1+t\vartheta)}{1-2\vartheta}f^{*,2/5}(\phi_{\text{pore}})\right]C_{ITZ}^{pq},$$

$$(9)$$

where $\Phi\left(\sum_{ij}, \sigma_e, f^*(\phi_{\text{pore}})\right)$ is the yield function of concrete, $\sigma_{ij}'(x)$ is the macroscopic stress, σ_e is the equivalent yield stress, $\sum_{eq}$ is the Mises yield stress, $\sum_m$ is the hydrostatic stress, $f^*(\phi_{\text{pore}})$ is the porosity distribution function of the ITZ during the yielding process, $f_c(\phi_{\text{pore}})$ is the porosity distribution function when pore confluence begins, $f_{fra}(\phi_{\text{pore}})$ is the critical porosity distribution function when the material fractures, D' is the damage factor under load, ΔR is the pore size change value of ITZ, and R_N is the pore size characteristic value of ITZ.

Based on the fracture criterion, the fracture toughness equation of the coarse aggregate lock concrete is determined as

$$\widetilde{G}_{FAC} = \frac{2\pi(\sigma_e)^2}{\overline{C_{FAC}^{pq}}}, \qquad (10)$$

where $\widetilde{G}_{FAC}$ is the fracture toughness of coarse aggregate interlocking concrete.

3. Experimental Details

3.1. Raw Materials and Mixing Proportions.
Raw materials including local ordinary Portland cement of grade P.O 42.5 N from Guangzhou Yuebao Cement Co., local river sand with a fineness modulus of 2.3, and water were used throughout the study. Local limestone was used as a coarse aggregate, with a size ranging from 5 mm to 25 mm. Tables 1 and 2 show the mechanical and chemical properties of ordinary Portland cement. The physical properties of the river sand and coarse aggregates are presented in Table 3. In this experiment, the water-to-cement ratio (w/c) was 0.45, and the mixing proportion of concrete is shown in Table 4 (coarse aggregates increase by 5%, 10%, 15%, 20%, and 25% according to the volume percentage of the basic aggregate).

3.2. Specimen Casting and Curing Conditions.
The concrete specimens were prepared in accordance with Chinese standard JTG 3420-2020 [28]. The dimensions of the concrete specimens were 150 mm × 150 mm × 150 mm (144 pieces), 100 mm × 100 mm × 400 mm (108 pieces), and 150 mm × 150 mm × 300 mm (108 pieces), and the specimens were demolded after 24 h. Each sample was placed in saturated limewater to cure at room temperature (i.e., 20 ± 2°C/RH ≥ 95%) for 28 days in accordance with GB/T50081-2019 [29].

3.3. Experimental Methods

3.3.1. Test Method for Strength of the Coarse Aggregate Interlocking Concrete.
150 mm × 150 mm × 150 mm (144 pieces) specimens were used for the compressive strength test, 100 mm × 100 mm × 400 mm (108 pieces) were used for the flexural strength test, and 150 mm × 150 mm × 300 mm (108 pieces) were used for the axial compressive strength test for 28 days according to GB/T50081-2019 [29].

3.3.2. Test of Elastic Modulus of the Coarse Aggregate Interlocking Concrete.
The secant modulus under 30% axial compressive strength stress is taken as the elastic modulus value according to GB/T50081-2019 [29]. The size of the experimentally produced specimen is 150 mm × 150 mm × 300 mm (108 pieces).

TABLE 1: Mechanical properties of Portland cement (MPa).

Flexural strength (MPa)		Compressive strength (MPa)		Fineness	Setting time (h: m)	
3 days	28 days	3 days	28 days		Initial setting	Final setting
5.2	7.1	22.1	51.8	1.8	0 : 46	1 : 33

TABLE 2: Chemical properties of Portland cement (%).

Chemical component	Weight (%)	Chemical component	Weight (%)
SiO_2	21.50	TiO_2	0.23
Al_2O_3	4.50	Na_2O	0.33
Fe_2O_3	3	K_2O	0.39
CaO	65.70	SO_3	2
MgO	1.30	P_2O_5	0.27
MnO	0.14	Cl	0.01

TABLE 3: Physical properties of the aggregates.

Physical properties	Fine aggregate	Coarse aggregate
Type	Natural stand	Crushed stone
Size (mm)	0.16–2.5	5–20.5
Apparent density (kg/m^3)	2,540	2,590
24-hour water absorption (%)	3.06	2.17
Fineness modulus	2.37	——

TABLE 4: Mixing proportions of the coarse aggregate interlocking concrete (kg/m^3).

No.	Cement	Water	Sand	Base stone	Add stone	Water-reducing agent
PT-0	493.3	222	736	1428.6	0	2.22
PT-5	493.3	222	736	1428.6	509	2.22
PT-10	493.3	222	736	1428.6	1018	2.22
PT-15	493.3	222	736	1428.6	1527	2.22
PT-20	493.3	222	736	1428.6	2036	2.22
PT-25	493.3	222	736	1428.6	2545	2.22
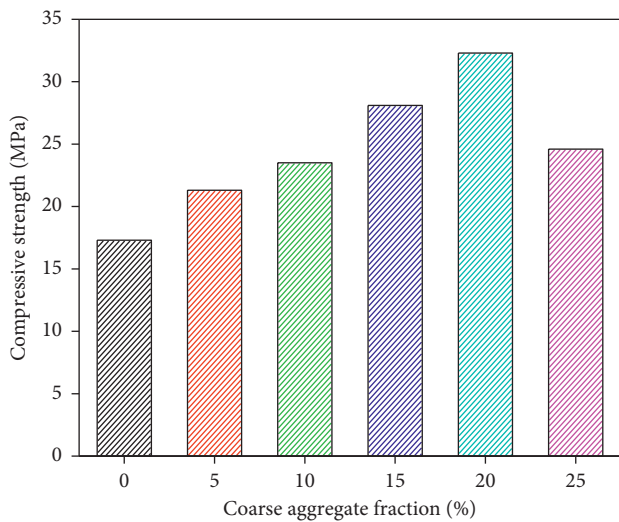
FIGURE 1: Compressive strength of coarse aggregate interlocking concrete subjected to different increasing amounts of coarse aggregates.
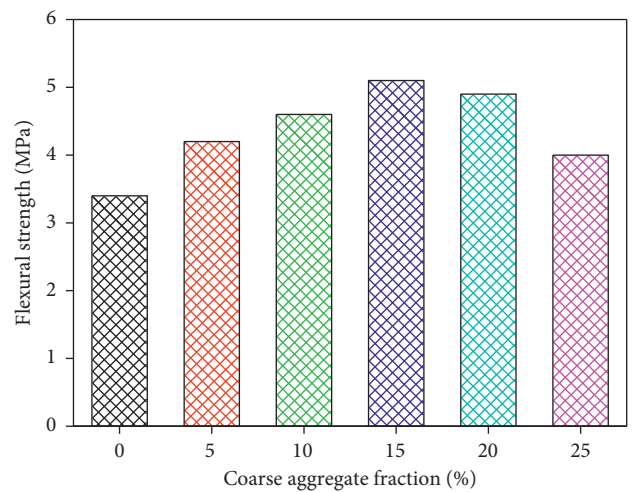
FIGURE 2: Flexural strength of coarse aggregate interlocking concrete subjected to different increasing amounts of coarse aggregates.
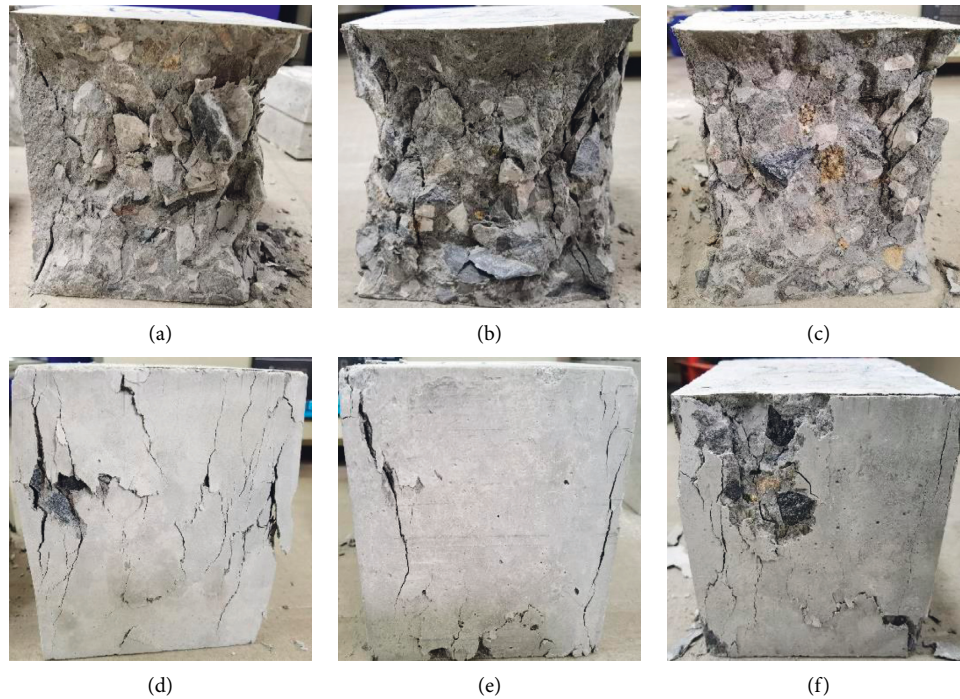
FIGURE 3: Failure mode of the coarse aggregate interlocking concrete subjected to different increasing amounts of coarse aggregates under compressive load. (a) PT-0. (b) PT-5. (c) PT-10. (d) PI5. (e) PT-20. (f) PT-25.

3.3.3. Test of Fracture Toughness of the Coarse Aggregate Interlocking Concrete. A notched three-point bending beam was used to determine the fracture toughness of coarse aggregate interlocking concrete. For crack generation, the specimen is made to produce cracks by cutting on the side of the specimen. The slit width is controlled at 3 mm ± 1 mm, the slit length is controlled at 80 mm ± 2 mm, and the angle between the joint surface and the specimen is 90° ± 0.5° according to GB/T50081-2019 [29]. The size of the experimentally produced specimen is 100 mm × 100 mm × 400 mm (108 pieces).

3.3.4. Mercury Intrusion Porosimetry (MIP) Analysis. Mercury intrusion porosimetry (MIP) is the most common method used to study the pore properties of cement-based materials. This method is relatively straightforward and generally yields reproducible pore size distributions. The significant characteristic parameters, such as the total pore diameter, total porosity, and theoretical pore diameter, can be deduced from these pore size distributions. With increasing pressure, mercury is pressed into the pore structures of concrete samples. After the mercury fills the samples, the relationship between the intrusion pressure and the pore radius can be obtained. The fine particles of concrete (5 groups and 6 solid samples in each group) were subjected to mercury intrusion test analysis.

4. Results and Discussion

4.1. Experimental Values of Mechanical Characteristics of Coarse Aggregate Interlocking Concrete. Figures 1 and 2
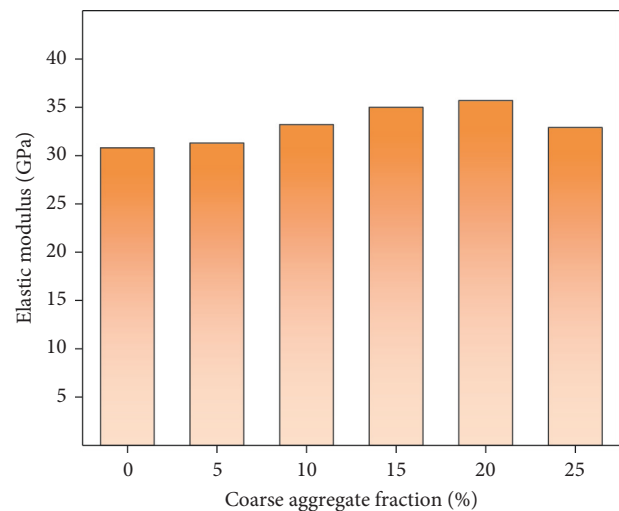

FIGURE 4: Elastic modulus of the coarse aggregate interlocking concrete subjected to different increasing amounts of coarse aggregates.

show the experimental results of compressive and flexural strength of coarse aggregate interlocking concrete. The results show the following: (1) The macroscopic mechanical strength increases as the volume rate of the coarse aggregate increases. (2) When the volume fraction of the external coarse aggregate is 0%–20%, the strength increases with the increase in the aggregate replacement rate. When the volume rate of coarse aggregate is 15%~20%, the compressive and flexural strengths reach the maximum values, which are increased by 40% and 36%, respectively. (3) However, when
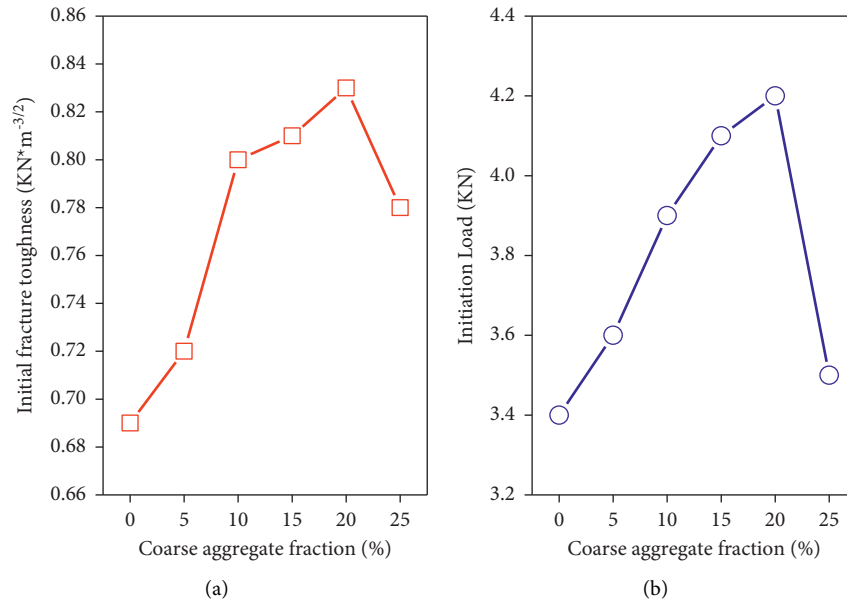
FIGURE 5: Initiation load and initial fracture toughness of the coarse aggregate interlocking concrete.
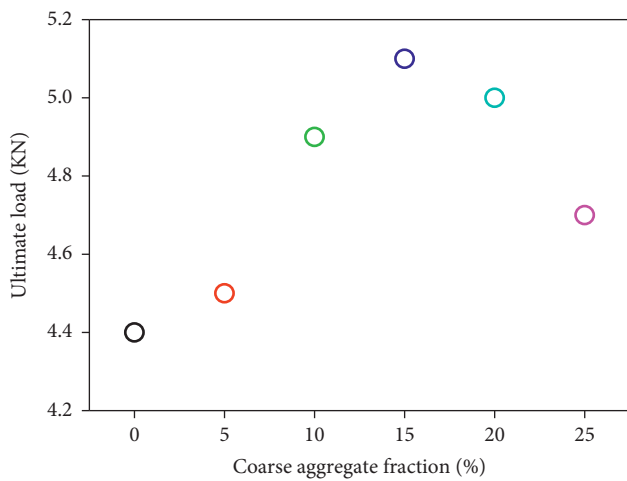

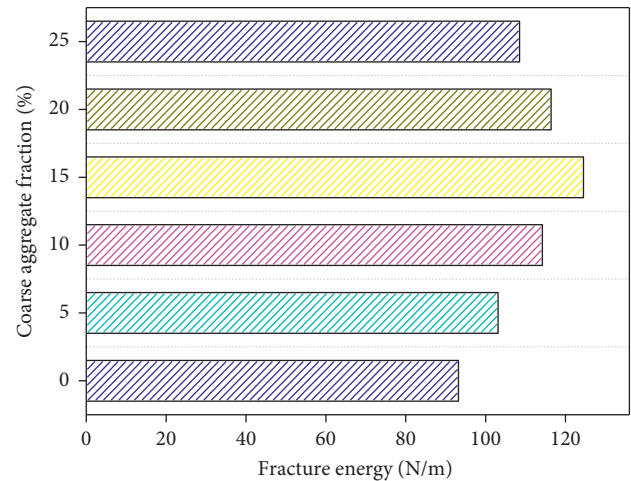FIGURE 6: Ultimate load of the coarse aggregate interlocking concrete.

FIGURE 7: Fracture energy of the coarse aggregate interlocking concrete.

the volume rate of the coarse aggregate is 25%, the macromechanical properties are significantly decreased. This is because too much coarse aggregate in the concrete makes compaction difficult, which reduces the mechanical strength. However, due to the interlocking effect between the aggregates, the final mechanical strength is still higher than the reference value.

In addition, the comparative analysis of the interface morphology subjected to compression fracture is shown in Figure 3. The results show the following: (1) The increase in the volume ratio of the coarse aggregate promotes the formation of the spatial distribution of the mutual embedment and occlusion of aggregates during the concrete hydration process. (2) The increase in coarse aggregate also reduces the distribution probability of through cracks under load. (3) When the volume ratio of coarse aggregate is 20%,

there is no obvious crack in the core part of the specimen during crushing failure. Figure 4 shows the elastic modulus of the coarse aggregate interlocking concrete. 5%, 10%, 15%, and 20% of the aggregate volume increased by 3.3%, 6.6%, 13%, and 19.8% compared with the elastic modulus of the benchmark group, respectively. Subsequently, when the volume of the aggregate is 25%, the elastic modulus began to decrease. The variation and evolution are similar as the abovementioned results of strength characteristics.

4.2. Experimental Values of Fracture Characteristics of Coarse Aggregate Interlocking Concrete. Figures 5 and 6 show the results of initial fracture load, ultimate fracture load, and initial fracture toughness during fracture experiment of the coarse aggregate interlocking concrete. Compared with the benchmark concrete, with the increase in aggregate volume,
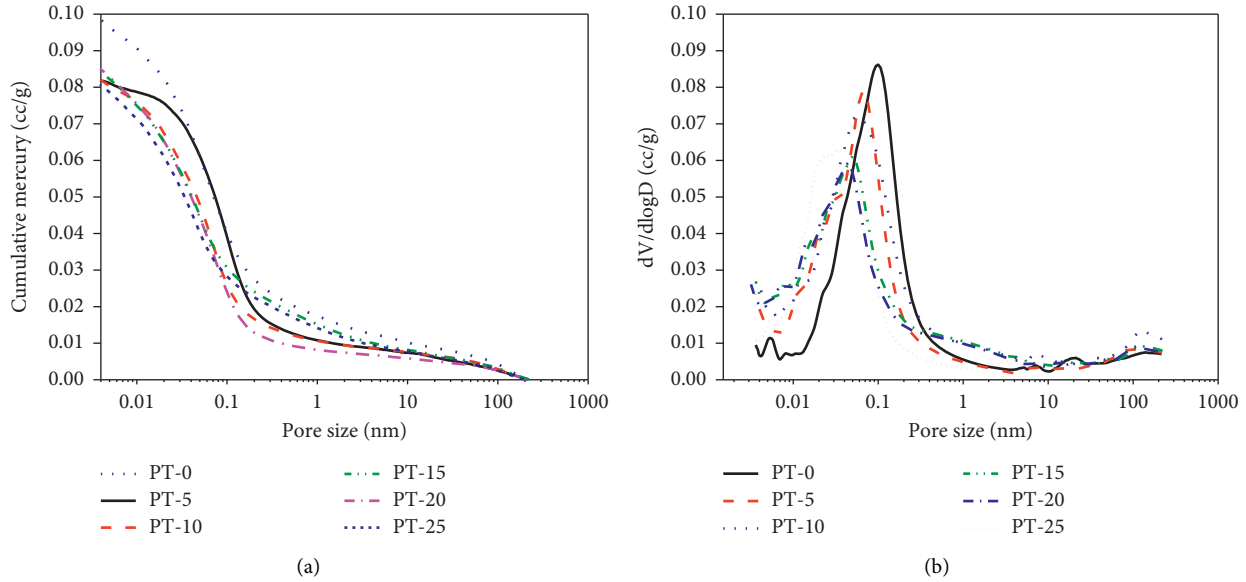
(a)

(b)

FIGURE 8: Pore size distribution of the coarse aggregate interlocking concrete. (a) Cumulative mercury. (b) Pore size distribution.
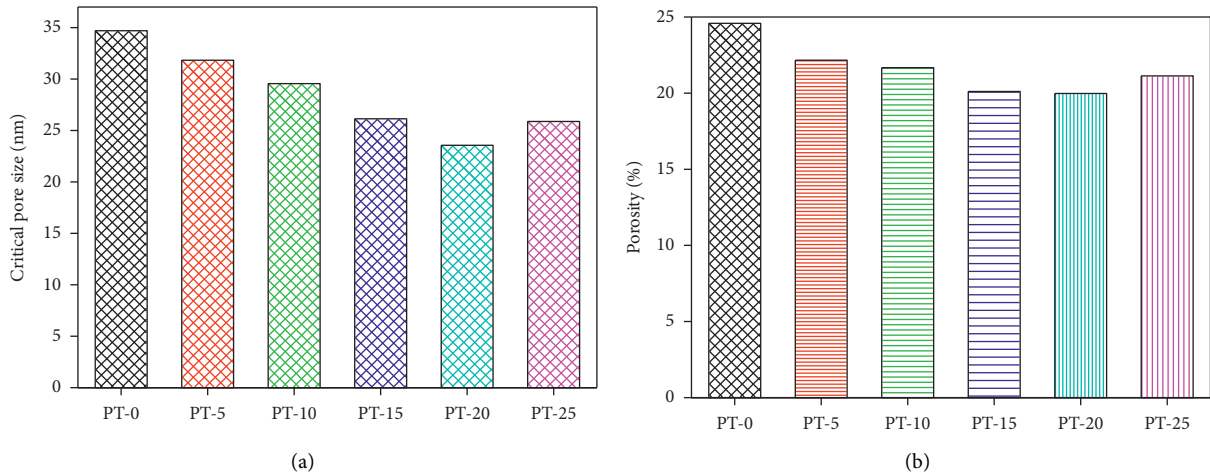

(a)

(b)

FIGURE 9: Pore parameters of the coarse aggregate interlocking concrete. (a) Critical pore size. (b) Porosity.

the cracking load shows an increasing trend. However, when the aggregate volume increases by 20%, the crack initiation load begins to show a downward trend. When the increase in the volume of the coarse aggregate is 0%–20%, the reason for the phenomenon of crack initiation and ultimate load enhancement is that more aggregate makes the material inside the concrete fill and compact, which improves the overall compactness of the material. When the increment reaches 20%–25%, the workability of concrete will be affected by the excessive coarse aggregate, which will reduce the cohesion of concrete and generate more internal cracks. This leads to a reduction in the initial and ultimate loads during the concrete fracture process.

According to the classical calculation equations in fracture mechanics, the test fracture energy under different coarse aggregate volume increments of the coarse aggregate interlocking concrete can be obtained and is shown in Figure 7. The results show the following: (1) When the volume increase in the coarse aggregate is 0%–20%, the

fracture energy shows an increasing trend. For every 5% increase in volume, the fracture energy increases by 12.3%, 17.6%, and 19.4%, respectively. In the fracture process, a certain friction force is formed between the coarse aggregates, which indirectly increases the bite force between the coarse aggregate and the cementitious material, and the fracture energy is improved. (2) However, when the volume increase fraction of the coarse aggregate reaches 25%, the fracture energy shows a downward trend (compared to 20% aggregate volume fraction, it decreased to 25.3%). When the volume increase of the coarse aggregate reaches 25%, the bite force between the materials begins to decrease due to the decrease in the compactness, which causes the evolution of the fracture energy to show a downward trend.

4.3. Pore Size Distribution of Coarse Aggregate Interlocking Concrete. Variations in the pore size distribution of the coarse aggregate interlocking concrete obtained from the
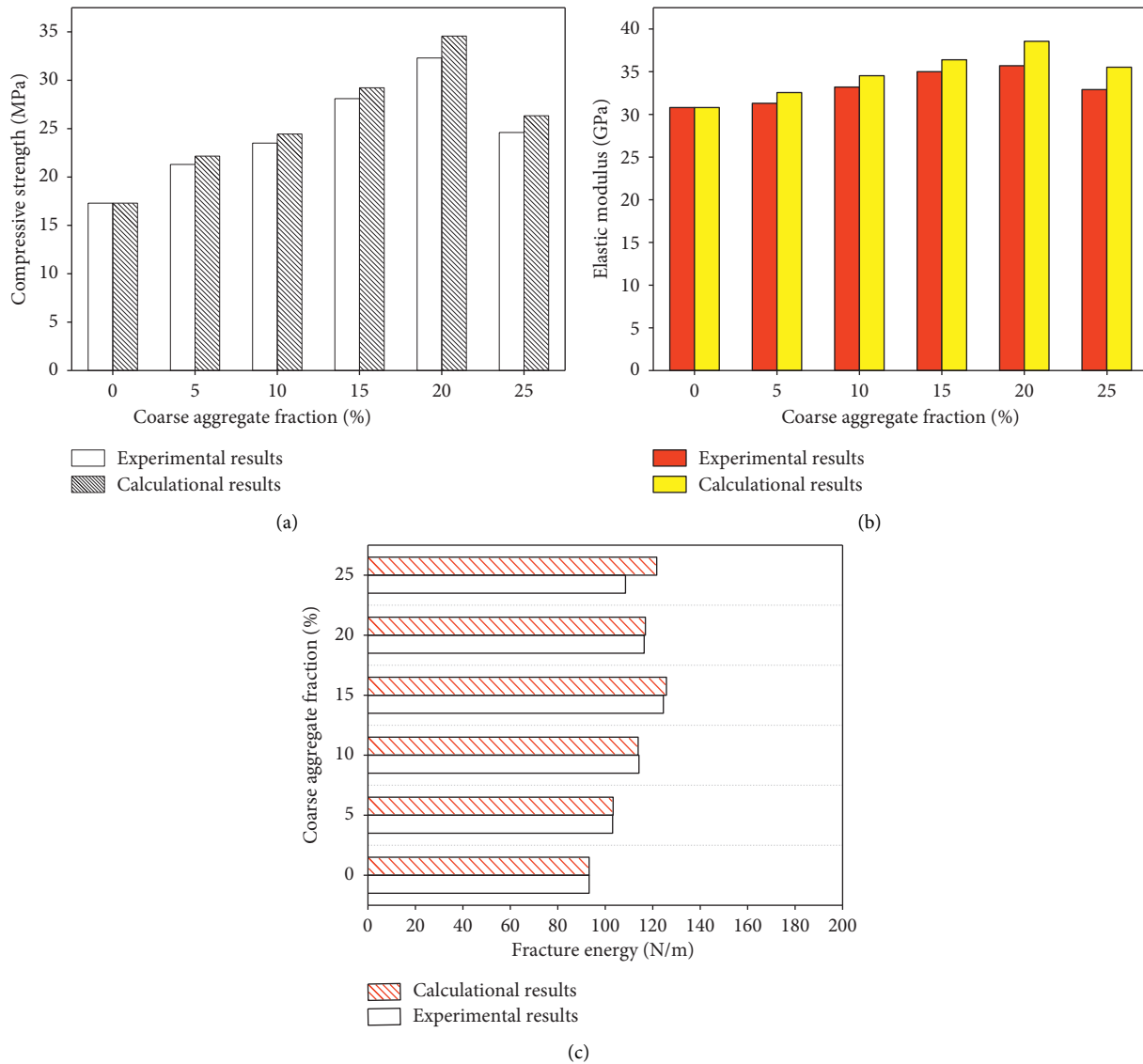
(a)

(b)

(c)

FIGURE 10: Comparison results of experiment and simulation calculation of the coarse aggregate interlocking concrete. (a) Compressive strength. (b) Elastic modulus. (c) Fracture energy.

pore size distribution curves based on MIP testing data are shown in Figure 8. Characteristic pore parameters such as porosity and critical pore size are shown in Figure 9. We can obtain the following: (1) With the increase in coarse aggregate volume, the porosity and critical pore size of concrete gradually decrease. (2) The appropriate increase in the volume of the coarse aggregate not only plays the role of the original strength skeleton but also improves the internal compactness of the concrete and reduces the internal pore density, which improves the ultimate strength and fracture resistance of the concrete. (3) However, the pore density increases when the volume increase of coarse aggregate is 20%~25% based on the influence of workability and insufficient wrapping of cementitious materials, in which the ultimate strength and fracture energy are significantly reduced. In summary, the coarse aggregate has an important relationship with the construction of pore structure of concrete. The change of porosity and critical pore size

significantly affects the fracture toughness and ultimate strength, which provides relevant calculation parameters for the theoretical simulation calculation in this paper.

4.4. Comparison of the Fracture Characteristics Calculated by the Mesoscopic Model and Experimental Results. This section reports the results of the fracture characteristics based on the mesoscopic model (equations (8)–(10)). The comparison results and errors are shown in Figures 10 and 11. Comparing the calculation results with the experimental results, we can find the following: (1) For the simulation of compressive strength and elastic modulus, the simulation results are higher than the experimental results. However, as the volume of coarse aggregate increases, the calculation error gradually stabilizes (3~4%). The accuracy of the calculation results of higher volume increase of the coarse aggregate (>20%) is not ideal. This may be attributed to the fact that
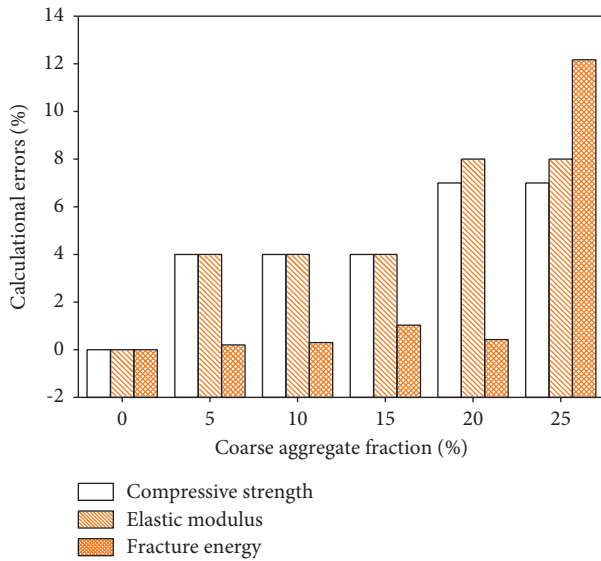
Figure 11: Calculated error values.

when the amount of coarse aggregates exceeds 20%, the distribution of aggregates inside the cement matrix is intricate and complex, which is prone to produce uneven forces on the aggregates, thus causing the calculation results to be affected and producing large fluctuations and errors. (2) For the simulation results of fracture energy, the simulation results have the same laws as the experimental results and the calculation error is small (the increase of coarse aggregate is less than 20%, and the error is 2%). The simulation results can well reflect the fracture energy development characteristics of the concrete fracture process. However, when the volume increase of coarse aggregate is large (>20%), the simulation results of fracture energy have very large errors. How to improve the accuracy of related calculation results in the future is the research content that the model still needs to consider in the future. In summary, the mesoscale multimechanical model established in this paper has certain theoretical basis and calculation accuracy.

5. Conclusions

A mesoscopic model, based on the micromechanics RVE model and fracture mechanics mechanism, was validated and applied to the experimental test for calculating the influence of coarse aggregate on fracture characteristics of the concrete. The following conclusions of this study can be drawn:

(1) Experiments and theoretical studies are conducted on the ultimate strength and fracture characteristics of concrete. The increase in coarse aggregate can significantly improve the macroscopic strength and fracture resistance of concrete within a certain range. However, as the volume increases, due to the influence of too much coarse aggregate on the working performance, the wrapping performance of the cementitious material, the pore size, and the

macromechanical properties decrease (still higher than the reference value).

(2) Based on the new model, some mesoscopic mechanical models were established for describing the mechanism of coupling relationship between pore size, mechanical strength, and fracture characteristics. The proposed model was proved to be effective for evaluating mechanical response of the coarse aggregate interlocking concrete.

Data Availability

The research data used to support the findings of this study are included within the article.

Disclosure

Conflicts of Interest

The authors declare that they have no conflicts of interest.

Authors' Contributions

Ben Li and Ying Yu contributed equally to this work.

Acknowledgments

References

[1] C. Zhang, X. Hu, T. Sercombe, Q. Li, Z. Wu, and P. Lu, "Prediction of ceramic fracture with normal distribution pertinent to grain size," *Acta Materialia*, vol. 145, pp. 41–48, 2018.

[2] R. Xu and X. Hu, "Effects of nano-grain structures and surface defects on fracture of micro-scaled polysilicon components," *Journal of the American Ceramic Society*, vol. 103, no. 6, pp. 3757–3762, 2020.

[3] B. Yuan, Y. Hu, and X. Hu, "Critical bending load of CFRP panel with shallow surface scratch determined by a tensile strength model," *Composites Science and Technology*, vol. 191, Article ID 108072, 2020.

[4] G. Sun, Y. Zhang, W. Sun, Z. Liu, and C. Wang, "Multi-scale prediction of the effective chloride diffusion coefficient of concrete," *Construction and Building Materials*, vol. 25, no. 10, pp. 3820–3831, 2011.

[5] Y. Zhou, Z. Fan, J. Du, L. Sui, and F. Xing, "Bond behavior of FRP-to-concrete interface under sulfate attack: an experimental study and modeling of bond degradation," *Construction and Building Materials*, vol. 85, pp. 9–21, 2015.

[6] T. Luping, "Engineering expression of the ClinConc model for prediction of free and total chloride ingress in submerged marine concrete," *Cement and Concrete Research*, vol. 38, no. 8-9, pp. 1092–1097, 2008.

[7] X. Han, Y. Chen, X. Hu, W. Liu, Q. Li, and S. Chen, "Granite strength and toughness from small notched three-point-bend specimens of geometry dissimilarity," *Engineering Fracture Mechanics*, vol. 216, Article ID 106482, 2019.

[8] D. R. Rilem, "Determination of the fracture energy of mortar and concrete by means of three-point bend tests on notched beams," *Materials and Structures*, vol. 18, no. 106, pp. 285–290, 1985.

[9] Z. P. Bažant, "Size effect in blunt fracture: concrete, rock, metal," *Journal of Engineering Mechanics*, vol. 110, no. 4, pp. 518–535, 1984.

[10] M. Zhang, G. Ye, and K. van Breugel, "Multiscale lattice Boltzmann-finite element modelling of chloride diffusivity in cementitious materials. Part I: Algorithms and implementation," *Mechanics Research Communications*, vol. 58, pp. 53–63, 2014.

[11] M. Zhang, G. Ye, and K. van Breugel, "Multiscale lattice Boltzmann-finite element modelling of chloride diffusivity in cementitious materials. Part II: simulation results and validation," *Mechanics Research Communications*, vol. 58, no. 28, pp. 64–72, 2014.

[12] O. Truc, J. P. Ollivier, and L. O. Nilsson, "Numerical simulation of multi-species diffusion," *Materials and Structures*, vol. 33, pp. 566–573, 2010.

[13] A. Boddy, E. Bentz, M. D. A. Thomas, and R. D. Hooton, "The University of Toronto chloride transport model: an overview and sensitivity study," *Cement and Concrete Research*, vol. 12, pp. 827–837, 2001.

[14] F. P. Glasser, J. Marchand, and E. Samson, "Durability of concrete-degradation phenomena involving detrimental chemical reactions," *Cement and Concrete Research*, vol. 11, no. 38, pp. 226–246, 2008.

[15] R. A. Cook and K. C. Hover, "Mercury intrusion porosimetry of cement-based materials and associated correction factors," *Construction and Building Materials*, vol. 4, no. 7, pp. 231–240, 2007.

[16] J. Kaufmann, F. Winnefeld, and R. Zurbriggen, "Polymer dispersions and their interaction with mortar constituents and ceramic tile surfaces studied by zeta-potential measurements and atomic force microscopy," *Cement and Concrete Composites*, vol. 34, no. 5, pp. 604–611, 2012.

[17] M. V Tran and B. Stitmannaithum, "Chloride penetration into concrete using various cement types under flexural cyclical load and tidal environment," *The IES Journal Part A: Civil & Structural Engineering*, vol. 13, pp. 201–214, 2015.

[18] A. Hillerborg, "Results of three comparative test series for determining the fracture energyG F of concrete," *Materials and Structures*, vol. 18, no. 5, pp. 407–413, 1985.

[19] D. G. Zollinger, T. Tang, and R. H. Yoo, "Fracture toughness of concrete at early ages," *ACI Materials Journal*, vol. 90, no. 5, pp. 463–471, 1993.

[20] S. Dehghanpoor Abyaneh, H. S. Wong, and N. R. Buenfeld, "Modelling the diffusivity of mortar and concrete using a three-dimensional mesostructure with several aggregate shapes," *Computational Materials Science*, vol. 78, no. 5, pp. 63–73, 2013.

[21] K. M. A. Sohel, K. Al-Jabri, M. H. Zhang, and J. Y. R. Liew, "Flexural fatigue behavior of ultra-lightweight cement composite and high strength lightweight aggregate concrete," *Construction and Building Materials*, vol. 173, pp. 90–100, 2018.

[22] S. Pyo, S. Y. Abate, and H.-K. Kim, "Abrasion resistance of ultra high performance concrete incorporating coarser aggregate," *Construction and Building Materials*, vol. 165, no. 165, pp. 11–16, 2018.

[23] M. Shafieifar, M. Farzad, and A. Azizinamini, "Experimental and numerical study on mechanical properties of ultra high performance concrete (UHPC)," *Construction and Building Materials*, vol. 156, no. 156, pp. 402–411, 2017.

[24] M. K. Lee and B. I. G. Barr, "An overview of the fatigue behaviour of plain and fibre reinforced concrete," *Cement and Concrete Composites*, vol. 26, no. 4, pp. 299–305, 2004.

[25] S. Seitl, V. Bílek, Z. Keršner, and J. Veselý, "Cement based composites for thin building elements: fracture and fatigue parameters," *Procedia Engineering*, vol. 2, no. 1, pp. 911–916, 2010.

[26] J. Wang, P. A. M. Basheer, S. V. Nanukuttan, A. E. Long, and Y. Bai, "Influence of service loading and the resulting microcracks on chloride resistance of concrete," *Construction and Building Materials*, vol. 108, pp. 56–66, 2016.

[27] V. Picandet, A. Khelidj, and G. Bastian, "Effect of axial compressive damage on gas permeability of ordinary and high-performance concrete," *Cement and Concrete Research*, vol. 31, no. 11, pp. 1525–1532, 2001.

[28] *JTG 3420-2020*, Test Methods of Concrete and Cement for Highway Engineering, Beijing, 2020.

[29] *GB/T 50081-2019, Standard for Test Method of Mechanical Properties on Ordinary concrete*, Beijing, 2019.

Research Article

Effect of Superabsorbent Polymer (SAP) Internal Curing Agent on Carbonation Resistance and Hydration Performance of Cement Concrete

Jieting Xu,[1] Xiao Qin ⓘ,[1] Zhenying Huang,[2] Yongkang Lin,[1] Ben Li,[1] and Zhengzhuan Xie[3]

[1]*Advanced and Sustainable Infrastructure Materials Group, School of Transportation and Civil Engineering and Architecture, Foshan University, Foshan 528225, Guangdong, China*
[2]*Guangzhou Huahui Traffic Technology Co, Ltd., Guangzhou 510355, China*
[3]*Guangxi Key Lab of Road Structure and Materials, Nanning 530007, Guangxi, China*

Correspondence should be addressed to Xiao Qin; qinnao@126.com

To clarify the influencing mechanism of superabsorbent polymer (SAP) internal curing agent on the carbonation resistance of cement concrete, accelerated carbonation experiment was conducted to explore the effect of particle size and dosage of SAP on carbonation depth. The hydration performance of internally cured concrete at different ages was studied by Fourier transform infrared spectroscopy (FTIR) test and X-ray diffraction (XRD) test. Combined with the scanning electron microscope (SEM) test, the hydration filling effect of internal curing on the microstructure of concrete was analyzed; meanwhile, the influence mechanism of SAP on carbonation resistance was revealed. The results showed that (i) when the particle size and dosage of SAP were 100 mesh and 0.200%, the carbonation depth of internally cured concrete was only 56.5% of the control group on day 28; (ii) the $Ca(OH)_2$ absorption peak area of SAP-concrete in the FTIR spectra could be increased by 3.38 times than that of the control group, and more C_2S and C_3S were translated into $Ca(OH)_2$, which helped to improve the hydration degree of cement concrete; (iii) the hydration products of day 56 were increased significantly and the remaining pores formed by SAP gels were gradually filled by hydration products, which enhanced the compactness and carbonation resistance of cement concrete.

1. Introduction

The corrosion of steel bars caused by carbonation is one of the main factors causing durability failure of concrete structures [1]. For bridge members, the carbonation reaction occurs accompanied by the erosion of acidic substances during the service period, which probably causes the destruction of passivation film, further the corrosion and expansion of steel bars [2]. Eventually, some cracks and spalling appear in the protective cover of concrete. In addition, microcracks caused by drying shrinkage and self-shrinkage are generated frequently due to the water evaporation and hydration reaction of concrete during the molding process, which probably provide several channels for CO_2 or other acidic substances to enter the concrete, accelerating the carbonation process. Therefore, the

shrinkage microcrack must be suppressed to improve the carbonation resistance of concrete.

Internal curing is considered to be one of the most promising shrinkage and crack resistance technologies. The internal curing material incorporated in concrete can release some extra curing water in time to maintain high humidity internal environment and promote further hydration of the binding material. To date, SAP is one of the best internal curing materials with excellent water absorption and release properties [3–5]. Moreover, the effect of SAP on reducing the shrinkage and crack of concrete was proved, presented in relevant studies that the shrinkage decreased by approximately 31–41%, when the SAP dosage was 2.0% [6, 7].

For practical engineering, the investigation of carbonation resistance in concrete has application significance. Nevertheless, most of the existing research focuses on the

mechanical and engineering properties and durability, including frost resistance and antipermeability of internal curing cement concrete and mortar, but relatively few concentrate on carbonation resistance [8–11]. The specific studies status about this topic is shown as follows. The effect of SAP curing has been studied, and the experimental results of Beushausen et al. [12] and Shi et al. [13] showed that SAP could improve carbonation performance. Zhang et al. [14] found that the connectivity between pores was blocked by SAP after hygroscopic expansion by adding the appropriate amount of prewater absorption and preabsorption of 1% silver nitrate solution SAP in concrete, which would improve the carbonation resistance of concrete. Guo et al. [15] revealed the enhancing mechanism of SAP on carbonation resistance of concrete on the microscopic level.

The carbonation resistance of concrete mainly depends on the microcracks, which could be influenced by the hydration degree and products. As for the effect of SAP on hydration, Jiang et al. [16] found that the early hydration reaction (0-7d) of concrete was delayed by the addition of SAP. Zhao et al. [17] investigated the influence of nano-SiO_2 and SAP on the hydration process of early-age cement paste by the low-field nuclear magnetic resonance technology (LF-NMR). The result showed that the beginning time of each stage and the hydration duration were prolonged with the increase of SAP dosage. Qin et al. [18, 19] studied the microstructure of concrete through mercury intrusion porosimetry (MIP) and XRD, which concluded that the amount of ettringite was increased in concrete cured by SAP. Qin et al. [20] found that the hydration degree of concrete could be greatly improved by smaller-sized SAP in the long term by investigating the transformation rule of water form during the internal curing process.

The above research indicated that SAP had a positive impact on the carbonation and hydration performance of concrete. However, the existing research focuses on the direct index, including pores and microstructure, to study the influence of internal curing on carbonation resistance, and lacks the research on the interlock that how the hydration degree influences the compactness of the structure and reduces the microcracks, which affects the carbonation performance of concrete. Therefore, the relationship between hydration and carbonation also needs to be established to further explore the influencing mechanism on carbonation resistance. Otherwise, the engineering environment of the component was also important for its service performance, so it urgently needed to be considered. Nevertheless, former research has been conducted mainly in ordinary cement concrete, but few have been carried out for bridge deck concrete in hot and humid areas.

Regarding this situation, the factors including high CO_2 content, high temperature, and wet weather might accelerate the carbonation and the destruction of bridge deck concrete. In this case, the setting of each parameter in the carbonation test should be simulated to the actual engineering background. Meanwhile, it is necessary to illuminate the influencing mechanism of SAP on carbonation, which would promote its application in engineering to reduce durability damage caused by carbonation.

In this work, on the basis of fully considering the inherent properties of hot and humid regions, the varying rule of carbonation depth of cement concrete with SAPs of different particle sizes and dosages was studied by accelerated carbonation experiment. The hydration degree and products were investigated based on the FTIR and XRD tests. In addition, the $Ca(OH)_2$ absorption peak area of the control group and internal curing group at different ages was calculated quantitatively. In particular, an SEM test was conducted to observe the microstructure and remaining pores in concrete formed by SAP gels. Finally, the influencing mechanism of SAP on carbonation resistance was revealed by analyzing the carbonation depth, hydration performance, and microstructure characteristics of SAP-concrete.

2. Materials and Preparation

2.1. Materials

2.1.1. Superabsorbent Polymer (SAP). Sodium polyacrylate SAP was used as an internal curing agent in this study, whose particle sizes included 221–864 μm (SAP-20), 117–140 μm (SAP-100), and 74–104 μm (SAP-150). SAP was a white particle or powder, and the microstructure of SAP dry powder is shown in Figure 1. The liquid absorption rate of SAP with different meshes in cement paste was tested using the tea bag method ($W/C = 0.37$). Table 1 presents the specific technical indices and the measured absorption rate of SAP.

2.1.2. Cement. On the basis of GB 175–2020 [21], ordinary Portland cement (PO.42.5) with Blaine fineness of 3570 cm^2/g was selected in this article. The physical and mechanical properties are detailed in Table 2.

2.1.3. Aggregate. The coarse aggregate (limestone) from Jiangmen, Guangdong Province in China, was used in this study, which included two types of 4.75–9.5 mm and 9.5–19 mm, and the applying mass ratio was 2 : 8. The fine aggregate was manufactured sand of fineness modulus of 2.80. The gradation curve is shown in Figure 2.

2.1.4. Water Reducer and Water. Polycarboxylate superplasticizer (HPWR-Q8011) with a water reduction rate of 26% and a gas content of 2.5% was employed. Experimental water was Foshan tap water, which met the technical requirements of JGJ 63–2006 [22].

2.2. Mix Proportion of Concrete. The theoretical internal curing water introduction amount and SAP content (mass ratio of binding materials) were calculated based on the SAP's water absorption in water at 30 min (see Table 1) and the Powers Formula (as (1)). In order to explore the effect of the dosage and particle size on carbonation resistance and hydration degree on cement, SAPs of three different particle sizes and dosages were applied in this study. The mix proportions of concrete used in this article are listed in Table 3. The mixing procedure is illustrated in Figure 3.
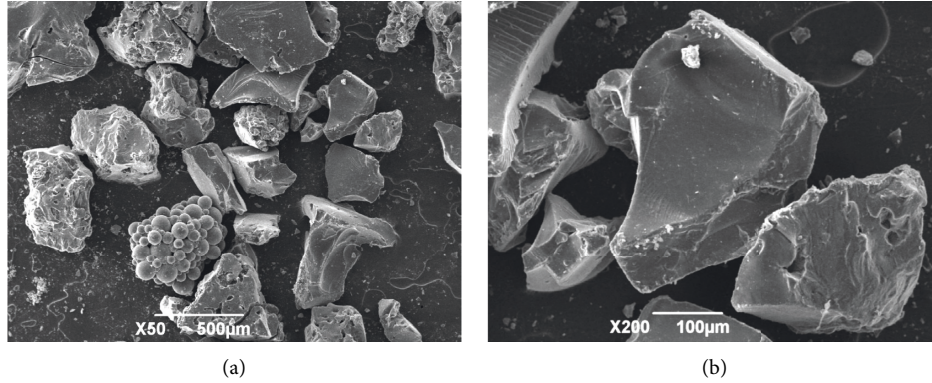
(a)

(b)

FIGURE 1: Micromorphology of SAPs in the dry state. (a) 50 times; (b) 200 times.

TABLE 1: Main technical indicators of SAP.

Density/(kg/m³)	pH/(1% moisture dispersion)	Saturated absorption time/s	Absorptance/(g/g)	Water absorption/(g/g)		
				20–60 mesh	100–120 mesh	150–200 mesh
0.75	5.5–6.8	< 28	450–550	17.2	14.2	12.3

TABLE 2: Physical and mechanical properties of cement.

Normative indices	Setting time/min		Flexural strength/MPa		Compressive strength/MPa	
	Initial set	Final set	3 d	28 d	3 d	28 d
	203	450	5.9	7.7	27.4	45
PO.42.5	≥45	≤600	≥3.5	≥6.5	≥17.0	≥42.5
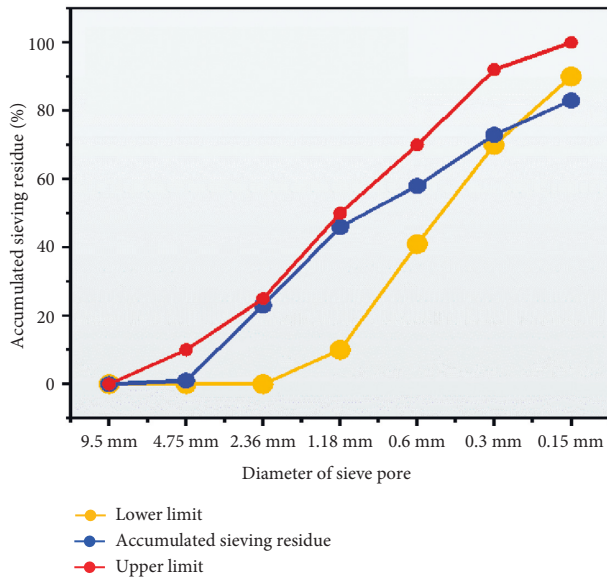
FIGURE 2: Fine aggregate gradation curve.

$$\frac{W}{C} \le 0.36, \left(\frac{W}{C}\right)_{IC} = 0.18\left(\frac{W}{C}\right),$$

$$0.36 \le \left(\frac{W}{C}\right)_{IC} \le 0.42, \left(\frac{W}{C}\right)_{IC} = 0.42 - \left(\frac{W}{C}\right), \quad (1)$$

where $(W/C)_{IC}$ is the additional water-cement ratio required for internal curing.

3. Testing Method

3.1. Accelerated Carbonation Test. Carbonation resistance could be characterized by measuring the carbonation depth of concrete. The test (the process of the test, see Figure 4) was conducted by the HTX-12 concrete carbonation box produced by North-South Instrument and Equipment Co., Ltd. The carbonation resistance of concrete was tested after 28 days of curing according to JTG3420-2020 [23]. The test of carbonation depth was recorded on days 3, 7, 14, and 28. A similar specimen of $100\,mm \times 100\,mm \times 400\,mm$ was prepared as a carrier for internal curing, which contained three parallel specimens in one group, and the bottom and surface were sealed with paraffin, leaving four sides. The specimens were placed in the testing space at $20 \pm 5°C$ and $70 \pm 5\%$ RH and the concentration of CO_2 was $20 \pm 3\%$. After testing treatment, the specimen was taken out and split on the press, and the thickness was decreased to $50\,mm$. The remaining specimen was put back in the carbonation box with a paraffin sealing section. The carbonation depth was calculated according to equation (2). Furthermore, in order to better investigate the influence of SAP on the carbonation performance of cement concrete, a coefficient of "relative carbonation rate" was defined and shown in equation (3).

TABLE 3: Mix proportion of internal curing pavement concrete.

Concrete type	SAP	W_{IC}/(kg/m³)	SAP dosage/kg	Compositions of pavement concrete/(kg/m³)					
				Cement	Water	Sand	4.75–9.5 mm Coarse	9.5–19 mm Coarse	Water reducer
S-Non	-	0	-						
S-20-0.200%	SAP-20	16.75	0.974						
S-150-0.200%	SAP-150	11.98	0.974	487	180.2	776	790	198	4.87
S-100-0.170%		11.76	0.828						
S-100-0.200%	SAP-100	13.83	0.974						
S-100-0.225%		15.56	1.096						
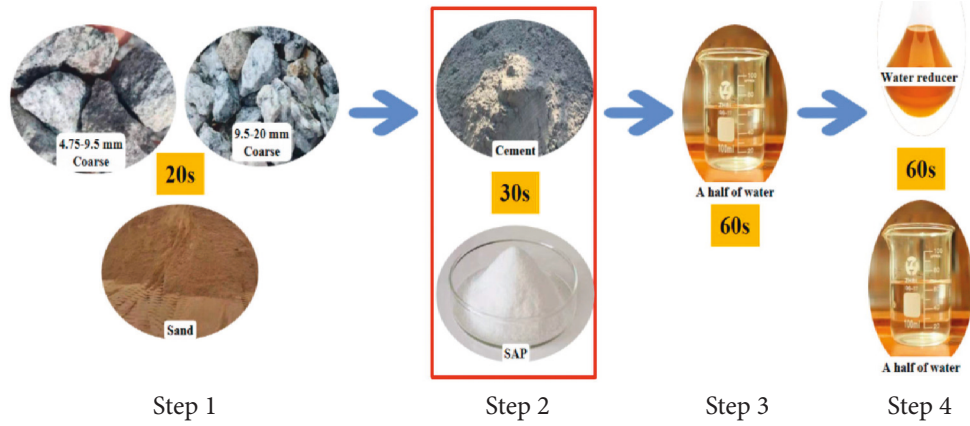
FIGURE 3: Preparing procedure of internal curing concrete with SAP.
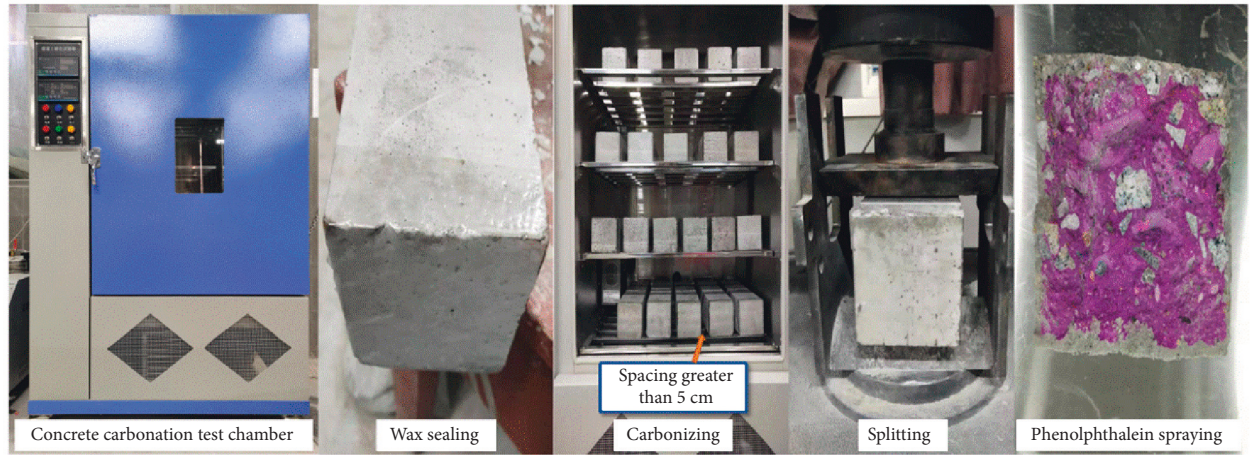
FIGURE 4: Process of concrete carbonation test.

$$\overline{d}_t = \frac{1}{n} \sum_{i=1}^{n} di, \tag{2}$$

where $\overline{d}_t$ is the average carbonation depth (mm) after carbonation (d); d_i is the carbonation depth of each measuring point (mm); n is the total number of measuring points. (Each specimen included 10 data in this study.)

$$\alpha_R = \frac{d_n}{d_0}, \tag{3}$$

where α_R is the relative carbonation rate; d_n is the average carbonation depth (mm) of the SAP curing group at

different ages; d_0 is the average carbonation depth (mm) of the control group at different ages.

3.2. Hydration Performance Test

3.2.1. FTIR Test.
To investigate the hydration degree of different experimental groups in Table 3, the FTIR test was carried out by FTIR-960 Fourier transform infrared spectrometer. The samples (approximately 0.02 g) were made with potassium bromide into thin slices using the specimen at the curing age of day 3, day 14, day 28, and day 56, respectively. The schematic of this test is presented in

Figure 5(a). The scanning wave number range was 4000–400 cm^{-1} and the resolution was 4.0 cm^{-1}.

It is worth noting that there were few studies on quantitative analysis of cement composition based on the FTIR technique [24]. A method for quantitative analysis of hydration degree was applied in this article. The absorption peak area of Ca(OH)$_2$ was quantitatively compared S-Non with the optimal SAP curing group. The tangent of the extreme points on both sides of the absorption peak was selected as the corrected baseline to calculate the absorption peak area, the baseline positioning, and peak area calculation (O$_1$, O$_2$, and O$_3$ are the reference points for peak area calculation), as shown in Figure 5(b).

3.2.2. XRD Test.

In order to further explore the influence of internal curing material on the internal hydration degree of cement, XRD was performed to characterize the valuation of hydration products. The samples chosen in this test contained three different curing ages of day 3, day 14, and day 28. The analysis angle range was 5°–80° with 40 kV voltage and 40 mA current.

3.3. SEM.

The carbonation resistance of internal curing concrete was closely related to its microstructure, and the macroscopic properties might be explained. Thus, SEM was used to characterize the microstructure and hydration products of concrete by a Japan Hitachi coldfield scanning electron microscope. The secondary electron resolution of SEM is 1.4 nm, and the magnification was 5000 times and 10000 times.

4. Results and Discussions

4.1. Influence Mechanism of Carbonation Resistance

4.1.1. Carbonation Resistance of Concrete with SAP of Different Particle Sizes.

The carbonation depth variation and relative carbonation rate of concrete with SAP of different particle sizes are shown in Figures 6 and 7, respectively.

From Figure 6, it can be seen that the incorporation of SAP had different effects on the carbonation resistance of concrete and the carbonation depth increased step by step with the extension of age. Among them, 100 mesh SAP had the minimum carbonation depth at the given time, followed by 150 mesh, which indicated that 100-mesh SAP had the best improvement effect on concrete. From the view of the relative carbonation rate in Figure 7, it can be discovered that the carbonation depth of the S-100-0.200% and S-150-0.200% groups were 56.5% and 88.3% compared to that of the control group on day 28, respectively. This phenomenon may be related to the distribution and internal curing range of SAP particles in concrete. The liquid absorption rate of 100 mesh is higher than 150 mesh, so the curing range of 100 mesh SAP internal curing water is larger, which reflects the better carbonation resistance.

Based on the above analysis, it can be speculated that for the given dosage, the larger the particle size is, the larger the curing range is provided, and the excellent carbonation

resistance may be presented. But it was interesting to find that the carbonation depth of the curing group was deeper than that of S-Non when the mesh was 20. Otherwise, the carbonation depth of concrete with 20-mesh SAP was 50.3% higher than that of the control group on day 3, but on day 28, only 9.9%, which demonstrated that the carbonation effect of 20-mesh SAP was gradually improved with the extension of age. In addition, SAP of 20 mesh may promote the generation of large remaining pores due to the large particle size of SAP and high liquid absorption rate, resulting in more channels for CO$_2$ to enter the internal concrete.

4.1.2. Carbonation Resistance of Concrete with SAP of Different Dosages.

To search the effect of SAP dosage on carbonation resistance, 3 dosages of 100-mesh SAP were chosen in this section, and the results are presented in Figures 8 and 9.

As shown in Figures 8 and 9, the carbonation resistance of concrete was enhanced to a certain degree. With the increase of SAP dosage, the carbonation depth of concrete decreased first and then increased on day 28. As the results show, the carbonation depth of internal curing groups of S-100-0.175%, S-100-0.200%, and S-100-0.225% were 9.0%, 24.7%, and 14.0%, respectively, less than that of the control group, while on day 28, there were 35.8%, 43.5%, and 18.2%, respectively, which decreased more significantly. Based on this phenomenon, it could be concluded that the dosage of 0.225% has the worst carbonation resistance among different dosages. Moreover, with the increase of age, the improving effect of internal curing material SAP on the carbonation resistance of cement concrete became more obvious. The addition of SAP could enhance the carbonation resistance of concrete, which could be interpreted as that SAP can absorb more internal curing water and gradually release the water absorbed in the mixing process during curing age, improving the relative humidity of concrete under the action of difference ion concentration and humidity. In this case, the microcracks in concrete are reduced, which could block the channels of CO$_2$ effectively. Therefore, the carbonation resistance of concrete is enhanced.

There is no doubt that the larger the curing range is, the more the microcracks may be inhibited, benefitting from the curing effect with the greater dosage, but it was interesting to note that the great dosage of 0.225% had the deepest carbonation depth. This is because the "microagglomeration" phenomenon is easy to occur in the process of cement concrete mixing, and the unsaturated SAP is wrapped with a layer of SAP saturated with water, which leads to further absorption of internal curing water being hindered and the internal curing effect weakened. In consequence, the carbonation resistance could be improved with a moderate dosage of SAP.

4.2. Hydration Degree Analysis Based on FTIR and XRD

4.2.1. Analysis of FTIR Spectra.

The influence of SAP on the hydration degree of cement could be inferred by the vibration peaks of each functional group measured by the FTIR test. The FTIR spectra of the control group
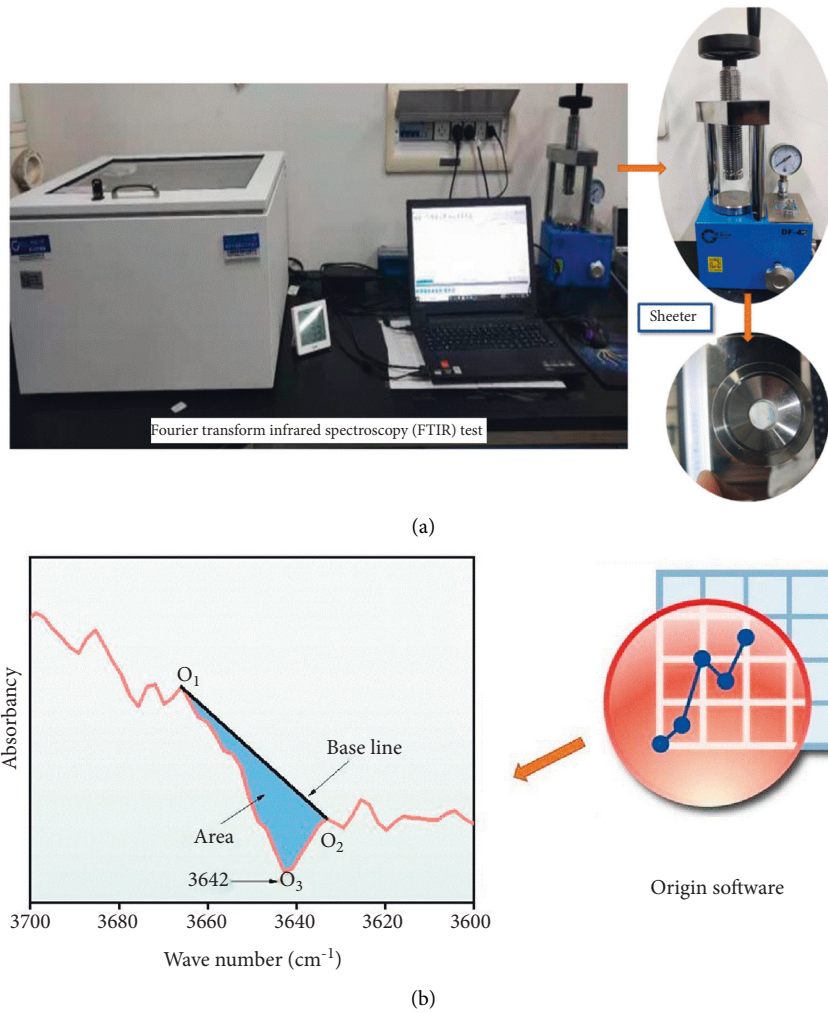
(a)

(b)

FIGURE 5: FTIR test: (a) process of preparation of thin slice samples; (b) calculation of peak area of $Ca(OH)_2$.
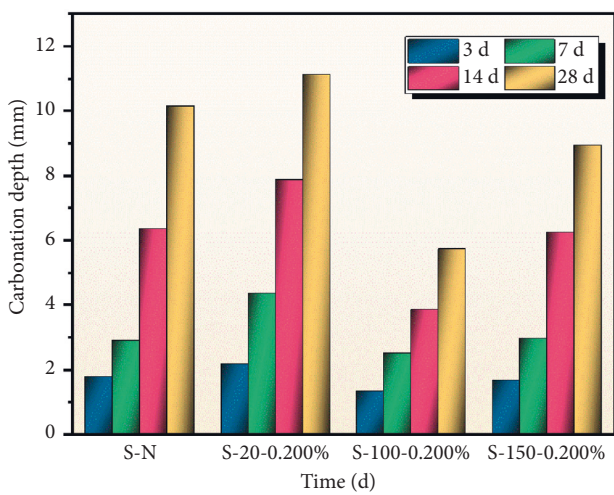

FIGURE 6: Carbonation depth of concrete with SAP of different sizes.
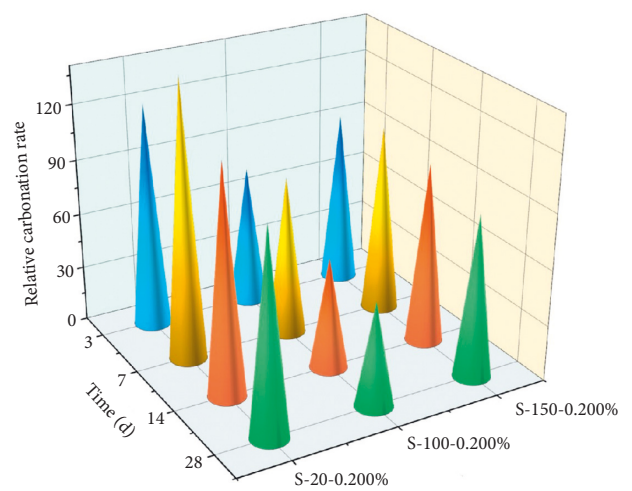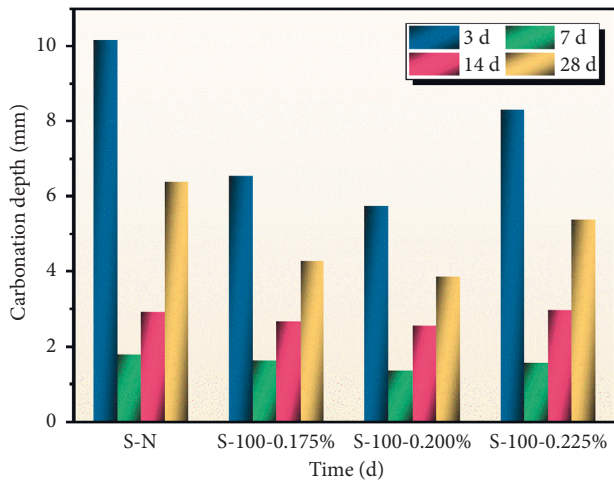

FIGURE 7: Relative carbonation rate of concrete with SAP of different sizes.

(Figure 10(a)) and S-100-0.200% (Figure 10(b)) (optimal group in carbonation test) were investigated and compared, whose age ranged from day 3 to day 56. At the same time, the effect of SAP particle size on the hydration of cement was studied by analyzing the FTIR spectra of day 56 (Figure 11).

FIGURE 8: Carbonation depth of concrete with SAP of different dosages.
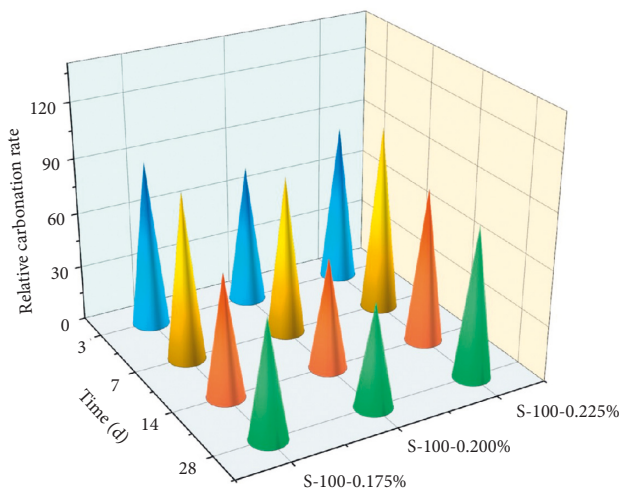
FIGURE 9: Relative carbonation rate of concrete with different dosages.

From Figures 10 and 11, it can be observed that the position and shape of the characteristic peaks of each functional group were basically the same in FTIR spectra between the two groups, but the absorption intensity of the absorption peak was different, which indicated that the addition of SAP promoted the hydration process of cement and led to the relative content variation of cement concrete components. The functional groups of OH^- and CO_3^{2-} mainly appeared in the high wavenumber region from 4000^{-1} to $300\,cm^{-1}$ and the stretching vibration peak of H-O-H (near $3432\,cm^{-1}$) was the absorption peak of water molecules. The characteristic peak of $CaCO_3$ ($1423\,cm^{-1}$) was caused by the CO_3^{2-} formed from the reaction of the alkali in the cement and CO_2 in the air, which induced the 'carbonation' phenomenon appearing in the cement. Therefore, the contact between CO_2 and H_2O should be avoided during the preparation, storage, and test of samples.

The absorption peak (below $1300\,cm^{-1}$) was caused by the vibration of the silica or alumina groups and the asymmetric stretching vibration peaks of Si-O in the silica tetrahedron around $1081\,cm^{-1}$ and $1024\,cm^{-1}$. The bending vibration peak of Si-O-Si (around $692\,cm^{-1}$) identified the degree of polymerization of the silicate grid, and the higher the peak value was, the higher degree of polymerization would be. The above peaks of Si-O and Si-O-Si combined with the bending vibration peak in the Si-O plane ($463\,cm^{-1}$) corresponded to the characteristic peaks of the C-S-H gel. Vibration peaks of Al-O ($874\,cm^{-1}$) were related to the generation of AFt or AFm. Although the variation of the main peak was not obvious with the advancement of the hydration process, the peak type of several small peaks in the range of $1300\,cm^{-1}$–$450\,cm^{-1}$ absorption peak developed rapidly. It could be explained that the aggregation degree of silicon (aluminum) oxygen polyhedron network structure on the surface of cement particles decreases, which leads to the tendency to be single in the oligomeric structure; thus, the symmetry of the structure is improved.

Figure 11 presents the FTIR spectra of concrete with SAP of different particle sizes at day 56. Compared with the S-Non, the characteristic peaks of hydration products of the internal curing group with 0.200% dosage were strengthened. The characteristic peak of the internal curing group was significantly enhanced to be about $874\,cm^{-1}$, and the absorption peak area of $Ca(OH)_2$ in S-100-0.200% was the largest, which demonstrated the degree of hydration was high, followed by 150 mesh. Meanwhile, the water absorption was improved with the increase in particle size, which was attributed to the hydration of cement.

As for the effect of SAP dosage on the hydration degree of cement, it was quantitatively analyzed by calculating the area ratio of $Ca(OH)_2$ absorption peak of the internal curing group with SAP of various dosages and S-Non at different ages (Figure 12).

It can be seen in Figure 12 that the ratio of $Ca(OH)_2$ absorption peak ($3642\,cm^{-1}$) shows the trend of decreasing-increasing in the SAP curing group and control group at different ages. The $Ca(OH)_2$ absorption peaks of S-100-0.175%, S-100-0.200%, and S-100-0.225% were 1.92 times, 1.95 times, and 1.74 times than that of the control group, respectively. It could be concluded that the early hydration of cement concrete can be enhanced with the addition of SAP. Interestingly, it was found that the absorption peak of $Ca(OH)_2$ in internal curing groups with three particle sizes was smaller than that S-Non at day 28. This phenomenon could be interpreted that the internal humidity of cement concrete gradually decreases with the continuous hydration. Then the internal water is gradually released, which promotes the secondary hydration of unhydrated cement and some part of $Ca(OH)_2$ is consumed. Thus, the hydration degree in the later stage is improved effectively. Compared with the control group at the age of day 56, SAP curing groups increased by 0.7 times, 3.36 times, and 1.03 times, respectively.

According to the above results, the dosage of 0.200% is considered the optimal dosage, which has the best enhancing effects. With the appropriate particle size and dosage, the hydration degree of cement can be improved and internal microcracks may be reduced, which would enhance structural compactness and promote carbonation resistance.
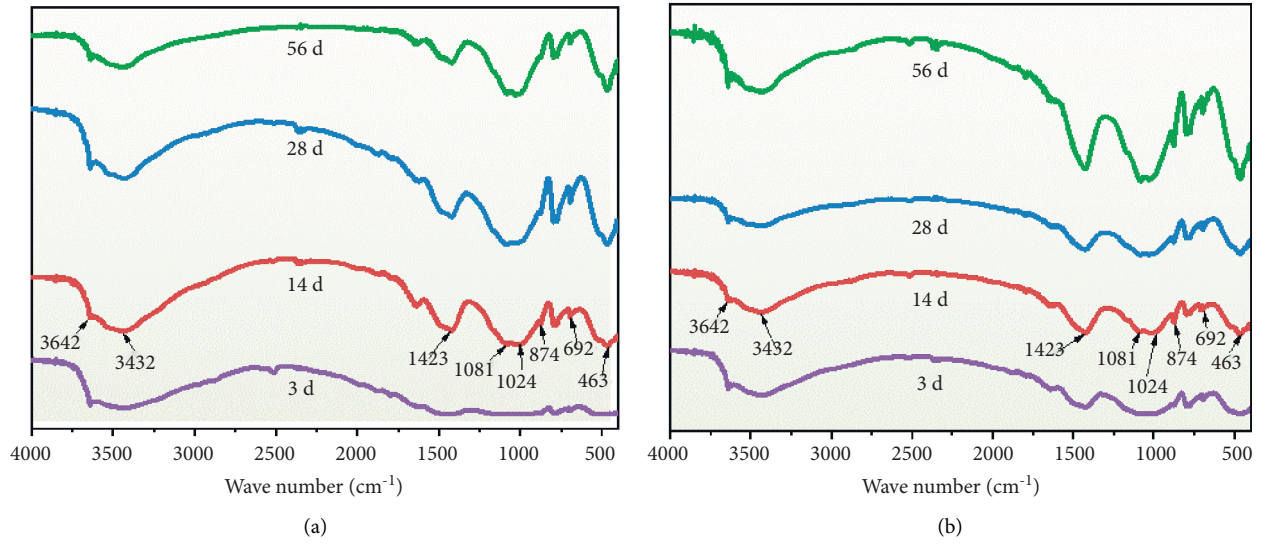
(a)

(b)

FIGURE 10: FTIR spectra of different ages: (a) S-Non; (b) S-100-0.200%.
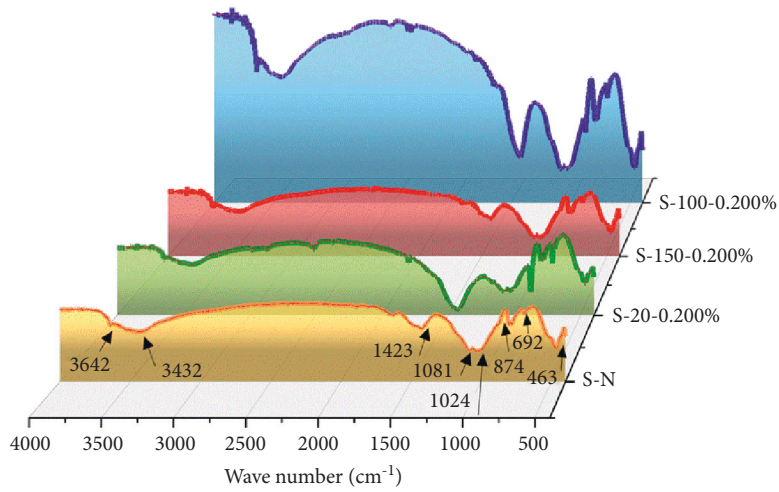

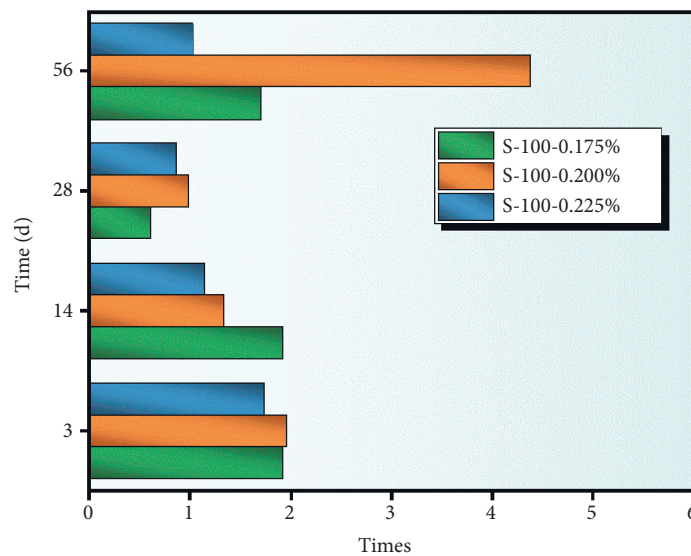FIGURE 11: FTIR spectra of different particle sizes for 56 d.

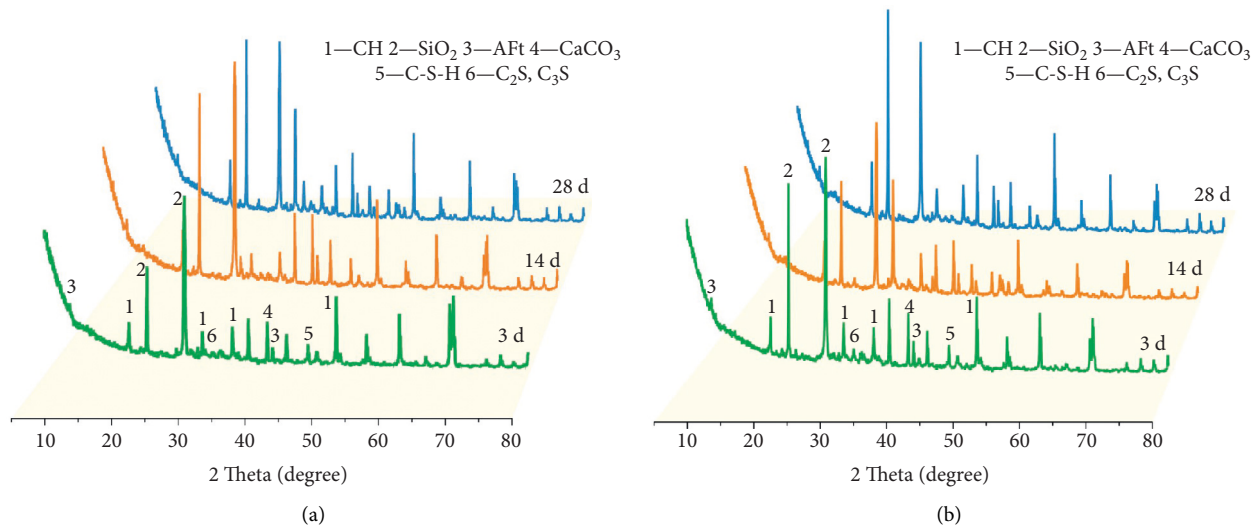FIGURE 12: Ratio of Ca(OH)$_2$ peak area in hydration products at different ages.

Figure 13: XRD results at different ages: (a) S-Non; (b) S-100-0.200%.

4.2.2. Analysis of XRD Pattern. For better understanding of the hydration degree of internal curing concrete, the comparison of the XRD spectrum between S-Non and S-100-0.200% on day 3, day 14, and day 28 is depicted in Figure 13

In Figure 13, it can be clearly obtained that $Ca(OH)_2$, C-S-H gel, and AFt were the main hydration products corresponding to the diffraction peaks of concrete. Besides, SiO_2 from binding material and fine aggregate minerals and the carbonation product of $CaCO_3$ existed. There was no obvious new diffraction peak in the XRD spectrum of S-100-0.200% on day 3, day 14, and day 28, which indicated that the type of hydration product was not changed with the incorporation of SAP.

Compared with the two groups, the content of hydration products was raised with the increase of age. The $Ca(OH)_2$ and AFt diffraction peaks in S-100-0.200% were significantly higher than S-Non. The strongest diffraction peaks of $Ca(OH)_2$ between the group without SAP and internal curing group were 486 Å and 902 Å, and those of C_2S and C_3S were 428 Å and 284 Å, respectively. It could be explained that SAP can promote the consumption of C_2S and C_3S, leading to the generation of more $Ca(OH)_2$.

The above analysis proves once again that the hydration degree of cement concrete is improved through SAP's water release effect; thereby, the microcracks are decreased and the density of the structure is increased, which would prevent the harmful substances such as carbon dioxide from entering the concrete.

4.3. Microstructure and Influence Mechanism of Carbonation. The factors affecting the carbonation resistance of internal curing concrete mainly include the following two aspects: (1) the compactness of concrete filled by the hydration products generated in the hydration process; (2) the balance between remaining pores formed by SAP gels and hydration product filling effect. Therefore, microstructure analysis of cement concrete and the remaining pores formed by SAP gels should

be implemented in the research on carbonation resistance of concrete.

SEM micrographs of S-Non and S-100-0.200% at the magnification of 5000 times at different ages are illustrated in Figures 14 and 15. It can be observed that the number of hydration products of the two groups increased gradually with the increment of age within day 56. The hydration degree of cement concrete structure in the control group is low. Figures 14(a) to 14(d) show that the pores between particles were large with microholes, which led to the distribution of relatively loose microstructure. Compared with the two groups, it can be found that the hydration products in S-Non were less than those in the internal curing group and only a few $Ca(OH)_2$ and a small amount of C-S-H were identified, which was improved at day 56. Obviously, cotton flocculent fibrous C-S-H appeared at day 14 in the S-100-0.200%, and the internal structure became dense. At day 56, a large amount of C-S-H gel was produced, which indicated a higher degree of hydration.

Combined with the micromorphology of internal pores (Figure 16) and the remaining pores formed by SAP gels panorama of S-100-0.200% (Figure 17), the connection between microstructure and performance results of SAP-concrete was clarified, and the influence mechanism of carbonation on internal curing could be mainly interpreted.

As seen in Figure 16, the abundance of hydration products inside the internal pores included the layered $Ca(OH)_2$, flocculent and fibrous C-S-H gel, and a small amount of AFt, which were closely intertwined and overlapped, showing the discontinuous three-dimensional network structure distribution. A large number of C-S-H gel and the accumulation of hydration products on day 56 are presented in Figure 16(b), which indicates the quantity of hydration products was increased and the dense structure was formed; thus, S-100-0.200% showed a better performance than the control group in hydration degree and carbonation test.
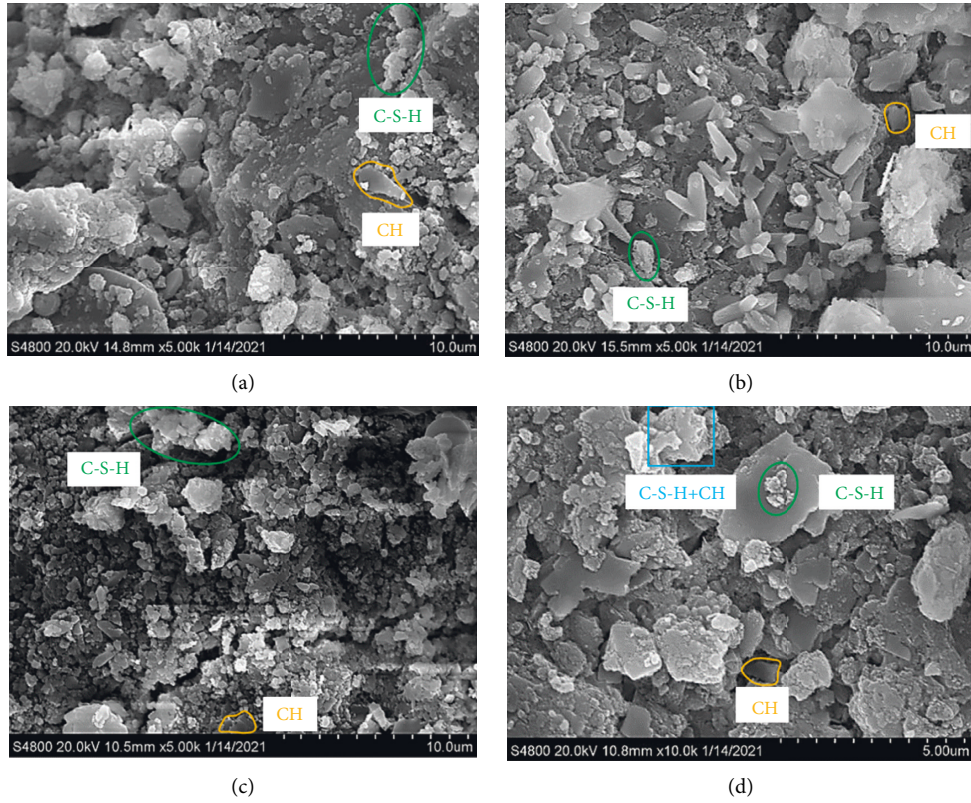
FIGURE 14: Micromorphology of cement concrete at different ages of control group: (a) 3 d, (b) 14 d, (c) 28 d, and (d) 56 d.
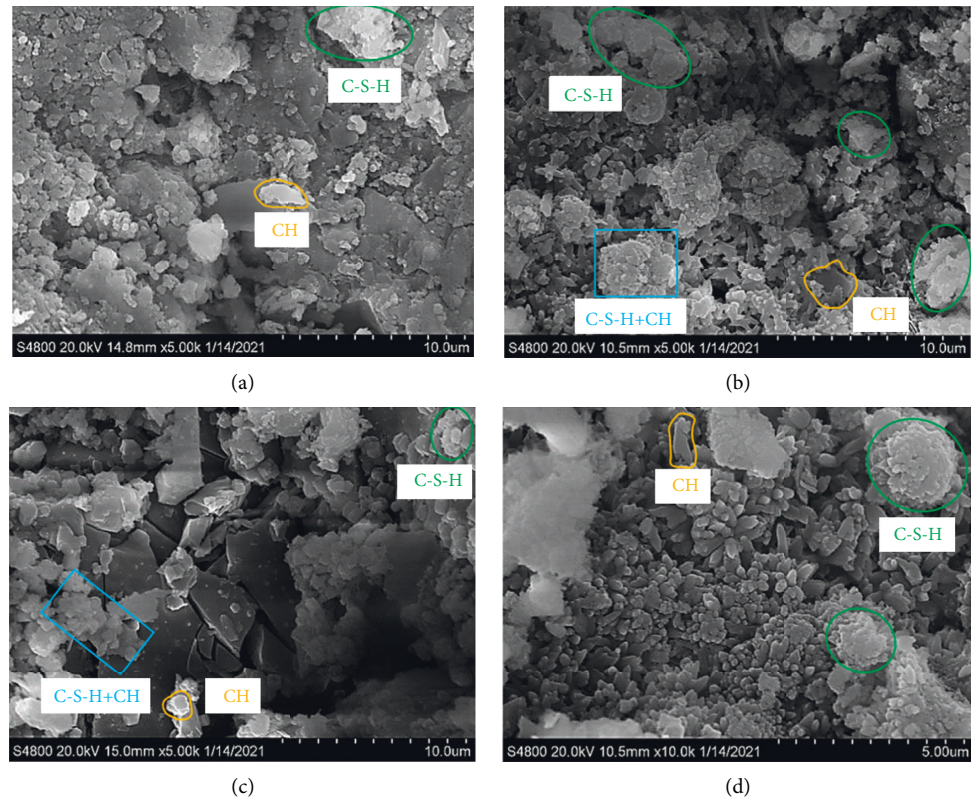

FIGURE 15: Micromorphology of cement concrete at different ages of S-100-0.200%: (a) 3 d (b) 14 d, (c) 28 d, and (d) 56 d.
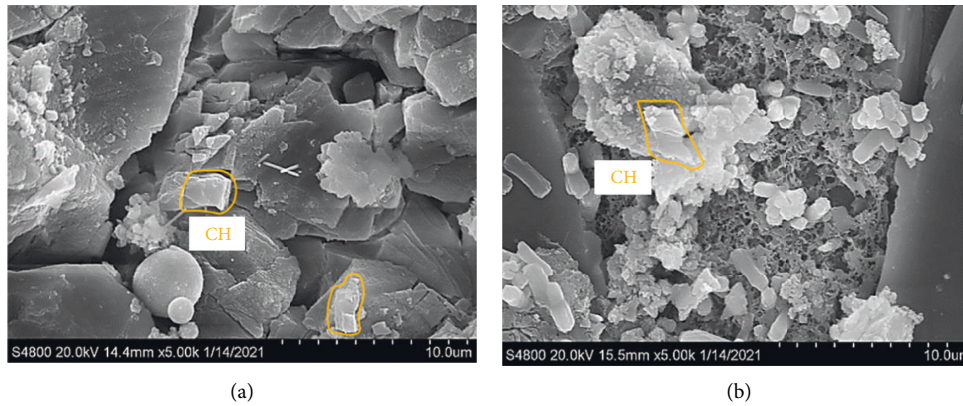
(a)

(b)

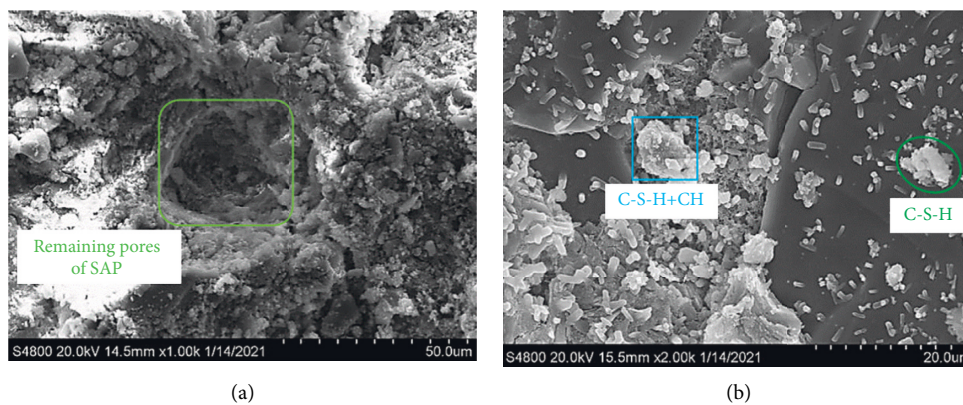FIGURE 16: Micromorphology of internal pores of S-100-0.200%: (a) 28 d; (b) 56 d.

(a)

(b)

FIGURE 17: Remaining pores formed by SAP gels panorama of S-100-0.200%: (a) 28 d; (b) 56 d.

As observed in Figure 17(a), the remaining pores formed by SAP gels on day 28 were filled with flocculent SAP and surrounded by a C-S-H gel layer with different thicknesses, which was formed by the diffusion of the slurry around the SAP hole to SAP. It could be analyzed that the large pores would be formed after water release; however, the pore filling of the gel layer is limited and the hydration products are mainly used to fill the opening pores capillary. Failure to achieve effective filling would accelerate the carbonation reaction with the increase of concrete pores, which is a good explanation for the above interesting phenomenon that the particle size of 20 mesh has the worst carbonation resistance among the internal curing group. Moreover, it can be observed from Figure 17(b) that the remaining pores formed by SAP gels could be well filled by hydration products during the internal curing process, which was closely integrated with the boundary; thus, the invasion of CO_2 was blocked.

The improving mechanism of hydration performance and carbonation resistance of SAP-concrete could be concluded based on the above analysis. On the one hand, SAP can compensate for the internal humidity of concrete and make the humidity distribution more uniform during the curing process, which could promote the hydration degree of cement and inhibit the microcracks; otherwise, more hydration products are produced to fill the inside structure. On the other hand, the filling relationship between hydration products and remaining pores formed by SAP gels could be better balanced with the moderate dosage and particle size. Thus, the compactness and integrity of concrete structures are enhanced. The denser the concrete is, the slower the diffusion rate of CO_2 and the smaller the residual pores are. At the same time, the content of alkaline substances is increased; therefore, the more corrosive substances (mainly CO_2 and some H^+, SO_4^{2-}) are needed to consume when entering the internal concrete, which mitigates the diffusion rate of CO_2. Thereby, the carbonation resistance of concrete was reinforced.

5. Conclusions

The carbonation test and hydration degree test included FTIR and XRD of internal curing cement with SAPs of different particle sizes and dosages studied in this article. The micromorphology and remaining pores formed by SAP gels panorama were also investigated to further understand the influence mechanism of internal curing with SAP. The conclusions were summarized as follows:

(1) The carbonation depth of cement concrete at different ages was measured in this research. The carbonation resistance first increased and then decreased with the increase of SAP particle size and

dosage. S-100-0.200% had the best performance, with the carbonation depth of only 56.5% of the control group on day 28. Furthermore, those of S-100-0.175% and S-100-0.225% were 35.8% and 18.2% lower than that of S-Non, respectively. The results showed that the carbonation resistance could be improved effectively by selecting the appropriate SAP particle size and dosage.

(2) The conclusion that the addition of SAP could promote the hydration degree was proved by qualitatively and quantitatively analyzing FTIR spectra and XRD. The area of $Ca(OH)_2$ absorption peak in S-100-0.200% was 3.36 times larger than that of S-Non at day 56. The strongest diffraction peaks of $Ca(OH)_2$ between the control group and S-100-0.200% were 486 Å and 902 Å, and those of C_2S and C_3S were 428 Å and 284 Å, which demonstrated that more C_2S and C_3S translated into $Ca(OH)_2$.

(3) The abundant hydration products in the cement concrete of S-100-0.200% had evenly filled up the remaining pores formed by SAP gels and a dense microstructure was formed, which improved the compactness of concrete and prevented carbon dioxide from entering; thus, the carbonation resistance was enhanced.

(4) The appropriate particle size and dosage obtained by optimization are 100 mesh and 0.200% when W/C is 0.37.

Further work can be performed to simulate the multiple environmental coupled effects like carbonation, salt freeze-thaw cycle, sulfate dry-wet cycle, acid rain, and fatigue load. The resistance performance of SAP-concrete under the multiple environmental coupled effect should be explored and the influencing mechanical properties need to be further clarified.

Data Availability

The data used to support the findings of this study are included within the article.

Conflicts of Interest

The authors declare that there are no conflicts of interest regarding the publication of this article.

Acknowledgments

References

[1] X. Zhang, B. Liu, L. Yang, and Y. Luo, "Experimental study on concrete carbonation performance under the influence of different temperature and strength," *Building Structure*, vol. 50, no. 24, pp. 110–115, 2020.

[2] T. Li, X. Liu, and Y. Zhang, "Carbonization mechanism of reactive powder concrete with sea-water and sea sand," *Materials Reports*, vol. 34, no. 4, pp. 8042–8050, 2020.

[3] F. Tong, Q. Ma, and X. Hu, "Triaxial shear test on hydrochloric acid-contaminated clay treated by lime, crushed concrete, and super absorbent polymer," *Advances in Materials Science and Engineering*, vol. 201913 pages, Article ID 3865157, 2019.

[4] X. Qin, A. Shen, J. Li, and Z. Xie, "Water transport characteristics and mechanical properties of internal curing pavement concrete," *Journal of Building Materials*, vol. 34, no. 3, pp. 606–614, 2021.

[5] D. Shen, C. Liu, J Jiang, J. Kang, and M. Li, "Influence of super absorbent polymers on early-age behavior and tensile creep of internal curing high strength concrete," *Construction and Building Materials*, vol. 258, pp. 120068–120079, 2020.

[6] I. S. Kim, S. Y. Choi, Y. S. Choi, and E. I. Yang, "Effect of internal pores formed by a superabsorbent polymer on durability and drying shrinkage of concrete specimens," *Materials*, vol. 14, no. 18, p. 5199, 2021.

[7] X. Zheng, M. Han, and L Liu, "Effect of superabsorbent polymer on the mechanical performance and microstructure of concrete," *Materials*, vol. 14, no. 12, p. 3232, 2021.

[8] B. J. Olawuyi, A. J. Babafemi, and W. P. Boshoff, "Early-age and long-term strength development of high-performance concrete with SAP," *Construction and Building Materials*, vol. 267, p. 121798, 2021.

[9] D. Dai, J. Peng, X. Zhao, G. Li, and L. Bai, "Strength and road performance of superabsorbent polymer combined with cement for reinforcement of excavated soil," *Advances in Civil Engineering*, vol. 202116 pages, Article ID 9170431, 2021.

[10] X. Qin, J. Xu, A. Shen, and Z. Lyu, "Salt frost resistance and fatigue characteristics of self-curing pavement concrete," *Bulletin of the Chinese Ceramic Society*, vol. 40, no. 8, pp. 2784–2793, 2021.

[11] S. Gupta, "Effect of presoaked superabsorbent polymer on strength and permeability of cement mortar," *Magazine of Concrete Research*, vol. 70, no. 9, pp. 473–486, 2018.

[12] H. Beushausen, M. Gillmer, and M. Alexander, "The influence of superabsorbent polymers on strength and durability properties of blended cement mortars," *Cement and Concrete Composites*, vol. 52, pp. 73–80, 2014.

[13] C. Shi, G. Lyu, X. Ma, J. Zhang, and J. Liu, "Influence of SAP on the properties of self- compacting concrete," *Materials Reports*, vol. 29, no. 20, pp. 118–124, 2015.

[14] L. Zhang, X. Kong, F. Xing, X. Fu, and B. Dong, "Chloride ion invasion and carbonation property of internal cured concrete with super-absorbent polymer," *Journal of Henan University of Science and Technology(Natural Science)*, vol. 40, no. 1, pp. 60–65+7, 2019.

[15] Y. Guo, Z. Huang, W. Wang, A. Shen, and D. Li, "Investigation of carbonation resistance and mechanism of SAP internal curing concrete in humid and hot environment," *Journal of Building Materials*, vol. 25, no. 1, pp. 16–23, 2022.

[16] Y. Jiang, Z. Jin, Y. Chen, and J. Fan, "Effect of super-absorbent polymer on hydration and compressive strength of concrete," *Materials Reports*, vol. 31, no. 24, pp. 40–44+49, 2017.

[17] H. Zhao, Y. Wan, J. Xie, and K. D. X. S. R. G. Jiang, "Effects of nano-SiO2 and SAP on hydration process of early-age cement paste using LF-NMR," *Advances in Materials Science and Engineering*, vol. 2020, Article ID 6089482, 9 pages, 2020.

[18] G. Qin, M. Gao, C. Pang, and W. Sun, "Research on performance ImproVement of ExpansiVe concrete with internal curing agent SAP and its action mechanism," *Journal of Building Materials*, vol. 14, no. 3, pp. 394–399, 2011.

[19] L. P. Esteves, "On the hydration of water-entrained cement-silica systems: combined SEM, XRD and thermal analysis in cement pastes," *Thermochimica Acta*, vol. 518, no. 1-2, pp. 27–35, 2011.

[20] X. Qin, A. Shen, Z. Lyu, and L. J. H. Shi, "Research on water transport behaviors and hydration characteristics of internal curing pavement concrete," *Construction and Building Materials*, vol. 248, pp. 118714–118728, 2020.

[21] GB 175-2020, *Common portland cement*, Standards Press of China, China, 2007.

[22] JGJ 63-2006, *Standard of Water for concrete*, pp. 3-4, ChinaChina Architecture & Building Press, 2006.

[23] JTG3420-2020, *Testing Methods of Cement and Concrete for Highway Engineering*, pp. 237–239, China Communications Press, China, 2020.

[24] R. Hu, W. Liu, L. Xu, L. Jin, and J. G. Liu, "Online analysis method of cement raw materials based on fourier transform infrared spectroscopy," *Spectroscopy and Spectral Analysis*, vol. 40, no. 1, pp. 41–47, 2020.

Research Article

Effect of Aromatic Petroleum Resin on Microstructure of SBS Modified Asphalt

Hongjuan Wu [ID],[1] **Peng Chen** [ID],[2] **Chengqin Chen** [ID],[1] **and Wei Zhang** [ID][1]

[1]*School of Civil Engineering, Northwest Minzu University, Lanzhou 730000, China*
[2]*Beijing CCCC Qiaoyu Science and Technology CO.LTD, Beijing 271000, China*

Correspondence should be addressed to Peng Chen; zjqychenpeng1983@yeah.net and Chengqin Chen; cccnmu@126.com

In this paper, aromatic petroleum resin (APR) was used as raw material. The fluorescence microscopic photography of styrene-butadiene-styrene block copolymer (SBS) modified asphalt with different contents of APR was carried out, and the effect of APR on the dispersion of SBS modified asphalt was quantitatively studied. The nano-surface morphology of SBS modified asphalt with different APR contents was tested by atomic force microscope (AFM), and the effects of APR content on AFM nanoscale parameters such as roughness and maximum amplitude were analyzed. In addition, this paper also tested the basic technical indexes of SBS modified asphalt with different APR contents and revealed its improvement law on the pavement performance of SBS modified asphalt. The results show that the use of APR is beneficial to the shearing of SBS into smaller particles. The larger the amount of APR, the smaller the maximum particle size and average particle size of SBS in asphalt and the smaller the roughness and maximum amplitude of SBS modified asphalt. APR can improve the viscosity and low-temperature ductility of SBS asphalt to a certain extent. High-temperature storage stability is improved obviously; SBS modified asphalt mixed with APR has a more dense spatial cross-linking structure after thorough development. The research results are helpful to reveal the mechanism of APR improving the performance of SBS polymer asphalt.

1. Introduction

SBS modified asphalt is the most widely used polymer asphalt in China, accounting for more than 95% of China's polymer asphalt market. Taking SBS as the main polymer, it has derived the largest polymer asphalt market in the world. SBS is dispersed in asphalt in a swelling state, and the particle size can reach micron level [1]. However, due to the large density gap between SBS and asphalt, the segregation of SBS has been perplexing asphalt production and transportation enterprises. Researchers have tried to use a variety of methods to improve the technical properties of SBS modified asphalt and achieved certain results. Among them, new modifiers are an important way. A variety of materials have been used to improve many technical properties of SBS modified asphalt, such as TiO$_2$/PS-rGO [2], nano-Al$_2$O$_3$ [3], polyphosphoric acid [4], polysulfide regenerant [5], nano-montmorillonite [6],

methylene diphenyl diisocyanate [7], multi-dimensional nanomaterials [8], polystyrene grafted activated waste rubber powder [9, 10], oil [11], multi-layered CNTs [12–14], nano-organic palygorskite [15], silica fume [16], and nano-CuO and MWCNT [17].

It can be seen that the use of new modifiers is the mainstream method to improve the technical performance of SBS modified asphalt. In recent years, APR has been used as additives in many fields, and it has good compatibility with asphalt [18–20]. APR refers to a resin material formed by polymerization of olefins or cyclo-olefins containing nine carbon atoms or copolymerization with aldehydes, aromatics, and terpenes [21–24]. APR appears as light yellow to light brown flake or blocks solid, the average molecular weight is 500–1000, the relative density is 0.97–1.04, the softening point is 40-l40°C, the glass transition temperature is 81°C, the refractive index is 1.512, the base value is less than 4, the acid value is less

than 0.1, the bromine value is 7–50, and the iodine value is 30–140 [25, 26]. APR has a ring structure with high cohesion, good acid resistance, chemical resistance, water resistance and weather resistance, but its adhesion is poor. APR has good compatibility with phenolic resin, coumarone resin, polymerized styrene butadiene rubber (SBR), and SBS. It is soluble in acetone, methyl ethyl ketone, cyclohexane, dichloromethane, ethyl acetate, benzene, toluene, and solvent gasoline, but it has poor compatibility with natural rubber and is insoluble in ethanol and water [27–30]. APR is often used as tackifying resins for preparing pressure-sensitive adhesives, hot-melt pressure-sensitive adhesives, and rubber adhesives. Some scholars have also done some related research work on the influence of substances with similar properties to APR on the properties of SBS modified asphalt Zhang W. et al. [31] reported that C9 petroleum resin can improve the storage stability of SBS modified asphalt. Tang et al. [21] revealed that aromatic oil and petroleum resin have good compatibility with SBS, which is conducive to the shear and dispersion of SBS in asphalt. Nie et al. [32] used bio-oil to increase the compatibility between SBS polymer particles and light oil.

In the research methods of SBS modified asphalt, fluorescence microscopy has become an important technology to study SBS modified asphalt. SBS modifier can emit light with a longer wavelength when excited by a short light wave. At present, the acquisition of fluorescent micro-red-green-blue picture (RGB) is relatively mature but still limited to the limitation of interdisciplinary disciplines. When acquiring micro-quantitative parameters, the fixed equal threshold method is generally used to binarize the RGB diagram of SBS modified asphalt. The thickness of each picture is different, which leads to a lot of information being enlarged or reduced, which greatly limits the accuracy of quantitative analysis of the microparameters of SBS modified asphalt by fluorescence microscopy. In addition, AFM technology has become an important means to study asphalt and modified asphalt. Some progress has been made in the measurement method of nano-morphology of asphalt, the relationship between morphology characteristics and macro-mechanical parameters, and the influencing factors of morphology characteristics. However, it is still in its infancy in terms of morphology characteristics and correlation energy. The quantitative analysis of different phases in the asphalt AFM phase diagram will become a breakthrough in this field.

In conclusion, there are not many studies on the action mechanism and effect of APR on SBS modified asphalt. Based on the existing research, this article used APR as the raw material and used a fluorescence microscope to explore its influence on the dispersion of SBS polymer in asphalt. With the help of AFM, the influence law of APR on the nano-surface morphology of SBS modified asphalt was explored, and the technical indexes of APR/SBS modified asphalt were tested. The research results are helpful to reveal the mechanism of APR improving the performance of SBS polymer asphalt.

2. Test Design

2.1. Materials.
The KLMY (90#) asphalt used in this article was produced by PetroChina Company Limited (Karamay, China). The technical indexes are shown in Table 1. SBS modifier was produced by Baling Petrochemical Co. Ltd. (Yueyang, China). The technical indexes are shown in Table 2. SBS polymer is used in a 1 : 1 ratio of linear-SBS and star-SBS, and the mixing amount is 4.5% (asphalt mass percentage). The sulfur-based stabilizer was produced by Sichuan Kelutai Transportation Technology Co. Ltd. (Chengdu, China). The technical indexes are shown in Table 3, and the content is 0.2% (percentage of asphalt mass). The APR was produced by Jinan Dahui Chemical Technology Co. Ltd. (Jinan, China), and its technical indexes are shown in Table 4.

The preparation method of SBS modified asphalt used in this paper is as follows. The 90# asphalt is heated to 175°C~185°C, then SBS polymer is added into the asphalt, and the shearing instrument is used to operate at a high speed of 4500 r/min for 50 min. During this period, sulfur-based stabilizers and APR are slowly mixed. After shearing and dispersion, SBS polymer asphalt can be obtained by stirring at 170°C~180°C for 2 h.

2.2. Test Design.
In this paper, the quality of SBS in SBS modified asphalt is used as a benchmark, and the content of APR is 0%, 5%, 10%, 15%, and 20%, respectively. The fluorescence microscopic images of SBS polymer asphalt were obtained by fluorescence microscope, and the dispersion effect of APR on SBS in asphalt was analyzed. The nano-surface morphology of SBS polymer asphalt was photographed with the help of the atomic force microscope to study the influence of APR on the nano-morphology of SBS modified asphalt. Finally, the conventional technical properties of APR/SBS modified asphalt were tested.

2.3. Test Specimen Preparation and Test Method

2.3.1. Preparation and Test Method of Fluorescent Micro-Asphalt Specimen.
The preparation method of fluorescent micro-asphalt specimen is as follows. Take an appropriate amount of asphalt (2 drops of asphalt in this paper) and drop it on the slide. Put the cover glass on the asphalt. No external force can be applied artificially to prevent the distribution form of polymer in the asphalt from changing due to the intervention of external force. Then, place the slide in the oven at 180°C for 1~2 min to prevent the influence of bubbles in asphalt and uneven cover glass on image quality. The glass slide can be taken out after the asphalt is covered with the cover glass and cooled naturally at 20°C~30°C. If there are many bubbles in the sample, it shall be discarded. Figure 1 is an example of the specimens prepared in this paper and a photo of the fluorescence microscopic test point.

The fluorescence microscope used in this paper is 27C-LQ type produced by Shanghai Putuo Photoelectric Instrument Co. Ltd. When excited by a short wave of light

TABLE 1: Technical indexes of KLMY 90# asphalt.

Technical indexes		Measured value
Penetration at 25°C, 0.1 mm		88.4
Ductility at 10°C, cm		54.3
Softening point, °C		46.9
RTFOT[1]	Mass change, %	0.42
	Penetration ratio, %	62.7
	Residual ductility at 10°C, cm	14.6

[1]RTFOT: rolling thin film oven test.

TABLE 2: Technical indexes of SBS.

Technical indexes	Linear-SBS	Star-SBS
S/B	30/70	40/60
Volatile, %	0.6	0.6
Ash, %	0.13	0.15
300% constant tensile stress, MPa	2.1	2.3
Tensile strength, MPa	16.34	8.2
Elongation at break, %	813	573
Permanent set, %	28.5	38.4
Shore hardness, A	76	71
Melt index, g/10 min	1.97	0.86

TABLE 3: Technical indexes of stabilizer.

Physical form	Proportion	Combustion temperature
Gray black powder	1.4 (25°C)	269°C

TABLE 4: Technical indexes of APR.

Technical indexes	Measured value
Flash point, °C	260
Kinematic viscosity at 100°C, mm^2/s	14
Ash content, %	0.03
Density, g/cm^3	1.05
Characteristic	Green liquid

wave after the SBS modifier is swelled in asphalt, it can emit light with a longer wavelength, while asphalt and APR do not excite any light. Therefore, the polymer phase and asphalt phase can be clearly distinguished under the fluorescence microscope. Because the fluorescence microscope uses the reflected light field imaging, the real distribution and morphological structure of polymer in asphalt can be clearly observed. In this paper, asphalt specimens are photographed with a fluorescence microscope at 400 times magnification. Asphalt and APR are red, while SBS is yellow. After proofreading, the side length of each fluorescence micrograph is 156 μm.

2.3.2. Preparation and Test Method of AFM Specimen

Preparation Method of AFM Sample. Heat the asphalt to the flowing state, take an appropriate amount of asphalt and drop it on the glass slide (10 drops of asphalt are used in this paper), and then place the glass slide in a horizontal oven at 180°C for 1 min. The asphalt can be basically kept flat without overflow. Then, put the glass slide into the

environmental chamber (the carrier remains horizontal) and reduce the asphalt temperature from 180°C to 25°C at a cooling rate of 8°C/min, and the asphalt AFM sample can be successfully prepared. AFM specimens were scanned by atomic force microscope in tap mode at 25°C. The parameters during the AFM test are as follows. The number of samples is 255, the scan size is 10 μm × 10 μm, and the drive amplitude is 300.00 MV. Figure 2 shows the AFM specimen preparation and test process.

3. Results and Discussion

3.1. Effect of APR on the Dispersion of SBS Modifier. Fluorescence microscopic images of undeveloped SBS asphalt were taken. At this time, SBS has become micron fine particles through high-speed shear. However, since the adsorption swelling process of SBS polymer particles on light components in asphalt has not been completed, SBS particles are granular, as shown in Figures 3–7. Figures 3–7 show the fluorescence micrographs of SBS asphalt with different contents of APR.

Figures 3–7 show that the addition of APR has a certain effect on the particle size of SBS particles dispersed in asphalt. The larger the content of APR, the smaller the particle size of SBS. It can be considered that APR is beneficial for SBS to be sheared into finer particles under the condition of the constant shear process.

3.2. Quantitative Analysis of Influence Law of Dispersion Performance. Process the SBS asphalt fluorescence micrograph and unify the pixel size (255 × 200 in this paper); the "imread" command in the MATLAB tool is used to obtain the RGB image of the fluorescence micrograph, and the "im2bw" command is used to obtain the binary image under an appropriate threshold. With the help of the Image-Pro Plus tool, the number of SBS particles and the number of pixels occupied by each SBS particle in the binary image can be counted, and then the area proportion of SBS can be calculated. The particle size, average particle size, maximum particle size, etc. of each SBS particle can also be calculated according to the relationship between the number of pixels and the actual size of the picture. Figure 8 shows an example of a picture processing process.

During the test, the method of increasing the test samples is adopted in order to avoid the influence of the discreteness of a single micro-image on the results. The number of each sample is 5~10, and the representative pictures are shown in Figures 9–13.

The binarization process adopts the processing method of dynamic threshold, and the binarization thresholds of Figures 9–13 are 0.680, 0.751, 0.525, 0.512, and 0.589, respectively. This processing method reduces the problem of the large error caused by using a single threshold in the binarization process of different images and lays a foundation for particle size statistics and image assignment analysis. The particle size distribution of SBS polymer particles with different contents of APR can be observed intuitively in Table 5.
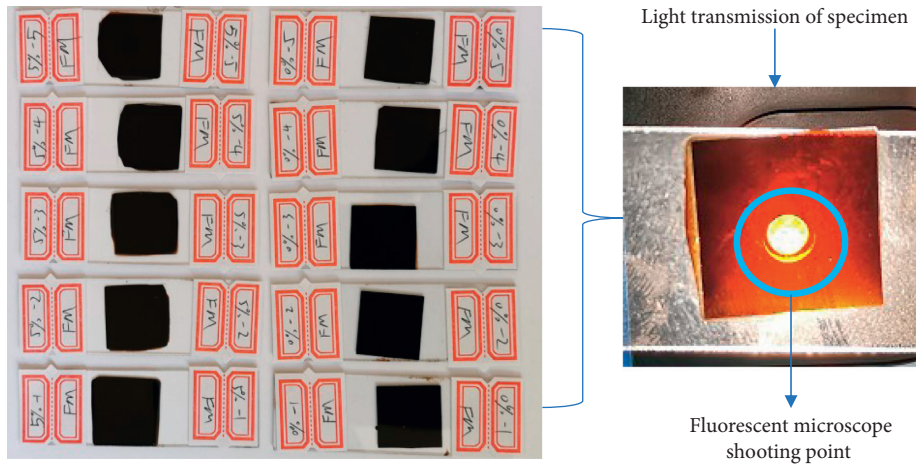
Light transmission of specimen

Fluorescent microscope shooting point

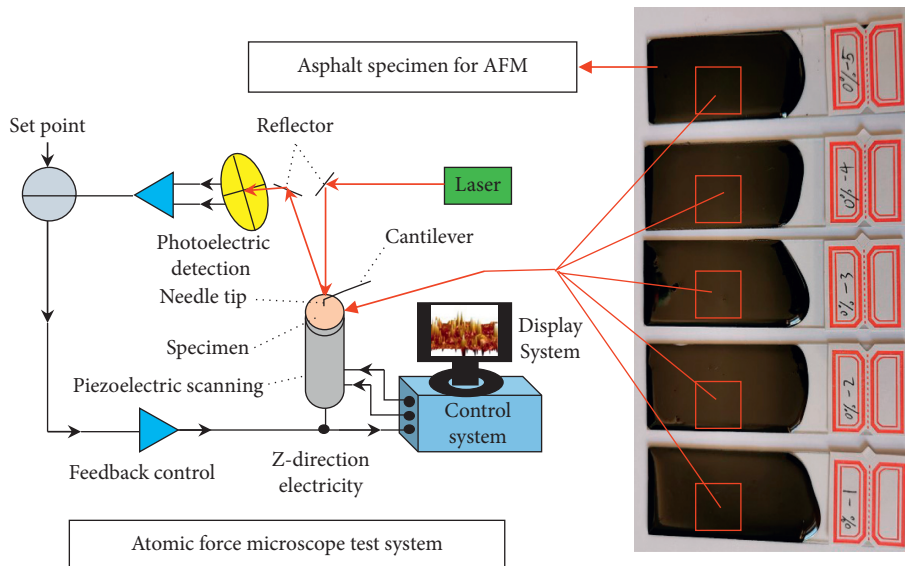FIGURE 1: An example of the specimens prepared in this paper and a photo of the fluorescence microscopic test point.

Asphalt specimen for AFM

Set point

Reflector

Laser

Photoelectric detection

Cantilever

Needle tip

Specimen

Display System

Piezoelectric scanning

Control system

Feedback control

Z-direction electricity

Atomic force microscope test system

FIGURE 2: The AFM specimen preparation and test process in this paper.

60 μm
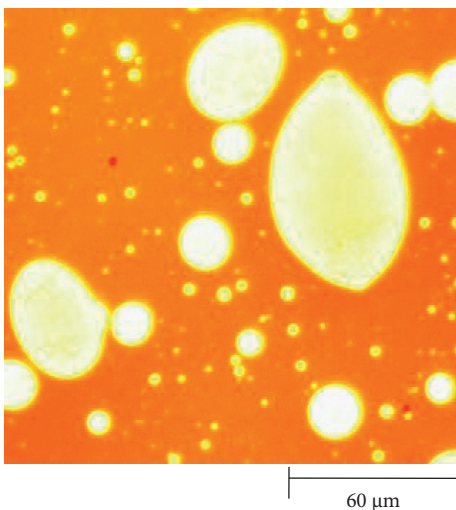
FIGURE 3: Fluorescence micrographs of undeveloped SBS modified asphalt with 0% content of APR.

60 μm
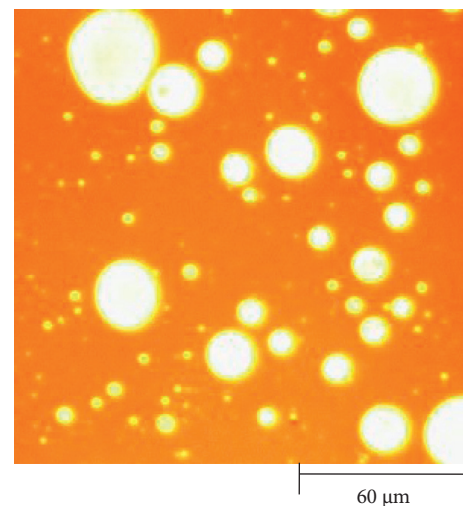
FIGURE 4: Fluorescence micrographs of undeveloped SBS modified asphalt with 5% content of APR.
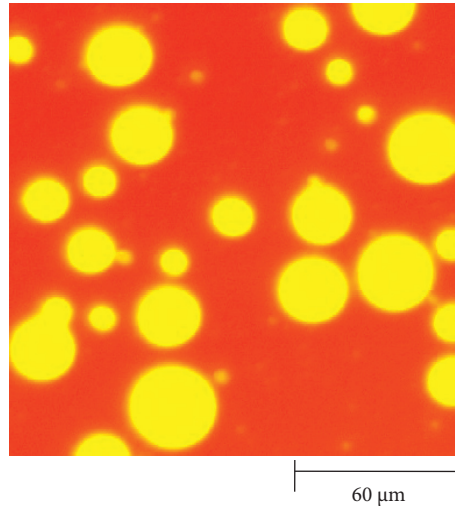
FIGURE 5: Fluorescence micrographs of undeveloped SBS modified asphalt with 10% content of APR.
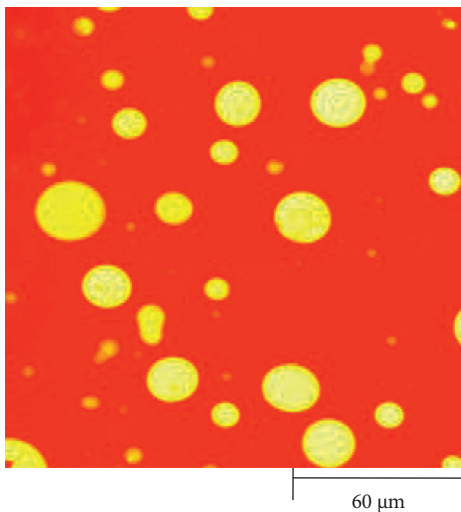
FIGURE 6: Fluorescence micrographs of undeveloped SBS modified asphalt with 15% content of APR.
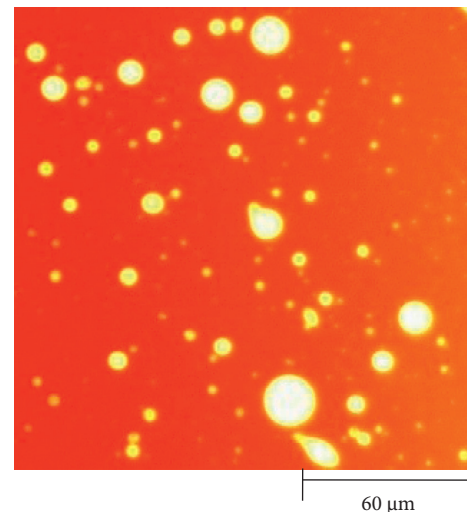

FIGURE 7: Fluorescence micrographs of undeveloped SBS modified asphalt with 20% content of APR.

Table 5 shows the maximum particle size, average particle size, and area proportion of SBS counted/measured with the help of the Image-Pro Plus tool. From the measurement results, the larger the content of APR, the smaller the maximum particle size and average particle size of SBS modifier particles. Although there is a positive correlation between the area proportion of SBS and the content of APR, the increasing trend is not obvious. The fundamental reason is that the decisive factor of the area proportion of SBS is the content of SBS. Figure 14 shows the test results of the average particle size of SBS polymer with different contents of APR.

Equations (1) and (2) are the calculation equations of the content of APR and the maximum particle size and average particle size of the SBS modifier based on the test results.

$$P_{max} = 0.157C^2 - 5.867C + 72.84R^2 = 0.934, \qquad (1)$$

$$P_{avg} = -0.40C + 13.08R^2 = 0.965, \qquad (2)$$

where P_{max} is the maximum particle size of SBS modifier, μm; P_{avg} is the average particle size of SBS modifier, μm; C is the content of APR, %; and R is the related coefficient.

Since the APR is a resin substance formed by polymerization of olefins or cycloolefins or copolymerization with aldehydes, aromatics, terpenes, and so on, combined with the research results in Sections 3.1 and 3.2, it can be boldly guessed that the addition of APR makes some substances have a related effect with SBS, which makes the swelling of SBS in asphalt easier and allows it to swell into particles with smaller particle size. As a result, the swelling degree of SBS modified asphalt mixed with APR is much higher.

3.3. Effect of APR on Nano-Morphology of SBS Modified Asphalt

3.3.1. Nanoscale Parameters of Asphalt. The height information of the asphalt surface is collected by AFM, and the scanning results are read by NanoScope Analysis software,
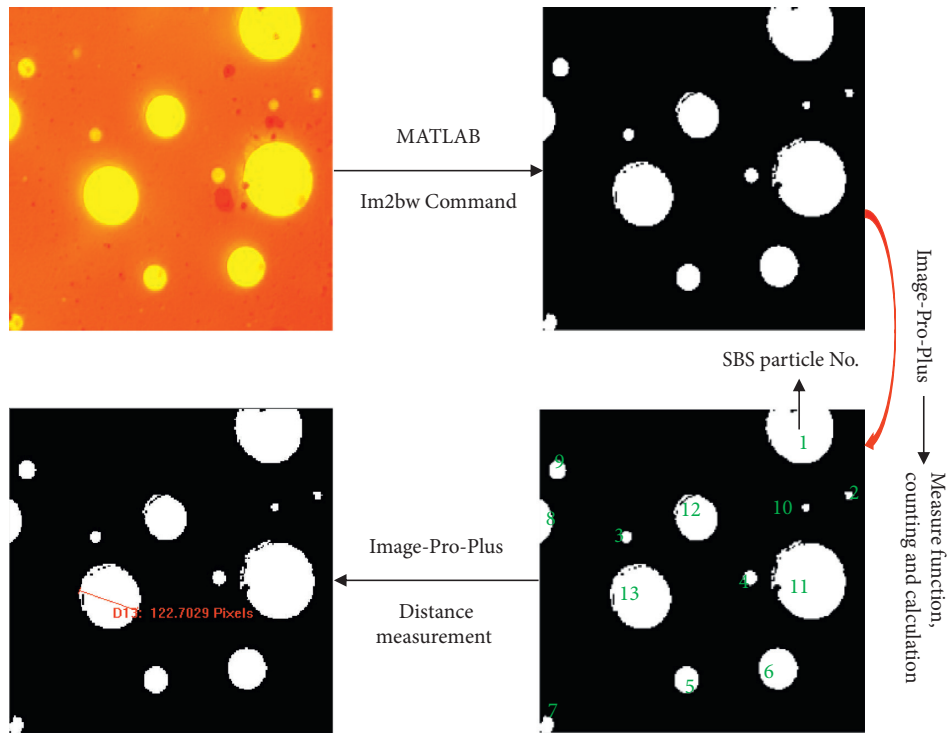
Figure 8: An example of a picture processing process.
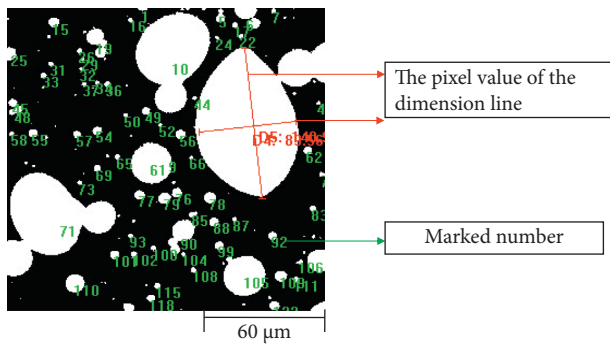

Figure 9: Fluorescence microscopic binarization image of SBS modified asphalt with 0% content of APR.
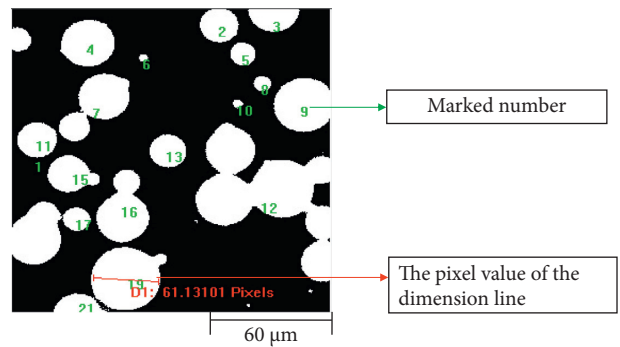

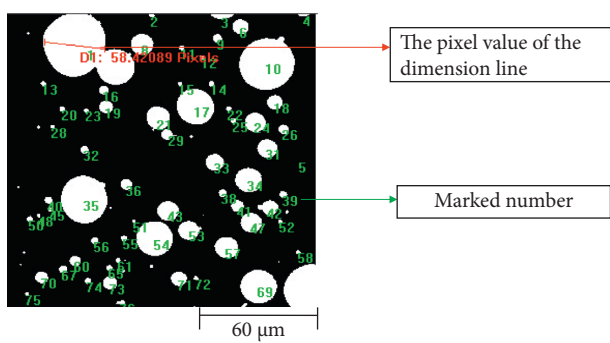Figure 11: Fluorescence microscopic binarization image of SBS modified asphalt with 10% content of APR.

Figure 10: Fluorescence microscopic binarization image of SBS modified asphalt with 5% content of APR.
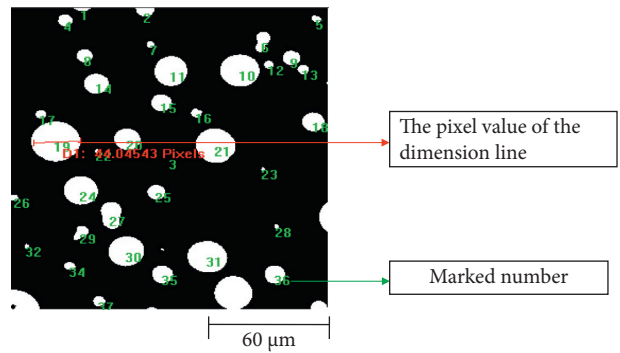

Figure 12: Fluorescence microscopic binarization image of SBS modified asphalt with 15% content of APR.
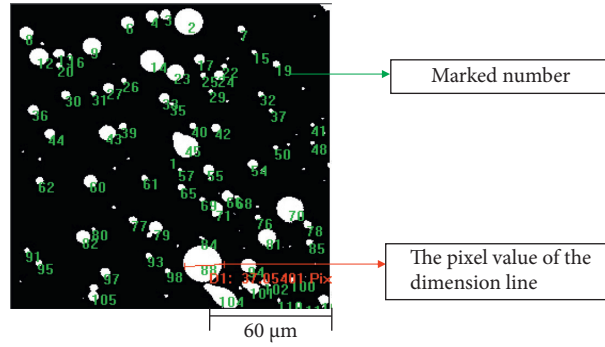
FIGURE 13: Fluorescence microscopic binarization image of SBS modified asphalt with 20% content of APR.

TABLE 5: Maximum particle size and average particle size of SBS.

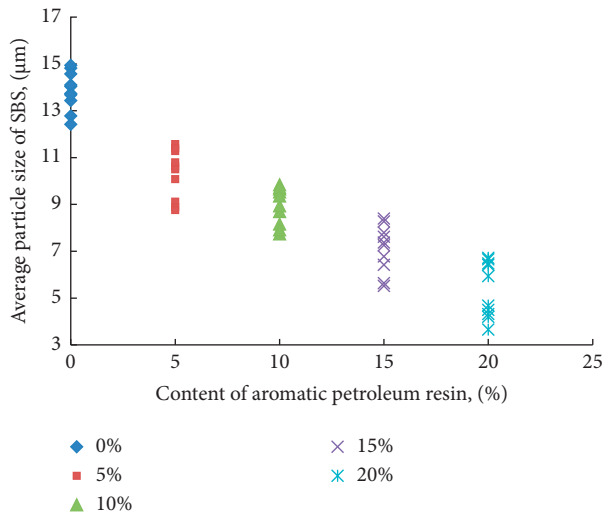| Content of APR, %	Maximum particle size, μm	Average particle size, μm	Proportion of SBS area, %
0	76.8	13.8	9.59
5	37.92	10.2	9.64
10	34.8	9	9.72
15	23.4	7.2	9.79
20	16.2	5.4	9.77

FIGURE 14: Relationship between average particle size of SBS modifier and content of APR.

and then the roughness value can be automatically calculated.

The roughness selected in this paper is the root mean square roughness (R_q), and the calculation method is shown in the following equation [33, 34]:

$$R_q = \left(\frac{\left(\iint [h(x, y) - h_0]^2 \mathrm{d}A \right)}{\left(\iint \mathrm{d}A \right)} \right)^{1/2}, \quad (3)$$

where A is the scanning area, $10 \,\mu\text{m} \times 10 \,\mu\text{m}$; $h(x, y)$ is the height function, nm; and h_0 is the reference height, nm, and its calculation method is shown in the following equation [35]:

$$h_0 = \frac{\left(\iint (h(x, y) \mathrm{d}S) \right)}{\left(\iint \mathrm{d}S \right)}. \quad (4)$$

Figure 12 shows the method to obtain the root mean square roughness. The roughness of the selected area can be quickly read by using the roughness module of NanoScope Analysis software.

During the test, it is found that for the same kind of asphalt, under the same test conditions (the cooling rate during forming shall be strictly controlled), the roughness of different test areas (in units of $10 \,\mu\text{m} \times 10 \,\mu\text{m}$) is relatively stable, and the test error is about 3%. It also provides a guarantee that the roughness can be used as an AFM nanoscale parameter. Figure 15 shows an example of the roughness test method.

This paper defines that the nanoscale parameter (maximum amplitude) based on AFM is the difference between the maximum height ($h_{\max}$) and the minimum height ($h_{\min}$) in the three-dimensional space of height (h). As shown in Figure 16, $h_{\max}$ and $h_{\min}$ can be read or calculated by NanoScope Analysis software. During the test, it is found that for the same kind of asphalt, under the same test conditions (the cooling rate during forming shall be strictly controlled), the maximum amplitude of different test areas (in units of $10 \,\mu\text{m} \times 10 \,\mu\text{m}$) is relatively stable, and the test error is about 5%. It provides a guarantee that the maximum amplitude can be used as an AFM nanoscale parameter.

3.3.2. Effect of APR Content on Nano-Morphology of SBS Modified Asphalt. In this paper, the AFM specimens of SBS modified asphalt with APR content (SBS mass percentage) of 0%, 5%, 10%, 15%, and 20% were prepared. All tested modified asphalt had been sheared and developed for 2 h. During the preparation of the AFM specimens, the cooling rate of the modified asphalt was controlled at 8°C/min, from 180°C to 25°C, and the scanning of the nano-topography was completed at a temperature of 25°C. There are five groups of data for each content of APR. The nanoscale parameters of

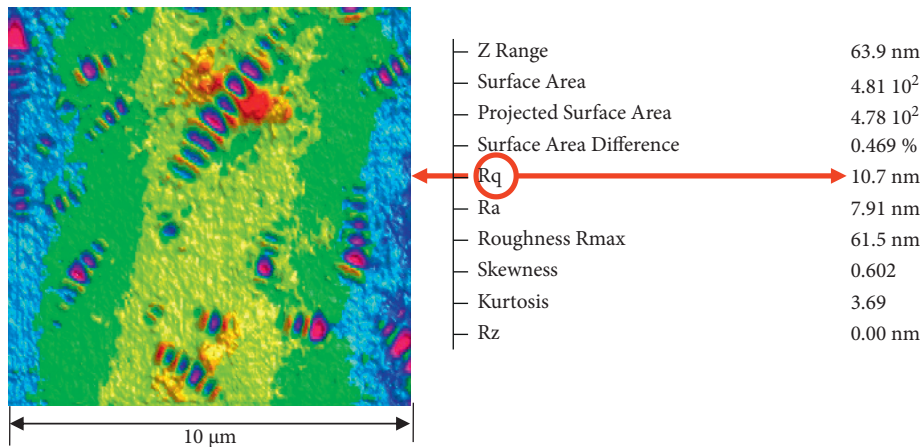| Z Range | 63.9 nm |
Surface Area	$4.81 \ 10^2$
Projected Surface Area	$4.78 \ 10^2$
Surface Area Difference	0.469 %
Rq	10.7 nm
Ra	7.91 nm
Roughness Rmax	61.5 nm
Skewness	0.602
Kurtosis	3.69
Rz	0.00 nm

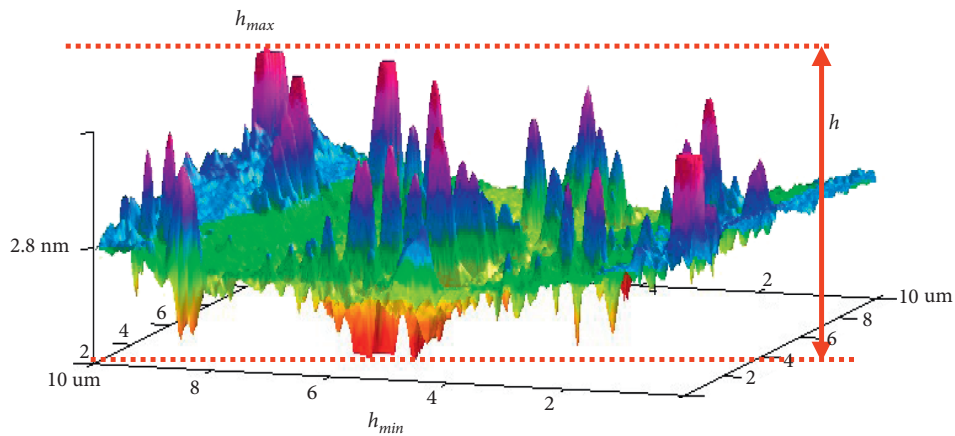FIGURE 15: Test method of the roughness.

FIGURE 16: Test method of the maximum amplitude.

SBS modified asphalt with different APR contents are calculated according to the AFM image. The calculation results are shown in Figures 17 and 18.

Figure 17 shows that with the gradual increase in the content of APR, the roughness of SBS modified asphalt shows a gradual decrease trend. When there is no APR, the roughness of SBS modified asphalt is basically maintained at about 9 nm, while when the content of APR reaches 20%, this value is reduced to about 6 nm. These phenomena suggest that APR has a certain interference effect on the formation of the bee-like structure of SBS modified asphalt. Although there is no unified view on the formation reason of bee-like structure, scholars generally believe that roughness, as an index reflecting bee-like structure, has a certain relationship with the technical performance of asphalt. It is generally believed that for the same modified asphalt, the greater the roughness, the stronger the viscosity and the stronger the anti-segregation and anti-ageing performance.

Figure 18 shows the maximum amplitude of SBS modified asphalt with different APR contents. With the continuous increase of the content of APR, the maximum amplitude of SBS modified asphalt shows a gradually decreasing trend, which just reflects the relationship between roughness and the content of APR. When there is no APR,

the maximum amplitude of SBS modified asphalt is maintained at about 90 nm, while when the content of APR reaches 20%, this value decreases to about 40 nm, which is very obvious. According to the relevant research, for the same modified asphalt, the maximum amplitude often exists on the bee-like structure, and its numerical value seriously affects the roughness value. Therefore, when the maximum amplitude of asphalt is smaller, the stronger the viscosity is, the stronger the anti-segregation and anti-ageing performance will be.

3.4. Influence of APR on Technical Indexes of SBS Modified Asphalt.
After the SBS modified asphalt with different contents of APR was adequately developed, the technical indexes of SBS asphalt with different contents of APR were tested, such as penetration (25°C), 48 h softening point difference, rotational viscosity (135°C), softening point, and ductility (5°C). The test results are summarized in Table 6.

Table 6 shows that softening point, an index of high-temperature viscosity of SBS asphalt, is not sensitive to the use of APR. However, when the amount of APR continues to increase, the penetration, as one of the conditional viscosity indexes of SBS modified asphalt, gradually decreases. At the
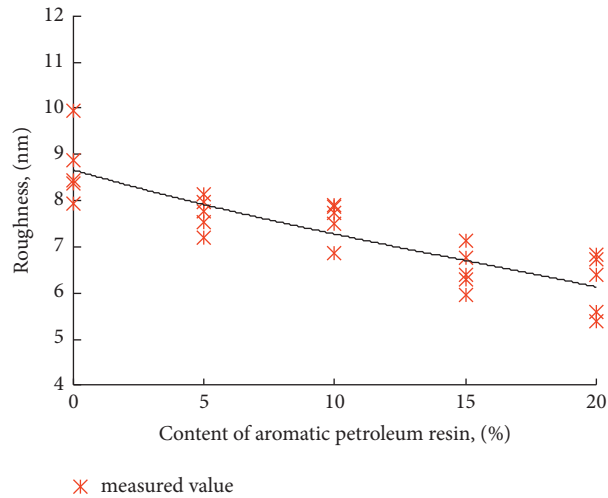
FIGURE 17: The roughness of SBS modified asphalt with different APR contents.
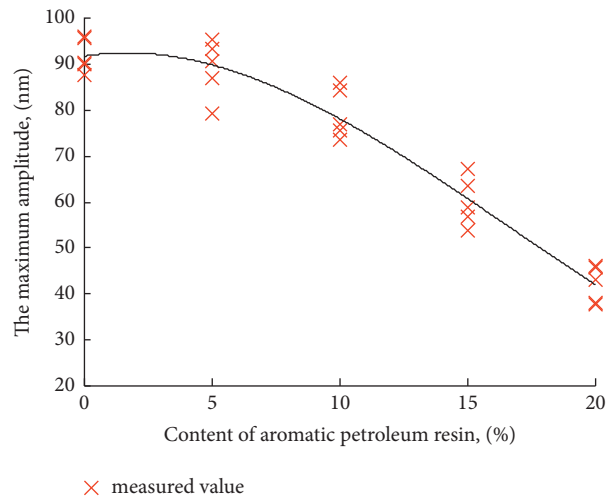

FIGURE 18: The maximum amplitude of SBS modified asphalt with different APR contents.

TABLE 6: Technical performance of SBS modified asphalt with different contents of APR.

APR content, %	Penetration at 25°C, 0.1 mm	48 h softening point difference, °C	Viscosity at 135°C, Pa·S	Softening point, °C	Ductility at 5°C, cm
0	65.4	3.4	1.688	80.6	34.6
5	63.5	2.9	1.721	79.5	36.5
10	62.4	2.2	1.796	79.1	37.7
15	61.9	1.6	1.875	80.3	38.4
20	61.2	1.0	1.901	79.5	40.3

same time, the viscosity at 135°C increased significantly, and the ductility at 5°C, an index characterizing the low-temperature ductility of asphalt, also increased. These phenomena indicate that the addition of APR can improve the viscosity and low-temperature performance of SBS modified asphalt.

It is particularly worth mentioning that the 48 h softening point difference of SBS asphalt has changed significantly with the use of APR. When the content of APR is 20%, the value is only 29% when the amount is 0%. This

phenomenon shows that the high-temperature storage stability of SBS modified asphalt has been greatly improved by the addition of APR.

This phenomenon can be explained by the micro-image of SBS asphalt after development. Figures 19 and 20 show the fluorescence micrographs when the content of APR is 0% and 20%, respectively.

Figures 19 and 20 show that APR can make SBS polymer easier to be sheared during shearing. SBS particles with small particle sizes have a more thorough swelling state after
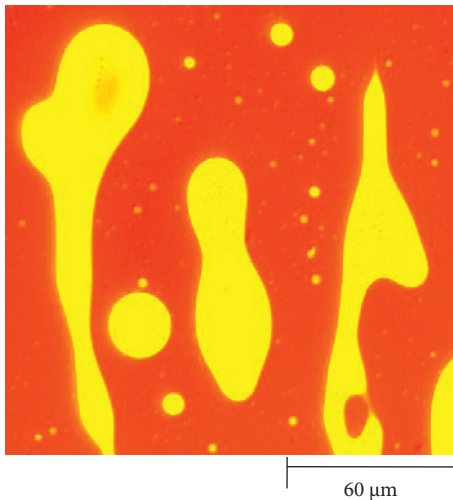
FIGURE 19: Fluorescence microscopic binarization image of complete development of SBS modified asphalt with 0% content of APR.
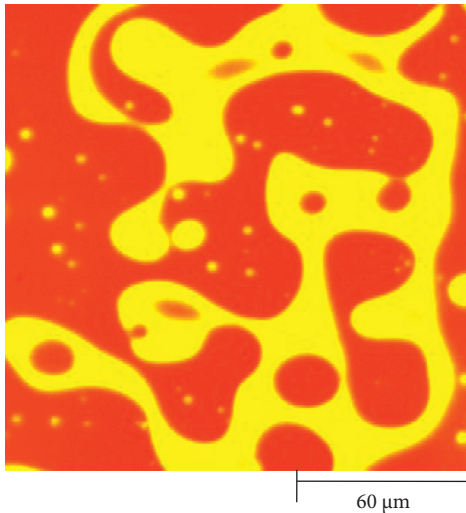

FIGURE 20: Fluorescence microscopic binarization image of complete development of SBS modified asphalt with 20% content of APR.

thorough development, and the network structure formed by the product of vulcanization reaction with sulfur-based stabilizer is denser. This also explains the differences in technical performance in Table 6.

4. Conclusions

In this paper, based on the existing research, the influence of APR on the dispersion of SBS polymer in asphalt was studied with the help of a fluorescence microscope. With the help of the atomic force microscope, the effect of SBS on the nano-surface morphology of SBS modified asphalt was studied. The technical performance of APR/SBS modified asphalt was tested.

Comparing SBS modified asphalt with different contents of APR, it is found that the larger the content, the smaller the

maximum particle size and average particle size of SBS particles. The addition of APR is conducive to the dispersion of SBS into smaller particles in the process of shearing and swelling. AFM test results show that with the increase of the content of APR, the roughness and maximum amplitude of SBS modified asphalt are smaller, indicating that APR also has a significant impact on the nano-morphology of SBS modified asphalt. From the macro-performance test results, APR can improve the viscosity and low-temperature ductility of SBS polymer asphalt to a certain extent and significantly improve the high-temperature storage stability of SBS polymer asphalt.

Data Availability

The data used to support the findings of this study are included within the article.

Conflicts of Interest

The authors declare that they have no conflicts of interest.

Acknowledgments

References

[1] W. Zhang, F. Wang, J. Shi, Z. Li, and X. Liang, "Experimental study on nano-parameters of styrene-butadiene-styrene block copolymer modified bitumen based on atomic force microscopy," *Polymers*, vol. 11, no. 6, p. 989, 2019.

[2] J. Yang, Y. Muhammad, C. Yang et al., "Preparation of TiO2/PS-rGO incorporated SBS modified asphalt with enhanced resistance against ultraviolet aging," *Construction and Building Materials*, vol. 276, Article ID 121461, 2021.

[3] F. B. Bhat and M. M. Mir, "A study investigating the influence of nano Al2O3 on the performance of SBS modified asphalt binder," *Construction and Building Materials*, vol. 271, Article ID 121499, 2021.

[4] L. Li, Z. Li, Y. Wang, X. Li, and B. Li, "Relation between adhesion properties and microscopic characterization of polyphosphoric acid composite SBS modified asphalt binder," *Frontiers in Materials*, vol. 8, Article ID 633439, 2021.

[5] X. Zhang, X. Zhou, L. Chen, F. Lu, and F. Zhang, "Effects of poly-sulfide regenerant on the rejuvenated performance of SBS modified asphalt-binder," *Molecular Simulation*, vol. 47, no. 17, pp. 1423–1432, 2021.

[6] F. Ye, W. Yin, H. Lu, and Y. Dong, "Property improvement of Nano-Montmorillonite/SBS modified asphalt binder by naphthenic oil," *Construction and Building Materials*, vol. 243, Article ID 118200, 2020.

[7] J. H. Ting, E. Khare, A. DeBellis et al., "Role of methylene diphenyl diisocyanate (MDI) additives on SBS-modified asphalt with improved thermal stability and mechanical

performance," *Energy & Fuels*, vol. 35, no. 21, Article ID 17641, 2021.

[8] Z. Chen, D. Zhang, Y. Zhang, H. Zhang, and S. Zhang, "Influence of multi-dimensional nanomaterials composite form on thermal and ultraviolet oxidation aging resistances of SBS modified asphalt," *Construction and Building Materials*, vol. 273, Article ID 122054, 2021.

[9] B. Liu, J. Li, M. Han, Z. Zhang, and X. Jiang, "Properties of polystyrene grafted activated waste rubber powder (PS-ARP) composite SBS modified asphalt," *Construction and Building Materials*, vol. 238, Article ID 117737, 2020.

[10] C. Qian and W. Fan, "Evaluation and characterization of properties of crumb rubber/SBS modified asphalt," *Materials Chemistry and Physics*, vol. 253, Article ID 123319, 2020.

[11] J. Xu, J. Pei, J. Cai, T. Liu, and Y. Wen, "Performance improvement and aging property of oil/SBS modified asphalt," *Construction and Building Materials*, vol. 300, Article ID 123735, 2021.

[12] X. Zhang, X. Zhou, W. Ji, F. Zhang, and F. Otto, "Characterizing the mechanical properties of Multi-Layered CNTs reinforced SBS modified Asphalt-Binder," *Construction and Building Materials*, vol. 296, Article ID 123658, 2021.

[13] R. Wang, M. Yue, Y. Xiong, and J. Yue, "Experimental study on mechanism, aging, rheology and fatigue performance of carbon nanomaterial/SBS-modified asphalt binders," *Construction and Building Materials*, vol. 268, Article ID 121189, 2021.

[14] X. Zheng, W. Xu, and S. Xie, "Study on ultraviolet aging mechanism of carbon nanotubes/SBS composite-modified asphalt in two-dimensional infrared correlation spectroscopy," *Materials*, vol. 14, no. 19, p. 5672, 2021.

[15] S. Liu, Y. Gao, J. Jin et al., "Synergy effect of nano-organic palygorskite on the properties of star-shaped SBS-modified asphalt," *Polymers*, vol. 13, no. 6, p. 863, 2021.

[16] X. Zheng, W. Xu, H. Feng, and K. Cao, "High and low temperature performance and fatigue properties of silica fume/SBS compound modified asphalt," *Materials*, vol. 13, no. 19, p. 4446, 2020.

[17] N. Amini, H. Latifi, and P. Hayati, "Effects of nano-CuO, MWCNT and SBS on the aging of asphalt binder: FTIR and XRD analyses," *Jordan Journal of Civil Engineering*, vol. 15, pp. 277–291, 2021.

[18] M. Elkashef, M. D. Elwardany, Y. Liang et al., "Effect of using rejuvenators on the chemical, thermal, and rheological properties of asphalt binders," *Energy & Fuels*, vol. 34, no. 2, pp. 2152–2159, 2020.

[19] T. Wang, T. Yi, and Z. Yuzhen, "The compatibility of SBS-modified asphalt," *Petroleum Science and Technology*, vol. 28, no. 7, pp. 764–772, 2010.

[20] Z. Liu, M. Xuan, Z. Zhao, Y. Cong, and K. Liao, "A study of the compatibility between asphalt and SBS," *Petroleum Science and Technology*, vol. 21, no. 7-8, pp. 1317–1325, 2003.

[21] P. Tang, L. Mo, C. Pan, H. Fang, B. Javilla, and M. Riara, "Investigation of rheological properties of light colored synthetic asphalt binders containing different polymer modifiers," *Construction and Building Materials*, vol. 161, pp. 175–185, 2018.

[22] A. V. Morozova and G. I. Volkova, "Effect of the petroleum resin structure on the properties of a petroleum-like system," *Petroleum Chemistry*, vol. 59, no. 10, pp. 1153–1160, 2019.

[23] M. I. L. Abutaqiya, A. A. AlHammadi, C. J. Sisco, and F. M. Vargas, "Aromatic ring index (ari): a characterization factor for nonpolar hydrocarbons from molecular weight and refractive index," *Energy & Fuels*, vol. 35, no. 2, pp. 1113–1119, 2021.

[24] E. Kraus, L. Orf, V. Sitnik et al., "Composition and surface energy characteristics of new petroleum resins," *Polymer Engineering & Science*, vol. 57, no. 9, pp. 1028–1032, 2017.

[25] M. Mousavi, T. Abdollahi, F. Pahlavan, and E. H. Fini, "The influence of asphaltene-resin molecular interactions on the colloidal stability of crude oil," *Fuel*, vol. 183, pp. 262–271, 2016.

[26] M. Lashkarbolooki and S. Ayatollahi, "Effects of asphaltene, resin and crude oil type on the interfacial tension of crude oil/brine solution," *Fuel*, vol. 223, pp. 261–267, 2018.

[27] I. A. Sizova, D. I. Panyukova, and A. L. Maksimov, "Hydrotreating of high-aromatic waste of coke and by-product processes in the presence of in situ synthesized sulfide nanocatalysts," *Petroleum Chemistry*, vol. 57, no. 14, pp. 1304–1309, 2017.

[28] E. Kraus, L. Orf, I. Starostina, A. Efimova, R. Perelygina, and O. Stoyanov, "Composite materials based on polyolefins with new petroleum resins," *Polymer Engineering & Science*, vol. 58, no. 12, pp. 2288–2292, 2018.

[29] A. A. Grin'ko, R. S. Min, T. A. Sagachenko, and A. K. Golovko, "Aromatic sulfur-containing structural units of resins and asphaltenes in heavy hydrocarbon feedstock," *Petroleum Chemistry*, vol. 52, no. 4, pp. 221–227, 2012.

[30] I. N. Frolov, T. N. Yusupova, M. A. Ziganshin, E. S. Okhotnikova, and A. A. Firsin, "Interpretation of thermal effects in differential scanning calorimetry study of asphalts," *Petroleum Chemistry*, vol. 58, no. 8, pp. 593–598, 2018.

[31] W. Zhang, L. Qiu, J. Liu et al., "Modification mechanism of C9 petroleum resin and its influence on SBS modified asphalt," *Construction and Building Materials*, vol. 306, Article ID 124740, 2021.

[32] X. Nie, Z. Li, H. Yao, T. Hou, X. Zhou, and C. Li, "Waste bio-oil as a compatibilizer for high content SBS modified asphalt," *Petroleum Science and Technology*, vol. 38, no. 4, pp. 316–322, 2020.

[33] W. Zhang, L. Zou, Z. Jia, F. Wang, Y. Li, and P. Shi, "Effect of thermo-oxidative ageing on nano-morphology of bitumen," *Applied Sciences*, vol. 9, no. 15, p. 3027, 2019.

[34] T. Su, T. Wang, C. Wang, and H. Yi, "The influence of salt-frost cycles on the bond behavior distribution between rebar and recycled coarse aggregate concrete," *Journal of Building Engineering*, vol. 45, Article ID 103568, 2022.

[35] Ž. Jelčić, V. O. Bulatović, K. J. Marković, and V. Rek, "Multi-fractal morphology of un-aged and aged SBS polymer-modified bitumen," *Plastics, Rubber and Composites*, vol. 46, no. 2, pp. 77–98, 2017.